VNIVERSITAT DE VALÈNCIA

IFIC
INSTITUT DE FÍSICA CORPUSCULAR

# Effective theory approaches to heavy meson resonances based on non-perturbative low energy two-meson dynamics

**Pedro Fernández Soler**
Tesis doctoral, julio 2019
Programa de Doctorat en Física

Directores:

Miguel Albaladejo Serrano, Juan M. Nieves Pamplona
y Eulogio Oset Báguena

**Dr. Miguel Albaladejo Serrano**, Investigador Científico de Thomas Jefferson National Accelerator Facility,
**Dr. Juan Miguel Nieves Pamplona**, Investigador Científico del Consejo Superior de Investigaciones Científicas, y
**Dr. Eulogio Oset Báguena**, Catedrático de Física Teórica de la Universidad de Valencia,

> CERTIFICAN: Que la presente memoria *Effective theory approaches to heavy meson resonances based on non-perturbative low energy two-meson dynamics* ha sido realizada bajo su dirección en el Departamento de Física Teórica de la Universidad de Valencia por D. Pedro Fernández Soler como Tesis para obtener el grado de Doctor en Física.

Y para que así conste, en cumplimiento con la legislación vigente, presentan ante el Departamento de Física Teórica, la referida memoria, firmando el presente certificado.

Valencia, a 20 de junio de 2019.

Miguel Albaladejo Serrano    Juan Miguel Nieves Pamplona    Eulogio Oset Báguena

# Contents

# AGRADECIMIENTOS

Resulta difícil pensar en estos últimos años de mi vida sin recordar a las personas que, ya sea por implicación directa o efecto colateral, irremediablemente forman parte de esta etapa vital que es “el doctorado”. Las eventuales dificultades, desafíos y alegrías de este tiempo influyen en mi relación con muchas de estas personas, haciendo que sienta los límites de lo profesional y lo personal algo difusos. Por este motivo, me gustaría agradecer a quienes me han acompañado durante los últimos años, de los que seguro siempre guardaré un grato recuerdo. Sin duda, si he conseguido llevar a término esta tesis ha sido gracias a su apoyo y ayuda.

En primer lugar, quiero agradecer a mis directores. Sin su guía y experiencia, nada de esto habría sido posible. Juan, Miguel y Eulogio, habéis sido para mi ejemplos de rigor y saber hacer, de honestidad profesional. Agradezco la exigencia y paciencia que habéis tenido conmigo y, sobre todo, el cariño incondicional con el que me habéis tratado desde el primer día. Me siento afortunado de haber contado con vuestro apoyo, atención y comprensión durante estos años, a pesar de las adversidades. Si este trabajo es mejorable, no sería por vuestra falta de empeño, sino por mis limitaciones. No puedo olvidar mencionar a Enrique, pues indudablemente el camino del doctorado lo emprendí en Granada. Si ahora soy consciente de que ignoro muchas cosas, entonces, en aquellos primeros pasos, lo era menos. Gracias por tu paciencia, cercanía y dedicación en mis inicios antes de la tesis, siempre recordaré esa época con afecto.

*I would also like to thank those people with whom I have had the good fortune to collaborate. I would like to thank Zhi-Feng Sun, Melahat Bayar, Feng-Kun Guo, Pablo Ortega, Menglin Du, Christoph Hanhart, Ulf Meißner and Deliang Yao. Specially, I would like to warmly thank Feng-Kun, Philipp Gubler, Makoto Oka and Zhi-Feng for being so kind and welcoming during my stay in China, and for the many interesting discussions.*

A Edu, Javi, Vinicius, Rafa, Asia y Gustavo por las risas, complicidad y apoyo constantes. Ha sido un placer compartir tantas frustraciones, memes y experiencias con vosotros. A Carlos, Francesca y Astrid, por vuestra ayuda y los agradables momentos durante los primeros años. A Miguel Escudero, Arkaitz, Neus y Julián, compañeros con los que ha sido una suerte coincidir, aunque fuese poco tiempo. A Manolo y Luís, por los numerosos consejos, anécdotas y compañía durante la pausa del café. *I could not forget to thank Jorgivan, Uchino and Rafi, for the very funny moments, conversations and discussions.* A Sergi González-Solís, por la ayuda, apoyo y las numerosas conversaciones y discusiones que amenizaron, haciendo más llevaderos, aquellos meses en Pekín. Ha sido muy enriquecedor conoceros y para mi es un regalo haber compartido tan buenos momentos con vosotros.

Por último, quisiera agradecer a aquellos que siempre, no solo durante los últimos años, han demostrado tener en mi una fe y confianza ciegas. A mi familia y amigos, ya sabéis quienes sois, aquellos que no entienden a qué me he estado dedicando exactamente durante estos años. Pero sobre todo a ti, Fer, que me has acompañado en todas las etapas. Gracias por tu amor, paciencia y apoyo continuado e incansable. Tú y Popi habéis sido mi fuente de alegría diaria.

Valencia, 2 de julio de 2019.
Pedro Fernández Soler.

# RESUMEN EN ESPAÑOL

En la actualidad, el Modelo Estándar de Física de partículas es el marco teórico que mejor explica la evidencia disponible sobre procesos mediados por las fuerzas débil, electromagnética y fuerte en la naturaleza. Los fenómenos físicos gobernados por estas tres interacciones fundamentales se describen en términos de un conjunto de partículas elementales y una sofisticada arquitectura basada en simetrías. En el Modelo Estándar, la Cromodinámica Cuántica (QCD) es la teoría cuántica de campos que explica los fenómenos asociados a la fuerza fuerte. Sin embargo, QCD no se puede resolver en general y, desafortunadamente, tan solo es posible utilizarla de modo aproximado, o implementando la teoría en un espacio-tiempo discretizado (LQCD). Debido a sus propiedades, no es posible realizar cálculos perturbativos en el régimen de bajas energías, donde la interacción entre las partículas fundamentales—quarks y gluones—es demasiado intensa. Y precisamente, es este régimen de bajas energías el que es necesario estudiar para entender el espectro hadrónico, es decir, las partículas que existen y sus propiedades (masas, anchuras, espín...). Con frecuencia, la interpretación de los numerosos hadrones o resonancias asociadas con la interacción fuerte se basa en aproximaciones de la teoría subyacente (QCD), como los denominados Modelos de Quarks Constituyentes (CQMs) o las Teorías Efectivas de Campos (EFTs). Mención aparte merece LQCD, que aún contando con la limitación que supone simular hadrones físicos (límite quiral y/o utilizar quarks $c$ y $b$ en el retículo), ha experimentado un considerable avance en los últimos años. No obstante, los resultados de LQCD para describir resonancias todavía presentan errores sistemáticos relacionados, no sólo con el límite del continuo, sino principalmente con la dificultad de describir procesos de dispersión de hadrones. En esta tesis hemos estudiado, desde un punto de vista teórico en el marco de EFTs, la naturaleza y fenomenología asociada a una clase especial de estados mesónicos con contenido de quarks *charm* (quark $c$) y *bottom* (quark $b$). Los hadrones que consideramos en este trabajo podrían identificarse como moléculas mesónicas (en un sentido amplio del término), es decir, sus propiedades y fenomenología se pueden explicar, en gran medida, gracias a la interacción fuerte de otros dos mesones más fundamentales. Además, estos estados que llamaremos exóticos, son difíciles de interpretar en el contexto de CQMs.

Esta tesis se estructura en dos partes. La primera, Capítulos 2 y 3, está dedicada a la presentación del formalismo utilizado en la descripción de la interacción entre mesones. Las simetrías exactas y aproximadas de QCD juegan un papel de especial relevancia en este contexto. En el Capítulo 2 describimos el método utilizado para obtener amplitudes de dispersión consistentes con unitariedad no perturbativa en canales acoplados. También se discute el papel crucial que juegan unitariedad y la estructura analítica de las amplitudes de dispersión con las propiedades de los hadrones exóticos que se estudian en esta tesis. Cabe destacar que tanto los conceptos de molécula hadrónica, como de EFTs, se basan en la existencia de una escala que delimita el régimen de bajas energías. La descripción molecular es apropiada en el contexto de estados mesón-mesón interactuando a energías bajas, en particular, lo suficientemente pequeñas para no resolver longitudes de onda del orden del tamaño de los hadrones involucrados, y otros fenómenos asociados a física de cortas distancias. Las simetrías exactas y aproximadas de QCD en el régimen de bajas energías son muy útiles, ya que guían/determinan la construcción de EFTs. Prestaremos una atención especial a la Simetría Quiral ($\chi$Sym), a la Simetría de Sabor de Quarks

Pesados (HQFS) y a la Simetría de Espín de Quarks Pesados (HQSS). En el Capítulo 3 discutimos de modo general estas simetrías aproximadas de QCD. Describimos cómo pueden emplearse en la construcción de Lagrangianos efectivos para la interacción mesón-mesón a bajas energías. Construimos EFTs que incorporan, por un lado, el octete de pseudo bosones de Nambu-Goldstone $(\pi^0, \pi^\pm, K^0, \bar{K}^0, K^\pm, \eta)$, resultantes de la rotura dinámica de $\chi$Sym, y por otro, los mesones pesados con contenido de quark $c$ y $b$ explícito en términos de multipletes de SU(3) y dobletes de HQSS.

En la segunda parte de esta memoria se detallan los resultados obtenidos. En el Capítulo 4, discutimos las predicciones de una extensión unitaria de la teoría quiral para mesones pesados (HM$\chi$PT). Esta se utiliza para describir la interacción de pseudo-escalares ligeros ($\pi$, $K, \eta$) y mesones pesados, pseudo-escalares y vectoriales, con contenido de un quark *charm* ($D^{(*)}$, $D_s^{(*)}$) y *bottom* ($\bar{B}^{(*)}$, $\bar{B}_s^{(*)}$). Unitarizamos las amplitudes de dispersión deducidas de un Lagrangiano quiral de segundo orden, incorporando, además de $\chi$Sym, unitariedad y simetrías de espín y sabor de quarks pesados. Nos referiremos a este esquema como NLO UHM$\chi$PT. Las amplitudes describen la interacción en onda $S$ de estos hadrones, en canales acoplados, para todas las configuraciones de números cuánticos de isospín ($I$) y de extrañeza ($S$) posibles. El momento angular total viene dado por el espín del mesón pesado, $J = 0$ ó $J = 1$, mientras que en todos los casos la paridad de los sistemas es +1. Por tanto, estamos estudiando los sectores $J^P = 0^+$ y $1^+$ con un quark pesado. Los parámetros del modelo se fijaron en un trabajo previo, analizando longitudes de dispersión correspondientes a varios canales y diferentes masas de pión, obtenidas en cálculos de LQCD. En primer lugar estudiamos las predicciones de este formalismo para el sector $(S, I) = (0, 1/2)$. Se trata del sector al que pertenece la resonancia escalar $D_0^*(2400)$, que no fue incluido en el análisis de longitudes de dispersión mencionado. Extendemos nuestro esquema a volúmenes espaciales finitos, y comparamos los niveles de energía obtenidos para diferentes tamaños de la caja con resultados recientes de LQCD. Se consideran los canales más relevantes: $D\pi$, $D\eta$ y $D_s\bar{K}$. Nuestras predicciones son remarcablemente consistentes con los resultados de LQCD, sin ajustar ningún parámetro, lo cual le da gran verosimilitud teórica al resto de predicciones del modelo en otros sectores. Encontramos dos polos en las amplitudes de dispersión con masas ($M$) y anchuras ($\Gamma$), $(M, \Gamma/2) = \left(2105^{+6}_{-8} - i\,102^{+10}_{-12}\right)$ MeV y $\left(2451^{+36}_{-26} - i\,134^{+7}_{-8}\right)$ MeV, que identificamos con dos resonancias escalares. El estado más ligero (pesado) se acopla de forma dominante al canal $D\pi$ ($D_s\bar{K}$). Se trata de un resultado muy interesante, ya que la Colaboración Particle Data Group sólo recoge un estado en el *Review of Particle Physics*, la resonancia $D_0^*(2400)$. La existencia de dos estados escalares ya ha sido sugerida en investigaciones previas, y nuestro trabajo constituye una evidencia a favor de esta interpretación. Además, exploramos el origen de esta estructura de dos polos, y encontramos que es consecuencia directa de la simetría SU(3) de sabor que incorpora la interacción. La estructura de simetría subyacente nos permite dar una interpretación interesante de los mesones escalares con contenido $c\bar{q}$ ($\bar{q} = \bar{u}, \bar{d}, \bar{s}$) más ligeros. En este esquema la resonancia $D_{s0}^*(2317)$ y el estado escalar de masa $\sim 2.1$ GeV, encontrado en el sector de la $D_0^*(2400)$, son miembros del mismo anti-triplete de SU(3). Por último, gracias a HQFS y HQSS, obtenemos que este patrón de dos estados no existe solamente para mesones escalares con contenido *charm*, sino que también con *bottom*, y además en ambos sectores para las resonancias axiales ($J^P = 1^+$).

En los Capítulos 5 y 6 utilizamos de nuevo las amplitudes NLO UHM$\chi$PT. En primer lugar, discutimos cómo este esquema es capaz responder varias cuestiones que surgen en la espectroscopia de dichos estados, *i)* por qué las predicciones de CQMs para los estados escalar y axial son tan diferentes de las masas experimentales de las resonancias $D_{s0}^*(2317)$ y $D_{s1}^*(2460)$; *ii)* por qué el estado escalar con contenido de extrañeza $[c\bar{s}]$, $D_{s0}^*(2317)$, *aparentemente* es más ligero que su compañero sin extrañeza $[c\bar{u},\, c\bar{d}]$, $D_0^*(2400)$; *iii)* por qué la diferencia de masas de los estados $D_{s1}^*(2460)$ y $D_{s0}^*(2317)$ es idéntica a la existente entre los mesones $D_{(s)}^*$ y $D_{(s)}$, y tan distinta de las predicciones de modelos de quarks. Los tres interrogantes encuentran respuesta gracias a la interpretación de los estados $c\bar{q}$ escalar y axial como moléculas mesónicas. A continuación, utilizamos las amplitudes de dispersión NLO UHM$\chi$PT en onda $S$ deducidas en el Capítulo 4 para analizar los datos experimentales de LHCb sobre la desintegración $B^- \to D^+\pi^-\pi^-$. Mostramos cómo dichas amplitudes ajustan los resultados experimentales de modo satisfactorio, comparando directamente con los resultados proporcionados por la Colaboración LHCb. Se trata de un resultado relevante, ya que en nuestro caso, la dinámica de canales acoplados y la estructura de dos polos determinan fuertemente el comportamiento de la fase de la amplitud de onda $S$. Esta dependencia en la fase no se distingue claramente en la amplitud experimental, debido a la incertidumbre de los datos y a que la resolución en energía es insuficiente. Una determinación experimental más precisa podría constituir la prueba definitiva para dilucidar la estructura de dos estados predicha por UHM$\chi$PT. Además, proponemos una simulación de QCD en el retículo para confirmar la estructura de dos polos. Tal y como se discutirá en el Capítulo 4, el más ligero de los dos estados es miembro de un antitriplete de SU(3)—compañero de la $D_{s0}^*(2317)$—mientras que el origen de la segunda resonancia, el estado más pesado, se encuentra en una representación irreducible distinta. La predicción de este último hadrón exótico es consecuencia directa de la naturaleza molecular de la interacción y la simetría SU(3) de los mesones constituyentes. Investigando cómo varía la masa de este estado en función de la masa de los quarks ligeros, en el límite de SU(3) y para masas de bosones de Goldstone lo suficientemente grandes, encontramos que se convierte en un estado ligado. Por tanto, este estado, en principio, se podría obtener en una hipotética simulación de LQCD reproduciendo dichas condiciones.

La serie de aplicaciones que involucra las estructuras de dos polos y de SU(3) de las amplitudes NLO UHM$\chi$PT concluye en el Capítulo 6. En esta parte de la tesis estudiamos los factores de forma hadrónicos escalares involucrados en la descripción de las desintegraciones débiles semileptónicas exclusivas $D \to \pi\bar{\ell}\nu_\ell$, $D \to \bar{K}\bar{\ell}\nu_\ell$, $\bar{B} \to \pi\ell\bar{\nu}_\ell$ y $\bar{B}_s \to K\ell\bar{\nu}_\ell$. Abordamos el problema empleando un formalismo dispersivo en canales acoplados, basado en la representación de Muskhelishvili-Omnès (MO), que incorpora las amplitudes NLO UHM$\chi$PT como punto de partida. Estas amplitudes contienen la estructura de dos estados y el patrón SU(3) de sabor mencionados anteriormente. Analizamos la influencia en los factores de forma de las resonancias escalares, con quarks $b$ y $c$, encontradas en el Capítulo 4. Los factores de forma escalares juegan un papel potencialmente relevante en la medida experimental de los elementos de la matriz de Cabbibo-Kobayashi-Maskawa (CKM), que a su vez, son una de las múltiples formas disponibles en la actualidad para explorar la validez y posibles extensiones del Modelo Estándar. Aunque los factores de forma escalares no sean tan importantes como los vectoriales, sí que tienen un impacto indirecto en la determinación de los elementos de la matriz de CKM, porque ambos factores de forma tienen que ser iguales a $q^2 = 0$ (con $q^\mu$ el momento transferido entre el mesón pesado y el ligero). Estas funciones no se pueden calcular mediante QCD perturbativa, por lo que actualmente la mejor fuente de información se obtiene de simulaciones de QCD en el retículo y reglas de suma en el cono de luz (LCSR). Ninguno de estos métodos puede usarse en el rango completo de $q^2$ permitido en la desintegración. En nuestro estudio, empleamos la información disponible sobre los factores de forma escalares para determinar los parámetros libres de la representación dispersiva de MO. Mostramos cómo es posible describir con precisión los resultados existentes de LQCD y LCSR sobre los factores de forma escalares de las desintegraciones semileptónicas $D \to \pi\bar{\ell}\nu_\ell$, $D \to \bar{K}\bar{\ell}\nu_\ell$, $\bar{B} \to \pi\ell\bar{\nu}_\ell$ y $\bar{B}_s \to K\ell\bar{\nu}_\ell$. Además, predecimos la dependencia de $q^2$ de los factores de forma escalares en todo el rango cinemático, incluyendo algunas transiciones que no se habían estudiado antes, y que calculamos aquí por primera vez: $D \to \eta\bar{\ell}\nu_\ell$, $D_s \to K\bar{\ell}\nu_\ell$, $D_s \to \eta\bar{\ell}\nu_\ell$ y $\bar{B} \to \eta\ell\bar{\nu}_\ell$. Para finalizar, determinamos los elementos de la matriz CKM $|V_{cd}| = 0.244 \pm 0.022$, $|V_{cs}| = 0.945 \pm 0.041$ y $|V_{ub}| = (4.3 \pm 0.7) \times 10^{-3}$ involucrados en las desintegraciones analizadas. Además, proporcionamos el valor de los factores de forma vectoriales a $q^2 = 0$: $|f_+^{D\to\eta}(0)| = 0.01 \pm 0.05$, $|f_+^{D_s\to K}(0)| = 0.50 \pm 0.08$, $|f_+^{D_s\to\eta}(0)| = 0.73 \pm 0.03$ y $|f_+^{\bar{B}\to\eta}(0)| = 0.82 \pm 0.08$, que pueden usarse como alternativa en un futuro para determinar los elementos de la matriz CKM, cuando estén disponibles las correspondientes distribuciones diferenciales de desintegración.

En el Capítulo 7, proponemos una nueva parametrización para los factores de forma hadrónicos en la desintegración semileptónica $\bar{B} \to D\ell\bar{\nu}_\ell$, basándonos también en una representación dispersiva de tipo MO. Considerando de forma combinada tanto las medidas experimentales de la anchura diferencial de desintegración, como los resultados de LQCD, determinamos de forma precisa el elemento de la matriz CKM $|V_{cb}| = 41.01(75) \times 10^{-3}$ y el cociente $\mathcal{R}_D = \mathcal{BR}(\bar{B} \to D\tau\bar{\nu}_\tau)/\ \mathcal{BR}(\bar{B} \to D\ell\bar{\nu}_\ell) = 0.301(5)$. Los coeficientes de esta nueva parametrización los denominamos momentos de fase, debido a que involucran la integral de la fase de los factores de forma a modo de reglas de suma. Estos momentos de fase contienen información valiosa acerca de la interacción $\bar{B}\bar{D}$ en onda $S$ y $P$, de la cual se tiene muy poca información actualmente. Encontramos evidencia en favor de la existencia de, al menos, un estado ligado y uno virtual generados por la interacción $\bar{B}\bar{D}$ en onda $S$, sujetos a incertidumbres debidas a la influencia de posibles efectos inelásticos potencialmente importantes. Este esquema podría ser aplicado también a cualquier otra desintegración semileptónica que involucre la transición $b \to c$.

En el Capítulo 8, prestamos una atención especial al papel de la interacción, entre estados obtenidos en modelos quark y grados de libertad mesón-mesón, en la dinámica de las resonancias $D_{s0}^*(2317)$ y $D_{s1}^*(2460)$. Consideramos un potencial efectivo mesón-mesón efectivo en onda $S$, generado a partir del intercambio de componentes $c\bar{s}$ de espín-paridad $J^P = 0^+$ y $1^+$ obtenidas en CQM. La interacción entre los bosones de Goldstone y los mesones $D$ y $D^*$ se obtiene del orden más bajo de HM$\chi$PT. La interacción resultante es unitarizada en canales acoplados y es consistente con HQFS y HQSS. Empleamos la información (niveles de energía) disponible de LQCD sobre las resonancias $D_{s0}^*(2317)$ y $D_{s1}^*(2460)$ para fijar el acoplamiento entre grados de libertad quark-antiquark y mesón-mesón. Estudiamos en detalle la importancia de los estados CQM en la generación dinámica y estructura de estas resonancias. Los resultados revelan que, de acuerdo con diversos análisis anteriores, la naturaleza de estos hadrones es dominantemente molecular ($\sim$ 60-70%). Por otro lado, comparamos las predicciones del formalismo NLO UHM$\chi$PT utilizado en los Capítulos 4, 5 y 6, con los resultados de QCD en el retículo. Resulta que ambos formalismos, el nuevo incorporando el intercambio de grados de libertad $c\bar{s}$ a las amplitudes obtenidas en HM$\chi$PT a nivel árbol, y el discutido previamente a segundo orden—únicamente en términos de mesones $D_{(s)}^{(*)}$ y mesones de Goldstone—, son equivalentes en el régimen de bajas energías y los dos reproducen razonablemente los resultados de LQCD. Concluimos que los dos esquemas contienen la misma dinámica gracias al ajuste de las constantes de baja energía fenomenológicas, dando lugar a descripciones similares de los estados $D_{s0}^*(2317)$ y $D_{s1}^*(2460)$. Sin embargo, la inclusión de los estados de CQM se manifiesta a energías mayores, que quedan fuera del rango de aplicabilidad de las amplitudes efectivas.

En el Capítulo 9, generalizamos estas ideas al sector del quark $b$. Estudiamos el efecto del intercambio de estados CQM $b\bar{s}$ en la interacción $\bar{B}^{(*)}K$ y ajustamos los niveles de energía disponibles, obtenidos en en simulaciones de QCD en el retículo, sobre los compañeros de las resonancias $D_{s0}^*(2317)$ y $D_{s1}^*(2460)$ en el sector *bottom*. Estos mesones exóticos, denominados $\bar{B}_{s0}^*$ y $\bar{B}_{s1}^*$, no han sido descubiertos experimentalmente todavía. Encontramos evidencia de un estado ligado escalar $\bar{B}K$ y otro axial $\bar{B}^{(*)}K$ con masas $5709 \pm 8$ MeV y $5755 \pm 8$ MeV, respectivamente. Nuestras predicciones para la masa de estas resonancias son muy similares a las obtenidas en el análisis del trabajo de LQCD, y en contraste con la situación del Capítulo 8, encontramos una componente molecular ligeramente menor ($\sim 50\%$) que para el caso de los estados $D_{s0}^*(2317)$ y $D_{s1}^*(2460)$.

Consideramos de nuevo el escalar $D_{s0}^*(2317)$ en el Capítulo 10. En este capítulo proponemos la desintegración $B_c \to J/\psi D^+ K^0$, con el objetivo de investigar la naturaleza de la resonancia $D_{s0}^*(2317)$ por medio de la interacción de estados finales del par $D^+K^0$.[1] En particular, gracias a la interacción fuerte de este par de mesones, que describimos con amplitudes de dispersión basadas en UHM$\chi$PT a primer orden, se incorpora la resonancia $D_{s0}^*(2317)$ como un estado ligado. Su efecto en la distribución de eventos, como función de la masa invariante del par $D^+K^0$, presenta un exceso característico en la región de energías cercana al umbral de producción del par de mesones. Es un resultado relevante, ya que se trata de un comportamiento muy distinto al que cabría esperar a partir del espacio fásico en ese mismo rango de energía. Por otro lado, también calculamos la anchura de desintegración $B_c \to J/\psi D_{s0}^*(2317)$, lo que nos permite construir un nuevo observable independiente de normalización y asociado directamente con la naturaleza molecular de la resonancia $D_{s0}^*(2317)$.

Continuamos con el Capítulo 11, donde estudiamos el estado exótico $Z_c(3900)$. Exploramos las predicciones en volúmenes finitos de un modelo para la interacción en onda $S$ de los canales $J/\psi\pi$ y $D\bar{D}^*$. Este modelo se desarrolló en un trabajo anterior, y se empleó con éxito para estudiar la información experimental disponible en su momento acerca del estado $Z_c(3900)$. Dos escenarios resultaron compatibles con los datos de la Colaboración BESIII. En uno de ellos, el $Z_c(3900)$ se identificaba con una resonancia, y en el otro, con un estado virtual. Con el objetivo de descartar una u otra interpretación, en este capítulo analizamos la información disponible sobre esta resonancia en LQCD. Así comparamos los niveles de energía que se obtienen en cada uno de los escenarios anteriores, con los resultados existentes de QCD en el retículo, obtenidos para un único volumen. Encontramos que la información de la simulación no es suficiente para favorecer ninguna de las dos interpretaciones. Discutimos cómo información adicional de niveles de energía para volúmenes distintos podría ser determinante para resolver la situación, ya que ambos escenarios dan lugar niveles de energía con dependencias de volumen sustancialmente diferentes.

En el Capítulo 12 estudiamos la interacción en onda $S$ de los estados $B$, $B^*$ y los mesones vectoriales $\rho$ y $\omega$, para las configuraciones de espín total $J = 0$, 1 y 2. En este estudio exploratorio, empleamos el formalismo de *Local Hidden Gauge* (LHG), basado en

---

[1] En el momento en que se realizó este estudio, esta desintegración no se había medido todavía.

una extensión de la teoría quiral de perturbaciones para incluir los mesones vectoriales. Investigamos cómo las amplitudes de dispersión son consistentes con HQSS, encontrando que la interacción LHG al orden más bajo satisface dicha simetría, salvo por contribuciones pequeñas, con origen en términos de contacto y provenientes del intercambio de mesones pesados. A continuación, exploramos el contenido espectroscópico de las amplitudes, teniendo en cuenta la contribución proveniente de la anchura del mesón $\rho$, así como de diagramas tipo caja construidos a partir de vértices con intercambio de un pión. Predecimos un conjunto de cuatro resonancias con paridad positiva y contenido de quark $b$, generadas por la dinámica mesón-mesón $B^{(*)}\rho$ en onda $S$: dos estados vector-axial y dos resonancias adicionales con $J^P = 0^+$ y $2^+$. Fijamos las constantes de renormalización de la teoría ajustando la masa y anchura del estado de espín 2 a los valores experimentales de la resonancia $B_2^*(5747)$. El resto de estados son, por tanto, predicciones. Encontramos un acuerdo razonable entre las propiedades de una de las resonancias predichas para $J = 1$, generada por la interacción $\rho B$, y los valores nominales de la resonancia $B_1(5721)$. El análisis de la estructura HQSS de la interacción nos conduce a una posible interpretación de las resonancias $B_1(5721)$ y $B_2^*(5747)$ como componentes, en cierta aproximación, del mismo doblete $\mathcal{L}^\pi$ de HQSS, donde $\mathcal{L}^\pi$ son los números cuánticos de espín-paridad de los grados de libertad ligeros.

Por último, en el Capítulo 13 recopilamos las conclusiones más importantes de esta memoria.

Los contenidos de esta tesis se basan en los artículos de investigación publicados en las Refs. [1–9] durante el desarrollo de la misma.

# ABSTRACT

The Standard Model (SM) of Particle Physics is currently established as the theory which better encodes our knowledge regarding the weak, electromagnetic and strong elementary forces of nature. It provides a description of these interactions based on an ensemble of fundamental degrees of freedom and a sophisticated apparatus of symmetries. Quantum Chromodynamics (QCD) governs the phenomena associated to the strong interactions, although its properties make extremely difficult its direct application in some circumstances: in the regime of low energies, where the interaction of the fundamental degrees of freedom—the quarks and gluons—is so strong that forbids any perturbative calculation. In particular, the diverse and rich experimentally observed spectrum of hadrons since the beginning of the 20th century up to the present days, belongs to this nonperturbative regime of QCD. The way to understand from QCD the masses, widths and some other properties of hadrons is nowadays based on approximations to the underlying theory. Among the most successful examples, we will consider in this work Constituent Quark Model (CQM), Effective Field Theory (EFT) approaches and Lattice Quantum Chromodynamics (LQCD). This dissertation provides a theoretical effective description of a special class of hadronic meson states with charm and bottom quark content and their associated phenomenology. The considered states are difficult to be accomodated in CQMs and are candidates to be interpreted as meson molecules. This relies on the assumption that their main properties can be described by means of an effective low energy interaction of two more fundamental mesons. In this picture, the physical interpretation of the exotic hadron states considered in the forthcoming chapters could be envisioned as originated by the interaction between other—more fundamental but nevertheless composite—objects.

This thesis is structured in two parts. In the first part, containing Chapters 2 and 3, we present the theoretical formalism used to describe the interaction of the meson degrees of freedom. In Chapter 2, we introduce a nonperturbative construction of $S$-wave scattering amplitudes consistent with exact two-body unitarity in coupled channels. The roles of unitarity and of the analytic structure of the scattering amplitudes, and their relations with the appearance of resonances are also discussed. These amplitudes should be understood to be valid at low energies, since they are effective descriptions of the dynamics of the relevant degrees of freedom. We stress that the molecular picture, and in general the concept of EFT, relies on the assumption of a separation of energy regimes regulated by a scale $\Lambda$. It is adequate when the energy is sufficiently low to prevent the resolution of wavelengths $\lambda \sim h/\Lambda$, typically smaller than the hadron sizes, associated with short-distance physics. Besides, we establish a link between the nonperturbative amplitudes and the low energy dynamical information of the mesonic degrees of freedom. On the other hand, the low energy symmetries of the underlying theory, QCD, provide very useful constraints on the amplitudes. We will pay special attention to Chiral Symmetry ($\chi$Sym), Heavy Quark Flavour Symmetry (HQFS) and Heavy Quark Spin Symmetry (HQSS). In Chapter 3 we provide a general overview of these approximate symmetries of QCD, and how they can be used to construct the low energy meson-meson interactions by means of effective Lagrangians. The latter incorporate, on the one hand, the light-pseudoscalar degrees of freedom $(\pi^0, \pi^\pm, K^0, \bar{K}^0, K^\pm, \eta)$ as the octet of pseudo Nambu-Goldstone bosons, resulting from the breaking of $\chi$Sym and, on the other hand, the heavy-light mesons as SU(3) multiplets and HQSS doublets. We finish Part I constructing the

effective Lagrangians that will be used later in the subsequent chapters.

The research studies are presented in Part II. We shall begin with Chapter 4, where we investigate the predictions of the Next-to-Leading Order (NLO) Unitary Heavy Meson Chiral Perturbation Theory (UHM$\chi$PT) scheme. The amplitudes, which describe the $S$-wave coupled-channel scattering in all the possible strangeness-isospin $(S, I)$ sectors, were determined in a previous work using LQCD information on the pion mass dependence of several scattering lengths. Our purpose is to test the predictions for $(S, I) = (0, 1/2)$ quantum numbers. This is the sector of the open-charm scalar resonance $D_0^*(2400)$, which was not considered in the set of aforementioned LQCD scattering lengths. We compare the energy levels obtained for different finite volumes with the first LQCD results on this sector involving all the relevant two-meson channels: $D\pi$, $D\eta$ and $D_s\bar{K}$. We find that our predictions turn out to be remarkably consistent with the LQCD results, even though there are no free parameters in our scheme. This agreement supports the numerous additional predictions of the model in other sectors, which thereafter are also presented. Interestingly, we find out evidence for two scalar states—instead of the currently accepted single $D_0^*(2400)$—associated to a two-pole structure of the amplitude. The two poles are located at $\left(2105^{+6}_{-8} - i\,102^{+10}_{-12}\right)$ MeV and $\left(2451^{+36}_{-26} - i\,134^{+7}_{-8}\right)$ MeV, with the largest couplings to the $D\pi$ and $D_s\bar{K}$ channels, respectively. This pattern of two states was already suggested in previous studies, and our work provides a strong support to that scenario. Besides, we also unravel the origin of the two-pole structure: it is rooted in the SU(3) symmetry encoded in the interaction, inherited from the use of amplitudes consistent with $\chi$Sym. It allows us to interpret the lowest-lying scalar open charm mesons as SU(3) partners, conforming a triplet. Finally, exploiting HQSS and HQFS we conclude that this pattern is not only reproduced in the scalar bottom sector, but also for axial open charm and bottom resonances.

In Chapters 5 and 6, we further explore the consequences of the NLO UHM$\chi$PT scheme. In Chapter 5, we pay attention to two aspects that might serve as a further test of the validity of the approach to describe open charm and bottom scalar and axial resonances. We demonstrate how the two-meson coupled-channels EFT scheme incorporating $\chi$Sym, HQSS, HQFS and two-body unitarity constraints provides successful answers to several puzzles arising in the spectroscopy of heavy-light mesons. It simultaneously explains *i*) why the CQM expectations for the charm-strange scalar and axial states were so different from the experimental masses of the $D_{s0}^*(2317)$ and $D_{s1}(2460)$; *ii*) why the scalar charm-strange resonance $D_{s0}^*(2317)$ seemed to be lighter than the non-strange partner, $D_0^*(2400)$; and finally, *iii*) why the experimental mass splitting between the $D_{s0}^*(2317)$ and $D_{s1}(2460)$ states is so different from that found in CQM approaches, most importantly, why it is almost identical to the splitting of the lowest-lying $D_{(s)}$ and $D_{(s)}^*$ mesons. The answers are all based on a meson-meson molecular interpretation of the scalar and axial resonances. Lately, we further test the validity of the amplitudes by using them to analyze the experimental data on the angular moments of the $B^- \to D^+\pi^-\pi^-$ decay, measured by the LHCb collaboration. We find out that the NLO UHM$\chi$PT $S$-wave amplitudes successfully reproduce the experimental results reported by the LHCb collaboration. Furthermore, we directly compare our $S$-wave decay amplitude with that obtained by LHCb from a best fit to data and find out a remarkable agreement between both amplitudes. Interestingly, in our case, the two-meson coupled-channel dynamics and the two-pole structure are strongly reflected in the phase-behaviour. However, this behaviour cannot be disentangled from the experimental amplitude, because of the lack of energy resolution and the limited available statistics. A finer experimental determination might constitute a definitive test of the two-pole structure predicted by the UHM$\chi$PT approach. Additionally, we propose a LQCD simulation to further unveil certain aspects related to the realization of the two-pole structure. The lighter scalar state of the two poles, as it is discussed in Chapter 4, is associated with a member of the SU(3) triplet—it would be a partner of the $D_{s0}^*(2317)$—while the origin of the higher one is rooted on a different SU(3) component of the interaction. We show that, from the light-quark mass dependence of the pole position for large enough Goldstone masses in the SU(3) limit, the higher resonance pole evolves into a bound state, and consequently, it might be found on a lattice simulation reproducing such conditions.

The series of applications involving the two-pole and SU(3) structures of the NLO UHM$\chi$PT amplitudes concludes in Chapter 6. There, we study scalar hadronic form factors which enter in the description of weak semileptonic exclusive decays of bottom and charm heavy-light mesons into a Goldstone boson, both in the strange and nonstrange sectors, $D \to \pi\bar{\ell}\nu_\ell$, $D \to \bar{K}\bar{\ell}\nu_\ell$, $\bar{B} \to \pi\ell\bar{\nu}_\ell$ and $\bar{B}_s \to K\ell\bar{\nu}_\ell$. It is accomplished by means of a coupled-channel dispersive approach that incorporates the NLO UHM$\chi$PT amplitudes as input, carrying the "two-pole" structure and SU(3) information of scalar open-charm and bottom resonances discussed in Chapter 4. One of the reasons that makes the study of the open-charm and bottom scalar states important can be traced to their influence on the shape of the scalar hadronic form factors, that describe the mentioned weak decays. The role of the QCD form factors in weak decays is essential to extract the values of the Cabibbo–Kobayashi–Makawa (CKM) matrix elements, and, as it is well-known, the determination of the CKM parameters is currently part of the plethora of available validity tests of the SM and its possible extensions. Although in practice, in many cases, the role of the scalar form factors may not be as important as that of vector form factors, in others the situation might be different because of their indirect impact on the values of the latter ones at $q^2 = 0$ (with $q^\mu$ the transferred momentum between the heavy and light mesons). Currently, there exist information on these scalar form factors from LQCD and light-cone sum rules (LCSR) computations, since these quantities cannot be obtained using pertubative QCD. None of these approaches can be used in the whole $q^2$ range accessed in the decay. In our study, we use the available information on scalar form factors to constrain our Muskhelishvili–Omnès (MO) dispersive approach, finding out that we are able to simultaneously describe fairly well LQCD and LCSR results on weak semileptonic exclusive transitions $D \to \pi\bar{\ell}\nu_\ell$, $D \to \bar{K}\bar{\ell}\nu_\ell$, $\bar{B} \to \pi\ell\bar{\nu}_\ell$ y $\bar{B} \to K\ell\bar{\nu}_\ell$. Furthermore, we predict the scalar form factors in all the kinematic range, including some transitions which have not been studied yet, and that are determined here for the first time, namely, $D \to \eta\bar{\ell}\nu_\ell$, $D_s \to K\bar{\ell}\nu_\ell$, $D_s \to \eta\bar{\ell}\nu_\ell$ and $\bar{B} \to \eta\ell\bar{\nu}_\ell$. Finally, we extract the values $|V_{cd}| = 0.244 \pm 0.022$, $|V_{cs}| = 0.945 \pm 0.041$ and $|V_{ub}| = (4.3 \pm 0.7) \times 10^{-3}$ for the involved CKM matrix elements. Additionally, we provide the following vector form factors at $q^2 = 0$: $|f_+^{D\to\eta}(0)| = 0.01 \pm 0.05$, $|f_+^{D_s\to K}(0)| = 0.50 \pm 0.08$, $|f_+^{D_s\to\eta}(0)| = 0.73 \pm 0.03$ and $|f_+^{\bar{B}\to\eta}(0)| = 0.82 \pm 0.08$, which might constitute alternatives to determine the CKM elements when experimental measurements of the corresponding differential decay rates become available.

In Chapter 7, a new model-independent parametrization is proposed for the hadronic form factors in the semi-leptonic $\bar{B} \to D\ell\bar{\nu}_\ell$ decay. By a combined consideration of the recent experimental and LQCD data, we determine precisely the CKM matrix element $|V_{cb}| = 41.01(75) \times 10^{-3}$ and the ratio $\mathcal{R}_D = \frac{\mathcal{BR}(\bar{B}\to D\tau\bar{\nu}_\tau)}{\mathcal{BR}(\bar{B}\to D\ell\bar{\nu}_\ell)} = 0.301(5)$. The coefficients in this parametrization, related to phase shifts by sumrule-like dispersion relations and hence called phase moments, encode important scattering information of the $\bar{B}\bar{D}$ interactions which are poorly known so far. Thus, we find strong hints about the existence of at least one bound and one virtual $\bar{B}\bar{D}$ $S$-wave $0^+$ states, subject to uncertainties produced by potentially sizeable inelastic effects. This formalism is also applicable for any other semileptonic processes induced by the weak $b \to c$ transition.

In Chapter 8, we pay special attention to the interplay between CQM and meson-meson degrees of freedom in the description of the $D_{s0}^*(2317)$ and its HQSS partner $D_{s1}(2460)$ resonances. We consider an effective two-meson interaction allowing the exchange of genuine scalar and axial-vector CQM components, in a formalism consistent again with unitarity, $\chi$Sym, HQSS and HQFS. We will use the most recent LQCD information on the charm-strange scalar and axial resonances to constrain the effective approach, and to study the influence of the CQM degrees of freedom in the dynamical generation and compositeness of the $D_{s0}^*(2317)$ and $D_{s1}(2460)$ resonances. Our findings are very much in line with previous analyses, pointing out to a dominant ($\sim$ 60-70%) molecular nature for both states. We further compare the predictions obtained using the NLO UHM$\chi$PT finite volume amplitudes—employed in Chapters 4, 5 and 6—with the LQCD results. It turns out that both approaches, the new one incorporating CQM states into the two-meson dynamics, and the previously discussed one—solely in terms of heavy-light meson and Goldstone degrees of freedom—are equivalent at low energies, and are able to describe the available LQCD data. We conclude that, in both cases, the low energy dynamics is properly encoded in the phenomenological low energy constants, leading to similar descriptions of the physical systems. Nevertheless, the influence of the inclusion of CQM states shows up at higher energies, which due to the effective nature of both approaches, might not be reliable in either case.

Chapter 9 is the extension of the discussion of Chapter 8 to the bottom sector. We use the same formalism to analyze the LQCD information on the bottom partners of the $D_{s0}^*(2317)$ and $D_{s1}(2460)$, which have not been experimentally found yet. We successfully describe the LQCD energy levels and make predictions for the mass of the bottom-strange scalar and axial resonances, showing-up as two-meson bound states with masses of $5709 \pm 8$ MeV and $5755 \pm 8$ MeV, respectively. Our predictions for these exotic hadrons turn out to be in good agreement with those reported in the LQCD works. In contrast with the situation in Chapter 8, we find slightly smaller molecular contributions ($\sim$ 50%) in the compositeness structure of the bottom-strange HQSS doublet.

In Chapter 10, we propose the weak decay of a $B_c$ meson into $J/\psi K^0 D^+$ in order to learn about the nature of the $D_{s0}^*(2317)$ resonance from the $K^0 D^+$ final state interaction. By the time the work was performed, this decay mode had not been measured. In particular, due to the strong interaction of the $K^0 D^+$ final states, which we compute in the framework of Leading Order (LO) UHM$\chi$PT amplitudes, the $D_{s0}^*(2317)$ turns out to be generated as a bound state. We find out that it would strongly influence the line shape of the $K^0 D^+$ invariant mass distribution of events in the proposed decay, in the low energy region close to the $K^0 D^+$ threshold. We further compute the width for the coalescence production of the $D_{s0}^*(2317)$ in the final state, which allows us to construct a ratio in terms of the invariant mass distribution and the aforementioned width. This ratio can be used to make predictions of a new normalization independent observable directly associated with the molecular nature of the $D_{s0}^*(2317)$.

We continue with Chapter 11, where we study the charmonium charged exotic state,

$Z_c(3900)$. We explore the predictions for finite volumes of a previously determined $S$-wave $D^*\bar{D}$ and $J/\psi\pi$ coupled-channel interaction, consistent with HQSS. This scheme is able to describe the experimental information available concerning the $Z_c(3900)$ resonance, where two scenarios were found compatible with the BESIII data, namely: the $Z_c(3900)$ as a narrow resonance or as a virtual state. For that reason, on this chapter we compare the volume dependence of the energy levels obtained in both scenarios with the single-volume LQCD results of the same system. We find out that the lattice information is not enough to favour any of the two interpretations. However, we conclude that energy levels coming from one or more additional lattice volumes could be essential in order to resolve the situation, since for certain sizes both scenarios show different volume dependence.

In Chapter 12 we explore the open-bottom meson sector by studying the $S$-wave interaction of $B$ and $B^*$ mesons with $\rho$ and $\omega$ mesons for all possible spins: $J = 0, 1, 2$. In this exploratory study, we adopt the Local Hidden Gauge (LHG) formalism. It is based on an extension of Chiral Perturbation Theory ($\chi$PT) extension to include vector mesons as gauge bosons of a hidden local SU(3) symmetry. We investigate whether this formalism is consistent with HQSS, and conclude that the leading LHG interaction satisfies HQSS. However, we identify small breaking contributions which come from the exchange of heavy vector mesons and the contact terms. These breaking terms are not problematic since they are consistently small, given that they are originated from subleading HQSS pieces. We construct unitary scattering vector-vector and vector-pseudoscalar amplitudes based on low energy LHG input potentials, and explore their spectroscopic content. We further take into account the effects due to the width of the $\rho$ meson, as well as the box-diagrams contribution incorporating one pion exchange vertices. In this way, we are able to predict a set of four open-bottom resonances with positive parity, generated by the dynamics of two-meson $S$-wave $B^{(*)}\rho$ interaction: Two axial-vector states and two additional resonances with spins $J = 0$ and 2. We fix the free parameters of the theory by matching the mass and width of the $J = 2$ state to the average values corresponding to the $B_2^*(5747)$. Thus, the rest of states are predictions of the scheme. We find an interesting agreement between one of our predicted $J = 1$ states, generated by the $\rho B$ interaction, and the nominal values of the $B_1(5721)$ resonance. Thanks to the analysis of the HQSS structure of the interaction we can provide a possible interpretation of these two narrow resonances, since in this formalism, they are originated in great measure by the same interaction and they could be identified as the members of a $J^P = (1^+, 2^+)$ HQSS doublet.

Finally, in Chapter 13 we summarize the main results obtained in this thesis.

The contents of this work are based on the research papers of Refs. [1–9] performed during the development of this thesis.

# Chapter 1

# Introduction

## 1.1 Motivation and scope

The contents of this manuscript constitute a varied set of studies which share many similarities. From all, the most important is that the studies are devoted to the theoretical description of low energy scattering of two-meson systems. The physical situations explored are motivated by the presence, either confirmed or hypothetical, of one or several meson resonances with exotic properties. From that perspective, the present research could be placed in the broad field of the old problem of hadron spectroscopy. The path that has led to the establishment of the SM as the paradigm of particle physics, and QCD as the fundamental theory of the strong interactions, has been guided, to a large degree, by the efforts on understanding the spectroscopy of the strong interactions.

The low energy regime of the strong interactions is populated by a rich variety of unstable particles, which number has steadily grown up boosted by the experimental efforts of many research groups. Since the beginning of the 21st century, the advent of powerful experimental facilities has motivated a renewed attention to the QCD spectrum of states at scales of the order of the charm and bottom mass; these scales would correspond to resonance masses of the order of 2 and 5 GeV, respectively. The interplay between theory and experiment has crystallized in a picture where the symmetries play a central role for classifying the different states according to internal degrees of freedom or quantum numbers.

Nowadays, a combined effort between LQCD simulations and experiment is boosting the exploration of this area of knowledge. Among all the theoretical approaches to the low energy QCD spectrum of hadrons, one of the most relevant and historically celebrated ones are the CQMs. Any technical and detailed description of these schemes is beyond the scope of this thesis, nevertheless we shall briefly refer to them for illustrative purposes.

The QCD bound states are supposed to manifest as colorless objects, leading to mesons, baryons, glueballs or multiquark states among many other possibilities. Even though any of these systems is extremely difficult to be described by the fundamental theory, CQMs aim to derive their properties in terms of an *effective* interaction of the constituents quarks [10–12]. The Gell-Mann eightfold way [10] is one of the most famous attempts towards understanding the spectrum of low energy mesons and baryons by using symmetry arguments. Up to 2003, they had succeeded in describing the spectrum of meson and baryons, with a few exceptions like the case of the $\Lambda(1405)$ and the Roper baryon resonances [13, 14].

We particularize now the discussion to the systems studied in this dissertation, focusing on the situation of the “open heavy flavour” or “heavy-light” mesons: boson states which contain a heavy charm or bottom valence quark. They were described as combinations of quark–anti-quark pairs, and interestingly, in Ref. [11] Godfrey and Isgur proposed, in their relativistic quark model, the existence of excited states with different quantum numbers, both in the open charm and bottom sectors. Years later, in 2003, the charm-strange scalar[1] ($J^P = 0^+$) and axial-vector ($1^+$) isoscalar mesons,

$$\begin{aligned} D_{s0}^*(2317) &\sim \left|J^P = 0^+;\, I = 0;\, S = 1\right\rangle \\ D_{s1}(2460) &\sim \left|J^P = 1^+;\, I = 0;\, S = 1\right\rangle \end{aligned} \tag{1.1}$$

were discovered [15, 16], and identified with the lowest-lying $P$-wave quark-model excitations of the $S$-wave states $D_s$ and $D_s^*$—where the latter have $J^P = 0^-$ and $1^-$ quantum numbers, and masses 1968 and 2112 MeV, respectively. These $P$-wave mesons were found to have very small widths, decaying into channels with unexpected isospin and explicit strangeness, due to their low masses. The discovery of these exotic resonances challenged the CQM predictions, since they showed properties at odds with the quark model expectations: their experimental masses were found around 100 MeV below the expected values, and they were strikingly narrow. Additionally, such states were found slightly below the energy thresholds for the production of $DK$ and $D^*K$. The latter meson pairs, when coupled to zero orbital angular momentum—in a $S$-wave configuration—have the same quantum numbers as the $D_{s0}^*$ and $D_{s1}$ states,

$$\begin{aligned} \left|DK\,(I = 0, L = 0)\right\rangle &= \left|J^P = 0^+; I = 0; S = 1\right\rangle \\ \left|D^*K\,(I = 0, L = 0)\right\rangle &= \left|J^P = 1^+; I = 0; S = 1\right\rangle . \end{aligned} \tag{1.2}$$

As a consequence of the proximity of the $D^{(*)}K$ threshold energies to the scalar and axial resonances, the hypothesis of the "molecular nature" of these states quickly raised. A hadronic molecule is a composite state made out of two weakly bound hadrons, $DK$ and $D^*K$ pairs in the case of the $D_s^*$ states. On the other hand, from a formal point of view, any reference to the nature of a state would be linked to the structure of its wave function. This may be problematic, since the wave function is not an observable. However, at least in the case of bound states with *small* binding energies, one could identify the imprints of their existence on low energy observables involving the scattering constituents, such as the scattering length. This is the case of the paradigmatic deuteron, in which its properties are explained in terms of the nucleonic degrees of freedom—even though they are ultimately determined by QCD.

Here comes a very important concept: how to quantify up to what values it can be assumed that the binding energy is small. This is at the core of not only the low energy description of QCD, but of any Effective Theory. To address such question, we need to introduce a scale in the problem, necessary to identify the relevant degrees of freedom (the mesons in the case of a molecule) as well as the high and low energy regimes. We shall refer as small binding energies $B$ those which satisfy $|\vec{k}| << \Lambda$, where the wave number $|\vec{k}| \approx \sqrt{2\mu B}$ would be the off-shell center of mass momentum of the constituent mesons inside the molecule ($\mu$ is their reduced mass), and $\Lambda$ is the mentioned scale. In a hadronic molecule, the latter should be small enough to make some bound state properties insensitive to the details of the interaction at short distances. In this way, the constituent hadrons would be the relevant degrees of freedom. One could think that the scale $\Lambda$ should be related to the smallest resolution needed to resolve the system, a typical hadron scale of the order of $\sim 0.5 - 1$ fm, determined by the size of the involved hadrons. This is to

---

[1] In the following we use the isospin $I$, total spin $J$, parity $P$ and strangeness $S$ quantum numbers to identify the different sectors.

say

$$\Lambda = \frac{h}{\lambda} \approx 1 - 2 \text{ GeV} \tag{1.3}$$

although, we shall consider the conservative value of $\Lambda \approx 1$ GeV. In the cases of the deuteron or the $D^*_{s0}$ and $D_{s1}$, it turns out that the wave numbers are approximately 36, 198 and 193 MeV. Clearly, the latter two cases are not as good as the first one, but $|\vec{k}| << \Lambda$ is definitely not a bad approximation. This would point out that a low energy description of the $D^*_{s0}/D_{s1}$ states in terms of the $DK/D^*K$ meson-pairs should be sufficiently accurate to capture essential features of these resonances. Therefore, the picture of the $D^*_{s0}(2317)$ as a bound state—$DK$ molecule—would qualitatively be interpreted using the following schematic superposition

$$\begin{aligned}|D^*_{s0}\rangle = {} & \alpha_1 \left|DK\,(I=0, L=0)\right\rangle + \alpha_2 \left|c\bar{s}\left({}^{2S+1}L_J = {}^3P_0\right)\right\rangle \\ & + \alpha_3 \left|D_s\eta\,(L=0)\right\rangle + \alpha_4 \left|D^*K^*\,(I=0, L=0)\right\rangle + \dots\end{aligned} \tag{1.4}$$

if $|\alpha_1|$ is significantly larger than the rest of $|\alpha_j|$ $(j \neq 1)$. Throughout this work, we will study exotic states (resonances) which are candidates to fit into a hadronic molecule description, motivated by the closeness of their masses to the energy thresholds for the production of $S$-wave two meson systems—with the same quantum numbers. We will extend these ideas not only to bound state candidates, but also to wide resonances, although the picture of a molecule gets more complicated, and there is not a straightforward interpretation of the associated quantum mechanical structure. Nevertheless, even if different approaches are able to provide a satisfactory description of some properties of a given state, they might differ in other predictions. In this way, the molecular scenarios can accommodate resonances with exotic quantum numbers, and relate different exotic states by means of the symmetry properties of the interaction between the constituent hadrons. Some of these results might not be easy to accommodate within CQM schemes.

In general, whenever the scattering observables could be influenced by the existence of resonances, we shall need an appropriate description of the amplitude accounting for the final state interaction of the mesonic degrees of freedom. That is the case in all the physical situations discussed in the following chapters. We will use in our analyses phenomenological information from both experiment and LQCD results. Thus, for instance, we will consider the volume dependence of lattice hadron eigenenergies, experimental event distributions or experimental masses and widths. On the other hand, we shall also speculatively explore, from a theoretical point of view, some situations in which the meson dynamics may lead to interesting predictions for unmeasured observables.

Before moving into the theoretical formalism, let us first take a quick overview of the heavy meson systems studied in this work.

## 1.2 Some exotic heavy mesons

Here, we will introduce some theoretical aspects and experimental evidences about different exotic mesons, this is to say, states that cannot be easily accommodated within CQMs, that will be studied in this thesis.

### 1.2.1 Heavy light mesons

In this sector, we will study some even parity resonances which may be organized in terms of their associated valence $Q\bar{q}$ structure. The presence of the heavy charm (or bottom) quark implies the validity, up to $\Lambda_{\rm QCD}/m_Q$ corrections, of HQSS [17–21], with $m_Q$ the heavy quark mass, and $\Lambda_{\rm QCD} \approx 250$ MeV a typical scale related to the dynamics of the light degrees of freedom. Thus, in a good approximation, the spin of the heavy quark $s_Q$ is decoupled from the total angular momentum of the light degrees of freedom $j_{\bar{q}}$, and hence they are separately conserved. This gives rise to the arrangement of the heavy-light mesons in doublets, classified by the total angular momentum and parity, $j_{\bar{q}}^P$, of their light degrees of freedom content, and with total spin $J = j_{\bar{q}} \pm 1/2$ and parity $P$. For the $P$-wave $Q\bar{q}$ mesons, the expected HQSS doublets are,[2] on the one hand, $j_{\bar{q}}^P = 1/2^+$ with $J^P = 0^+, 1^+$ mesons, and, on the other hand, $j_{\bar{q}}^P = 3/2^+$ with $J^P = 1^+, 2^+$ mesons. Furthermore, according to their light flavour content the heavy-light $P$-wave doublets will be classified into strangeness $S$ and isospin $I$ combinations, $(S, I)$. Finally, all this structure can be put in correspondence in both the charm and bottom sectors by means of HQFS, so that the HQSS doublets existing in each $(S, I)$ configuration in the charm sector will have the analogue partners in the bottom one. In Table 1.1, we show possible experimental candidates for the different $j_{\bar{q}}^P$ HQSS doublets in all sectors, together with the average values for the masses and widths taken from the Review of Particle Physics (RPP) [14]. From all the configurations, we shall pay attention to the lowest lying even-parity doublets, those corresponding to the $j_{\bar{q}}^P = 1/2^+$ configuration of the light degrees of freedom.

- **The $j_{\bar{q}}^P = 1/2^+$ doublet in the $(S, I) = (1, 0)$ sector**

**Charm sector.** About ten years before the discovery of the positive parity $D_{s0}^*(2317)$ and $D_{s1}(2460)$ resonances, two positive parity $J^P = 1^+$ and $J^P = 2^+$ charmed-strange resonances, $D_{s1}(2536)$ and $D_{s2}^*(2573)$, had already been reported and confirmed by the ARGUS and CLEO collaborations [22–24]. These narrow states have almost degenerate masses and might be identified with the $j_{\bar{q}}^P = 3/2^+$ doublet. The current average values quoted in the RPP [14] are $(M, \Gamma) = (2535.10 \pm 0.06, 0.92 \pm 0.05)$ MeV and $(2569.1 \pm 0.8, 16.9 \pm 0.8)$ MeV for the $1^+$ and $2^+$, respectively. These values were consistent with the results of CQMs [11, 25, 26] for this HQSS doublet. On the other hand, these CQMs made predictions for the members of the $j_{\bar{q}}^P = 1/2^+$ HQSS doublet. Thus, the $0^+$ and $1^+$ mesons of this multiplet were expected to be almost degenerated and quite broad, decaying into $D^{(*)}K$ through $S$-wave, and separated by around 80 MeV. However, neither of these properties are consistent with the observed $D_{s0}^*(2317)$ and $D_{s1}(2460)$ states [15, 16]. They are very narrow, located below the $D^{(*)}K$ thresholds, and have a mass splitting of the order of $\sim m_\pi$, see Fig. 1.1.

This triggered an intense debate on the nature of those resonances, leading to a wide variety of interpretations among which we highlight their assignment to $c\bar{s}$ states [27–29] and two-meson or four-quark systems [30–44].

There is another essential tool to explore the low energy hadron spectrum of QCD,

---

[2] The parity of the light degrees of freedom in this case is +, that corresponds to an odd parity $\bar{q}$ antiquark orbiting in $P$ wave around the heavy quark $Q$, while the total angular momentum of the light degrees of freedom is determined by the sum of the spin 1/2 of the $\bar{q}$ antiquark and its orbital angular momentum ($L = 1$).

**Table 1.1:** Quantum number configurations leading to HQSS meson doublets. Within CQM approaches, their valence content will be $Q\bar{q}$, with $\bar{q} = \bar{u}/\bar{d}$ or $\bar{s}$ for $(S, I) = (0, 1/2)$ or $(1, 0)$ sectors, respectively. We also give the isospin average mass and width ($M$ and $\Gamma$) of possible experimental candidates, in units of MeV, taken from the RPP [14]. Below, $\vec{L}$ is the orbital angular momentum, $\vec{j}_{\bar{q}}$ labels the angular momentum of the light degrees of freedom and $\vec{J} = \vec{j}_{\bar{q}} + \vec{S}_Q$ is the total spin of the quark-antiquark system, with $\vec{S}_Q$ the spin of the heavy quark. The parity of the $Q\bar{q}$ state is given by $P = (-1)^{L+1}$.

| $L$ | $j_{\bar{q}}^P$ | $J^P$ | $c\bar{q}$ | $(M, \Gamma)$ | $b\bar{q}$ | $(M, \Gamma)$ |
|---|---|---|---|---|---|---|
| 0 | $\frac{1}{2}^-$ | $0^-$ | $D$ | $(1867.24 \pm 0.04, [11.19 \pm 0.04] \cdot 10^{-10})$ | $\bar{B}$ | $(5279.48 \pm 0.10, [4.174 \pm 0.008] \cdot 10^{-10})$ |
| | | $1^-$ | $D^*$ | $(2008.55 \pm 0.04, < 1.09)$ | $\bar{B}^*$ | $(5324.65 \pm 0.25, ?)$ |
| 1 | $\frac{1}{2}^+$ | $0^+$ | $D_0^*$ | $(2335 \pm 15, 248 \pm 22)$ | $\bar{B}_0^*$ | $(?)$ |
| | | $1^+$ | $D_1$ | $(2427 \pm 36, 384^{+130}_{-105})$ | $\bar{B}_1$ | $(?)$ |
| | $\frac{3}{2}^+$ | $1^+$ | $D_1^*$ | $(2422.0 \pm 1.2, 28.4 \pm 3.3)$ | $\bar{B}_1^*$ | $(5726.0 \pm 1.5, 29 \pm 3)$ |
| | | $2^+$ | $D_2^*$ | $(2463.1 \pm 0.7, 47.1 \pm 0.8)$ | $\bar{B}_2^*$ | $(5738.4 \pm 0.5, 22 \pm 3)$ |
| | | | $c\bar{s}$ | | $b\bar{s}$ | |
| 0 | $\frac{1}{2}^-$ | $0^-$ | $D_s$ | $(1968.34 \pm 0.07, [13.1 \pm 0.1] \cdot 10^{-10})$ | $\bar{B}_s$ | $(5366.89 \pm 0.19, [4.36 \pm 0.01] \cdot 10^{-10})$ |
| | | $1^-$ | $D_s^*$ | $(2112.2 \pm 0.4, < 1.9)$ | $\bar{B}_s^*$ | $(5415.4^{+1.8}_{-1.5}, ?)$ |
| 1 | $\frac{1}{2}^+$ | $0^+$ | $D_{s0}^*$ | $(2317.7 \pm 0.6, < 3.8)$ | $\bar{B}_{s0}^*$ | $(?)$ |
| | | $1^+$ | $D_{s1}$ | $(2459.5 \pm 0.6, < 3.5)$ | $\bar{B}_{s1}$ | $(?)$ |
| | $\frac{3}{2}^+$ | $1^+$ | $D_{s1}^*$ | $(2535.10 \pm 0.06, 0.92 \pm 0.05)$ | $\bar{B}_{s1}^*$ | $(5828.63 \pm 0.27, 0.5 \pm 0.4)$ |
| | | $2^+$ | $D_{s2}^*$ | $(2569.1 \pm 0.8, 16.9 \pm 0.8)$ | $\bar{B}_{s2}^*$ | $(5839.85 \pm 0.17, 1.47 \pm 0.33)$ |

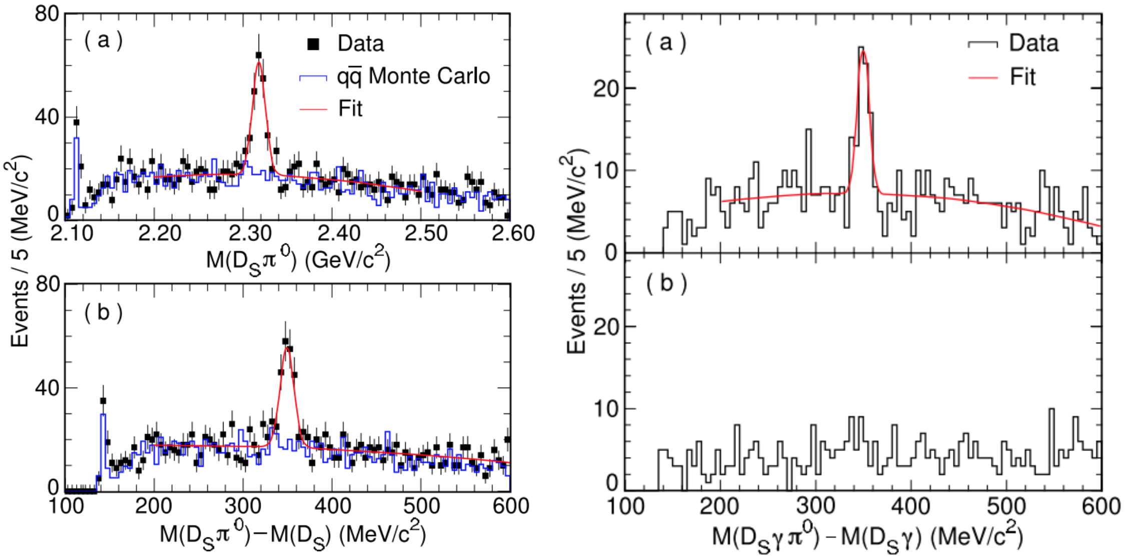

**Figure 1.1:** Peaks associated to the experimental measurement of the $D^*_{s0}$ (left) and $D_{s1}$ (right) in their isospin violating decay modes $D_s\pi$ and $D^*_s\pi$, respectively. Figures are taken from Ref. [16] .

which is the information obtained from LQCD. The latest LQCD simulations [45–47] have achieved a good description of these charmed-strange resonances when $D^{(*)}K$ interpolators are included in the set of used operators. Notably, the mass of the $D^*_{s0}(2317)$ was found to be overestimated if the $DK$ interpolators were omitted, which gives further support to the idea of a necessary interplay between CQM configurations and nearby $D^{(*)}K$ thresholds.

We will extensively refer to these exotic states in the forthcoming pages, specifically, they will be discussed in Chapters 4, 5, 6, 8, and 10.

**Bottom sector.** As we have already mentioned, in the heavy quark limit the dynamics of systems containing a single heavy quark becomes also independent of the flavour of the heavy quark (see for instance [21]). Hence the bottom-strange sector is expected to present a pattern similar to that of the charm-strange one described above, in particular there should exist bottom partners of the $D^*_{s0}(2317)$ and $D_{s1}(2460)$ resonances. Furthermore, since the $b$ quark is heavier than the $c$ quark, the $\mathcal{O}(1/m_Q)$ corrections are expected to be smaller, and thus the HQSS relations should be more accurate. In these circumstances, the $b\bar{s}$ $j^P_{\bar{q}} = 1/2^+$ doublet is a good scenario to discuss the interplay between CQM states and meson-meson channels with thresholds located close to the former. Studying the bottom sector is thus relevant to unveil the nature of the $D^*_{s0}(2317)$ and $D_{s1}(2460)$, and elucidate the role played by this interplay in the dynamics of these states in both heavy flavour sectors.

Unfortunately, unlike the $c\bar{s}$ spectrum, the lowest-lying positive parity $b\bar{s}$ states have not been fully discovered. While experimental searches have successfully observed narrow candidates for the $j^P_{\bar{q}} = 3/2^+$ doublet $\bar{B}_{s1}(5830)$ and $\bar{B}^*_{s2}(5840)$ [48, 49], the lower mass $j^P_{\bar{q}} = 1/2^+$ doublet states still wait to be observed. Note that the dynamics of the $j^P_{\bar{q}} = 3/2^+$ doublet is not entirely governed by $\chi$Sym, since the $\bar{B}^{(*)}K^*$ channel, involving the light vector meson $K^*$, should be considered. On the other hand, this situation may have some resemblances to the existing one back in 2003, when the $D^*_{s0}$ was discovered.

Under this lack of experimental data, many theoretical predictions have been produced within a wide variety of techniques (CQMs [26,50–52], EFT [33,37,42,53–56], and LQCD [57,58]). A special attention deserves the recent LQCD study of the even-parity isoscalar $b\bar{s}$ energy-levels carried out in Ref. [58]. There, clear signatures for the $\bar{B}_{s1}(5830)$ and $\bar{B}^*_{s2}(5840)$ are found above the $\bar{B}^{(*)}K$ thresholds. Below these thresholds, two QCD bound states are identified using a combination of quark-antiquark and $\bar{B}^{(*)}K$ interpolating fields, and assuming that the mixing with $\bar{B}_s^{(*)}\eta$ and the isospin-violating decays $\bar{B}_s^{(*)}\pi$ are negligible. A $J^P = 0^+$ bound state with mass $5.711 \pm 0.023$ GeV is predicted, and with some further assumptions, a $1^+$ state is also found with a mass of $5.750 \pm 0.025$ GeV [58].

We shall consider these states in Chapters 4 and 5, where we will show predictions for the bottom-strange $j_{\bar{q}}^P = 1/2^+$ doublet, while in Chapter 9 we will further discuss the influence of CQM states on the dynamics of these resonances.

- **The $j_{\bar{q}}^P = 1/2^+$ doublet in the $(S, I) = (0, 1/2)$ sector.**

Possible candidates for the members of the $j_{\bar{q}}^P = 1/2^+$ HQSS doublet in the $(S, I) = (0, 1/2)$ sector are denoted as $(D_0^*, D_1)$. While the $D_{s0}^*(2317)$ is very narrow and its mass is well measured [14], the situation for the broad $D_0^*(2400)$ is less clear: the reported mass values for the $D_0^*(2400)^0$ at $B$-factories, $(2308 \pm 36)$ MeV (Belle [59]) and $(2297 \pm 22)$ MeV (*BABAR* [60]), differ from that in $\gamma\, A$ reactions, $(2407 \pm 41)$ MeV (FOCUS [61]), while the LHCb value for the charged partner lies in between [62]. These analyses use Breit–Wigner parametrizations and assume a single scalar particle. See Fig. 1.2 gathering all the experimental results mentioned above. Therein, we can appreciate how the set of measurements seem to be scattered in the area ranging from 2.2 GeV up to the $D\eta$ threshold. Although they coincide for the width, the masses appear distributed in two distinct regions of low (2.3 GeV) and higher masses (2.4 GeV), whereas the LHCb result lies in between. From the experimental results gathered in Fig. 1.2, one might be tempted to suggest the possible existence of two scalar $D_0^*$-like states instead of the single established one. In Chapter 4, we will provide further theoretical arguments supporting this scenario.

Definitely, the situation of the $D_0^*$ state deserves some attention. Additionally, a better understanding of the $D_0^*(2400)$ is important because its properties influence the shape of the scalar form factor $f_0$ in semileptonic $D \to \pi$ decays [40,63], and indirectly it has some impact in the form factor $f_+$ that determines $|V_{cd}|$ [64–68]. The bottom analogue, which is still missing, is even more interesting because of the existing tension between the determinations of $|V_{ub}|$ from inclusive and exclusive $\bar{B}$ decays [69,70], and the implications on the unitarity triangle [71,72] and on new physics limits [73].

Different schemes have described the $j_{\bar{q}}^P = 1/2^+$ doublet members as mostly $c\bar{q}$ states [53,74,75], as mixture of $c\bar{q}$ with meson-meson components [76], as purely tetraquarks [77–79], or as heavy–light meson molecules [33,37,38,40,80] motivated by the closeness of the two-meson thresholds (as suggested by the physics of the $D_{s0}^*(2317)$ and the $DK$ threshold [30,32,34,38,39,44]).

There have also been LQCD simulations in the charmed scalar sector. The first LQCD study of $D\pi$, $D\eta$, and $D_s\bar{K}$ coupled-channel scattering (for $m_\pi \simeq 391$ MeV) was recently reported by the Hadron Spectrum collaboration [81]. Therein, a bound state with a large coupling to $D\pi$ is found and assigned to the $D_0^*(2400)$. These results constitute a very important step towards the understanding of the interaction of charmed mesons and

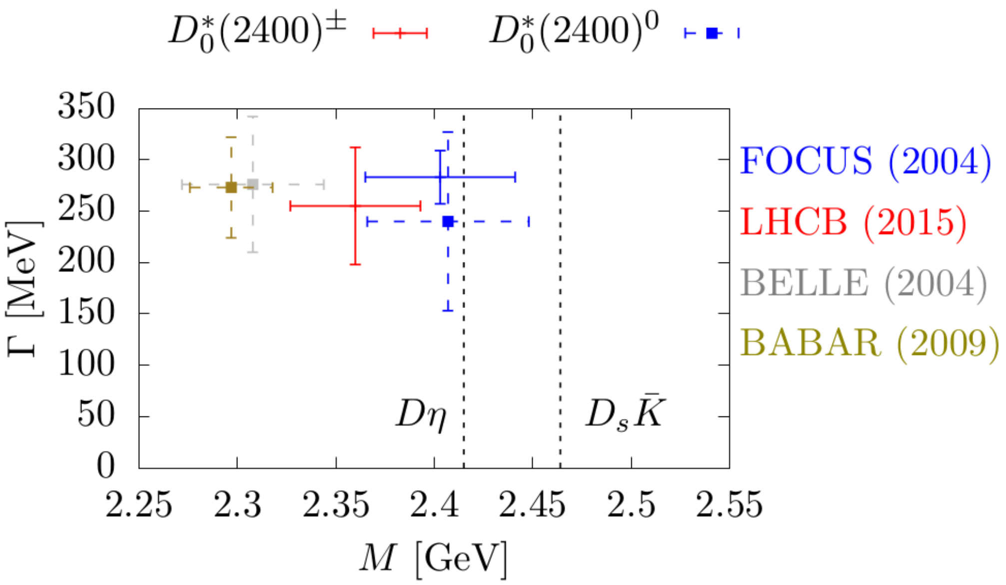

**Figure 1.2:** Experimental mass $M$ and total width Γ of the charged and neutral $D_0^*(2400)$. The values and uncertainties shown are those provided by different experimental facilities [59–62]. The vertical dashed lines show the energies of the nearby $D\eta$ and $D_s\bar{K}$ thresholds, which coupled in $S$-wave and $I = 0$ have the same quantum numbers as $D_0^*(2400)$.

light pseudoscalars. In Chapter 4 we shall pay special attention to these LQCD results, in particular, to the information concerning the volume dependence of the energy levels reported in Ref. [81].

### 1.2.2 The charmonium $Z_c(3900)$ state

In addition to the heavy-light states introduced in the former Sec. 1.2.1, we will also pay attention in Chapter 11 to this exotic state belonging to the charmonium spectrum. Since the discovery of the $X(3872)$ in 2003 [82], the charmonium and charmonium-like spectrum are being continuously enlarged with new so-called $XYZ$ states [83–85], many of which do not fit properly in the conventional quark models (see for instance Ref. [11]). The relevance of meson-meson channels can be grasped from the fact that all the charmonium states predicted below the lowest hidden-charm threshold ($D\bar{D}$) have been experimentally confirmed, but above this energy most of the observed states cannot be unambiguously identified with any of the predicted charmonium $c\bar{c}$ states.

Amongst the $XYZ$ states, the $Z_c(3900)^\pm$ was simultaneously discovered by the BESIII and Belle collaborations [86, 87] in the $e^+e^- \to Y(4260) \to J/\psi\pi^+\pi^-$ reaction, where a clear peak very close to the $D^*\bar{D}$ threshold, around 3.9 GeV, is seen in the $J/\psi\pi$ spectrum. Later on, an analysis [88] based on CLEO-c data for the reaction, $e^+e^- \to \psi(4160) \to J/\psi\pi^+\pi^-$, confirmed the presence of this resonant structure as well, although with a somewhat lower mass. The BESIII collaboration [89, 90] has also reported a resonant-like structure in the $\bar{D}^*D$ spectrum for the reaction $e^+e^- \to \bar{D}^*D\pi$ at different $e^+e^-$ center of mass energies [including the production of $Y(4260)$]. This structure, with quantum numbers favoured to be $J^P = 1^+$, has been cautiously called $Z_c(3885)^\pm$, because its fitted mass and width showed some differences with those attributed to the $Z_c(3900)^\pm$. Whether both sets of observations correspond to the same state needs to be confirmed, though there is a certain consensus that this is indeed the case, and the peaks reported as the $Z_c(3885)^{\pm}$ and $Z_c(3900)^{\pm}$ are originated by the same state seen in different channels. Moreover, evidence for its neutral partner, $Z_c(3900)^0$, has also been reported [88, 91].

The nature of the $Z_c\,(3900)^{\pm}$ is intriguing. On one hand, it couples to $D^*\bar{D}$ and $J/\psi\pi$, and therefore one assumes it should contain a constituent $c\bar{c}$ quark–anti-quark pair. On the other hand, it is charged and hence it must also have another constituent quark–anti-quark pair, namely $u\bar{d}$ (for $Z_c^+$). Its minimal structure would be then $c\bar{c}u\bar{d}$, which automatically qualifies it as a non-$q\bar{q}$ (exotic) meson. Being a candidate for an exotic hidden charm state, it has triggered much theoretical interest. An early discussion of possible structures for the $Z_c\,(3900)^{\pm}$ was given in Ref. [92]. The suggested interpretations cover a wide range: a $\bar{D}^*D$ molecule [93–100], a tetraquark [101–107], an object originated from an attractive $\bar{D}^*D^*$ interaction [108], a simple kinematic effect [109, 110], a cusp enhancement due to a triangle singularity [111], or a radially excited axial meson [112]. In Ref. [113], it was argued that this structure cannot be a kinematical effect and that it must necessarily be originated from a nearby pole. Consequences from some of these models have been discussed in Ref. [114]. The non-compatibility (partial or total) of the properties of the $Z_c$ deduced in different approaches clearly hints why the actual nature of this state has attracted so much attention.

Hopefully, in this chapter we have conveyed a clear message: in the field of heavy meson spectroscopy new experimental information is being continuously added, and it presents many issues not yet fully understood on theoretical grounds. In this regard, in this thesis we try to shed some light into several of these aspects.

# Part I

# Formalism

# Chapter 2

# NON-PERTURBATIVE AMPLITUDES

The present knowledge of the low energy regime of the strong interactions manifests as a quite subtle picture, mixture of fundamental principles and phenomenological information. In the SM, the strong force is explained by the quantum field theory of color interactions, QCD. It is a renormalizable gauge theory in which the quarks are the fundamental building blocks, matter fields interacting *via* the exchange of gauge bosons, the gluons, which also carry the color charge associated to the strong interaction. Among all the features of QCD, there are two aspects that make this theory very special in the regime of low energies, and rely on the research efforts of the hadron community since the beginning of the last century until the present days. These are *confinement* and *asymptotic freedom*.

The confinement phenomenon follows from the fact that neither quarks nor gluons have ever been observed as free states. Its formulation is stated simply by saying that quarks and gluons always combine into color-singlet states. Even if there is no analytic proof of confinement in four space-time dimensions for non-abelian theories, it is undisputedly assumed to be a property of the interaction of quarks and gluons [115]. On the other hand, asymptotic freedom [116–118] is a theoretical consequence stemming from the non-abelian nature of QCD, further verified by experiments, see *e.g*, [14, 119]. It predicts that the strength of the renormalized coupling between quarks and gluons decreases with increasing energy scales. In contrast, the interaction between quarks and gluons becomes more and more intense for decreasing energy scales. Therefore, unfortunately it is not possible to use perturbation theory in the strong coupling constant, $\alpha_s$, to compute observables at a small enough scale. Such scale is commonly referred to as the confinement scale or $\Lambda_{\mathrm{QCD}}$, and could be regarded as a fundamental parameter of QCD, which would replace the dimensionless parameter $\alpha_s$ *via* dimensional transmutation [120]. Formally, it is not clear how to state a precise definition and determine $\Lambda_{\mathrm{QCD}}$. One could identify this scale with that introduced during the integration of the renormalization group equations which describe the running of $\alpha_s(\mu^2)$, in a way that $\alpha_s(\mu^2) \to \infty$ for $\mu \to \Lambda_{\mathrm{QCD}}$. Nevertheless, its value depends on the specific renormalization scheme and the quark flavours considered. Furthermore, since the $\beta$ function entering in the renormalization group equation in practice is computed up to a given order in perturbation theory, the solution for $\alpha_s(\mu^2)$ is not valid for such scales approaching $\Lambda_{\mathrm{QCD}}$. Thus, nowadays the growing of $\alpha_s$ with decreasing scales is a working assumption consistent with confinement.

The two aspects discussed above point to two different regimes of QCD, separated by a scale of the order of $\Lambda_{\mathrm{QCD}}$. Thus, if one intends to apply QCD to processes involving momentum transfers of order $\mathcal{O}(\Lambda_{\mathrm{QCD}})$, just like the case of the low energy scattering of an open-flavour heavy meson off a light pseudo-scalar meson, one necessarily needs to consider alternative methods to perturbation theory, which are generally referred to as non-perturbative approaches. For example, this is the case of LQCD, $\chi$PT and other QCD-inspired EFTs or models like CQM ones. The initial efforts for understanding strong interactions were pursued in the spirit of the program developed by Heisenberg [121, 122] in terms of observable objects. The theory of the scattering matrix [123], or $S$-matrix theory [124], makes emphasis on a *black-box* description of strong interacting processes constrained by the general principles of Lorentz invariance, causality and unitarity as well as quantum symmetries [125]. The knowledge of the interaction is translated to the knowledge of a set of complex functions (scattering amplitudes) depending on the kinematic variables. A further step was taken by Mandelstam in two-body scattering with the maximum analyticity hypothesis, connecting causality with the properties of the scattering amplitudes when promoting the variables $s$, $t$ and $u$ to be complex valued. Though there is no a complete proof of the connection of analyticity and causality in relativistic quantum field theory—it is manifest in non-relativistic scattering for certain types of finite range potentials [126]—this connection is extensively considered as a requirement of any effective theory of the strong interactions. Therefore, according to the Mandelstam conjecture [127] the scattering amplitudes would be analytic functions in the complex $s$, $u$ and $t$ planes up to singularities required by physical features. These singularities can have a kinematic origin, such as the branch cuts, due to unitarity and crossing symmetry, or a dynamical one, like the simple poles associated to bound and resonant states.

**The role of unitarity.** The low energy spectrum of QCD is populated by a rich number of short-lived states decaying into multi-hadron states. We are interested in meson resonances with charm and bottom content, which either are seen, or expected, to decay into two hadron states. On the other hand, these resonant states have a strong influence in the dynamics of the decaying products. In particular, we will pay special attention to some exotic states which nature has not been fully understood by established theoretical CQMs or even in some LQCD computations.

As we shall justify later, and already mentioned above, resonance states are associated with pole singularities in the scattering amplitudes. In our case, we are interested in those which can be classified as dynamically generated [128–137]. This concept may somehow be diffuse for a classification of hadrons. We will be concerned with singularities that can be generated in the scattering amplitudes *via* a unitarization program. This is to say, singularities mainly produced by the unitarization of the hadron loops. This brings us to the concept of unitarity and its relation with resonances.

Unitarity is a constraint on the scattering amplitudes, which has its origin in the conservation of probability. It induces a nonlinear relation between the real and imaginary parts of the scattering amplitude, and it also manifests in the form of bounds on its magnitude. The nonlinear relation implies that this requirement is satisfied only perturbatively in any field theory, in a way that higher orders will always be necessary to fulfil the unitary relation. Furthermore, whenever the interaction is strong, the behaviour of the amplitude may saturate the mentioned unitarity bounds—specially in the case of the presence of resonances—and in such situations unitarity plays an essential role. This is the motivation that triggered the efforts towards exploring approximate ways to restore exact unitarity in perturbative (or kernel) scattering amplitudes. As a few examples, we will quote the Inverse Amplitude Method [138–141], the Numerator Denominator or N/D method [142], and the unitary extension of $\chi$PT [130, 132].

## 2.1 Unitarity and $T$-matrix

In this section, the consequences of unitarity are briefly introduced in the context of the $T$-matrix operator. The formal development of the theory of quantum scattering is devoted to the description of transitions among asymptotically free *incoming* and *outgoing* quantum states, symbolically denoted in the following as $|\mathrm{in}\rangle$ and $|\mathrm{out}\rangle$ respectively. In an operator notation, the observables are computed by means of the transition probability amplitude $\mathrm{S}_{\mathrm{in,out}}$,

$$\mathrm{S}_{\mathrm{in,out}} = \langle \mathrm{out}| \, \mathbf{S} \, |\mathrm{in}\rangle \tag{2.1}$$

where $\mathbf{S}$ is the scattering operator. It embodies all the possible effects on the incoming and outgoing states due to the interaction, which can be made explicit by rewriting it in terms of the transition operator or $T$-matrix $\mathbf{T}$,

$$\mathbf{S} = \mathbb{I} - i\mathbf{T}. \tag{2.2}$$

Unitarity is the necessary requirement for probability conservation [125],

$$\mathbf{S}\mathbf{S}^{\dagger} = \mathbf{S}^{\dagger}\mathbf{S} = \mathbb{I}, \tag{2.3}$$

which follows from a natural constraint: the outcome of any scattering process described by the theory will always be a combination—or superposition—of asymptotic states. For simplicity, let us choose an orthonormal and complete discrete set of asymptotic states $O = \{|\alpha_j\rangle\}_{j=1}^{N}$. The statement above is translated to the equality,

$$\sum_{j=1}^{N} |\langle \alpha_{\mathrm{j}}| \, \mathbf{S} \, |\mathrm{in}\rangle|^2 = 1, \tag{2.4}$$

from where the condition in Eq. (2.3) can be derived, since $|\mathrm{in}\rangle$ is a linear combination of states of $O$. In the language of $T$-matrix, unitarity reads,

$$i\left(\mathbf{T} - \mathbf{T}^{\dagger}\right) = \mathbf{T}\mathbf{T}^{\dagger}, \tag{2.5}$$

or equivalently,

$$i\left(\left(\mathbf{T}^{\dagger}\right)^{-1} - \mathbf{T}^{-1}\right) = \mathbb{I}, \tag{2.6}$$

Let us pay attention to the particular matrix element among the states $|\mathrm{a}\rangle, \ |\mathrm{b}\rangle \in O$. Introducing the notation $\mathrm{T}_{ba} = \langle b| \, \mathbf{T} \, |a\rangle$ Eqs. (2.5) and (2.6) lead to

$$i\left(\mathrm{T}_{ba} - \mathrm{T}^{\dagger}_{ba}\right) = \sum_{j=1}^{N} \mathrm{T}_{b\alpha_j}\mathrm{T}^{\dagger}_{\alpha_j a}, \tag{2.7}$$

$$i\left(\left(\mathrm{T}^{\dagger}\right)^{-1}_{ba} - \left(\mathrm{T}\right)^{-1}_{ba}\right) = \langle b| \left(\sum_{j=1}^{N} |\alpha_j\rangle\langle\alpha_j|\right) |a\rangle . \tag{2.8}$$

.

## 2.2 Unitarity and partial waves

### 2.2.1 $T$-matrix normalization

First of all, we shall state the necessary conventions and definitions in the theoretical description of the scattering of a heavy meson ($H$) off a light meson ($\phi$). Let us identify

$p_1$ and $p_2$ as the four-momenta of the initial heavy and light mesons respectively, while $p_3$ and $p_4$ will denote those of the heavy and light mesons in the final state. For simplicity, we will limit here the discussion to spinless mesons.[1] We denote as $\mathcal{P}_{i(f)} \equiv p_{1(3)} + p_{2(4)}$ the total initial (final) momentum of the system. For the masses, we will use the notation $M_{H_i}$ in the case of the heavy mesons, and $m_{\phi_i}$ for the light ones. We normalize the one-particle momentum and total momentum states as follows,

$$\langle p|p'\rangle = (2\pi)^3\,(2p^0)\delta^3(\vec{p}-\vec{p}\,'), \tag{2.9}$$

$$\langle \mathcal{P}|\mathcal{P}'\rangle = (2\pi)^4\delta^4\left(\mathcal{P}-\mathcal{P}'\right). \tag{2.10}$$

The pair of mesons conform a two-body state

$$|H(p_H)\phi(p_\phi)\rangle \equiv |\mathcal{P}\rangle \otimes |p_H p_\phi\rangle_{\mathcal{P}} \tag{2.11}$$

with definite conserved internal quantum numbers, *e.g.*, isospin $(I)$, parity $(P)$ and other discrete symmetries that determine the sector. In general, there may be different combinations of meson species—referred to as channels—leading to the same quantum numbers of the two-particle state in a given sector. For a total number of channels $n$, we denote the two-body states as $H_j\phi_j$, where $j = 1,\ldots,n$ labels the channel. The scattering process,

$$H_i\left(p_1\right)\phi_i\left(p_2\right) \to H_j\left(p_3\right)\phi_j\left(p_4\right) \tag{2.12}$$

will be described by the amplitude,

$$\mathrm{T}_{ji} = \langle H_j\left(p_3\right)\phi_j\left(p_4\right);\sigma|\,\mathbf{T}\,|H_i\left(p_1\right)\phi_i\left(p_2\right);\sigma\rangle \tag{2.13}$$

where $\sigma$ denotes the quantum numbers that identify the sector. This means that the transition probability amplitude is

$$\mathrm{S}_{ji} = \delta_{ij}(4p_1^0p_2^0)(2\pi)^6\delta^3\left(\vec{p}_1-\vec{p}_3\right)\delta^3\left(\vec{p}_2-\vec{p}_4\right) - \mathrm{i}\mathrm{T}_{ji}. \tag{2.14}$$

It is convenient to make the total momentum conservation $\mathcal{P}$ explicitly manifest rewriting the amplitude (2.13) in terms of the following reduced matrix element

$$\mathrm{T}_{ji} = (2\pi)^4\delta^4\left(\mathcal{P}_j-\mathcal{P}_i\right) \times T^{\sigma}_{ji}(p_1,p_2,p_3,p_4), \tag{2.15}$$

keeping in mind that there should be an extra label $(\mathcal{P} = \mathcal{P}_{i(f)})$ in the amplitude $T^{\sigma}_{ji}$ identifying the total four momentum configuration of the system. The amplitude in Eq. (2.15) is a Lorentz scalar and, therefore, it will only depend on the well-known Mandelstam variables, which are defined in the usual way

$$\begin{aligned} s &\equiv \left(p_1+p_2\right)^2 = \left(p_3+p_4\right)^2, \\ t &\equiv \left(p_1-p_3\right)^2 = \left(p_2-p_4\right)^2, \\ u &\equiv \left(p_1-p_4\right)^2 = \left(p_2-p_3\right)^2 \end{aligned} \tag{2.16}$$

These variables are not independent of each other, and they are related

$$s+t+u = M_1^2 + m_2^2 + M_3^2 + m_4^2 \equiv \Sigma. \tag{2.17}$$

---

[1] Most of the results are extended in the case of particles with spin interacting in $S$-wave, after averaging over third spin components.

Thus, the dependence of the reduced amplitude may be simply stated as $T^{\sigma}_{ji}(s,t)$. Within our conventions, we can write the differential cross section in the center of momentum or zero momentum (cm) frame, *i.e.*, in the frame satisfying $\mathcal{P} = (\sqrt{s}, \vec{0})$, as follows,

$$\left.\frac{\mathrm{d}\sigma_{ji}}{\mathrm{d}\Omega}\right|_{\mathrm{cm}} = \frac{1}{64\pi^2 s}\frac{|\vec{q}\,|}{|\vec{p}\,|}\left|T^{\sigma}_{ji}(s,t)\right|^2 \tag{2.18}$$

where $|\vec{p}\,|$ and $|\vec{q}\,|$ are the magnitude of the incoming and outgoing cm momenta, respectively. Their expressions are compactly written in terms of the Khällén function $\lambda(x,y,z) = x^2 + y^2 + z^2 - 2(xy + yz + zx)$,

$$\begin{aligned} |\vec{p}\,| &= \frac{\sqrt{\lambda(s, M_1^2, m_2^2)}}{2\sqrt{s}}, \\ |\vec{q}\,| &= \frac{\sqrt{\lambda(s, M_3^2, m_4^2)}}{2\sqrt{s}}. \end{aligned} \tag{2.19}$$

In the rest of the chapter, we will omit the sector label "$\sigma$" in $T^{\sigma}_{ji}(s,t)$ and we will simply refer to this function as $T_{ji}(s,t)$.

### 2.2.2 Expansion in partial waves

Let us choose a special coordinate system with the $z$-axis pointing in the direction of the cm relative three-momentum $\vec{p}$ of the initial particles. The dependence on the orientation of the initial and final momenta is encoded in the $t$ variable,

$$t = -\frac{s^2 - s\Sigma + \Delta_i\Delta_j - 4|\vec{p}\,||\vec{q}\,|\; s\cos\theta}{2s}, \tag{2.20}$$

where $\theta$ is the angle formed by $\vec{p}$ and $\vec{q}$ in the cm frame, and we have introduced the shorthand $\Delta_i \equiv M_i^2 - m_i^2$. Thus $T_{ji}(s,t)$ (or equivalently $T_{ji}(s,\theta)$) admits an expansion in powers of $\cos\theta$ [125],

$$T_{ji}(s,\theta) = \sum_{J=0}^{\infty} T^{(J)}_{ji}(s)(2J+1)P_J(\cos\theta). \tag{2.21}$$

This is the so-called partial-wave expansion of $T_{ji}(s,t)$. The $P_J$ functions are the Legendre polynomials, a set of orthogonal polynomials of order $J$, and $T^{(J)}_{ji}(s)$ is called the partial wave amplitude. This expansion is obtained after rewriting the two-particle states in Eq. (2.13) in terms of angular momentum states $|JM\rangle$. Since we consider spinless states, the total angular momentum ($\vec{J}$) and orbital angular momentum ($\vec{L}$) are equal $\vec{L} = \vec{J}$. The partial wave amplitudes may be labelled in terms of the relative orbital quantum number $l$,

$$T^{(l)}_{ji}(s) = \frac{1}{2}\int_{-1}^{+1} \mathrm{d}(\cos\theta)\; T_{ji}(s,\theta)P_l(\cos\theta), \tag{2.22}$$

where the orthogonality property of the Legendre polynomials,

$$\int_{-1}^{+1} \mathrm{d}x P_l(x)P_{l'}(x) = 2\delta_{ll'}/(2l+1), \tag{2.23}$$

has been used.

The constraints that unitarity imposes are specially manifest in the partial wave form of the amplitude. Let us insert the expansion of (2.21) on the left and right-hand sides of Eq. (2.7). For the left-hand side we get,

$$i\left(\mathrm{T}_{ji}-\mathrm{T}_{ji}^{\dagger}\right)=i(2\pi)^4\delta^4(\mathcal{P}_i-\mathcal{P}_f)\sum_{l=0}^{\infty}\left(T_{ji}^{(l)}(s)-T_{ji}^{\dagger(l)}(s)\right)(2l+1)P_l(\cos\theta). \tag{2.24}$$

In the case of the right-hand side of Eq. (2.7), which involves the sum over the matrix elements of all the intermediate transitions, we need to sum over the complete set of $|p_{H_m}p_{\phi_m}\rangle$ states,

$$\mathbb{I}=\sum_{m=1}^{n}\iint_{\mathbb{R}^6}\frac{\mathrm{d}^3\vec{p}}{(2\pi)^3\,2p^0}\frac{\mathrm{d}^3\vec{p}\,'}{(2\pi)^3\,2p^0\,'}\left|p_{H_m}p'_{\phi_m}\right\rangle\left\langle p_{H_m}p'_{\phi_m}\right|, \tag{2.25}$$

to obtain[2]

$$\begin{aligned}\sum_{m=1}^{n}\mathrm{T}_{jm}\mathrm{T}_{mi}^{\dagger}=&\sum_{m=1}^{n}\iint_{\mathbb{R}^6}\frac{\mathrm{d}^3\vec{p}}{2p^0}\frac{\mathrm{d}^3\vec{p}\,'}{2p^0\,'}\frac{1}{(2\pi)^6}\;T_{jm}(s,\theta'')\,T_{mi}^{\dagger}(s,\theta')\\&\times\,(2\pi)^4\delta^4(\mathcal{P}_j-\mathcal{P}_m)\,(2\pi)^4\delta^4(\mathcal{P}_i-\mathcal{P}_m)\end{aligned} \tag{2.26}$$

where $\theta'$ ($\theta''$) is the angle formed by the cm momenta of the intermediate two-meson state $|p_{H_m}p_{\phi_m}\rangle$ and the initial (final) pair. We take the cm momentum of the initial state in the $z$ direction and that of the final pair in the $yz$-plane; with $\theta$ its polar angle (see Fig. 2.1). Defining the well-known Lorentz invariant two-body phase-space operator,

$$\begin{aligned}\iint\mathrm{dLIPS}_m\{\dots\}\equiv&\iint_{\mathbb{R}^6}\frac{\mathrm{d}^3\vec{p}}{2p^0}\frac{\mathrm{d}^3\vec{p}\,'}{2p^0\,'}\frac{1}{(2\pi)^6}\;(2\pi)^4\,\delta^4\left(\mathcal{P}_i-\mathcal{P}_m\right)\{\dots\}\\=&\int_0^{2\pi}\mathrm{d}\phi'\int_{-1}^{1}\mathrm{d}(\cos\theta')\frac{1}{16\pi^2}\frac{|\vec{p}_m|}{\sqrt{s}}\{\dots\},\end{aligned} \tag{2.27}$$

where $\phi'$ is the azimuthal angle of the momentum of the intermediate state. Thus, we find

$$\begin{aligned}\sum_{m=1}^{n}\mathrm{T}_{jm}\mathrm{T}_{mi}^{\dagger}=&(2\pi)^4\,\delta^4\left(\mathcal{P}_i-\mathcal{P}_j\right)\sum_{m=1}^{n}\iint\mathrm{dLIPS}_m T_{jm}(s,\cos\theta'')T_{mi}^{\dagger}(s,\cos\theta')\\=&(2\pi)^4\,\delta^4\left(\mathcal{P}_i-\mathcal{P}_j\right)\sum_{m=1}^{n}\sum_{l,l'=0}^{\infty}(2l+1)\,(2l'+1)\,T_{jm}^{(l')}(s)T_{mi}^{\dagger(l)}(s)\\&\times\iint\mathrm{dLIPS}_m P_l(\cos\theta')P_{l'}(\cos\theta'')\end{aligned} \tag{2.28}$$

Taking into account the addition theorem for spherical harmonics $Y_l^m(\theta,\phi)$ [125, 143],

$$P_{l'}(\cos\theta'')=\frac{4\pi}{2l'+1}\sum_{m'=-l'}^{l'}Y_{l'}^{*\,m'}(\theta,\phi=\frac{\pi}{2})Y_{l'}^{m'}(\theta',\phi') \tag{2.29}$$

---

[2] We truncate the full QCD coupled channel space and we only consider $n$ two meson (one heavy and one light) channels.

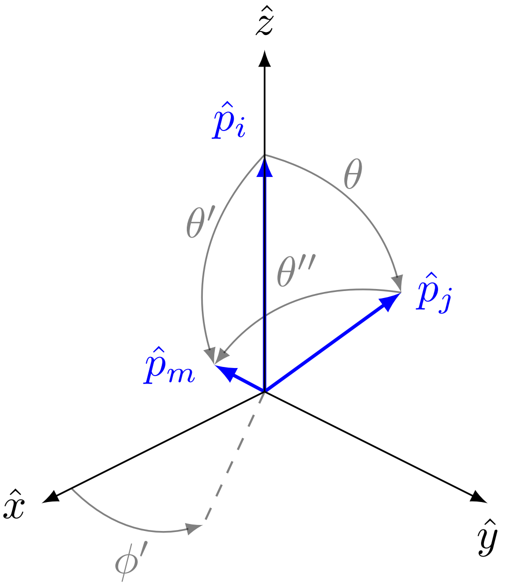

**Figure 2.1:** Definition of the angles $\phi$, $\theta$, $\theta'$ and $\theta''$ formed by the vectors $\vec{p}_{i(j)}$ and $\vec{p}_m$, which correspond to the cm momenta of the initial (final) and intermediate two-particle states entering the partial wave decomposition of $\mathrm{T}_{jm}\mathrm{T}^\dagger_{mi}$, see Eq. (2.26).

with $\cos\theta'' = \sin\theta\sin\theta'\sin\phi' + \cos\theta\cos\theta'$, the angular integrations that are implicit in the $\iint \mathrm{dLIPS}_m$ can be performed [144, 145]

$$\begin{aligned}\int_{-1}^{+1} \mathrm{d}(\cos\theta') P_l(\cos\theta') \int_0^{2\pi} \mathrm{d}\phi' P_{l'}(\cos\theta'') &= \int_{-1}^{+1} \mathrm{d}(\cos\theta') P_l(\cos\theta') \left(2\pi P_{l'}(\cos\theta) P_{l'}(\cos\theta')\right) \\ &= \frac{4\pi}{2l+1}\delta_{ll'} P_l(\cos\theta). \end{aligned} \tag{2.30}$$

With the above result, Eq. (2.28) becomes,

$$\sum_{m=1}^{n} \mathrm{T}_{jm}\mathrm{T}^\dagger_{mi} = (2\pi)^4\,\delta^4\left(\mathcal{P}_i - \mathcal{P}_j\right) \sum_{m=1}^{n} \frac{|\vec{p}_m\,|}{4\pi\,\sqrt{s}} \sum_{l=0}^{\infty} (2l+1)\, P_l(\cos\theta) T^{(l)}_{jm}(s) T^{\dagger(l)}_{mi}(s) \tag{2.31}$$

Finally, we gather the results of Eqs. (2.24) and (2.31) for the left and right hand sides of the unitarity condition of Eq. (2.7) , and we obtain for each partial wave

$$i\left(T^{(l)}_{ji}(s) - T^{\dagger(l)}_{ji}(s)\right) = \sum_{m=1}^{n} \frac{|\vec{p}_m\,|}{4\pi\,\sqrt{s}} T^{(l)}_{jm}(s) T^{\dagger\,(l)}_{mi}(s). \tag{2.32}$$

This equation represents a constraint of the partial wave amplitudes, which should be satisfied for cm energies in a certain range. We can bound such energy regime as

$$\mathbb{L} \equiv [s_0, s_{>2}) \tag{2.33}$$

where $s_0$ denotes the smallest energy threshold—the energy necessary for two-particle production—and $s_{>2}$ denotes the energy threshold for the production of the lowest-lying intermediate state of more than two particles. At energies larger than $s_{>2}$, the relation of Eq. (2.32) should be modified in order to include the effect of intermediate states with three or more particles. However, we will not consider their influence, *i.e.*, assume in the following that $s_{>2} \to \infty$, restricting the discussion exclusively to the case of two-body unitarity in coupled channels.

## 2.3 Analytic properties of partial wave amplitudes

The analytic structure of the functions $T^{(l)}(s)$ plays a very important role relating the scattering observables to the properties of the interaction. The analyticity of the scattering amplitude is well understood under certain conditions, where it turns out to be highly relevant, for example, in the case of the non-relativistic interactions with *reasonable*[3] potentials [146]. Analyticity may be linked to strong consistency conditions, such as causality, giving rise to a dispersive treatment of scattering amplitudes in non-relativistic collisions [126]. Whether this connection—which would promote the analytic properties of scattering amplitudes to the category of physical principles—is valid in the general case of any proper Quantum Field Theory is still an open question. Nevertheless, the assumption of such properties is a rather common working hypothesis, which has proven to be very fruitful in the description of the scattering phenomena.

In this context, the partial wave amplitude $T^{(l)}(s)$ is regarded as a (complex) function defined in the complex $s$-plane: $\mathbb{C}_s$. The main assumption is that the amplitudes will have as few singularities as possible. Any singularity must be required by some physical cause. Hence, there exists an analytic continuation of $T^{(l)}(s)$ onto most of the complex plane $\mathbb{C}_s$, such that the physical values that $T^{(l)}(s)$ takes on the scattering line, $s \in \mathbb{L}$, are the boundary values,

$$T^{(l)}(s) \text{ [physical]} = \lim_{\epsilon \to 0^+} T^{(l)}(s + i\epsilon), \;\; s \in \mathbb{L}, \tag{2.34}$$

In other words, all the physical information is encoded in the singularities of the partial wave amplitude—and all of them are of physical origin. In the following, whenever we write "$i\epsilon$" we will implicitly assume that the limit $\epsilon \to 0^+$ is being taken. It is a key further assumption that the partial wave amplitude is a real function in some segment of the real $s$-axis disjoint from $\mathbb{L}$. When one takes into account the latter property, Hermitian analyticity [147, 148]

$$T^{(l)}_{ji}(s^*) = \left(T^{(l)}_{ji}(s)\right)^\dagger \tag{2.35}$$

allows for an analytic continuation from $s + i\epsilon$ onto the lower half-plane, and we have

$$T^{(l)}_{ji}(s + i\epsilon) - T^{\dagger(l)}_{ji}(s + i\epsilon) = T^{(l)}_{ji}(s + i\epsilon) - T^{(l)}_{ji}(s - i\epsilon) \equiv \operatorname{Disc} T^{(l)}_{ji}(s + i\epsilon). \tag{2.36}$$

Eq (2.36), together with the unitarity condition in Eq. (2.32), provide a strong constraint on the analytic structure of the partial wave amplitudes,

$$i \operatorname{Disc} T^{(l)}_{ii}(s + i\epsilon) = -2 \operatorname{Im} T^{(l)}_{ii}(s + i\epsilon) = \sum_{m=1}^{n} \frac{\sigma_m(s + i\epsilon)}{4\pi} |T^{(l)}_{im}(s + i\epsilon)|^2, \;\; s \in \mathbb{L}. \tag{2.37}$$

As we can read from Eq. (2.37), the imaginary part is proportional to a linear combination of the functions $\sigma_m(s)$. Let us look in detail to these quantities which are defined as follows,

$$\sigma_j(s) \equiv \frac{|\vec{p}_j|}{\sqrt{s}} = \frac{\sqrt{(s - (M_j + m_j)^2)(s - (M_j - m_j)^2)}}{2s}. \tag{2.38}$$

---

[3] Here reasonable stands for a particular class of finite range potentials which behave properly in the $r \to \infty$ limit.

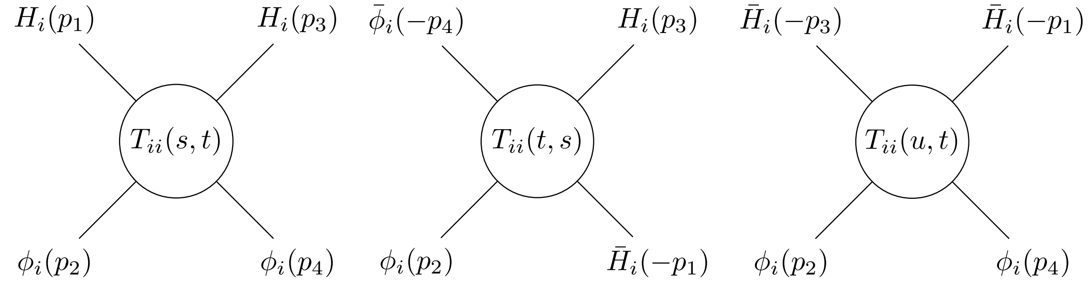

**Figure 2.2:** The $s$, $t$ and $u$ channels described by the $T_{ii}(s,t)$ amplitude according to crossing symmetry.

Note that $\sigma_j(s)$ describes a multi-valued function. When $s \in \mathbb{C}_s$, the function $\sigma_j(s)$ has two branches, with the branch points located at $s_0^{(j)} \equiv (M_j + m_j)^2$ and $s_-^{(j)} \equiv (M_j - m_j)^2$ [149]. These points are commonly referred to as the threshold and pseudo-threshold, respectively. The branch cut is chosen to be the line segment $]-\infty, s_-^{(j)}] \bigcup [s_0^{(j)}, +\infty[$ . It is also usual to denote the $[s_0^{(j)}, +\infty[$ segment, which is included in $\mathbb{L}$, as the right hand cut. Therefore, from Eq. (2.37) we deduce that $\mathrm{Im} T_{ii}^{(l)}(s)$ will inherit as many right hand cuts as the number of channels considered. Besides, to each cut there will be associated two branches or Riemann Sheet (RS)s of $T_{ij}^{(l)}(s)$, although for the moment we will concentrate on the so called physical sheet, satisfying Eq. (2.32) on the upper lip, *i.e.*, $\mathrm{Im}\, T_{ii}(s + i\epsilon) < 0$ $(s \in \mathbb{L})$.

**Left hand cuts.** There exists additional cuts required by crossing symmetry. These kind of processes are depicted in Fig. 2.2. Let us briefly focus on the full amplitude $T_{ii}(s,t)$. The Mandelstam variables (2.16) are commonly used to identify the three processes depicted in Fig. 2.2, and related by crossing symmetry. In each of them, one of the three variables plays the role of the invariant mass squared, so that we will refer to them as the $s$, $t$ and $u$-modes or, redundantly, channels. The same amplitude describes the different modes, the difference is that in each case the Mandelstam variables take real values in non-overlapping regions, so in practice they could be regarded as three independent functions. On the other hand, it may be interesting to suggest that all these processes are described by the same function. Once the kinematic variables are promoted to be complex, each of the three disjoint regions may be connected in the complex plane by analytic continuation. The three amplitudes would become the boundary values of the same function $T(s,t,u)$, allowing then relating any of the modes to the other two. This assumption was originally made by Mandelstam [127], and generally it is adopted as the starting point to derive the analytic properties of the partial wave amplitudes. If unitarity is taken into account in the crossed $u$-mode, for fixed $t$, we would expect a right hand cut structure on the $u$ complex plane in the same way as for the $s$-mode. The cut in the $u$-plane is the line segment $\mathbb{L}_u \equiv [(M_i + m_i)^2, \infty)$, and it induces an additional cut structure of $T_{ii}(s,t)$ on $\mathbb{C}_s$, for the values

$$\mathbb{U} \equiv \{s = \Sigma - t - u \ : \ u \in \mathbb{L}_u\}\, (t \text{ fixed}). \tag{2.39}$$

The set of values $\mathbb{U}$ is traditionally called a left-hand cut. This singularity structure accounting for crossed $u$-mode processes is propagated to the partial wave amplitude when integrating in the angular variable $\theta$ (see Eq. (2.21)). We will briefly illustrate later, with a simple example, how $u$-mode physics induce left hand cut structures into the partial wave amplitudes of the $s$-channel.

**Poles.** So far we have considered two-particle states, though in the physical situation there may well be necessary to include one particle states $|p\rangle$ in a given quantum sector. If such states have a mass $M_r$ larger than the lowest two-particle threshold, $M_r^2 > s_0$, then they will be unstable and allowed to decay into $|pp'\rangle$ products. On the other hand, states satisfying $M_r^2 < s_0$ will be kinematically stable. Therefore they should be included in the Hilbert space, *i.e.*, they should be accounted in the identity resolution (2.25) by adding the corresponding terms,

$$\sum_{b=1}^{n_b} \int_{\mathbb{R}^3} \frac{\mathrm{d}^3\vec{p}_b}{(2\pi)^3 2p_b^0} |p_b\rangle\langle p_b| = \sum_{b=1}^{n_b} \int_{\mathbb{R}^4} \frac{\mathrm{d}^4 p_b}{(2\pi)^3}\ \Theta(p_b^0)\delta(p_b^2 - M_r^2)\ \ |p_b\rangle\langle p_b| \tag{2.40}$$

where $n_b$ denotes the total number of such one-particle stable states. The latter are known as *bound* states, while unstable states are called *resonances*. When the contribution in Eq. (2.40) is implemented into the unitarity relation of Eq. (2.7)—similarly as it was done in Eq. (2.26) for the two-particle states—we find for each of the bound states the following term,

$$\begin{aligned}
\langle H_j\phi_j|\, \mathrm{T}^\dagger \mathrm{T}\, |H_i\phi_i\rangle &= \int_{\mathbb{R}^4} \frac{\mathrm{d}^4 p_b}{(2\pi)^3}\ \Theta(p_b^0)\delta(p_b^2 - M_r^2)\, \langle H_j\phi_j|\, \mathrm{T}^\dagger\, |p_b\rangle\langle p_b|\, \mathrm{T}\, |H_i\phi_i\rangle \\
&= \int_{\mathbb{R}^4} \frac{\mathrm{d}^4 p_b}{(2\pi)^3}\ \Theta(p_b^0)\delta(p_b^2 - M_r^2)\, \left\langle p_{H_j}p_{\phi_j}\right|T^\dagger\, |b\rangle\langle b|\, T\, |p_{H_i}p_{\phi_i}\rangle \\
&\quad \times (2\pi)^4\delta^4(P_i - p_b)(2\pi)^4\delta^4(p_b - P_j) + \ldots \\
&= 2\pi\delta(P_i^2 - M_r^2)\, \left\langle p_{H_j}p_{\phi_j}\right|T^\dagger\, |b\rangle\langle b|\, T\, |p_{H_i}p_{\phi_i}\rangle\big|_{P_i^2 = M_r^2} \\
&\quad \times (2\pi)^4\delta^4(P_j - P_i) + \ldots
\end{aligned} \tag{2.41}$$

Eq. (2.41) represents the contribution of a bound state of mass $M_r$ to the right-hand side of the $T$-matrix unitarity relation (2.7). When Eq. (2.7) is expressed in terms of the reduced matrix element in Eq. (2.15), we find

$$\begin{aligned}
i\left(T_{ji}(s,t) - T_{ji}^\dagger(s,t)\right) &= 2\pi\delta(s - M_r^2)\, \left\langle p_{H_j}p_{\phi_j}\right|T^\dagger\, |b\rangle\langle b|\, T\, |p_{H_i}p_{\phi_i}\rangle\big|_{s=M_r^2} + \ldots \\
&\equiv 2\pi\delta(s - M_r^2) \times \mathrm{g}_j^*\mathrm{g}_i + \ldots
\end{aligned} \tag{2.42}$$

$$\Rightarrow \mathrm{Im}\ T_{ji}(s,t) = -\pi\delta(s - M_r^2)\mathrm{g}_j^*\mathrm{g}_i + \ldots \tag{2.43}$$

The result obtained in Eq. (2.43) is traditionally referred to as a pole term contribution, since this is the imaginary part that would produce an amplitude of the form

$$T_{ji}(s,t) = \frac{\mathrm{g}_i\mathrm{g}_j^*}{s - M_r^2} + \ldots \tag{2.44}$$

The former statement can be checked applying the famous result from complex analysis known as the *Sokhotski-Plemelj* theorem:

$$\lim_{\epsilon\to 0^+} \frac{1}{x - a \pm i\epsilon} = \mathrm{P}\frac{1}{x - a} \mp i\pi\delta(x - a), \tag{2.45}$$

to the physical amplitude $T_{ji}(s+i\epsilon,t)$ (2.44)—the symbol "P" in Eq. (2.45) denotes the principal value. We conclude that for each bound state there will be a simple-pole singularity (Eq. (2.44)), and the associated residue $\mathrm{g}_i\mathrm{g}_j^*$ will depend on the strength of the overlap between the bound and the two-particle states $\langle p_{H_j}p_{\phi_j}|\,T^\dagger\,|b\rangle\langle b|\,T\,|p_{H_i}p_{\phi_i}\rangle|_{s=M_r^2}$. When the $|p_{H_i}p_{\phi_i}\rangle$ states are expressed in the cm two particle state basis, it turns out that the residue $(\mathrm{g}_i\mathrm{g}_j^*)$ is real and proportional to the Legendre polynomial $P_J(x)$, with $J$ the spin of the bound state [125], $\mathrm{g}_i\mathrm{g}_j^*\equiv g_ig_j^*P_J(x)$. Therefore, a bound state pole will also appear in the partial wave amplitude satisfying $l=J$ (we recall that for simplicity we are studying here scattering of spin zero particles).

**Particle exchanges in crossed process.** The above discussion, combined with the Mandelstam hypothesis, would indicate that the existence of bound states in the $u$-channel

$$T_{ii}(u,t)\sim\tilde{\rho}_u/(u-M_u^2), \tag{2.46}$$

would generate non-analytic structures in the complex $s$-plane $\mathbb{C}_s$ of the type (2.17)

$$T_{ii}(s,t)\sim\tilde{\rho}_u/(\Sigma-t-s-M_u^2). \tag{2.47}$$

The particle exchange in a crossed process is an example of a left-hand cut structure induced on the partial wave amplitudes, because, for the amplitude of Eq. (2.47), we would have the partial wave projection (2.21),

$$T_{ii}^{(l)}(s)\sim\frac{1}{2}\int_{-1}^{+1}\mathrm{d}x\frac{\rho_uP_J(x)}{\Sigma-t(x)-s-M_u^2}P_l(x) \tag{2.48}$$

$$=\frac{1}{2}\int_{-1}^{+1}\mathrm{d}x\frac{1}{2|\vec{p}_i|^2}\frac{\rho_uP_J(x)P_l(x)}{x-\mathfrak{g}(s,m,M,M_u)} \tag{2.49}$$

where we have introduced

$$\mathfrak{g}(s,m,M,M_u)=\frac{-s^2+s\Sigma-2sM_u^2+\Delta_i^2}{4s\,|\vec{p}_i|^2}, \tag{2.50}$$

as well as $\tilde{\rho}_u=\rho_uP_J(x)$. For illustration, for $S$-wave $J=l=0$ we would find

$$T_{ii}^{(0)}(s)\sim\frac{1}{2}\int_{-1}^{+1}\mathrm{d}x\frac{\rho_u}{2\,|\vec{p}_i|^2}\frac{P_0(x)\,P_0(x)}{x-\mathfrak{g}(s,m,M,M_u)} \tag{2.51}$$

$$=\frac{\rho_u}{2\,|\vec{p}_i|^2}\ln\left(\frac{\mathfrak{g}(s,m,M,M_u)+1}{\mathfrak{g}(s,m,M,M_u)-1}\right) \tag{2.52}$$

$$=\frac{\rho_u}{2\,|\vec{p}_i|^2}\ln\left(\frac{1}{s}\frac{\Delta_i^2-s\,M_u^2}{\Sigma-M_u^2-s}\right). \tag{2.53}$$

From Eq. (2.53) we learn that the partial wave amplitude will develop an imaginary part whenever the argument of the logarithm, $\ln(z)$, becomes negative. Once again, given that Hermitian analyticity requires $(T_{ii}^{(l)}(s))^*=T_{ii}^{(l)}(s^*)$, we would have a discontinuity: $\mathrm{Disc}[\ln(z)]=\ln(z+i\epsilon)-\ln(z-i\epsilon)=2\pi i$, with $z<0$. In this example, there are two branch points of the $1/s$ logarithm at 0 and $-\infty$, plus the two located at $s_b=\Delta_i^2/M_u^2$ and $s_b'=\Sigma-M_u^2$ associated to the second logarithm. The location of the left hand cuts stemming from $u$-mode bound states would be $\mathbb{U}=\{\,]-\infty,0]\bigcup[s_b,s_b']\,\}$.

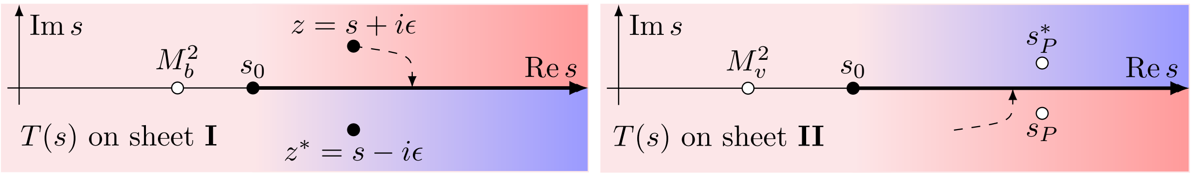

**Figure 2.3:** Schematic plot of the analytic structure for the two branches (labelled as sheet I and II) of an elastic partial wave amplitude $T(s)$ in the complex $s$-plane—neglecting left-hand cuts. The solid thick black arrow starting at $s_0$ depicts the branch cut, and the dashed arrow points into the direction approaching the physical values of the amplitude (see Eq. (2.34)) in both sheets. The blank circles represent the location of simple poles.

One could pay attention to a physical system where this cut would appear, like for example, the amplitude of the $D\bar{K}$ scattering in $S$-wave—therefore $J^P = 0^+$—in the strangeness-isospin $(S, I) = (-1, 0)$ sector. The $u$-mode associated to this system would be the $DK$ elastic scattering, which in $S$-wave in the $(S, I) = (1, 0)$ sector is well known for the existence of a scalar particle, $D_{s0}^*(2317)$, satisfying $M_u = M_{D_{s0}^*} < M_D + m_K$. This scenario is exactly the situation discussed in the former paragraph. If we use the numerical values of the particle masses to find the location of the left hand cuts we find $\mathbb{U} = \{(-\infty, 0] \bigcup [(1.403)^2, (1.454)^2]\}$ (units of GeV$^2$). These contributions are "quite far" from the $D\bar{K}$ scattering line, since the threshold is located at $2.365^2$ GeV$^2$. For that reason, left hand cut terms like the one in Eq. (2.53) may be regarded as a mild effect, when it comes to describe the physical amplitude $T_{D\bar{K}}^{(0)}(s)$ on the scattering line (note that the term (2.53), for large $s$, is suppressed behaving like $\sim 1/s \times \ln s$) .

This is just a simple illustration on how this type of singularities could arise in partial wave amplitudes. The actual general case is more complicated involving further cuts and, given that we will always neglect the energy dependence of such contributions, we will omit a thorough derivation. (The reader may find it, for example, in the textbook [125]). Another reason is that, as it has been shown, a proper management of such singularities requires *a priori* a deep knowledge about the interaction, such as the possible existence of bound states. This, in general, will not be the case, and we shall see how in our phenomenological treatment the effects induced by this unified consideration of the ($s$-$t$-$u$)-channels are only approximately taken into account.

**Resonances and Riemann sheets.** In the case of resonant states, since their only difference with bound states is the matter of stability, one may think that they would also be associated with pole singularities in $\mathbb{C}_s$ at positions, lets say $s_P$,[4] but satisfying $\mathrm{Re}\, s_p > s_0$ and $\mathrm{Im}\, s_p \neq 0$ to prevent spoil unitarity on the scattering line (2.32). These poles would influence a dispersive representation of $T_{ji}^{(l)}(s)$—since it necessarily would have contributions from the residues $g_i g_j^*$ of the resonance poles. In general, $g_i g_j^*$ will be complex and therefore contribute to the absorptive part of the amplitude, spoiling unitarity again. For this reason, resonances do manifest as poles in different Riemann sheets of $T_{ji}^{(l)}(s)$, but not in the first one.

In Fig. 2.3, a sketch of the analytic structure of an elastic $S$-wave amplitude, $T(s)$, is shown. Therein, we can distinguish the two sheets on the left and right panels, denoted as I—the physical sheet—and II respectively. These are the two branches associated to the

---

[4] Note that each complex pole would have a complex conjugate partner due to Hermitian analyticity, as deduced from Eq. (2.35).

right hand cut starting at $s_0$. The different colors represent the values of $T(s)$ around the cut, and we can see how a path crossing the upper lip of the physical sheet is connected with the lower lip of the second sheet. On the right panel, two complex conjugate poles $s_P$ and $s_P^*$ are shown. From the two poles, the most important would be the lower one, $s_P$, since it lies on the region that is connected with the physical sheet, and consequently, will have a strong impact on the line-shape of the physical amplitude (note that red and blue colors represent the different values of $T(s)$ along the cut). This pole is parametrized in terms of the mass $M_\mathrm{r}$ and width $\Gamma_\mathrm{r}$ of the associated particle, $s_P = (M_\mathrm{r} - i\Gamma_\mathrm{r}/2)^2$, a reminiscence from quantum mechanics [150]. On the same sheet, we distinguish another class of poles which are known as *virtual* poles, associated to virtual states. These would be located on the real axis at values $s = M_v^2 < s_0$. In a situation without bound state poles, the latter may play a role, influencing the low energy region if they are located close enough to $s_0$.

In order to find the analytic continuation into the second sheet, as well as for future purposes, it is convenient to express the unitarity condition in Eq. (2.37) in terms of the *inverse* of the partial wave amplitude $T_{ji}^{(l)}(s)$. For simplicity we will denote the latter here as $T_{ji}^{-1}(s) \equiv (T^{-1}(s))_{ji}$, omitting the "$l$" (wave) label. One easily finds,

$$\mathrm{Disc}\, T_{ji}^{-1}(s+i\epsilon) = 2i\,\mathrm{Im}\, T_{ji}^{-1}(s+i\epsilon) = 2i\,\frac{\sigma_i(s+i\epsilon)}{8\pi}\delta_{ij},\;\; s \in [s_0^{(i)}, +\infty[\,. \tag{2.54}$$

From Eq. (2.54) we learn that the inverse amplitude will also inherit the right hand cut structure carried by the function $\sigma_i(s)$. The values of $T^{-1}(s+i\epsilon)$ on the upper lip of the right hand cut satisfy

$$T_{ji}^{-1}(s+i\epsilon) = (T^{-1})_{ji}^{\mathrm{II}}(s-i\epsilon) \tag{2.55}$$

where the label "II" is used to denote the second sheet of $T_{ji}^{-1}$. On the other hand, one can use the following trivial identity (2.36)

$$T_{ji}^{-1}(s+i\epsilon) = T_{ji}^{-1}(s-i\epsilon) + \mathrm{Disc}\, T_{ji}^{-1}(s+i\epsilon), \tag{2.56}$$

in order to find an analytic continuation of $T_{ji}^{-1}(s)$ (and therefore, of $T_{ji}(s)$) onto the second sheet [133]

$$\begin{aligned}(T^{-1})_{ji}^{\mathrm{II}}(s-i\epsilon) &= T_{ji}^{-1}(s-i\epsilon) + \mathrm{Disc}\, T_{ji}^{-1}(s+i\epsilon),\\ &= T_{ji}^{-1}(s-i\epsilon) + 2i\,\frac{\sigma_i(s+i\epsilon)}{8\pi}\delta_{ij} \qquad (2.57)\\ \Rightarrow (T^{-1})_{ji}^{\mathrm{II}}(s) &= T_{ji}^{-1}(s) - 2i\,\frac{\sigma_i(s)}{8\pi}\delta_{ij}. \qquad (2.58)\end{aligned}$$

Eq. (2.58) constitutes a proper analytic continuation onto the second sheet of $T^{-1}(s)$ provided the function $\sigma(s)$ enters evaluated on the first sheet, *i.e.*, $\sigma(s+i\epsilon) > 0$ for $s \geqslant s_0^{(i)}$.

### 2.3.1 Phase shifts, inelasticities and low energy parametrization

In many situations, it is important to have a parametrization of the partial wave amplitude. At low energies, one can always model the line shape of a physical amplitude in a way consistent with unitarity. In this regime, one might consider the case of elastic scattering, either because the inelastic channels are closed or maybe because the influence of such higher channels is expected to be small. If so, we learn from unitarity and analyticity that the partial wave amplitude is a complex analytic function with a right hand cut along the scattering line $\mathbb{L}$. The physical amplitude can be parametrized as $T(s) = N(s)e^{i\delta(s)}$, *i.e.*, in terms of a phase $\delta(s)$, called phase shift. Alternatively, one also has that the $S$-matrix is a complex number of unit modulus, $S(s) = e^{2i\delta(s)}$. Recalling that Eq. (2.37) in the elastic case reads $\operatorname{Im} T(s) = -\sigma(s)|T(s)|^2/8\pi$ , we thus have,

$$T^{(l)}(s) = -8\pi \frac{\sin \delta^{(l)}(s)}{\sigma(s)} e^{i\delta^{(l)}(s)}, \tag{2.59}$$

$$S^{(l)}(s) \equiv e^{2i\delta^{(l)}(s)} = 1 - i\frac{\sigma(s)}{4\pi} T^{(l)}(s). \tag{2.60}$$

For finite range interactions, it is in general possible to perform the following low energy expansion[5] [151, 152],

$$|\vec{p}\,|^{2l+1} \cot \delta^{(l)}(s) = -\frac{1}{a_l} + \frac{1}{2} r_l\, |\vec{p}\,|^2 + \mathcal{O}(|\vec{p}\,|^4), \tag{2.61}$$

where $a_l$ and $r_l$ in the case of $S$-waves ($l = 0$) are known as the scattering length and effective range, respectively—note that the sign in front of $a_l$ is a convention and it may be different in other works. The parameters $a_0$ and $r_0$ can be related to the elastic partial wave amplitude combining Eq. (2.60), $\sigma(s) = |\vec{p}\,|/\sqrt{s}$ and $S(s) = e^{2i\delta(s)} = (\cot \delta(s) + i) / (\cot \delta(s) - i)$,

$$|\vec{p}\,| \cot \delta(s) = -8\pi \sqrt{s}\, T^{-1}(s) + i\, |\vec{p}\,|. \tag{2.62}$$

From Eq. (2.62), we find the formula of the scattering length in terms of the $S$-wave amplitude

$$a_0 = \lim_{s \to s_0} \frac{T(s)}{8\pi \sqrt{s}}. \tag{2.63}$$

In the coupled channels case, we will extend the phase shift parametrization of Eq. (2.60) to introduce, for each channel, the phase shifts ($\delta^{(l)}_m(s)$) and inelasticities ($\eta^{(l)}_m(s)$) through,

$$S^{(l)}_{mm}(s) \equiv \eta^{(l)}_m(s) e^{2i\delta^{(l)}_m(s)} = 1 - i\frac{\sigma_m(s)}{4\pi} T^{(l)}_{mm}(s), \;(m = 1, \ldots, n). \tag{2.64}$$

The inelasticities parametrize the dynamical absorptive effects deviating the $S$-matrix diagonal elements from having modulus unity. These effects come into play at energies big enough to open higher channels. Therefore, they enter in different energy regions, satisfying $0 \leqslant \eta_i(s) \leqslant 1$ whenever $s \geqslant s^{(i)}_0$. The exception is the lightest channel $i = 1$, for which $\eta_1(s)$ is one in the elastic regime of energies $s_0 \leqslant s < s^{(2)}_0$, recovering Eq. (2.60). Furthermore, using the condition $S(s)S^{\dagger}(s) = \mathbb{I}$, one can readily show that $\eta_1(s) = \eta_2(s)$ in the region $s^{(2)}_0 \leqslant s < s^{(3)}_0$, when there are only two coupled channels open.

---

[5] The exceptional case in which the expansion is not possible would be in the presence of a bound state pole located at threshold. In the case where there exist a weakly bound state $s_b$, $s_b < s_0$, $\cot \delta(s_b) = i$ and Eq. (2.61) becomes, for $S$-wave, $\gamma = 1/a_0 + \gamma^2 r_0/2$, with $\gamma = \text{Abs}|\vec{p}(s_b)|$.

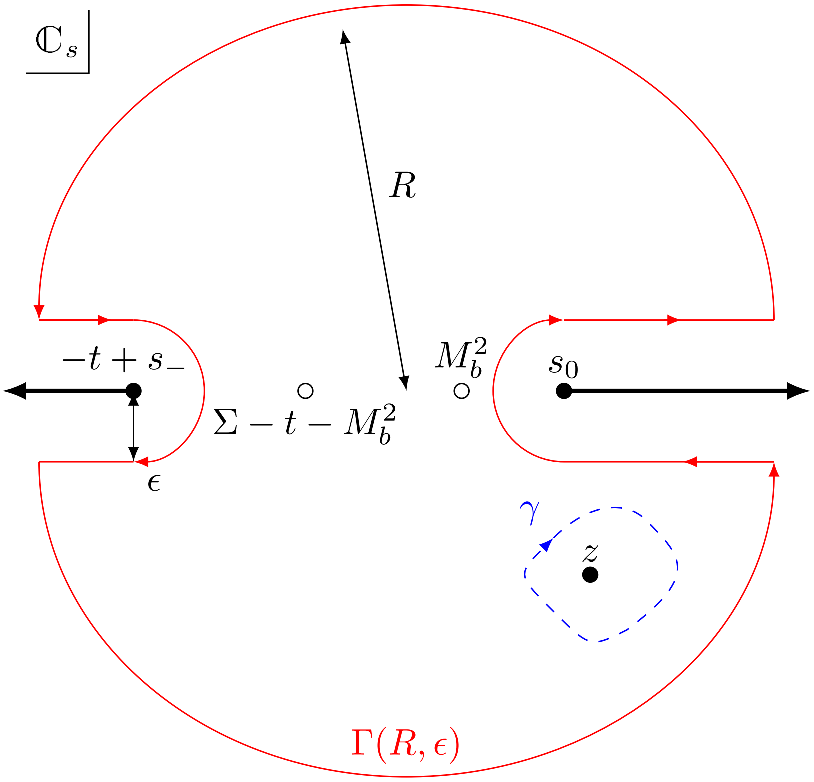

**Figure 2.4:** Analytic structure of the function $T(s)/(s-z)$ on the complex $s$-plane $\mathbb{C}_s$.

**Dispersion relations.** Nevertheless, even if the analytic structure of the partial wave amplitudes provides useful constraints, these, are not enough *per se* to describe physical systems. In any case, what one effectively does is to encode the dynamical information of the amplitudes in different places, like the pole positions, residues, phase shifts and inelasticities. Let us consider a single-channel $T(s,t)$ for a fixed $t$-value. Formally, our amplitude $T(z)$ can be represented as an integral in the complex plane $\mathbb{C}_s$ along a closed, counter-clockwise oriented path $\gamma$ including $z$, by means of Cauchy's Residue Theorem,

$$T(z) = \frac{1}{2\pi i}\int_\gamma \mathrm{d}z' \frac{T(z')}{z'-z} \tag{2.65}$$

provided $T(z)$ is analytic inside $\gamma$. Now, if the contour $\gamma$ is enlarged to the circuit $\Gamma(R,\epsilon)$, see Fig. 2.4, Eq. (2.65) is no longer valid and should be modified to accommodate all the new enclosed singularities of $T(z')/(z'-z)$. Let us assume that we *know* in advance that there exist real poles, like in the situation depicted in Fig. 2.4. In that case we should rewrite Eq. (2.65) including all the pole contributions on the left hand side,

$$T(z) + \frac{g^2}{M_b^2 - z} + \frac{g_u^2}{\Sigma - t - M_b^2 - z} = \frac{1}{2\pi i}\int_{\Gamma(R,\epsilon)} \mathrm{d}z' \frac{T(z')}{z'-z} \tag{2.66}$$

while the right-hand side integral can be divided into three main pieces: the straight segments, that enclose the left and right branch cuts, and the two circular curves on the upper and lower half planes. If, as we enlarge the circuit $\Gamma$, the integrand vanishes[6]—

---

[6] It should be mentioned that one can always perform a Cauchy representation of the function $T(z)/(z-z_1)\cdots(z-z_n)$ such that the integrand evaluated on the circular path—of large enough radius $R$—gives

$|T(R\,e^{i\phi})| \to 0$ for $R \to \infty$ ($\phi \in (0,\pi) \bigcup (\pi, 2\pi)$)— the contribution of the circular integrals can be neglected for large values of $R$. Hence, in the limit of vanishing $\epsilon$ and very large $R$ we are left with the contribution of the straight segments along the upper and lower lip of the cuts, which gives,

$$\begin{aligned} T(z) + \frac{g^2}{M_b^2 - z} + & \frac{g^2}{\Sigma - t - M_b^2 - z} \\ &= \frac{1}{2\pi i}\int_{\mathbb{U}} \frac{\operatorname{Disc} T(z'+i\epsilon)}{z'-z}\mathrm{d}z' + \frac{1}{2\pi i}\int_{s_0}^{\infty} \frac{\operatorname{Disc} T(z'+i\epsilon)}{z'-z}\mathrm{d}z' \end{aligned} \tag{2.67}$$

Eq. (2.67) stems from the simplified analytic structure represented in Fig. 2.4. In general, as already mentioned, the left-hand cut structure could be more complicated. In this work we aim to describe the interaction of hadrons at low energies, therefore, we will pursue a sufficiently accurate description of the amplitude $T(z)$ for values in the region close to $s_0$. The exact structure of the left-hand cut contributions has a small effect on the amplitude in the scattering line, since it will give rise to mild $s$-dependences for $s > s_0$, as long as the cuts are sufficiently separated. Furthermore, the low energy constants will effectively account for these effects, and the presence of resonances or weakly bound states makes even less relevant a correct treatment of the left-hand cut terms. The former discussion can alternatively be displayed in terms of the inverse amplitude $T^{-1}(z)$—recall Eq. (2.54)—by writing the following dispersive representation [132],

$$T^{-1}(z) = \mathcal{Q}(z) + \frac{1}{2\pi i}\int_{s_0}^{\infty} \frac{\operatorname{Disc} T^{-1}(z'+i\epsilon)}{z'-z}\mathrm{d}z' \tag{2.68}$$

In Eq. (2.68), the energy dependence encoded in the function $\mathcal{Q}(z)$ accounts for the dynamics (bound states, left hand cut contributions, *etc*...), while the integral guarantees that the amplitude satisfies exact unitarity (2.54) by construction, since we can use Eq. (2.45) and get,

$$\begin{aligned} T^{-1}(s+i\epsilon) &= \mathcal{Q}(s) + \frac{1}{8\pi^2}\int_{s_0}^{\infty} \frac{\sigma(z'+i\epsilon)}{z'-s-i\epsilon}\mathrm{d}z' \\ &= \mathcal{Q}(s) + \frac{1}{8\pi^2}\mathrm{P}\int_{s_0}^{\infty} \frac{\sigma(z'+i\epsilon)}{z'-s}\mathrm{d}z' + i\frac{\sigma(s+i\epsilon)}{8\pi}. \end{aligned} \tag{2.69}$$

In the next section we shall see how it is possible to establish a connection between the function $\mathcal{Q}(s)$ and the dynamics of the scattering constituents. With this link, the formulation in Eq. (2.69) would allow for a program to construct amplitudes satisfying symmetry constraints, and, at the same time, consistent with unitarity. The drawback is that, in most of the approximations for $\mathcal{Q}(s)$, the exact crossing structure is lost. As commented before, some mild contributions may be considered as absorbed in the free parameters, since, at least we need to introduce one subtraction in order to make finite the principal part integral in Eq. (2.69).

## 2.4 The Bethe-Salpeter resummation

We discuss here the method that we shall utilize to build unitary amplitudes in a coupled-channels formalism, starting from kernel amplitudes consistent with a set of symmetry

---

a vanishing contribution.

properties. The general idea was originally proposed in the work of Oller and Oset [130] as an approach to the lowest-lying unflavoured meson resonances in the scalar sector. There, the applicability of the tree level $\chi$PT amplitudes was extended by means of the restoration of exact two-body unitarity. This approach was in the spirit of previous attempts of describing meson-nucleon resonances by Kaiser, Siegel and Weise [128, 129]. Whereas in the latter cases the idea was based on the resolution of $S$-wave non-relativistic Lippmann-Schwinger and Schrödinger equations with *pseudo*-potentials obtained from $\chi$PT amplitudes, in the case of Ref. [130] the tree-level amplitudes were directly iterated in a set of algebraic Lippmann-Schwinger equations with relativistic propagators. The approach has been successively extended to study dynamically generation of resonances in meson-meson [130, 132, 153–155] or meson-baryon [131, 133, 156] in a diversity of situations and sectors in order to assess and/or incorporate the dynamical generation of resonances.

**Dynamically generated resonances.** As we have discussed in the previous section, one particle (stable or unstable) states are associated to poles in partial wave amplitudes on its different sheets. When constructing the dispersive representation, its presence has always been imposed in advance. As it may seem natural to think, in a real situation without enough information this is a clear disadvantage, since such approach lacks of predictivity in that sense. On the other hand, amplitudes obtained in perturbation theory would never contain any further pole singularity than those introduced at the Lagrangian level. One should use nonperturbative methods, such as scattering equations or infinite resummations of diagrams in order to generate pole singularities. In this context, when an amplitude obtained after some sort of nonperturbative method contains poles, either in the first or second Riemann sheets, the latter are called *dynamically generated* poles or resonances, specially when their dynamics is decisively influenced by the unitarity hadron loops.

**The Bethe-Salpeter Equation (BSE).** Let us rewrite the kinematic variables $s$, $t$ and $u$ resorting to the following notation for the $i \to j$ process,

$$H_i(\frac{P}{2}+p)+\phi_i(\frac{P}{2}-p)\to H_j(\frac{P}{2}+q)+\phi_j(\frac{P}{2}-q). \tag{2.70}$$

The variables in Eq. (2.70), in terms of the Mandelstam variables, correspond to $s=P^2$, $t=(p-q)^2$ and $u=(p+q)^2$. The amplitude of the process will be written as $T_{ij}^{(P)}(p,q)$, making the off-shell dependence explicit. In this language, the BSE equation reads [132] (see also [157]),

$$T_{ji}^{(P)}(p,q)=V_{ji}^{(P)}(p,q)+\sum_{a=1}^{n} i\int_{\mathbb{R}^4}\frac{\mathrm{d}^4k}{(2\pi)^4}\frac{V_{ai}^{(P)}(p,k)}{\Delta^{-1}(\frac{P}{2}-k,m_a)}\frac{T_{ja}^{(P)}(k,q)}{\Delta^{-1}(\frac{P}{2}+k,M_a)}. \tag{2.71}$$

It relates the complete off-shell amplitudes $T_{ji}^{(P)}(p,q)$ with the full set of two-particle irreducible (2PI) diagrams without unitarity cuts, $V_{ji}^{(P)}(p,k)$ (red dashed circles in Fig. 2.5), plus the renormalized full propagators $\Delta(p,m)=(p^2-m^2+i\epsilon)^{-1}$ (double lines in Fig. 2.5) of the heavy $H_\ell$ ($M_\ell$) and light $\phi_\ell$ ($m_\ell$) mesons. In what follows, in many ocassions, we will refer to the 2PI amplitudes as *potentials*. Eq. (2.75) can be understood diagrammatically as the resummation depicted in Fig. 2.5—note that one can iterate the solution by insertions of $T_{ja}^{(P)}(k,q)$ on the right hand side. The limitation of the BSE lies in the

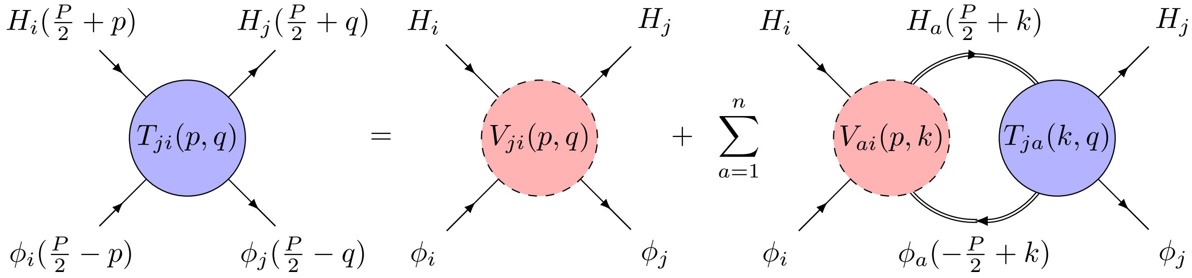

**Figure 2.5:** Diagrammatic formulation of the Bethe-Salpeter Equation

knowledge of the dynamics, which would determine $V_{ji}^{(P)}(p,q)$ and $\Delta(p,m)$. One could use a perturbative kernel for $V_{ji}^{(P)}(p,q)$ and $\Delta(p,m)$ derived from some effective quantum field theory to get consecutive approximations to the exact $T_{ji}^{(P)}(p,k)$. In that case, the necessary renormalization constants—to regularize the subsequent ultraviolet (UV) divergent loop integrals—would reflect the lack of knowledge of the short distance physics (or approximated nature of the solution). These low energy constants will account for some contributions from higher orders.

**On-shell scheme.** A very important simplification for the resummation of (2.75) is found when off-shell effects are neglected in the loop integral. This step is justified if, as it was shown in the case of the $\pi$-$\pi$ interaction involving chirally invariant 2PI amplitudes [132], the off-shell contributions lead to power-like divergences with the same structure as the potential. These divergencies can be absorbed by renormalizing the low energy constants in the $V_{ji}^{(P)}(p,k)$ amplitudes. This is also the case for the $H^{(*)}\phi$ scattering, which is also governed by the chiral counting rules.

The partial wave decomposition of the half off-shell two-particle amplitude ($P = (\sqrt{s},\vec{0})$) is,

$$V_{ai}^{(P)}(p,k) = \sum_{l=0}^{\infty}(2l+1)P_l(\cos\theta_{\vec{p},\vec{k}})V_{ai}^{(l)}(s,k^2,P\cdot k) \tag{2.72}$$

where we have taken into account that on-shell, $p^2 = (m_i^2 + M_i^2)/2 - s/4$, and that $p^0$ is a function of $s$. Besides, $\theta_{\vec{p},\vec{k}}$ is the angle formed by $\vec{p}$ and $\vec{k}$. Using a similar expression for $T_{ja}^{(P)}(k,q)$, we find,

$$\begin{aligned}\sum_{l=0}^{\infty}(2l+1)P_l(\cos\theta_{\vec{p},\vec{q}})T_{ji}^{(l)}(s) &= \sum_{l=0}^{\infty}(2l+1)P_l(\cos\theta_{\vec{p},\vec{q}})V_{ji}^{(l)}(s)\\ +\sum_{a=1}^{n}\sum_{l,l'=0}^{\infty}(2l+1)(2l'+1)\; i\int_{\mathbb{R}^4}\frac{\mathrm{d}^4k}{(2\pi)^4}&\frac{V_{ai}^{(l)}(s,k^2,P\cdot k)}{\Delta^{-1}(\frac{P}{2}-k,m_a)}\frac{T_{ja}^{(l')}(s,k^2,P\cdot k)}{\Delta^{-1}(\frac{P}{2}+k,M_a)}\\ &\times P_l(\cos\theta_{\vec{p},\vec{k}})P_{l'}(\cos\theta_{\vec{q},\vec{k}}).\end{aligned} \tag{2.73}$$

At this point, we recall Eq. (2.30) to perform the angular integration. Using that

$$\int_{-1}^{+1}\mathrm{d}\Omega(\hat{k})P_l(\cos\theta_{\vec{p},\vec{k}})P_{l'}(\cos\theta_{\vec{q},\vec{k}}) = \frac{4\pi}{2l+1}\delta_{ll'}P_l(\cos\theta_{\vec{q},\vec{p}}). \tag{2.74}$$

we get,

$$T^{(l)}_{ji}(s) = V^{(l)}_{ji}(s) + \sum_{a=1}^{n} \, i\, 4\pi \int \frac{\mathrm{d}k^0\, |\vec{k}|^2 \mathrm{d}|\vec{k}|}{(2\pi)^4} \frac{V^{(l)}_{ai}(s, k^2, P\cdot k)}{\Delta^{-1}(\frac{P}{2} - k, m_a)} \frac{T^{(l)}_{ja}(s, k^2, P\cdot k)}{\Delta^{-1}(\frac{P}{2} + k, M_a)}. \tag{2.75}$$

Now, within the on-shell approximation, where $k^2$ and $P \cdot k$ in the arguments of $V^{(l)}_{ai}$ and $T^{(l)}_{ja}$ are approximated by their on-shell values, we finally obtain,

$$T^{(l)}_{ji}(s) = V^{(l)}_{ji}(s) + \sum_{a=1}^{n} V^{(l)}_{ai}(s) G_a(s) T^{(l)}_{ja}(s) \tag{2.76}$$

with the loop function of the two mesons associated to the channel “a” given by,

$$G_a(s) = i \int_{\mathbb{R}^4} \frac{\mathrm{d}^4 k}{(2\pi)^4} \frac{1}{((P-k)^2 - m_a^2 + i\epsilon)\,(k^2 - M_a^2 + i\epsilon)}. \tag{2.77}$$

The $k^0$ integral can be performed taking into account that the integrand has poles located at positions $\tilde{k}^0_{m^\pm} = \sqrt{s} \mp (E_m - i\epsilon)$ and $\tilde{k}^0_{M^\pm} = \mp(E_M - i\epsilon)$, where $E_x^2(\vec{k}) = \vec{k}^2 + x^2$ $(x = m, M)$. Thus, choosing an appropriated closed path—as we did to build the dispersive representation (2.67) (see Fig. 2.4)—we can close the $k^0$ integral on a segment of the real axis $[-R, R]$ using a semicircle line of radius $R$, clockwise oriented. In the limit $R \to \infty$ the contribution from the semicircular path vanishes, and we obtain the $k^0$ integral in terms of the residues at the poles with negative imaginary parts $\tilde{k}^0_{m^-}$ and $\tilde{k}^0_{M^-}$

$$\begin{aligned} G_a(s) =& -2\pi i \int_{\mathbb{R}^3} \frac{\mathrm{d}^3 k}{(2\pi)^4} i \left[ \frac{1}{\left(\tilde{k}^0_{m^-} - \tilde{k}^0_{m^+}\right)\left(\tilde{k}^0_{m^-} - \tilde{k}^0_{M^-}\right)\left(\tilde{k}^0_{m^-} - \tilde{k}^0_{M^+}\right)} \right. \\ &+ \left. \frac{1}{\left(\tilde{k}^0_{M^-} - \tilde{k}^0_{m^+}\right)\left(\tilde{k}^0_{M^-} - \tilde{k}^0_{m^-}\right)\left(\tilde{k}^0_{M^-} - \tilde{k}^0_{M^+}\right)} \right] \\ =& \int_{\mathbb{R}^3} \frac{\mathrm{d}^3 k}{(2\pi)^3} \frac{E_m + E_M}{2 E_m E_m} \frac{1}{s - (E_m + E_M)^2 + i\epsilon}. \end{aligned} \tag{2.78}$$

We shall need some regularization in order to deal with the logarithmic UV divergence of Eq. (2.78). We will come back to this point later. Performing the change of variables $z' = (E_m + E_M)^2$ we obtain (the angular integration gives $4\pi$),

$$G_a(s) = \int_{s_0}^{\infty} \mathrm{d}z' \frac{\sigma(z')}{8\pi^2} \frac{1}{s - z' + i\epsilon}, \tag{2.79}$$

which has a suitable form to extract the imaginary part of the loop function (2.45). Thus, one gets,

$$\operatorname{Im} G_\ell(s + i\epsilon) = -\frac{|\vec{p}_\ell(s)|}{8\pi\sqrt{s}} = -\frac{\sigma(s + i\epsilon)}{8\pi}. \tag{2.80}$$

Eq. (2.76) can be easily solved, either in terms of the amplitude or its inverse. Using the matrix notation $T(s)$ and $V(s)$—in the space of coupled channels—to respectively denote the partial wave and 2PI amplitudes, plus introducing $[G(s)]_{ij} = G_i(s)\delta_{ij}$, the solution is,

$$T(s) = [\mathbb{I} - V(s)G(s)]^{-1}\, V(s) \tag{2.81}$$

$$T^{-1}(s) = V^{-1}(s) - G(s) \tag{2.82}$$

where we have omitted the partial wave labels. The amplitude obtained solving Eq. (2.81) or (2.82) satisfies exact unitarity across the right hand cut (2.54). This is thanks to the imaginary part of the loop function (2.80), since $\mathrm{Im}\, T^{-1}(s) = -\mathrm{Im}\, G(s)$. Recall that the two-particle irreducibility of the amplitudes implies that these are real functions free of right hand cuts for energies $s \in \mathbb{L}$. In this on-shell approximation, the physics encoded in the kernel 2PI amplitudes of the matrix $V^{-1}(s)$ in Eq. (2.82), characterize the $\mathcal{Q}(s)$ function introduced in the dispersive representation of Eq. (2.69). It is illustrative to compare Eq. (2.82) with the elastic dispersive representation of $T^{-1}(s) - T^{-1}(s_1)$, where $s_1$ is a subtraction point. From Eq. (2.69) we get

$$\begin{aligned} T^{-1}(s) &= \underbrace{\left(T^{-1}(s_1) - \mathcal{Q}(s_1)\right)}_{\equiv\alpha} + \mathcal{Q}(s) + \frac{1}{8\pi^2}\int_{s_0}^{\infty} \frac{\sigma(z'+i\epsilon)(s-s_1)}{(z'-s_1)(z'-s)}\mathrm{d}z' \\ &= \alpha + \mathcal{Q}(s) + \frac{1}{8\pi^2}\int_{s_0}^{\infty} \frac{\sigma(z'+i\epsilon)(s-s_1)}{(z'-s_1)(z'-s)}\mathrm{d}z'. \end{aligned} \tag{2.83}$$

While solving the on-shell BSE (with $G(s)$ in the form (2.79)), we find

$$\begin{aligned} T^{-1}(s) &= \underbrace{\left(T^{-1}(s_1) - V^{-1}(s_1)\right)}_{\equiv\alpha'} + V^{-1}(s) + G(s) - G(s_1) \\ &= \alpha' + V^{-1}(s) + \frac{1}{8\pi^2}\int_{s_0}^{\infty} \frac{\sigma(z'+i\epsilon)(s-s_1)}{(z'-s_1)(z'-s)}\mathrm{d}z'. \end{aligned} \tag{2.84}$$

In this way, we realize how the energy dependence of the functions $\mathcal{Q}(s)$ is clearly in correspondence with the dynamics associated to the 2PI amplitudes [132]. In Eqs. (2.83) and (2.84) the undetermined constant factors, $\alpha$ and $\alpha'$, arise from the renormalization scheme—in this case, subtracting the value of $T$ at $s_1$. Hence, we shall have that an amplitude $T(s)$ calculated using a regularized loop function, $G^{(\mathrm{R})}(\Lambda, s)$, will be equivalent to a once-subtracted dispersive representation (2.83) provided,

$$T^{-1}(s) = V^{-1}(s, \Lambda) - G^{(\mathrm{R})}(\Lambda, s), \tag{2.85}$$

where the regulator ($\Lambda$) dependence of $G^{(\mathrm{R})}$ should be absorbed by the low energy constants of the 2PI amplitudes. Consequently, the observables would not be sensitive to ambiguities in the regularization procedure. This could not be always the case, given that in practice it may not be feasible to include the *full* set of 2PI amplitudes and some truncation will be implemented. Hence, one should expect some (mild) dependence of the observables on the UV regulator. In all the cases, the input consists on phenomenological perturbative amplitudes—*potentials*—which are calculated at some order and, consequently, depend on a finite set of low energy constants. Whenever the changes experimented by $T(s)$—due to different values of the regulator—are significant, these would be pointing out that the role of higher orders could be important. Conversely, from an alternative perspective, we see that the regulator effectively accounts for part of the higher order contributions.

## 2.5 The unitary $T$-matrix in coupled channels

In the rest of the dissertation we shall make extensive use of the formalism introduced up to this point. The purpose of this section is to summarize the results gathering the relevant expressions in a common place. In all the situations, we will deal with systems in which the relevant degrees of freedom must be considered in the formalism of coupled channels. As already derived in the previous section, a unitary $T$-matrix in the space of $N$ coupled channels is obtained by solving the algebraic equation (2.85)

$$T^{-1}(s) = V^{-1}(s) - G^{(\mathrm{R})}(s), \tag{2.86}$$

$$G^{(\mathrm{R})}(s) = \mathrm{diag}\left(G_1^{(\mathrm{R})}(s), \ldots, G_N^{(\mathrm{R})}(s)\right), \tag{2.87}$$

in which we omit the regulator dependence of the input tree level amplitudes $V$ and of the loop function matrix $G^{(\mathrm{R})}$, although, they should be implicitly understood to be there. Besides, we may use different regularization "R" schemes for the loop function—either because we explore implications of previously fixed unitary models, or in order to compare different regularization procedures. For convenience, all the necessary formulae concerning the regulated loop function can be found in appendix A.

We shall also search for poles in the complex $s$-plane $\mathbb{C}_s$. As already discussed in Sec. 2.3, we will be able to reach the different $2^N$ Riemann sheets by performing the analytic continuation of Eq. (2.58) on the diagonal elements of the inverse amplitude $T^{-1}$. Thanks to Eq. (2.86), this operation may be applied to the set of loop functions carrying the right hand cut structure

$$\{G_{11}^{(\mathrm{R}),\xi_1}, G_{22}^{(\mathrm{R}),\xi_2}, \ldots, G_{NN}^{(\mathrm{R}),\xi_N}\} \tag{2.88}$$

where each of the variables $\xi_i$ can take the values $\xi_i = 0$ or 1, and denote if the analytic continuation

$$G_{ii}^{(\mathrm{R})}(s) \to G_{ii}^{(\mathrm{R})}(s) + i\frac{\sigma_i(s)}{8\pi}\,\xi_i, \quad s \in \mathbb{C}\ , \tag{2.89}$$

has or has not been performed in each channel. Consequently, the vectors $\vec{\xi} = (\xi_1, \ldots, \xi_N)$ serve to label the possible sheets, with $\vec{\xi} = \vec{0}$ referring to the physical, first Riemann sheet. Nevertheless, we will be interested in those sheets analytically connected with the first one—the physical sheet—on the upper lip of each cut, and refer to it, with some abuse of notation, as the unphysical or "second" sheet. If, as we have previously introduced, we label the different thresholds as

$$s_0^{(1)} \equiv (M_{H_1} + m_{\phi_1})^2\,, \tag{2.90}$$

$$s_0^{(2)} \equiv (M_{H_2} + m_{\phi_2})^2\,, \tag{2.91}$$

$$\cdots$$

$$s_0^{(N)} \equiv (M_{H_N} + m_{\phi_N})^2\,, \tag{2.92}$$

the mentioned second sheet is defined, for a given cm energy satisfying $s_0^{(n+1)} >\mathrm{Re}\{s\} > s_0^{(n)}$, as $\xi_i = 1$ for $i = 1, 2, \ldots, n$ and $\xi_i = 0$ for $i > n$. On the other hand, for each pole singularity located at the position $s_P = (M - i\Gamma/2)^2$, we identify the couplings of the associated resonance to the channels $i$ and $j$ by means of the residue of the $T$-matrix (see Eq. (2.44) and the related discussion),

$$\begin{aligned} T_{ij}(s) &\approx \frac{g_i g_j}{s - s_P}, \ s \approx s_P \\ g_i g_j &= \mathrm{Res}\,[T_{ij}; s_P] \end{aligned} \tag{2.93}$$

either for a pole on the physical or unphysical sheet. The residue can be numerically computed by means of an integral along a circle of radius $\rho$ enclosing $s_P$:

$$\mathrm{Res}\left[T_{ij};s_P\right] = \frac{1}{2\pi i}\int_0^{2\pi} \mathrm{d}\theta\, T_{ij}(s_P+\rho e^{i\theta})i\rho e^{i\theta}. \tag{2.94}$$

It should be noted that some caution is needed, since $\rho$ should be chosen small enough to avoid including further singularities different to $s_P$ inside the contour.

In the following chapter we shall focus on the kernel potentials that will model the low energy $S$-wave interaction of the degrees of freedom. These will be chosen on the light of the symmetries of the underlying theory, QCD.

### 2.5.1 Finite volume

In hadron spectroscopy, LQCD is playing a very important role [70, 158, 159]. The path integral formulation of QCD on Euclidean $\mathbb{R}^4$ space-time is numerically evaluated, replacing the latter by a discretized lattice of points [160], that is further bounded to a finite volume $V \times T \in \mathbb{R}^3 \times \mathbb{R}$.

The properties of hadrons, associated to QCD one-particle eigenstates,

$$\mathbf{H}_{\mathrm{QCD}}\left|m_i,\vec{p};\sigma\right\rangle = E_{\vec{p}}^{\sigma,i}\left|m_i,\vec{p};\sigma\right\rangle \tag{2.95}$$

are extracted from Euclidean correlation functions [159] computed on the lattice, thanks to the behaviour of the correlator at large time separations,

$$\begin{aligned}\int \mathrm{d}^3x\, e^{-i\vec{p}\vec{x}}\left\langle 0\right| O^\sigma(x)\, O^\sigma(0)^\dagger \left|0\right\rangle \propto \sum_i |\alpha_i|^2\frac{e^{-E_{\vec{p}}^{\sigma,i}|x_0|}}{2E_{\vec{p}}^{\sigma,i}}&\\ +\,\mathcal{O}\left[\text{two-particle eigenstates}\right]+\dots&\end{aligned} \tag{2.96}$$

The correlation functions are built out from operators $O^\sigma(x)$ with definite quantum numbers "$\sigma$" on the Heisenberg representation,[7] $O^\sigma(x) = e^{\mathbf{H}_{\mathrm{QCD}}|x_0|-i\mathbf{P}x}O(0)e^{-\mathbf{H}_{\mathrm{QCD}}|x_0|+i\mathbf{P}x}$. They are often constructed in a way such that their overlap ($\alpha_i$) with the desired QCD eigenstate $\left|m_i,\vec{p};\sigma\right\rangle$ is maximal, since as shown in Eq. (2.96), in principle one should expect contributions coming from all the QCD eigenstates allowed by the quantum numbers at stake.

The case of resonant unstable states cannot be treated as illustrated in Eq. (2.96) since they appear as poles on the unphysical sheet of the scattering amplitudes. Ideally, one probably would like to have a way to access the scattering amplitudes *via* LQCD. Unfortunately, it is not possible to obtain *directly* this information using LQCD computations: on the Euclidean lattice there is no difference between $|\mathrm{in}\rangle$ and $|\mathrm{out}\rangle$ states, and the matrix elements (2.1), (2.14) are real valued.[8] Therefore, using lattice correlation functions it is not possible to directly detect changes in the amplitude phase due to the interaction. This result is known as the Maiani-Testa theorem [161].

Instead, the information on these states, and on scattering in general, should be obtained from the dependence of the energy spectrum of eigenstates on the size of the finite

---

[7] We recall that Heisenberg representation describes the time evolution in the Minkowski space of an operator $\phi$ driven by a time independent Hamiltonian $H = H_0 + H_I$ as $\phi_H(t) = e^{iHt}\phi e^{-iHt}$.

[8] There is no such concept of "asymptotic state" in a confined space-time.

volume $V$, as well as the difference with the free (noninteracting two particle) spectrum. This approach was proposed by Lüscher in 1985-1986 [162–164] in the context of non-relativistic elastic scattering of two particles. Essentially, it establishes a relation between the interacting energies $E_{\vec{p}}(L)$ and the scattering phase shifts in a cubic volume $V = L^3$ configuration with periodic field boundary conditions. This approach, as well as its extensions and generalizations, has been widely used in the recent LQCD analysis of hadron systems.

In our case, in many situations we will use as input the lattice information on the volume dependence, $E_{\vec{p}}(L)$, obtained for different two-meson systems, with the purpose of learning about their properties and constrain the two-body interaction, $V(s)$. The LQCD results are subject to a series of artifacts (unphysical pion masses, finite lattice spacing, *etc...*) which arise during their technical implementation. They vary from one study to another, to make profit from the LQCD input it is necessary to adapt the unitary approach discussed in the previous section, and try to implement the lattice characteristics. We highlight in what follows the most important points which are common to all lattice studies.

- In general, the simulations can be performed in one or several volumes with different geometry and boundary conditions. However, in this thesis we will always have spatial cubic isotropic lattices, which gives rise to volumes of side length $L$ and periodic boundary conditions.

- Lorentz invariance under space-time transformations is only recovered in the continuum limit. The lattice spacing of the spatial coordinates, $a$, restricts the maximum momentum available to the Brillouin zone $p_i < \pi/a$, introducing an ultraviolet cut-off. The symmetry under continuous spatial $O(3)$ rotations is reduced to the set of discrete rotations of the cubic point group $O_h$. In particular, the irreducible representation that corresponds to $S$-wave is the one denoted as $\mathrm{A}_1^+$, which also comprises $D$-waves [164]. Nevertheless, we shall neglect the mixing between $S$- and with $D$-waves when considering finite volume results from the $\mathrm{A}_1^+$ sector.

- The practical lattice implementations might involve unphysical hadron masses and energy-momentum dispersion relations, therefore, in those cases we will consistently implement the same kinematic conditions. Some of these effects may be due to the use of finite volumes, finite lattice sizes and unphysical quark masses. The LQCD simulation of physical $u$ and $d$ quarks is very demanding from the computational point of view [165].

- The periodic boundary conditions introduce a maximal resolution of the possible three-momenta configuration of the states. The three-momentum states are quantized as $\vec{q}_{\vec{n}} = (2\pi/L) \times \vec{n}$, $\vec{n} \in \mathbb{Z}^3$ [160, 166].

We extend the unitarized $T$-matrix scheme, presented in previous sections, to finite volumes implementing periodic boundary conditions [41, 167]. In this way, we would directly compare with the LQCD results. For simplicity, we will first consider a single channel case. The generalization to coupled channels is straightforward. The finite volume $T$-matrix, $\widetilde{T}(s, L)$, can be employed to determine the discrete spectrum of eigenenergies $s^* = (E^*)^2$, $s^* \in \mathbb{R}$:

$$\left[\widetilde{T}\left((E^*)^2, L\right)\right]^{-1} = \widetilde{V}^{-1}\left((E^*)^2, L\right) - \widetilde{G}^{(\mathrm{R})}\left((E^*)^2, L\right) = 0 \tag{2.97}$$

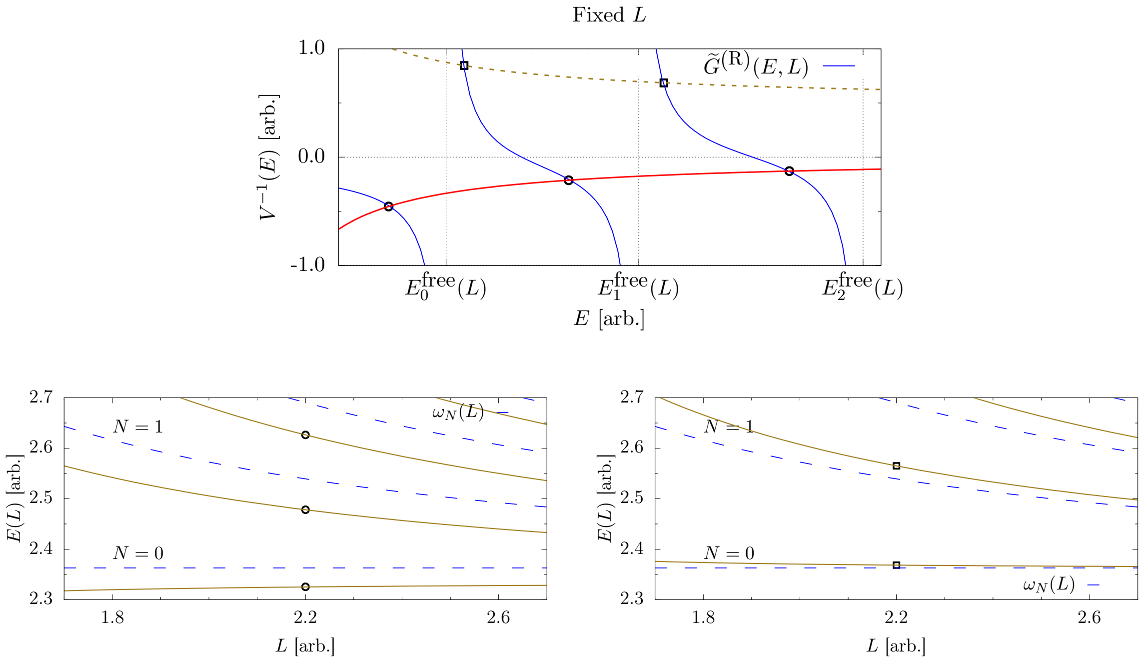

**Figure 2.6:** Example of the energy levels solution of $\widetilde{T}^{-1}(E,L) = 0$ (Eq. (2.97)) using the finite volume loop function of Eq. (2.100). In the top panel, the energy dependence of $\widetilde{G}^{(\mathrm{R})}(E,L)$ for a fixed box size is shown in blue—note how the latter is made up of a sum of poles (2.100) located at the free energies $E_N^{\mathrm{free}}(L)$—together with two cases of elastic repulsive (dashed-green) and attractive (solid-red lines) interaction potential $V$. Therein, black circles (squares) correspond to the eigenenergies solution of (2.97), in the attractive (repulsive) case. In the bottom left (right) panels, the volume dependence of the spectrum of eigenenergies for an attractive (repulsive) case is shown. The points correspond to the fixed volume solutions of the upper plot. Note how the interaction shifts the energy levels towards smaller or larger energies compared to the noninteracting ones (blue dashed lines).

where the difference with respect the on-shell Bethe-Salpeter equation (see Eqs. (2.85) and (2.86)) is in the three-momentum integral, that must be replaced by discrete sums over the allowed momenta,

$$\int_{\mathbb{R}^3} \frac{\mathrm{d}^3 q}{(2\pi)^3} \to \sum_{\vec{n}\in\mathbb{Z}^3} \frac{1}{L^3}. \tag{2.98}$$

For 2PI amplitudes not involving loops, the finite box corrections to the infinite volume potentials $V$ are exponentially suppressed [162], and will not be considered in this work. On the other hand, as already mentioned, we will take into account the unphysical lattice meson masses when solving the energy levels from Eq. (2.97).

The eigenenergies associated to the allowed discrete two-meson "scattering states" in the finite box are obtained from the singularities of $\widetilde{T}$, zeros of $\widetilde{T}^{-1}$, from Eq. (2.97). Let us introduce here the cm *free energies*,

$$E_{\vec{n}}^{\mathrm{free}}(L) = E_{\vec{n}}^{m}(L) + E_{\vec{n}}^{M}(L) = \sqrt{\vec{q}_{\vec{n}}^{\,2} + m^2} + \sqrt{\vec{q}_{\vec{n}}^{\,2} + M^2}. \tag{2.99}$$

The dependence on the square of the three-momentum in Eq. (2.99) allows us to label the free energies by means of their associated integer magnitude number $\mathfrak{m} \equiv \vec{n}^2 =$

$|\vec{q}_{\vec{n}}|^2 L^2/(4\pi^2)$. Let us denote the set of values of $\mathfrak{m}$ as $\mathbb{M}$. We realize that each value of $\mathfrak{m} \in \mathbb{M}$ will have a different associated multiplicity, $\mathcal{M}(\mathfrak{m})$, *i.e.*, a different number of $\vec{n}$ configurations leading to the same $\mathfrak{m}$ (for further details on this issue see, *e.g.*, Ref. [168]).[9] Note that not all values of $\mathfrak{m}$ are allowed, thus for instance the multiplicity of $\mathfrak{m} = 7$ is zero. With this information, the UV renormalized finite volume version of the loop function (2.78) can be obtained through the replacement (2.98) as the sum,

$$\widetilde{G}^{(\mathrm{R})}(s = E^2, L) = \sum_{\mathfrak{m} \in \mathbb{M}}^{\mathfrak{m}_{\max}} \frac{\mathcal{M}(\mathfrak{m})}{L^3} \frac{E^{\mathrm{free}}_{\mathfrak{m}}(L)}{2E^m_{\mathfrak{m}}(L) E^M_{\mathfrak{m}}(L)} \frac{1}{E^2 - \left(E^{\mathrm{free}}_{\mathfrak{m}}(L)\right)^2}. \tag{2.100}$$

The upper value of the sum is needed to render finite the loop function. It would correspond to the use of a hard UV cutoff in the momentum integration of the loop function in Eq. (2.78) for infinite volume. The finite volume loop function can be renormalized using different procedures, as we will see later.

From Eq. (2.100), we learn that in the limit of vanishing interaction, $\widetilde{V} \to 0$, we can interpret the $\widetilde{T}$ singularities satisfying $\widetilde{V}^{-1}(E^*, L) = \widetilde{G}(E^*, L)$, as the noninteracting eigenenergies. For each value of $L$, we expect a tower of energies $E^* = E^{\mathrm{free}}_{\mathfrak{m}}$ satisfying the condition above. The interaction ($V \neq 0$) will hence deviate the eigenenergies $E^*$ from the values $E^{\mathrm{free}}_{\mathfrak{m}}$. On the upper panel of Fig. 2.6, we show (blue solid lines) the finite volume loop function for a fixed volume size. Two cases of an attractive and repulsive interaction are shown, and the associated eigenenergies solution of (2.97) are depicted as black circles and squares, respectively. On the lower panels, the energy levels obtained in the two sample cases of interaction are illustrated; we can see the effect of the interaction on the shift of the solid lines associated to the volume dependence of the eigenvalues with respect to the free energy levels (dashed blue lines in the plots).

Note that, neglecting finite volume effects in the potential $V^{-1}$, one obtains the infinite volume $T$-matrix precisely for the eigenenergies, $E^*$, found in the LQCD simulation—carried out for the volume $L$—since they satisfy $V^{-1}(E^*) = \widetilde{G}^{(\mathrm{R})}(E^*, L)$, and therefore

$$T^{-1}(E^*) = \widetilde{G}^{(\mathrm{R})}(E^*, L) - G^{(\mathrm{R})}(E^*). \tag{2.101}$$

In the above equation, the meson masses correspond to those found in the LQCD simulation. The difference $\widetilde{G}^{(\mathrm{R})}(E^*, L) - G^{(\mathrm{R})}(E^*)$ is related with the Luscher $Z_{00}$ function [163], as it was shown in Ref. [167] (see also Ref. [169]). In addition, $T^{-1}(E^*)$ can be used to obtain the cm two-meson phase shifts.

As we have seen, the lattice input can be used to determine the interaction $V$. This might, in turn, imply that the finite volume and discretization effects will be propagated into the low energy parameters entering in the kernel potentials. Henceforth, we shall keep in mind this issue in some of the future chapters when interpreting the corresponding results.

---

[9] Hence, for example, $\mathcal{M}(0) = 1$, $\mathcal{M}(1) = 6$, $\mathcal{M}(2) = 12$, *etc...* For $\vec{n}^2 = 2$, one has $(\pm1, \pm1, 0)$, $(\pm1, 0, \pm1)$, $(0, \pm1, \pm1)$ which gives rise to 12 different momenta.

# Chapter 3

# INTERACTIONS

## 3.1 Preliminary remarks

In the previous chapter we have presented the formalism to describe the interaction of multiple two-meson channels in a way consistent with the constraints of exact two-body unitarity, and the low energy analytic structure of the scattering amplitudes. The nonperturbative $T$-matrix was obtained using kernel potentials for the two-meson degrees of freedom and performing a nonperturbative resummation to restore exact coupled-channels unitary. In the present chapter we will discuss how to incorporate the symmetry properties of QCD to the strong interacting meson system, and more specifically, how to employ the underlying QCD information to construct the 2PI amplitudes (potentials). The latter will be obtained from effective Lagrangians, that incorporate the imprints of the exact and approximate relevant QCD symmetries in a situation where the relevant degrees of freedom are mesons and not quark and gluons. To achieve this goal, we shall firstly focus in Sec. 3.2 on the symmetry properties of QCD in the heavy and light quark sectors. The light-quark chiral symmetry and its breaking pattern is essential; its role and the identification of each member of the octet of light pseudoscalar mesons as a pseudo Nambu-Goldstone boson (pNGB) will be discussed. On the other hand, heavy quark symmetries are very useful in the classification and understanding of the QCD spectrum in the heavy quark sectors. How to implement these symmetries on the meson degrees of freedom will be discussed in Section 3.3. Finally, in Section 3.4 we will present the interaction Lagrangians that will be later employed in Chapters 4, 5, 6, 8, and 9.

**Effective field theory.** The concept of effective theories [170] is a hot-topic, guiding an important subset of research efforts in particle physics in the last three decades, up to the present days. Even if each effective theory might be very different from the rest, all of them are based on the same idea: the existence of a relevant scale, $\Lambda$, which allows to construct an approximate (effective) theory in terms of some small physical quantity $q$. The applicability of the approximated theory will be restricted to the situations in which $q/\Lambda \lesssim 1$, and its usefulness lies on the fact that, in such regime, the details of the *real* theory at scales larger than $\Lambda$ are not essential. In that sense, it will involve the degrees of freedom which are relevant in its regime of applicability—if $\Lambda$ is an energy scale, one might neither explicitly include particles heavier than $\Lambda$ nor physics details at distances shorter than $1/\Lambda$. All these effects will be encoded in the low energy parameters of the effective theory. In the case of effective field theories [170], the goal is to construct the most general Lagrangian consistent with a given set of symmetries, as well as other general requirements [171–173].[1] In our case, we will deal with the low energy regime of the strong interactions. Hence, it will be necessary to impose the symmetries of QCD.

---

[1] It should provide the most general amplitude "consistent with analyticity, unitarity, cluster decomposition and the assumed symmetry principles" [173] (in a perturbative manner).

The number of possible terms in the effective Lagrangian is infinite since in general there will be infinite operators satisfying the requirements mentioned above. By assigning a *counting rule* to the different building blocks of the Lagrangian, these pieces are organized in terms of their contributions to the scattering amplitudes of a particular topology by means of powers of $(q/\Lambda)^N$. Therefore, the observables computed perturbatively will be known at a determined level of precision, which may be improved by including more terms (higher order contributions $(q/\Lambda)^{N'}$, $N' > N$). Each new term in the Lagrangian will be accompanied, in general, by an undetermined coefficient, a Low Energy Constant (LEC), parametrizing our "ignorance" about the UV behaviour of the underlying (*real*) theory. As mentioned above, the LECs effectively incorporate effects from short distance physics and from heavier degrees of freedom that have been integrated out in the path integral. In $\chi$PT, the Weinberg's power counting [173] ensures that at a given order, provided one includes all the allowed operators, the field theory is renormalizable; the new ultraviolet divergences arising at higher orders can be absorbed by the new renormalized LECs. This is a general property of well-defined effective field theories [174]: they are renormalizable order by order, and renormalizability stems from the fact that one is considering all the necessary effective operator structures which provide the most general amplitude satisfying the demanded symmetry properties.

The contents of this chapter constitute a sequential exposition of the most relevant aspects behind the construction of the effective field Lagrangians that we will consider in the research applications. A more systematic and thorough review of the crucial features involving the light-quark symmetries of QCD may be found in the textbooks [175,176]. Concerning the construction of effective Lagrangians of QCD involving Goldstone boson degrees of freedom we quote the historical papers [177–179] as well as the reviews [180–182]. Finally, the heavy quark symmetries and their interplay with $\chi$Sym in the construction of effective Lagrangians can be found in Refs. [19,21,183–185].

## 3.2 Quantum Chromodynamics and its approximate symmetries

Quarks and gluons are the fundamental degrees of freedom of the strong interaction. QCD is a gauge theory invariant under local SU(3)—color—transformations of the quark and gluon fields. As already mentioned, one of the most relevant properties of QCD is the so-called *asymptotic freedom* and its implications on low energy perturbative calculations. We shall see how, nevertheless, it is possible to use QCD to learn about the nature of the strong dynamics at low energies by exploiting its approximate symmetries, as well as their breaking pattern.

Let us consider the term in the QCD Lagrangian density containing the quark fields $\psi_{\rm f}^{\rm c}$, with the index c and f labelling the three colors and six flavours respectively. It is convenient to gather the quark fields into color triplets $\psi_{\rm f} = (\psi_{\rm f}^1,\ \psi_{\rm f}^2,\ \psi_{\rm f}^3)^{\rm T}$, and furthermore, introduce additional notation to distinguish the light and heavy quark flavour sectors: $q_{\rm f} \equiv \psi_{\rm f}$ for ${\rm f} = u,\ d,\ s$ and $Q_{\rm f} \equiv \psi_{\rm f}$ for ${\rm f} = c,\ b,\ t$, with bare masses $m_{\rm f}$ and $M_{\rm f}$ in each case. The separation of the quarks into these two sectors may be justified by the existence of the scale $\Lambda_{\rm QCD}$ and the fact that the current quark masses satisfy $m_q < \Lambda_{\rm QCD} \ll m_Q$ [14]. In this context, the term of the QCD Lagrangian containing the fermion matter fields is,

$$\mathcal{L}^{\text{QCD}} = \mathcal{L}^{\text{QCD}}_{\text{light}} + \mathcal{L}^{\text{QCD}}_{\text{heavy}} \tag{3.1}$$

$$= \sum_{\text{f}=u,d,s} \bar{q}_{\text{f}} \left(i\not{D} - m_{\text{f}}\right) q_{\text{f}} + \sum_{\text{f}=c,b,t} \bar{Q}_{\text{f}} \left(i\not{D} - M_{\text{f}}\right) Q_{\text{f}}. \tag{3.2}$$

The covariant derivative, $D_\mu$, is a matrix in color space

$$D_\mu = \partial_\mu + ig\text{A}_\mu(x), \tag{3.3}$$

with $\text{A}_\mu(x) = \sum_{i=1}^{8} A^i_\mu(x) T^i$, where $T^i$ are the eight generators of SU(3) acting in the color space—they are traceless and satisfy $[T^a, T^b] = i\sum_{j=1}^{8} f_{abj} T^j$, with $f_{abc}$ the structure constants of the SU(3) Lie algebra. The constant $g$ is the gauge coupling that defines the strong coupling constant $\alpha_s = g^2/4\pi$. The covariant derivative contains the gluon fields $A^i_\mu(x)$, ensuring the invariance under local color SU(3) transformations, $U_{\text{c}}(x) \in \text{SU(3)}$ (c),

$$\psi_{\text{f}}(x) \underset{\text{c}}{\rightarrow} U_{\text{c}}(x)\,\psi_{\text{f}}(x) = \exp\left(-i\sum_{j=1}^{8} \alpha^j_{\text{c}}(x) T^j_{\text{c}}\right)\psi_{\text{f}}(x), \tag{3.4}$$

$$\text{A}_\mu(x) \underset{\text{c}}{\rightarrow} U_{\text{c}}(x)\,\text{A}_\mu(x)\,U^{-1}_{\text{c}}(x) + \frac{i}{g}\left(\partial_\mu U_{\text{c}}(x)\right) U^{-1}_{\text{c}}(x), \tag{3.5}$$

$$D_\mu\psi_{\text{f}}(x) \underset{\text{c}}{\rightarrow} U_{\text{c}}(x)\,D_\mu\psi_{\text{f}}(x). \tag{3.6}$$

Note that in Eq. (3.2) we are omitting the gauge fixing and kinetic gluon terms. The latter is $-\text{Tr}(\text{F}^{\mu\nu}\text{F}_{\mu\nu})/2$, with

$$\text{F}^{\mu\nu} = \partial^\mu\text{A}^\nu - \partial^\nu\text{A}^\mu + ig\left[\text{A}^\mu, \text{A}^\nu\right], \tag{3.7}$$

the gluon gauge field strength tensor. Even if it is not possible to use QCD to describe multi-quark systems involving low momentum transfers, the study of its properties in certain limits is extremely useful. Here we will focus on two limits which involve the two separate terms $\mathcal{L}^{\text{QCD}}_{\text{light}}$ and $\mathcal{L}^{\text{QCD}}_{\text{heavy}}$, namely, the limit of vanishing light quark masses $m_{\text{f}} \to 0$ and the limit of infinite heavy quark mass $M_{\text{f}} \to \infty$. The interest in these limiting cases—despite not being strictly realized in nature—is justified by the fact that the confinement scale, $\Lambda_{\text{QCD}}$, the energy scale associated to the nonperturbative phenomena in strong interactions, is much larger that the mass of any of the light quarks and, at the same time, much smaller than the mass of the heavy quarks. As a consequence, whenever we deal with the interaction of quarks at energies of the order $\Lambda_{\text{QCD}}$ one may consider the limits $m_i/\Lambda_{\text{QCD}} \to 0$ and $\Lambda_{\text{QCD}}/M_i \to 0$ to be a good approximation. In each of these limits, QCD exhibits different approximate symmetries. As we will see, they turn to be essential in the understanding of hadron systems at low and intermediate energies: Chiral and Heavy Quark symmetries.

**Chiral symmetry.** First, let us begin rewriting the QCD Lagrangian term containing only the light quark fields,

$$\mathcal{L}^{\text{QCD}}_{\text{light}} = \sum_{\text{f}=u,d,s} \bar{q}_{\text{f}} i\not{D} q_{\text{f}} - \sum_{\text{f}=u,d,s} \bar{q}_{\text{f}} m_{\text{f}} q_{\text{f}}, \tag{3.8}$$

in terms of the chiral projections $q_{\mathrm{f}^L_R} \equiv P^\chi_\mp q_\mathrm{f}$ and $\bar{q}_{\mathrm{f}^L_R} = \bar{q}_\mathrm{f} P^\chi_\pm$, where the projectors are given by

$$P^\chi_\pm = (1 \pm \gamma_5)/2. \tag{3.9}$$

The Lagrangian of Eq. (3.8) now reads

$$\begin{aligned}\mathcal{L}^{\mathrm{QCD}}_{\mathrm{light}} &= \sum_{\mathrm{f}=u,d,s} \left(\bar{q}_{\mathrm{f}L} i\not{D} q_{\mathrm{f}L} + \bar{q}_{\mathrm{f}R} i\not{D} q_{\mathrm{f}R}\right) - \sum_{\mathrm{f}=u,d,s} \left(\bar{q}_{\mathrm{f}L} m_\mathrm{f} q_{\mathrm{f}R} + \bar{q}_{\mathrm{f}R} m_\mathrm{f} q_{\mathrm{f}L}\right) \\ &= \bar{q}_L i\not{D} q_L + \bar{q}_R i\not{D} q_R - \left(\bar{q}_L \hat{m} q_R + \bar{q}_R \hat{m} q_L\right).\end{aligned} \tag{3.10}$$

We have introduced in Eq. (3.10) the notation in flavour space $q = (q_u, q_d, q_s)^\mathrm{T}$, for both left and right fields, and $\hat{m} = \mathrm{diag}(m_u, m_d, m_s)$. The QCD Lagrangian for the three lightest flavours in the massless limit reads,

$$\mathcal{L}^{\mathrm{QCD}}_0 = \bar{q}_L i\not{D} q_L + \bar{q}_R i\not{D} q_R. \tag{3.11}$$

The Lagrangians of Eqs. (3.2), (3.10) and (3.11) are invariant under local color transformations (see Eqs. (3.4), (3.5), (3.6)), parity (P)

$$\begin{aligned}\psi_\mathrm{f}(x^0, \vec{x}) &\underset{\mathrm{P}}{\rightarrow} \gamma^0 \psi_\mathrm{f}(x^0, -\vec{x}) \\ q_{f^L_R}(x^0, \vec{x}) &\underset{\mathrm{P}}{\rightarrow} \gamma^0 q_{f^R_L}(x^0, -\vec{x})\end{aligned} \tag{3.12}$$

and charge conjugation (C)

$$\begin{aligned}\psi_\mathrm{f}(x) &\underset{\mathrm{C}}{\rightarrow} i\gamma^2\gamma^0 \left[\bar{\psi}_\mathrm{f}(x)\right]^\mathrm{T} \text{ (same for } q_{\mathrm{f}L(R)}), \\ \bar{\psi}_\mathrm{f}(x) &\underset{\mathrm{C}}{\rightarrow} -\left[\psi_\mathrm{f}(x)\right]^\mathrm{T} i\gamma^2\gamma^0 \text{ (same for } \bar{q}_{\mathrm{f}L(R)}),\end{aligned} \tag{3.13}$$

transformations of the quark fields—"T" denotes transposition in Dirac space. Additionally, due to the absence of the mass term, the Lagrangian in Eq. (3.11) is invariant under independent global SU(3) transformations in flavour space of the chiral fields,

$$\begin{aligned}q_L &\xrightarrow[\mathrm{SU}(3)_L]{} Lq_L = \exp\left(-i\sum_{j=1}^{8} \alpha^j_L T^j\right) q_L \\ q_R &\xrightarrow[\mathrm{SU}(3)_R]{} Rq_R = \exp\left(-i\sum_{j=1}^{8} \alpha^j_R T^j\right) q_R.\end{aligned} \tag{3.14}$$

The latter group of transformations is known as the chiral group, which in tensor notation is denoted as $G = \mathrm{SU}(3)_L \otimes \mathrm{SU}(3)_R$. Therefore, if $g = (L, R) \in G$, the action of the chiral group on the chiral fields $(q_L, q_R)$ is simply $(Lq_L, Rq_R)$. We refer to the invariance of $\mathcal{L}^{\mathrm{QCD}}_{\mathrm{light}}$ in the limit of vanishing quark masses as the $\chi$Sym of QCD. The Lagrangian of Eq. (3.11) is also invariant under $U(1)$ transformations $\exp(-i\Theta_{L/R})$ of the left and right quark fields, satisfying $\Theta_L = \Theta_R$ and $\Theta_L = -\Theta_R$. The former transformation leads to the quark—or baryon—number conservation, while the latter is only a symmetry at the classical level, that is broken by the axial anomaly.

As already mentioned, $\chi$Sym is only approximate and it is *explicitly* broken by the quark masses,

$$\mathcal{L}^{\mathrm{QCD}}_{\mathrm{light}} \underset{G}{\rightarrow} \mathcal{L}^{\mathrm{QCD}}_{\mathrm{light}} - \left(\bar{q}_L \left(L^\dagger \hat{m} R - \hat{m}\right) q_R + \bar{q}_R \left(R^\dagger \hat{m} L - \hat{m}\right) q_L\right). \tag{3.15}$$

Nevertheless, it is interesting to note that in the of case equal quark masses $m_u = m_d = m_s \neq 0$, Eq. (3.15) tells us that there is still a symmetry if the transformation is chosen of the type $L = R = U$, with $U \in \mathrm{SU}(3)$. Such set of transformations $V \equiv (U, U)$ is called the group of vector transformations, $\mathrm{SU}(3)_V$, a subgroup of the chiral transformations $G$.

The rest of transformations in the chiral group $G$ are obtained introducing the axial transformations $A \equiv (-U, U)$, $\mathrm{SU}(3)_A$, for which $L = -R$. The axial together with the set of vector transformations lead to $(L, R) = (V - A) \oplus (V + A)$, or $G = \mathrm{SU}(3)_V \otimes \mathrm{SU}(3)_A$.

Thus, in the scenario of equal $u$, $d$ and $s$ masses, the invariance of Eq. (3.15) under the action of vector group will imply that hadrons could be organized as members of multiplets associated to irreducible representations of $\mathrm{SU}(3)_V$, with degenerate masses. This invariance of the strong interactions was proposed by Gell-Mann and Ne'eman in the famous eightfold way [186], promoting $SU(2)$ isospin symmetry to SU(3) in order to accommodate the strangeness quantum number. It works well in the case of the octet of lightest pseudoscalar mesons $\phi_m = \{\pi^\pm, K^\pm, \pi^0, \eta, K^0, \bar{K}^0\}$ and baryons $\phi_b = \{p, n, \Sigma^\pm, \Sigma^0, \Xi^-, \Xi^0, \Lambda\}$, and much better in the case of $SU(2)_V$ or isospin. The consideration of infinitesimal chiral transformations in the expressions of Eq. (3.14) leads to the following transformation properties under vector and axial flavour rotations,

$$\begin{aligned} q \xrightarrow[\mathrm{SU}(3)_V]{} Vq &= \exp\left(-i\sum_{j=1}^{8} \alpha_V^j T^j\right) q \\ q \xrightarrow[\mathrm{SU}(3)_A]{} Aq &= \exp\left(-i\sum_{j=1}^{8} \alpha_A^j T^j \gamma_5\right) q, \end{aligned} \tag{3.16}$$

where the different parameters are related by $\alpha^j_{\substack{V\\A}} = (\alpha_R \pm \alpha_L)/2$. Unlike the case of vector transformations, $\mathcal{L}^{\mathrm{QCD}}_{\mathrm{light}}$ is only invariant under $\mathrm{SU}(3)_A$ in the chiral limit, *i.e.*, when all quark are massless. The Noether charges associated to the conservation of axial and vector transformations (3.16) are

$$Q^j_A(x^0) = \int_{\mathbb{R}^3} d^3x \bar{q}(x) T^j \gamma^0 \gamma_5 q(x), \ (j = 1, 2, \ldots, 8) \tag{3.17}$$

$$Q^j_V(x^0) = \int_{\mathbb{R}^3} d^3x \bar{q}(x) T^j \gamma^0 q(x), \ (j = 1, 2, \ldots, 8). \tag{3.18}$$

The eight axial and vector charge operators transform as pseudoscalar and scalar objects under parity (3.12) and, as a consequence, the action of the axial charges onto QCD energy eigenstates, $H^0_{\mathrm{QCD}} |\alpha, \eta_{\mathrm{P}}\rangle = E_\alpha |\alpha, \eta_{\mathrm{P}}\rangle$ (with $\eta_{\mathrm{P}}$ the parity quantum number of the state), will turn negative parity eigenstates into positive ones and *viceversa*:

$$\begin{aligned} |\alpha, j, \eta'_P\rangle &\equiv Q^j_A |\alpha, \eta_P\rangle \\ \hat{\mathrm{P}} |\alpha, j, \eta'_P\rangle &= \hat{\mathrm{P}} Q^j_A \hat{\mathrm{P}}^{-1} \hat{\mathrm{P}} |\alpha, \eta_P\rangle \\ &= -\eta_{\mathrm{P}} |\alpha, j, \eta'_P\rangle \end{aligned}$$

where $\hat{\mathrm{P}}$ denotes the parity operator and the relation $\dot{Q}^a_A = [H^0_{\mathrm{QCD}}, Q^a_A] = 0$ would ensure the degeneracy of the states. The (Wigner-Weyl) realization of $\chi$Sym in nature, even if approximate, would produce a *parity doubling* of the spectrum, *i.e.*, there would be a spectrum of degenerate SU(3) multiplets, each with two versions showing opposite parities. In contrast, this is not the case of the observed approximate $\mathrm{SU}(3)_V$ multiplets

$\phi_m(\eta_{\rm P} = -1)$ and $\phi_b(\eta_{\rm P} = +1)$, there is no trace of such degenerate chiral partners with parity $\eta'_{\rm P} = -\eta_{\rm P}$.

On the other hand, if we assume that the (approximate) $\chi$Sym of the strong interaction is dynamically broken into $\text{SU}(3)_V$, according to the Goldstone theorem [187,188] for each of the eight broken generators of $\text{SU}(3)_A$ there will be a massless spin zero boson, the so-called Nambu-Goldstone bosons [187,189,190] denoted here as $\xi_j(x)$, $j = 1, 2, ..., 8$. Since the set of fields will still be invariant under vector transformations, they will fulfil an octet representation of $\text{SU}(3)_V$. The quantum numbers of such bosons are obtained from the transformation properties of $Q_A^j(x)$, and therefore, they have negative parity.

Due to the explicit breaking of $\chi$Sym (3.15), the Nambu-Goldstone bosons acquire finite masses. Additionally, such breaking in the quark masses also introduces differences between the masses of the members of the $\text{SU}(3)_V$ multiplets. Nevertheless, if the breaking is small, in that case one would expect that the mass of these bosons would be smaller than the rest of the hadron spectrum. This picture gives an explanation to the lightness of the triplet of pions (in the case of $\text{SU}(2)_V$) or the octet of pseudoscalars $\phi_m$ (in the case of $\text{SU}(3)_V$) compared to the rest of hadrons. Then, it might seem reasonable to identify the octet of pseudoscalars $\phi_m$ with the mentioned massive modes or pNGBs.

There is no need to know how QCD undergoes the symmetry breaking in order to appreciate the consequences of the existence of these approximate massless modes in the low energy regime of QCD. All of them are encoded in the possible effective Lagrangians valid at low energies made out with the pNGB, plus other additional degrees of freedom relevant in each case.

**Heavy quark symmetries.** The symmetries arising in hadron systems containing heavy quarks can be also inferred from QCD. For a hadron system containing heavy quarks, these will manifest differently depending on the number and type of heavy quarks present. Let us pay attention to mesons containing only one heavy quark $Q$ (heavy-light mesons).

Inside a heavy-light meson $Q\bar{q}$, the heavy quark $Q$ interacting with the light degrees of freedom, the *brown muck*, exchanges momenta much smaller than its mass $m_Q$. In first approximation, the heavy quark momentum $p_Q^\mu$ is close to $m_Q v^\mu$,

$$p_Q^\mu = m_Q v^\mu + k^\mu, \tag{3.19}$$

where $v^\mu$ is the four velocity ($v^2 = 1$) of the hadron ($p_H^\mu = m_H v^\mu$, with $p_H$ and $m_H$ the hadron momentum and mass). The "residual" momentum $k$ is of order $\Lambda_{\rm QCD}$.

In the $m_Q \to \infty$ limit, the heavy quark is on-shell, since $v \cdot k \sim \mathcal{O}(\Lambda_{\rm QCD})$ and $p_Q^2 \sim m_Q^2(1 + \mathcal{O}(\Lambda_{\rm QCD})/m_Q)$, hence, the heavy quark and the hadron that contains it have the same velocity. In this heavy quark limit, the strong interaction effects—encoded in the residual momentum $k$—would not change the four velocity. This is the velocity superselection rule, which requires dealing with the velocity variable as an additional fundamental parameter.

To deduce the further implications of the heavy quark limit it is very useful to construct an effective Lagrangian for the heavy quark $Q_v$ with four-velocity $v$. This is achieved encoding the strong interaction effects in an expansion in powers of $1/m_Q$ and the strong coupling $\alpha_s(m_Q)$. The applicability of the effective interaction will thus be constrained to small residual momenta $k$ compared with the heavy quark mass scale: $k/m_Q \ll 1$. This is the reason why in the case of heavy-light mesons, such as $D$ and $B$ mesons, the leading corrections due to the finite $c$ and $b$ quark masses are of the order of $\Lambda_{\rm QCD}/m_c$ and $\Lambda_{\rm QCD}/m_b$ in each case.

Let us consider the heavy quark field $Q(x)$ with an almost on-shell momentum $p_Q = m_Q v + k$ inside of a heavy-light meson. From the QCD Lagrangian (3.2) we have

$$\mathcal{L}^{Q}_{\rm QCD} = \bar{Q}\left(i\not{D} - m_Q\right)Q. \tag{3.20}$$

Its free propagator is $i(\not{p}_Q + m_Q)/(p_Q^2 - m_Q^2 + i\epsilon)$, which, in the heavy quark limit, simplifies to $i(\mathbb{I} + \not{v})/(2vk + i\epsilon)$. The operators $\Pi_\pm \equiv (\mathbb{I} \pm \not{v})/2$ behave like projectors, $\Pi_\pm\Pi_\pm = \Pi_\pm$ and $\Pi_\pm\Pi_\mp = 0$. In the $Q$ rest frame, $v = (1, \vec{0})$, and we have $\Pi_+ Q = 1/2\,\mathrm{diag}(1,1,0,0)\,Q$, and hence $\Pi_+$ projects the Dirac four-spinor $Q$ into the particle bispinor. It is convenient to introduce the components,

$$Q_v(x) = e^{im_Q vx}\,\Pi_+\,Q(x) \tag{3.21}$$

$$\mathfrak{Q}_v(x) = e^{im_Q vx}\,\Pi_-\,Q(x) \tag{3.22}$$

So that $Q(x) = e^{-im_Q vx}[Q_v(x) + \mathfrak{Q}_v(x)]$. The purpose of the exponential factors is to extract the explicit $m_Q$ dependence of the fields. If we use Eqs. (3.21) and (3.22) to rewrite the QCD Lagrangian (3.20) we find,

$$\begin{aligned}\mathcal{L}^{Q}_{\rm QCD}(x) = {} & \bar{Q}_v(x)\ [iv\cdot D]\ Q_v(x) \\ & - \bar{\mathfrak{Q}}_v(x)\ [iv\cdot D]\ \mathfrak{Q}_v(x) - 2m_Q\bar{\mathfrak{Q}}_v(x)\mathfrak{Q}_v(x) \\ & + \bar{Q}_v(x)\left[i\not{D}\right]\mathfrak{Q}_v(x) + \bar{\mathfrak{Q}}_v(x)\left[i\not{D}\right]Q_v(x).\end{aligned} \tag{3.23}$$

We see in Eq. (3.23) that the field $Q_v(x)$ describes massless degrees of freedom while $\mathfrak{Q}_v(x)$ is related to fluctuations with twice the heavy quark mass. The latter heavy degrees of freedom must be removed. Both fields are coupled in the last two terms, which describe the creation or annihilation of heavy quark–antiquark pairs. The virtual quantum fluctuation can only propagate over a short distance $\Delta x \sim 1/m_Q$ [185]. We see that the first term is invariant under heavy quark spin rotations. In a general frame one can always define generators of spin symmetry in terms of a set of three orthonormal vectors orthogonal to $v$ (see, *e.g.* Ref. [185]), still finding that the first term of Eq. (3.23) is invariant under spin rotations. Additionally, this term in Eq. (3.23) has no explicit dependence on the heavy quark mass, and it provides the same free propagator $i(\mathbb{I} + \not{v})/(2vk + i\epsilon)$ which would be obtained from the relativistic one in the heavy quark limit. The invariance under $SU(2)_S$ rotations of the heavy quark spin is called HQSS of QCD, while the independence on $m_Q$ is referred to as HQFS.

The heavy degrees of freedom represented by $\mathfrak{Q}_v(x)$ can be integrated out using the equations of motion of QCD [21, 191],

$$\left(i\not{D} - m_Q\right)Q(x) = 0 \tag{3.24}$$

$$\begin{aligned}\left(i\not{D} - m_Q\right)Q(x) &= \left(i\not{D} - m_Q\right)e^{-im_Q\,vx}\left[Q_v(x) + \mathfrak{Q}_v(x)\right] \\ &= e^{-im_Q\,vx}\left(i\not{D} - 2m_Q\Pi_-\right)\left[Q_v(x) + \mathfrak{Q}_v(x)\right] \\ &= e^{-im_Q\,vx}\left(i\not{D}Q_v(x) + \left[i\not{D} - 2m_Q\right]\mathfrak{Q}_v(x)\right).\end{aligned} \tag{3.25}$$

From where it follows,

$$\mathfrak{Q}_v(x) = \left[2m_Q - i\not{D}\right]^{-1}\, i\not{D}Q_v(x) \approx \frac{1}{2m_Q}\,i\not{D}Q_v(x) + \mathcal{O}\left[(1/2m_Q)^2\right]. \tag{3.26}$$

If we take Eq. (3.26) into account, we derive the subleading $1/m_Q$ terms—tree-level in $\alpha_s$—in Eq. (3.23) for the interaction of the $Q_v(x)$ field,

$$\mathcal{L}(x) = \bar{Q}_v(x)\ [iv \cdot D]\ Q_v(x) + \frac{1}{2m_Q}\bar{Q}_v(x)\left[i\not{D}i\not{D}\right] Q_v(x) + \mathcal{O}\left[(1/2m_Q)^2\right]. \tag{3.27}$$

Now, we recall the definition of the covariant derivative in terms of the gluon fields $A^a_\mu(x)$, which allows us expressing $\not{D}\not{D}$ as follows

$$\not{D}\not{D} = D_\mu D^\mu + \frac{[\gamma^\mu, \gamma^\nu]}{4} ig\mathrm{F}_{\mu\nu} \equiv D_\mu D^\mu + g\,\frac{\sigma^{\mu\nu}}{2}\,\mathrm{F}_{\mu\nu} \tag{3.28}$$

where $\mathrm{F}^{\mu\nu}$ denotes the gluon field strength tensor (see Eq. (3.7)). The subleading $1/m_Q$ interaction terms in the Lagrangian (3.27) break HQFS, but, from the two structures stemming by the terms in Eq. (3.28) only the second one breaks the invariance under spin rotations in Dirac space. The light degrees of freedom are blind to the flavour (mass) and spin orientation of the heavy quark. They only experience its color field, which extends over large distances because of confinement.

We shall make use of these two approximate symmetries arising in heavy-light systems. In the following sections we will concentrate on the effective interactions involving heavy-light mesons and pNGBs, which have been employed throughout the different chapters of this thesis.

## 3.3 The building blocks

### 3.3.1 The Nambu-Goldstone bosons

As we have seen in Sec. 3.2, the pNGBs are associated to the dynamical symmetry breaking pattern

$$G = L \otimes R \to H = V \otimes V \tag{3.29}$$

where $G$ denotes the group of chiral transformations, and $V$ the subgroup of vector transformations. The set of Goldstone fields is introduced through the field multiplet $\xi(x)$, that in each point $x$ is a real vector in a space of dimension $n = n_G - n_V$. To build effective Lagrangians in terms of the Goldstone degrees of freedom, it is necessary to know the transformation properties of the latter under the symmetry groups. For that, a mapping $\xi' = f(g, \xi)$ relating the fields with the group elements $g \in G$ is necessary. Besides, in order to be a representation of the group $G$ the mapping should satisfy $f(gg', \xi) = f(g, f(g', \xi))$. The symmetry breaking pattern (3.29), states that the vacuum is invariant under the action of the elements of $H$. If the vacuum is identified with the field configuration $\xi = O$, the mapping should be such that $O = f(h, O)$, with $h \in H$. It will also satisfy $f(g, O) = f(gh, O)$, and therefore, it will describe the transformation properties of the Goldstone fields by group elements defined on the quotient $G/H$, *i.e.*, the set of left cosets: $G/H = \{\{gh|h \in H\}|g \in G\}$. That this mapping indeed exists, it is an isomorphism and it is unique, has been discussed in detail in the literature [171, 172], here we will simply explore the implications.

The isomorphic relation allows to identify the Goldstone fields with a group element. Choosing a representative group element, $\mathfrak{g} = (\mathcal{L}, \mathcal{R}) \in G$, of each left coset $\{\mathfrak{g}h|h \in H\} \in$

$G/H$, we would have the transformation properties,

$$\xi = f(\mathfrak{g}h, O) \tag{3.30}$$
$$\xi' = f(g,\xi) = f(g\mathfrak{g}h, O). \tag{3.31}$$

In this context, we can always arrange the left coset $\mathfrak{g}h$ as (the following equalities are understood $\forall \mathcal{V} \in V$)

$$\begin{aligned}\mathfrak{g} \circ h &= (\mathcal{L}\mathcal{V}, \mathcal{R}\mathcal{V}),\\ &= (\mathbb{I}, \mathcal{R}\mathcal{L}^\dagger) \circ (\mathcal{L}\mathcal{V}, \mathcal{L}\mathcal{V}),\\ &= \underbrace{(\mathbb{I}, \mathcal{R}\mathcal{L}^\dagger)}_{\mathfrak{g}} \circ \underbrace{(\mathcal{V}, \mathcal{V})}_{h},\end{aligned} \tag{3.32}$$

note that alternatively one could have chosen the element $\mathfrak{g} = (\mathcal{L}\mathcal{R}^\dagger, \mathbb{I})$ as the representative of the left coset. The action of the chiral transformations on $\mathfrak{g}h$ is

$$\begin{aligned}g \circ (\mathfrak{g} \circ h) &= (L, R) \circ (\mathbb{I}, \mathcal{R}\mathcal{L}^\dagger) \circ (\mathcal{V}, \mathcal{V}),\\ &= (L, R\mathcal{R}\mathcal{L}^\dagger) \circ (\mathcal{V}, \mathcal{V}),\\ &= (\mathbb{I}, R\mathcal{R}\mathcal{L}^\dagger L^\dagger) \circ (L\mathcal{V}, L\mathcal{V}),\\ &= \underbrace{(\mathbb{I}, R\mathcal{R}\mathcal{L}^\dagger L^\dagger)}_{g\mathfrak{g}} \circ \underbrace{(\mathcal{V}, \mathcal{V})}_{h}.\end{aligned} \tag{3.33}$$

Finally, we arrive to the matrix relating the Goldstone fields and the left coset (Eqs. (3.30) and (3.32)) $U(x) = \mathcal{R}\mathcal{L}^\dagger(x)$, which should transform according to $U'(x) = RU(x)L^\dagger$ (Eqs. (3.31) and (3.33)).

As it is customary, the SU(3) field matrix $U(x)$ is parametrized by means of the generators of SU(3) in terms of the exponential mapping

$$U(x) := \exp\left(i\,\frac{\sum_{a=1}^{n} \xi_a(x) T^a}{F}\right) \tag{3.34}$$

$$= \exp\left[\frac{i}{F}\begin{pmatrix} \pi^0 + \frac{\eta}{\sqrt{3}} & \sqrt{2}\pi^+ & \sqrt{2}K^+ \\ \sqrt{2}\pi^- & -\pi^0 + \frac{\eta}{\sqrt{3}} & \sqrt{2}K^0 \\ \sqrt{2}K^- & \sqrt{2}\bar{K}^0 & -\frac{2}{\sqrt{3}}\eta \end{pmatrix}\right] \tag{3.35}$$

where $F$ is the pion decay constant in the three-flavour chiral limit. For convenience, we will denote the matrix of pseudoscalar mesons in Eq. (3.35) as $\hat{\xi}(x) := \sum_a T_a \xi_a(x)$, hence,

$$\hat{\xi}(x) := \begin{pmatrix} \pi^0 + \frac{\eta}{\sqrt{3}} & \sqrt{2}\pi^+ & \sqrt{2}K^+ \\ \sqrt{2}\pi^- & -\pi^0 + \frac{\eta}{\sqrt{3}} & \sqrt{2}K^0 \\ \sqrt{2}K^- & \sqrt{2}\bar{K}^0 & -\frac{2}{\sqrt{3}}\eta \end{pmatrix}. \tag{3.36}$$

The realization of $G$ on the set of matrix fields (3.35) is conveniently described by the mapping

$$U'(x) = f\left(g, U(x)\right) = RU(x)L^\dagger,\ g = (L, R) \in G. \tag{3.37}$$

From Eq. (3.37) we see that the vacuum configuration should correspond to $\xi_j = \mathcal{O}_j = 0$, in order to have $\mathcal{O} = f[h, \mathcal{O}]$: $\mathbb{I} = f[h, \mathbb{I}] = V \mathbb{I} V^\dagger$. The realization of $G$ in terms of the fields $\xi_j$ is much more complicated, involving non-linear relations among them.

Note that the Goldstone fields are pseudoscalar fields, therefore, from Eq. (3.35) we can derive the action of a parity operation on $U$: $U \underset{\mathrm{P}}{\longrightarrow} U^\dagger$. On the other hand, charge conjugation implies $U \underset{\mathrm{C}}{\longrightarrow} U^{\mathrm{T}}$, where transposition should be understood in terms of the matrix expansion $\exp(X) = (\mathbb{I} + X + XX/2 + \dots)$. These properties are summarized here,

$$U(x) \underset{G}{\longrightarrow} R U(x) L^\dagger, \tag{3.38}$$

$$U(x) \underset{\mathrm{P}}{\longrightarrow} U^\dagger(x^0, -\vec{x}), \tag{3.39}$$

$$U(x) \underset{C}{\longrightarrow} U^{\mathrm{T}}(x). \tag{3.40}$$

We finally make explicit the convention between pNGBs particle and isospin states that will be used in the next chapters. We shall always—with the exception of Chapter 12—use the isospin convention

$$\begin{aligned} \bar{u} &= |1/2, -1/2\rangle \\ \bar{d} &= -|1/2, +1/2\rangle, \end{aligned} \tag{3.41}$$

which induces a minus sign between particle and antiparticle states in the following isospin multiplets $|\xi; I, I^3\rangle$:

$$\left|\pi^\pm\right\rangle = \mp \left|\pi; 1, \pm 1\right\rangle, \; \left|\pi^0\right\rangle = + \left|\pi; 1, 0\right\rangle. \tag{3.42}$$

$$\left|K^+\right\rangle = + \left|K; \frac{1}{2}, +\frac{1}{2}\right\rangle, \; \left|K^0\right\rangle = + \left|K; \frac{1}{2}, -\frac{1}{2}\right\rangle. \tag{3.43}$$

$$\left|\bar{K}^0\right\rangle = - \left|\bar{K}; \frac{1}{2}, +\frac{1}{2}\right\rangle, \; \left|K^-\right\rangle = + \left|\bar{K}; \frac{1}{2}, -\frac{1}{2}\right\rangle. \tag{3.44}$$

### 3.3.2 The heavy mesons

In section 3.2 we have introduced the two important symmetries that arise in heavy-light hadron systems when the heavy quark limit is considered: HQSS and HQFS. The case of charm and bottom mesons, which constitute the core of all the applications discussed in this thesis, is a very suitable scenario to learn about the consequences of these two approximate symmetries. For the charm sector, they may not be as good as in the case of the bottom one, since $\mathcal{O}(\Lambda_{\mathrm{QCD}}/m_Q)$ corrections are expected. HQSS predicts that for each $Q\bar{q}$ state with quantum numbers[2] $N^{2S+1}L_J$, there will be another one, $N^{2S'+1}L_{J'}$, approximately degenerated in mass,which is obtained by a flip of the spin state of the heavy quark: $\left|S_Q, S_Q^3\right\rangle \to \left|S_Q, -S_Q^3\right\rangle$. For that reason, since both the spin $S_Q = 1/2$ and total angular momentum $J$ are conserved quantities, the heavy mesons could be classified in degenerate doublets depending on the spin of the light degrees of freedom $j_{\bar{q}}$, satisfying $J = j_{\bar{q}} + S_Q$. Note that the spin-parity of the light degrees of freedom will be also

---

[2] Here we use the spectroscopic notation with $\vec{S} = \vec{S}_Q + \vec{S}_{\bar{q}}$ and $\vec{J} = \vec{L} + \vec{S}$, the total spin and angular momentum of the quark antiquark pair. In addition, $\vec{L}$ and $N$ refer to the orbital angular momentum and the radial excitation.

conserved. It is assumed that, as it is the case of CQM, the lowest excitations correspond to the smaller values of $L$. In this way, the $S$-wave states ($L = 0$) would form the lowest lying heavy-light HQSS doublets with quantum numbers $J^P = (0^-, 1^-)$—the parity is $P = \eta_Q \eta_{\bar{q}} (-1)^L = (-1)^{L+1}$ where the intrinsic parities $\eta_Q$ and $\eta_{\bar{q}}$ of the quark and antiquark are opposite $\eta_Q = -\eta_{\bar{q}}$. The spin-parity of the light degrees of freedom in this case are $j_{\bar{q}} = 1/2^-$, that correspond to those of a light antiquark orbiting in $S$-wave around the heavy quark. Thus, these $J^P = (0^-, 1^-)$ mesons are, in spectroscopic notation, the ${}^1S_0$ and ${}^3S_1$ states. The next excitation would correspond to $P$-wave ($L = 1$) states of positive parity: ${}^{2S+1}L_J = {}^3P_0$ and ${}^{2S+1}L_J = {}^3P_1$, that would form the doublet $J^P = (0^+, 1^+)$. The configuration of the light degrees of freedom are now $j_{\bar{q}}^P = 1/2^+$, obtained out of a light antiquark orbiting in $P$-wave around the heavy quark. In $P$-wave, the light degrees of freedom can also be $3/2^+$, that, when coupled with the spin of the heavy quark, give rise to another HQSS doublet $J^P = (2^+, 1^+)$, ${}^3P_2$ and ${}^3P_1$. This doublet is not degenerated with the previous $j_{\bar{q}}^P = 1/2^+$ doublet, since the light degrees of freedom configuration is different. Note, however, that HQSS is only an approximate symmetry, there will exist some mixing between the two $J^P = 1^+$ states.

We should consider the HQSS $Q\bar{q}$ doublets $(P, P^*)$ on the same footing. To achieve this, for instance in the case of $S$-wave mesons, we first introduce the field $H_a^{(Q)}$ [21, 183, 192],

$$H_a^{(Q)} = \frac{1+\not{v}}{2} \left( P_{a\,\mu}^{*(Q)} \gamma^\mu - P_a^{(Q)} \gamma_5 \right), \tag{3.45}$$

which combines the $\mathrm{SU}(3)_V$ multiplet of pseudoscalar heavy-meson fields

$$P_a^{(Q)} = \left( Q\bar{u}, Q\bar{d}, Q\bar{s} \right) \tag{3.46}$$

and their vector partners $P_a^{*(Q)}$, with the condition $v \cdot P_a^{*(Q)} = 0$. We recall that in the heavy quark limit, the projected field $Q_v(x)$ in Eq. (3.23) annihilates a heavy quark with velocity $v$. Hence, the fields (3.46) will consequently annihilate a heavy meson moving with a fixed four velocity $v$—we dropped the $v$ label in Eqs. (3.45) and (3.46) to alleviate notation, though, it must be understood to be there. Furthermore, as in the case of Eq. (3.23), we would like also to remove any trivial dependence on the heavy quark mass. The point is that the mass independence should be manifest on the matrix elements relating transitions between heavy meson states $|H\rangle = P_a^{(Q)\dagger} |0\rangle$. Given our relativistic normalization of one-particle states (see Eq. (2.9)) we would have

$$\langle 0| a_P(\vec{p}\,') a_P^\dagger(\vec{p}) |0\rangle = (2\pi)^3 (2p^0) \delta^3(\vec{p} - \vec{p}\,'), \tag{3.47}$$

where $a_P^{(\dagger)}$ denotes the Fock destruction (creation) operator of a given relativistic heavy meson field $P(x)$. In order to remove the mass dependence in Eq. (3.47)—encoded in $p^0 = \sqrt{\vec{p}^2 + m_H^2}$—we should consider the $P_a^{(Q)}$ fields in Eqs. (3.45) and (3.46) with a different normalization satisfying $a_P \sim \sqrt{m_H} a_H$ [21], such that it would give

$$\langle 0| a_H(\vec{p}\,') a_H^\dagger(\vec{p}) |0\rangle \xrightarrow[m_H \to \infty]{} (2\pi)^3 (2v^0) \delta^3(\vec{k} - \vec{k}\,') \tag{3.48}$$

where $k$ represents the $\mathcal{O}(\Lambda_{QCD})$ residual momentum introduced in Eq. (3.19). As a consequence of the different normalization, the heavy meson states in the effective theory will have dimensions $E^{-3/2}$. In addition, we recall the convention of Eq. (3.41), which induces a minus sign between the $D^+ \sim c\bar{d}$ (and $\bar{B}^0 \sim b\bar{d}$) particle and isospin doublets $|H; I, I^3\rangle$,

$$\begin{aligned} |D^+\rangle &= -\left|D; \frac{1}{2}, +\frac{1}{2}\right\rangle, \ |D^0\rangle = +\left|D; \frac{1}{2}, -\frac{1}{2}\right\rangle \\ |\bar{B}^0\rangle &= -\left|\bar{B}; \frac{1}{2}, +\frac{1}{2}\right\rangle, \ |B^-\rangle = +\left|\bar{B}; \frac{1}{2}, -\frac{1}{2}\right\rangle. \end{aligned} \tag{3.49}$$

On the other hand, within the HQSS formalism the even parity $Q\bar{q}$ states, associated to the $j^P_{\bar{q}} = 1/2^+$ HQSS doublet, are described by the matrix field $J^{(Q)}_a$ [193],

$$J^{(Q)}_a = \frac{1+\not{v}}{2}\left(Y^{*(Q)}_{a\,\mu}\gamma_5\gamma^\mu + Y^{(Q)}_a\right), \tag{3.50}$$

with $v^\mu Y^{*(Q)}_{a\,\mu} = 0$. The $Y_a$ and $Y^*_a$ fields respectively annihilate the $0^+$ and $1^+$ meson states belonging to the $j_{\bar{q}} = 1/2^+$ doublet.

Under a parity transformation we have

$$H^{(Q)}(x^0, \vec{x}) \to \gamma^0 H^{(Q)}(x^0, -\vec{x})\gamma^0, \qquad v^\mu \to v_\mu. \tag{3.51}$$

The field $H^{(Q)}_a$ transforms as a $(2, \bar{3})$ under the heavy spin $\otimes$ SU(3)$_V$ symmetry [183], this is to say:

$$H^{(Q)}_a \to S_Q\left(H^{(Q)}U^\dagger\right)_a. \tag{3.52}$$

The hermitian conjugate field is defined by:

$$\bar{H}^{(Q)a} = \gamma^0[H^{(Q)}_a]^\dagger\gamma^0, \tag{3.53}$$

and transforms as a $(\bar{3}, 2)$ [183]:

$$\bar{H}^{(Q)a} \to \left(U\bar{H}^{(Q)}\right)^a S^\dagger_Q. \tag{3.54}$$

The matrix field $J^{(Q)}_a$ satisfies transformation relations identical to those in Eqs. (3.51)–(3.54).

We shall summarize here the transformation properties of the $H^{(Q)}$, $\bar{H}^{(Q)}$, $J^{(Q)}$ and $\bar{J}^{(Q)}$ degrees of freedom under chiral,

$$\begin{aligned} H^{(Q)}_a &\xrightarrow[G]{} \left[H^{(Q)}U^\dagger_\chi\right]_a \\ \bar{H}^{(Q)}_a &\xrightarrow[G]{} \left[U_\chi\bar{H}^{(Q)}\right]_a \end{aligned} \tag{3.55}$$

$$\begin{aligned} J^{(Q)}_a &\xrightarrow[G]{} \left[J^{(Q)}U^\dagger_\chi\right]_a \\ \bar{J}^{(Q)}_a &\xrightarrow[G]{} \left[U_\chi\bar{J}^{(Q)}\right]_a \end{aligned} \tag{3.56}$$

parity,

$$\begin{aligned} H^{(Q)}_a(x^0, \vec{x}) &\xrightarrow[\mathrm{P}]{} \gamma^0 H^{(Q)}_a(x^0, -\vec{x})\gamma^0 \\ \bar{H}^{(Q)}_a(x^0, \vec{x}) &\xrightarrow[\mathrm{P}]{} \gamma^0 \bar{H}^{(Q)}_a(x^0, -\vec{x})\gamma^0 \end{aligned} \tag{3.57}$$

$$\begin{aligned} J_a^{(Q)}(x^0,\vec{x}) &\underset{\mathrm{P}}{\rightarrow} \gamma^0 J_a^{(Q)}(x^0,-\vec{x})\gamma^0 \\ \bar{J}_a^{(Q)}(x^0,\vec{x}) &\underset{\mathrm{P}}{\rightarrow} \gamma^0 \bar{J}_a^{(Q)}(x^0,-\vec{x})\gamma^0 \end{aligned} \tag{3.58}$$

and heavy quark spin rotations

$$\begin{aligned} H_a^{(Q)} &\xrightarrow[SU(2)_Q]{} S_Q H_a^{(Q)} \\ \bar{H}_a^{(Q)} &\xrightarrow[SU(2)_Q]{} \bar{H}_a^{(Q)} S_Q^\dagger \end{aligned} \tag{3.59}$$

$$\begin{aligned} J_a^{(Q)} &\xrightarrow[SU(2)_Q]{} S_Q J_a^{(Q)} \\ \bar{J}_a^{(Q)} &\xrightarrow[SU(2)_Q]{} \bar{J}_a^{(Q)} S_Q^\dagger \end{aligned} \tag{3.60}$$

where now $U_\chi = U_\chi(L,R)$ is a SU(3) matrix depending on the specific $(L,R)$ transformation. The chiral transformation $U_\chi$ should satisfy $V = U_\chi(V,V)$. On the other hand, it should be noted that the action of consecutive P$G$P transformations on $H$ should give the same result as the one obtained by the only action of $G$. Hence we have,

$$\begin{aligned} H(x) &\underset{\mathrm{P}}{\rightarrow} \gamma^0 H(x^0,-\vec{x})\gamma^0 \\ &\underset{G}{\rightarrow} \gamma^0 H(x^0,-\vec{x})\gamma^0 U_\chi^\dagger(L,R) \\ &\underset{\mathrm{P}}{\rightarrow} H(x) U_\chi^\dagger(R,L) \overset{!}{=} H(x) U_\chi^\dagger(L,R) \end{aligned} \tag{3.61}$$

where we have taken into account the action of parity on the group elements of $G$: $\mathrm{P}L(R)\mathrm{P}^{-1} = R(L)$, and the last equality stems from the assumption $[P,G]=0$.

Equations (3.55) and (3.59) imply that the field $H_a^{(Q)}$, which contains the matter fields $P^{(Q)}$, $P^{*\,(Q)}$, transforms as an antitriplet under the unbroken $\mathrm{SU}(3)_V$ subgroup of $\chi$Sym and as a doublet under HQSS. Matter fields have a well defined transformation rule under the unbroken vector $\mathrm{SU}(3)_V$ symmetry, but they do not necessarily form representations of the spontaneously broken $\chi$Sym. To construct the chiral Lagrangian, it is useful to define an $H_a^{(Q)}$ field that transforms under the full $\mathrm{SU}(3)_L \otimes \mathrm{SU}(3)_R$ $\chi$Sym group in such a way that the transformation reduces to $H_a^{(Q)} V^\dagger$ under the unbroken vector subgroup. The transformation of $H_a^{(Q)}$ under $\mathrm{SU}(3)_L \otimes \mathrm{SU}(3)_R$ is not uniquely defined, but one can show that all such Lagrangians are related to each other by field redefinitions, and so, they make the same predictions for any physical observable [180, 194].

For example, we could pick a field $\hat{H}_a^{(Q)}$ that transforms as,

$$\hat{H}_a^{(Q)} \underset{G}{\rightarrow} \hat{H}_b^{(Q)} L_{ba}^\dagger, \; (U_\chi = L) \tag{3.62}$$

under chiral $\mathrm{SU}(3)_L \otimes \mathrm{SU}(3)_R$. This transformation is a little unusual in that it singles out a special role for the $\mathrm{SU}(3)_L$ transformation. Furthermore, for this choice the parity transformation of Eq. (3.57) and the relation of Eq. (3.61) are not compatible. To solve the problem, the transformation under parity needs to be changed to

$$\hat{H}_a^{(Q)}(x^0,\vec{x}) \underset{\mathrm{P}}{\rightarrow} \gamma^0 \hat{H}_a^{(Q)}(x^0,-\vec{x})\gamma^0 U^\dagger(x^0,-\vec{x}) \tag{3.63}$$

with $U(x)$ the exponential map introduced in Eq. (3.35) and transforming as showed in Eqs. (3.38) and (3.39). Clearly, Eq. (3.62) is not symmetric under $L \leftrightarrow R$, which causes the parity transformation rule to involve the $U(x)$ field. It is convenient to have a more symmetrical transformation for $H_a^{(Q)}$, which will allow us consistently use the simple parity transformation of Eq. (3.57).

## 3.4 Effective Lagrangians

**External sources.** The construction of low energy effective Lagrangians of QCD is based on approximations of the generating functional $Z_{\rm QCD}$ by the ones obtained in the different effective theories $Z_{\rm eff}$ [177–179]. The symmetry requirements are inherited by the amplitudes, since when these functions are invariant under *local* chiral transformations they satisfy the so-called Takahashi-Ward identities [195,196]. The program is to consider the action of local $G$ transformations $(L(x), R(x))$,

$$U'(x) = R(x)U(x)L^\dagger(x),\ \ L(x), R(x) \in {\rm SU}(3) \tag{3.64}$$

which are the local version of the global chiral transformations in Eq. (3.37). One also needs the associated external currents $\ell^\mu(x)$ and $r^\mu(x)$. The transformation properties of the left and right fields are obtained requiring local invariance of the chiral QCD Lagrangian, $\mathcal{L}_0^{\rm QCD}(x)$ in Eq. (3.11), including external classical sources [177–179],

$$\mathcal{L}^{\rm QCD}_{v,\,a,\,s,\,p}(x) = \mathcal{L}_0^{\rm QCD}(x) + \bar q(x)\gamma^\mu \left(v_\mu(x) + a_\mu(x)\gamma_5\right) q(x) - \bar q(x)\left(s(x) - i\,\gamma_5 p(x)\right) q(x) \tag{3.65}$$

where the external fields $v_\mu(x) \equiv (r_\mu(x) + \ell_\mu(x))/2$ and $a_\mu(x) \equiv (r_\mu(x) - \ell_\mu(x))/2$ are the vector and axial sources, respectively, while $s(x)$ and $p(x)$ are the scalar and pseudoscalar densities. These objects are all hermitian, colorless matrices of dimension 3 × 3 in flavour space. Under a local chiral rotation $(L(x), R(x))$ of the quark fields (recall the chiral projectors $P_\pm^\chi$ given in Eq. (3.9)),

$$\begin{aligned} q(x) &\xrightarrow[G]{} \left[R(x)P_+^\chi + L(x)P_-^\chi\right] q(x) \\ \bar q(x) &\xrightarrow[G]{} \bar q(x)\left[P_-^\chi R^\dagger(x) + P_+^\chi L^\dagger(x)\right] \end{aligned} \tag{3.66}$$

the transformation rules of the external fields are,

$$r_\mu(x) \xrightarrow[G]{} R(x)\, r_\mu(x)\, R^\dagger(x) + i\, R(x)\partial_\mu R^\dagger(x), \tag{3.67}$$

$$\ell_\mu(x) \xrightarrow[G]{} L(x)\, \ell_\mu(x)\, L^\dagger(x) + i\, L(x)\partial_\mu L^\dagger(x), \tag{3.68}$$

$$[s(x) + i\,p(x)] \xrightarrow[G]{} R(x)\,[s(x) + i\,p(x)]\, L^\dagger(x). \tag{3.69}$$

With the help of Eqs. (3.67) and (3.68) we can construct a chirally covariant derivative

$$D_\mu {\rm O} := \partial_\mu {\rm O}\ +\ i{\rm O}\ell_\mu - i r_\mu {\rm O} \tag{3.70}$$

for any object O transforming as $U$ in Eq. (3.64), $D_\mu$O itself transforms in the same way as O—this is the requirement of a covariant derivative. The left and right sources, $\ell_\mu(x)$ and $r_\mu(x)$, serve to effectively incorporate the electromagnetic and weak couplings between the quarks and the photon as well as the weak bosons [182]. Recalling Eqs. (3.12) and (3.13) one can also derive the transformation rules of the external fields to guarantee parity and charge conjugation invariance of $\mathcal{L}^{\rm QCD}_{v,\,a,\,s,\,p}$ in Eq. (3.65), which read [180]

$$r_\mu(x) \xrightarrow[{\rm P}]{} \ell_\mu(x), \tag{3.71}$$

$$\ell_\mu(x) \xrightarrow[{\rm P}]{} r_\mu(x), \tag{3.72}$$

$$[s(x) + i\,p(x)] \xrightarrow[{\rm P}]{} [s(x) + i\,(-p(x))]\,, \tag{3.73}$$

and,

$$r_\mu(x) \underset{\mathrm{C}}{\rightarrow} -\ell_\mu^{\mathrm{T}}(x), \tag{3.74}$$

$$\ell_\mu(x) \underset{\mathrm{C}}{\rightarrow} -r_\mu^{\mathrm{T}}(x), \tag{3.75}$$

$$[s(x) + i\,p(x)] \underset{\mathrm{C}}{\rightarrow} \left[s^{\mathrm{T}}(x) + i\,p^{\mathrm{T}}(x)\right]. \tag{3.76}$$

We recall that the QCD Lagrangian (Eq. (3.8)) would be recovered setting the sources to the values $\ell_\mu = r_\mu = p = 0$ and $s = \mathrm{diag}(m_u, m_d, m_s)$. In our effective Lagrangian, in terms of the Goldstone degrees of freedom, we use the *same* sources and densities. Note that the transformation rules of $\ell_\mu$ and $r_\mu$ in Eq. (3.67) and (3.68) depend explicitly on derivatives of the $L(x)$ and $R(x)$ matrices, therefore, these fields will only enter through the chiral covariant derivative in Eq. (3.70). We will incorporate the pseudoscalar and scalar densities using the linear combination

$$\chi \coloneqq 2B_0\,(s + i\,p)\,. \tag{3.77}$$

With the transformation properties $\chi \underset{G}{\rightarrow} R\chi L^\dagger$, $\chi \underset{\mathrm{P}}{\rightarrow} \chi^\dagger$ and $\chi \underset{\mathrm{C}}{\rightarrow} \chi^{\mathrm{T}}$ given by Eqs. (3.69), (3.73) and (3.76), respectively. The quantity $B_0$ appearing in Eq. (3.77) is related to the scalar singlet quark condensate through $3F^2B_0 = -\langle 0|\,\bar{q}q\,|0\rangle$, and its value is a measure of the dynamical breaking of chiral symmetry [180]. The explicit breaking of chiral symmetry is implemented by introducing, as in the case of (3.65), the source,

$$\chi = 2B_0 \begin{pmatrix} \hat{m} & 0 & 0 \\ 0 & \hat{m} & 0 \\ 0 & 0 & m_s \end{pmatrix} \tag{3.78}$$

where we do not distinguish the masses of the $u$ and $d$ quarks and take a common mass, $\hat{m}$, in the isospin symmetric limit. Before continuing, we need the power counting assignment of the different building blocks. The expansion of the low energy interaction of pNGBs is in terms of their (small) momentum $p$ momentum over the typical hadron scale $\Lambda_\chi = 4\pi F \sim 1$ GeV [194]. Any derivative of a Goldstone field is counted as $\mathcal{O}(p)$, with $p$ denoting the momentum of the Goldstone boson. Hence, we account $U$ and $D_\mu U$ as $\mathcal{O}(p^0)$ and $\mathcal{O}(p)$ respectively. The action of charge conjugation and parity onto $D_\mu U$ have the same effect as in the case of $U$. The scalar source $\chi$ is counted, as we shall see soon, as $\mathcal{O}(p^2)$. We can build the lowest order effective Lagrangian for the interaction of pNGBs, invariant under parity, charge conjugation and incorporating the masses of the Goldstone bosons via Eq. (3.78), as follows

$$\mathcal{L}_1^{(2)} = \frac{F^2}{4}\mathrm{Tr}\left[D_\mu U (D^\mu U)^\dagger\right] + \frac{F^2}{4}\mathrm{Tr}\left[\chi U^\dagger + U\chi^\dagger\right]. \tag{3.79}$$

By expanding $U$ and $U^\dagger$ in Eq. (3.79) in terms of the Goldstone fields $\phi_i$ we identify the kinetic terms: $1/2\partial_\mu\phi_i\partial^\mu\phi_i^\dagger - 1/2\,m_i^2\phi_i\phi_i^\dagger$—the $F^2/4$ factors therein ensure the correct normalization of these terms and the $m_i$ coefficients stand for the bare masses of the pseudoscalar fields. Hence, the pieces quadratic in the fields $(\phi_i\phi_i^\dagger)$ allow us to rewrite Eq. (3.78) in terms of the masses of the pseudoscalar mesons: $m_\pi^2 = 2B_0\hat{m}$, $m_K^2 =$

$B_0(\hat{m}+m_s)$ and $m_\eta^2 = \frac{2}{3}B_0(\hat{m}+2m_s)$,

$$\chi = \begin{pmatrix} m_\pi^2 & 0 & 0 \\ 0 & m_\pi^2 & 0 \\ 0 & 0 & 3m_\eta^2 - 2m_K^2 \end{pmatrix}. \tag{3.80}$$

which would complete the kinetic term of the Goldstone fields. For that reason, the source $\chi$ is considered as $\mathcal{O}(p^2)$. A further relation can be obtained by this identification, the so-called Okubo mass formula [197]: $m_\eta^2 = (4m_K^2 - m_\pi^2)/3$.

### 3.4.1 Heavy-light—pNGB's interaction

**Incorporating heavy mesons as matter fields.** As we have stated, the goal is to construct an effective Lagrangian describing the scattering of the pNGB's off heavy-light pseudoscalar mesons. The latter can be included in different ways, and firstly, following Refs. [198, 199] we will consider them as matter fields. Let us refer to the field describing the heavy-light pseudoscalar meson degrees of freedom as $P$, which should transform appropriately under the symmetry groups. The advantage of this approach is that this is the canonical way to describe the interaction of pNGB's with relativistic baryons, and one can use the ideas developed for the pion nucleon interaction [200, 201], since both baryons and heavy mesons have non vanishing masses in the chiral limit. This approach is commonly known as Heavy Meson Chiral Perturbation Theory (HM$\chi$PT). We retake here part of the discussion in Sec. 3.3.2. We will consider the heavy mesons as a SU(3) anti-triplet (regarding these states as $Q\bar{q}$ with $q = u, d, s$). Therefore, under a chiral transformation they will transform as

$$P \underset{G}{\rightarrow} PM^\dagger(L,R) \tag{3.81}$$

$$P^\dagger \underset{G}{\rightarrow} M(L,R)P^\dagger \tag{3.82}$$

where $M$ denotes a SU(3) matrix, which in principle can depend on the chiral transformation. This matrix should satisfy $M(V,V) = V$ for a vector transformation. As we have already discussed in Sec. 3.3.2 around Eq. (3.61), there is ambiguity concerning the form of $M(L,R)$, and this will have repercussion on the transformation properties of the heavy-light degrees of freedom under parity (we follow here the discussion of the book [21]). To solve this issue, it is convenient to introduce the square root of $U(x)$ field [202]

$$u(x) = \sqrt{U(x)} = \exp\left(\frac{i}{2F}\hat{\xi}(x)\right) \tag{3.83}$$

with $\hat{\xi}$ denoting the matrix of pNGB fields of Eq. (3.35). The new field introduced in Eq. (3.83) satisfies $uu = U$, therefore, a chiral transformation (3.37) acting on this object would result in

$$u(x) \underset{G}{\rightarrow} \mathcal{M}(L,R)u(x)L^\dagger = Ru(x)\mathcal{M}^\dagger(L,R). \tag{3.84}$$

The matrix $\mathcal{M}(L,R)$ is a unitary matrix which is not only a function of the $L$ and $R$ matrices, but also of the fields in $\hat{\xi}$, consequently it is also space-time dependent: it is local. In the construction of chiral Lagrangians with matter fields it is common to choose $M = \mathcal{M}$, we shall do the same here. In practice [21], this choice requires a redefinition of the heavy meson fields $\tilde{P} \coloneqq Pu^\dagger$ which would admit the simpler parity transformation of Eq. (3.57). The complicated transformation property (3.84) may not be convenient in order to build invariant objects. This issue is overcome if we consider the combinations

$$V_\mu = \frac{1}{2}\left(u^\dagger\,\partial_\mu u + u\,\partial_\mu u^\dagger\right) \tag{3.85}$$

$$A_\mu = \frac{1}{2}\left(u^\dagger\,\partial_\mu u - u\,\partial_\mu u^\dagger\right) \tag{3.86}$$

since their chiral transformation are much simpler, and reads

$$V_\mu \underset{G}{\rightarrow} MV_\mu M^\dagger + M\partial_\mu M^\dagger \tag{3.87}$$

$$A_\mu \underset{G}{\rightarrow} MA_\mu M^\dagger. \tag{3.88}$$

From Eqs. (3.87) and (3.88) we see that $V_\mu$ transforms as a vector gauge field—note that $u(x) \underset{\mathrm{P}}{\rightarrow} u^\dagger(x^0, -\vec{x})$,

$$V_\mu(x) \underset{\mathrm{P}}{\rightarrow} V^\mu(x^0, -\vec{x}) \tag{3.89}$$

$$A_\mu(x) \underset{\mathrm{P}}{\rightarrow} -A^\mu(x^0, -\vec{x}). \tag{3.90}$$

This gauge field is also known as the chiral connection. Therefore, analogously to Eq. (3.70), the gauge field can be used to define a chiral covariant derivative of the anti-triplet $P$

$$\begin{aligned} D_\mu P &\equiv \partial_\mu P + PV_\mu^\dagger \\ D_\mu P^\dagger &\equiv \partial_\mu P^\dagger + V_\mu P^\dagger \end{aligned} \tag{3.91}$$

Using Eq. (3.91) we can construct the simplest chiral invariant Lagrangian describing the interaction of the $\mathrm{SU}(3)_V$ anti-triplet of heavy mesons $P$ and the octet of Goldstone bosons $\hat{\xi}$ as,

$$\mathcal{L}^{P\phi} = D^\mu P D_\mu P^\dagger - \overset{\circ}{M}{}_Q^2\, PP^\dagger. \tag{3.92}$$

which includes the nonvanishing bare mass of the heavy-light mesons $\overset{\circ}{M}_Q$ in the chiral limit. The heavy-light masses are counted as $\mathcal{O}(p^0) \sim \mathcal{O}(\Lambda_\chi) \approx 1$ GeV, similarly, the momentum of the heavy mesons—derivatives of $P$ and $P^\dagger$—which does neither vanish in the chiral limit, is counted as $\mathcal{O}(p^0)$. Therefore, the LO $P\phi \to P\phi$ interaction in Eq. (3.92) is $\mathcal{O}(p^1)$ coming from terms involving one vector current (3.85)—$u \sim \mathcal{O}(p^0)$, $\partial_\mu u \sim \mathcal{O}(p^1)$,

$$\begin{aligned} \mathcal{L}^{P\phi} = {}& \partial^\mu P \partial_\mu P^\dagger - \overset{\circ}{M}{}_Q^2\, PP^\dagger \\ & + \underbrace{\partial_\mu P V^\mu P^\dagger - PV_\mu \partial^\mu P^\dagger}_{=:\mathcal{L}^{P\phi}_{\mathrm{LO}}} + \mathcal{O}\left(\phi_i^4/F^4\right) \end{aligned} \tag{3.93}$$

Note that the $P\phi \to P\phi$ amplitudes from Eq. (3.93) require expanding the vector current up to second order in the Goldstone fields, while at first order we would have a vanishing contribution: $V^\mu \approx i\partial^\mu\hat{\xi} + (i\partial^\mu\hat{\xi})^\dagger = 0$.

Concerning the applications to be discussed in this thesis, we shall need the first subleading $\mathcal{O}(p^2)$ interaction, $\mathcal{L}^{P\phi}_{\text{NLO}}$. It will incorporate sources like $\chi$ in Eq. (3.80), which provide the mass differences among the members of the anti-triplet $P$ incorporating the explicit $\text{SU}(3)_V$ breaking through the Goldstone masses. One thus should consider order $\mathcal{O}(p^2)$ blocks, $B$, such that terms of the form $PBP^\dagger$ and $D_\mu P\tilde{B}^{\mu\nu}D_\nu P^\dagger$ remain invariant under chiral transformations. The blocks should transform as

$$B \underset{G}{\longrightarrow} MBM^\dagger, \tag{3.94}$$

which may be achieved through the structures $u^\dagger\hat{B}u^\dagger + u\hat{B}^\dagger u$, with $\hat{B} = \chi, D_\mu U$—note that we do not need $\hat{B} = U$ since $u^\dagger U u^\dagger = \mathbb{I}$. In addition, $uD_\mu U^\dagger u = uD_\mu(uu)^\dagger u = -u^\dagger D_\mu U u^\dagger$. We introduce the following hermitian operators,

$$\chi_+ := u\chi^\dagger u + u^\dagger\chi u^\dagger \sim \mathcal{O}(p^2) \tag{3.95}$$

$$u_\mu := iu^\dagger D_\mu U u^\dagger \sim \mathcal{O}(p^1) \tag{3.96}$$

which allow the construction of the following $\mathcal{O}(p^2)$ invariants,

$$\chi_+,\ \text{Tr}\left[\chi_+\right],\ u_\mu u^\mu,\ \text{Tr}\left[u_\mu u^\mu\right],\ u^\mu u^\nu,\ \text{Tr}\left[u^\mu u^\nu\right]. \tag{3.97}$$

Gathering the possible combinations in Eq. (3.97) the NLO Lagrangian reads,

$$\begin{aligned}\mathcal{L}^{P\phi}_{\text{NLO}} &= P\left(-h_0\,\text{Tr}\left[\chi_+\right] - h_1\,\chi_+ + h_2\,\text{Tr}\left[u_\mu u^\mu\right] - h_3\,u_\mu u^\mu\right)P^\dagger \\ &\quad + D_\mu P\left(h_4\,\text{Tr}\left[u^\mu u^\nu\right] - h_5\left\{u^\mu, u^\nu\right\} - h_6\left[u^\mu, u^\nu\right]\right)D_\nu P^\dagger.\end{aligned} \tag{3.98}$$

Each coefficient $h_i$ $(i = 0, 1, ..., 6)$ accompanying the corresponding invariant term is a real undetermined parameter, a LEC. Before continuing, it should be mentioned that the invariant $D_\mu P\left[u^\mu, u^\nu\right]D_\nu P^\dagger$ contributes at least at order $\mathcal{O}(p^3)$, and consequently, it should not be considered. Let us rewrite this (apparently) order $\mathcal{O}(p^2)$ contribution stemming from the partial derivatives in the covariant derivative $D_\mu = \partial_\mu + \mathcal{O}(p)$,

$$\begin{aligned}\partial_\mu P\left[u^\mu, u^\nu\right]\partial_\nu P^\dagger &= \partial_\mu\left(P\left[u^\mu, u^\nu\right]\partial_\nu P^\dagger\right) \\ &\quad - P\left(\left[\partial_\mu u^\mu, u^\nu\right] + \left[u^\mu, \partial_\mu u^\nu\right]\right)\partial_\nu P^\dagger \\ &\quad - P\left[u^\mu, u^\nu\right]\partial_\mu\partial_\nu P^\dagger\end{aligned} \tag{3.99}$$

Paying attention to the three pieces in Eq. (3.99), the first one gives a surface term contribution to the action, which is neglected. The second one is of order $\mathcal{O}(p^3)$, while the third one is zero since, in terms of Feynman $P\phi \to P\phi$ amplitudes, we would have $\partial_\mu\partial_\nu P^\dagger = \partial_\nu\partial_\mu P^\dagger$.

Let us note that blocks of the form $PC^\mu D_\mu P^\dagger + D_\mu P C^{\mu\dagger}P^\dagger$ do not contribute to the scattering at order $\mathcal{O}(p^2)$. These terms would also require $C^\mu$ transforming as the axial chiral current $A^\mu$ in Eq. (3.88) under $G$. We could consider $C^\mu = u^\mu$, which would provide the term $P\left(V^\mu u_\mu + u_\mu V^{\mu\dagger}\right)P^\dagger$. The latter one does not contribute to $P\phi \to P\phi$ amplitudes, since it would require keeping one derivative in $V^\mu$, and—as we have seen before—the vector current vanishes when expanded in terms of one derivative of Goldstone fields.

We conclude that the NLO Lagrangian depends solely on five LECs [198],

$$\begin{aligned}\mathcal{L}^{P\phi}_{\text{NLO}} &= P\left(-h_0\,\text{Tr}\left[\chi_+\right] - h_1\,\chi_+ + h_2\,\text{Tr}\left[u_\mu u^\mu\right] - h_3\,u_\mu u^\mu\right)P^\dagger \\ &\quad + D_\mu P\left(h_4\,\text{Tr}\left[u^\mu u^\nu\right] - h_5\left\{u^\mu, u^\nu\right\}\right)D_\nu P^\dagger.\end{aligned} \tag{3.100}$$

We need the dimensionfull $h_4$ and $h_5$ parameters to satisfy that $h_{4,5}\,\overset{\circ}{M}{}_Q^{2}$ are of natural size. This further requirement guaranties that $\mathcal{O}(p^2)$ contributions are smaller than the $\mathcal{O}(p)$ ones. As we will see, this is well satisfied. We could use some experimental input in order to fix one of the LECs in Eq. (3.100). If we expand the explicit chiral symmetry breaking blocks containing the Goldstone masses ($\chi_+ \sim \chi$), we will obtain a modified kinetic term for each heavy light meson depending on $h_0$ and $h_1$. Noting that the contribution of $h_0$ is the same for all the members of the anti-triplet, the values of the physical $Q\bar{u}$, $Q\bar{d}$ and $Q\bar{s}$ heavy-light meson masses can be used to fix the constant $h_1$. The latter incorporates the mass splitting of the anti-triplet of $Q\bar{q}$ degrees of freedom: it has a contribution to the kinetic chiral mass $\overset{\circ}{M}_Q$ of each meson leading to $M^2_{Q\bar{s}} - M^2_{Q\bar{l}} = 4h_1(m_K^2 - m_\pi^2)$ $(l = u, d)$. Hence, it can be fixed to reproduce the mass splitting of, for example, the charm and charm-strange pseudoscalar mesons $D$ and $D_s$. Using the isospin symmetric physical masses of the different particles the value of $h_1$ is 0.42, of order one—and therefore of *natural* size, as expected in a well defined EFT.

One may wonder how the interaction is consistent with heavy quark spin symmetry requirements. The answer is simple, since the formalism described throughout the present section can be applied to the $S$-wave $P^*\phi \to P^*\phi$ interaction, using the *same* amplitudes to describe both systems. In this way we would be incorporating the requirement that, at leading order in the heavy quark mass expansion, the interaction of the members of the HQSS doublet ($P$ and $P^*$) and the light degrees of freedom are identical. Of course, $\Lambda_{\rm QCD}/m_Q$ corrections to this limit will always be present, and in principle, one could expect differences in the values of the LECs describing both $J^P = 0^+$ and $J^P = 1^+$ ($S$-wave $P^{(*)}\phi$).

**Incorporating heavy mesons as hyperfields.** We consider here the heavy meson fields in the form previously introduced in Sec. 3.3.2, through Eqs. (3.45) and (3.53). However, first of all we will focus exclusively on their transformation properties under the groups $\mathrm{SU}(3)_V \otimes \mathrm{SU}(2)_{S_Q}$. Due to their transformation properties under the heavy quark spin and chiral symmetries (see Eqs. (3.52) and (3.54)), the associated building blocks should be considered in the form

$$\left\langle H_b C^b_a \Gamma \bar{H}^a \right\rangle \tag{3.101}$$

where symbol "$\langle \ldots \rangle$" stands for the trace in Dirac space, $C^a_b$ $(a, b = 1, 2, 3)$ denotes a $3 \times 3$ matrix in flavour space and $\Gamma$ refers to a matrix in Dirac space. We can derive the chirally covariant kinetic term, see Eq. (3.92), for the fields $H$ and $\bar{H}$, which would ultimately provide the leading order Lagrangian describing $H\phi \to H\phi$ amplitudes, by simply writing,

$$\mathcal{L}^{H\phi} = \frac{1}{2}\left\langle D_\mu H D^\mu \bar{H} \right\rangle - \frac{1}{2} m_H^2 \left\langle H\bar{H} \right\rangle . \tag{3.102}$$

The covariant derivatives above are the same as those introduced in Eqs. (3.91), with the correspondences $P \leftrightarrow H$ and $P^\dagger \leftrightarrow \bar{H}$. The factors 1/2 ensure that from Eq. (3.102) we recover the kinetic term of the $P$ and $P^*$ matter fields. On the other hand, we keep in mind that there should not be explicit dependence on $m_H$ in the heavy quark formalism. Therefore, as we did with the heavy quark field $Q(x)$ in Eq. (3.21), we reparametrize the fields $H$ and $\bar{H}$ as follows: $H \to e^{-im_H vx} H$; $\bar{H} \to e^{im_H vx} \bar{H}$. After performing these replacements in Eq. (3.102) the kinetic mass terms disappear and we obtain the following terms,

$$\begin{aligned}\mathcal{L}^{H\phi} &= \frac{1}{2} i v^\mu m_H \left\langle \left(\partial_\mu H \bar{H} - H \partial_\mu \bar{H}\right) \right\rangle \\ &+ \frac{1}{2} i v^\mu m_H \left\langle H \left(V_\mu^\dagger - V_\mu\right) \bar{H} \right\rangle \\ &+ \frac{1}{2} \left\langle \partial_\mu H \partial^\mu \bar{H} \right\rangle \\ &+ \frac{1}{2} \left\langle \partial_\mu H V^\mu \bar{H} + H V_\mu^\dagger \partial^\mu \bar{H} \right\rangle \\ &+ \frac{1}{2} \left\langle H V_\mu^\dagger V^\mu \bar{H} \right\rangle . \end{aligned} \tag{3.103}$$

The remaining explicit $m_H$ dependence is absorbed by introducing the non-relativistic fields $P^{(Q)}$ and $P_\mu^{(Q)*}$, which have a different normalization: $H^{(Q)} \sim \sqrt{m_H} H$ (see Eqs. (3.46) and (3.48)). Besides, we use $V_\mu^\dagger = -V_\mu$ (which can be deduced from its definition (3.85)) and we also rewrite the first term involving only one partial derivative neglecting its surface contribution to the action,

$$\begin{aligned}\mathcal{L}^{H\phi} = &-i v^\mu \left\langle H^{(Q)} \partial_\mu \bar{H}^{(Q)} \right\rangle + \frac{1}{2m_H} \left\langle \partial_\mu H^{(Q)} \partial^\mu \bar{H}^{(Q)} \right\rangle \\ &+ \frac{1}{2m_H} \left\langle H^{(Q)} V_\mu^\dagger V^\mu \bar{H}^{(Q)} \right\rangle \\ &- i v_\mu \left\langle H^{(Q)} V_\mu \bar{H}^{(Q)} \right\rangle \\ &+ \frac{1}{2m_H} \left\langle \partial_\mu H^{(Q)} V^\mu \bar{H}^{(Q)} + H^{(Q)} V_\mu^\dagger \partial^\mu \bar{H}^{(Q)} \right\rangle . \end{aligned} \tag{3.104}$$

Among all the terms in Eq. (3.104), those without the field $V_\mu$ (first line) correspond to the kinetic pieces of the heavy meson field. The second line has no tree level contribution to the $P\phi$ scattering. The third and fourth lines give instead contributions to the $P\phi$ scattering amplitude. We note that they are of the same order, $\mathcal{O}(p)$, in the chiral counting, since all of them involve a single power of the chiral connection $V_\mu$. Moreover, with respect to the interaction term in the third line, the terms in the fourth are suppressed since they involve a derivative of the heavy field $H^{(Q)}$ and a factor $1/m_H$. These latter terms are thus necessarily included in the NLO lagrangian of Eq. (3.100). Therefore, the only LO term is:

$$\mathcal{L}_1^{H\phi} = -\frac{i}{2} v^\mu \left\langle H^{(Q)} \left(u^\dagger \partial_\mu u + u \partial_\mu u^\dagger\right) \bar{H}^{(Q)} \right\rangle . \tag{3.105}$$

The Lagrangian of Eq. (3.105) provides the LO (Weinberg-Tomozawa) $S$-wave $P\phi$ interaction, written in a formalism where HQSS and HQFS are made explicit.

There is one more term which can be built involving one derivative of Goldstone fields. This would be of the form $\left\langle H^{(Q)} i A^\mu \gamma_\mu \gamma_5 \bar{H}^{(Q)} \right\rangle$, with the $\gamma_\mu\gamma_5$ matrix which ensures parity invariance. This term would allow the existence of tree level amplitudes corresponding to one Goldstone exchange between heavy mesons, because, as opposed to the case of the vector current, $A_\mu \approx i\partial_\mu \hat{\xi}/2F + \mathcal{O}(p^3)$. Such Lagrangians provide $PP^*\phi$ and $P^*P^*\phi$ $P$-wave couplings. On the other hand, they will only contribute to the $S$-wave $H\phi \to H\phi$ scattering through $t$-channel diagrams, which give a very small contribution [40,63], and consequently, we will not consider them.

The correspondence between the fields $P^{(Q)} \sim \sqrt{m_Q}P$ can be used to determine the scaling of the NLO LECs in the Lagrangian (3.100) with the mass of the heavy quark. On the other hand, in order to satisfy HQFS, the LECs $h^{(\mathrm{c})}$ and $h^{(\mathrm{b})}$ associated to charm and bottom heavy mesons fields $P$ should scale properly. We identify these rules absorbing the corresponding $\sqrt{m_Q}$ factors in the fields $P$ and taking into account the $m_Q$ factors coming from the derivatives acting on the heavy fields in Eq. (3.100)

$$\begin{aligned} \frac{h_i^{(\mathrm{c})}}{m_c} &\sim \frac{h_i^{(\mathrm{b})}}{m_b},\ i = 0, 1, \ldots, 3 \\ h_i^{(\mathrm{c})} m_c &\sim h_i^{(\mathrm{b})} m_b,\ i = 4, 5. \end{aligned} \tag{3.106}$$

To finish this section, we will discuss the contribution to the $H\phi \to H\phi$ $S$-wave scattering coming from the possible exchange of positive parity heavy-light states. This will be studied in Chapters 8 and 9. We will consider the $s$-channel exchange of the lowest-lying $P$-wave heavy-light $Q\bar{q}$ states obtained in CQMs. We have previously introduced the $(0^+, 1^+)$ doublet in Sec. 3.3.2 through the hyperfield $J^{(Q)}$ given in Eq. (3.50)—which is the analogue of $H^{(Q)}$ in the case of the $(0^-, 1^-)$ HQSS doublet. Thus, the lowest order Lorentz invariant term relating the coupling $H\phi$ pairs to intermediate $j_{\bar{q}}^P = 1/2^+$ heavy-light mesons takes the form [4]

$$\begin{aligned} \mathcal{L}^{\mathrm{ex}} &= c \left\langle H^{(Q)} i A_\mu \gamma^\mu \gamma_5 \bar{J}^{(Q)} \right\rangle + c \left\langle J^{(Q)} i A_\mu \gamma^\mu \gamma_5 \bar{H}^{(Q)} \right\rangle \\ &= i \frac{c}{2} \left\langle H^{(Q)} \left( u^\dagger \partial_\mu u - u \partial_\mu u^\dagger \right) \gamma^\mu \gamma_5 \bar{J}^{(Q)} \right\rangle + \mathrm{h.c.} \end{aligned} \tag{3.107}$$

which is consistent with chiral, HQSS and parity invariance. The parameter $c$ is an undetermined low energy constant which will regulate the strength of the coupling of the $P$-wave scalar HQSS doublet to the $S$-wave $P\phi$ and $P^*\phi$ pairs. Since the nonrelativistic $H$ and $J$ fields have dimensions of $E^{3/2}$, we find that $c$ is dimensionless—recall the constraint $[\mathcal{L}(x)] \sim E^4$ in order to obtain a dimensionless action. Note that, even though it does not depend on the flavour of the heavy quark, one could expect corrections of the order $\Lambda_{\mathrm{QCD}}/m_Q$ and, therefore, the values in the charm and bottom sector should not be exactly the same.

# Part II

# Applications

# Chapter 4

# THE TWO-POLE STRUCTURE OF THE $D_0^*(2400)$

## 4.1 Introduction

In this chapter we study the heavy–light pseudoscalar meson $J^P = 0^+$ scattering in the strangeness-isospin $(S, I) = (0, 1/2)$ sector, and present a strong case for the existence of two poles in the $D_0^*(2400)$ energy region (and similarly in the bottom sector). The affirmative evidence comes from a remarkably good agreement between our *parameter-free predicted* energy levels and the LQCD results reported in Ref. [81]. This two-pole structure was previously claimed in Refs. [33,37,38,199], and finds now a strong support. Its dynamical origin is elucidated from the light-flavour SU(3) structure of the interaction, and we find that the lower pole is the SU(3) partner of the $D_{s0}^*(2317)$. Predictions for other $(S, I)$ sectors, including bottom ones, are also given. For a brief review about the current status of the experimental information concerning the $D_0^*(2400)$ we refer to Sec. 1.2.1. This chapter is based in the findings of Ref. [3].

## 4.2 Formalism

### 4.2.1 Unitary $T$-matrix

We consider the $S$-wave $D\pi$, $D\eta$, and $D_s\bar{K}$ coupled-channel scattering. A unitary $T$-matrix, $T(s)$, can be written [203,204] following Eq. (2.86), $T^{-1}(s) = V^{-1}(s) - G^{(\mathrm{R})}(s)$, with $s \equiv E^2$ the cm energy squared. The kernel $V$ will be discussed in the next section. The diagonal matrix $G^{(\mathrm{R})}$ (see Eq. (2.87)) is constructed from the two-meson loop function, $G_{ii}^{(\mathrm{R})}(s) = G^{(\mathrm{D})}(s, m_i, M_i)$ [205], where $m_i$ and $M_i$ are the masses of the light and heavy pseudoscalar mesons in the channel $i$, respectively. It carries the unitarity cut and it is regularized with a subtraction constant $a(\mu)$ (at a scale $\mu = 1$ GeV), see Eq. (A.1) in Appendix A for details. The matrix $V(s)$ containing the interaction potentials is made out from tree level amplitudes obtained from the $\mathcal{O}(p^2)$ HM$\chi$PT Lagrangian of Ref. [198], that we have previously introduced in Eqs. (3.93) and (3.100). The tree level amplitudes depend on six LECs, $h_{0,\ldots,5}$. For the LECs and the subtraction constant $a(\mu)$ we use the values and uncertainties obtained in Ref. [205] from a fit to LQCD results of the $S$-wave charm–light pseudoscalar-meson scattering lengths in several $(S, I)$ sectors. Notice that the channel $(0, 1/2)$ was not included in the fit carried out in [205].

**Table 4.1:** Coefficients entering the tree level scattering amplitudes of Eq. (4.3) for the different $(S, I)$ sectors.

| $(S,I)$ | channel | $C_{\mathrm{LO}}$ | $C_0$ | $C_1$ | $C_{24}$ | $C_{35}$ |
|---|---|---|---|---|---|---|
| (-1,0) | $D\bar{K} \to D\bar{K}$ | $-1$ | $m_K^2$ | $m_K^2$ | 1 | $-1$ |
| (-1,1) | $D\bar{K} \to D\bar{K}$ | 1 | $m_K^2$ | $-m_K^2$ | 1 | 1 |
| (0,3/2) | $D\pi \to D\pi$ | 1 | $m_\pi^2$ | $-m_\pi^2$ | 1 | 1 |
| (0,1/2) | $D\pi \to D\pi$ | $-2$ | $m_\pi^2$ | $-m_\pi^2$ | 1 | 1 |
|  | $D\eta \to D\eta$ | 0 | $m_\eta^2$ | $-m_\pi^2/3$ | 1 | $\frac{1}{3}$ |
|  | $D_s\bar{K} \to D_s\bar{K}$ | $-1$ | $m_K^2$ | $-m_K^2$ | 1 | 1 |
|  | $D\pi \to D\eta$ | 0 | 0 | $-m_\pi^2$ | 0 | 1 |
|  | $D\pi \to D_s\bar{K}$ | $-\sqrt{\frac{3}{2}}$ | 0 | $-\sqrt{6}(m_K^2 + m_\pi^2)/4$ | 0 | $\sqrt{\frac{3}{2}}$ |
|  | $D_s\bar{K} \to D\eta$ | $-\sqrt{\frac{3}{2}}$ | 0 | $+\sqrt{6}(5m_K^2 - 3m_\pi^2)/12$ |  |  |
| (1,0) | $DK \to DK$ | $-2$ | $m_K^2$ | $-2m_K^2$ | 1 | 2 |
|  | $DK \to D_s\eta$ | $-\sqrt{3}$ | 0 | $-(5m_K^2 - 3m_\pi^2)/\sqrt{12}$ | 0 | $\frac{1}{\sqrt{3}}$ |
|  | $D_s\eta \to D_s\eta$ | 0 | $m_\eta^2$ | $-2(m_\eta^2 - m_\pi^2/3)$ | 1 | $\frac{4}{3}$ |
| (1,1) | $D_s\pi \to D_s\pi$ | 0 | $m_\pi^2$ | 0 | 1 | 0 |
|  | $DK \to DK$ | 0 | $m_K^2$ | 0 | 1 | 0 |
|  | $DK \to D_s\pi$ | 1 | 0 | $-(m_\pi^2 + m_K^2)/2$ | 0 | 1 |
| (2,1/2) | $D_sK \to D_sK$ | 1 | $m_K^2$ | $-m_K^2$ | 1 | 1 |

### 4.2.2 NLO amplitudes

With the conventions used in Eqs. (3.42), (3.43), (3.44) and (3.49) the tree level transitions among the different channels in all $(S, I)$ sectors can be computed from the LO and NLO HM$\chi$PT Lagrangians (3.93) and (3.100). Note that the amplitudes, as in Ref. [198, 205], are projected into isospin $|\pi D\rangle$ and $|DK\rangle$ states—a different ordering might influence crossed transitions by inducing minus signs into Clebsch-Gordan coefficients. The expansion of the LO and NLO Lagrangians in terms of two pNGB fields yields

$$\mathcal{L}_{\rm LO} = \frac{1}{8F^2}\left(\partial_\mu P\left[\hat{\xi},\partial^\mu\hat{\xi}\right]P^\dagger - P\left[\hat{\xi},\partial^\mu\hat{\xi}\right]\partial_\mu P^\dagger\right) \tag{4.1}$$

$$\begin{aligned}\mathcal{L}_{\rm NLO} &= \frac{1}{2F^2}\left(P\left(-h_0{\rm Tr}\left\{\hat{\xi}\chi\hat{\xi}\right\} - h_1\hat{\xi}\chi\hat{\xi}\right)P^\dagger\right)\\ &+ \frac{1}{F^2}\left(P\left(h_2{\rm Tr}\left\{\partial_\mu\hat{\xi}\partial^\mu\hat{\xi}\right\} - h_3\partial_\mu\hat{\xi}\partial^\mu\hat{\xi}\right)P^\dagger\right)\\ &+ \frac{1}{F^2}\left(\partial_\mu P\left(h_4{\rm Tr}\left\{\partial^\mu\hat{\xi}\partial^\nu\hat{\xi}\right\} - h_5\left\{\partial^\mu\hat{\xi},\partial^\nu\hat{\xi}\right\}\right)\partial_\nu P^\dagger\right),\end{aligned} \tag{4.2}$$

which give the amplitudes with the following Lorentz structure

$$\begin{aligned}V(s,t,u) = \frac{1}{F^2}&\left(C_{\rm LO}\,(s-u)/4\right.\\ &- 4C_0h_0 + 2C_1h_1\\ &- 2C_{24}\left(2h_2\,p_2\cdot p_4 + h_4\left[(p_1\cdot p_2)(p_3\cdot p_4) + (p_1\cdot p_4)(p_2\cdot p_3)\right]\right)\\ &\left.+ 2C_{35}\left(h_3\,p_2\cdot p_4 + h_5\left[(p_1\cdot p_2)(p_3\cdot p_4) + (p_1\cdot p_4)(p_2\cdot p_3)\right]\right)\right).\end{aligned} \tag{4.3}$$

The different $C_i$ factors appearing in Eq. (4.3) are constant coefficients associated to the specific transition and $(S,I)$ considered sector. Their values can be found in Table. 4.1. Note that the amplitudes of Eq. (4.3) need to be projected into $S$-wave.

Above threshold, we adopt the parametrization of the $S$-matrix in terms of phase shifts $[\delta_i(s)]$ and inelasticities $[\eta_i(s)]$ of each channel $i$ introduced in Sec. 2.3.1, which are related to the diagonal elements of $T$ by means of Eq. (2.64). Bound, resonant, and virtual states are associated to poles in different RSs of the $T$-matrix. In our three-channel problem, RSs are denoted as $(\xi_1\,\xi_2\,\xi_3)$, $\xi_i = 0,1$, and are defined through the analytical continuations of Eq. (2.89). Thus, (000) is the physical RS. The coupling $g_i$ of a pole to the channel $i$ is obtained from the residue $(g_i^2)$ of $T_{ii}$ as discussed in Eq. (2.93).

**Finite volume.** In order to compare with the LQCD results, we follow the program described in Sec. 2.5.1 calculating the UHM$\chi$PT amplitude in a finite box, $\widetilde{T}(s,L) = V^{-1}(s) - \widetilde{G}(s)$. The finite volume loop functions are calculated as follows [41,167]:

$$\begin{aligned}\widetilde{G}_{ii}(s,L) &= G_{ii}(s)\\ &+ \lim_{q_{\rm max}\to\infty}\left\{\frac{1}{L^3}\sum_{\vec{n}}^{|\vec{q}|<q_{\rm max}}\frac{1}{2E_{m_i}E_{M_i}}\frac{E_{m_i}+E_{M_i}}{s-(E_{m_i}+E_{M_i})^2+i\epsilon} - G^{\rm (SC)}(s,m_i,M_i)\right\}\end{aligned} \tag{4.4}$$

with $G^{\rm (SC)}(s,m_i,M_i)$ the loop function regularized with a sharp cutoff $q_{\rm max}$, that is send to infinity, given in Eq. (A.5). The kernel potentials $V(s)$ do not involve loops and therefore, do not receive finite volume corrections. Hence, the energy levels are obtained as poles of $\widetilde{T}(s,L)$—as denoted in Eq. (2.97)—and they can be directly compared with those obtained in LQCD simulations.

Here we compare with the results of Ref. [81], where energy levels relevant to the $D\pi$, $D\eta$, and $D_s\bar{K}$ channels at different volumes are reported. We employ the meson masses of that reference in the evaluation of $V(s)$ and $\widetilde{G}_{ii}(s)$.

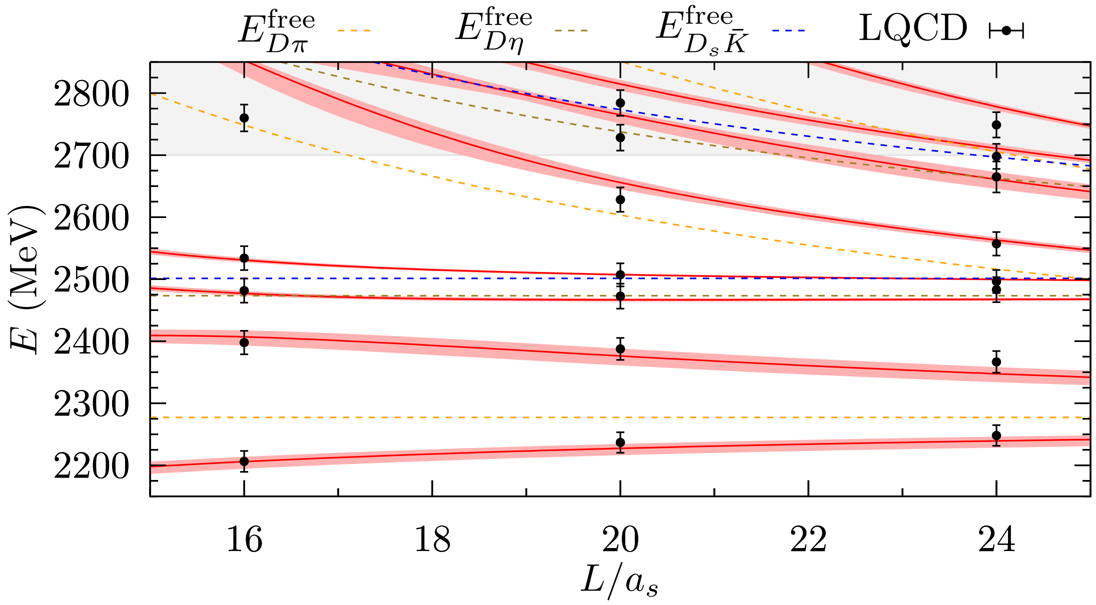

**Figure 4.1:** Comparison of Ref. [81] $(0, 1/2)$ energy levels (black dots) with our predictions (red lines and bands) from Eq. (2.97). The bands represent the $1\sigma$ uncertainties derived from the LECs fitted in Ref. [205], and $a_s = 0.12$ fm [81] .

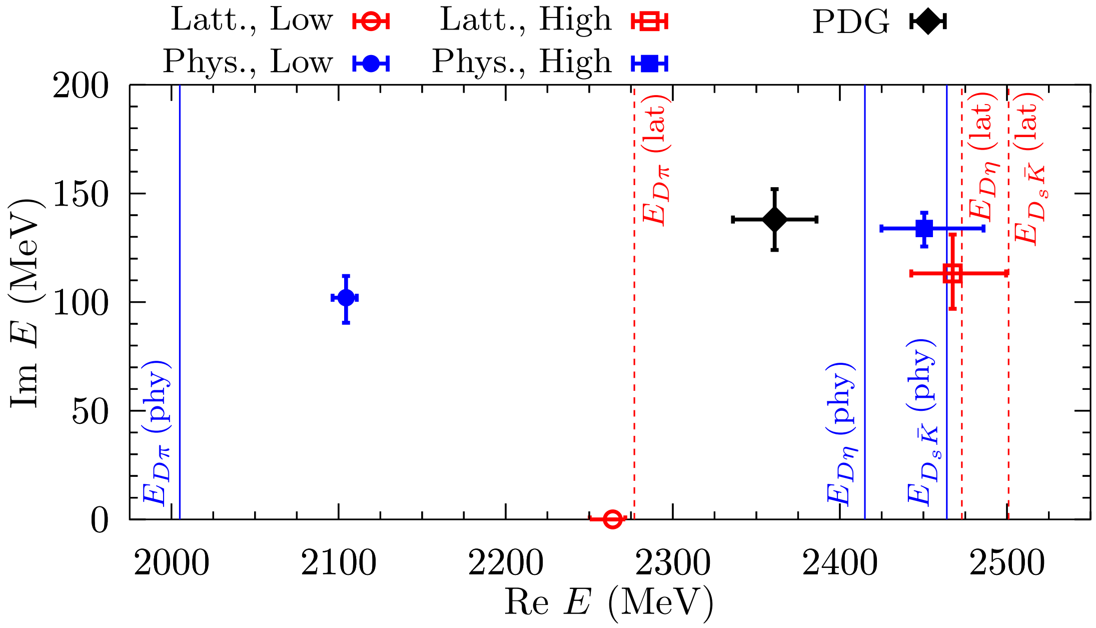

**Figure 4.2:** Complex energy plane location of the two-pole-structure collected in Table 4.2. Empty red (filled blue) symbols stand for the poles obtained when the LQCD [81] (physical) masses are used. The black diamond represents the isospin average of the PDG values for $D_0^*(2400)^0$ and $D_0^*(2400)^+$ [206].

## 4.3 Results

The predicted $(0, 1/2)$ energy levels as a function of $L$ are shown in Fig. 4.1. The region above 2.7 GeV (shaded in Fig. 4.1) is beyond the range of applicability of our $\mathcal{O}(p^2)$ chiral unitary formalism. Below that energy, the agreement of our computed energy levels with

| Masses | $M$ (MeV) | $\Gamma/2$ (MeV) | RS | $\lvert g_{D\pi}\rvert$ | $\lvert g_{D\eta}\rvert$ | $\lvert g_{D_s\bar{K}}\rvert$ |
|---|---|---|---|---|---|---|
| lattice | $2264^{+\ 8}_{-14}$ | 0 | (000) | $7.7^{+1.2}_{-1.1}$ | $0.3^{+0.5}_{-0.3}$ | $4.2^{+1.1}_{-1.0}$ |
| | $2468^{+32}_{-25}$ | $113^{+18}_{-16}$ | (110) | $5.2^{+0.6}_{-0.4}$ | $6.7^{+0.6}_{-0.4}$ | $13.2^{+0.6}_{-0.5}$ |
| physical | $2105^{+6}_{-8}$ | $102^{+10}_{-12}$ | (100) | $9.4^{+0.2}_{-0.2}$ | $1.8^{+0.7}_{-0.7}$ | $4.4^{+0.5}_{-0.5}$ |
| | $2451^{+36}_{-26}$ | $134^{+7}_{-8}$ | (110) | $5.0^{+0.7}_{-0.4}$ | $6.3^{+0.8}_{-0.5}$ | $12.8^{+0.8}_{-0.6}$ |

**Table 4.2:** Position ($\sqrt{s} = M - i\Gamma/2$), couplings (in GeV) and RS of the two poles found in the $(0, 1/2)$ sector using LQCD [81] or physical masses.

those obtained in the LQCD simulation is excellent. This is remarkable, since no fit to the LQCD results is performed. The error bands in Fig. 4.1 correspond to $1\sigma$ uncertainties propagated from the LECs determined in Ref. [205].

The level below $D\pi$ threshold is interpreted in Ref. [81] as a bound state associated to the $D_0^*(2400)$. For infinite volume and with the lattice meson masses, our $T$-matrix also presents this pole. The second level, lying between the $D\pi$ and $D\eta$ thresholds, is very shifted with respect to both of them, hinting at the presence of another pole in infinite volume, that we find slightly below the $D\eta$ threshold. Both poles are collected in the upper half of Table 4.2 and represented with empty red symbols in Fig. 4.2.

Next, we study the spectroscopic content of our UHM$\chi$PT amplitudes when the physical masses are employed. The poles found are also collected in Table 4.2, and shown in Fig. 4.2. Comparing the couplings, we see that the bound state below the $D\pi$ threshold evolves into a resonance above it when physical masses are used (notice that the threshold decreases from 2277 MeV to 2005 MeV). Such an evolution is typically found for $S$-wave poles (*e.g.*, for the $\sigma$ meson [134, 207]). The second pole moves very little and its couplings are rather independent of the meson masses. For physical masses, it is a resonance located between the $D\eta$ and the $D_s\bar{K}$ thresholds in the (110) RS, continuously connected to the physical sheet. The mass of the $D_0^*(2400)$ reported by the Particle Data Group (PDG) [206] lies between those of the two poles found here, whereas the widths are similar (Fig. 4.2). We conclude the $D_0^*(2400)$ structure is produced by two different states (poles), alongside with complicated interferences with the thresholds. This two-pole structure was previously reported in Refs. [33, 37, 38, 199], and it receives here a robust support.

Phase shifts and $|T_{ii}(s)|^2$ are shown in Fig. 4.3. The lower pole causes a very mild effect in the $D\eta$ and $D_s\bar{K}$ amplitudes. It couples mostly to $D\pi$ where a peak around 2.1 GeV is clearly seen, while the phase goes through $\pi/2$ at $\sqrt{s} \simeq 2.2$ GeV. The higher pole manifests itself in a more subtle way. It produces a small enhancement in the $D\pi$ amplitude, but the strongest effect is a clear peak in the $D_s\bar{K}$ amplitude around 2.45 GeV. However, the shape is quite non-conventional. Despite the relatively large width, the amplitude shows a narrow peak stretched between two cusps at the $D\eta$ and $D_s\bar{K}$ thresholds. Such a behaviour provides a possible test of the two-pole structure. The *BABAR* and Belle data for $B \to D_s^- K\pi$ show an enhancement in the $D_s^- K$ invariant mass distribution [208, 209] (see also Ref. [210]). This might confirm the features of the second pole found here, although better statistics data are required.

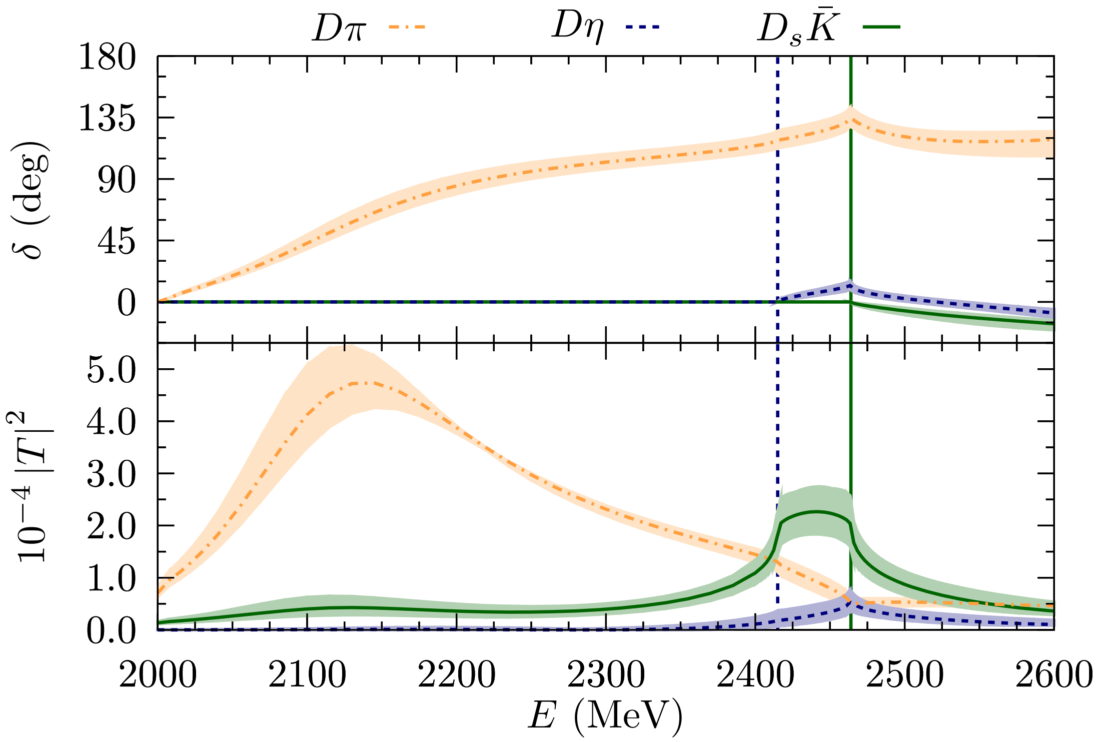

**Figure 4.3:** Phase shift and modulus squared of the diagonal $D\pi$, $D\eta$ and $D_s\bar{K}$ UHM$\chi$PT amplitudes, $T_{ii}(s)$, in the $(0, 1/2)$ sector.

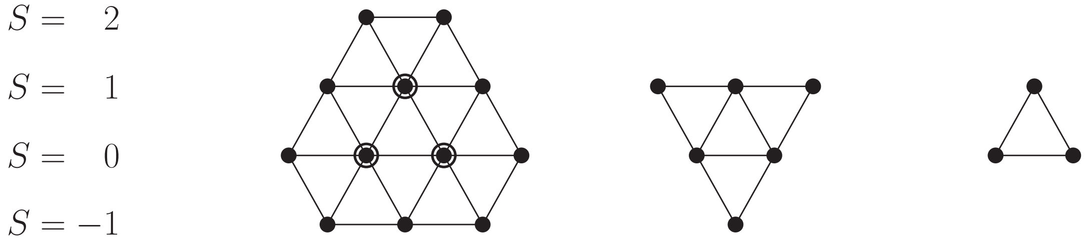

**Figure 4.4:** Weight diagrams of the $\overline{\mathbf{15}}$, $\mathbf{6}$ and $\overline{\mathbf{3}}$ irreps.

## 4.4 SU(3) study

To gain further insights, we study the evolution of the two poles in the light-flavour SU(3) limit, *i.e.*, when all light and heavy meson masses take common values, $m_i = m$ and $M_i = M$, respectively. Similar analyses were done in Refs. [33,38]. In this limit, the heavy–light meson scattering decomposes into irreducible representation (irrep) components as $\overline{\mathbf{3}}\otimes\mathbf{8} = \overline{\mathbf{15}}\oplus\mathbf{6}\oplus\overline{\mathbf{3}}$ (Fig. 4.4), and the potential matrix can be diagonalized, $V_d(s) = D^\dagger V(s) D = \mathrm{diag}\,(V_{\overline{\mathbf{15}}}, V_{\mathbf{6}}, V_{\overline{\mathbf{3}}})$. Since the three channels have a common subtraction constant [205], the $T$-matrix is diagonalizable, $T_d(s) = D^\dagger T(s) D = \mathrm{diag}(T_{\overline{\mathbf{15}}}, T_{\mathbf{6}}, T_{\overline{\mathbf{3}}})$, where $T_A^{-1}(s) = V_A^{-1}(s) - G(s, m, M)$, $A \in \{\overline{\mathbf{15}}, \mathbf{6}, \overline{\mathbf{3}}\}$. At chiral $\mathcal{O}(p)$, $V_d(s) = f(s)\,\mathrm{diag}(1, -1, -3)$, with $f(s)$ positive in the scattering region, showing that the interaction in the $\mathbf{6}$ and $\overline{\mathbf{3}}$ ($\overline{\mathbf{15}}$) irreps is attractive (repulsive). The most attractive irrep, $\overline{\mathbf{3}}$, admits a $c\bar{q}$ ($q = u, d, s$) configuration. At $\mathcal{O}(p^2)$, the potentials receive corrections, but these qualitative features remain.

We can connect the physical and SU(3) symmetric cases by continuously varying the

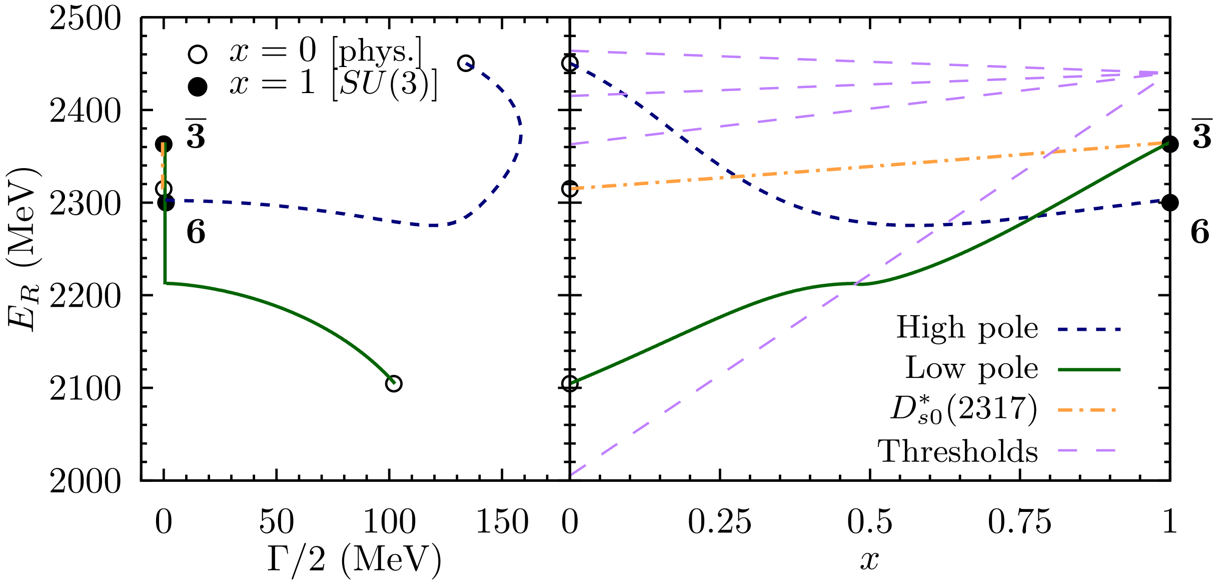

**Figure 4.5:** Evolution from the physical to the flavour SU(3) symmetric cases of $(0, 1/2)$ and $(1, 0)$ poles $\sqrt{s} = E_R - i\Gamma/2$. The blue short dashed, green solid and the orange dashed dotted lines represent the higher and lower $D_0^*(2400)$ and the $D_{s0}^*(2317)$, respectively. Left: path followed by the poles in the complex plane. Right: evolution of $E_R$ with $x$. The purple long dashed lines stand for the $D\pi$, $D\bar{K}$, $D\eta$, and $D_s\bar{K}$ thresholds (from bottom to top).

meson masses as:

$$m_i = m_i^{\text{phy}} + x(m - m_i^{\text{phy}}) \;, \tag{4.5}$$

and analogously for $M_i$. Thus, $x = 0$ ($x = 1$) corresponds to the physical (SU(3) symmetric) case. Numerically, we take $m = 0.49$ GeV and $M = 1.95$ GeV. The evolution of the poles with $x$ is shown in Fig. 4.5. The lower $D_0^*(2400)$ pole found in the physical case (in the (100) RS) connects with a bound state of $T_{\bar{\mathbf{3}}}$ in the SU(3) limit, whereas the higher pole (in the (110) RS) connects with a virtual ($V_{\mathbf{6}}$ is not attractive enough to bind) state generated in $T_{\mathbf{6}}$.[1]

In the $(S, I) = (1, 0)$ sector involving the $DK$ and $D_s\eta$ channels, and using the same input and physical masses, we find a bound state at $2315^{+18}_{-28}$ MeV [205] which is naturally identified with the $D_{s0}^*(2317)$. Its evolution is also shown in Fig. 4.5, and we see that it emerges from the $T_{\bar{\mathbf{3}}}$ pole. Hence, the $D_{s0}^*(2317)$ and the lower $D_0^*(2400)$ poles are flavour SU(3) partners.

## 4.5 Pole predictions in other sectors.

We now discuss other sectors in the physical case. The energies of the relevant two-meson thresholds have been included in Table 4.3 whereas the pole positions are collected in Table 4.4. The $(S, I) = (-1, 0)$ involves only the $D\bar{K}$ channel, and it is part of the $\mathbf{6}$

---

[1] In the physical case, the RSs are specified by $(\xi_1\,\xi_2\,\xi_3)$, with $\xi_i = 0$ or 1 [Eq. (2.89)]. In the SU(3) symmetric case, since all channels have the same threshold, there are only two RSs, the physical [(000)] and the unphysical [(111)] sheets. To connect the lower pole in the physical case, located in the (100) RS, with the $T_{\bar{\mathbf{3}}}$ pole, in the (000) RS, we vary the parameter $\xi_1 = 1 - x$. For the higher pole, one has to evolve $\xi_3 = x$ to connect (110) (physical case) with (111) (SU(3) limit).

**Table 4.3:** Threshold energies, $E_{\rm th}$, of the different relevant channels with $J^P = 0^+, 1^+$ in both charm and bottom, $(0,1/2)$ and $(1,0)$ sectors.

| Channel | $D\pi$ | $D\eta$ | $D_s\bar{K}$ | $D^*\pi$ | $D^*\eta$ | $D_s^*\bar{K}$ |
|---|---|---|---|---|---|---|
| $E_{\rm th}$ [MeV] | 2005.26 | 2415.09 | 2463.92 | 2146.74 | 2556.57 | 2607.75 |
| Channel | $\bar{B}\pi$ | $\bar{B}\eta$ | $\bar{B}_s\bar{K}$ | $\bar{B}^*\pi$ | $\bar{B}^*\eta$ | $\bar{B}_s^*\bar{K}$ |
| $E_{\rm th}$ [MeV] | 5417.50 | 5827.33 | 5862.47 | 5462.69 | 5872.51 | 5911.05 |
| Channel | $DK$ | $D_s\eta$ | - | $D^*K$ | $D_s^*\eta$ | - |
| $E_{\rm th}$ [MeV] | 2362.87 | 2516.13 | - | 2504.35 | 2659.96 | - |
| Channel | $\bar{B}K$ | $\bar{B}_s\eta$ | - | $\bar{B}^*K$ | $\bar{B}_s^*\eta$ | - |
| $E_{\rm th}$ [MeV] | 5775.11 | 5914.68 | - | 5820.30 | 5963.26 | - |

irrep, which is weakly attractive. Indeed, we find a virtual pole, at $2342^{+13}_{-41}$ MeV, roughly 20 MeV below threshold, which has a sizeable influence on the $D\bar{K}$ scattering length [205]. The $(S,I) = (1,1)$ sector, involving the $D_s\pi$ and $DK$ channels, has contributions from the **6** and the repulsive $\overline{\mathbf{15}}$. Because of this, we do not find any pole that can be associated to a physical state.

### 4.5.1 Heavy-quark mass scaling of the LECs in the $D\phi$ interactions at NLO

In the bottom sector, due to the HQFS, we foresee a similar pattern. Thanks to heavy quark symmetry, the $D\phi$ and $\bar{B}\phi$ interactions share the same effective Lagrangian with the correspondence $D \leftrightarrow \bar{B}$. The heavy flavor scaling of the NLO LECs $h_i$'s is discussed in Refs. [55, 198, 205] and given here in Eq. (3.106), equivalently,

$$h^B_{0,1,2,3} = \frac{\bar{m}_B}{\bar{m}_D} h^D_{0,1,2,3}\,, \qquad h^B_{4,5} = \frac{\bar{m}_D}{\bar{m}_B} h^D_{4,5}\,. \tag{4.6}$$

Here $\bar{m}_D$ ($\bar{m}_B$) is the average of the physical masses of the $D$ ($\bar{B}$) and $D_s$ ($\bar{B}_s$) mesons. In addition, as already mentioned in Sec. 4.2, in the unitarized amplitudes there appears one subtraction constant, $a(\mu)$, with $\mu = 1$ GeV the scale introduced in dimensional regularization. In the $(S,I) = (0,1/2)$ channel, the subtraction constants in the charm, denoted by $a^D(\mu)$, and in the bottom, denoted by $a^B(\mu)$, sectors are related as follows [37]:

1. First, given the phenomenological value of $a^D(\mu)$, a sharp-cutoff, $q_{\rm max}$, is determined by requiring the dimensionally (A.1) and the sharp-cutoff regularized (A.5) $D_s\bar{K}$ loop functions to be equal at threshold [211]

$$a(\mu) = -\frac{2}{m_1+m_2}\left\{ m_1 \ln\frac{q_{\rm max} + \sqrt{q^2_{\rm max}+m_1^2}}{\mu} + m_2 \ln\frac{q_{\rm max} + \sqrt{q^2_{\rm max}+m_2^2}}{\mu} \right\}, \tag{4.7}$$

with $m_1 = M_{D_s}$ and $m_2 = m_{\bar{K}}$. This cutoff turns out to be $q_{\rm max} = 0.72^{+0.07}_{-0.06}$ GeV.

**Table 4.4:** Pole positions $(M, \Gamma/2)$ in units of MeV. The *Lower* poles shown are always found in $(1,0,0)$ Riemann sheet, while the *Higher* ones are located in the $(1,1,0)$, except for the $(S,I) = (1,0)$, where poles are in the physical sheet $(0,0)$. Couplings are in units of GeV. In addition, the poles in the $(S,I) = (-1,0)$ correspond to virtual states, since they are found in the (1) sheet (there is only one, $D^{(*)}\bar{K}/B^{(*)}\bar{K}$, channel).

| Sector | $(M, \Gamma/2)$ | $\lvert g_1\rvert$ | $\lvert g_2\rvert$ | $\lvert g_3\rvert$ |
|---|---|---|---|---|
| $(S,I) = (0,1/2)$ | | | | |
| $D_0^*$ Lower | $\left(2105^{+6}_{-8}, 102^{+10}_{-12}\right)$ | $9.4^{+0.2}_{-0.2}$ | $1.8^{+0.7}_{-0.7}$ | $4.4^{+0.5}_{-0.5}$ |
| $D_0^*$ Higher | $\left(2451^{+35}_{-26}, 134^{+7}_{-8}\right)$ | $5.0^{+0.7}_{-0.4}$ | $6.3^{+0.8}_{-0.5}$ | $12.8^{+0.8}_{-0.6}$ |
| $D_1$ Lower | $\left(2247^{+5}_{-6}, 107^{+11}_{-10}\right)$ | $10.1^{+0.2}_{-0.2}$ | $1.3^{+0.4}_{-0.5}$ | $5.0^{+0.4}_{-0.4}$ |
| $D_1$ Higher | $\left(2555^{+47}_{-30}, 203^{+8}_{-9}\right)$ | $5.3^{+0.4}_{-0.3}$ | $5.3^{+0.6}_{-0.4}$ | $13.1^{+0.8}_{-0.6}$ |
| $B_0^*$ Lower | $\left(5535^{+9}_{-11}, 113^{+13}_{-17}\right)$ | $25.0^{+0.7}_{-0.7}$ | $3.8^{+1.5}_{-1.5}$ | $14.6^{+0.5}_{-0.4}$ |
| $B_0^*$ Higher | $\left(5852^{+11}_{-12}, 36 \pm 5\right)$ | $7.9^{+1.0}_{-0.8}$ | $14.4^{+0.6}_{-0.4}$ | $23.4^{+1.1}_{-0.8}$ |
| $B_1$ Lower | $\left(5584^{+9}_{-11}, 119^{+14}_{-17}\right)$ | $25.5^{+0.7}_{-0.8}$ | $4.0^{+1.5}_{-1.5}$ | $14.9^{+0.5}_{-0.4}$ |
| $B_1$ Higher | $\left(5912^{+9}_{-10}, 42^{+5}_{-4}\right)$ | $8.7^{+0.8}_{-0.6}$ | $15.0^{+0.3}_{-0.3}$ | $24.0^{+0.7}_{-0.6}$ |
| Sector | $(M, \Gamma/2)$ | $\lvert g_1\rvert$ | $\lvert g_2\rvert$ | |
| $(S,I) = (1,0)$ | | | | |
| $D_{s0}^*$ | $\left(2315^{+18}_{-28}, 0\right)$ | $9.5^{+1.2}_{-1.1}$ | $7.5^{+0.5}_{-0.5}$ | |
| $D_{s1}$ | $\left(2456^{+15}_{-21}, 0\right)$ | $10.4^{+0.8}_{-0.7}$ | $7.6^{+0.5}_{-0.4}$ | |
| $B_{s0}^*$ | $\left(5720^{+16}_{-23}, 0\right)$ | $23.1^{+1.8}_{-1.7}$ | $18.9^{+0.5}_{-0.6}$ | |
| $B_{s1}$ | $\left(5772^{+15}_{-21}, 0\right)$ | $22.8^{+1.9}_{-1.7}$ | $18.8^{+0.6}_{-0.7}$ | |
| Sector | $(M, \Gamma/2)$ | $\lvert g_1\rvert$ | | |
| $(S,I) = (-1,0)$ | | | | |
| V $(c)$ $0^+$ | $\left(2342^{+13}_{-41}, 0^{+0}_{-0}\right)$ | $9.4^{+6.0}_{-2.2}$ | | |
| V $(c)$ $1^+$ | $\left(2353^{+21}_{-14}, 84^{+42}_{-60}\right)$ | $12.5^{+9.3}_{-1.3}$ | | |
| V $(b)$ $0^+$ | $\left(5763^{+9}_{-36}, 0^{+0}_{-0}\right)$ | $22.7^{+28.6}_{-7.4}$ | | |
| V $(b)$ $1^+$ | $\left(5791^{+17}_{-51}, 0^{+48}_{-0}\right)$ | $32.4^{+77.1}_{-10.0}$ | | |

2. Next, $q_{\max}$ is used to determine $a^B(\mu)$ by requiring that the dimensionally and the sharp-cutoff regularized $\bar{B}_s\bar{K}$ loop functions to be also equal at threshold.

LECs and subtraction constants for $D\phi$ and $\bar{B}\phi$ interactions used in this work are collected in Table 4.5. Those in the charm sector, together with their uncertainties, are taken from Ref. [205]. Note that the values shown on Table 4.5 correspond to redefinitions of the LECs appearing in the HM$\chi$PT amplitudes of Eq. (4.3): $h_{4,5}^{\prime, D(B)} \equiv \bar{m}_{D(B)}^2 h_{4,5}^{D(B)}$, $h_{24} \equiv h_2 + h_4'$ and $h_{35} \equiv h_3 + 2h_5'$.

**Table 4.5:** LECs and subtraction constants $a(\mu = 1$ GeV) used in this work to compute the unitary $D\phi$ and $\bar{B}\phi$ UHM$\chi$PT amplitudes

| | $a$ | $h_0$ | $h_1$ | $h_{24}$ | $h_4'$ | $h_{35}$ | $h_5'$ |
|---|---|---|---|---|---|---|---|
| $D\phi$ | $-1.88^{+0.07}_{-0.09}$ | 0.014 | 0.42 | $-0.10^{+0.05}_{-0.06}$ | $-0.32^{+0.35}_{-0.34}$ | $0.25 \pm 0.13$ | $-1.88^{+0.63}_{-0.61}$ |
| $\bar{B}\phi$ | $-3.41^{+0.03}_{-0.04}$ | 0.038 | 1.17 | $-0.27 \pm 0.15$ | $-0.90^{+0.97}_{-0.93}$ | $0.68 \pm 0.36$ | $-5.23^{+1.74}_{-1.69}$ |

### 4.5.2 $J^P = 0^+$ bottom and $J^P = 1^+$ bottom and charm resonances

We conclude that also in the bottom sector and for $(S, I) = (0, 1/2)$ there is a two-pole structure, located at $(5535^{+9}_{-11}, 113^{+15}_{-17})$ MeV and $(5852^{+11}_{-12}, 36 \pm 5)$ MeV. For $(S, I) = (1, 0)$, we find a state with a mass of $5720^{+16}_{-23}$ MeV, bound by about 50 MeV, as the $D_{s0}^*(2317)$ in the charm sector. All these pole positions are very similar to those found already at $\mathcal{O}(p)$ [37]. In the $(-1, 0)$ sector, we find a virtual state located almost at threshold, which can also appear as a bound state considering the $\mathcal{O}(p^2)$ parameter uncertainties. As in the charm case, we do not find physical poles in the $(1, 1)$ sector that could be identified with the $X(5568)$, recently reported by the D0 Collaboration [212], but not seen in other experiments [213, 214]. We conclude the $X(5568)$ is not generated by the $\bar{B}_s\pi - \bar{B}K$ rescattering [215] (see also Refs. [216–218]).

Finally, we recall that HQSS relates the $0^+$ and $1^+$ sectors, and thus in the latter we find a similar pattern of bound, resonant and virtual states [33,34,37,54,55]. We highlight the predictions for the $\bar{\mathbf{3}}$ multiplet, where we find $2456^{+15}_{-21}$ MeV and $\left(2247^{+5}_{-6} - i\,107^{+11}_{-10}\right)$ MeV, for the $D_{s1}(2460)$ and a new $D_1$ resonance, respectively. In the bottom sector, we predict $5772^{+15}_{-21}$ MeV and $\left(5584^{+9}_{-11} - i\,119^{+14}_{-15}\right)$ MeV for the $B_{s1}$ and the lowest $B_1$. The higher $D_1$ and $B_1$ poles stemming from the $\mathbf{6}$ will presumably be affected by channels involving $\rho$ mesons [1, 219]. For $(S, I) = (-1, 0)$, we find, as in the $0^+$ case, an axial state located almost at threshold in the bottom sector, while for charmed mesons the pole (virtual) moves deep in the complex plane.

## 4.6 Conclusions

We have first studied the $D\pi$, $D\eta$ and $D_s\bar{K}$ scattering in the $J^P = 0^+$ and $(S, I) = (0, 1/2)$ sector. Although so far only one meson, the $D_0^*(2400)$, has been reported in experiments [206], we present a strong support for the existence of two poles in the $D_0^*(2400)$ mass region: the physical amplitudes, that contain two poles, when put in a finite volume produce energy levels that successfully describe the LQCD results obtained in Ref. [81] without adjusting any parameter. The two poles are located at $\left(2105^{+6}_{-8} - i\,102^{+10}_{-12}\right)$ MeV and $\left(2451^{+36}_{-26} - i\,134^{+7}_{-8}\right)$ MeV, with the largest couplings to the $D\pi$ and $D_s\bar{K}$ channels, respectively. A group theoretical analysis shows that the lower pole and the $D_{s0}^*(2317)$ complete the $\bar{\mathbf{3}}$ multiplet, being thus flavour SU(3) partners, with the mass of the lower nonstrange resonance smaller than that of the strange one. We expect the two-pole structure to produce distinctive features in $D\pi$, $D\eta$ and $D_s\bar{K}$ invariant mass spectra in high-energy reactions, such as $\bar{B}$ decays. In particular, despite of its large width, the higher pole shows up as a narrow peak in the $D_s\bar{K} \to D_s\bar{K}$ amplitude and should produce a sizeable near-threshold enhancement. Note that clear $D_s\bar{K}$ threshold enhancements have been already observed in $B$ decays [208, 209]. Future data from better statistics experiments, such as LHCb and Belle-II, will shed light into their origin. In Chapter 5 we will pay a special attention to the $B^- \to D^+\pi^-\pi^-$ reaction, recently measured by LHCb.

A similar resonance pattern is also found in the bottom sector. Besides the two-pole structure, we stress the possible existence of a near-threshold bound or virtual state in the $\bar{B}\bar{K}$ (or $BK$) channel, both for $0^+$ and $1^+$ sectors. These exotic states, with quark content $bs\bar{d}\bar{u}$, will have a large impact in the scattering length, and if bound they could only decay through weak and/or electromagnetic interactions.

The predicted phase shifts, both in the charm and bottom sectors, can be used as input to the Omnès representation of the scalar form factors describing heavy meson semileptonic decays [40, 63]. Thus, the special two-pole structure discussed here is also of interest to achieve an accurate determination of the CKM matrix elements. We will address this issue in Chapter 6.

It is also worthwhile to notice the resemblance between the results obtained here for the $D_0^*(2400)$ and the widely discussed two-pole structure of the $\Lambda(1405)$ linked to $\Sigma\pi$ and $N\bar{K}$ [204, 206, 220–222]. The existence of such a two-pole structure is rooted in both cases in chiral dynamics, which on one hand determines the interaction strength, and on the other hand ensures the lightness of pions and kaons. The latter is important to separate the two poles from higher hadronic channels. A two-pole structure driven by chiral dynamics is also found in Refs. [211, 223, 224] for the $K_1(1270)$.

# Chapter 5

# PUZZLES AND ANSWERS IN OPEN-CHARM MESON SPECTROSCOPY

## 5.1 Introduction

Until the beginning of the millennium, heavy-hadron spectroscopy was assumed to be well understood by means of the quark model [10, 11], which describes the positive-parity ground state charm mesons as bound systems of a heavy quark and a light antiquark in a $P$-wave. This belief was put into question in 2003, when the charm-strange scalar ($J^P = 0^+$) and axial-vector ($1^+$) mesons $D_{s0}^*(2317)$ [15] and $D_{s1}(2460)$ [16] were discovered (for recent reviews on new hadrons, see Refs. [84, 225–230]), since the states showed properties at odds with the quark model. Moreover, attempts to adjust the quark model raised more questions [231]. Various alternative proposals were put forward about the nature of these new states including $D^{(*)}K$ hadronic molecules (loosely bound states of two colorless hadrons) [30, 76], tetraquarks (compact states made of two quarks and two antiquarks) [232] and chiral partners (doublets due to the chiral symmetry breaking of QCD in heavy-light systems) [53, 233]. The situation became more obscure in 2004, when two new charm-nonstrange mesons, the $D_0^*(2400)$ [61] and $D_1(2430)$ [59], were observed. In brief, the experimental discoveries brought up three puzzles:

(1) Why are the $D_{s0}^*(2317)$ and $D_{s1}(2460)$ masses much lower than the quark model expectations for the lowest $0^+$ and $1^+$ $c\bar{s}$ mesons?

(2) Why is the mass difference between the $D_{s1}(2460)$ and the $D_{s0}^*(2317)$ equal to that between the ground state vector meson $D^{*+}$ and pseudoscalar meson $D^+$ within 2 MeV?

(3) Why are the $D_0^*(2400)$ and $D_1(2430)$ masses almost equal to or even higher than their strange siblings, a relationship exploited in many works [56, 234–236], although states with an additional strange quark are typically at least 100 MeV heavier since $m_s/m_d \simeq 20$, see, e.g., Ref. [206]?

Although their bottom cousins are still being searched for in high-energy experiments, it is natural to ask whether such puzzles will be duplicated there and in other sectors.

As outlined below, in recent works it was demonstrated that analyses combining EFT methods with LQCD allows one to resolve all those puzzles. These analyses suggest that all low-lying positive-parity heavy open-flavour mesons qualify as hadronic molecules. Here we add two crucial pieces to the existing line of reasoning, namely we propose a lattice QCD study at unphysical quark masses that will allow one to see the two-meson character of the mentioned states more explicitly, and we demonstrate that recent data on $B^- \to D^+\pi^-\pi^-$ show a nontrivial structure fully in line with the proposed dynamical picture.

**Table 5.1:** Predicted masses of the lowest positive-parity heavy-strange mesons in comparison with the measured values [206] and latest LQCD results, in units of MeV. These results were already presented in Chapter 4.

| | prediction | RPP | LQCD |
|---|---|---|---|
| $D_{s0}^*$ | $2315^{+18}_{-28}$ | $2317.7 \pm 0.6$ | $2348^{+7}_{-4}$ [45] |
| $D_{s1}$ | $2456^{+15}_{-21}$ | $2459.5 \pm 0.6$ | $2451 \pm 4$ [45] |
| $B_{s0}^*$ | $5720^{+16}_{-23}$ | – | $5711 \pm 23$ [58] |
| $B_{s1}$ | $5772^{+15}_{-21}$ | – | $5750 \pm 25$ [58] |

One reason why the analyses that led to the $D_0^*(2400)$ and $D_1(2430)$ resonance parameters in the RPP [206] should be questioned is that the amplitudes used were inconsistent with constraints from the chiral symmetry of QCD. As its chiral symmetry is spontaneously broken, the pions, kaons and eta arise as Goldstone Bosons with derivative and thus energy-dependent interactions even for $S$-wave couplings. The standard Breit Wigner (BW) resonance shapes used in the experimental analyses correspond, however, to constant couplings. Moreover, the energy range of these states overlaps with various $S$-wave thresholds that necessarily need to be considered in a sound analysis, as these thresholds can leave a remarkable imprint on observables as will be shown below. As we have discussed at length, a theoretical framework satisfying such requirements is provided by the Unitarized Chiral Perturbation Theory (U$\chi$PT) for heavy mesons [33, 34, 37, 38, 40, 42, 54, 199, 205, 237]: UHM$\chi$PT. In this approach, $\chi$PT at a given order is used to calculate the interaction potential which is then resummed in a scattering equation to fulfil exact two-body unitarity and allows for the generation of resonances as pioneered in Ref. [138]. Although there is no unique method for unitarization, different methods do not differ much as long as there are no prominent left-hand cuts [136], as is the case here. We will employ here the NLO version whose free parameters have been fixed to the Goldstone-Boson–charm-meson scattering lengths determined in fully dynamical LQCD in channels without disconnected diagrams [205]. Later it was demonstrated [3] (previous chapter) that these coupled-channel amplitudes properly predict the energy levels generated in LQCD (with a pion mass $M_\pi \simeq 391$ MeV) for the isospin-1/2 channel even beyond the threshold [81]. This means that now the scattering amplitudes for the coupled Goldstone-Boson–charm-meson system are available, and that are based on QCD. Moreover, those amplitudes allow us to identify the poles in the complex energy plane reflecting the lowest positive-parity meson resonances of QCD in the charm sector as well as in the bottom sector, once heavy quark flavor symmetry [185] is employed (see previous Chapter 4). The predicted masses for the lowest charm-strange positive-parity mesons are fully in line with the well-established measurements, and those for the bottom-strange mesons are consistent with LQCD results with an almost physical pion mass [58], see Table 5.1 where the uncertainties quoted stem from the one-sigma uncertainties of the parameters in the NLO UHM$\chi$PT determined in Ref. [205].

The first two of the puzzles listed above are solved in this picture: the $D^{(*)}K$ hadronic molecules do not correspond to the quark model $c\bar{s}$ states; spin symmetry predicts that the binding energies are independent of the heavy meson spin up to an uncertainty of about 10%, as the leading spin symmetry breaking interaction is also of NLO in the chiral expansion. Moreover, there are two poles, corresponding to two resonances, in the

**Table 5.2:** Predicted poles corresponding to the positive-parity heavy-light nonstrange mesons given as $(M, \Gamma/2)$, with $M$ the mass and $\Gamma$ the total decay width, in units of MeV. The current RPP [206] values are listed in the last column. These results were already obtained in Chapter 4

| | lower pole | higher pole | RPP |
|---|---|---|---|
| $D_0^*$ | $\left(2105^{+6}_{-8}, 102^{+10}_{-11}\right)$ | $\left(2451^{+35}_{-26}, 134^{+7}_{-8}\right)$ | $(2318 \pm 29, 134 \pm 20)$ |
| $D_1$ | $\left(2247^{+5}_{-6}, 107^{+11}_{-10}\right)$ | $\left(2555^{+47}_{-30}, 203^{+8}_{-9}\right)$ | $(2427 \pm 40, 192^{+65}_{-55})$ |
| $B_0^*$ | $\left(5535^{+9}_{-11}, 113^{+15}_{-17}\right)$ | $\left(5852^{+11}_{-12}, 36 \pm 5\right)$ | – |
| $B_1$ | $\left(5584^{+9}_{-11}, 119^{+14}_{-17}\right)$ | $\left(5912^{+9}_{-10}, 42^{+5}_{-4}\right)$ | – |

$I = 1/2$ and strangeness $S = 0$ channel. The predicted poles, located at the complex energies $M - i\,\Gamma/2$, for both scalar and axial-vector charm and bottom mesons are listed in Table 5.2. The masses for the lower nonstrange resonances are smaller than those for the strange ones, leading to the solution to the third puzzle as we already commented in Chapter 4. For comparison the currently quoted masses and widths of the $D_0^*(2400)^0$ and $D_1(2430)^0$ given in RPP are also listed.

This pattern of two $I = 1/2$ states emerges naturally in the underlying formalism since already leading order HM$\chi$PT interactions are attractive in two flavour multiplets, to which the two states belong: the anti-triplet and the sextet [3, 33]. These two scalar isospin $I = 1/2$ states were predicted in the earlier works of Refs. [33, 37], where, however, less refined amplitudes were employed.

Given the above discussion, it is important to test the scenario outlined above as much as possible. In this chapter we discuss two possible paths: On the one hand we propose a numerical experiment on the lattice, on the other hand we demonstrate that recent experimental data provide additional support of the nontrivial dynamics that leads to the existence of the light positive-parity open-charm states. This work is based on the results of Ref. [6].

**The sextet state.** If the mentioned states were $\bar{q}c$ states, they would all be members of the flavour anti-triplet—the presence of the sextet is a nontrivial prediction emerging from the meson-meson dynamics that the picture presented above is based on. We notice that while we predicted two $I = 1/2$ states (see Table 5.2), the Hadron Spectrum Collaboration reported only one, located just below the $D\pi$ threshold, in their lattice calculation at $M_\pi \simeq 391$ MeV [81]. This is in line with the expectation that the lower pole would become a bound state at $M_\pi \gtrsim 350$ MeV [205]. The authors of Ref. [81] report that they "do not find any further poles in the region where ... [their lattice analysis] constrained the amplitudes". This does on the other hand not exclude the presence of the second pole advocated in Ref. [3] as well as above: The quote simply reflects the fact that while various of the amplitudes employed in the analysis of Ref. [81] contained a second pole, its location was strongly parametrization-dependent [238]. With the quark masses used in Ref. [81], the predicted sextet pole is located deep in the complex plane [3], and thus it is not captured easily. The advantage of our amplitudes compared to those employed in the analysis of Ref. [81] is that they are constrained by both the pattern of chiral symmetry breaking of QCD as well as lattice data in additional channels. To further test our explanation for the light positive parity open charm states, we propose to search

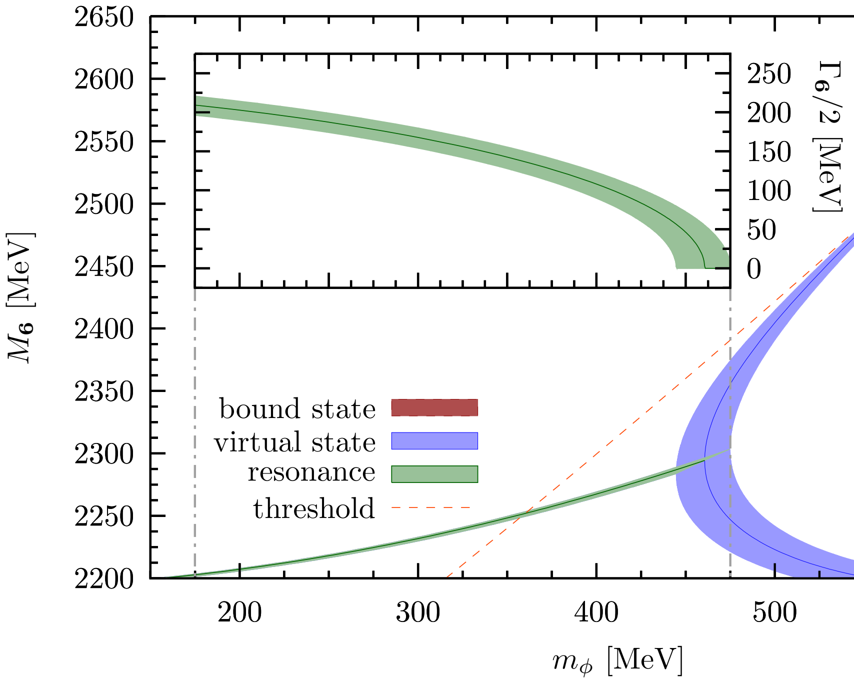

**Figure 5.1:** Illustration of the mass of the predicted sextet state at the SU(3) symmetric point as a function of the Goldstone boson mass $m_\phi$. Below $m_\phi \lesssim 475$ MeV, the pole is a resonance with its imaginary part ($\Gamma_{\mathbf{6}}/2$) shown in the inserted sub-figure. Above $m_\phi \simeq 475$ MeV, it evolves into a pair of virtual states, and finally it becomes a bound state at $m_\phi \simeq 600$ MeV.

for them in lattice studies at a SU(3) symmetric point, with a relatively large quark mass $m_u = m_d = m_s$, such that the lightest pseudoscalar-meson masses will be near or above $m_\phi \gtrsim 475$ MeV. We predict that the sextet pole will become a virtual state below threshold for such large quark masses, and that it would even become a bound state for higher quark masses. This behaviour is illustrated in Fig. 5.1, where one can see that now the pole is close to threshold, and it should be easy to detect in a lattice calculation.

Note that the trajectory of the pole displayed in Fig. 5.1, where resonance poles exist in the complex energy plane below threshold, is a common pattern for two-meson states in a relative $S$-wave. This feature is discussed in quite general terms in Ref. [239] (see also Refs. [134,207] for the $f_0(500)$ case) and was first presented for the open flavor states in the focus here in Ref. [199].

## 5.2 The $D\pi$ final state interaction in the $B^- \to D^+\pi^-\pi^-$ reaction

In the following, we show that our solution to these puzzles is backed by precise experimental data by showing that the amplitudes with the two $D_0^*$ states are fully consistent with the LHCb measurements of the reaction $B^- \to D^+\pi^-\pi^-$ [240], which are at present the best data providing access to the $D\pi$ system and thus to the nonstrange scalar charm mesons. Therefore, all the available theoretical, experimental and LQCD knowledge is consistent with the existence of two $D_0^*$ states in the mass region where there was believed to be only one $D_0^*(2400)$.

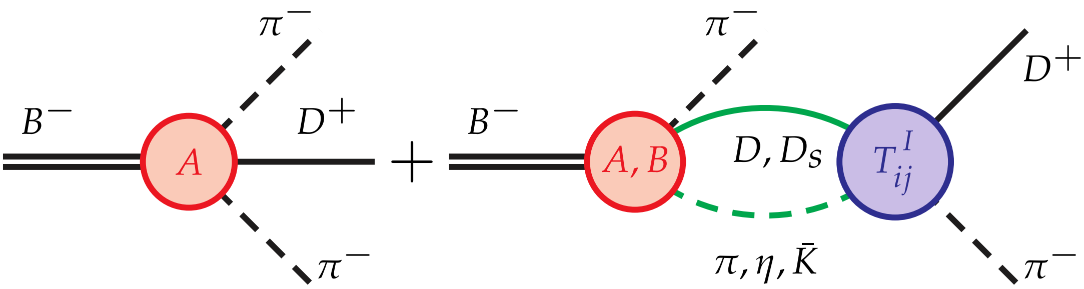

**Figure 5.2:** The decay amplitude for $B^- \to D^+\pi^-\pi^-$. Here, $A, B$ parametrize the production vertex, see Eq. (5.11), and $T^I_{ij}$ denotes the final state interactions between the charm and the light mesons.

### 5.2.1 Effective Lagrangian

We begin briefly discussing the effective Lagrangian for the weak decays $\bar{B} \to D$, with the emission of two light pseudoscalar mesons. They are induced by the Cabibbo-allowed transition $b \to c\bar{u}d$. In the phase space region near the $D\pi$ threshold, chiral symmetry puts constraints on one of the two pions while the other one moves fast and can be treated as a matter field. Moreover, its interaction with the other particles in the final state can be safely neglected. Then the relevant chiral effective Lagrangian reads [241],

$$\begin{aligned}\mathcal{L}_{\text{eff}} \;=\; & \bar{B}\big[c_1\,(u_\mu t M + M t u_\mu) + c_2\,(u_\mu M + M u_\mu)\,t \\ & + c_3\,t\,(u_\mu M + M u_\mu) + c_4\,(u_\mu\langle Mt\rangle + M\langle u_\mu t\rangle) \\ & + c_5\,t\langle M u_\mu\rangle + c_6\langle (M u_\mu + u_\mu M)\,t\rangle\big]\partial^\mu D^\dagger\,. \end{aligned} \tag{5.1}$$

Here, $\bar{B} = (B^-, \bar{B}^0, \bar{B}^0_s)$ and $D = (D^0, D^+, D^+_s)$ are the fields for bottom and charm mesons, $\langle \ldots \rangle$ denotes the trace in the SU(3) light-flavour space, and $u_\mu = i(u^\dagger\partial_\mu u - u\partial_\mu u^\dagger)$ (see Eq. (3.96)) is the axial current derived from chiral symmetry. The Goldstone Bosons are represented non-linearly *via* $u = \exp\big(i\phi/(\sqrt{2}F)\big)$ in Eq. (3.83), with $\phi$ a field matrix containing the light pseudoscalars and $F$ as the Goldstone-Boson decay constant in the chiral limit—in particular, we have that $\hat{\xi}$ in Eq. (3.35) satisfies $\hat{\xi} = \sqrt{2}\phi$. In addition, $t = uHu^\dagger$ is a spurion field with [241]

$$H = \begin{pmatrix} 0 & 0 & 0 \\ 1 & 0 & 0 \\ 0 & 0 & 0 \end{pmatrix}, \tag{5.2}$$

for Cabibbo-allowed decays. The matter field $M$, having the same form as $\phi$, describes the fast moving light meson. The $c_i$ $(i = 1, \ldots, 6)$ are LECs. This effective Lagrangian considers both chiral, for the regime with soft Goldstone Bosons, and SU(3) constraints, the latter of which has been considered in Ref. [241].

### 5.2.2 The $B^- \to \pi^-\pi^-D^+$ decay amplitude

The Feynman diagrams of the decay amplitude for $B^- \to D^+\pi^-\pi^-$ are shown in Fig. 5.2. Let us introduce the notation $p_{D^+}$, $p_{\pi^-}$ and $p^*_{\pi^-}$ to identify the four momenta of the final

$D$, fast and slow pion, respectively—note that, since we will pay attention to the regime involving small energies of the final $D^+\pi^-$ state, there will always be a relativistic pion carrying the rest of the total momenta $p_{B^-}$. All the channels ($D^+\pi^-$, $D^0\pi^0$, $D^0\eta$ and $D_s^+K^-$) coupled to $D^+\pi^-$ need to be considered in the intermediate states. The decay amplitude in the energy region up to 2.6 GeV, which is sufficient to study the low-lying scalar states, can be decomposed into $S$-, $P$- and $D$-waves,

$$\mathcal{A}(B^- \to D^+\pi^-\pi^-) = \sum_{L=0}^{2} \sqrt{2L+1}\mathcal{A}_L(s)P_L(z)\,, \tag{5.3}$$

where $\mathcal{A}_{0,1,2}(s)$ correspond to the amplitudes with $D^+\pi^-$ in the $S$ , $P$ and $D$ waves, respectively, and $P_L(z)$ are the Legendre polynomials. For the $P$- and $D$-wave amplitudes we use the same BW form as in the LHCb analysis [240]. Note that the coefficients/normalization entering the partial wave expansion of Eq. (5.3) are chosen as in Ref. [240], and are different from the standard form introduced in Eq. (2.21).

**Breit-Wigner amplitudes in $P$ and $D$ waves.** In the work of Ref. [240], the LHCb collaboration obtained the masses and widths of the vector ($J^P = 1^-$) resonances, $D^*$ and $D^*(2680)$, and the tensor state ($J^P = 2^+$) $D_2(2460)$, which are present in the $L = 1$ and $L = 2$ partial wave amplitudes. In order to analyze their data, we choose to represent the $P$ and $D$ partial waves in the same way. We consider BW amplitudes

$$\mathcal{A}_1(s) = a_1 T_1^{D^*}(s) + b_1 T_1^{D^*(2680)}(s),\ a_1, b_1 \in \mathbb{C} \tag{5.4}$$

$$\mathcal{A}_2(s) = a_2 T_2^{D_2(2460)}(s),\ a_2 \in \mathbb{C}, \tag{5.5}$$

where the complex undetermined coefficients $a_1$, $b_1$ and $a_2$ will be fitted to the experimental data. The functions $T_L^{\mathrm{R}}(s)$ are the BW corresponding to a $D^+\pi^-$ resonance “R”, with mass $M$, total width $\Gamma$, and appearing in the partial wave amplitude $L$,

$$T_L^{\mathrm{R}}(s) = R(s) \times X\left(|\vec{p}(s)|\, r\right) \times X\left(|\vec{p}^{\,*}(s)|\, r\right) \times \left|\frac{\vec{p}(s)}{\vec{p}(M^2)}\right|^L \left|\frac{\vec{p}^{\,*}(s)}{\vec{p}^{\,*}(M^2)}\right|^L M\Gamma \tag{5.6}$$

where $\vec{p}^{\,*}(s)$ and $\vec{p}(s)$ denote the three momentum of the slow—belonging to the $D^+\pi^-$ system—and fast pion, in the $D^+\pi^-$ cm frame. Their expressions will be given later in the next section. The parameter “$r$” is called the barrier radius, and we take the value $r = 4.0\ \mathrm{GeV}^{-1}$ as in Ref. [240]. The BW amplitudes of Eq. (5.6) depend on two further functions, the radial function $R(s)$,

$$R(s) = \frac{1}{(M^2 - s) - iM\tilde{\Gamma}\left(\sqrt{s}\right)}, \tag{5.7}$$

$$\tilde{\Gamma}(x) = \Gamma \times \left[\frac{|\vec{p}^{\,*}(x^2)|}{|\vec{p}^{\,*}(M^2)|}\right]^{2L+1} \times \frac{M}{x} \times X^2\left(|\vec{p}^{\,*}(x^2)|\, r\right). \tag{5.8}$$

**Table 5.3:** Numerical values of the mass and width of the different resonances included as relativistic BW amplitudes in $P$ and $D$ partial waves (see Eqs. (5.3), (5.4) and (5.5)), taken from Ref. [240].

| state | $L$ | $M$ [MeV] | $\Gamma$ [MeV] |
|---|---|---|---|
| $D^*$ | 1 | 2006.98 | 2.1 |
| $D_1^*(2680)$ | 1 | 2681.10 | 186.7 |
| $D_2^*(2460)$ | 2 | 2463.70 | 47.0 |

and the Blatt-Weiskopf barrier factors $X\,(x)$

$$X\,(x) = \begin{cases} 1 & L=0, \\ \sqrt{\dfrac{1+x_0^2}{1+x^2}} & L=1, \\ \sqrt{\dfrac{x_0^4+3x_0^2+9}{x^4+3x^2+9}} & L=2, \end{cases} \tag{5.9}$$

$$x_0 = \left(\left|\vec{k}(M^2)\right| r\right), \text{ with } \vec{k} = \vec{p}^{\,*} \text{ or } \vec{p}. \tag{5.10}$$

Note that the BW form in Eq. (5.6) may be different with respect to other standard versions, since we are including the normalization factors $M\Gamma/\left|\vec{p}^{\,*}(M^2)\right|^L \left|\vec{p}(M^2)\right|^L$ in order to have $T_L^{\rm R}(M^2) \sim 1$, which turns out convenient in the numerical calculations—with the purpose of avoiding coefficients $a_1$, $b_1$ and $a_2$ showing ridiculously different scales. As already mentioned, we use the values of mass and width for the different resonances obtained in the LHCb fit (see Tables III and IV in Ref. [240]) using relativistic BW. The values can be found here in Table 5.3.

**$S$-wave amplitude.** However, for the $S$-wave we employ

$$\begin{aligned} \mathcal{A}_0(s) \;=\; & A\Bigg\{E_\pi\left[2+G_1(s)\left(\frac{5}{3}T_{11}^{1/2}(s)+\frac{1}{3}T^{3/2}(s)\right)\right] \\ & +\frac{1}{3}E_\eta G_2(s)T_{21}^{1/2}(s)+\sqrt{\frac{2}{3}}E_{\bar{K}}G_3(s)T_{31}^{1/2}(s)\Bigg\} \\ & +BE_\eta G_2(s)T_{21}^{1/2}, \end{aligned} \tag{5.11}$$

where $A$ and $B$ are two independent couplings following from SU(3) flavor symmetry [241], and $E_{\pi,\eta,\bar{K}}$ are the energies of the light mesons. In terms of the LECs appearing in the effective Lagrangian of Sec. 5.2.1, the parameters $A$ and $B$ in Eq. (5.11) can be expressed as $A = \sqrt{2}(c_1+c_4)/F$ and $B = 2\sqrt{2}(c_2+c_6)/(3F)$. Here the $T_{ij}^I(s)$ are the UHM$\chi$PT $S$-wave scattering amplitudes for the coupled-channel system with total isospin $I$, where $i, j$ are channel indices with $1, 2$ and $3$ referring to $D\pi$, $D\eta$ and $D_s\bar{K}$, respectively. These scattering amplitudes were determined in Ref. [205] where also all the parameters were fixed, and they can be found in Chapter 4. The unitarity relation of Eq. (2.32) is readily adapted to the present situation in the case of the $S$-wave decay amplitude $\mathcal{A}_{0,i}$,

$$\operatorname{Im}\mathcal{A}_{0,i}(s) = -\sum_j T_{ij}^*(s)\rho_j(s)\mathcal{A}_{0,j}(s), \tag{5.12}$$

with $\rho_j(s) = \sigma_j(s)/8\pi$ the two-body phase space factor for channel-$j$. Equation (5.12) is satisfied as long as $\operatorname{Im} G_i(s) = -\rho_i(s)$ (see Eq. (2.80)), which allows us to represent $G_i(s)$ via a once-subtracted dispersion relation [242]. The same subtraction constant, $a_A$, is taken for all channels, and it constitutes one more free parameter. The amplitude of Eq. (5.11) embodies chiral symmetry constraints and coupled-channel unitarity, and thus has a sound theoretical foundation. Here the final state interaction between the two $\pi^-$ mesons is neglected because the two pions are in an isospin-tensor state, and they have a large relative momentum so that they quickly fly away from each other.

## 5.3 Angular moments

Following Ref. [243], the angular moments of order $L$ are defined as the weighted sum of the events in each bin of energy, where the sum should be performed over all the possible angles of the $D^+\pi^-$ system relative to the remaining—fast—pion. The weights for each angular moment are given by the corresponding Legendre Polynomial[1] of order $L$—for further details, the reader may see p. 12 of Ref. [243], and also Sec. V of Ref. [240]. The—unnormalized—angular moments of the $B^- \to D^+\pi^-\pi^-$ decay, can be written as follows,

$$\langle P_L \rangle \sim \int_{-1}^{+1} \frac{\mathrm{dEvents}}{\mathrm{d}\cos\phi \; \mathrm{d}m_{D^+\pi^-}} \times P_L(\cos\phi)\; \mathrm{d}\cos\phi \tag{5.13}$$

where $\phi$ is the angle between the three-momentum of the pion in the $D^+\pi^-$ system relative to the three-momentum of the remaining pion, in the $D^+\pi^-$ frame.

### 5.3.1 The partial decay rate

The experimental event distribution is proportional to the partial decay rate [206],

$$\mathrm{d}\Gamma = \frac{1}{(2\pi)^3}\frac{1}{32 m_{B^-}^3} \left|\mathcal{A}\left(B^- \to D^+\pi^-\pi^-\right)\right|^2 \mathrm{d}m_{D^+\pi^-}^2 \; \mathrm{d}m_{\pi^-\pi^-}^2, \tag{5.14}$$

where $m_{B^-}$, $m_{D^+\pi^-}^2$ and $m_{\pi^-\pi^-}^2$ label the mass of the decaying $B$ meson, the invariant mass squared of the $D^+\pi^-$ and $\pi^-\pi^-$ pairs, respectively. The goal now is to express $\mathrm{d}\Gamma$ as a function of $m_{D^+\pi^-}$ and $\cos(\phi)$ as in Eq. (5.13), because,

$$\frac{\mathrm{dEvents}}{\mathrm{d}\cos\phi \; \mathrm{d}m_{D^+\pi^-}} \propto \frac{\mathrm{d}\Gamma}{\mathrm{d}\cos\phi \; \mathrm{d}m_{D^+\pi^-}}. \tag{5.15}$$

Recalling the definitions,

$$m_{D^+\pi^-}^2 = (p_{D^+} + p_{\pi^-}^*)^2 \tag{5.16}$$

$$m_{\pi^-\pi^-}^2 = (p_{\pi^-} + p_{\pi^-}^*)^2\,, \tag{5.17}$$

where we have denoted as $p_{\pi^-}^* = \left(p_{\pi^-}^{0,*}, \vec{p}_{\pi^-}^{\,*}\right)$ the momentum of the—slow—pion belonging to the $D^+\pi^-$ system. In the $D^+\pi^-$ cm frame we have,

$$\begin{aligned} m_{D^+\pi^-}^2 &= (p_{D^+} + p_{\pi^-}^*)^2 && (5.18)\\ &= \left(p_{D^+}^0 + p_{\pi^-}^{0,*}\right)^2 \equiv s && (5.19)\end{aligned}$$

---

[1] The Legendre polynomials have been introduced in Chapter 2, see also Eq. (2.23) in Sec. 2.2.2 for details on their normalization.

On the other hand, in the same frame,

$$
\begin{aligned}
m^2_{\pi^-\pi^-} &= \left(p_{\pi^-} + p^*_{\pi^-}\right)^2 && (5.20)\\
&= p^2_{\pi^-} + \left(p^*_{\pi^-}\right)^2 + 2 p_{\pi^-} p^*_{\pi^-} && (5.21)\\
&= 2 m^2_{\pi^-} + 2 p^0_{\pi^-} p^{0,\,*}_{\pi^-} - 2\,|\vec{p}_{\pi^-}|\,|\vec{p}^{\,*}_{\pi^-}| \cos\phi . && (5.22)
\end{aligned}
$$

At this point, is convenient to bring here total four-momentum conservation,

$$
\begin{aligned}
p_{B^-} &= p_{D^+} + p_{\pi^-} + p^*_{\pi^-} && (5.23)\\
p_{B^-} - p_{\pi^-} &= p_{D^+} + p^*_{\pi^-} && (5.24)\\
\Rightarrow \left(p_{B^-} - p_{\pi^-}\right)^2 &= s, && (5.25)
\end{aligned}
$$

which leads to the following expressions of the magnitude of the three-momentum in terms of the variable $s$ defined in Eq. (5.19),

$$
\begin{aligned}
|\vec{p}^{\,*}_{\pi^-}| &= \frac{\lambda^{1/2}(s, m^2_{\pi^-}, m^2_{D^+})}{2\sqrt{s}} && (5.26)\\
|\vec{p}_{\pi^-}| &= \frac{\lambda^{1/2}(m^2_{B^-}, m^2_{\pi^-}, s)}{2\sqrt{s}}, && (5.27)
\end{aligned}
$$

together with the energies

$$
\begin{aligned}
p^{0\,*}_{\pi^-} &= \frac{s + m^2_{\pi} - m^2_{D^+}}{2\sqrt{s}} && (5.28)\\
p^{0}_{\pi^-} &= \frac{m^2_{B^-} - s - m^2_{\pi}}{2\sqrt{s}}. && (5.29)
\end{aligned}
$$

We must rewrite the differential decay rate in terms of the new variables $\sqrt{s} \equiv m_{D^+\pi^-}$ and $\cos\phi$. The transformation between the old variables—$m^2_{D^+\pi^-}$, $m^2_{\pi^-\pi^-}$—and the new ones—$\sqrt{s}$, $\cos\phi$—are given by Eqs. (5.19) and (5.22). We shall need the Jacobian matrix of the transformation:

$$
\begin{aligned}
J\left[\sqrt{s}, \cos(\phi)\right] &= \begin{pmatrix} \frac{\partial m^2_{D^+\pi^-}}{\partial \sqrt{s}} & \frac{\partial m^2_{D^+\pi^-}}{\partial \cos\phi} \\ \frac{\partial m^2_{\pi^-\pi^-}}{\partial \sqrt{s}} & \frac{\partial m^2_{\pi^-\pi^-}}{\partial \cos\phi} \end{pmatrix}, && (5.30)\\
&= \begin{pmatrix} 2\sqrt{s} & 0 \\ 2\left(p^0_{\pi^-} p^{0\,*}_{\pi^-}\right)' - 2\left[|\vec{p}_{\pi^-}|\,|\vec{p}^{\,*}_{\pi^-}|\right]' \cos\phi & -2\,|\vec{p}_{\pi^-}|\,|\vec{p}^{\,*}_{\pi^-}| \end{pmatrix}. && (5.31)
\end{aligned}
$$

where $[\ldots]'$ denotes a derivative with respect to $\sqrt{s}$. We get,

$$
\mathrm{d}\Gamma = \frac{1}{(2\pi)^3} \frac{1}{32 m^3_{B^-}} \left|\mathcal{A}\right|^2 4\sqrt{s}\,|\vec{p}_{\pi^-}|\,|\vec{p}^{\,*}_{\pi^-}|\,\mathrm{d}\left(\sqrt{s}\right) \mathrm{d}\cos\phi . \tag{5.32}
$$

Alternatively, coming back to the notation $\sqrt{s} \to m_{D^+\pi^-}$, we finally get the differential decay rate in terms of the $D^+\pi^-$ invariant mass and—what is called in Ref. [240]—the helicity angle of the $D^+\pi^-$ system, *i.e.*, the angle between the momentum of the pion in the $D^+\pi^-$ system relative to the momentum of the other pion, evaluated in the $D^+\pi^-$ frame,

$$
\frac{\mathrm{d}\Gamma}{\mathrm{d}\cos\phi\ \mathrm{d}m_{D^+\pi^-}} = \frac{1}{64\pi^3 m^3_{B^-}} \sqrt{s}\,|\vec{p}_{\pi^-}|\,|\vec{p}^{\,*}_{\pi^-}|\,\left|\mathcal{A}\right|^2 . \tag{5.33}
$$

With the relations of Eqs. (5.3), (5.13), (5.15) and (5.33) we finally obtain the angular moments as,

$$\langle P_L \rangle \sim \int_{-1}^{+1} |\mathcal{A}|^2 \, |\vec{p}^{\,*}_{\pi^-}| \, |\vec{p}_{\pi^-}| \times P_L(\cos\phi) \mathrm{d}\cos\phi \tag{5.34}$$

$$= |\vec{p}^{\,*}_{\pi^-}| \, |\vec{p}_{\pi^-}| \int_{-1}^{+1} \left| \mathcal{A}_0 P_0(z) + \sqrt{3}\mathcal{A}_1 P_1(z) + \sqrt{5}\mathcal{A}_2 P_2(z) \right|^2 \times P_L(z) \mathrm{d}z \tag{5.35}$$

where we should keep in mind that we do not consider partial waves with $L > 2$. After the $\phi$ integration—for $L = 0$, 1, 2 and 3—the result is,

$$\begin{aligned} &\int_{-1}^{+1} \mathrm{d}z \, \left| \mathcal{A}_0 P_0(z) + \sqrt{3}\mathcal{A}_1 P_1(z) + \sqrt{5}\mathcal{A}_2 P_2(z) \right|^2 \times P_L(z) \\ &= \begin{cases} 2\left(\mathcal{A}_0\mathcal{A}_0^* + \mathcal{A}_1\mathcal{A}_1^* + \mathcal{A}_2\mathcal{A}_2^*\right), & (L=0) \\ \frac{2}{5\sqrt{3}}\left(5\left(\mathcal{A}_0\mathcal{A}_1^* + \mathcal{A}_1\mathcal{A}_0^*\right) + 2\sqrt{5}\left(\mathcal{A}_1\mathcal{A}_2^* + \mathcal{A}_2\mathcal{A}_1^*\right)\right), & (L=1) \\ \frac{2}{\sqrt{5}}\left(\mathcal{A}_0\mathcal{A}_2^* + \mathcal{A}_2\mathcal{A}_0^*\right) + \frac{4}{5}\mathcal{A}_1\mathcal{A}_1^* + \frac{4}{7}\mathcal{A}_2\mathcal{A}_2^*, & (L=2) \\ \frac{6}{7}\sqrt{\frac{3}{5}}\left(\mathcal{A}_1\mathcal{A}_2^* + \mathcal{A}_2\mathcal{A}_1^*\right), & (L=3) \end{cases} \end{aligned} \tag{5.36}$$

Let us introduce the notation $\mathcal{A}_i\mathcal{A}_j^* + \mathcal{A}_j\mathcal{A}_i^* = 2\,|\mathcal{A}_i|\,|\mathcal{A}_j|\cos\left(\delta_j - \delta_i\right)$, with $\delta_i$ the phases of $\mathcal{A}_i$. In this way, we can directly compare with the LHCb results of Ref. [240] directly with

$$\langle P_0 \rangle \propto |\vec{p}^{\,*}_{\pi^-}| \, |\vec{p}_{\pi^-}| \left(|\mathcal{A}_0|^2 + |\mathcal{A}_1|^2 + |\mathcal{A}_2|^2\right), \tag{5.37}$$

$$\langle P_2 \rangle \propto |\vec{p}^{\,*}_{\pi^-}| \, |\vec{p}_{\pi^-}| \left(\frac{2}{5}|\mathcal{A}_1|^2 + \frac{2}{7}|\mathcal{A}_2|^2 + \frac{2}{\sqrt{5}}|\mathcal{A}_0|\,|\mathcal{A}_2|\cos\left(\Delta\delta_2\right)\right), \tag{5.38}$$

$$\langle P_{13} \rangle \equiv \langle P_1 \rangle - \frac{14}{9}\langle P_3 \rangle \propto |\vec{p}^{\,*}_{\pi^-}| \, |\vec{p}_{\pi^-}| \left(\frac{2}{\sqrt{3}}|\mathcal{A}_0|\,|\mathcal{A}_1|\cos\left(\Delta\delta_1\right)\right). \tag{5.39}$$

where $\Delta\delta_{1,2} \equiv \delta_{1,2} - \delta_0$ are the phase differences of $P$- and $D$-waves relative to the $S$-wave, respectively. Instead of $\langle P_1 \rangle$ and $\langle P_3 \rangle$, we propose to analyze the linear combination $\langle P_{13} \rangle$, since besides being only dependent on the $S$-$P$ interference—up to $L = 2$—is particularly sensitive to the $S$-wave phase motion. The angular moments in Eqs. (5.37), (5.38) and (5.39) contain important information about the partial-wave phase variations. Neglecting partial waves above $L \geqslant 3$ is consistent in the energy region of interest to analyze the LHCb data.

## 5.4 Results

### 5.4.1 Fit

We fit $N_{\text{data}} = 27$ data points of each LHCb moment (see Eq. (5.13)), up to the energy $M_{D^+\pi^-} = 2.54$ GeV, minimizing the merit function,

$$\chi^2(a_1, b_1, a_2, a_A, A, B) = \sum_{k=\{0,2,13\}} \sum_{n=1}^{N_{\text{data}}} \frac{\left(\langle P_k^{\text{th}} \rangle - \langle P_k^{\text{LHCb}} \rangle\right)^2}{\left(\Delta \langle P_k^{\text{LHCb}} \rangle\right)^2} \tag{5.40}$$

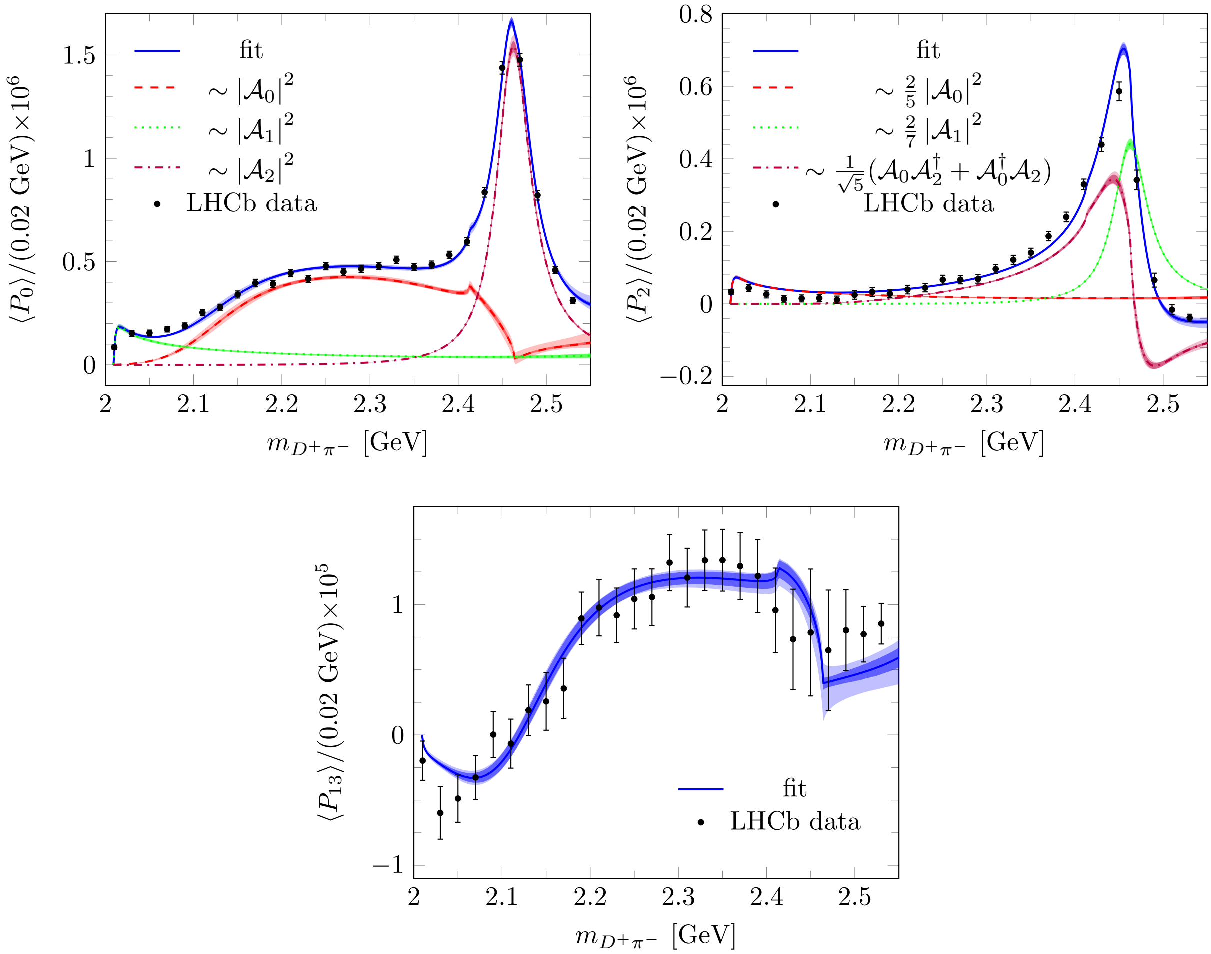

**Figure 5.3:** Fit to the LHCb data of the angular moments $\langle P_0\rangle$, $\langle P_2\rangle$ and $\langle P_{13}\rangle \equiv \langle P_1\rangle - 14\langle P_3\rangle/9$ for the $B^- \to D^+\pi^-\pi^-$ reaction [240]. The largest error among $\langle P_1\rangle$ and $14\langle P_3\rangle/9$ in each bin is taken as the error of $\langle P_{13}\rangle$ to compute the chi-square. The solid blue lines show our results, with the darker error bands corresponding to the one-sigma statistical uncertainties propagated from the fit procedure (see caption in Table 5.4 for details), while the outer bands—in lighter blue color—were obtained by adding in quadrature the $1\sigma$ uncertainties propagated from the LECs entering the UHM$\chi$PT amplitudes in the $S$-wave decay amplitude. The rest of coloured bands displayed represent the different contributions to each angular moment governed by different partial waves as can be seen in Eqs. (5.37), (5.38) and (5.39)

**Table 5.4:** Parameters obtained from the fit to the LHCb data on the angular moments in the decay $B^- \to D^+\pi^-\pi^-$ [240] (see Eq. (5.40)). The first quoted errors correspond to statistical $1\sigma$ confident-level uncertainties propagated from a large set of Montecarlo synthetic fits to randomly generated data samples assuming Gaussian statistics: $\left\langle P_k^{\text{LHCb,synth}} \right\rangle \sim \mathcal{N}(\mu = P_k^{\text{LHCb}}, \sigma = \Delta P_k^{\text{LHCb}})$. The second errors correspond to uncertainties propagated from fits where the input LECs entering the $S$-wave NLO UHM$\chi$PT amplitudes—determined in Ref. [205], (see Table 4.5)—were varied covering $1\sigma$ hyperellipses in the LECs parameter space.

| parameter | result |
|---|---|
| $a_1$ | $1.3(0.1)(0.1) + i\,(-0.8(0.1)(0.1))$ |
| $b_1 \times 10^3$ | $-2.0(0.9)(1.3) + i\,(1.5(0.7)(0.7))$ |
| $a_2 \times 10^2$ | $-1.5(0.1)(0.2) + i\,(1.9(0.1)(0.2))$ |
| $A \times 10^2$ | $-8.4(0.4)(1.6)$ |
| $B$ | $0.3(0.0)(0.1)$ |
| $a_A$ | $1.1(0.1)(0.3)$ |
| $\chi^2$/d.o.f. | $\frac{126.21}{81-9} = 1.75$ |

with $\left\langle P_k^{\text{th}} \right\rangle$ denoting the angular moments given by Eqs. (5.37), (5.38) and (5.39), which are obtained in terms of the $S$, $P$ and $D$ partial wave amplitudes introduced in Eqs. (5.4), (5.5) and (5.11). There is a total of 9 undetermined parameters $\{a_1, b_1, a_2, a_A, A, B\}$—recall that $a_1$, $b_1$ and $a_2$ are complex constants. As already explained, in addition to $S$-wave $D\pi$ amplitude given in Eq. (5.11), we include the resonances $D^*$ and $D^*(2680)$ in the $P$-wave and $D_2(2460)$ in the $D$-wave. The best fit has $\chi^2$/d.o.f. $= 1.75$ and the best fit parameters obtained are collected in Table 5.4. A comparison of the best fit with the LHCb data is shown in Fig. 5.3, where the darker inner bands reflect the one-sigma errors obtained from a bootstrap Montecarlo propagation assuming Gaussian statistics. The outer bands have been obtained by adding in quadrature to the former the uncertainties resulting from propagation of the LECs $1\sigma$ errors—note that the LECs enter the $S$-wave decay amplitude in Eq. (5.11) *via* the NLO UHM$\chi$PT amplitudes $T$. It is worthwhile to notice that in $\langle P_{13} \rangle$, where the $D_2(2460)$ does not play any role, the data show a significant variation between 2.4 and 2.5 GeV. Theoretically this feature can now be understood as a signal for the opening of the $D^0\eta$ and $D_s^+K^-$ thresholds at 2.413 and 2.462 GeV, respectively, which leads to two cusps in the amplitude. This effect is amplified by the higher $D_0^*(2400)$ pole which is relatively close to the $D_s\bar{K}$ threshold on the unphysical sheet.

### 5.4.2 $S$-wave amplitude

One might wonder if the discrepancy between our amplitude and the data for $\langle P_{13} \rangle$ at low energies points at a deficit of the former. Fortunately the LHCb Collaboration provides more detailed information on their $S$-wave amplitude in Ref. [240]: in their analysis a series of anchor points were defined where the strength and the phase of the $S$-wave amplitude were extracted from the data. Then cubic splines were used to interpolate between these anchor points. In Fig. 5.4 our $S$-amplitude fixed in the previous section is

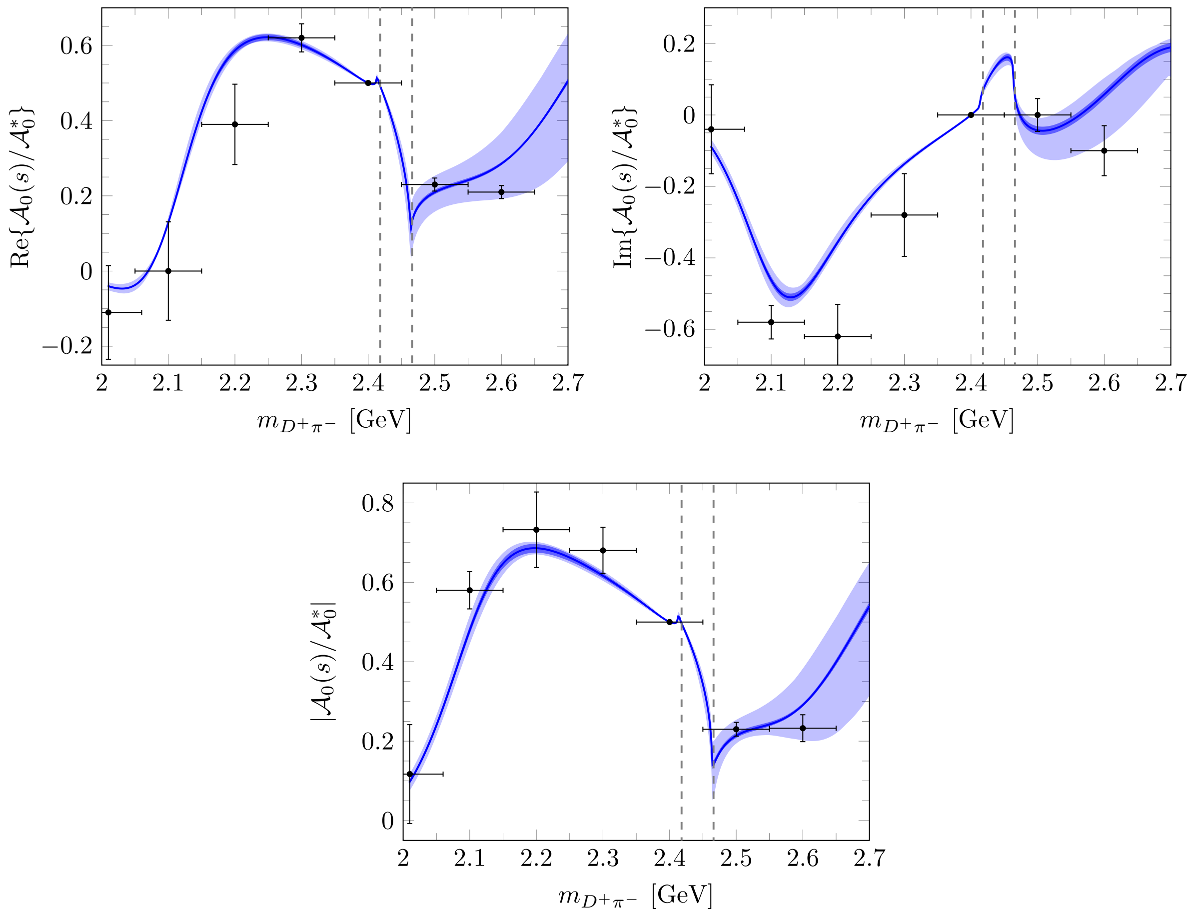

**Figure 5.4:** Comparison of the $S$-wave amplitude determined in this work to the $S$-wave anchor points found in the experimental analysis, shown as black data points [240]. The blue lines give the best fit results and the blue bands quantify the uncertainties that emerged from the fitting procedure—see caption of Fig. 5.3 and Table 5.4 for details on the error determination. The fitting range extends up to 2.55 GeV. The dashed perpendicular lines indicate the location of the $D\eta$ and $D_s\bar{K}$ threshold, respectively. Note how the $S$-wave amplitude provided in Ref. [240] is normalized to 1/2 at the energy 2.4 GeV, henceforth, we have also set $\mathcal{A}_0^* = 2\mathcal{A}_0\left([2.4\ \text{GeV}]^2\right)$.

compared to the LHCb anchor points. Not only does this figure show very clearly that the strength of the $S$-wave amplitude—largely determined by the fits to lattice data—is fully consistent with the one extracted from the data for $B^- \to D^+\pi^-\pi^-$. Additionally, it also shows the importance of the $D\eta$ and $D_s\bar{K}$ cusps and, thus, of the role of the higher pole in the $I = 1/2$ and $S = 0$ channel—even more clearly than the angular moments discussed above.

This clearly highlights the importance of a coupled-channel treatment for this reaction. An updated analysis of the LHC Run-2 data is called for to confirm the prominence of the two cusps. Notice that the shape of the $S$-wave is determined by only two real parameters ($B/A$, $a_A$), while its phase motion is largely determined from unitarity, Eq. (5.12).

## 5.5 Conclusions

In summary, we have demonstrated that amplitudes fixed from QCD input for the pNGB scattering off charm mesons not only resolve some longstanding puzzles in charm-meson spectroscopy but also are at the same time fully consistent with recent LHCb data on $B$ decays, which provide by far the most precise experimental information for the $D\pi$ system. The amplitudes have a pole corresponding to the $D_{s0}^*(2317)$ in the isoscalar strangeness $S = 1$ channel, and two poles in the $I = 1/2$ nonstrange channel [3]. The latter pair of poles should replace the lowest $J^P = 0^+$ charm nonstrange meson, $D_0^*(2400)$, listed in the RPP [206]. Similarly, the broad $D_1(2430)$ listed in RPP should also be replaced by two $J^P = 1^+$ states.

It should be stressed that the observation that certain scattering amplitudes employ poles does not necessarily imply that the corresponding states need to be interpreted as molecular states. However, the $S$-wave molecular admixture of a near-threshold state can be quantified from the scattering length directly [244]. Applying this argument to the $DK$ scattering length in the $D_{s0}^*(2317)$ channel, predicted in Ref. [205] and determined using LQCD [46], reveals that the molecular component of the $D_{s0}^*(2317)$ is larger than 70%, a conclusion confirmed later in Ref. [44, 45, 245] for both the $D_{s0}^*(2317)$ and the $D_{s1}(2460)$. All the poles listed in Tables 5.1 and 5.2 are spin-flavour partners, due to approximate QCD symmetries. Therefore, they should be envisioned as to have the same origin, i.e., hadronic molecules generated from coupled-channel two-hadron chiral dynamics.

Treating other narrow heavy mesons, such as the $D_1(2420)$ and the $D_2(2460)$, as matter fields leads to additional molecular states such as the $J^P = 1^-$ $D_{s1}^*(2860)$ [246] and its partners. In fact, the interactions of Goldstone bosons with matter fields are relatively weak at low energies because of the chiral symmetry of QCD. Even though, hadronic molecular states can be still generated. One would expect that the $S$-wave attractive interaction of other hadrons with heavy mesons, not suppressed by chiral symmetry, may produce hadron-hadron states as well, analogous to nuclei. These states are not the exclusive origin of higher resonances, but they are important contributors to the hadron zoo. Given more and more $S$-wave thresholds at higher energies, quark models are expected to become less and less reliable.

We therefore conclude that the long accepted paradigm underlying open-flavour heavy meson spectroscopy that identifies all ground states with $c\bar{q}$ or $b\bar{q}$ quark model states, is no longer tenable. In a broader view, the hadron spectrum must be viewed as more than a collection of quark model states, but rather as a manifestation of a more complex dynamics that leads to an intricate pattern of various types of states that can only be understood by a joint effort from experiment, LQCD and phenomenology. We close the chapter by summarizing a few suggestions that will provide further, non-trivial tests of the scenario proposed here:

- Measuring the angular moments, in particular $\langle P_1 \rangle - 14\langle P_3 \rangle/9$, with unprecedented accuracy for the $B \to D^{(*)}\pi\pi$ and $B \to D_s^{(*)}\bar{K}\pi$ reactions. This can be done at LHCb and Belle-II. We expect to see nontrivial cusp structures at the $D^{(*)}\eta$ and $D_s^{(*)}\bar{K}$ thresholds in the former, and near-threshold enhancement in the $D_s^{(*)}\bar{K}$ spectrum in the latter [3].

- Measuring the hadronic width of the $D_{s0}^*(2317)$, predicted to be of about 100 keV in the molecular scenario [205, 247], while much smaller otherwise. This will be measured by the $\overline{\text{P}}$ANDA experiment.

- Checking the existence of the sextet pole in LQCD with a relatively large SU(3) symmetric quark mass.

- Searching for the predicted analogous bottom positive-parity mesons both experimentally and in LQCD.

## Chapter 6

# SCALAR FORM FACTORS IN $H_{(s)} \to \phi\ell\bar{\nu}_\ell$ $(H = B, D)$ SEMILEPTONIC DECAYS

## 6.1 Introduction

Exclusive semileptonic decays play a prominent role in the precise determination of the CKM matrix elements, which are particularly important to test the SM—any violation of the unitarity of the CKM matrix would reveal new physics beyond the SM (see for instance the review on the CKM mixing parameters by the PDG [206]). Experimental and theoretical efforts have been devoted to multitude of inclusive and exclusive semileptonic decays driven by electroweak charge currents. For instance, the $K_{\ell 3}$ decays and those of the type $H \to \phi\,\bar{\ell}\,\nu_\ell$ and $H \to \phi\,\ell\,\bar{\nu}_\ell$ (hereafter denoted by $H_{\ell 3}$ or $H \to \phi$), where $H \in \{D,\, \bar{B}\}$ is an open heavy-flavour pseudoscalar meson and $\phi \in \{\pi,\, K,\, \bar{K},\, \eta\}$ denotes one of the Goldstone bosons due to the spontaneous breaking of the approximate chiral symmetry of QCD, are important in the extraction of some of the CKM matrix elements. Experimentally, significant progresses have been achieved and absolute decay branching fractions and differential decay rates have been accurately measured [248–257]. On the theoretical side, determinations of the form factors in the vicinity of $q^2 = 0$ (with $q^2$ the invariant mass of the outgoing lepton pair) using LCSR have significantly improved their precision [258, 259], and have reached the level of two-loop accuracy [260]. Meanwhile, improvements have been made by using better actions in LQCD, which have allowed to extract CKM matrix elements with significantly reduced statistical and systematical uncertainties [66, 261–266]. As a result of this activity in the past decade, lattice calculations on the scalar form factors in heavy-to-light semileptonic transitions have been also reported by the different groups (see the informative review by the Flavour Lattice Averaging Group (FLAG) [70]).

The extraction of the CKM mixing parameters from $K_{\ell 3}$ and/or $H_{\ell 3}$ decays relies on the knowledge of the vector $[f_+(q^2)]$ and scalar $[f_0(q^2)]$ hadronic form factors that determine the matrix elements of the charged current between the initial and final hadron states.[1] Various parametrizations, such as the Isgur–Scora–Grinstein–Wise updated model [267] or the series expansion proposed in Ref. [268], are extensively used in LQCD and experimental studies. In this chapter, based on the findings of Ref. [8], we will study the scalar form factors in $H_{\ell 3}$ decays by using the MO formalism, which is a model independent approach to account for $H\phi$ coupled-channel re-scattering effects. The coupled-channel MO formalism has been extensively applied to the scalar $\pi\pi$, $\pi K$ and $\pi\eta$ form factors, see, e.g., Refs [269–273]. It builds up an elegant bridge to connect the form factors with the

---

[1] The contribution of the scalar form factor to the decay width is suppressed since it vanishes in the limit of massless leptons. However, both scalar and vector form factors take the same value at $q^2 = 0$, and thus an accurate determination of the $q^2-$dependence of the scalar form factor can be used to constrain the vector one in this region.

corresponding $S$-wave scattering amplitudes via dispersion relations. The construction of those equations is rigorous in the sense that the fundamental principles, such as unitarity and analyticity, and the proper QCD asymptotic behaviour are implemented. The first attempts to extend this method to the investigation of the scalar $H \to \phi$ form factors were made in Refs. [40, 63, 67, 68, 274–278], but just for the single-channel case. A similar dispersive MO approach has been also employed to study the semileptonic $\bar{B} \to \rho l \bar{\nu}_l$ [277, 279–281] and $\bar{B}_s \to \bar{K}^* l \bar{\nu}_l$ [277] decays and the possible extraction of the CKM element $|V_{ub}|$ from data on the four-body $\bar{B} \to \pi\pi l \bar{\nu}_l$ and $\bar{B}_s \to \bar{K}\pi l \bar{\nu}_l$ decay-modes.

The study of heavy-light form factors using the MO representation incorporating coupled-channel effects has not been undertaken yet. This is mainly because of the poor knowledge on the $H\phi$ interactions up to very recent years. However, a few intriguing positive-parity charmed mesons, like the $D_{s0}^*(2317)$, have been recently discovered [206], giving support to a new paradigm for heavy-light meson spectroscopy [6] that questions their traditional $q\bar{q}$ constituent quark model interpretation. Hence, the study of the $H\phi$ interactions aiming at understanding the dynamics of these newly observed states has become an interesting subject by itself, see, e.g., Refs. [3, 33, 34, 37, 38, 42, 199, 237, 282–285] for phenomenological studies and [45–47, 81, 205, 286, 287] for LQCD calculations. For the $D_{\ell 3}$ decays, several LQCD results on the relevant form factors have been recently reported, see, e.g., Refs. [261, 262, 266]. This situation makes timely the study of the scalar $D \to \phi$ form factors by means of the MO representation incorporating our current knowledge of $D\phi$ interactions. The extension to the $H = \bar{B}$ case is straightforward with the help of HQFS. Based on HQFS, the LECs involved in the $D\phi$ interactions or $D \to \phi$ semileptonic form factors are related to their analogues in the bottom sector by specific scaling rules. It is then feasible either to predict quantities in the bottom (charm) sector by making use of the known information in the charm (bottom) case or to check how well HQFS works by testing the scaling rules.

In the present study, we construct the MO representations of the scalar form factors, denoted by $f_0(s)$, for the semileptonic $D \to \pi$ and $D \to \bar{K}$ transitions, which are related to the unitarized $S$-wave scattering amplitudes in the $D\phi$ channels with strangeness ($S$) and isospin ($I$) quantum numbers $(S, I) = (0, \frac{1}{2})$ and $(S, I) = (1, 0)$, respectively. These amplitudes are obtained by unitarizing the $\mathcal{O}(p^2)$ heavy-meson chiral perturbative ones [198], with LECs determined from the lattice calculation [205] of the $S$-wave scattering lengths in several $(S, I)$ sectors. The scheme provides an accurate description of the $D\phi$ interactions in coupled channels. For instance, as it is shown in Ref. [3] and in the previous Chapter 4, the finite volume energy levels in the $(S, I) = (0, 1/2)$ channel calculated with the unitarized amplitudes, without adjusting any parameter, are in an excellent agreement with those recently reported by the Hadron Spectrum Collaboration [81].

The unitarized chiral scattering amplitudes are used in this work as input to the dispersive integrals. However, these amplitudes are valid only in the low Goldstone-boson energy region. Hence, asymptotic behaviours at high energies for the phase shifts and inelasticities are imposed in the solution of the MO integral equations. The Omnès matrices obtained in this way incorporate the strong final state interactions, and the scalar form factors are calculated by multiplying the former by polynomials. The (*a priori* unknown) coefficients of the polynomials are expressed in terms of the LECs appearing at NLO in the chiral expansion of the form factors [184, 288].

The scheme employed in the charm sector is readily extended to the bottom one. Afterwards, the LECs could be either determined by fitting to the results obtained in the LQCD analyses of the $D \to \pi(\bar{K})$ decays carried out in Refs. [261, 262, 266] or to the LQCD and LCSR combined $\bar{B} \to \pi$ and $\bar{B}_s \to K$ scalar form factors reported in Refs. [66,263–265] and [258–260], respectively. In both scenarios LQCD and LCSR results are well described using the MO dispersive representations of the scalar form factors constructed in this work.

However, our best results are obtained by a simultaneous fit to all available results, both in the charm and bottom sectors. As mentioned above, all of the LECs involved in the $\bar{B}_{(s)}\phi$ interactions or $\bar{B}_{(s)} \to \bar{\phi}$ semileptonic transitions are related to those in the charm sector by making use of the heavy quark scaling rules [288], which introduce some constraints between the polynomials that appear in the different channels. Thus, assuming a reasonable effect of the HQFS breaking terms, a combined fit is performed to the $D \to \pi/\bar{K}$ and the $\bar{B} \to \pi$ and $\bar{B}_s \to K$ scalar form factors, finding a fair description of all the fitted data, and providing reliable predictions of the different scalar form factors in the whole semileptonic decay phase space, which turn out to be compatible with other theoretical determinations by, e.g., perturbative QCD [289, 290]. The results of the fit allow also to predict the scalar form factors for the $D \to \eta$, $D_s \to K$ and $D_s \to \eta$ transitions in the charm sector, and for the very first time for the $\bar{B} \to \eta$ decay. In some of these transitions, the form factors are difficult for LQCD due to the existence of disconnected diagrams of quark loops.

Based on the results of the combined fit, and taking advantage of the fact that scalar and vector form factors are equal at $q^2 = 0$, we extract all the heavy-light CKM elements and test the second-row unitarity by using the $|V_{cb}|$ value given in the PDG [206]. We also predict the different form factors above the $q^2$−regions accessible in the semileptonic decays, up to energies in the vicinity of the involved thresholds, which should be correctly described within the employed unitarized chiral approach.

This chapter is organized as follows. In Subsec. 6.2.1, we introduce the definitions of the form factors for $H_{\ell 3}$ decays. A general overview of the MO representation of the scalar form factors is given in Subsec. 6.2.2, while the input for the MO problem and the solutions are discussed in Subsec. 6.2.3. In Subsec. 6.2.4, we derive the scalar as well as vector form factors at NLO in heavy-meson chiral perturbation theory and then perform the aforementioned matching between the MO and the chiral representations close to the corresponding thresholds. Section 6.3 comprises our numerical results and discussions, with details of the fits given in Subsecs. 6.3.1 and 6.3.2. With the results of the combined charm-bottom fit, in Sec. 6.3.3, we extract the related CKM elements and make predictions for the values of $f_+(0)$ in various transitions. Predictions for flavour-changing $b \to u$ and $c \to d, s$ scalar form factors above the $q^2$−regions accessible in the semileptonic decays are given and discussed in Subsec. 6.3.4. We summarize the results of this work in Sec. 6.4. Finally, some further results for $b \to u$ form factors, obtained with quadratic MO polynomials, are shown in Sec. 6.5.

## 6.2 Theoretical framework

### 6.2.1 Form factors in $H_{\ell 3}$ decays

For a semileptonic decay of the type $H(p) \to \bar{\phi}(p')\,\ell(p_\ell)\,\bar{\nu}_\ell(p_\nu)$, the Lorentz invariant Feynman amplitude is proportional to

$$\begin{aligned}\mathcal{M} \propto & \frac{G_F}{\sqrt{2}}\Big\{\bar{u}(p_\ell)\gamma^\mu(1-\gamma_5)v(p_\nu)\Big\}\times \\ & \Big\{V_{Qq}\,\langle\bar{\phi}(p')|\bar{q}\gamma_\mu(1-\gamma_5)Q|H(p)\rangle\Big\}\ ,\end{aligned} \tag{6.1}$$

where $G_F$ is the Fermi constant, and $V_{Qq}$ is the CKM matrix element corresponding to the flavour changing $Q \to q$ transition. The terms in the first and second curly brackets stand for the weak and hadronic matrix elements, respectively. In the hadronic matrix element, the axial-vector part vanishes due to parity and total angular momentum conservation, while the remaining vector part is parametrized in a conventional form as

$$\begin{aligned}\langle\bar{\phi}(p')|\bar{q}\gamma^\mu Q|H(p)\rangle =& f_+(q^2)\left[\Sigma^\mu - \frac{m_H^2 - M_\phi^2}{q^2}q^\mu\right] \\ &+ f_0(q^2)\frac{m_H^2 - M_\phi^2}{q^2}q^\mu\ ,\end{aligned} \tag{6.2}$$

where $f_+(q^2)$ and $f_0(q^2)$ are the vector and scalar form factors, respectively, with $q^\mu = p^\mu - p'^\mu$ and $\Sigma^\mu = p^\mu + p'^\mu$. Note that both form factors should be equal at $q^2 = 0$. As discussed in Ref. [291], they specify the $P$-wave ($J^P = 1^-$) and $S$-wave ($J^P = 0^+$) of the crossed-channel matrix elements,

$$\langle 0|\bar{q}\gamma^\mu Q|H(p)\phi(-p')\rangle = \langle\bar{\phi}(p')|\bar{q}\gamma^\mu Q|H(p)\rangle\ . \tag{6.3}$$

Both the scalar and vector form factors contribute to the differential decay rate, see e.g., Ref. [70]. Nevertheless, when the lepton mass is neglected, the differential decay rate in the $H-$meson rest frame can be simply expressed in terms of the vector form factor via

$$\frac{\mathrm{d}\Gamma(H \to \bar{\phi}\ell\bar{\nu}_\ell)}{\mathrm{d}q^2} = \frac{G_F^2}{24\pi^3}|\vec{p}\,'|^3|V_{Qq}|^2|f_+(q^2)|^2\ . \tag{6.4}$$

It is then possible to extract the CKM element $|V_{Qq}|$ even for a single value of the four-momentum transfer, provided one simultaneously knows the vector form factor and the experimental differential decay width. A possible choice is $q^2 = 0$, where the scalar and vector form factors coincide, $f_+(0) = f_0(0)$.

In the next two subsections, Subsecs. 6.2.2–6.2.3, we give specific details on the MO representation of the form factors. For brevity, in some occasions we will focus on the formalism for the case of the charm sector ($H = D$). The extension to the bottom sector ($H = \bar{B}$) is straightforward using HQFS, though some aspects are explicitly discussed in Subsec. 6.2.3.

### 6.2.2 Muskhelishvili–Omnès representation

We now discuss the dispersive representation of the scalar form factors within the MO formalism. Throughout this work, isospin breaking terms are not considered, and therefore it is convenient to work with the isospin basis. Before proceeding, we first discuss the relation of the form factors expressed in the particle and isospin bases. We start defining the phase convention for isospin states as illustrated in Subsec. 3.3.1 of Chapter 3 through Eqs. (3.42), (3.43) and (3.44) for the pNGBs, whereas for the heavy mesons the conventions are those in Eq. (3.49) introduced in Subsec. 3.3.2 of the same chapter. The form factors involving the $c \to d$ transition are those appearing in the $D^0 \to \pi^-$, $D^+ \to \pi^0$, $D^+ \to \eta$, and $D_s^+ \to K^0$ semileptonic decays. (Note that $D^0 \to \pi^-$ and $D^+ \to \pi^0$ transitions are related by an isospin rotation.) The details of these form factors close to the zero recoil point, where the outgoing Goldstone boson is at rest, are greatly influenced by the $\pi D$, $D\eta$, and $D_s\bar{K}$ scattering amplitudes in the $(S, I) = (0, 1/2)$ sector. Note that to be consistent with the convention of Refs. [198, 205] and previous Chapter 4, we use $\pi D$ instead of $D\pi$ to construct the isospin 1/2 state. We then define the vector-column $\vec{\mathcal{F}}^{(0,1/2)}$ as

$$\vec{\mathcal{F}}^{(0,1/2)}(s) \equiv \begin{pmatrix} \sqrt{\frac{3}{2}} f_0^{D^0\to\pi^-}(s) \\ f_0^{D^+\to\eta}(s) \\ f_0^{D_s^+\to K^0}(s) \end{pmatrix} . \tag{6.5}$$

We shall use the shorthand $f_0^{D\pi}(s) = f_0^{D^0\to\pi^-}(s)$, $f_0^{D\eta}(s) = f_0^{D^+\to\eta}(s)$, and $f_0^{D_s\bar{K}}(s) = f_0^{D_s^+\to K^0}(s)$. Likewise for the $c \to s$ transitions, we have the $D^0 \to K^-$, $D^+ \to \bar{K}^0$, and $D_s^+ \to \eta$ semileptonic decays, related to the $DK$ and $D_s\eta$ scattering amplitudes in the $(S, I) = (1, 0)$ sector. We thus define:[2]

$$\vec{\mathcal{F}}^{(1,0)}(s) \equiv \begin{pmatrix} -\sqrt{2} f_0^{D^0\to K^-}(s) \\ f_0^{D_s^+\to\eta}(s) \end{pmatrix} , \tag{6.6}$$

for which we will also use the notation $f_0^{D^0\to K^-}(s) = f_0^{DK}(s)$ and $f_0^{D_s^+\to\eta}(s) = f_0^{D_s\eta}(s)$. Here, and again to be consistent with the convention of Refs. [198,205], we use $DK$ instead of $KD$ to construct the isoscalar state, which is just the opposite convention to that used for the isospin $\pi D$ state. With these definitions, the unitarity relation for any of the $\vec{\mathcal{F}}(s)$ can be compactly written as:

$$\begin{aligned} \frac{\vec{\mathcal{F}}(s+i\epsilon) - \vec{\mathcal{F}}(s-i\epsilon)}{2i} &= \operatorname{Im} \vec{\mathcal{F}}(s+i\epsilon) \\ &= T^*(s+i\epsilon)\Sigma(s)\vec{\mathcal{F}}(s+i\epsilon) , \end{aligned} \tag{6.7}$$

where $T(s)$ stands for the coupled-channel $S$-wave scattering amplitude in the corresponding $(S, I)$ sector, which will be discussed further in Sec. 6.2.3. The diagonal matrix $\Sigma(s)$ contains the phase space factors. For $(0, 1/2)$, one has

$$\Sigma(s) = 2\,\mathrm{diag}\left(\sigma_{D\pi}(s), \sigma_{D\eta}(s), \sigma_{D_s\bar{K}}(s)\right) , \tag{6.8}$$

whereas in the $(1, 0)$ sector including two coupled channels we have

$$\Sigma(s) = 2\,\mathrm{diag}\left(\sigma_{DK}(s), \sigma_{D_s\eta}\right) . \tag{6.9}$$

The function $\sigma_{ab}(s)$ was already introduced in Eq. (2.38), and we reproduce it here including a Heaviside step function:

$$\sigma_{ab}(s) = \frac{\lambda^{1/2}(s, m_a^2, m_b^2)}{2s} \Theta\left[s - (m_a + m_b)^2\right] . \tag{6.10}$$

---

[2] Here also $D^0 \to K^-$ and $D^+ \to \bar{K}^0$ form factors are related by an isospin rotation.

which ensures the reality of the form factors below the lowest threshold. Invariance under time-reversal together with the optical-theorem leads to

$$\operatorname{Im} T^{-1}(s+i\epsilon) = -\Sigma(s) \tag{6.11}$$

In this convention, the $T$- and $S$-matrices are related by

$$S(s) = \mathbb{I} + 2i\Sigma^{\frac{1}{2}}(s)T(s)\Sigma^{\frac{1}{2}}(s) \tag{6.12}$$

The unitarity relation of Eq. (6.7) can be used to obtain dispersive representations for the form factors. We start considering the $D \to \pi$ transition in the single channel case (elastic unitarity) where the form factor satisfies

$$\operatorname{Im} f_0^{D\pi}(s) = [t^{\pi D}(s)]^* \sigma_{D\pi}(s) f_0^{D\pi}(s)\ , \quad s \equiv q^2\ , \tag{6.13}$$

with $t^{\pi D}(s)$ the $\pi D$ $S$-wave elastic scattering amplitude. Equation (6.13) admits an algebraic solution [292],

$$f_0^{D\to\pi}(s) = \Omega(s)P(s)\ , \tag{6.14}$$

where $P(s)$ is an undetermined polynomial, and the Omnès function $\Omega(s)$ is given by

$$\Omega(s) = \exp\left[\frac{s}{\pi}\int_{(m_D+M_\pi)^2}^{\infty} \mathrm{d}s' \frac{\delta(s')}{s'(s'-s)}\right]\ , \tag{6.15}$$

with $\delta(s)$ the elastic $0^+$ $\pi D$ phase shift, in accordance with the Watson final state interaction theorem [293]. This was the scheme adopted in the previous studies carried out in Refs. [40, 63, 67, 68, 274–276, 278].

For coupled channels the solution for $\vec{\mathcal{F}}(s)$ takes the form:

$$\vec{\mathcal{F}}(s) = \Omega(s)\cdot\vec{\mathcal{P}}(s) \tag{6.16}$$

being $\vec{\mathcal{P}}(s)$ a vector of polynomials with real coefficients and $\Omega(s)$ the Omnès matrix that satisfies[3]

$$\operatorname{Im}\Omega(s+i\epsilon) = T^*(s+i\epsilon)\Sigma(s)\Omega(s+i\epsilon) \tag{6.19}$$

which leads to the following unsubtracted dispersion relation:

$$\Omega(s+i\epsilon) = \frac{1}{\pi}\int_{s_{\mathrm{th}}}^{\infty} \frac{T^*(s')\,\Sigma(s')\,\Omega(s')}{s'-s-i\epsilon}\mathrm{d}s'\ , \tag{6.20}$$

---

[3] Taking into account that the $\Omega(s)$ matrix should have only a right-hand cut and it should be real below all thresholds, Eq. (6.19) is equivalent to

$$\Omega(s+i\epsilon) = H(s+i\epsilon)\Omega(s-i\epsilon). \tag{6.17}$$

with $H(s) = (\mathbb{I} + 2iT(s)\Sigma(s))$. Furthermore since $H(s)H^*(s) = \mathbb{I}$, though $H(s)$ is not the $S$-matrix in the coupled-channel case, it follows

$$\det[\Omega(s+i\epsilon)] = e^{2i\phi(s)}\det[\Omega(s-i\epsilon)] \tag{6.18}$$

with $\exp 2i\phi(s) = \det[H(s)]$. This is to say that the determinant of the matrix $\Omega(s)$ satisfies a single-channel Omnès-type relation [294], which is extensively used in this work to check the accuracy of the numerical calculations. Note that above all thresholds, $\det[H(s)] = \det[S(s)]$ and therefore in the elastic case ($\eta_i \to 1\ \forall i$), $\phi(s) = \sum_{i=1}^{n}, \delta_i(s)$, with $n$ the number of channels.

with $s_{\rm th}$ the lowest threshold, which is referred to as the MO integral equation [295]. Taking a polynomial $\vec{P}(s)$ of rank $(n-1)$ would require the knowledge of $\vec{\mathcal{F}}(s)$ for $n$ values of $s$. Unlike the single channel case, there is no analytical solution [in the sense of Eq. (6.15)] for the coupled-channel MO problem and it has to be solved numerically. The MO equation can be written in an alternative form:

$$\begin{aligned} \mathrm{Re}\,\Omega(s) &= \frac{1}{\pi}\mathcal{P}\int_{s_{\rm th}}^{\infty}\frac{\mathrm{d}s'}{s'-s}\mathrm{Im}\,\Omega(s'), \\ \mathrm{Im}\,\Omega(s) &= X(s)\,\mathrm{Re}\,\Omega(s)\ , \end{aligned} \tag{6.21}$$

with $\mathcal{P}\int$ denoting the principal value and

$$X(s) = \mathrm{Im}\,T(s)\,[\mathrm{Re}\,T(s)]^{-1}\ , \tag{6.22}$$

which is expressed in terms of the $T$-matrix and encodes the information on the $D\phi$ rescattering. The linear MO system, Eq. (6.21), can be solved by following the appropriate numerical method described in Ref. [294].

### 6.2.3 Input and MO solutions

To solve the MO equation and obtain the $\Omega(s)$ matrix, the $T$-matrix is needed as an input. We will use here the amplitudes based on unitarized chiral effective theory as computed in Refs. [198,205] and presented in the previous Chapter 4. Because of the normalizations used in Eqs. (6.7) and (6.11), the unitarized amplitude calculated in Chapter 4, denoted here by $T_U(s)$, is related to the $T$-matrix introduced in the above subsection by:

$$T(s) = -\frac{1}{16\pi}T_U(s)\ . \tag{6.23}$$

Since the amplitudes are based on chiral potentials, the obtained $T$-matrices are only valid in the energy region not far from the corresponding thresholds. We thus adopt such $T$-matrices only up to a certain value of $s$, denoted by $s_m$. Above that energy, the $T$-matrix elements are computed as an interpolation between their values at $s=s_m$ and the asymptotic values at $s=\infty$. The interpolation still gives a unitary $T$-matrix since, as we will specify below, it is actually performed on the phase shifts and the inelasticities. Moreover, the approximation of quasi-two-body channels cannot hold for arbitrarily large energies and Eq. (6.7) is a reasonable approximation to the exact discontinuity only in a finite energy range. However, as we are interested in constructing the form factors in a finite energy region also, the detailed behaviour of the spectral function at much higher energies should be, in principle, unimportant. As we will see below, this is not entirely correct, in particular for the $\bar{B}\to\pi$ semileptonic transition, because of the large $q^2-$phase space accessible in this decay. Nevertheless, we will assume that Eq. (6.7) holds up to infinite energies, only requiring that the $T$-matrix behaves in a way that ensures an appropriate asymptotic behaviour of the form factors, and we will discuss the dependence of our results on the contributions from the high energy region. In general, except for the $\bar{B}$ decays,[4] the asymptotic conditions on the $T$-matrix are chosen such that:

$$\lim_{s\to\infty}|T_{ij}(s)| = 0 \quad \text{for} \quad i\neq j\ , \tag{6.24}$$

$$\lim_{s\to\infty}\sum_{i=1}^{n}\delta_i(s) = n\pi\ , \tag{6.25}$$

---

[4] We will specifically discuss the situation for these transitions below.

where $n$ is the number of channels involved in the $T$-matrix and $\delta_i(s)$ are the phase shifts. These conditions ensure (in general) that the unsubtracted dispersion relation for the Omnès matrix in Eq. (6.20) has a unique solution, albeit a global normalization [295] (see also in particular Sec. 4.3 of Ref. [294]). The condition of Eq. (6.25) guaranties that

$$\lim_{s\to\infty} \det\left[\Omega(s)\right] \to 1/s^n \tag{6.26}$$

as can be deduced from the discussion of Eqs. (6.17) and (6.18). Note that the normalization of the Omnès matrix is completely arbitrary, and the computed form factors do not depend on it.[5]

In what follows, we detail the $T$-matrices and the specific shape of the asymptotic conditions for the two coupled-channel cases $[(S,I) = (1,0)$ and $(0,1/2)]$ that will be analyzed below.

- **The** $(S,I) = (1,0)$ **sector**

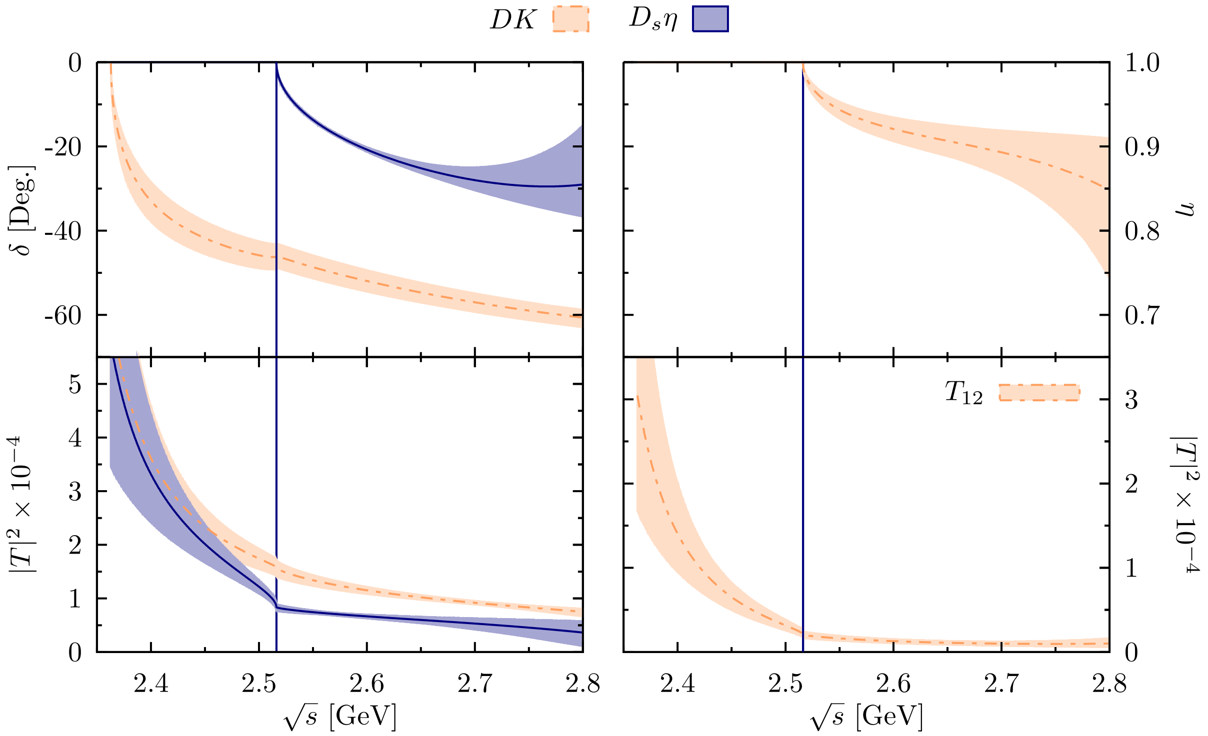

**Figure 6.1:** Phase shifts, inelasticities [see Eq. (6.27)] and amplitude moduli from $T_U^{(1,0)}$. The vertical line indicates the $D_s\eta$ threshold. Error bands have been obtained by Monte Carlo propagating the uncertainties of the LECs quoted in Ref. [205].

In this sector, we will consider two coupled channels, $DK$ (1) and $D_s\eta$ (2), and above all thresholds, the $T$-matrix is parametrized in terms of two phase shifts and one inelas-

---

[5] For example, let us consider Omnès matrices $\Omega$ and $\bar{\Omega}$ normalized to $\Omega(0) = \mathbb{I}$ or $\bar{\Omega}(s_n) = A$ ($s_n$ the normalization point, $s_n \leqslant s_{\rm th}$ and $A$ a real matrix), respectively. The matrix $\bar{\Omega}(s)$ is readily obtained from $\Omega(s)$ as $\bar{\Omega}(s) = \Omega(s)\Omega^{-1}(s_n)A$. The form factors can then also be written as $\vec{\mathcal{F}}(s) = \Omega(s)\vec{\mathcal{P}}(s) = \bar{\Omega}(s)A^{-1}\Omega(s_n)\vec{\mathcal{P}}(s) \equiv \bar{\Omega}(s)\vec{\bar{\mathcal{P}}}(s)$, where the definition of $\vec{\bar{\mathcal{P}}}(s)$ reabsorbs the constant matrix $A^{-1}\Omega(s_n)$.

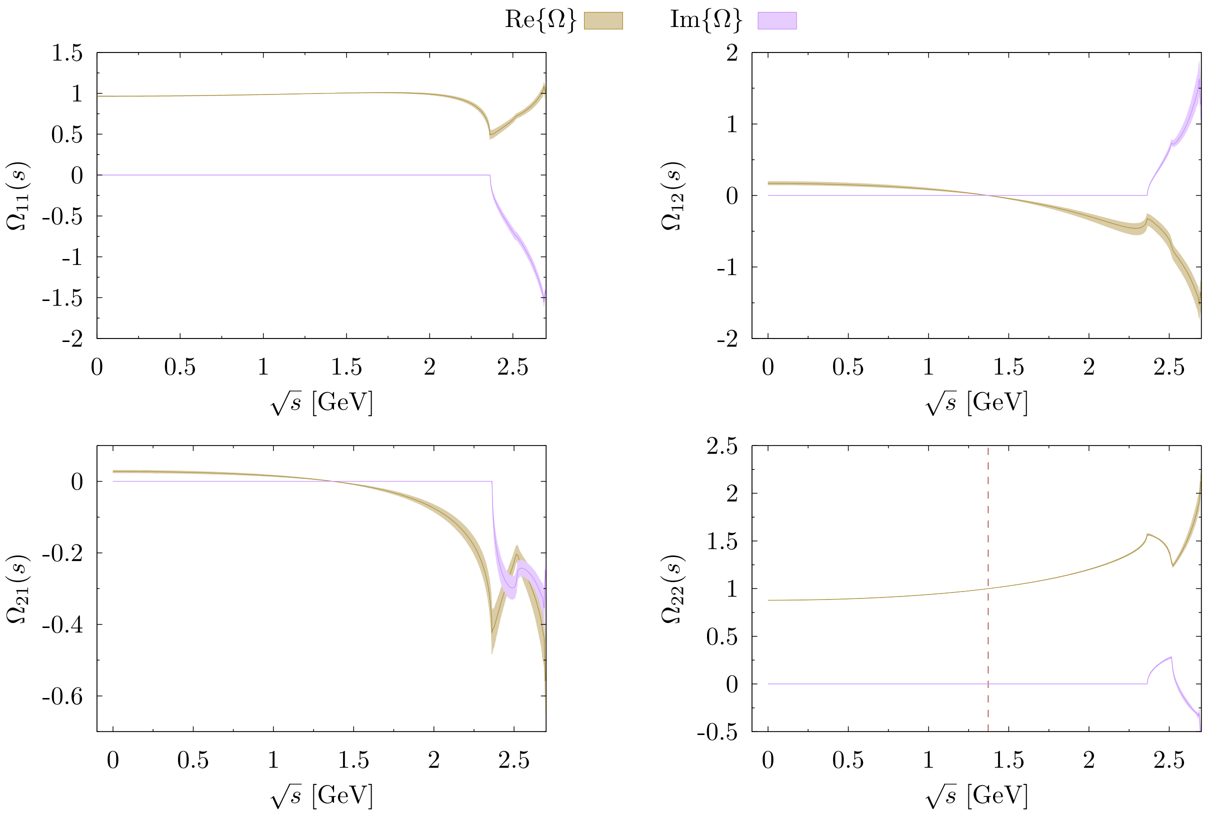

**Figure 6.2:** $(S, I) = (1, 0)$ Omnès matrix solution of the MO integral equation (6.21) with the contour condition $\Omega\left((m_D - M_K)^2\right) = \mathbb{I}$, and asymptotic phase shifts $\delta_{DK}(\infty) = 2\pi$ and $\delta_{D_s\eta}(\infty) = 0$. Error bands have been obtained by Monte Carlo propagating the uncertainties of the LECs quoted in Ref. [205]. The dashed vertical line indicates $q^2_{\max} = (m_D - M_K)^2$.

ticity parameter,

$$T(s) = \begin{pmatrix} \frac{\eta(s)e^{2i\delta_1}-1}{2i\sigma_1(s)} & \frac{\sqrt{1-\eta^2}e^{i\phi_{12}}}{2\sqrt{\sigma_1(s)\sigma_2(s)}} \\ \frac{\sqrt{1-\eta^2}e^{i\phi_{12}}}{2\sqrt{\sigma_1(s)\sigma_2(s)}} & \frac{\eta(s)e^{2i\delta_2}-1}{2i\sigma_2(s)} \end{pmatrix} \tag{6.27}$$

with the phase $\phi_{12} = \delta_1 + \delta_2 + \mathrm{mod}(\pi)$ and $0 \leqslant \eta \leqslant 1$. To solve the MO integral equation [cf. Eq. (6.21)], we use a $T$-matrix of the form

$$T(s) = \begin{cases} -\frac{1}{16\pi}T_U^{(1,0)}(s) & s_{\text{th}} \leqslant s \leqslant s_m \ , \\ T_H(s) & s \geqslant s_m \ , \end{cases} \tag{6.28}$$

with $s_{\text{th}} = (m_D + M_K)^2$ the lowest threshold, $T_U$ defined in Eq. (2.86) and $T_H$ the asymptotic matrix that will be discussed below. $T_U$ is computed following the prescriptions of Sec. 2.5 and the kernel potentials introduced in Sec. 4.2.2 of previous Chapter 4 (see Eqs. (4.2) and Tables 4.1 and 4.5). Phase shifts, inelasticities and amplitude moduli from $T_U^{(1,0)}$ are displayed in Fig. 6.1 up to $\sqrt{s} = 2.8$ GeV, slightly above $s_m = (2.7\text{ GeV})^2$. Above this scale, the $T$-matrix elements are computed as an interpolation between their values at $s = s_m$ and the asymptotic values at $s = \infty$, given in Eqs. (6.24) and (6.25).

Thus, $T_H$ is constructed from Eq. (6.27) using the following parametrizations for phase shifts and inelasticities:

$$\begin{aligned}\delta_i(s) &= \delta_i(\infty) + [\delta_i(s_m) - \delta_i(\infty)]\frac{2}{1+(s/s_m)^{3/2}}, \\ \eta(s) &= \eta(\infty) + [\eta(s_m) - \eta(\infty)]\frac{2}{1+(s/s_m)^{3/2}}\end{aligned} \tag{6.29}$$

as suggested in Ref. [294]. As discussed above, the Omnès matrix is uniquely determined by choosing $\eta(\infty) = 1$ and $\delta_1(\infty) + \delta_2(\infty) = 2\pi$. The only remaining freedom is the distribution of $2\pi$ over the two phase shifts. Note that, $\delta_i(s_m)$ is defined modulo $\pi$ and this ambiguity is fixed by continuity-criteria. Here for the $DK - D_s\eta$ coupled channels, we choose $\delta_1(\infty) = 2\pi$, $\delta_2(\infty) = 0$. Different choices of the asymptotic values or of the interpolating functions in Eq. (6.29) will modify the shape of the Omnès solution far from the chiral region. The numerical effect of such freedom on the derived scalar form factors should be safely compensated by the undetermined polynomial in front of the Omnès matrix.

In Fig. 6.2, we show the solution of the MO integral equation (6.21), with the input specified above, and the contour condition $\Omega(q^2_{\text{max}}) = \mathbb{I}$, with $q^2_{\text{max}} = (m_D - M_K)^2$. We display results only up to $s = s_m$ that would be later used to evaluate the scalar form factors entering in the $D \to \bar{K}$ and $D_s \to \eta$ semileptonic transitions. Note that the imaginary parts are zero below the lowest threshold $s_{\text{th}} = (m_D + M_K)^2$, and how the opening of the $D_s\eta$ threshold produces clearly visible effects in the Omnès matrix. At very high energies, not shown in the figure, both real and imaginary parts of all matrix elements go to zero, as expected from Eq. (6.26).

- **The** $(S, I) = (0, 1/2)$ **sector**

**<u>Charm sector</u>:** Here we consider three channels, $D\pi$ (1), $D\eta$ (2), and $D_s\bar{K}$ (3), and above all thresholds, the $S$-matrix can be still specified[6] by the elastic parameters, i.e., three phase shifts and three inelasticities [296, 297],

$$S(s) = \begin{pmatrix} \eta_1 e^{2i\delta_1} & \gamma_{12}e^{i\phi_{12}} & \gamma_{13}e^{i\phi_{13}} \\ \gamma_{12}e^{i\phi_{12}} & \eta_2 e^{2i\delta_2} & \gamma_{23}e^{i\phi_{23}} \\ \gamma_{13}e^{i\phi_{13}} & \gamma_{23}e^{i\phi_{23}} & \eta_3 e^{2i\delta_3} \end{pmatrix}, \tag{6.30}$$

Furthermore, the parameters in the off-diagonal elements are related to the diagonal ones $\delta_i$ and $\eta_i$ by

$$\begin{aligned}\gamma_{ij}^2 &= \frac{1}{2}\left(1 + \eta_k^2 - \eta_i^2 - \eta_j^2\right), \quad i \neq j \neq k \neq i\,, \\ \phi_{ij} &= \delta_i + \delta_j + \alpha_{ij} + \text{mod}(\pi), \quad i, j, k = 1, 2, 3\,,\end{aligned}$$

and $\alpha_{ij}$ is determined as

$$\sin\alpha_{ij} = \sqrt{\frac{1}{4\eta_i\eta_j}\left[\frac{\gamma_{ik}^2\gamma_{jk}^2}{\gamma_{ij}^2} - (\eta_i - \eta_j)^2\right]} \equiv X_{ij}\ . \tag{6.31}$$

---

[6] The $T$-matrix is obtained from Eq. (6.30).

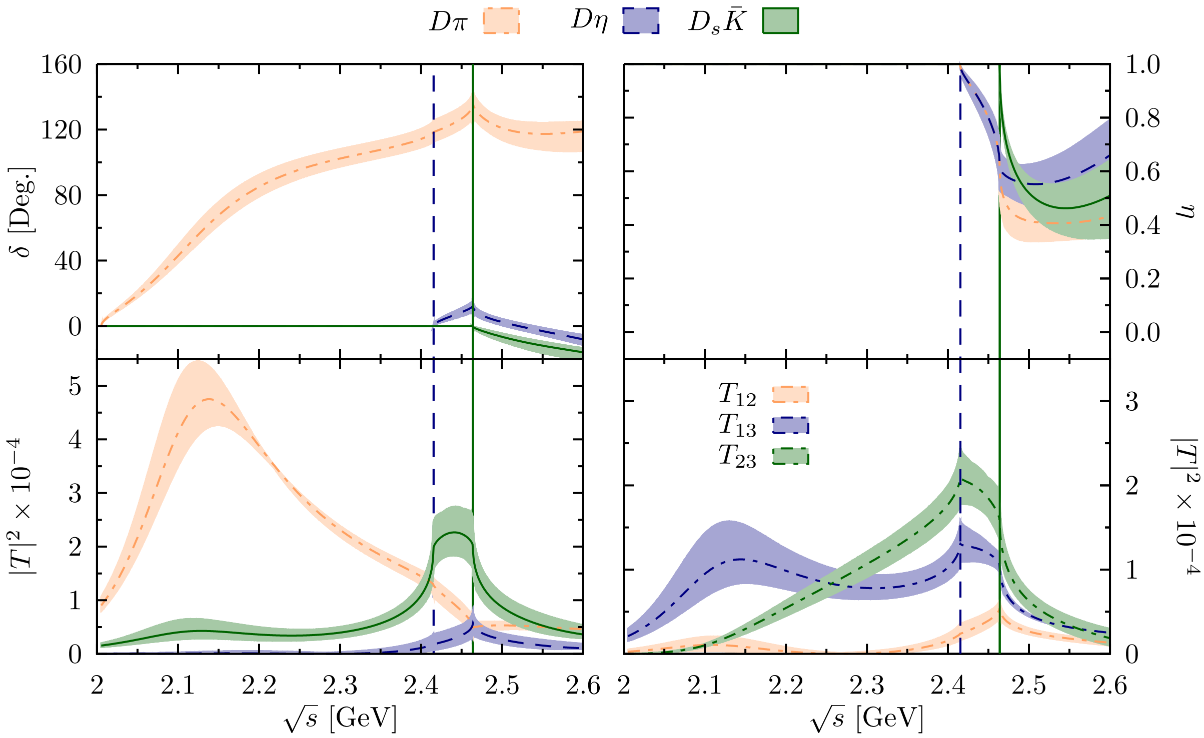

**Figure 6.3:** Phase shifts, inelasticities and amplitude moduli from $T_U^{(0,1/2)}$ in the charm sector. The vertical lines indicate the $D\eta$ and $D_s\bar{K}$ thresholds. Error bands have been obtained by Monte Carlo propagating the uncertainties of the LECs quoted in Ref. [205].

Note that the solutions for $\alpha_{ij}$ can be either $\arcsin(X_{ij})$ or $\pi-\arcsin(X_{ij})$. The inelasticity parameters should satisfy the following boundary conditions:

$$\begin{aligned} 0 &\leqslant \eta_i \leqslant 1\,, \\ |1-\eta_j-\eta_k| &\leqslant \eta_i \leqslant 1-|\eta_j-\eta_k|, \quad i\neq j\neq k\,. \end{aligned} \tag{6.32}$$

To solve the MO integral Eq. (6.21), we use a $T$-matrix similar to that in Eq. (6.28), with the obvious substitution of $T_U^{(1,0)}(s)$ by $T_U^{(0,\frac{1}{2})}(s)$. In addition, $s_{\text{th}} = (m_D + M_\pi)^2$ and we now take $s_m = (2.6\text{ GeV})^2$. Phase shifts, inelasticities and amplitude moduli from $T_U^{(1,0)}$ are displayed in Fig. 6.3 for $s_{\text{th}} \leqslant s \leqslant s_m$. Above $s_m = (2.6\text{ GeV})^2$, $T_H$ is constructed from Eq. (6.30) using interpolating parametrizations for phase shifts and inelasticities similar to those given in Eq. (6.29), imposing continuity of phase shifts and of the $T$-matrix, and taking

$$\begin{aligned} \delta_1(\infty) &= 3\pi\,, \quad \delta_i(\infty)=0, \quad i=2,3\,, \\ \eta_j(\infty) &= 1\,, \quad j=1,2,3\,. \end{aligned} \tag{6.33}$$

With the input specified above, the three-dimensional $(S,I)=(0,1/2)$ Omnès matrix can be numerically computed and its complex elements are shown in Fig. 6.4 up to $\sqrt{s}\leqslant 2.6$ GeV.

**Bottom sector:** In Figs. 6.5 and 6.6, we show phase shifts, inelasticities and the solution of the MO integral equation for the $(S,I)=(0,1/2)$ channel in the bottom

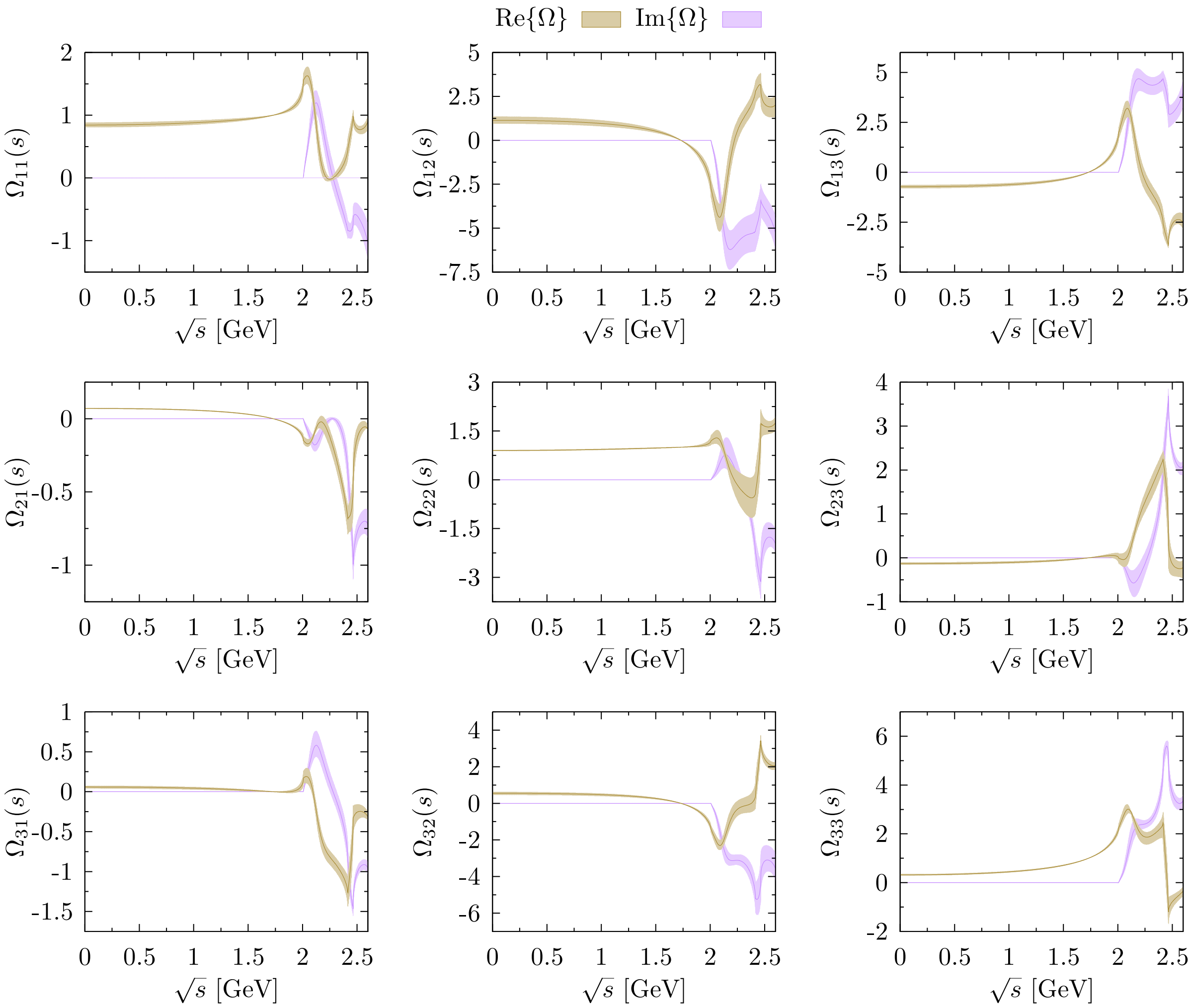

**Figure 6.4:** Charm $(S, I) = (0, 1/2)$ Omnès matrix solution of the MO integral equation (6.21) with the contour condition $\Omega\left((m_D - M_\pi)^2\right) = \mathbb{I}$, and asymptotic phase shifts $\delta_{D\pi}(\infty) = 3\pi$, $\delta_{D\eta}(\infty) = 0$ and $\delta_{D_s\bar{K}}(\infty) = 0$. Error bands have been obtained by Monte Carlo propagating the uncertainties of the LECs quoted in Ref. [205].

sector. The chiral amplitudes[7] are used in Eq. (6.20) up to $s_m = (6.25\text{ GeV})^2$, and from there on, the asymptotic forms of the amplitudes are employed. As we will show in the next section, in the case of $\bar{B}$ decays, the accessible phase space is quite large, and $q^2$ varies from around $m_B^2$ at zero recoil $[q^2_{\rm max} = (m_B - M_\phi)^2]$ down to zero, when the energy of the outgoing light meson is about $m_B/2$ far from the chiral domain. The $\bar{B}\pi$ scalar form factor decreases by a factor of five, and the LQCD results around $q^2_{\rm max}$ and the LCSR predictions in the vicinity of $q^2 = 0$ are not linearly connected. In the present approach, as we will discuss, we multiply the MO matrix $\Omega$ by a rank-one polynomial, and thus the extra curvature provided by the MO matrix becomes essential. While $\Omega(s)$ around $q^2_{\rm max}$ is rather insensitive to the adopted asymptotic behaviour of the $T$-matrix, since it is dominated by the integration region close to threshold $(s < s_m)$ where the

---

[7] The values of the involved LECs in the $\bar{B}\phi$ interactions are determined from their analogues in the charm sector by imposing the heavy-quark mass scaling rules discussed in Sec. 4.5.1 of previous Chapter 4.

chiral amplitudes are being used,[8] this is not the case for low values of $q^2$ close to 0, quite far from the two-body scattering thresholds. This unwanted dependence, due to the large extrapolation, could be compensated in the form factors by using higher rank polynomials, but that would introduce additional undetermined parameters. Conversely, this dependence of $\Omega(0)$, relative to the results at $q^2_{\rm max}$, on the details of the amplitudes at high energies will be diminished by solving a MO integral equation involving several subtractions, instead of the unsubtracted one of Eq. (6.20). This, however, will also introduce some more free parameters [40]. The situation is better in the charm sector, where the needed $q^2$−range is much reduced, and thus most of the contributions to the MO matrix come from an integration region within the chiral regime. Indeed, in the bottom sector we need to use $\delta_1(\infty) = 2\pi, \delta_2(\infty) = 2\pi$ and $\delta_3(\infty) = 0$, instead of the choice of Eq. (6.33) used for the charm decays, to find acceptable fits to the LQCD and LCSR predictions of the $\bar{B}\pi$ and $\bar{B}_sK$ scalar form factors. With this choice, we find theoretically sound fits where the LECs[9] that determine the rank-one Omnès polynomials describe the LQCD data close to $q^2_{\rm max}$, within the range of expected validity of the chiral expansion, while the LCSR results are reproduced thanks to the non-linear behaviour encoded in the

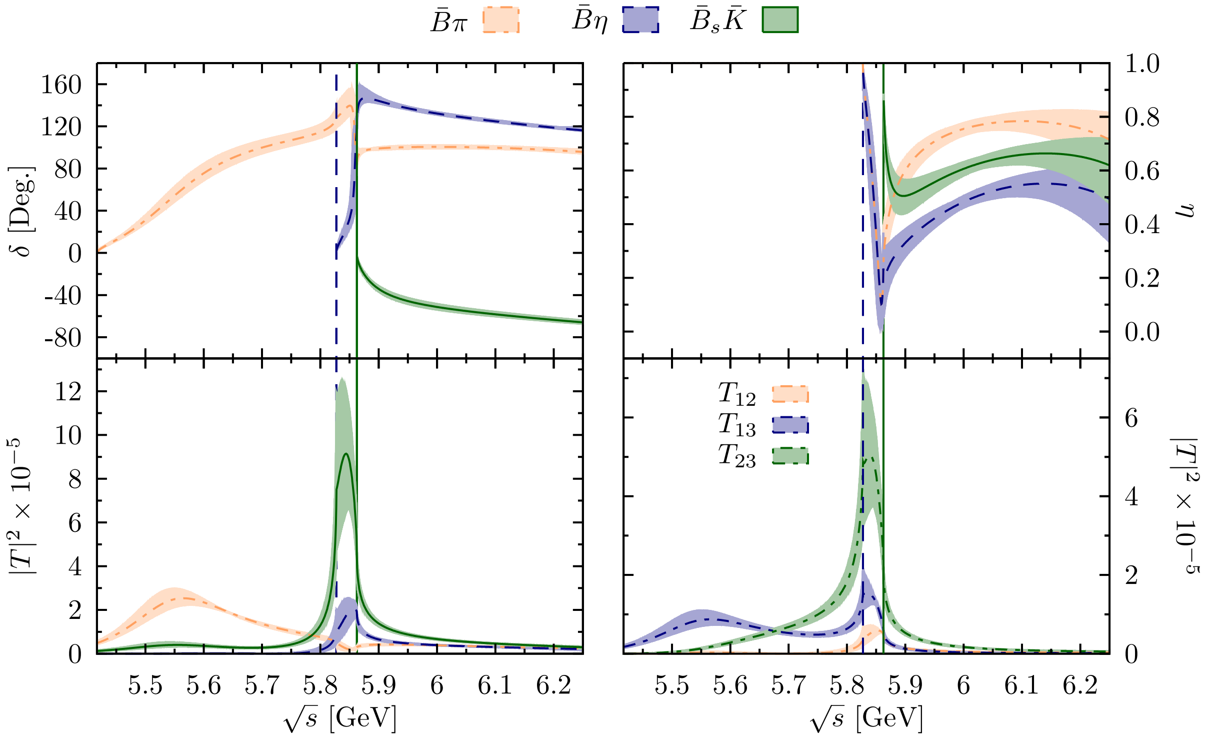

**Figure 6.5:** Phase shifts, inelasticities and amplitude moduli from $T_U^{(0,1/2)}$ in the bottom sector. The vertical lines indicate the $\bar{B}\eta$ and $\bar{B}_s\bar{K}$ thresholds. The values of the involved LECs in the $\bar{B}\phi$ interactions are determined from their analogues in the charm sector by imposing the heavy-quark mass scaling rules discussed in Sec. 4.5.1. Error bands have been obtained by Monte Carlo propagating the uncertainties of the LECs quoted in Ref. [205].

---

[8] In general, the MO matrix in the chiral domain, between the $q^2_{\rm max}$ and scattering (below $s_m$) regions is rather insensitive to the high energy behaviour of the amplitudes.

[9] These are $\beta_1^P$ and $\beta_2^P$, to be introduced in Subsec. 6.2.4, that appear in the chiral expansion of the form factors at NLO.

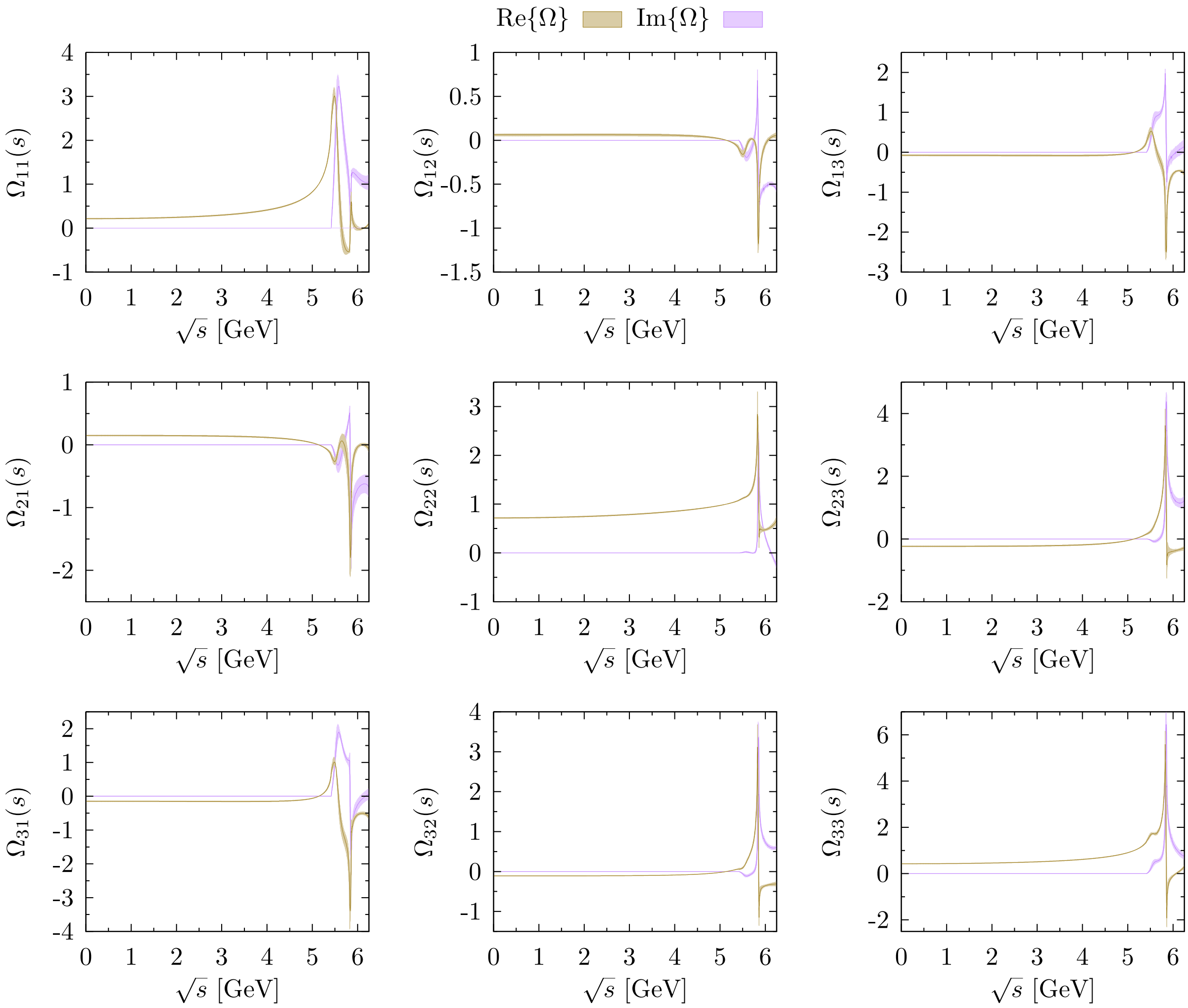

**Figure 6.6:** Bottom $(S, I) = (0, 1/2)$ Omnès matrix solution of the MO integral equation (6.21) with the contour condition $\Omega\left((m_B - M_\pi)^2\right) = \mathbb{I}$, and asymptotic phase shifts $\delta_{\bar{B}\pi}(\infty) = 2\pi$, $\delta_{\bar{B}\eta}(\infty) = 2\pi$ and $\delta_{\bar{B}_s\bar{K}}(\infty) = 0$. Error bands have been obtained by Monte Carlo propagating the uncertainties of the LECs quoted in Ref. [205].

MO matrix $\Omega(s)$. This picture will be reinforced by the consistent results that will be obtained, assuming a reasonable effect of the HQFS breaking terms, from combined fits to the $D \to \pi/\bar{K}$ and the $\bar{B} \to \pi$ and $\bar{B}_s \to K$ scalar form factors.

We do not really have an explanation of why the above choice of phase shifts at infinity works better in the bottom sector than the usual one in Eq. (6.33) adopted in the charm meson decays. We would like, however, to mention the different behaviour of the unitarized chiral phase shifts in the charm and bottom sectors. In both cases, the chiral amplitudes give rise to two resonances [3] (see Chapter 4): the first one, the non-strangeness flavour partner of the $D^*_{s0}(2317)$, quite broad, and located around 100 MeV above the $D\pi$ or $\bar{B}\pi$ thresholds and the second one placed below the heaviest of the thresholds, $D_s\bar{K}$ and $\bar{B}_s\bar{K}$, respectively. In the charm sector, the second resonance does not produce clear signatures in the phase shifts of the two open channels $D\pi$ and $D\eta$, while it is clearly visible in the phase shifts of the bottom $\bar{B}\pi$ and $\bar{B}\eta$ channels. Moreover, the second resonance is significantly narrower for the latter heavy-quark sector than for the former one (70 MeV versus 270 MeV).

Note also that now $\lim_{s\to\infty}\sum_{i=1}^{3}\delta_i(s) = 4\pi > 3\pi$, which implies a slightly faster decreasing of the MO matrix elements at high energies.

### 6.2.4 Chiral expansion of the form factors and the MO polynomial

Once the Omnès matrix is obtained, the form factor $\vec{\mathcal{F}}(s)$ is determined, according to Eq. (6.16), up to a polynomial $\vec{\mathcal{P}}(s)$ that contains unknown coefficients. We will match the dispersive and the NLO chiral representations of the form factors in a region of values of $s$ where the latter are supposed to be still valid. Besides the theoretical benefit of this constraint, it has also the practical advantage of expressing the coefficients of the polynomials in terms of the few LECs used in the chiral expansion of the form factors. Since, as will be discussed below (cf. Eqs. (6.39) and (6.40) and the discussion that follows), the NLO chiral expansion of the form factors used here is appropriate only up to terms linear in $s$, we should also take linear forms for the MO polynomials,

$$\vec{\mathcal{P}}(s) = \vec{\alpha}_0 + \vec{\alpha}_1\, s\ . \tag{6.34}$$

Since the Omnès matrix elements asymptotically behave as $1/s$ [see Eq. (6.26)], due to the chosen asymptotic conditions, this implies that the form factors will tend to a constant[10] for $s\to\infty$. Note that one would rather expect the form factors to vanish in this limit [298]. To achieve such asymptotic behaviour one should employ order zero polynomials. However, since we are interested in the region $0 \leqslant s \leqslant s_{\max}$, with $s_{\max}$ in the vicinity of $(m_H - M_\phi)^2$, we prefer to keep the linear behaviour of the polynomials, since this allows for a better matching of the coefficients $\vec{\alpha}_{0,1}$ with the LECs that appear in the NLO chiral calculation of the form factors.

- **Form factors in heavy meson chiral perturbation theory**

The leading-order (LO) coupling of the charm ($D$ and $D_s$) or bottom ($\bar{B}$ and $\bar{B}_s$) mesons to the Nambu–Goldstone bosons of the spontaneous breaking of the approximate chiral symmetry of QCD, through the charged, left-handed current $J^\mu = \left(\bar{Q}\gamma_L^\mu u, \bar{Q}\gamma_L^\mu d, \bar{Q}\gamma_L^\mu s\right)^T$, with $Q = c, b$, and $\gamma_L^\mu = \gamma^\mu(1-\gamma_5)$, is described by the following chiral effective Lagrangian [184,288,299]

$$\mathcal{L}_0 = \sqrt{2}f_{\mathcal{P}}\left(i\,\mathring{m}\mathcal{P}^*_\mu + \partial_\mu\mathcal{P}\right)u^\dagger J^\mu\ . \tag{6.35}$$

where $\mathcal{P}$ and $\mathcal{P}^*$ are the pseudoscalar and vector heavy-light mesons with content ($Q\bar{u}$, $Q\bar{d}$, $Q\bar{s}$), respectively, which behave as SU(3) light flavour triplets. Here $\mathring{m}$ denotes the degenerate mass of the $P_{(s)}$ and $P^*_{(s)}$ mesons in the chiral and heavy-quark limits, and $f_{\mathcal{P}}$ is the pseudoscalar heavy-light meson decay constant defined as

$$\langle 0|J^\mu|\mathcal{P}(p_1)\rangle = i\,\sqrt{2}f_{\mathcal{P}}\,p_1^\mu\ . \tag{6.36}$$

---

[10] This not strictly true in the case of $\bar{B}_{(s)}$−decays since, as discussed above, different asymptotic conditions have been assumed in the bottom sector and the Omnès matrix elements are expected to decrease slightly faster than $1/s$.

The chiral block is defined by $u^2 = U = \exp[i\sqrt{2}\Phi/F_0]$ as in Eq. (3.83), where $\hat{\xi} = \sqrt{2}\Phi$ is the octet of the Nambu–Goldstone bosons given in Eq. (3.36), and $F_0$ the pion decay constant in the chiral limit (we will take the physical value for the decay constant $F_0 \simeq$ 92 MeV). The relevant NLO chiral effective Lagrangian reads [288]

$$\mathcal{L}_1 = -\beta_1^P \mathcal{P}\, u\, (\partial_\mu U^\dagger) J^\mu - \beta_2^P (\partial_\mu \partial_\nu \mathcal{P})\, u\, (\partial^\nu U^\dagger)\, J^\mu \ . \tag{6.37}$$

We need the LO $\mathcal{P}\mathcal{P}^*\phi$ interaction as well, which is given by [184, 288, 299] ,

$$\mathcal{L}_{\mathcal{P}\mathcal{P}^*\phi} = \tilde{g}\left(\mathcal{P}^*_\mu u^\mu \mathcal{P}^\dagger + \mathcal{P}\, u^\mu \mathcal{P}^{*\dagger}_\mu\right) \ , \tag{6.38}$$

where $u_\mu$ was introduced in Eq. (3.96) and $\tilde{g} \sim g\mathring{m}$, with $g \sim 0.6$ a dimensionless and heavy quark mass independent constant. The topologies of relevant Feynman diagrams are shown in Fig. 6.7. The vector and scalar form factors, in the (strangeness, isospin) basis, at $\mathcal{O}(E_\phi)$ (i.e., NLO) in the chiral expansion read [288]

$$\begin{aligned} f_+^{[P\phi](S,I)}(s) =& \frac{\mathcal{C}^{(S,I)}_{[P\phi]}}{\sqrt{2}F_0}\Bigg[\frac{f_P}{\sqrt{2}} + \sqrt{2}\frac{\tilde{g}\,\mathring{m}\,f_P}{m_R^2 - s} \\ & + \beta_1^P - \frac{\beta_2^P}{2}(\Sigma_{P\phi} - s)\Bigg], \end{aligned} \tag{6.39}$$

$$\begin{aligned} f_0^{[P\phi](S,I)}(s) =& \frac{\mathcal{C}^{(S,I)}_{[P\phi]}}{\sqrt{2}F_0}\Bigg[\left(\sqrt{2}\frac{\tilde{g}\,\mathring{m} f_P}{m_R^2} + \beta_1^P\right)\frac{\Delta_{P\phi} - s}{\Delta_{P\phi}} \\ & + \left(\sqrt{2}f_P - \beta_2^P(\Sigma_{P\phi} - s)\right)\frac{\Delta_{P\phi} + s}{2\,\Delta_{P\phi}}\Bigg], \end{aligned} \tag{6.40}$$

where $\Delta_{P\phi} = m_P^2 - M_\phi^2$ and $\Sigma_{P\phi} = m_P^2 + M_\phi^2$ with $P \in \{Q\bar{s}, Q\bar{d}, Q\bar{u}\}$ and $\phi \in \{\pi,\ K, \bar{K}\ \eta\}$. The coefficients $\mathcal{C}^{(S,I)}_{[P\phi]}$ are collected in Table 6.1. Moreover, we have fixed $m_R$ to $m_{D^*}$ ($m_{B^*}$) and to $m_{D_s^*}$ ($m_{B_s^*}$) for the $(S, I) = (0, 1/2)$ and $(S, I) = (1, 0)$ charm (bottom) channels, respectively. In principle, at LO in the heavy quark expansion, $m_R$ should be set to $\mathring{m}$, however the use of the physical vector mass is quite relevant for the vector form factor, because of the propagator structure, though it has much less relevance for the scalar form factor that we study in this work. We should also note that all kinematical factors are always calculated using physical masses of the involved mesons. It is worthwhile to notice that $s$ is of the order $m_P^2 \sim \mathcal{O}(E_\phi^0)$, $(\Delta_{P\phi} - s) \sim \mathcal{O}(E_\phi)$ and $(\Sigma_{P\phi} - s) \sim \mathcal{O}(E_\phi)$, and $(\Delta_{P\phi} + s) \sim \mathcal{O}(E_\phi^0)$, so that a small change of $\mathcal{O}(E_\phi)$ in $(\Delta_{P\phi} + s)$ only leads to a higher order effect. Thus, $(\Delta_{P\phi} + s)$ should be regarded as basically a constant with $s \sim m_P^2$, and the expression in Eq. (6.40) should be matched to a rank-1 MO polynomial as mentioned before (see below for details of the matching).

Finally, we should mention that the LECs $\beta_1^P$ and $\beta_2^P$ scale with the heavy quark mass as [288]

$$\beta_1^P \sim \sqrt{m_P}, \qquad \beta_2^P \sim 1/\sqrt{m_P^3} \tag{6.41}$$

neglecting logarithmic corrections.

- **Matching**

At energies close to the thresholds, the scalar form factors in Eq. (6.16) should have the same structure as the ones obtained from chiral perturbation theory, given in Eq. (6.40).

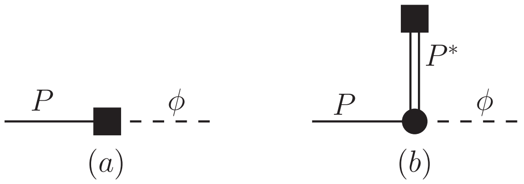

**Figure 6.7:** Topologies of the relevant Feynman diagrams contributing to the hadronic matrix elements. The solid circle denotes the LO $\mathcal{P}\mathcal{P}^*\phi$ interaction and the solid square represents the left-handed current.

**Table 6.1:** Strangeness-isospin coefficients appearing in the chiral expansion of the form factors.

| $(S, I)$ | $(1,0)$ | | $(0, \frac{1}{2})$ | | |
|---|---|---|---|---|---|
| channel | $DK$ | $D_s\eta$ | $D\pi$<br>$\bar{B}\pi$ | $D\eta$<br>$\bar{B}\eta$ | $D_s\bar{K}$<br>$\bar{B}_s\bar{K}$ |
| $\mathcal{C}$ | $-\sqrt{2}$ | $-\sqrt{\frac{2}{3}}$ | $\sqrt{\frac{3}{2}}$ | $\frac{1}{\sqrt{6}}$ | $1$ |

We match the two representations at a point $s = s_0$ located in the valid region of the chiral expansion. Namely, we take $s_0 = q^2_{\text{max}} = (m_P - M_\pi)^2$ for the $(0, 1/2)$ form factors, and $s_0 = (m_D - M_K)^2$ for the charm $(1, 0)$ case, since this is the point in which the momentum of the lightest meson is zero. Imposing that the dispersive form factors and their first derivative to be equal to the chiral ones at $s = s_0$, the coefficients in the polynomials, Eq. (6.34), can be expressed as:

$$\begin{aligned} \vec{\alpha}_0 &= \Omega^{-1}(s_0) \cdot \vec{\mathcal{F}}_\chi(s_0) - \vec{\alpha}_1\, s_0, \\ \vec{\alpha}_1 &= \Omega^{-1}(s_0) \cdot \left[\vec{\mathcal{F}}'_\chi(s_0) - \Omega'(s_0) \cdot \Omega^{-1}(s_0) \cdot \vec{\mathcal{F}}_\chi(s_0)\right], \end{aligned} \tag{6.42}$$

where the $'$ stands for a derivative with respect to $s$. The vectors $\vec{\mathcal{F}}_\chi$ contain the chiral form factors,

$$\vec{\mathcal{F}}_\chi^{(0,\frac{1}{2})}(s) \equiv \left(f_0^{D\pi^{(0,\frac{1}{2})}}, f_0^{D\eta^{(0,\frac{1}{2})}}, f_0^{D_sK^{(0,\frac{1}{2})}}\right)^T, \tag{6.43}$$

$$\vec{\mathcal{F}}_\chi^{(1,0)}(s) \equiv \left(f_0^{DK^{(1,0)}}, f_0^{D_s\eta^{(1,0)}}\right)^T, \tag{6.44}$$

with all the elements given in Eq. (6.40). Similar expressions are used for the $(0, \frac{1}{2})$ channel in the bottom sector. In other words, the vectors $\vec{\mathcal{F}}_\chi(s)$ contain the form factors defined in Eqs. (6.5) and (6.6), but computed according to the chiral expansion.

It is worth noting that the NLO LECs $\beta_1^P$ and $\beta_2^P$ determined from a fit to data using the MO scheme would have some residual dependence on the matching point. To minimize such dependence, we have chosen $s_0 = q^2_{\text{max}}$, where the momentum of the Goldstone bosons is close to zero and higher order chiral corrections are expected to be small. Different choices of the matching point, within the chiral regime, will amount to changes in the fitted (effective) $\beta_1^P$ and $\beta_2^P$ LECs driven by higher order effects.

In the charm $(1,0)$ sector, due to the presence of the $D^*_{s0}(2317)$ state as a bound state in the $T$-matrix, the solution of Eq. (6.16) gets modified. The contribution from $D^*_{s0}(2317)$ is easily incorporated as follows:

$$\Omega^{(1,0)} \cdot \vec{\mathcal{P}}^{(1,0)}(s) \to \Omega^{(1,0)} \cdot \left\{ \frac{\beta_0\, \vec{\Gamma}}{s - s_p} + \vec{\mathcal{P}}^{(1,0)}(s) \right\}, \tag{6.45}$$

where $\beta_0$ is an unknown parameter which characterizes the coupling of $D^*_{s0}(2317)$ to the left-hand current. $\vec{\Gamma}$ contains the couplings of the $D^*_{s0}(2317)$ to the $DK$-$D_s\eta$ system,[11] namely, $\vec{\Gamma} = (g_{DK}, g_{D_s\eta})^T$. As it was shown previously (see Table 4.4), this bound state is dynamically generated in the unitarized amplitudes $T_U^{(1,0)}(s)$ presented in Chapter 4, that we also employ here. The couplings are computed from the residue of the amplitude at the pole as in Eq. (2.93). The $D^*_{s0}(2317)$ pole position $s_p = (M - i\Gamma/2)^2$, together with $g_{DK}$ and $g_{D_s\eta}$, are collected in Table 4.4.

## 6.3 Numerical results and discussion

**Table 6.2:** Masses and decay constants (in MeV units) used in this work and taken from the PDG [206] and FLAG [70] reviews.

| Goldstone | | charm sector | | bottom sector | |
|---|---|---|---|---|---|
| $M_\pi$ | 139 | $m_D$ | 1869.6 | $m_B$ | 5279.5 |
| $M_K$ | 496 | $m_{D_s}$ | 1968.5 | $m_{B_s}$ | 5366.8 |
| $M_\eta$ | 547 | $f_D$ | 147.6 | $f_B$ | 135.8 |
| $F_0$ | 92.4 | $f_{D_s}$ | 174.2 | $f_{B_s}$ | 161.5 |
| | | $m_{D*}$ | 2008.6 | $m_{B*}$ | 5324.7 |
| | | $m_{D_s^*}$ | 2112.1 | | |

So far, the theoretical MO representations of the scalar form factors have been constructed. In this section, we want to confront the so-obtained form factors to the LQCD and LCSR results. In what follows, we first fit to the $\bar{B} \to \pi$ and $\bar{B}_s \to \bar{K}$ scalar form factors, where we expect the $1/m_P$ corrections to the chiral expansion in Eq. (6.40) to be substantially suppressed. Next, we will carry out a combined fit to all the data in both charm and bottom sectors, by adopting some (approximate) heavy-quark flavor scaling rule [288] for the $\beta_1^P$ and $\beta_2^P$ LECs in Eq. (6.40). Using the results of our combined fit, we will: i) determine the CKM elements, $|V_{cd}|$, $|V_{cs}|$ and $|V_{ub}|$, ii) predict form factors, not computed in LQCD yet, and that can be used to over-constrain the CKM matrix elements from analyses involving more semileptonic decays, and iii) predict the different

---

[11] Note that the first term in the bracket of Eq. (6.45) should have a more general form, $\frac{\vec{\beta}_0}{s-s_p}$, with $\vec{\beta}_0$ a vector with two independent components, $\vec{\beta}_0 = (\beta_0^a, \beta_0^b)^T$. The specific form in Eq. (6.45) reduces the number of free parameters, by forcing $\beta_0^a/\beta_0^b = g_{DK}/g_{D_s\eta}$. On the other hand, this has the effect that the form factors $f_0^{DK}$ and $f_0^{D_s\eta}$ are not exactly independent of the choice of the point $s_n$ where one normalizes the Omnès matrix, $\Omega(s_n) = \mathbb{I}$. Nonetheless, we have checked that this choice, varying $s_n$ from zero to $q^2_{\rm max}$, has no practical effect in the determination of $\beta_0$, which indicates that our assumption is reasonable. We also remark that this discussion has no effect at all in the $(0,1/2)$ sector.

form factors above the $q^2-$regions accessible in the semileptonic decays, up to moderate energies amenable to be described using the unitarized coupled-channel chiral approach.

Masses and decay constants used in this work are compiled in Table 6.2. In addition, the mass of the heavy-light mesons in the chiral limit, see Eq. (6.35), is set to $\mathring{m} = (m_P + m_{P_s})/2$, for simplicity the same average is used to define $\bar{m}_P$ in the Sec. 4.5.1 and in the relations given in Eq. (6.52). The $\mathcal{P}\mathcal{P}^*\phi$ axial coupling constant $\tilde{g}$ in Eq. (6.38) can be fixed by calculating the decay width of $D^{*+} \to D^0\pi^+$ [206], which leads[12] to $g \sim 0.58$ and hence $\tilde{g}_{D^*D\pi} \sim 1.113$ GeV. In the bottom sector we use a different value for $g$, around 15% smaller, consistent with the lattice calculation of Ref. [300], where $g \sim 0.51$ (or $\tilde{g}_{\bar{B}^*\bar{B}\pi} \sim 2.720$ GeV) was found. Note that the difference is consistent with the expected size of heavy-quark-flavour symmetry violations. In addition, there exist sizeable SU(3) corrections to the overall size of the $\mathcal{P}^*$ pole contribution to both $f_+$ and $f_0$ form factors. Thus, such contribution is around $\sim 20\%$ smaller for $\bar{B}^*\bar{B}_sK$ than for $\bar{B}^*\bar{B}\pi$ [275, 278]. According to [301] this suppression is mainly due to a factor $F_\pi/F_K \sim 0.83$ [70]. We will implement this correction in the pole contribution to $f_0$ in Eq. (6.40) when the Goldstone boson is either a kaon or an eta meson (for simplicity, we also take $F_\eta \approx F_K$), and both in the bottom and charm sectors.

### 6.3.1 Fit to the LQCD+LCSR results in the bottom sector

We are first interested in the $\bar{B} \to \phi$ transitions induced by the $b \to u$ flavour-changing current, which include $\bar{B} \to \pi$, $\bar{B} \to \eta$ and $\bar{B}_s \to K$. The scalar form factors involved in those transitions can be related to the Omnès matrix through

$$\begin{pmatrix} \sqrt{\frac{3}{2}} f_0^{\bar{B}^0\to\pi^+}(s) \\ f_0^{B^-\to\eta}(s) \\ f_0^{\bar{B}_s^0\to K^+}(s) \end{pmatrix} = \Omega_{\bar{B}}^{(0,\frac{1}{2})}(s) \cdot \vec{\mathcal{P}}_{\bar{B}}^{(0,\frac{1}{2})}(s) \; . \tag{6.46}$$

Within the present approach, and considering just rank-one MO polynomials, there are only two undetermined parameters: the NLO LECs $\beta_1^P$ and $\beta_2^P$ that appear in the chiral expansion of the form factors in Eq. (6.40). We fit these parameters, in the bottom sector, to LQCD (UKQCD [265], HPQCD [66, 263] and Fermilab Lattice & MILC (to be referred to as FL-MILC for brevity) [264]) and LCSR [258, 259] results for the scalar form factors in $\bar{B}^0 \to \pi^+$ and $\bar{B}_s^0 \to K^+$ semileptonic decays. Lattice results are not available for the whole kinematic region accessible in the decays, and they are restricted to large values of $q^2 \geqslant 17$ GeV$^2$, where momentum-dependent discretization and statistical errors are under control. To constrain the behaviour of the scalar form factors at small values of $q^2$, we take four LCSR points (equally-spaced) in the interval $q^2 = 0 - 6$ GeV$^2$ for each decay.

The UKQCD Collaboration [265] provides data for both $\bar{B} \to \pi$ and $\bar{B}_s \to K$ form factors together with statistical and systematic correlation matrices for a set of three form factors computed at different $q^2$ (Tables VIII and IX of this reference). In the case of HPQCD [263] $\bar{B}_s \to K$ and FL-MILC [264] $B \to \pi$ form factors, we have read off four points from the final extrapolated results (bands) given in these references, since in both cases, originally only four momentum configurations ($0 \to 0$, $0 \to 1$, $0 \to \sqrt{2}$ and $0 \to \sqrt{3}$) were simulated. Finally, we also include in the fit the five $B \to \pi$ points provided by the HPQCD Collaboration in the erratum of Ref. [66].

---

[12] Errors on $g$ determined from the decay $D^{*+} \to D^0\pi^+$ are very small of the order of 1%.

We address the uncorrelated merit function, $\chi^2_{\mathrm{u}}$,

$$\chi^2_{\mathrm{u}} = \sum_{i=1} \frac{\left(f_0(q_i^2) - f_0^i\right)^2}{\left(\Delta f_0^i\right)^2} , \tag{6.47}$$

used in the uncorrelated data sets $\{f_0^i, \Delta f_0^i\}_{i=1}^{N_{\mathrm{data}}}$. On the other hand, the correlated merit function $\chi^2_{\mathrm{cov}}$ accounting for the information of the correlation matrices in UKQCD data is defined as

$$\chi^2_{\mathrm{cov}} = \sum_{i,j=1} \left[f_0(q_i^2) - f_0^i\right](\mathcal{C}^{-1})_{ij}\left[f_0(q_j^2) - f_0^j\right] , \tag{6.48}$$

with the covariance matrix $\mathcal{C}$ constructed from the statistical and systematic correlation matrices and uncertainties given in Ref. [265]. Above, $f_0(q^2)$ stands for the theoretical scalar form factor obtained from the MO representation.

Thus, the $\chi^2$ reads

$$\begin{aligned} \chi^2 &= (\chi^2_{\mathrm{cov}})^{\bar{B}\to\pi}_{\mathrm{UKQCD}} + (\chi^2_{\mathrm{cov}})^{\bar{B}_s\to K}_{\mathrm{UKQCD}} + (\chi^2_{\mathrm{u}})^{\bar{B}\to\pi}_{\mathrm{FL-MILC}} \\ &+ (\chi^2_{\mathrm{u}})^{\bar{B}\to\pi}_{\mathrm{HPQCD}} + (\chi^2_{\mathrm{u}})^{\bar{B}_s\to K}_{\mathrm{HPQCD}} \\ &+ (\chi^2_{\mathrm{u}})^{\bar{B}\to\pi}_{\mathrm{LCSR}} + (\chi^2_{\mathrm{u}})^{\bar{B}_s\to K}_{\mathrm{LCSR}} , \end{aligned} \tag{6.49}$$

The chi-squared fit results are

$$\begin{aligned} \beta_1^B &= (0.27 \pm 0.12 \pm 0.07)\ \mathrm{GeV} \\ \beta_2^B &= (0.037 \pm 0.004 \pm 0.003)\ \mathrm{GeV}^{-1} \end{aligned} \tag{6.50}$$

with $\chi^2/dof = 4.2$ for 25 degrees of freedom, and a correlation coefficient 0.999 between the two fitted parameters. The first set of errors in the parameters is obtained from the minimization procedure, assuming Gaussian statistics, while the second one accounts for the uncertainties of the LECs quoted in Ref. [205] that enter in the definition of the chiral amplitudes. Such a correlation coefficient so close to 1 indicates that the considered data can not properly disentangle both LECs,[13] and that different $(\beta_1^B, \beta_2^B)$ pairs belonging to the straight line

$$\frac{\beta_1^B - \overline{\beta}_1^B}{\sigma_{\beta_1^B}} = \frac{\beta_2^B - \overline{\beta}_2^B}{\sigma_{\beta_2^B}} \tag{6.51}$$

in the vicinity of the best fit values $(\overline{\beta}_1^B, \overline{\beta}_2^B)$ quoted in Eq. (6.50) lead to similar descriptions of the data (see the dashed-blue line in the right panel of Fig. 6.10). The scalar form factors obtained are displayed in Fig. 6.8. We find a fair description of the LQCD and LCSR results for the $\bar{B}_s^0 \to K^+$ scalar form factor, while we face some problems for the $\bar{B}^0 \to \pi^+$ decay. The large value of $\chi^2/dof$ reported in Eq. (6.50) is mainly due to the existing tension between the LQCD results from different collaborations in this latter decay. The disagreement between UKQCD and HPQCD $\bar{B}^0 \to \pi^+$ scalar form factors was already highlighted in the top-right panel of Fig. 23 of the UKQCD work [265], where it is noted that the HPQCD calculation used only a single lattice spacing.

---

[13] This can be easily understood since these LECs enter in the definition of $\vec{\alpha}_0$ and $\vec{\alpha}_1$ in the combinations $\beta_1 - m_P^2\beta_2$ and $\beta_1 - m_P(m_P - 2M_\phi)\beta_2$ , which are identical up to some small SU(3) corrections.

In addition, as we discussed before, the $\bar{B}\pi-$scalar form factor decreases by a factor of five in the $q^2-$range accessible in the decay, and the LQCD results around $q^2_{\rm max}$ and the LCSR predictions in the vicinity of $q^2 = 0$ are not linearly connected at all. In the current scheme, where only rank-one MO polynomials are being used, this extra needed curvature should be provided by the $q^2-$dependence of the MO matrix, $\Omega$, whose behaviour near $q^2 = 0$, far from $q^2_{\rm max}$, is not determined by the behaviour of the amplitudes in the chiral regime. Indeed, it significantly depends on the high-energy input.[14] This is an unwanted feature, source of systematic uncertainties. To minimize this problem, in the next subsection we will perform a combined fit to transitions induced by the $b \to u$ and $c \to d, s$ flavour-changing currents. The latter ones describe $D \to \pi$ and $D \to \bar{K}$ semileptonic decays for which there exist recent and accurate LQCD determinations of the scalar form factors. Moreover, in these latter transitions the $q^2-$ranges accessible in the decays and the form factor variations are much limited and, thus, the input provided in the chiral regime becomes more relevant.

To finish this subsection, we would like to stress that given the large value found for $\chi^2/dof$, statistical errors should be taken with some care. Indeed, one can rather assume some systematic uncertainties affecting our results, that could be estimated by considering in the best fit alternatively only the HPQCD or the UKQCD and the FL-MILC sets of predictions. We will follow this strategy to obtain our final results for the CKM matrix elements and form factors at $q^2 = 0$ from the combined-fit to charm and bottom decays detailed in the next subsection.

### 6.3.2 Extension to the charm sector and combined fit

Besides the parameter $\beta_0$ introduced in Eq. (6.45) to account for the effects on the $D^*_{s0}(2317)$ state in the $c \to s$ decays, one should also take into account that the LECs $\beta^P_1$ and $\beta^P_2$ depend on the heavy quark mass. The scaling rules given in Eq. (6.41) can be used to relate the values taken for these LECs in the bottom ($\beta^B_i$) and charm sectors ($\beta^D_i$). We will assume some heavy quark flavour symmetry violations and we will use

$$\frac{\beta^D_1}{\beta^B_1} = \sqrt{\frac{\bar{m}_D}{\bar{m}_B}}(1+\delta), \quad \frac{\beta^D_2}{\beta^B_2} = \sqrt{\frac{\bar{m}^3_B}{\bar{m}^3_D}}(1-3\delta) \tag{6.52}$$

where, one should expect the new parameter, $\delta$, to be of the order $\Lambda_{\rm QCD}/\bar{m}_D$. Note that we are correlating the heavy quark flavour symmetry violations in the LECs $\beta_1$ and $\beta_2$. There is not a good reason for this other than avoiding to include new free parameters. On the other hand, at the charm scale, one might also expect sizeable corrections to the LO prediction $f_0(s) \sim \mathcal{C} \times f_P/F_0$ of Eq. (6.40), even more bearing in mind the large $(40-50\%)$ heavy-quark symmetry violations inferred from the ratio $f_B/f_D$ quoted in Table 6.2. (Note that at LO in the inverse of the heavy quark mass, this ratio should

---

[14] The results displayed in Fig. 6.8 might suggest that the present approach hardly provides enough freedom to simultaneously accommodate the near $q^2 = 0$ (LCSR) and $q^2_{\rm max}$ (LQCD) determinations of the $\bar{B}\pi$ scalar form factor. The situation greatly improves when only the HPQCD, among all LQCD calculations, $\bar{B}\pi$ results are considered in the $q^2_{\rm max}$ region, being then possible to find an excellent combined description of the LCSR and HPQCD results with $\chi^2 = 9.65$ for a total of 18 degrees of freedom (see dashed-red curve in the right plot of Fig. 6.10), which leads to $\chi^2/dof = 0.5$. The parameters $\beta^B_{1,2}$ come out still to be almost totally correlated as in Eq. (6.50), and moreover they lie, within great precision, in the straight line of Eq. (6.51), but in the $\beta^B_1 \sim 0.7$ GeV region.

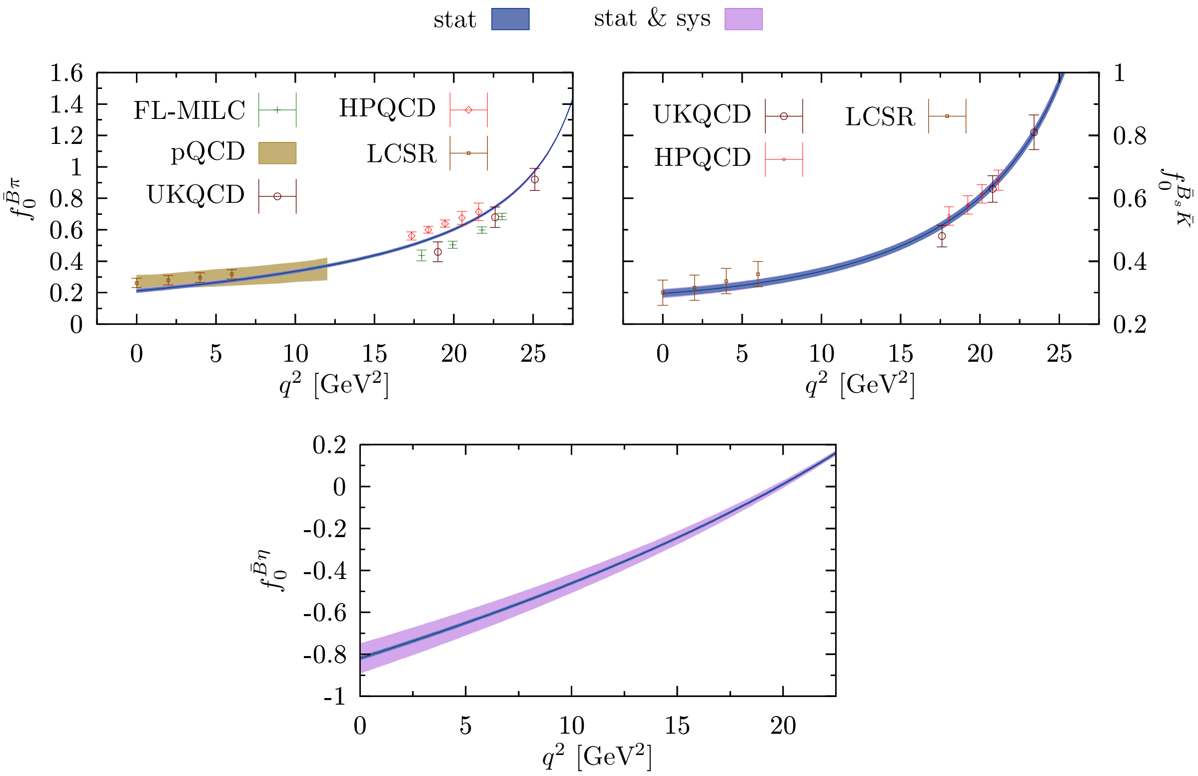

**Figure 6.8:** Fitted $\bar{B}^0 \to \pi^+$, $\bar{B}^0_s \to K^+$ (top) and predicted $\bar{B}^- \to \eta$ (bottom) scalar form factors. Besides the fitted data (UKQCD [265], HPQCD [66, 263], FL-MILC [264] and LCSR [258, 259]), and for comparison, predictions from the NLO perturbative QCD approach of Ref. [289] for the $\bar{B}^0 \to \pi^+$ decay are also shown. Statistical (stat) and statistical plus systematic (stat & sys) 68%-confident level (CL) bands are also shown. The systematic uncertainties are inherited from the errors on the LECs quoted in Ref. [205], that enter in the definition of the chiral amplitudes, and are added in quadratures to the statistical uncertainties to obtain the outer bands. To estimate the systematic uncertainties for each set of LECs we re-do the best fit.

scale as $(\bar{m}_D/\bar{m}_B)^{1/2}$). Thus, we have also introduced an additional parameter, $\delta'$, defined through the replacement

$$f_P \to f_P \times (1+\delta') \tag{6.53}$$

when Eq. (6.40) is applied to the $c \to d, s$ decays. Thus, we have three new parameters $\beta_0, \delta, \delta'$, which in addition to $\beta^B_{1,2}$, will be fitted to the LQCD & LCSR results for the scalar form factors in the $\bar{B} \to \pi$, $\bar{B}_s \to K$, $D \to \pi$ and $D \to \bar{K}$ semileptonic decays.

First we need to incorporate the $c \to d, s$ input into the merit function $\chi^2$, which was defined in Eq. (6.49) using only bottom decay results. In the last ten years, LQCD computations of the relevant $D \to \pi$ and $D \to \bar{K}$ semileptonic decay matrix elements have been carried out by the HPQCD [261, 262] and very recently by the ETM [266] Collaborations. Compared with the former, the latter corrects for some hypercubic effects, coming from discretization of a quantum field theory on a lattice with hypercubic symmetry [302], and uses a large sample of kinematics, not restricted in particular to the parent $D$ meson at rest, as in the case of the HPQCD simulation. Moreover, it is argued in Ref. [266] that the restricted kinematics employed in the simulations of Refs. [261, 262] may obscure the presence of hypercubic effects in the lattice data, and these corrections

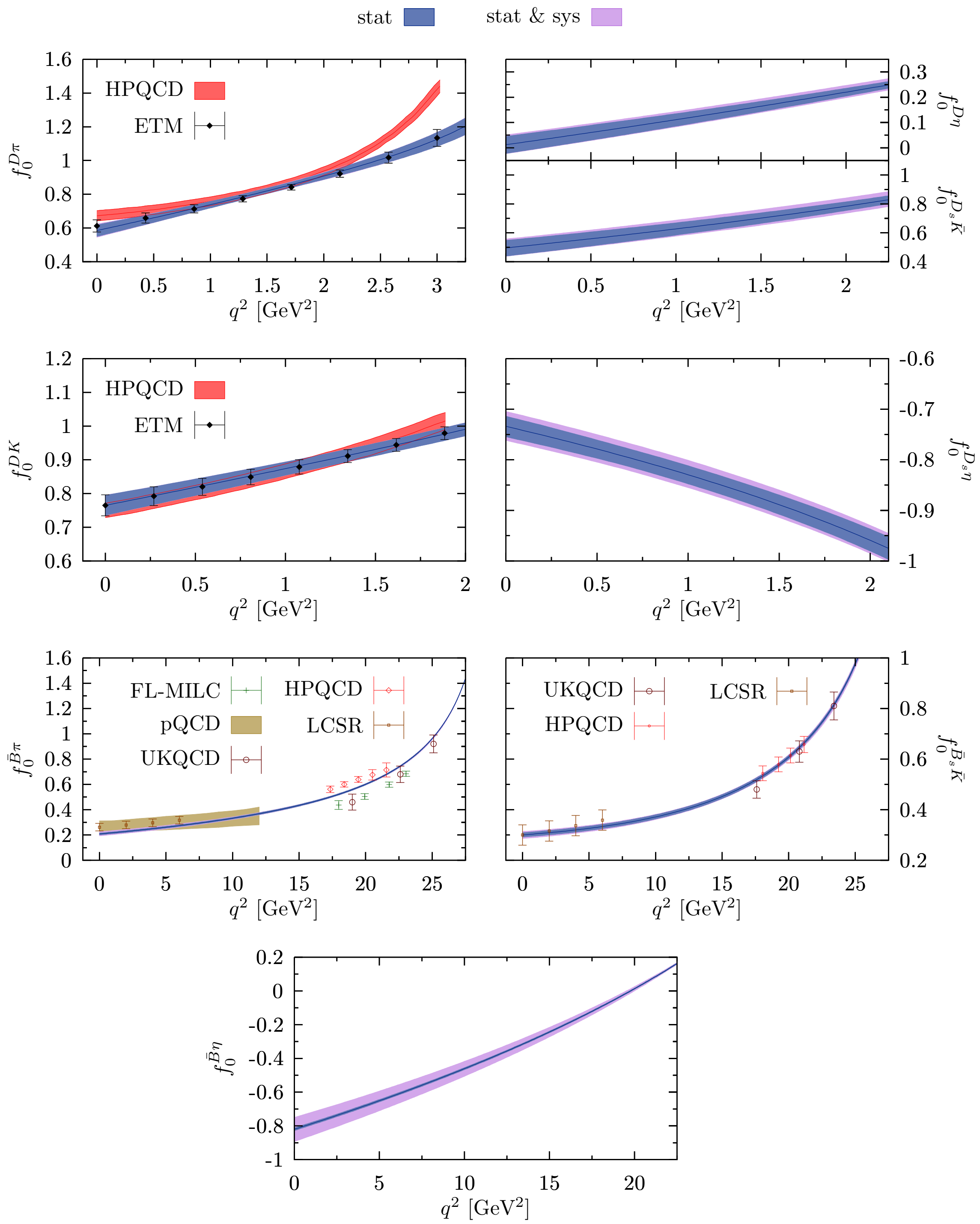

**Figure 6.9:** Scalar form factors from the $D_{\ell 3}$, $\bar{B}_{\ell 3}$ and $(\bar{B}_s)_{\ell 3}$ combined fit (see Table 6.3 for details). The three bottom panels are similar to those depicted in Fig. 6.8, but computed from the results of the combined best-fit. The four panels in the first two rows show form factors for $c \to d, s$ semileptonic transitions. Only ETM results, corrected for some hypercubic (discretization) effects [266], have been considered in the fit of Table 6.3. For comparison, predictions from the HPQCD [261, 262] Collaboration are also displayed. Differences between ETM and HPQCD sets of $D \to \pi$ and $D \to K$ form factors are clearly visible in the vicinity of $q^2_{\text{max}}$, in particular for the $D \to \pi$ case. Statistical (stat) and statistical plus systematic (stat & sys) 68%-confident level bands are also given and are calculated as explained in Fig. 6.8. Finally, predictions for the $D \to \eta$, $D_s \to K$ and $D_s \to \eta$ scalar form factors are also shown.

**Table 6.3:** Results from the bottom-charm combined fit, with $\chi^2$ defined in Eq. (6.54) and a total of 38 degrees of freedom. The first set of errors in the best-fit parameters is obtained from the minimization procedure, assuming Gaussian statistics, while the second one accounts for the uncertainties of the LECs quoted in Ref. [205] that enter in the definition of the chiral amplitudes. The LECs $\beta_0$ and $\beta_1^B$ ($\beta_2^B$) are given in units of GeV (GeV$^{-1}$).

| | | correlation matrix | | | | |
|---|---|---|---|---|---|---|
| | $\frac{\chi^2}{dof} = 2.77$ | $\beta_0$ | $\beta_1^B$ | $\beta_2^B$ | $\delta$ | $\delta'$ |
| $\beta_0$ | 0.152(14)(13) | 1.000 | 0.502 | 0.499 | $-0.490$ | 0.311 |
| $\beta_1^B$ | 0.22(4)(4) | 0.502 | 1.000 | 0.995 | $-0.965$ | 0.848 |
| $\beta_2^B$ | 0.0346(16)(15) | 0.499 | 0.995 | 1.000 | $-0.958$ | 0.845 |
| $\delta$ | 0.138(21)(18) | $-0.490$ | $-0.965$ | $-0.958$ | 1.000 | $-0.942$ |
| $\delta'$ | $-0.18(4)(2)$ | 0.311 | 0.848 | 0.845 | $-0.942$ | 1.000 |

can affect the extrapolation to the continuum limit in a way that depends on the specific lattice formulation. This might be one of the sources of the important discrepancies found between the $D \to \pi$ form factors reported by the HPQCD and ETM Collaborations in the region close to $q^2_{\max} = (m_D - M_\pi)^2$, as can be seen in the left top panel of Fig. 6.9.

Here, we prefer to fit to the most recent data together with the covariance matrices provided by the ETM Collaboration. This analysis is based on gauge configurations produced with $N_f = 2{+}1{+}1$ flavours of dynamical quarks at three different values of lattice spacing, and with pion masses as small as 210 MeV. Lorentz symmetry breaking due to hypercubic effects is clearly observed in the ETM data and included in the decomposition of the current matrix elements in terms of additional form factors. Those discretization errors have not been considered in the HPQCD analyses, and for this reason we have decided to exclude the results of these latter collaboration in our fits.

The scalar form factors involved in the $D \to \pi$ and $D \to \bar{K}$ transitions are related to the Omnès matrices displayed in Figs. 6.2 and 6.4 through[15] Eq. (6.16) and Eqs. (6.5) and (6.6). Hence, the bottom-charm combined $\chi^2$ now reads

$$\begin{aligned}\chi^2 &= (\chi^2_{\text{cov}})^{\bar{B}\to\pi}_{\text{UKQCD}} + (\chi^2_{\text{cov}})^{\bar{B}_s\to K}_{\text{UKQCD}} + (\chi^2)^{\bar{B}\to\pi}_{\text{FL-MILC}} \\ &+ (\chi^2)^{\bar{B}\to\pi}_{\text{HPQCD}} + (\chi^2)^{\bar{B}_s\to K}_{\text{HPQCD}} \\ &+ (\chi^2)^{\bar{B}\to\pi}_{\text{LCSR}} + (\chi^2)^{\bar{B}_s\to K}_{\text{LCSR}} \\ &+ (\chi^2_{\text{cov}})^{D\to\pi} + (\chi^2_{\text{cov}})^{D\to\bar{K}}\,, \end{aligned} \tag{6.54}$$

where we have added sixteen ETM points, eight for each of the two $D \to \pi$ and $D \to \bar{K}$ decay modes. Each of the new eight-point sets is correlated and the corresponding covariance matrices[16] have been obtained from the authors of Ref. [266]. Thus, we are fitting

---

[15] Notice that the particle charges are not specified in the notation used in Lattice QCD, for instance, $D^0 \to \pi^-$ in Eq. (6.5) is simplified to $D \to \pi$, to be used below and denoted by $D\pi$ in the lattice paper.

[16] The $D \to \pi$ and $D \to \bar{K}$ scalar form factor covariance-matrices have troublesome small eigenvalues, as small as $10^{-6}$ or even $10^{-9}$. Due to this, the fitting procedure could be easily spoiled since a tiny error in the fitting function yields a huge $\chi^2$ value (specific examples can be found in Ref. [303]). We have used the singular value decomposition (SVD) method to tackle this issue, which is widely used by a number of lattice groups [304–306].

five parameters to a total of 43 points. The best-fit results for the five unknown parameters and their Gaussian correlation matrix are collected in Table 6.3 and the resulting scalar form factors are shown in Fig. 6.9.

The results for the bottom scalar form factors are almost the same as the ones shown in Fig. 6.8, while the ETM $c \to d, s$ transition form factors are remarkably well described within the present scheme. As in the former best-fit to only the $\bar{B}_{(s)}$ results, the large value obtained for $\chi^2/dof$ is mainly due to the existing tension between the LQCD results from different collaborations in the $\bar{B} \to \pi$ decay.

Due to the hypercubic effects, there might be inconsistencies between the ETM and HPQCD analyses for the $D\pi$ scalar form factor in the region close to $q^2_{\rm max} = (m_D - M_\pi)^2$ [266]. As one can see, our result disagrees with the HPQCD data in that region too. We have checked that if we fit to the HPQCD instead of the ETM data in the charm sector, the best fit still tends to coincide with the ETM data. This observation is important and it seems to indicate that the Lorentz symmetry breaking effects in a finite volume, due to the hypercubic artifacts, could be important in the LQCD determination of the form factors in semileptonic heavy-to-light decays, as pointed out in Ref. [266].

The HQFS breaking parameters $\delta$ and $\delta'$ turn out to be quite correlated and their size is of the order $\Lambda_{\rm QCD}/m_c$. As expected, $\delta$ presents also a high degree of correlation with $\beta_1^B$ and $\beta_2^B$, and on the other hand, the combined fit does not reduce the large correlation between these two latter LECs, while the central values (errors) quoted for them in Table 6.3 are compatible within errors with (significantly smaller than) those given in Eq. (6.50), and obtained from the fit only to $b \to u$ transitions. In addition, the values quoted for $(\beta_1^B, \beta_2^B)$ in Table 6.3 perfectly lie in the straight line of Eq. (6.51), deduced from the fit to only bottom form factors carried out in the previous Sec. 6.3.1. Indeed, the straight line that one can construct with the results of Table 6.3 in the $(\beta_1^B, \beta_2^B)-$plane is practically indistinguishable from that of Eq. (6.51). All this can be seen in the left plot of Fig. 6.10, where both straight lines are depicted, together with the statistical 68% CL ellipses and the one-sigma-rectangle bands obtained by minimizing the merit function given in Eq. (6.49) or alternatively in Eq. (6.54), and considering only bottom or bottom and charm scalar form factors, respectively.

In the right plot of Fig. 6.10, we show the dependence of $\chi^2$ on $\beta_1^B$ for different situations. We display the combined charm-bottom and the bottom-only fits, and in both cases, we have considered results obtained when all $\bar{B} \to \pi$ LQCD form factors or only the HPQCD or the UKQCD and the FL-MILC subsets of results are considered in the fits. The circles stand for the different best-fit results, accounting for variations of $\chi^2$ up to one unit from the minimum value,[17] while the dashed and solid curves have been obtained by relating $\beta_1^B$ and $\beta_2^B$ through Eq. (6.51) and minimizing $\chi^2$ with respect to the other parameters, $\beta_0, \delta$ and $\delta'$, respectively. Several conclusions can be extracted from the results shown in the figure:

- The combined charm-bottom analyses (solid lines) provide large curvatures of $\chi^2$ as a function of $\beta_1^B$, hence leading to better determinations of this latter LEC, always in the 0.2 GeV region, as we also found in Eq. (6.49) from the best fit to only the bottom results. A value for $\beta_1^B$ close to this region, taking into account errors, is also found from a fit where only the bottom form factors are considered, but without including the HPQCD $\bar{B} \to \pi$ results (dashed-green curve). Only the dashed-red

---

[17] Thus, the ranges marked by the circles show the statistical errors of $\beta_1^B$ in each fit.

line (fit only to the bottom results, but without including in this case the UKQCD and FL-MILC $\bar{B} \to \pi$ scalar form factors) turns out to be incompatible with the combined fit presented in Table 6.3. Thus, we find some arguments to support the range of values quoted in Table 6.3 for the parameters $(\beta_1^B, \beta_2^B)$ that appear in the HM$\chi$PT expansion of the scalar form factors at the bottom scale.

- The existing tension between HPQCD, and UKQCD and FL-MILC sets of $\bar{B} \to \pi$ form factors leads to large values of $\chi^2$. Thus, as mentioned above, statistical errors should be taken with some care, and some systematic uncertainties would need to be considered in derived quantities, as for instance in the values of the form factors at $q^2 = 0$ or in the CKM mixing parameters. We note that this source of systematics also induces variations on the fitted parameters in Table 6.3 which range between 50% ($\beta_0$ and $\beta_2^B$) to 100% ($\beta_1^B$, $\delta$ and $\delta'$) of the statistical errors quoted in the table.

Our predictions for the scalar form factors for the $D_s \to \eta$, $D \to \eta$ and $D_s \to K$ transitions, for which there are no lattice results as yet, are also shown in Fig. 6.9. Note that transitions involving the $\eta$ meson in the final state are more difficult to be evaluated in LQCD simulations. Interestingly, the $D \to \eta$ scalar form factor in the three-channel $(0, 1/2)-$case is largely suppressed, similar to the component regarding the $K \to \eta$ transition in the strangeness-changing scalar form factors as shown in Ref. [270].

### Further considerations

We have also obtained results using constant and quadratic MO polynomials. In the first case, the dispersive representations of the form factors should be matched to the LO chiral ones, where the terms driven by the $\beta_1^P$ and $\beta_2^P$ LECs are dropped out. The first consequence is that bottom and charm sectors are no longer connected since, in addition, we are not enforcing the heavy-quark scaling law for the decay constants. To better describe the data, one might perform separate fits to bottom and charm form factors with free $\vec{\alpha}_0$ parameters in Eq. (6.34). Fits obviously are poorer, and moreover, they do not necessarily provide reliable estimates of the form factors at $q^2_{\rm max}$, since the fitted parameters are obtained after minimizing a merit function constructed out of data in the whole $q^2-$range accessible in the decays. For charm decays, the description of the $D \to \pi$ form factor is acceptable, while that of the $D \to \bar{K}$ is in comparison worse, mostly because the $s-$dependence induced by the $D^*_{s0}(2317)$ can not be now modulated by the MO polynomial. In the bottom sector, as one should expect, the simultaneous description of LQCD and LCSR form factors in the vicinity of $q^2_{\rm max}$ and $q^2 = 0$, respectively, becomes poorer. Indeed, since the LQCD input has a larger weight in the $\chi^2$ than the LCSR one, the latter form factors are totally missed by the new predictions, which now lie below the lower error bands of the LCSR results.

The consideration of quadratic MO polynomials solves this problem, as shown in Fig. 6.12 of Sec. 6.5. Indeed, it is now possible to improve the description of the $\bar{B} \to \pi$ LCSR form factors, providing still similar results in the $q^2_{\rm max}-$region, where the LQCD data are available. Thus, for instance, we get $f_+^{\bar{B}\to\pi}(0) = 0.248(10)$ using the new fit to be compared with 0.211(10) obtained using the parameters of the fit of Eq. (6.50) (form factors displayed in Fig. 6.8). Nevertheless, as we will see in the next subsection, there exist some other systematic errors, which practically account for the latter difference, and thus this source of uncertainty will be considered in the determination of the CKM matrix element $|V_{ub}|$. In addition, though the $\chi^2/dof$ obtained with quadratic MO polynomials is

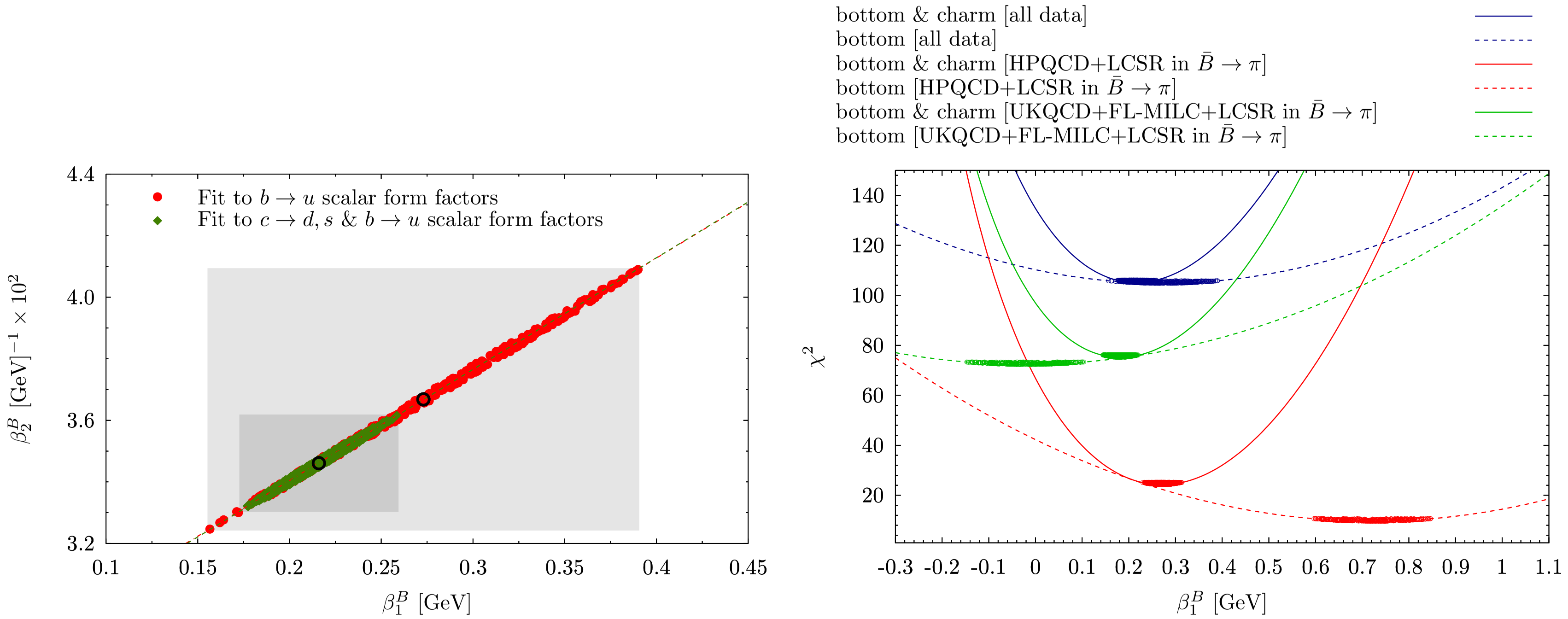

**Figure 6.10:** Left plot: Statistical 68% CL ellipses and one-sigma-rectangle bands in the $(\beta_1^B, \beta_2^B)$−plane obtained by minimizing the merit functions given in Eqs. (6.49) and (6.54). In addition the correlation relation of Eq. (6.51) is also displayed. A similar relation deduced from the best-fit results of Table 6.3 is also shown, though it is hardly distinguishable from the former one. Right plot: Dependence of $\chi^2$ on $\beta_1^B$ for different situations. The circles stand for the different best-fit results, accounting for variations of $\chi^2$ up to one unit from the minimum value, while the dashed and solid curves have been obtained by relating $\beta_1^B$ and $\beta_2^B$ through Eq. (6.51) and minimizing $\chi^2$ with respect to the other parameters, $\beta_0, \delta$ and $\delta'$, respectively.

better, it is still large (around 3.7) due to the tension between the $\bar{B} \to \pi$ LQCD results from different collaborations. Moreover $\beta_1^B$ and $\beta_2^B$ are still fully correlated, and the quadratic terms of the MO polynomials that multiply the elements $\Omega_{ij}$, $(i = 1,2,3,\ j = 2,3)$ of the matrix displayed in Fig. 6.6 are almost undetermined (see the large errors in the parameters $\alpha_{2,3}$ and especially $\alpha_{2,2}$ given in Table 6.4). Finally, the central-value predictions, that will be shown in Subsec. 6.3.4, for the form factors above $q^2_{\rm max}$ and to moderate energies amenable to be described using the unitarized coupled-channel chiral approach, are not affected by the inclusion of quadratic terms in the MO polynomials, though errors are enhanced. For all of this, we consider our best estimates for the form factors those obtained using rank-one polynomials.

We do not discuss quadratic terms in the charm-sector because rank-one MO polynomials led already to excellent reproductions of the form factors (see Fig. 6.9), in part due to the smaller $q^2-$range involved in these decays. Moreover a correct charm-bottom combined treatment will require the matching at Next-to-next-to-Leading Order (NNLO) in the chiral expansion, which is beyond the scope of this work.

### 6.3.3 Extraction of CKM elements and predictions

Taking advantage that scalar and vector form factors are equal at $q^2 = 0$, the results of the combined charm-bottom fit presented in the previous subsection can be used to extract the vector form factor, $f_+$, at $q^2 = 0$ for various semileptonic decays studied in this work. Moreover, given some experimental input for the quantity $|V_{Qq}|f_+(0)$, with $Qq = bu, cd$ or $cs$, we can extract the corresponding CKM matrix element using the present MO scheme. Measurements of the differential distribution $d\Gamma(H \to \bar{\phi}\ell\bar{\nu}_\ell)/dq^2$ at $q^2 = 0$ will directly provide model independent determinations of $|V_{Qq}|f_+(0)$,[18] while measurements of the total decay width could be used to estimate this latter quantity only after relying on some model for the $q^2-$dependence of $f_+$.

In the charm sector from the fit presented in Table 6.3 and Fig. 6.9, we find

$$f_+^{D\to\pi}(0) = 0.585(35)_{\rm stat}(19)_{\rm sys_1}(32)_{\rm sys_2}, \tag{6.55}$$

$$f_+^{D\to\bar{K}}(0) = 0.765(30)_{\rm stat}(4)_{\rm sys_1}(14)_{\rm sys_2}\ , \tag{6.56}$$

where the first and second sets of errors are similar to those quoted in Table 6.3 and account for statistical (propagated from the $1\sigma$ fluctuations of the fitted parameters) and chiral systematic (propagated from the errors of the LECs that enter in the computation of the MO matrix) uncertainties, respectively. The third set of errors ($\rm sys_2$) takes into account the variations that are produced when in the best fit one considers alternatively only HPQCD or UKQCD and FL-MILC $\bar{B} \to \pi$ form factors. The results of Eq. (6.55) and (6.56) are in good agreement with our preliminary estimates reported in [307], where we fitted only to the charm ETM LQCD form factors.

In combination with the experimental values

$$\begin{aligned} f_+^{D\to\pi}(0)|V_{cd}| &= 0.1426(19)\ , \\ f_+^{D\to\bar{K}}(0)|V_{cs}| &= 0.7226(34)\ , \end{aligned} \tag{6.57}$$

---

[18] Neglecting the lepton masses.

taken from the report by the Heavy Flavor Averaging Group (HFLAV) [308], we obtain

$$|V_{cd}| = 0.244(22) \tag{6.58}$$

$$|V_{cs}| = 0.945(41) \tag{6.59}$$

for the corresponding CKM matrix elements. The dominant error is the theoretical one affecting the determination of the form factors at $q^2 = 0$, within the scheme presented in this work. As expected, these results nicely agree with those reported by the ETM Collaboration [266] since we describe rather well the LQCD scalar form factors calculated in this latter work. The values of Eq. (6.58) agree within around $1\sigma$ with the average ones[19] given in Ref. [206],

$$|V_{cd}| = 0.220(5) \ , \tag{6.60}$$

$$|V_{cs}| = 0.995(16) \ . \tag{6.61}$$

On the other hand, the test of the second-row unitarity of the CKM matrix is satisfied within errors

$$|V_{cd}|^2 + |V_{cs}^2| + |V_{cb}|^2 = 0.95(9) \ , \tag{6.62}$$

where $|V_{cb}| = 0.0405(15)$ from PDG [206] has been used.

Likewise, in the bottom sector, we obtain from the combined bottom-charm fit

$$f_+^{\bar{B}\to\pi}(0) = 0.208(7)_{\text{stat}}(15)_{\text{sys}_1}(30)_{\text{sys}_2} \ , \tag{6.63}$$

where we see that the error budget is now dominated by the inconsistency between HPQCD and UKQCD and FL-MILC sets of results for $f_0^{\bar{B}\to\pi}$ for high $q^2$, above 17 GeV$^2$. Dropping out the UKQCD and FL-MILC sets of results for $\bar{B} \to \pi$, the LCSR and HPQCD results for this transition can be significantly better described simultaneously, leading to values of the form factor at $q^2 = 0$ around 0.24 for the combined charm-bottom fit, in the highest edge of the interval quoted in Eq. (6.63), and compatible within errors with the result of $0.26^{+0.04}_{-0.03}$ predicted in Ref. [258] using LCSR.[20] However, the description of the $\bar{B}_s \to K$ and $D \to \pi$ scalar form factors gets somewhat worse, being thus the situation unclear.

In principle, based on the above values, the CKM element $|V_{ub}|$ could be determined as in the charm sector. However, the full kinematic region in the bottom case is very broad, and the experimental determination of $f_+(0)|V_{ub}|$ might suffer from large systematic uncertainties. A customary way to extract $|V_{ub}|$ has been to perform a joint fit to the LQCD and LCSR theoretical results for $f_+(q^2)$ and to measurements of the differential decay width, with $|V_{ub}|$ being a free parameter, see, e.g., Refs. [276, 309, 310]. This is not feasible to us, since we only know the value of the vector form factor at zero momentum by using the relation $f_+(0) = f_0(0)$. However the latest Belle [255] and BaBar [256] works reported accurate measurements of the $\bar{B} \to \pi$ partial branching fractions in several bins of $q^2$ that are used to extract the $f_+$ form factor shape and the overall normalization determined by $|V_{ub}|$. As a result, Belle and BaBar obtained values of $(9.2 \pm 0.3) \times 10^{-4}$

---

[19] Determinations from leptonic and semileptonic decays, as well as from neutrino scattering data in the case of $|V_{cd}|$, are used to obtain the PDG averages.

[20] Fitting only to the $b \to u$ data and not considering UKQCD and FL-MILC sets of $\bar{B} \to \pi$ results, we find $f_0^{\bar{B}\to\pi}(0) \sim 0.27$, even in better agreement with the LCSR determination.

and $(8.7 \pm 0.3) \times 10^{-4}$ for $f_+(0)|V_{ub}|$, respectively. Though the latter values were extracted from direct fits to data, they might be subject to some systematic uncertainties, since they were obtained using some specific $q^2$ parametrizations (Becirevic and Kaidalov [311] and Boyd-Grinstein-Lebed [312] in the Belle and BaBar works, respectively). Nevertheless, we average both determinations and we take

$$f_+^{\bar{B}\to\pi}(0)|V_{ub}| = (8.9 \pm 0.3) \times 10^{-4} \ , \tag{6.64}$$

Using this latter value and our estimate for the form factor at $q^2 = 0$ given in Eq. (6.63), we get

$$10^3|V_{ub}| = 4.3(7) \tag{6.65}$$

There exist tensions between the inclusive and exclusive determinations of $|V_{ub}|$ [206]:

$$10^3|V_{ub}| = 4.49(16)(17) \qquad \text{(inclusive)}, \tag{6.66}$$

$$10^3|V_{ub}| = 3.72(19) \qquad \text{(exclusive)}. \tag{6.67}$$

and combining both values, R. Kowalewski and T. Mannel quote an average value of

$$10^3|V_{ub}| = 4.09(39) \tag{6.68}$$

in the PDG review [206], which is in good agreement with our central $|V_{ub}|$ result of Eq. (6.65). We should mention that it is higher than the typical values obtained from LQCD and LCSR determinations of the $\bar{B} \to \pi$ $f_+(q^2)$ form factor, combined with measurements of the $q^2$ distribution of the differential width. Thus, the FLAG review [70] gives an average value (in $10^3$ units) of $3.67 \pm 0.09 \pm 0.12$. Nevertheless, this latter value is still compatible, taking into account the uncertainties, with our result.

These extractions of the CKM elements rely strongly on the results either from LQCD in the high $q^2$ region or from LCSR in the vicinity of $q^2 = 0$ (the latter only in the bottom sector), which are used in the combined fit, and hence are not *ab initio* predictions. However, our extractions incorporate the influence of general $S$-matrix properties, in the sense that unitarity and analyticity are implemented in the MO representation of the scalar form factors. Moreover, one of the advantages of our approach is that we can make predictions for the channels related by chiral SU(3) symmetry of light quarks. In some of these channels, the form factors are difficult for LQCD due to the existence of disconnected diagrams of quark loops. The $D \to \eta$, $D_s \to K$, $D_s \to \eta$ and $\bar{B} \to \eta$ scalar form factors were already shown in Fig. 6.9 for the whole kinematical regions accessible in the decays. On the other hand, their values at $q^2 = 0$ are particularly important, since they might serve as alternatives to determine the CKM elements when experimental measurements of the corresponding differential decay rates become available. Our predictions for the absolute values of the vector form factors at $q^2 = 0$ are (we remind once more here that vector and scalar form factors coincide at $q^2 = 0$)

$$|f_+^{D\to\eta}(0)| = 0.01(3)_{\text{stat}}(2)_{\text{sys}_1}(4)_{\text{sys}_2}, \tag{6.69}$$

$$|f_+^{D_s\to K}(0)| = 0.50(6)_{\text{stat}}(3)_{\text{sys}_1}(5)_{\text{sys}_2}, \tag{6.70}$$

$$|f_+^{D_s\to\eta}(0)| = 0.734(21)_{\text{stat}}(21)_{\text{sys}_1}(3)_{\text{sys}_2}, \tag{6.71}$$

$$|f_+^{\bar{B}\to\eta}(0)| = 0.82(1)_{\text{stat}}(7)_{\text{sys}_1}(3)_{\text{sys}_2}, \tag{6.72}$$

$$|f_+^{\bar{B}_s\to K}(0)| = 0.301(9)_{\text{stat}}(11)_{\text{sys}_1}(26)_{\text{sys}_2} \tag{6.73}$$

For the decay $\bar{B}_s \to K$, we find, adding errors in quadrature, $f_+^{\bar{B}_s\to K}(0) = 0.30 \pm 0.03$ in perfect agreement with the results obtained from the LCSR ($0.30^{+0.04}_{-0.03}$ [259]) and HPQCD ($0.32 \pm 0.06$ [263]) analyses, but about 1 sigma above the LQCD result of the UKQCD Collaboration [265]. The single-channel Omnès-improved constituent quark model study of Ref. [278] led to $0.297 \pm 0.027$, which is also in good agreement with our result.

### 6.3.4 Scalar form factors above the $q^2_{\rm max}$−region

It is worth recalling here the relation between the results obtained for the form factors and the scattering amplitudes used as input of the MO representation. If we focus, for instance, on the charm form factors, the lightest open-charm scalar resonance, called $D_0^*(2400)$ by the PDG [206], lies in the $(S, I) = (0, 1/2)$ sector. In Refs. [33, 37, 199], two different states, instead of only one, were claimed to exist in the energy region around the nominal mass of the $D_0^*(2400)$. These studies were based on chiral symmetry and unitarity. This complex structure should be reflected in the scattering regime of the form factors. Indeed, this can be seen in the first row of panels of Fig. 6.11, where form factors for different semi-leptonic transitions are shown above the $q^2_{\rm max}$−region. As discussed in Sec. 6.2.3, here we use the $\mathcal{O}(p^2)$ HM$\chi$PT amplitudes obtained in Refs. [198, 205], which also successfully describe the $(0, 1/2)$ finite-volume energy levels reported in the recent LQCD simulation of Ref. [81] (see Chapter 4 for details) and, as we will see soon in Chapter 5, are consistent with the precise LHCb data [240] for the angular moments of the $B^- \to D^+\pi^-\pi^-$ [6]. These chiral amplitudes predict the existence of two scalar broad resonances, instead of only one, with masses around 2.1 and 2.45 GeV, respectively [3, 6], which produce some signatures in the $D \to \pi$, $D \to \eta$ and $D_s \to K$ form factors at around $q^2 = 4.4$ and 6 GeV$^2$, as can be appreciated in Fig. 6.11. The effect of this two-state structure is particularly visible in the $D_s \to K$ form factor. Note that this two-state structure should have also some influence in the region below $q^2_{\rm max}$, where we have fitted the LQCD data. Below $q^2_{\rm max}$, the sensitivity of the form factors to the details of the two resonances is however smaller than that of the energy levels calculated in the scattering region, since the former ones are given below the lowest threshold, while the latter ones are available at energies around and above it. Nonetheless, the success in describing the LQCD results for the $D \to \pi$ scalar form factor clearly supports the chiral input, and the predictions deduced from it, used in the current scheme. If better determined form factors were available in all of the channels, perhaps the two state structure for the $D_0^*(2400)$ could be further and more accurately tested.

A similar pattern is found in the bottom sector [3,6], as expected from the approximate heavy-flavour symmetry of QCD. The two-state structure is clearly visible, more than that in the charm sector, in the corresponding form factors (three bottom plots of Fig. 6.11), and it has a certain impact in the form factors close to $q^2_{\rm max}$, where LQCD results are available.

In the charm $(S, I) = (1, 0)$ sector the effect of the narrow $D_{s0}^*(2317)$ resonance, which is the SU(3) flavor partner of the lighter one of the two $D_0^*$ states, predicted by the unitarized NLO chiral amplitudes [3, 6], is clearly visible in the scalar $D \to \bar{K}$ and $D_s \to \eta$ form factors, and it fully dominates these form factors in the vicinity of the pole, as can be seen in the second row of panels of Fig. 6.11. Indeed, this state also influences the $D \to \bar{K}$ form factor below (near) $q^2_{\rm max}$, where the LQCD results are available,[21] and

---

[21] Indeed, the existence of the $D_{s0}^*(2317)$ was suggested in [40] by fitting the single channel MO represen-

the excellent description of the ETM results gives clear support to the coupled-channel MO representation of the $D \to \bar{K}$ and $D_s \to \eta$ scalar form factors derived in this work.

## 6.4 Summary and outlook

We have studied the scalar form factors that appear in semileptonic heavy meson decays induced by the flavour-changing $b \to u$ and $c \to d, s$ transitions using the MO formalism. The coupled-channel effects, due to re-scattering of the $H\phi$ $(H = D, \bar{B})$ system, with definite strangeness and isospin, are taken into account by solving coupled integral MO equations. We constrain the subtraction constants in the MO polynomials, which encodes the zeros of the form factors, thanks to light-quark chiral SU(3) and heavy-flavour symmetries.

The $H\phi$ interactions used as input of the MO equations are well determined in the chiral regime and are taken from previous work. In addition, some reasonable behaviours of the amplitudes at high energies are imposed, while appropriate heavy-flavour scaling rules are used to relate bottom and charm form factors. We fit our MO representation of the scalar form factors to the latest $c \to d, s$ and $b \to u$ LQCD and $b \to u$ LCSR results and determine all the involved parameters, in particular the two LECs ($\beta_1^P$ and $\beta_2^P$) that appear at NLO in the chiral expansion of the scalar and vector form factors near $q^2_{\rm max}$, which are determined in this work for first time. We describe the LQCD and LCSR results rather well, and in combination with experimental results and using that $f_0(0) = f_+(0)$, we have also extracted the $|V_{ub}|$, $|V_{cd}|$ and $|V_{cs}|$ CKM elements, which turn out to be in good agreement with previous determinations from exclusive decays.

We would like to stress that we describe extremely well the recent ETM $D \to \pi$ scalar form factor, which largely deviates from the previous determination by the HPQCD Collaboration, providing an indication that the Lorentz symmetry breaking effects in a finite volume, due to the hypercubic artifacts, could be important in the LQCD determination of the form factors in semileptonic heavy-to-light decays, as claimed in Ref. [266]. As it is also pointed out in the previous reference, this is a very important issue, which requires further investigations, since it might become particularly relevant in the case of the determination of the form factors governing semileptonic $\bar{B}-$meson decays into lighter mesons.

We have also predicted the scalar form factors, which are in the same strangeness-isospin multiplets as the fitted $D \to \pi$, $D \to \bar{K}$, $\bar{B} \to \pi$ and $\bar{B}_s \to K$ ones. Our prediction of the form factors in such channels ($D \to \eta$, $D_s \to K$, $D_s \to \eta$, and $B \to \eta$) are difficult for LQCD simulations due to the existence of disconnected diagrams. These form factors are related to the differential decay rates of different semileptonic heavy meson decays and hence provide alternatives to determine the CKM elements with the help of future experimental measurements.

Moreover, we also find that the $D \to \eta$ scalar form factor is largely suppressed compared to the other two components ($D \to \pi$, $D \to \bar{K}$) in the three-channel $(0, 1/2)-$multiplet, which is similar to what occurs for the $K \to \eta$ strangeness-changing scalar form factor in Ref. [270].

Our determination of the form factors has the advantage that the constraints from

---

tation of the $D \to \bar{K}$ scalar form factor, constructed out the unitarized LO chiral elastic $DK$ amplitude, to LQCD results of the scalar form factor below $q^2_{\rm max}$.

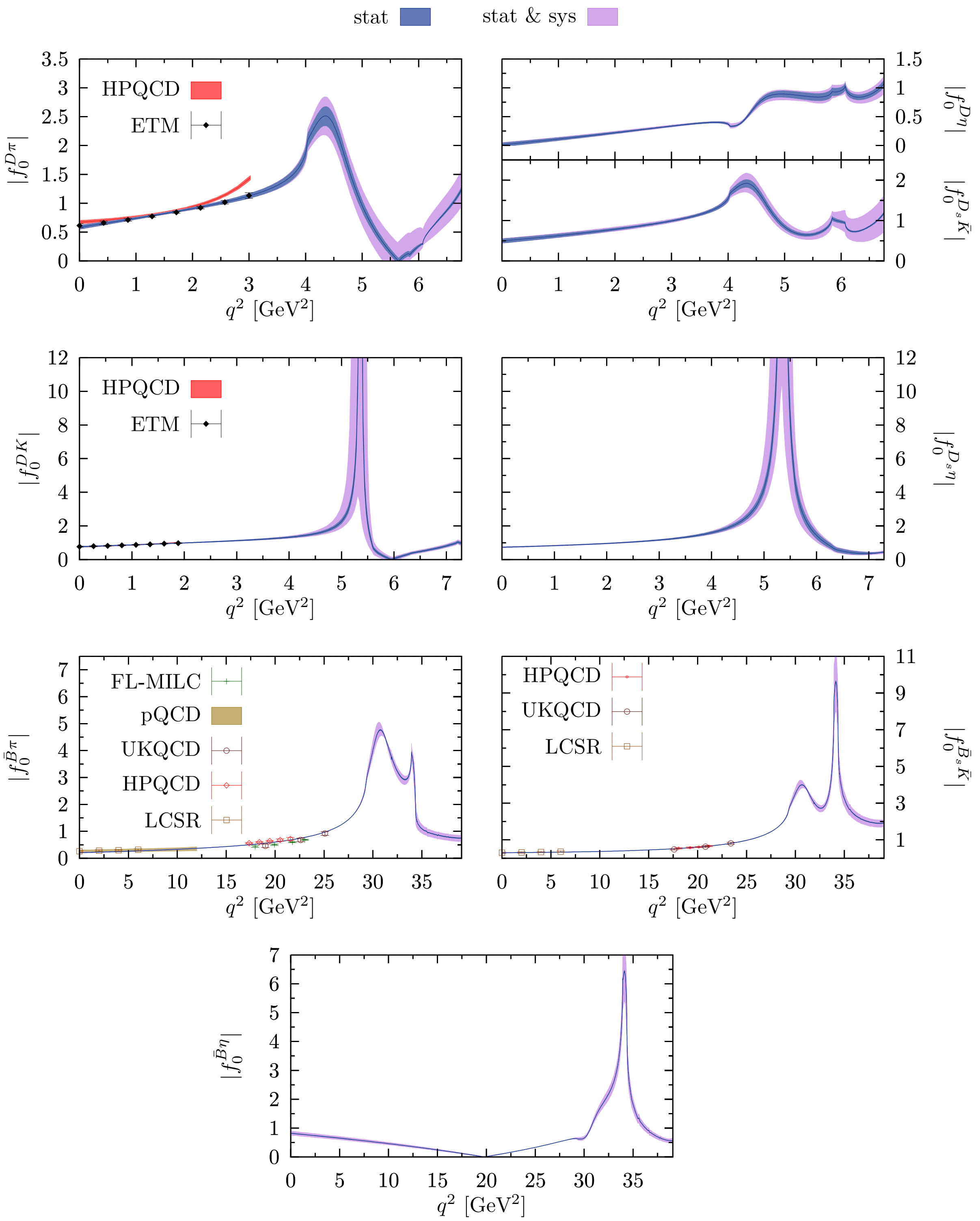

**Figure 6.11:** Scalar form factors for different $b \to u$ and $c \to d, s$ transitions. They have been computed in this work using the MO matrices derived in Sec. 6.2.3 from the NLO HM$\chi$PT amplitudes of Refs. [198, 205], and the LECs, compiled in Table 6.3, obtained from a fit to LQCD and LCSR results below $q^2_{\text{max}}$. Statistical (stat) and statistical plus systematic (stat & sys) 68%-confident level bands are also given and are calculated as explained in Fig. 6.8.

unitarity and analyticity of the $S$-matrix have been taken into account, as well as the state-of-the-art $H\phi$ chiral amplitudes. Thus, our predictions for the flavour-changing $b \to u$ and $c \to d, s$ scalar form factors above the $q^2-$region accessible in the semileptonic decays, depicted in Fig. 6.11, should be quite accurate[22] and constitute one of the most important findings of the current research. Indeed, we have shown how the form factors in this region reflect details of the chiral dynamics that govern the $H\phi$ amplitudes, and that give rise to a new paradigm for heavy-light meson spectroscopy [6] which questions the traditional $q\bar{q}$ constituent quark model interpretation, at least in the scalar sector.

As an outlook, the scheme presented here will also be useful to explore the $H\phi$ interactions by using the lattice data for the scalar form factors in semileptonic decays of $\bar{B}$ or $D$ mesons. As pointed out in Ref. [313], more data are needed to fix the LECs in the NNLO potentials. Since the dispersive calculation of $D\phi$ and $\bar{B}\phi$ scalar form factors depend on the scattering amplitudes of these systems, the LQCD results for the form factors can be used to mitigate the lack of data and help in the determination of the new unknown LECs.

One might also try to extend the MO representation to a formalism in a finite volume with unphysical quark masses, such that comparisons to the discretized lattice data could be directly undertaken. On the other hand, the chiral matching of the form factors can be carried out at higher order to take into account the expected sizeable corrections in SU(3) HM$\chi$PT. Moreover, this improved matching will in practice suppose to perform additional subtractions in the dispersive representations of the form factors, and it should reduce the importance of the high-energy input used for the $H\phi$ amplitudes. The high energy input turns out to be essential to describe the scalar $\bar{B} \to \pi$ form factor near $q^2 = 0$, and it represents one of the major limitations of the current approach.

Both improvements would lead to a more precise and model-independent determination of the CKM matrix elements related to the heavy-to-light transitions.

## 6.5 Bottom form factors and quadratic MO polynomials

**Table 6.4:** Results from the fit to the scalar $\bar{B} \to \pi$ and $\bar{B}_s \to K$ LQCD & LCSR form factors using rank-two MO polynomials (see Eq. (6.74)), and with $\chi^2$ defined in Eq. (6.49). There is a total of 22 degrees of freedom and the best-fit gives $\chi^2/dof = 3.7$. The LECs $\beta_1^B$, $\beta_2^B$ and $\alpha_{2,i}$ are given in units of GeV, GeV$^{-1}$ and GeV$^{-4}$, respectively.

| $\beta_1^B$ | $(\beta_2^B \times 10)$ | $(\alpha_{2,1} \times 10^3)$ | $(\alpha_{2,2} \times 10^3)$ | $(\alpha_{2,3} \times 10^3)$ |
|---|---|---|---|---|
| 0.74(22) | 0.53(8) | 0.24(6) | −0.1(7) | 1.0(8) |

We show in Fig. 6.12, the scalar $\bar{B} \to \pi, \eta$ and $\bar{B}_s \to K$ form factors obtained using rank-two MO polynomials. Specifically, we replace Eq. (6.34) by

$$\vec{\mathcal{P}}(s) = \vec{\alpha}_0 + \vec{\alpha}_1\, s + \vec{\alpha}_2\, s^2 \ , \tag{6.74}$$

---

[22] Note that for the moderate $q^2-$values shown in Fig. 6.11, the form factors are largely insensitive to the high-energy input in the MO dispersion relation, and they are almost entirely dominated by the low-energy (chiral) amplitudes.

where $\vec{\alpha}_2$, together with $\beta^B_{1,2}$, are fitted to the merit function defined in Eq. (6.49). (Note that $\vec{\alpha}_{0,1}$ are still expressed in terms of $\beta^B_{1,2}$.) Best fit results are compiled in Table 6.4.

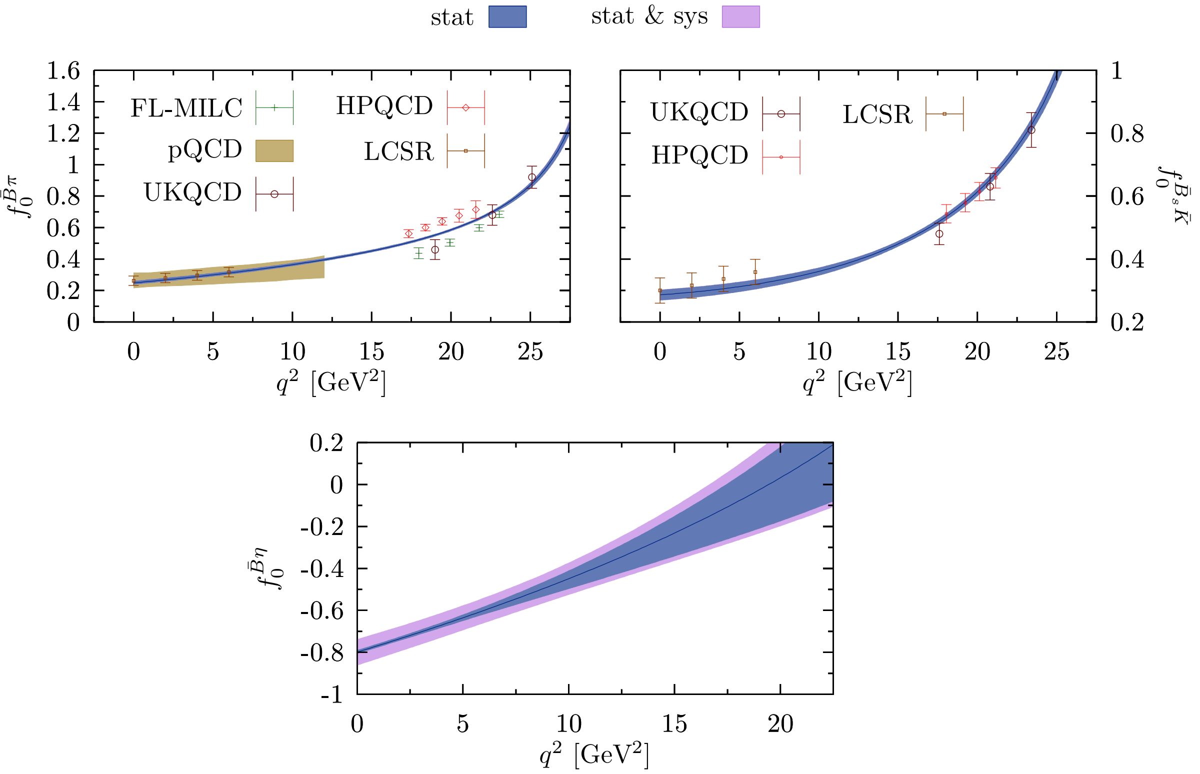

**Figure 6.12:** Same as Fig. 6.8, but using a quadratic MO polynomial (see Eq. (6.74)), and parameters given in Table 6.4.

# Chapter 7

# A NEW PARAMETRIZATION OF FORM FACTORS IN $\bar{B} \to D\ell\bar{\nu}_\ell$ DECAYS

## 7.1 Introduction

One of the most primary goals in flavor physics currently is to precisely determine the elements of the CKM matrix, since they afford a sharp probe of physics beyond the standard model (SM) as inputs of the CKM unitarity triangle. For that purpose, experimental and theoretical efforts are extensively devoted to study both inclusive and exclusive semileptonic decays of bottom hadrons. For the latter ones, different ways have been proposed to parametrize the hadronic form factors involved, the most commonly used of which are the Boyd-Grinstein-Lebed (BGL) [314] and Caprini-Lellouch-Neubert (CLN) [315] parametrizations. There is tension in the determination of some of the entries like $V_{cb}$ from $B$ meson decays, for which the result considering inclusive decays [316] is larger than the value obtained from exclusive ones—a discrepancy at 2-3$\sigma$ significance level exists, see *e.g.* Refs. [70, 308, 317, 318] for recent reviews. The main source of exclusive $V_{cb}$ determinations is the $\bar{B} \to D^{(*)}\ell\bar{\nu}_\ell$ semi-leptonic decay.

Since 2015, significant progress has been made. The Belle Collaboration measured the differential decay rates of the exclusive $\bar{B} \to D\ell\bar{\nu}_\ell$ [319] and $\bar{B} \to D^*\ell\bar{\nu}_\ell$ reactions [320] using their full data set; and there have been LQCD results on the form factors at non-zero recoils for $\bar{B} \to D\ell\bar{\nu}_\ell$ obtained by the HPQCD [321] and Fermilab Lattice plus MILC (FL-MILC) [322] Collaborations. It turns out that the CLN and BGL parametrizations lead to different values of the extracted $|V_{cb}|$, see *e.g.*, Refs [319,320,323,324]. For instance, the Belle determinations of this CKM matrix element from the $B \to \bar{D}\bar{\ell}\nu$ decay are $(39.86 \pm 1.33) \times 10^{-3}$ or $(40.83 \pm 1.13) \times 10^{-3}$ using the CLN or BGL parametrizations, respectively [319]. For comparison, the updated HFLAV averages for the inclusive determination of $|V_{cb}|_{\text{in}}$ are $(42.19 \pm 0.78) \times 10^{-3}$ or $(41.98 \pm 0.45) \times 10^{-3}$ depending on the used scheme [308]. It is pointed out in Refs. [323,325,326] that the CLN parametrization, based upon heavy quark effective theory, though very useful in the past, may no longer be adequate to cope with the accuracy of the currently available data. The BGL parametrization is a model-independent expansion in powers of a small variable $z$. To describe data, the expansion needs to be truncated at least at the $z^2$ order, leading to 3 unknown coefficients for each form factor. The relation $f^+ = f^0$ at $q^2 = 0$ imposes a constraint among these parameters, which on the other hand do not have an obvious physical interpretation, except for those of the leading term that could be related to the form factor normalization.

In this chapter, based on Ref. [9], we propose a new model-independent parametrization based on a dispersion relation. It is more efficient than the BGL one in the sense that modern high-accuracy data can be described with less parameters. Furthermore, the parameters are the moments of the phase of form factors and encode information of the $\bar{B}\bar{D}$ interactions. As will be shown below, the available Belle and LQCD data can be well reproduced truncating at the leading order, which has only one parameter for each form factor in addition to the normalization. This allows for an extraction of $|V_{cb}|$ with a smaller uncertainty of only 1.8%.

Furthermore, all the involved parameters are physically meaningful, encoding scattering information on elastic and inelastic $\bar{B}\bar{D}$ interaction through dispersion relations to phase shifts.

The $\bar{B}\bar{D}$ interaction, related to the $\bar{B} \to D$ transition amplitude by crossing, is poorly known so far, however, is utmost essential to explore the spectrum of hadrons containing one bottom quark ($b$) and one charm antiquark ($\bar{c}$), *i.e.*, $B_c$ mesons, see Ref. [327] for example. Up to now, the discovery of the $B_c$ mesons is restricted to two states only [14]: $B_c(6275)$ and $B_c(2S)(6871)$, both with $J^P = 0^-$ (although the vector $B_c^*(2S)$ was reported recently by both CMS [328] and LHCb [329], its mass has not been measured because of the unreconstructed low-energy photon in both experiments). In view of the well established bottomonium or charmonium spectra, it is clear that many $B_c$ states are still missing. Hopefully, states will be unravelled in the near future due to the advent of the LHCb, which is an efficient factory to produce $b\bar{c}$ or $bc$ states. Besides, prognosis of charmed-bottom hadrons from LQCD has been made very recently [330]. Our new parametrization, bringing information from semileptonic decays to the scattering problem, will definitely shed light on those newly predicted/discovered states.

## 7.2 New parametrization

To proceed, let us first introduce the semileptonic $\bar{B}(p) \to D(p')\ell(q_1)\bar{\nu}_\ell(q_2)$ differential decay rate [331]

$$\frac{\mathrm{d}\Gamma}{\mathrm{d}q^2} = \frac{8\mathcal{N}|\vec{p}^*|}{3}\left[\left(1+\frac{m_\ell^2}{2q^2}\right)|H_0|^2 + \frac{3m_\ell^2}{2q^2}|H_t|^2\right] , \tag{7.1}$$

with $q \equiv p - p' = q_1 + q_2$ and $|\vec{p}^*|$ is the modulus of the three-momentum of the $D$ meson in the $\bar{B}$ rest frame. The normalization factor is

$$\mathcal{N} = \frac{G_F^2}{256\pi^3}\eta_{\mathrm{EW}}^2|V_{cb}|^2\frac{q^2}{m_B^2}\left(1-\frac{m_\ell^2}{q^2}\right)^2 , \tag{7.2}$$

where $G_F = 1.166 \times 10^{-5}$ GeV$^{-2}$ is the Fermi coupling constant and the factor $\eta_{\mathrm{EW}} = 1.0066$ accounts for the leading order electroweak corrections [332]. Here $m_B$ ($m_D$) and $m_\ell$ denote the masses of the $B$ ($D$) meson and the lepton, respectively. We will use the values $m_D = 1867.22$ MeV, $m_B = 5279.47$ MeV and $m_\tau = 1776.91$ MeV. Furthermore, the helicity amplitude $H_0$ amounts to the longitudinal part of the spin-1 hadronic contribution, while $H_t$ corresponds to the spin-0 hadronic contribution, owing its presence to the off-shellness of the weak current. They are related to the conventional hadronic vector ($J^P = 1^-$) and scalar ($J^P = 0^+$) form factors, *i.e.*, $f_+(q^2)$ and $f_0(q^2)$, respectively, through

$$H_0 = \frac{2m_B|\vec{p}^*|}{\sqrt{q^2}}f_+(q^2) , \quad H_t = \frac{m_B^2 - m_D^2}{\sqrt{q^2}}f_0(q^2) . \tag{7.3}$$

At $q^2 = 0$, the two form factors coincide: $f_+(0) = f_0(0)$.

According to Refs. [298, 333, 334], and using general arguments from QCD, one expects vector and scalar form factors to fall off as $1/s$ (up to logarithms) when $|s| \to \infty$.

Thus, based on analyticity, unitarity and crossing symmetry, once-subtracted dispersion relations for each form factor admit solutions of the Omnès form

$$f_i(q^2) = f_i(s_0) \exp\left[\frac{q^2 - s_0}{\pi} \int_{s_{\rm th}}^{\infty} \frac{{\rm d}s}{s - s_0} \frac{\alpha^i(s)}{s - q^2}\right], \tag{7.4}$$

for $q^2 < s_{\rm th}$. In addition, $i = +, 0$, $s_{\rm th} = (m_B + m_D)^2$ is the $\bar{B}\bar{D}$ threshold, $s_0$ is the subtraction point and $\alpha^i(s)$ is the phase of the corresponding form factor. This solution can be easily obtained noticing that $f_i(s+i\epsilon)/f_i(s-i\epsilon) = \exp\left[2i\alpha^i(s)\,\theta(s - s_{\rm th})\right]$. It is worthwhile to emphasize that Eq. (7.4) holds even in the inelastic regime, *i.e.*, when channels with a higher threshold such as $\bar{B}^*\bar{D}^*$ are open. In the elastic region ($\sqrt{s} < m_{B^*} + m_D$ for $i = +$ and $\sqrt{s} < m_{B^*} + m_{D^*}$ for $i = 0$), the phase $\alpha^i(s)$ coincides with the $P$- and $S$-wave $\bar{B}\bar{D}$ scattering phase shift for $f^+$and $f^0$, respectively, according to the Watson's theorem [335].

In the physical $\bar{B} \to D\ell\bar{\nu}_\ell$ decay, the maximum value of $q^2$ is $q^2_{\rm max} = (m_B - m_D)^2$. Given that $s \geqslant s_{\rm th} \gg q^2_{\rm max} \geqslant q^2$, Eq. (7.4) can be recast into a new form,

$$f_i(q^2) = f_i(s_0) \prod_{n=0}^{\infty} \exp\left[\frac{q^2 - s_0}{s_{\rm th}} \mathcal{A}_n^i \frac{q^{2n}}{s_{\rm th}^n}\right] , \tag{7.5}$$

with the dimensionless coefficients (phase moments) defined as

$$\mathcal{A}_n^i \equiv \frac{1}{\pi} \int_{s_{\rm th}}^{+\infty} \frac{{\rm d}s}{s - s_0} \frac{\alpha^i(s)}{(s/s_{\rm th})^{n+1}} \ . \tag{7.6}$$

Since the power of $s$ in the denominator of the integrand above grows as $n + 1$, higher moments become sensitive only to the details of the form-factor phases $\alpha^i(s)$ in the vicinity of threshold. Equation (7.5) provides a new parametrization of the form factors in $\bar{B} \to D$ semileptonic decays. The coefficients $\mathcal{A}_n^i$ are called *phase moments* hereafter, due to the fact that they are related to the phases of the form factors in the physical $\bar{B}\bar{D}$ scattering region.

## 7.3 Fit to Belle and LQCD data

Let us first define the recoil variable $\omega = (m_B^2 + m_D^2 - q^2)/(2m_B m_D)$. It ranges from 1 at zero recoil, $q^2 = (m_B - m_D)^2$, to about $(m_B^2 + m_D^2)/(2m_B m_D) \approx 1.59$ at $q^2 = 0$, for the decays into electron or muon leptons. To determine the phase moments $\mathcal{A}_n^i$ introduced in Eq. (7.5), we perform a combined fit to the recent experimental data measured by Belle [319] together with the LQCD results of the vector and scalar form factors at non-zero recoil obtained by the HPQCD [321] and FL-MILC [322] collaborations.

The Belle data consist of the weighted averaged differential decay rates for 10 $\omega$-bins (see Table II of Ref. [319]), and should be confronted with

$$\frac{\Delta\Gamma_k}{\Delta\omega} = \frac{1}{\Delta\omega} \int_{\omega_{k,\rm min}}^{\omega_{k,\rm max}} \frac{{\rm d}\Gamma}{{\rm d}\omega} {\rm d}\omega \ , \quad k = 0, \cdots, 9 \ , \tag{7.7}$$

where the $\Delta\omega$ is the width of each bin, $\omega_{k,\rm min\,(max)}$ is the minimal (maximal) value of $\omega$ in the $k$th bin. The lepton masses, except for the tau case to be discussed later, are neglected.

**Table 7.1:** Results from the combined fit to Belle [319] and LQCD [321, 322] data.

| $\frac{\chi^2}{dof} = \frac{6.47}{22-4} \simeq 0.36$ | | Correlation matrix | | | |
|---|---|---|---|---|---|
| | | $f_0(0)$ | $\mathcal{A}_0^0$ | $\mathcal{A}_0^+$ | $\lvert V_{cb}\rvert \times 10^3$ |
| $f_0(0)$ | 0.658(17) | 1.000 | −0.979 | −0.978 | −0.818 |
| $\mathcal{A}_0^0$ | 1.38(12) | −0.979 | 1.000 | 0.957 | 0.801 |
| $\mathcal{A}_0^+$ | 2.60(12) | −0.978 | 0.957 | 1.000 | 0.774 |
| $\lvert V_{cb}\rvert \times 10^3$ | 41.01(75) | −0.818 | 0.801 | 0.774 | 1.000 |

The FL-MILC Collaborations [322] provide results both for both $f_+$ and $f_0$ at three different $\omega \in \{1.00, 1.08, 1.16\}$. The HPQCD Collaboration [321] presents their results in terms of the Bourrelly-Caprini-Lellouch (BCL, a simple alternative to BGL, see Ref. [310]) parametrization for the entire kinematic decay region (see the gray bands in the upper panel of Fig. 7.1). However, they only performed numerical lattice simulations for three different $q^2$ configurations, which lead to $\omega$ values in the range of $[1, \sim 1.11]$. Therefore, as done in Refs. [323, 324], we prefer to extract, from the BCL parametrization obtained in Ref. [321], three values for each of the form factors, $f_+$ and $f_0$, at $\omega \in \{1.00, 1.06, 1.12\}$. The 12 lattice data points with error-bars are shown in the upper panel of Fig. 7.1. We note that the HPQCD errors are significantly larger than the FL-MILC ones.

In our fit, in addition to the phase moments $\mathcal{A}_n^i$, the subtraction $f_0(s_0)$ and the CKM matrix element $|V_{cb}|$ are treated as free parameters as well. The kinematic constraint $f_+(0) = f_0(0)$ imposes a relation for the subtractions of both form factors

$$f_+(s_0) = f_0(s_0) \exp\left[\frac{s_0}{s_{\text{th}}}(\mathcal{A}_0^+ - \mathcal{A}_0^0)\right] . \tag{7.8}$$

We choose $s_0 = 0$ as the subtraction point, and find that a truncation of the the expansion in Eq. (7.5) to the first order, *i.e.*, $n = 0$, is sufficient to accurately describe the data as seen in Fig. 7.1. Consequently, we have a total of four free parameters: $f_0(0)$, $\mathcal{A}_0^0$, $\mathcal{A}_0^+$ and $|V_{cb}|$. Fit results are collected in Table 7.1, where the errors in brackets are obtained from the minimization procedure. Moreover, it is found that the precision of the data set at hand is not sufficient to reliably pin down the phase moments $\mathcal{A}_n^i$ with $n \geqslant 1$. We already observe large correlation in Table 7.1. In Fig. 7.1, the form factors and the differential decay rates from the combined fit are plotted as a function of $q^2$ in the whole kinematic region. We also show the prediction of the differential decay rate for the $\bar{B} \to D\tau\bar{\nu}_\tau$ decay. For comparison, the Belle and LQCD (HPQCD and FL-MILC) data are displayed as well.

From the best fit, we get

$$|V_{cb}| = (41.01 \pm 0.75) \times 10^{-3} , \tag{7.9}$$

which is in agreement with the determination reported in Ref. [319] using the BGL parametrization, but higher than the values obtained using the CLN one [319, 320, 323, 325, 326]. It also agrees with the world average of the inclusive determinations [308]. Our result confirms the conclusion that the previous tension between the exclusive and inclusive determinations was mostly due to the use of the CLN parametrization. The error in our determination is only 1.8%, which is lower than the 2.4% from the combined

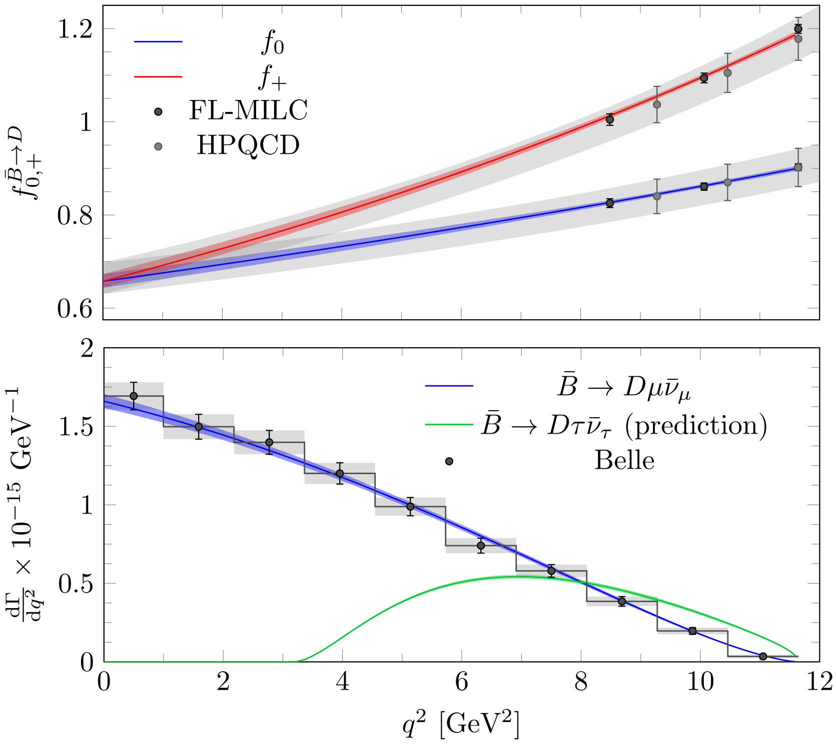

**Figure 7.1:** Upper panel: vector and scalar form factors. Lower panel: differential decay rates. The gray bands in the upper panel stand for the HPQCD results from the BCL continuous parametrization provided in [321].

fit in Ref. [323] to the experimental data (*BABAR* [336], Belle [319]) and LQCD results (HPQCD [321], FL-MILC [322]) using the BGL parametrization. Furthermore, as already commented, the fitted phase moments $\mathcal{A}_0^{0,+}$ provide valuable information to constrain the $\bar{B}D$ interaction.

With the parameters in Table 7.1, we predict the ratio

$$\mathcal{R}_D = \frac{\mathcal{BR}(\bar{B} \to D\tau\bar{\nu}_\tau)}{\mathcal{BR}(\bar{B} \to D\ell\bar{\nu}_\ell)} = 0.301(5)\,, \tag{7.10}$$

with $\ell = e$ or $\mu$. It is well consistent with the predictions using the LQCD form factors: $\mathcal{R}_D = 0.299(11)$ by FL-MILC [322] and $\mathcal{R}_D = 0.300(8)$ by HPQCD [321]. However, the central value is significantly smaller than the values measured by *BABAR*, $\mathcal{R}_D = 0.440(58)(42)$ [337], and by Belle, $\mathcal{R}_D = 0.375(64)(26)$ [338]. Yet, the deviation is 1.8 $\sigma$ from the former and only 1.0 $\sigma$ from the latter, given the large uncertainties in the experimental measurements. It is intriguing to see whether the deviation persists under more precise measurements.

We checked the dependence of the above results on the subtraction point $s_0$ by redoing fits with $s_0$ varied in the range $[0, q^2_{\rm max}]$. We find that the fit quality keeps exactly the same as for $s_0 = 0$, and the values of $|V_{cb}|$ and $\mathcal{R}_D$ are independent of the choice of $s_0$ as well. This is because in the Omnès representation, one is free to choose any $s_0$. The dependence of $s_0$ in the exponential in Eq. (7.4) or Eq. (7.5) is compensated by the parameter $f_0(s_0)$ that behaves as a normalization factor.

## 7.4 Comparison

For decades, the CLN parametrization [315] has been widely used. In the work of Ref. [315], the ratio

$$\begin{aligned} \frac{S_1(\omega)}{V_1(\omega)} &= \frac{(1+r)^2}{2r(1+\omega)}\frac{f_0(\omega)}{f_+(\omega)} \\ &= A\big[1 + B(\omega-\omega_0) + C(\omega-\omega_0)^2 + \cdots\big] \end{aligned} \tag{7.11}$$

is reported as a series of $\omega$ expanded around some $\omega_0$, with $r = m_D/m_B$. The coefficients $A, B$ and $C$ were determined from available LQCD results at that time, Heavy Quark Effective Theory (HQET), sum-rule calculations and unitary constrains, and included leading short-distance and $1/m_Q$ corrections [339, 340] as well. Given the above relations and our new parametrization of $f_{+,0}(q^2)$ in Eq. (7.5), we obtain the HQET prediction of the difference between $\mathcal{A}_0^+$ and $\mathcal{A}_0^0$ as

$$[\mathcal{A}_0^+ - \mathcal{A}_0^0]_{\mathrm{HQET}} = \frac{(1+r)^2}{1-2\omega_0 r + r^2} \ln \frac{(1+r)^2}{2rA(1+\omega_0)} \tag{7.12}$$

by matching at $\omega = \omega_0$. In Ref. [315], $A$ was given by expanding the results for the ratio of Eq. (7.11) for two different choices of $\omega_0$ (see Tables A.1 and A.2 of that reference). For $\omega_0 = 1$, $A = 1.0036$, while $A = 1.0018$ for $\omega_0 \simeq 1.267$. These spread of values for $A$ leads to

$$[\mathcal{A}_0^+ - \mathcal{A}_0^0]_{\mathrm{HQET}} \simeq 1.05 \sim 1.12\,. \tag{7.13}$$

As mentioned, Eq. (7.12) was obtained only from the constant term in Eq. (7.11). As a further check, we have also found the above difference of phase moments by matching the $(\omega - \omega_0)$ term

$$[\mathcal{A}_0^+ - \mathcal{A}_0^0]_{\mathrm{HQET}} = \frac{(1+r)^2}{2r}\frac{B(1+\omega_0)+1}{(1+\omega_0)} \tag{7.14}$$

which consistently gives values in the $0.98 \sim 1.12$ range.

The difference $[\mathcal{A}_0^+ - \mathcal{A}_0^0]$ can be also obtained from our results in Table 7.1,

$$[\mathcal{A}_0^+ - \mathcal{A}_0^0]_{\text{this work}} = 1.22\,(3)\,, \tag{7.15}$$

where we have taken into account the large statistical correlation between $\mathcal{A}_0^+$ and $\mathcal{A}_0^0$ to obtain the error above. Our result is larger than the HQET prediction in Eq. (7.13). This gives a strong indication that higher order HQET corrections, neglected in the CLN parametrization, are sizable, in agreement with the conclusion in Refs. [323, 325, 326].

## 7.5 Further considerations

As we stressed above, one of the advantages of the parametrization proposed in this work is that the fitted phase moments may be used to learn details on the $\bar{B}\bar{D}$ dynamics. Let us focus on $\mathcal{A}_0^0$, and let us note that if $\alpha^0(s)$ is replaced by the constant $\pi$ in Eq. (7.6), the zeroth order $S$-wave phase moment would be one (taking $s_0 = 0$). In the elastic region,

$\sqrt{s} < (m_{B^*} + m_{D^*})$, the phase $\alpha^0$ coincides with the $S$-wave $\bar{B}\bar{D}$ phase shift. Let us suppose that the integration in Eq. (7.6) is being dominated by phase-space regions close to threshold, then according to Levinson's theorem, it would be justified to replace $\alpha^0(s)$ by $\pi$ if there exists one, but only one, $\bar{B}\bar{D}$ bound state. This scenario will easily explain a value for $A_0^0$ of 1. Moreover, since the best fit value is 1.38(12), we might conjecture either the existence of two bound states or of one bound and one virtual state. We recall here that for an energy-independent interaction, which seems a reasonable approach to describe low energy $S-$wave $\bar{B}\bar{D}$ scattering, Levison's theorem establishes that $\delta(s_{\rm th}) = n_b\pi$, with $n_b$ the number of bound states of the potential[1], and $\delta(\infty) = 0$ [151]. In the case of two $\bar{B}\bar{D}$ bound states, we envisage a situation where the phase shift will take the value of $2\pi$ at threshold and after will decrease with $\sqrt{s}$ (positive scattering length), providing an integrated value larger than one for $\mathcal{A}_0^0$. In the second case, one bound and one virtual state, the phase shift will begin taking the value of $\pi$ at threshold, but it would grow in the vicinity of $s = s_{\rm th}$ (negative scattering length) to make possible the phase moment to reach magnitudes of around 1.4. We notice, however, the above discussion might be altered by inelastic-channel effects that will induce energy dependent interactions.

## 7.6 Summary

In this chapter, we have proposed a new model-independent parametrization for the form factors in the semileptonic $\bar{B} \to D\ell\bar{\nu}_\ell$ decays. It provides an excellent simultaneous reproduction of experimental measurements of the differential decay rate and the LQCD results for $f_+$ and $f_0$, leading to a quite accurate determination of $|V_{cb}|$. We also confirm that the previous tension between the exclusive and inclusive determinations was mostly due to the use of the CLN parametrization. Furthermore, the fitted phase moments $\mathcal{A}_0^{0,+}$ provide valuable information to constrain the $S$- and $P$-wave $\bar{B}\bar{D}$ interactions. Any model for them should be consistent with the determination of these parameters extracted here from the $\bar{B} \to D$ semileptonic decays. As an example, we have given strong hints about the existence of at least one bound and one virtual $\bar{B}\bar{D}$ $S$-wave $0^+$ states, subject to uncertainties produced by potentially sizeable inelastic effects. The same parametrization can be also employed to other $b \to c$ semileptonic processes such as $\bar{B} \to D^*\ell\bar{\nu}_\ell$ and $\Lambda_b \to \Lambda_c\ell\bar{\nu}_\ell$.

---

[1] An $S-$wave bound state of zero binding energy gives a contribution of $\pi/2$ instead of $\pi$.

# Chapter 8

# CONTRIBUTION OF CONSTITUENT QUARK MODEL $c\bar{s}$ STATES TO THE DYNAMICS OF THE $D^*_{s0}(2317)$ AND $D_{s1}(2460)$ RESONANCES

## 8.1 Introduction

In this chapter we shall focus on the most recent LQCD information concerning the charmed-strange scalar $D^*_{s0}(2317)$ and axial $D_{s1}(2460)$ resonances. These states have already been presented in Sec. 1.2.1 of Chapter 1, remarking the important role that are currently playing in the understanding of the spectroscopy of open-charm mesons. We have also illustrated how they can be associated with $P$-wave $c\bar{s}$ excitations from the perspective of their valence quark content, and at the same time, be considered as part of a HQSS doublet. In the course of the following pages, our aim is to develop a description of these states based on a UHM$\chi$PT interaction that explicitly includes the contribution of CQM bare degrees of freedom in a way consistent with HQSS and HQFS. To that end, we will follow the scheme detailed in Ref. [341], where the $(D\bar{D}^* + h.c.)$ two-meson channel was coupled to the $\chi_{c1}(2P)$ charmonium state, and the consequences for the $X(3872)$ and its spin-flavour partners, were examined. The contents of this chapter are based on the results obtained in Ref. [7].

If one accepts the predictions of generally successful CQMs, one should expect the charmed-strange $J^P = 0^+$ ground state to lie much closer to the $DK$ threshold than the physical $D^*_{s0}(2317)$, so the latter meson pair could act as an essential dynamical agent to reduce the mass of the bare meson state closer to the experimental value, as suggested by some authors [76]. Hence, in this picture, the physical $D^*_{s0}(2317)$ resonance would be the result of a strong renormalization of a bare $c\bar{s}$ component, rather than a new dynamical state generated from a strongly attractive $DK$ interaction. Nevertheless, since the required renormalization would be quite significant, one would expect, even in this context, that the $D^*_{s0}(2317)$ resonance will acquire a sizeable two-meson molecular probability. Indeed, the low-lying $P$-wave charmed-strange mesons were studied in Ref. [342] employing a widely used CQM [343–345], where the coupling between the quark-antiquark and meson-meson degrees of freedom was modeled with the $^3P_0$ transition operator [346]. In that work, where all the parameters were constrained from previous studies on hadron phenomenology, the bare $1^3P_0$ $c\bar{s}$ state[1] developed a large mass-shift as a consequence of its coupling with the $DK-$meson pair, becoming its mass closer to that of the physical

---

[1] As in previous chapters, we use the nomenclature $n\,^{2S+1}L_{2J+1}$ for the radial, spin, orbital and total angular momentum quantum numbers of a quark-antiquark state. In addition the parity of the state is $(-1)^{L+1}$.

$D_{s0}^*(2317)$ resonance. On the other hand, the dressed state contained a large molecular component that gave rise to a $DK-$meson pair probability of around 33% [342] in the final configuration of the meson.

In sharp contrast, the LQCD energy-levels reported in Refs. [46, 47] were analyzed in Ref. [245], employing an auxiliary potential method, where $DK$ molecular probabilities for the $D_{s0}^*(2317)$ much higher, of the order of 70%, were found. This result was consistent with the previous values obtained in Ref. [205]. The authors of this work performed a LQCD calculation of several heavy-light meson–Goldstone boson scattering lengths, that they used to fit the LECs entering in the unitarized NLO heavy meson chiral perturbation theory HM$\chi$PT coupled-channel $T-$matrix derived in Ref. [198]. The latter amplitudes were employed to estimate the $D_{s0}^*(2317)$ molecular component. These high values for the $DK$ probabilities[2] are similar to those obtained in Ref. [44] from the analysis of the experimental $DK$ invariant mass spectra of the reactions $B^+ \to \bar{D}^0 D^0 K^+$, $B^0 \to D^- D^0 K^+$ [348] and $B_s \to \bar{D}^0 K^- \pi^+$ [243] measured by the BaBar and LHCb Collaborations, respectively. In all cases an enhancement right above the threshold is seen and it is related in Ref. [44] to the presence of the $D_{s0}^*(2317)$. The latter is dynamically generated when LO HM$\chi$PT amplitudes are used as the kernel of a BSE, whose renormalized solutions fulfil exact elastic unitarity in coupled-channels.

The predominantly molecular structure of the $D_{s0}^*(2317)$ and $D_{s1}(2460)$ resonances has recently received an indirect robust theoretical support in Refs. [3, 6] (see also the review of Ref. [228]). The results for the first of these two references have already been discussed in Chapter 4, where the heavy-light pseudoscalar meson $J^P = 0^+$ scattering in the strangeness-isospin $(S, I) = (0, 1/2)$ sector was studied, and a strong case for the existence of two poles in the $D_0^*(2400)$ energy-region was presented. The dynamical origin of this two-pole structure was elucidated from the light-flavour SU(3) structure of the interaction, and we found that the lower pole would be the SU(3) partner of the $D_{s0}^*(2317)$. Thus, this latter state will have also clear hadron-molecular origin. A similar pattern was found for $J^P = 1^+$ and in the bottom sector. This in fact might solve a long-standing puzzle in charm-meson spectroscopy—as has been also discussed in the previous Chapter 5—since it would provide an explanation of why the masses, quoted in the PDG [206], of the non-strange mesons $D_0^*(2400)$ and $D_1(2430)$ are almost equal to or even higher than their strange siblings. Moreover, in Chapter 5 it has been further shown that the well-constrained amplitudes for Goldstone bosons scattering off charm mesons used in Chapter 4 are fully consistent with recent high quality data on the $B^- \to D^+\pi^-\pi^-$ final states provided by the LHCb experiment in Ref. [240]. Indeed, all these results suggest a new paradigm for heavy-light meson spectroscopy that questions their traditional $q\bar{q}$ CQM interpretation [6].

Most of these latter works [3,6,44,205] do not incorporate explicitly the bare $c\bar{s}$ degrees of freedom, whose effects are, in principle, encoded in the LECs that appear beyond LO in the chiral expansion, and in the non-perturbative re-summation employed to restore elastic coupled-channels unitarity. However, and depending on the proximity of the CQM states to the energy-region under study, this approximation might not be sufficiently accurate.

---

[2] Note that Ref. [205] made use of the Weinberg compositeness rule [244], which relates this probability to the scattering length in the limit of small binding energies. However, the works of Ref. [44, 245] employed a generalization [347] that remains valid for bound states, independently of their distance to threshold.

Such radically different pictures of the inner structure of the $D_{s0}^*(2317)$ make timely a re-analysis of this resonance, paying special attention to the interplay between meson molecular and CQM degrees of freedom. From that perspective, we will try to describe here the charm $0^+$ and $1^+$ LQCD energy-levels obtained in Ref. [45] using a HM$\chi$PT approach incorporating, for the very first time in this context, bare CQM scalar and axial degrees of freedom to the relevant two-meson channels. Such comparison will also serve to constrain/determine the LECs that appear in the approach.[3]

The recent LQCD simulation of Ref. [45] reported finite volume energy-levels from a high statistics study of the $J^P = 0^+$ and $1^+$ charmed-strange mesons, $D_{s0}^*(2317)$ and $D_{s1}(2460)$, respectively, where the effects of the nearby $DK$ and $D^*K$ thresholds were taken into account by employing the corresponding four-quark operators. As we will discuss below, the work of Ref. [45] represents a clear improvement on the pioneering ones of Refs. [46, 47]. Some of the energy-levels reported in Ref. [45] lie in the proximity of, when not above, the expected CQM bare masses of the ground scalar and axial charmed-strange states, being thus interesting to include explicitly these degrees of freedom in the scheme, since their effects might not be properly taken into account by simply including LECs. Moreover, in the present study, we will also include the next $(S = 1, I = 0)$ higher thresholds, $D_s^{(*)}\eta$, since they appear at energies below some of the finite-volume levels computed in Ref. [45].

This chapter is structured as follows. After this introduction, some novel aspects of the theoretical formalism are described in Sec. 8.2, where details about the $D^{(*)}K$ and $D_s^{(*)}\eta$ scattering amplitudes, the coupling of the meson-pair degrees of freedom with the bare CQM $c\bar{s}$ spectrum, the restoration of unitarity and the extension of the scheme to finite volume are discussed. In Sec. 8.3 our results for the finite volume $0^+$ and $1^+$ energy levels are presented and compared with the ones reported in Ref. [45]. The properties of the $D_{s0}^*(2317)$ and $D_{s1}(2460)$ mesons, in particular their molecular content, are discussed in this section. We also compute the energy levels obtained using the unitarized NLO HM$\chi$PT amplitudes derived in Refs. [198, 205], and extensively compare the predictions of this latter scheme with those deduced by including a bare CQM pole. The section concludes with predictions for $DK$ $S$-wave scattering phase shifts, and a discussion about a few aspects of the renormalization dependence of the results obtained in this work. The conclusions and a summary of results are presented in Sec. 8.4.

## 8.2 Theoretical formalism

We will briefly review here the most relevant aspects of the theoretical formalism, paying attention to the inclusion of the $D_s^{(*)}\eta$ channels and the coupling with the CQM bare states. The relevant effective Lagrangians have been introduced in Sec. 3.4.1 in terms of the heavy-light meson 3.3.2 and pNGBs 3.3.1 degrees of freedom.

### 8.2.1 Interactions

We are interested in the $S$-wave Goldstone boson ($K^+$, $K^0$ and $\eta$) scattering off charm mesons $P_a^{(*)} \equiv (D^{0(*)}, D^{+(*)}, D_s^{+(*)})$. We will generically refer as $\phi$ to the former mesons

---

[3] As it will be discussed below, LECs of our effective interaction in the charm and bottom sectors might be related by heavy-quark flavour symmetry. The present study is closely related to the contents of Chapter 9 where we study the same states in the bottom sector.

and $P^{(*)}$ to the latter ones. The heavy-light charm mesons are described in terms of the HQSS matrix field $H_a$ (3.45).

The Weinberg-Tomozawa Lagrangian (WTL), which was introduced in Eq. (3.105) of Sec. 3.4.1, describes the $S$-wave $P^{(*)}\phi$ chiral interaction at LO. In this case, we shall later distinguish between the unflavoured $\eta_8$ SU(3) state appearing in the octet of pNGBs and the physical state by incorporating the ideal mixing between the octet and singlet $\eta_1$ states. For that reason, we replace the field matrix $u$ in Eq. (3.83) by its modified version containing the singlet $\eta_1$ given by [184],

$$u = \exp\left(i\frac{\widetilde{M}}{\sqrt{2}f}\right), \tag{8.1}$$

with normalization $f \sim 93$ MeV and the matrix $\widetilde{M}$ reads,

$$\widetilde{M} = \begin{pmatrix} \frac{\pi^0}{\sqrt{2}} + \frac{\eta_8}{\sqrt{6}} + \frac{\eta_1}{\sqrt{3}} & \pi^+ & K^+ \\ \pi^- & -\frac{\pi^0}{\sqrt{2}} + \frac{\eta_8}{\sqrt{6}} + \frac{\eta_1}{\sqrt{3}} & K^0 \\ K^- & \bar{K}^0 & -\sqrt{\frac{2}{3}}\eta_8 + \frac{\eta_1}{\sqrt{3}} \end{pmatrix}, \tag{8.2}$$

where we explicitly consider the $\eta_1$ and $\eta_8$ unflavoured SU(3)states. On the other hand, within the HQSS formalism, the even parity CQM bare $c\bar{q}$ states, associated to the $j_{\bar{q}}^P = \frac{1}{2}^+$ HQSS doublet, are described by the matrix field $J_a$ [193] introduced in Eq. (3.50) (see Sec. 3.3.2 for details). Since in this chapter we will be interested in the $(S, I) = (1, 0)$ sector, in what follows and for simplicity we will denote the relevant heavy quark fields $Y_{c\bar{s}}^{(*)}$ entering the SU(3) anti-triplet $J_a$ as $Y^{(*)}$. The mass of CQM bare states, $\overset{\circ}{m}_{c\bar{s}}$, is a renormalization-dependent parameter of the scheme [341] that will be discussed below. At LO in the heavy quark expansion, there exists only one term invariant under Lorentz, parity, chiral and heavy quark spin transformations which was given in Eq. (3.107). It depends on a dimensionless undetermined LEC, $c$, that controls the strength of the vertex. This LEC, though it depends on the orbital angular momentum and radial quantum numbers of the CQM state, is in principle independent of the spin of the quark-model heavy-light meson, and of the light SU(3) flavour structure of the vertex. Thus, up to $\Lambda_{\rm QCD}/m_Q$ corrections, it can be used both for $J = 0$ and $J = 1$ in the charm and bottom sectors. Moreover, in the SU(3) limit, the same LEC governs the interplay between two-meson and quark model degrees of freedom in all isospin and strangeness channels. Let us consider the transitions involving pseudoscalar ($P$) heavy-light and Goldstone ($\phi$) mesons,

$$P_I\phi_I \to P_F\phi_F, \tag{8.3}$$

for which the tree level isoscalar[4] amplitude ($V_c$) deduced from the WTL of Eq. (3.105) reads [199]

$$\begin{aligned} V_c(s,u) &= -A\frac{(s-u)}{2f^2}, \\ A &= \begin{pmatrix} 1 & \sqrt{2/3} \\ \sqrt{2/3} & 0 \end{pmatrix}, \end{aligned} \tag{8.4}$$

---

[4] The phase convention for isospin states $|I, I_3\rangle$ are given in Eqs. (3.41), (3.43) and (3.49). Moreover, we use the order $DK$, as in Ref. [199], to construct the isoscalar amplitudes.

where channels 1 and 2 are $DK$ and $D_s\eta$, respectively, $s$ and $u$ are the usual Mandelstam variables and we have considered the $\eta-\eta'$ ideal mixing [349][5],

$$\begin{aligned}\eta_8 &= \frac{2\sqrt{2}}{3}\eta - \frac{1}{3}\eta', \\ \eta_1 &= \frac{1}{3}\eta + \frac{2\sqrt{2}}{3}\eta'.\end{aligned} \tag{8.5}$$

After projecting into $J=0$, we replace

$$\frac{(s-u)}{2} \quad\rightarrow\quad \frac{3s^2 - s\Sigma - \Delta_I\Delta_F}{4s} \tag{8.6}$$

with $\Sigma = (M_I^2 + m_I^2 + M_F^2 + m_F^2)$ and $\Delta_{I(F)} = (M^2_{I(F)} - m^2_{I(F)})$, where $M_{I(F)}$ and $m_{I(F)}$ are the masses of the initial (final) heavy-light charm and Goldstone mesons, respectively.

The WTL leads to similar isoscalar amplitudes for the transitions involving vector ($P^*$) heavy-light mesons,

$$P_I^*\phi_I \rightarrow P_F^*\phi_F\ . \tag{8.7}$$

Indeed, one gets in this case a potential[6] like that of Eq. (8.4), supplemented by a term $-\epsilon_I\cdot\epsilon_F$, where $\epsilon_{I(F)}$ is the polarization four-vector of the initial (final) heavy-light meson. This latter factor reduces, at LO, to 1 after projecting into $J=1$ ($S$-wave, i.e., zero orbital angular momentum). In summary, the amplitudes given in Eq. (8.4), together with the projection implicit in Eq. (8.6) provide the coupled-channel contact potential, $V_c(s)$, both in the $0^+$ and $1^+$ sectors.

Next, we consider transitions between CQM bare states [$Y^{(*)}$] and $P^{(*)}\phi$ meson pairs, $Y^{(*)}\rightarrow P^{(*)}\phi$. From Eq. (3.107) we find

$$\begin{aligned}V_{c\bar{s}}(s) &= -\tilde{A}\frac{ic}{f}\sqrt{M\ \overset{\circ}{m}_{c\bar{s}}}\frac{s+m^2-M^2}{\sqrt{s}}, \\ \tilde{A} &= \begin{pmatrix}1\\ \frac{1}{\sqrt{6}}\end{pmatrix},\end{aligned} \tag{8.8}$$

with $M$ an $m$ the masses of the $P^{(*)}$ and $\phi$ mesons, respectively.

Note that, here, by bare mass, we mean the mass of the CQM states when the LEC $c$ is set to zero, and thus it is not a physical observable. In the sector studied in this work, the coupling to the $P^{(*)}\phi$ meson pairs renormalizes this bare mass, as we will discuss

---

[5] The ideal mixing-angle turns out to be around $-19.5$ degrees, while the global fit to determine the $\eta-\eta'$ mixing angle carried out in [350] provided a value of $-13.3(5)$ degrees. There is an abundant literature on this subject, and more recent theoretical works (see for instance [284] and references therein) found higher absolute values for the mixing-angle, and therefore closer to the ideal one. Thus for instance, the authors of Ref. [351] quoted $-16.2^{+2.8}_{-2.9}$ degrees. Fine details of the $\eta-\eta'$ mixing are irrelevant for the exploratory study carried out in this work, since, as we will see, the influence of the $D_s^{(*)}\eta$ channels on the $D^*_{s0}(2317)$ and $D_{s1}(2460)$ dynamics is quite small, and can be taken into account by mild variations of the rest of the LECs of the scheme. Thus, for simplicity, we find sufficiently accurate to adopt the ideal mixing scheme. However, $\eta-\eta'$ mixing fine details are certainly relevant for studies on the number of colors and/or pion mass dependencies of the properties of these resonances, as the one carried out in [284], where $m_\pi$ is extrapolated until values close to 700 MeV.

[6] Now channels 1 and 2 are $D^*K$ and $D_s^*\eta$, respectively.

below. Since, in the effective theory, the UV regulator is finite, the difference between the bare and the physical resonance masses is a finite renormalization. This shift depends on the UV regulator since the bare mass itself depends on the renormalization scheme. The value of the bare mass, which is thus a free parameter, can either be indirectly fitted to experimental observations, or obtained from schemes that ignore the coupling to the mesons, such as some CQMs. In this latter case, the issue certainly would be to set the UV regulator to match the quark model and the HM$\chi$PT approaches [341].

The vertices in Eq. (8.8) can be used to compute the contribution $[V_{\rm ex}(s)]$ to $P^{(*)}\phi$ scattering via the exchange of intermediate even-parity charmed-strange mesons. It is given by [4, 341]

$$V_{\rm ex}(s) = \frac{V_{c\bar{s}}(s) V_{c\bar{s}}^\dagger(s)}{s - (\overset{\circ}{m}_{c\bar{s}})^2} \; . \tag{8.9}$$

Finally, the full effective potential, $V(s)$, consistent with HQSS is given by

$$V(s) = V_{\rm c}(s) + V_{\rm ex}(s), \tag{8.10}$$

that incorporates the interplay between meson-pairs and CQM degrees of freedom in the $P^{(*)}\phi$ dynamics [341].

Note that $V_{\rm c}(s)$ is obtained from $V_{\rm c}(s,u)$ in Eq. (8.4) using the projection implicit in Eq. (8.6). The LO potentials, $V_{\rm c}(s)$ and $V_{\rm ex}(s)$, are identical in the heavy-quark limit in both the $0^+$ and $1^+$ sectors. Here, we will include some HQSS breaking corrections stemming from the mass difference between pseudoscalar and vector heavy-light mesons and the masses of scalar and axial CQM bare states. The scheme derived here is similar to that followed in next Chapter 9, though here the $D_s^{(*)}\eta$ channel has been included, while the counterpart of this channel in the bottom-strange sector will not be considered in the forthcoming chapter.

### 8.2.2 Unitarity in coupled-channels

Elastic unitarity in coupled channels is restored by solving for each $J^P$ sector a BSE (2.81), using as kernel the HQSS effective potential of Eq. (8.10). The BSE is solved within the so-called on-shell approximation [132] (2.87) and using a Gaussian cut-off, $\Lambda$, to regularize/renormalize its UV behaviour. For further details on the conventions and normalizations employed here, we refer to the program described in Sec. 2.5 as well as Sec. 2.3.1 for the phase shifts definitions.

The expression for the regularized loop functions $G_\ell^{(\rm R)}(s) = G^{(\rm G)}(s, m_\ell, M_\ell)$ entering the loop matrix (2.87) can be found in Eq. (A.2) of Appendix A. In our two coupled channels context the $\ell = 1, 2$ particularize to channels $D^{(*)}K$, $D_s^{(*)}\eta$.

### 8.2.3 CQM states

We have seen that through the coupling of the CQM $c\bar{s}$ and the $P^{(*)}\phi$ degrees of freedom, the effective interaction incorporates a term ($V_{\rm ex}(s)$) driven by the exchange of bare CQM states ($Y^{(*)}$). Such a term introduces a pole in the two-meson tree-level amplitudes, Eq. (8.10), located at the bare mass value, $\sqrt{s} = \overset{\circ}{m}_{c\bar{s}}$. As already mentioned, it should be interpreted as the mass of the CQM state in the limit of vanishing coupling to the $P^{(*)}\phi$ meson-pairs ($c \to 0$), and therefore it is not an observable. The interaction with the meson cloud *dresses* the CQM state through loops [Eq. (2.87)], renormalizing its mass, and the dressed state might also acquire a finite width, when it is located above threshold. At energies far enough $\overset{\circ}{m}_{c\bar{s}}$, the contribution of $V_{\rm ex}$ can be regarded as small contact interaction that can be accounted for by means of a LEC. However, the exchange contribution becomes more important for higher energies approaching $\overset{\circ}{m}_{c\bar{s}}$, and its energy dependence might then not be safely ignored.

A priori, the value of $\overset{\circ}{m}_{c\bar{s}}$ is a free parameter of the present approach, and moreover it should depend on the renormalization scheme [341]. We will take predictions from quenched CQMs, which in principle do not include couplings with nearby meson-meson channels. In the $J^P = 0^+$ sector, quark models predict, in general, $c\bar{s}$ bare masses well above $M_D + m_K$, which lead to attractive $V_{\rm ex}$ exchange interactions at $DK$ threshold, which might help in forming the $D^*_{s0}(2317)$ resonance. Most quark models predict masses in the range of $2.45 - 2.51$ GeV for the $1^3P_0$ $c\bar{s}$ state [25, 26, 352, 353], significantly far from the $D^*_{s0}(2317)$ experimental mass. With the aim of improving these predictions, some other models [29, 354] incorporated a one-loop correction diagram to the one-gluon exchange (OGE) potential, adding a spin-dependent term to the quark-antiquark potential which affects mesons with different flavour quarks, such as the $c\bar{s}$ mesons. In these works, it is shown that this correction is rather small except for the $0^+$ sector, where large shifts are found and the mass of the CQM $1^3P_0$ state is significantly lowered ($\sim 100$ MeV). Indeed, it is found in the 2.35-2.38 GeV region—closer to but still above the experimental $D^*_{s0}(2317)$ mass. Nevertheless, these predicted states would be still above the $DK$ threshold and their width would be large due to the decay into final $DK$, and difficult to reconcile with the experiment that currently provides an upper bound of a few MeV for its total width,[7] as mentioned in the Introduction. Moreover, quark models including these modified OGE potential will still face difficulties to describe the $J^P = 1^+$ sector, where these corrections are quite small, and the experimental mass pattern is similar to that found in the isoscalar-scalar sector.

One should bear also in mind, as the one-loop OGE correction brings the bare state closer to the $DK$ threshold, the interplay between the two-meson channel and the CQM degrees of freedom might have a major impact on the description of the resonance properties and LQCD energy-levels.

Thus, in this study we will explore both types of CQMs. On one side, we will take the $\overset{\circ}{m}_{c\bar{s}}$ values for the $j^P_{\bar{q}} = \frac{1}{2}^+$ charmed-strange meson doublet predicted in the CQM calculations of Refs. [345,356] (Set A in Table 8.1). Such CQM is based on the assumption that the light constituent quark mass and the exchange of pseudo-Goldstone bosons arise as a consequence of the spontaneous breaking of the chiral symmetry in QCD. Besides, the dynamics is completed with a perturbative OGE potential and a non-perturbative screened confining interaction [343, 345]. On the other hand, another set of bare masses (Set B in Table 8.1) will be employed, predicted within the same CQM but supplemented by the one-loop OGE corrections derived in Ref. [354] (see Ref. [356] for further details).

In contrast to the bottom sector studied in next Chapter 9, we see in Table 8.1 how the values of the bare masses lie close to the $D_s^{(*)}\eta$ threshold and, consequently, this channel has been incorporated to the formalism.

---

[7] Being the $D^*_{s0}(2317)$ resonance located below the $DK$ threshold, all its hadronic decays are suppressed by isospin symmetry. Depending on different dynamical assumptions, decay widths, within molecular schemes, from 10 keV to more than 100 keV have been predicted [247, 285, 355].

**Table 8.1:** The two sets of $\overset{\circ}{m}_{c\bar{s}}$ CQM bare masses and the $D^{(*)}K$ and $D_s^{(*)}\eta$ averaged threshold energies (in MeV units) used in this work, taken from Ref. [356]. In addition, we take an average kaon mass of $m_K = 495.6$ MeV.

| $J^P$ | [Set A] $\overset{\circ}{m}_{c\bar{s}}$ | [Set B] $\overset{\circ}{m}_{c\bar{s}}$ | $(M_{D^{(*)}} + m_K)$ | $(M_{D_s^{(*)}} + m_\eta)$ |
|---|---|---|---|---|
| $0^+$ | 2510.7 | 2382.9 | 2362.8 | 2516.1 |
| $1^+$ | 2593.1 | 2569.7 | 2504.2 | 2660.0 |
| $1^+ - 0^+$ | 82.4 | 186.8 | | |

### 8.2.4 NLO corrections

We will also use the $\mathcal{O}(p^2)$ NLO UHM$\chi$PT amplitudes presented in Subsects. 4.2.1 and 4.2.2 in Chapter 4. The consideration of the contributions from explicit exchanges of CQM states, in addition to the LO HM$\chi$PT amplitudes, contemplated in the previous subsections provides a different perspective to the physiognomy of the $P^{(*)}\phi$ interactions. Thus, it is worth discussing if there exists an energy-regime where the LO & CQM scheme might mimic the NLO amplitudes, and when the CQM effects cannot be properly accounted for by the LECs that appear beyond LO in the chiral expansion. Such study could provide further insights on the energy range of applicability of the unitarized effective theory. Hence, in addition to results obtained with a LO & CQM interaction, we will also show results from the $(S, I) = (1, 0)$ NLO UHM$\chi$PT amplitudes employed in previous Chapters 4, 6 and 5.

### 8.2.5 Poles, couplings and compositeness condition for bound states

The interplay between meson-meson and CQM $c\bar{s}$ states might dynamically generate new states that arise as poles of the scattering amplitudes on the complex $s-$plane. There exist two thresholds $s_0^{(1,2)}$ (see Eq. (2.92)) in our two-channel problem, therefore, RSs are denoted as $(\xi_1\,, \xi_2)$, $\xi_i = 0, 1$, and are defined in the whole complex plane through analytical continuations of the loop functions [133] in Eq. (2.89). With the definitions stated in Sec. 2.5, $(0, 0)$ is the physical RS (or first Riemann sheet (FRS)), while the unphysical sheet (second Riemann sheet (SRS)), is defined by requiring continuity across the unitarity cut between its fourth quadrant and the first one of the physical one. Therefore, the definition of the SRS of the amplitudes varies below and above the highest threshold (branch point of the $T-$matrix) [133], and it corresponds to (10) or (11) when the real part of $s$ is above $s_0^{(1)}$, but below $s_0^{(2)}$, or above both thresholds, respectively (see Ref. [133] and Sec. 2.5 in Chapter 2 for some more details).

The mass ($M_R$) and the width ($\Gamma_R$) of the bound state/resonance are obtained from the position of the pole on the complex energy plane $\sqrt{s_R} = M_R - i\,\Gamma_R/2$, whereas the coupling $g_i$ of the resonance to the channel $i$ is obtained from the residue (2.93) of $T_{ij}(s)$ at the pole position. The residues can be used to get information on the compositeness of the bound states. Motivated by the Weinberg compositeness condition [244, 357, 358], the probability of finding the $D^{(*)}K$ or $D_s^{(*)}\eta$ molecular component in the bound state wave function is given by [347, 359–361],

$$P_j = -g_j^2 \left. \frac{\partial G_j}{\partial s} \right|_{s=M_b^2} , \tag{8.11}$$

where $M_b$ is the bound state mass. The energy dependence of the potential produces probabilities in Eq. (8.11) that deviate from one. We will restrict the discussion to the case of bound states. The evaluation of Eq. (8.11) for resonances gives rise to complex values of $P_j$, loosing then a straightforward probabilistic interpretation. (Further details can be found, for instance, in section 4.2 of Ref. [341]. See also Refs. [359, 362, 363].)

### 8.2.6 Finite volume and details of the LQCD simulation

As mentioned in Sec. 8.1, the simulation of Ref. [45] reported finite volume energy-levels from a high statistics study of the $D^*_{s0}(2317)$ and $D_{s1}(2460)$ resonances, taking into account effects of the nearby $DK$ and $D^*K$ thresholds by employing appropriate four-quark operators. Six ensembles with $N_f = 2$ non-perturbatively $\mathcal{O}(a)$ improved clover Wilson sea quarks at lattice-spacing $a = 0.071$ fm were employed in Ref. [45], covering different spatial volumes and pion masses: linear lattice size ($L$) of 1.7 fm to 4.5 fm were realized for $m_\pi = 290$ MeV and 3.4 fm and 4.5 fm for an almost physical pion mass of 150 MeV. Thus, the work of Ref. [45] represents a clear improvement on the pioneering ones of Refs. [46, 47], where an ensemble with $m_\pi = 156$ MeV, at a fairly coarse lattice spacing of $a = 0.09$ fm and a small spatial lattice extent of $L = 2.9$ fm ($Lm_\pi = 2.29$) were analyzed using the effective range approximation to extract infinite volume results. Thus, the use of a finer lattice spacing in Ref. [45] is important since discretization effects can be substantial for observables involving charm quarks, while exploring the dependence on the spatial volume is needed, since contributions which are exponentially suppressed in $Lm_\pi$ (that are ignored in the Lüscher formalism) may not be small for $Lm_\pi = 2.29$.

Nevertheless, we should warn the reader that by employing $N_f = 2$ dynamical fermions, effects arising from strange sea quarks are omitted in Ref. [45], with the expectation that the valence strange quark provides the dominant contribution. This seems to be the case, as can be inferred from Fig. 10 of this latter reference, where the splittings found in Ref. [45] of the two lowest states, with the noninteracting threshold for the scalar and axial-vector channels, for $m_\pi = 290$ MeV and 150 MeV and various volumes are compared to the $m_\pi = 156$ MeV 2+1 dynamical quarks results obtained in Ref. [47] for $Lm_\pi = 2.29$. The latter single-volume splittings lie in the volume-dependence curves derived in Ref. [45], but with significant larger errors. Firstly because the number of gauge configurations used in Ref. [45] is around one order of magnitude larger than that computed in Ref. [47], and secondly, perhaps, as a consequence of the discretization errors that should be higher in this LQCD simulation (see for instance the sizable breaking of Lorentz symmetry in the heavy-light meson dispersion relation given in Eq. (2) and Table VI of Ref. [47]).

To compare with the energy-levels reported in Ref. [45], we consider our scheme, based on unitarized HM$\chi$PT and the contribution of CQM states, in a cubic box of side $L$, and periodic boundary conditions for the fields. The three momentum is quantized $\vec{q} = \frac{2\pi}{L}\vec{n}$ ($\vec{n} \in \mathbb{Z}^3$). The integrals in the loop functions $G(s)$ are replaced by their finite volume versions , $\widetilde{G}(s, L) = \text{diag}\left[\widetilde{G}_{D^{(*)}K}(s, L), \widetilde{G}_{D_s^{(*)}\eta}(s, L)\right]$ [167, 169], involving the sum over all possible $\vec{q}$,

$$\begin{aligned} \widetilde{G}_j(s,L) &= \frac{1}{L^3}\sum_{\vec{n}\in\mathbb{Z}^3} \frac{\Omega(\vec{q})e^{-2(\vec{q}^{\,2}-\vec{k}^{\,2})/\Lambda^2}}{s-\left[\omega_{P_j^{(*)}}(\vec{q})+\omega_{\phi_j}(\vec{q})\right]^2}, \\ \Omega(\vec{q}) &= \frac{\omega_{P_j^{(*)}}+\omega_{\phi_j}}{2\omega_{P_j^{(*)}}\omega_{\phi_j}}, \end{aligned} \tag{8.12}$$

where $\omega_i(\vec{q}) = (\mathcal{M}_i^2+\vec{q}^{\,2})^{\frac{1}{2}}$, with $\mathcal{M}_i$ the mass of the heavy-light meson or the Goldstone boson for $i = P^{(*)}$ or $\phi$, respectively. (We have adopted relativistic dispersion relations as in Ref. [45].) Up to the order considered in this work, there are no finite volume corrections to the potential, so the full volume dependence is carried by the loop function $\widetilde{G}$ defined in a finite box. As explained in Sec. 2.5.1, the energy-levels $E(L)$ ($s = E^2$, $E \in \mathbb{R}$) are computed from the poles of $\widetilde{T}(s,L)$ in Eq. (2.97) for each size of the box, $\det\widetilde{T}^{-1}(s,L) = \det(V^{-1}(s) - \widetilde{G}(s,L)) = 0$. The spectrum becomes discrete, with levels that, in principle, can be associated to two-meson ($P^{(*)}\phi$) scattering states. In the non-interacting case, the free energies (2.99), $E^{\rm free}_{D^{(*)}K}(\vec{q})$ and $E^{\rm free}_{D_s^{(*)}\eta}(\vec{q})$ are recovered (there should not be room to confusion noting that, now, the subindex is used to distinguish free energies related to the two channels instead of labelling the three-momentum as in Eq. (2.99)). Hence, the continuous volume dependent curves that will be presented below are essentially the Lüscher curves obtained from the phase shift by solving

$$\delta(q) + \phi(\hat{q}) = n\pi \tag{8.13}$$

with $\hat{q} = qL/2\pi$ and $\phi(\hat{q})$ determined by the Lüscher function (see Eq. (6.13) of Ref. [164]).

On the other hand, for a proper comparison with the results of Ref. [45], it is necessary to use the lattice meson masses obtained in that simulation. That work reported two different sets of results that correspond to two different pion masses used to compute the energy-levels. We will label here the two sets of LQCD levels by Ensembles I and II, for $m_\pi = 290$ MeV and 150 MeV, respectively. We take the $\pi$, $K$, $D$ and $D^*$ masses, for the different box-sizes considered in each of the ensembles, from Table I of Ref. [45]. Besides, the $0^-$ and $1^-$ $D_s^{(*)}$ masses for the Ensemble II are taken from Table VII ($L/a = 64$) of Ref. [45], while for Ensemble I the masses of the charmed-strange heavy-light mesons have been obtained using the values of $(m_{0^+} - m_{0^-})$ and $(m_{1^+} - m_{1^-})$ displayed in Fig. 13 of the latter reference, and taking for the $m_{0^+}$ and $m_{1^+}$ masses the $L/a = 64$ values reported in Table III of the same work (Ref. [45]). Hence, we neglect any dependence on $L$ in the masses of $0^-$ and $1^-$ $c\bar{s}$ ground states.[8] The masses used in this work are compiled in Table 8.2.

The mass of the $\eta$ meson is not reported in Ref. [45] either, so we estimated its value, as function of the volume and pion mass, using the Okubo mass formula [197] as follows

$$m_\eta^{\rm lat} = m_\eta^{\rm exp} + m_8^{\rm lat} - m_8^{\rm exp}\,, \tag{8.14}$$

---

[8] It is not straightforward to extract the masses of the $0^-$ and $1^-$ $D_s^{(*)}$ mesons, for each of the pion masses and volumes studied in Ref. [45], from the results reported in that work. Note, however, that volume effects in the masses of these mesons are expected to be even smaller than for the $D-$meson, and that these masses enter only through the small effects originated from the coupled-channels dynamics, when the $D_s^{(*)}\eta$ components are considered.

**Table 8.2:** LQCD masses (in MeV units) of the $0^-$ and $1^-$ $D_s^{(*)}$ mesons used in this work. They have been obtained from Tables III, VII and Fig. 13 of Ref. [45] [we always use the results corresponding to the highest volume ($L/a = 64$); see discussion in the text for details]. We also give experimental masses, taken from the RPP [206], and the difference between the experimental and lattice spin-averaged $D_s$ masses.

| | Ensemble I | Ensemble II | Exp |
|---|---|---|---|
| $M_{D_s}$ | 1978(4) | 1976.9(2) | 1968.28 |
| $M_{D_s^*}$ | 2100(7) | 2094.9(7) | 2112.1 |
| $\bar{M}^{\rm exp} - \bar{M}^{\rm lat}$ | 5(5) | 9.6(7) | |

with $m_8^2 = (4m_K^2 - m_\pi^2)/3$. Finally for unphysical pion masses, the CQM bare masses are also corrected using the difference between the experimental and lattice spin-averaged $D_s$ masses,

$$\overset{\circ}{m}{}_{c\bar{s}}^{\rm lat} = \overset{\circ}{m}_{c\bar{s}} + \bar{M}^{\rm lat} - \bar{M}^{\rm exp}, \tag{8.15}$$

with $\bar{M} = (M_{D_s} + 3M_{D_s^{(*)}})/4$.

Uncertainties in all input lattice mesons masses (Table I of Ref. [45] and Table 8.2 of this work), as well as in $\overset{\circ}{m}{}_{c\bar{s}}^{\rm lat}$, are taken into account in the error budget of our final results, as we will detail in the next section.

To end this subsection, we would like to stress that considering the LQCD meson masses, for finite volumes and unphysical pions, it is important to set up correctly the thresholds and to properly compute the loop function in a finite box. However, the current approach will still suffer from some systematic errors, mostly because we have not considered the dependence of the Goldstone decay constant, that appears in the WTL interaction, on the volume and the unphysical pion mass (such information is not given in Ref. [45]), and we still use its value in the infinite-volume chiral limit.[9] Nevertheless, some of this dependence might be partially reabsorbed in the parameters fitted to the LQCD energy-levels, and we certainly benefit from the fact that the pions simulated in Ref. [45] are quite light and close to the physical one.

## 8.3 Results and discussion

### 8.3.1 LO HMChPT+CQM analysis

#### Fit details

The $S$-wave $D^{(*)}K$ interaction in the LO+CQM interaction scheme depends on three, a priori, free parameters: the Gaussian cut-off $\Lambda$, the LEC $c$ (Eq. (8.8)) and the masses of the bare CQM $c\bar{s}$ state, $\overset{\circ}{m}_{c\bar{s}}$. Nevertheless, we will consider different CQM meson masses in the $0^+$ and $1^+$ sectors (Sets A and B in Table 8.1), as discussed in Sec. 8.2.3.

---

[9] We have simplified the discussion and have focused on $f$. An accurate treatment might require to go beyond LO in the chiral expansion, which in turn might create some problems of double counting with the contribution from CQM states. We will come back to this point below.

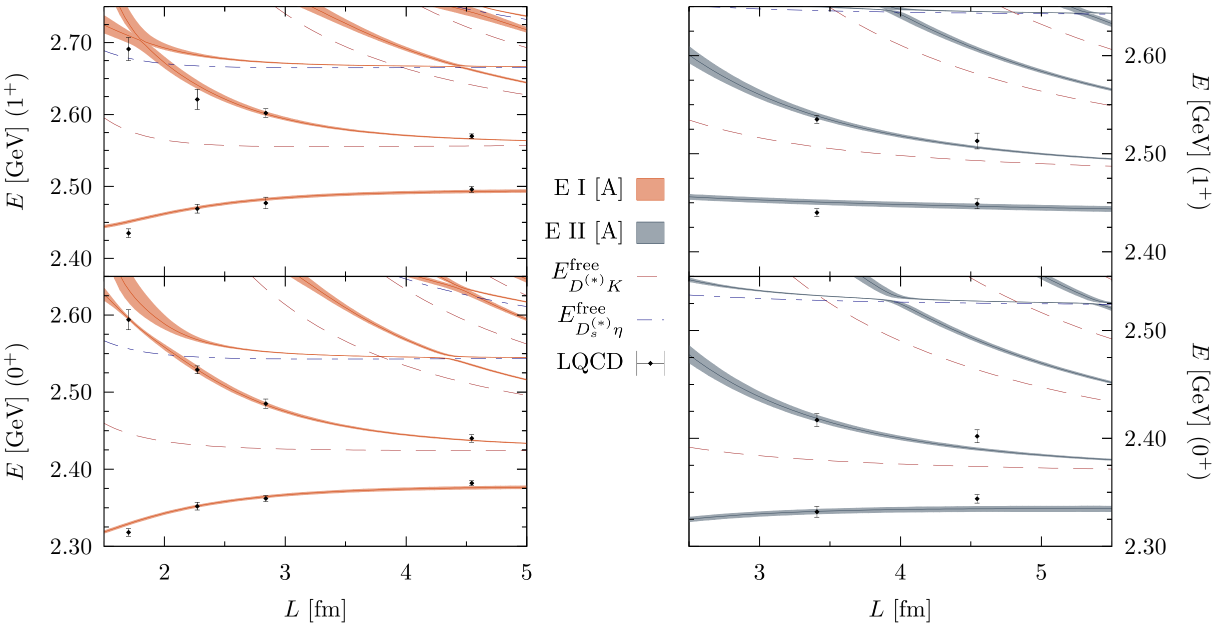

**Figure 8.1:** Black points: LQCD $J^P = 0^+$ (bottom panels) and $J^P = 1^+$ (top panels) energy-levels, taken from Ref. [45], for different volumes and pion masses. LQCD data for Ensembles I and II are depicted in the left and right panels, respectively. Solid lines: Energy-levels obtained from $0^+$ and $1^+$ combined fits to Ensembles I and II using the Set A of CQM bare masses, as a function of the box-size, $L$ (some volume interpolated meson masses are used to compute the continuous energy-levels for values of $L$ different than those employed in Ref. [45]). Details of the fits and some derived quantities are collected in Table 8.3. Statistical 68%-confident level (CL) bands are also shown. They are calculated from the distributions obtained from a sufficiently large number of fits to synthetic sets of LQCD data, randomly generated assuming that each of the LQCD energy-levels is Gaussian distributed. (Note that possible correlations between the different energy-levels are not considered, since these are not provided in Ref. [45].) In addition, in all synthetic fits, the LQCD meson masses for each volume are randomly chosen as well. For comparison, the free energies $E^{\rm free}_j$, $j = D^{(*)}K, D_s^{(*)}\eta$, for each volume and set of LQCD meson masses are also shown (dashed lines).

To determine the values of the LEC $c$, that controls the interplay between CQM and meson-pairs degrees of freedom, and the Gaussian cut-off, we perform, for each set (A and B) of bare CQM masses and lattice ensembles (I and II) a combined fit to the $0^+$ and $1^+$ energy-levels, using an uncorrelated merit function defined as,

$$\chi^2 = \sum_i \left( \frac{E_i^{lat} - E_i^{th}}{\Delta E_i^{lat}} \right)^2 , \tag{8.16}$$

where the sum spans over the $0^+$ and $1^+$ energy-levels compiled in Table III of Ref. [45]. For both $0^+$ and $1^+$ sectors, only two energy-levels for each volume are fitted. We have not considered in the fits the third $1^+$ level given in the last column of that table. It is rather insensitive to the spatial volume, suggesting only a small coupling to the $D^*K$ threshold and, in Ref. [45], it is identified with the $D_{s1}(2536)$ resonance, that would presumably have a large overlap with the $j_{\bar{q}}^P = \frac{3}{2}^+$ HQSS state.

We show in Figs. 8.1 and 8.2 the $0^+$ and $1^+$ energy-levels obtained using sets A and B of CQM bare masses, respectively. Fitted parameters and best fit $\chi^2/dof$ values are

**Table 8.3:** Best fit LO+CQM parameters, together with infinite volume properties (masses, $D^{(*)}K$ and $D_s^{(*)}\eta$ molecular components and couplings) of the lowest-lying $j_{\bar{q}}^P = \frac{1}{2}^+$ $D_s$ charm-strange meson doublet, determined from the fits to the lattice energy-levels obtained for each of the two lattice pion mass ensembles (I and II) calculated in Ref. [45], and using either Set A or B of bare CQM masses (see discussion in Sec. 8.2.3). $S$-wave isoscalar $D^{(*)}K$ scattering lengths ($a$) are also given, which are related to the amplitudes at threshold by $T\left[s = (M_{D^{(*)}} + m_K)^2\right] = -8\pi a\,(M_{D^{(*)}} + m_K)$, as in Ref. [45]. All these infinite volume quantities have been computed using physical meson masses. LQCD energy-levels and those determined in this work are shown in Figs. 8.1 and 8.2. Statistical 68%-CL errors on the best fit parameters and derived quantities are calculated from the distributions obtained after performing a sufficiently large number of fits to synthetic sets of LQCD data, as explained in the caption of Fig. 8.1. In addition, the $c-\Lambda$ correlation coefficients are $-0.81, -0.93, 0.08$ and $-0.80$ for fits AI, AII, BI and BII, respectively. Besides, in the Set C rows, we give the results obtained from a one-parameter (UV cutoff $\Lambda$)-fit that corresponds to an scheme where the LQCD energy-levels are described using finite-volume unitarized LO HM$\chi$PT amplitudes. This is to say, the LEC $c$ is fixed to zero, and therefore the contributions to the amplitudes of the exchange of even-parity charmed-strange CQM mesons are neglected. The volume dependence of the $0^+$ and $1^+$ energy-levels determined within this latter scheme are shown in Fig. 8.3 for the two lattice pion mass ensembles (I and II).

| | | | parameters | | | | infinite volume predictions | | | | | |
|---|---|---|---|---|---|---|---|---|---|---|---|---|
| Set | Ensemble | $J^P$ | $\overset{\circ}{m}_{c\bar{s}}$ [MeV] | $c$ | $\Lambda$ [MeV] | $\chi^2/dof$ | $M_b$ [MeV] | $P_{D^{(*)}K}$ [%] | $P_{D_s^{(*)}\eta}$ [%] | $a_{D^{(*)}K}$ [fm] | $g_{D^{(*)}K}$ [GeV] | $g_{D_s^{(*)}\eta}$ [GeV] |
| A | I | $0^+$ | 2511 | $0.62 \pm 0.04$ | $663^{+23}_{-27}$ | 1.8 | $2335 \pm 2$ | $67 \pm 1$ | $2.1 \pm 0.2$ | $-1.41^{+0.05}_{-0.06}$ | $10.6 \pm 0.2$ | $5.43 \pm 0.08$ |
| | | $1^+$ | 2593 | | | | $2465 \pm 2$ | $57 \pm 1$ | $1.9 \pm 0.2$ | $-1.16^{+0.03}_{-0.04}$ | $12.1^{+0.3}_{-0.2}$ | $5.83 \pm 0.06$ |
| | II | $0^+$ | 2511 | $0.61 \pm 0.09$ | $710^{+70}_{-60}$ | 3.1 | $2331 \pm 3$ | $64 \pm 2$ | $2.4 \pm 0.4$ | $-1.29^{+0.07}_{-0.08}$ | $10.9^{+0.4}_{-0.3}$ | $5.6 \pm 0.1$ |
| | | $1^+$ | 2593 | | | | $2460 \pm 3$ | $55^{+2}_{-1}$ | $2.2^{+0.4}_{-0.3}$ | $-1.07^{+0.05}_{-0.06}$ | $12.2^{+0.5}_{-0.4}$ | $6.0 \pm 0.1$ |
| B | I | $0^+$ | 2383 | $0.71 \pm 0.01$ | $426 \pm 14$ | 18.6 | $2330 \pm 2$ | $51 \pm 1$ | $0.51 \pm 0.06$ | $-1.36 \pm 0.05$ | $11.8^{+0.1}_{-0.2}$ | $4.95 \pm 0.1$ |
| | | $1^+$ | 2570 | | | | $2485 \pm 2$ | $67 \pm 1$ | $0.51 \pm 0.07$ | $-1.79 \pm 0.09$ | $11.0^{+0.2}_{-0.3}$ | $4.9 \pm 0.1$ |
| | II | $0^+$ | 2383 | $0.57^{+0.07}_{-0.08}$ | $580^{+80}_{-50}$ | 18.0 | $2320 \pm 4$ | $45^{+2}_{-1}$ | $1.2^{+0.3}_{-0.2}$ | $-1.04^{+0.09}_{-0.08}$ | $11.0^{+0.5}_{-0.6}$ | $5.0 \pm 0.1$ |
| | | $1^+$ | 2570 | | | | $2477 \pm 4$ | $60 \pm 2$ | $1.3^{+0.4}_{-0.2}$ | $-1.40 \pm 0.1$ | $11.1^{+0.4}_{-0.5}$ | $5.3^{+0.2}_{-0.1}$ |
| C | I | $0^+$ | – | 0 fixed | $1141 \pm 14$ | 4.5 | $2323 \pm 2$ | $65 \pm 1$ | $5.67 \pm 0.07$ | $-1.10 \pm 0.03$ | $10.9 \pm 0.1$ | $6.59 \pm 0.04$ |
| | | $1^+$ | – | | | | $2463 \pm 2$ | $65 \pm 1$ | $5.64 \pm 0.07$ | $-1.08 \pm 0.03$ | $11.7 \pm 0.1$ | $7.03 \pm 0.05$ |
| | II | $0^+$ | – | 0 fixed | $1140 \pm 20$ | 2.5 | $2323 \pm 3$ | $65 \pm 1$ | $5.66 \pm 0.1$ | $-1.11 \pm 0.05$ | $10.9 \pm 0.2$ | $6.58 \pm 0.07$ |
| | | $1^+$ | – | | | | $2463 \pm 3$ | $65 \pm 1$ | $5.64 \pm 0.1$ | $-1.08 \pm 0.04$ | $11.7 \pm 0.2$ | $7.03 \pm 0.07$ |

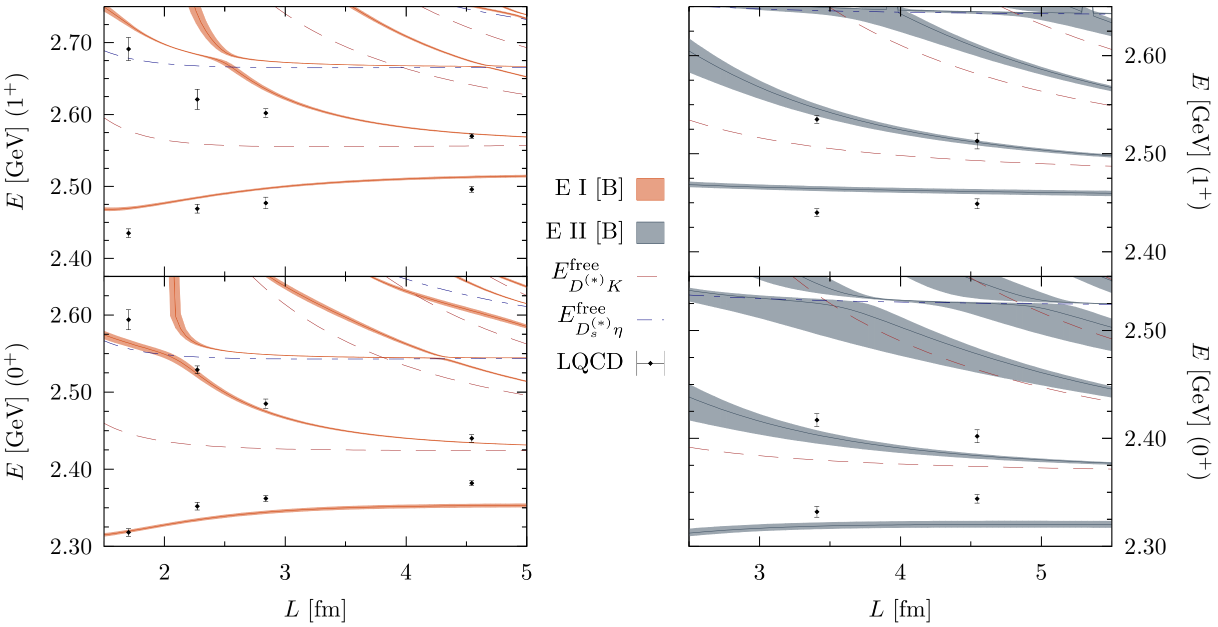

**Figure 8.2:** Same as Fig. 8.1, but in this case the predictions have been obtained using the Set B of CQM bare masses.

**Table 8.4:** Infinite volume properties of the second pole, resonance located above the $D^{(*)}K$ threshold, that appears in the unitarized amplitudes considered in Table 8.3. Note that now the couplings are complex in general, and we only give here the moduli.

| Set | Ensemble | $J^P$ | $M_R$ [MeV] | $\Gamma_R$ [MeV] | $\lvert g^R_{D^{(*)}K}\rvert$ [GeV] | $\lvert g^R_{D_s^{(*)}\eta}\rvert$ [GeV] |
|---|---|---|---|---|---|---|
| A | I | $0^+$ | $2689^{+25}_{-18}$ | $85 \pm 4$ | $3.5^{+0.1}_{-0.2}$ | $3.7 \pm 0.2$ |
| | | $1^+$ | $2772^{+24}_{-18}$ | $98 \pm 5$ | $4.3^{+0.1}_{-0.2}$ | $3.8 \pm 0.2$ |
| | II | $0^+$ | $2684^{+53}_{-45}$ | $85^{+8}_{-13}$ | $3.6^{+0.1}_{-0.5}$ | $3.6 \pm 0.4$ |
| | | $1^+$ | $2767^{+51}_{-44}$ | $98^{+10}_{-16}$ | $4.4^{+0.1}_{-0.4}$ | $3.8 \pm 0.4$ |
| B | I | $0^+$ | $2602 \pm 8$ | $97 \pm 3$ | $3.4 \pm 0.2$ | $4.2 \pm 0.1$ |
| | | $1^+$ | $2797 \pm 7$ | $91 \pm 2$ | $2.2 \pm 0.3$ | $4.6 \pm 0.1$ |
| | II | $0^+$ | $2527^{+33}_{-32}$ | $101^{+7}_{-17}$ | $4.9^{+0.1}_{-0.3}$ | $3.2 \pm 0.3$ |
| | | $1^+$ | $2713^{+36}_{-35}$ | $88^{+5}_{-12}$ | $4.5^{+0.2}_{-0.4}$ | $3.5^{+0.4}_{-0.3}$ |

collected in Table 8.3.

We see that the Set A of bare CQM masses provides a fairly good description of the volume dependence of the LQCD energy-levels in both the $J^P = 0^+$ and $1^+$ sectors, despite the large deviations from the free levels. There exists a very mild dependence of the UV cutoff and LEC $c$ on the pion mass, which however is not statistically significant. The $D_s^{(*)}\eta$ coupled channel effects are negligible, except perhaps for the highest levels calculated with the heaviest pion mass ensemble at the smallest of the volumes, since that threshold is located sufficiently more higher than the measured levels in Ref. [45]. (Note that $D_s^{(*)}\eta$ correlators are not considered in the LQCD study of the latter reference.) We find $c = 0.61(9)$ and $\Lambda = 710(70)$ MeV from the fit to the lightest pion mass ensemble.

This parameter is also determined in Chapter 9—based on Ref. [4]—from a similar analysis of the LQCD low-lying $0^+$ and $1^+$ $B_s-$energy-levels calculated in Ref. [58]. There, we shall see that we find $c = 0.75(6)$, with an UV cutoff in the range 620-770 MeV, which points out to some small dependence of the LEC $c$ on the heavy-flavour mass.

On the other hand, when the Set B of $0^+$ and $1^+$ CQM bare masses are used, we find unacceptable fits, with $\chi^2/dof$ values much larger than 1—above 18 for both pion mass ensembles. Indeed, as can be seen in Fig. 8.2, the set B leads to a really poor description of the LQCD data. For the latter, the HQSS breaking corrections thus look *i)* compatible with those encoded in the current scheme when the Set A of bare masses is used, but *ii)* much smaller than those implemented by the Set B of bare masses. The one-loop corrections [354] to the OGE potential implemented in Ref. [356] produce a $1^+ - 0^+$ shift of the bare CQM masses of around 190 MeV, while it is around only 80 MeV when these corrections are neglected (see Table 8.1). This is because, as we already mentioned, this correction mostly affects the $0^+$ sector [354]. Actually, because of the denominator in Eq. (9.3) and for fixed $c$ and $\Lambda$, the decrease of the $0^+$ bare mass produces an enhancement of the attraction close to the $DK$ threshold from the exchange of the CQM state. This effect is much less important in the $1^+$ sector, and thus the current scheme using Set B of bare masses produces a visible tension between the predicted $0^+$ and $1^+$ levels and the LQCD data (Fig. 8.2). The scheme tends to overestimate (underestimate) the attraction in the former (latter) energy-levels by around 10-20 MeV, amount significantly larger than the errors of the LQCD data. Therefore, this study strongly disfavors the bare masses found in Ref. [356], where the one-loop corrections derived in Ref. [354] are taken into account. These one-loop corrections to the OGE potential produced a much smaller HQSS breaking of the bare masses in the bottom sector, and thus nothing statistically meaningful could be concluded about this issue in the analysis carried out in Ref. [4] of the $B_s-$energy-levels reported in Ref. [58]. Due to the former discussion, we will always make reference to the results obtained from the Set A of CQM bare masses in the rest of the work.

Next, and once the parameters of the model have been fixed, we search for poles in the FRS (bound states) and SRS (resonances) of the isoscalar $S$-wave $D^{(*)}K$ and $D_s^{(*)}\eta$ amplitudes for the infinite volume case and using physical meson masses. For both sets of CQM bare masses, and in both $J^P = 0^+$ and $1^+$ sectors, we find a bound state (FRS) and a resonance (SRS). The masses and couplings [see Eq. (2.93)] of the lowest-lying $j_{\bar{q}}^P = \frac{1}{2}^+$ charm-strange meson doublet are compiled in Table 8.3, together with the $0^+$ and $1^+$ isoscalar $D^{(*)}K$ scattering lengths and the probabilities of the molecular $D^{(*)}K$ and $D_s^{(*)}\eta$ components [see Eq. (8.11)]. The properties of the additional $0^+$ and $1^+$ states, resonances located above the $D^{(*)}K$ threshold, are compiled in Table 8.4 for the different schemes presented in the previous table.

### Properties of the lowest-lying states: masses, molecular probabilities and couplings

We first pay attention to the mesons of the lowest-lying $j_q^P = \frac{1}{2}^+$ $D_s$ doublet. We see that the predicted mass of the $0^+$ bound state, using Set A of CQM bare masses, is only around 15 MeV higher than the experimental mass of the $D^*_{s0}(2317)$ and 75-80 MeV smaller than the CQM bare mass, while that of the $1^+$ nicely agrees, taking into account the errors, with the experimental mass of the $D_{s1}(2460)$ state. Nevertheless, this level of discrepancy can be well attributed to the presence of discretization errors, or some uncertainties in the determination of the mass of the charm quark in the lattice simulation. Actually, the results compiled in Table I of Ref. [45] show discrepancies of the order of 10 MeV between the experimental masses of the $D$ and $D^*$ mesons and the LQCD ones, determined from the lightest quark mass, which provides almost physical pion masses. We should also note some differences (1-2 $\sigma$'s) between the $0^+$ and $1^+$ masses found in this work and those reported in Table VII of Ref. [45], taken from the $m_\pi = 150$ MeV and $L = 64a$ ensemble. These might be due to the use here of physical meson masses, and also because the LQCD ones are accessed via the Lüscher's relation [Eq. (8.13)] using the effective range approximation. The approach followed here, where the two meson loop function is computed in a finite volume, the unknown LECs are determined from fits to the LQCD data, and finally poles are searched for in the infinite volume unitarized chiral amplitudes, provides a theoretically sound tool to analyze the LQCD energy-levels. A good example of the latter affirmation can be found in Ref. [3], where such approach led to the existence of two $D^*_0(2400)-$poles, instead of only one reported in the original lattice work of the Hadron Spectrum Collaboration [81], where the LQCD energy-levels were calculated (see also the discussion in Ref. [6], where it is emphasized how the two-pole pattern of the $D^*_0(2400)$, together with their SU(3) structure, provides a natural solution to a number of puzzles).

Interestingly, we appreciate in Fig. 8.1 a quite significant dependence of the lowest-lying LQCD energy-levels on the pion mass (differences between left and right plots), as it is also evident in the results of Table IV of Ref. [45]. Thus, the LQCD $0^+$ and $1^+$ masses reported in that table vary between 30 to 50 MeV, when the pion mass is reduced from 290 MeV down to 150 MeV. These changes are likely related to the modifications of the $DK$ and $D^*K$ thresholds. All of this clearly indicates that the $D^*_{s0}(2317)$ and $D_{s1}(2460)$ states should have a sizeable molecular component, and that any CQM $c\bar{s}$ component in their dynamics cannot be dominant, because it could not accommodate such visible dependence of their masses on the light quark mass, as exhibited by the LQCD data. These findings are corroborated by the molecular probabilities collected in Table 8.3. Using the modified Weinberg compositeness condition of Eq. (8.11), we derive the molecular $S$-wave $D^{(*)}K$ probabilities for the $D^*_{s0}(2317)$ and $D_{s1}(2460)$, which turn out to be around 65% and 56% for the scalar and axial states, respectively. On the other hand, $D^{(*)}_s\eta$ components are small for both mesons, of the order of 2%. The LQCD studies of Ref. [45–47] showed a non-zero overlap of the energy-levels related to the $D^*_{s0}(2317)$ and $D_{s1}(2460)$ and meson-meson lattice interpolating fields, but no precise information was provided on the percentage of meson-meson channels in the wave function of these states. Only in the latest work of Ref. [45], the compositeness probability is studied, and found to be 1 within errors (around 20-30%) for both states.

The large molecular probabilities found in this work confirm those reported in previous works [44,205,245] that, employing also unitarized meson-meson amplitudes, had already obtained molecular components of around 70% for the $D^*_{s0}(2317)$, as mentioned in the Introduction. In what respects the $D_{s1}(2460)$, the authors of Ref. [245] found a molecular probability of $0.57 \pm 0.22$ also in good agreement with our findings, although with a much larger error. The interesting and novel aspect of the present calculation is that the LO HM$\chi$PT interactions have been supplemented by those driven by the exchange of even-parity charmed-strange CQM mesons, and thus the couplings of CQM $c\bar{s}$ and $P^{(*)}\phi$

degrees of freedom have been explicitly taken into account.[10]

In Ref. [342] two-meson loops and CQM bare poles are also coupled. For the latter, the values of the bare masses are the same as those used here. The $D^{(*)}K$ interactions are derived from the same CQM used to compute the bare states, instead of using HM$\chi$PT. The $^3P_0$ model is employed to couple both types of degrees of freedom, and the quark model wave functions provide form-factors that regularize the meson loops. Thus, all the inputs in this approach are constrained/determined from previous studies. The masses of the $0^+$ and $1^+$ states found in Ref. [342] are about 10 and 25 MeV higher than the experimental ones, respectively. The coupling of the CQM mesons to the $DK$ and $D^*K$ thresholds is crucial to simultaneously lower the masses of the corresponding $D_{s0}^*(2317)$ and $D_{s1}(2460)$ states predicted by the naive quark model. Such effects are of the order of 60 and 85 MeV in the $0^+$ and $1^+$ sectors, respectively. However, in the study carried out in Ref. [342], the one-loop corrections derived in Ref. [354] are taken into account, and they lower the predicted mass of the $D_{s0}^*(2317)$ by more than 100 MeV. To this respect, we should repeat once more that the simultaneous analysis of the $0^+$ and $1^+$ LQCD energy-levels of Ref. [45] carried out in this work strongly disfavors such corrections. Molecular probabilities are reported in Ref. [342] to be around 33% and 54% for the $D_{s0}^*(2317)$ and $D_{s1}(2460)$, respectively. Though the latter one turns out to be in a nice agreement with our results, the former one is around twice smaller than that found here and in previous works [44, 205, 245], and it would contradict a dominant molecular picture for the $D_{s0}(2317)$. Moreover, this disparity between the molecular components in the scalar and axial states might also question that the $D_{s0}^*(2317)$ and $D_{s1}(2460)$ could form a HQSS doublet. Within our scheme, it is however natural to assign these two states to the $j_{\bar{q}}^P = 1/2^+$ HQSS doublet, assignation that gets further support from the observation that the experimental mass splitting between these two resonances is remarkably similar to that between the $D$ and $D^*$ mesons. Furthermore, interpreting the $D_{s0}^*(2317)$ and $D_{s1}(2460)$ as $DK$ and $D^*K$ bound states, the binding energies of both states will be very similar (approximately 46 MeV versus 54 MeV).

The couplings of the $D_{s0}^*(2317)$ and $D_{s1}(2460)$ to $D^{(*)}K$ and $D_s^{(*)}\eta$ are also compiled in Table 8.3. We see that the coupling of both states to the latter channel, though around a factor two smaller than to $D^{(*)}K$, is not negligible.[11] The analysis adopted in the original LQCD work of Ref. [45] led to $g_{D^{(*)}K}$ couplings of $11.0 \pm 1.3$ GeV and $13.8 \pm 1.3$ GeV for the $D_{s0}^*(2317)$ and $D_{s1}(2460)$, respectively. These values are in good agreement with the values found in this work. We would like to stress that the clear similarities between the couplings of both resonances reinforces our conclusion that they form a HQSS doublet. Moreover, as we shall discuss in next Chapter 9, $D_{s0}^*(2317)$ and $D_{s1}(2460)$ should be

---

[10] Other studies have done something similar (*e.g.* Ref. [245]) by including in the interactions a Castillejo-Dalitz-Dyson pole [364] to visualize a genuine (CQM) state that couples weakly to a meson-meson component. However, those studies do not make use of the HQSS to relate the interplay between both types of degrees of freedom in the $0^+$ and $1^+$ sectors, which will be fundamental to disfavor the Set B of CQM bare masses used in the study of Ref. [342], that will be discussed in the next paragraph, and that claimed a much smaller (∼30%) molecular components for the $D_{s0}^*(2317)$. Moreover, in some of these studies chiral symmetry is not fully used to constraint the $P^{(*)}\phi$ interactions, and different solutions were obtained with many sets of parameters, obviously correlated, though the claim in Ref. [245] was that the particular values of the parameters did not have a special significance, and all of them led to similar hadronic-molecular probabilities [245].

[11] The much larger differences found for the molecular probabilities are due, not only because it appears the square of the couplings, but also because the large distance of the $D_s^{(*)}\eta$ thresholds to the masses of the resonances.

heavy-flavour partners of the $\bar{B}_s$ scalar and axial mesons found in Ref. [4] at $5709 \pm 8$ and $5755 \pm 8$ MeV, respectively. Note that the mass shift, due to the breaking of HQSS, is much smaller in the bottom sector, and it turns out to be quite similar to $(M_{\bar{B}^*} - M_{\bar{B}})$, as expected.

### $D^{(*)}K$ scattering lengths

The $D^{(*)}K$ scattering lengths are negative (see Table 8.3), compatible with the interpretation of the $D_{s0}^*(2317)$ and $D_{s1}(2460)$ as bound states. Indeed, the zero-range approximation, $a_0 = -1/(2\mu B)^{\frac{1}{2}}$ [$B > 0$ and $\mu$ are the $D^{(*)}K$ binding energy and reduced mass, respectively], provides already the first significant digit ($-1$ fm). This simple formula also anticipates that $|a_{DK}| > |a_{D^*K}|$. Our predictions for the scattering lengths are consistent, within errors, with previous lattice determinations [45–47], particularly with the reanalysis of Ref. [245]; the bulk of the small differences existing among central values can be explained in terms of the differences between binding energies. The uncertainties on our estimates are significantly smaller than those affecting the LQCD ones. This is in line with the previous discussion about the errors on the masses of the $D_{s0}^*(2317)$ and $D_{s1}(2460)$ resonances, and it shows, once more, that the present analysis of the LQCD energy-levels leads to more precise results than those based on the Lüscher's relation using the effective range approximation.

### Second pole: resonances

Within the current scheme, the amplitudes include an explicit pole. It is therefore reasonable to assume that the CQM bare state does not disappear, but it gets dressed by the meson-meson interaction moving into the complex plane. In addition to a mass shift, the new state acquires a width since it can decay into $S$-wave $D^{(*)}K$ and $D_s^{(*)}\eta$ meson-pairs. The position and couplings of these extra poles, located in the SRS of the amplitudes, are collected in Table 8.4. We see that both in the $0^+$ and $1^+$ sectors, the resonances are relatively broad (85(4) and 98(5) MeV), respectively) and have similar couplings[12] to $D^{(*)}K$ and $D_s^{(*)}\eta$. On the other hand, the couplings of these resonances to $D^{(*)}K$ are around a factor of three smaller than those of the $D_{s0}^*(2317)$ and $D_{s1}(2460)$ states.

The masses of these higher states are 175 (330) and 110 (270) MeV above the $D_s^{(*)}\eta$ ($D^{(*)}K$) threshold. Thus, we should take these results with some caution, since most likely they should be affected by sizeable higher order chiral corrections and higher threshold-channels corrections. In other words, they are not as theoretically robust as those concerning the lowest-lying $D_{s0}^*(2317)$ and $D_{s1}(2460)$ states. As mentioned, these additional resonances are likely originated from the bare $c\bar{s}$-quark-model poles that are dressed by the $D^{(*)}K$ and $D_s^{(*)}\eta$ meson loops. In that case, the bare poles have been highly renormalized, moving to significant higher masses and acquiring a significant width. We should also bear in mind that radial excitations ($2^3P_0$) of the CQM states [26] or $D^{(*)}K^*$ two-meson loops, neither of them taken into account in this study, might lie in this region of energies, then having a certain impact in the dynamics of these resonances.

---

[12] The couplings are now complex in general, and we refer to the moduli.

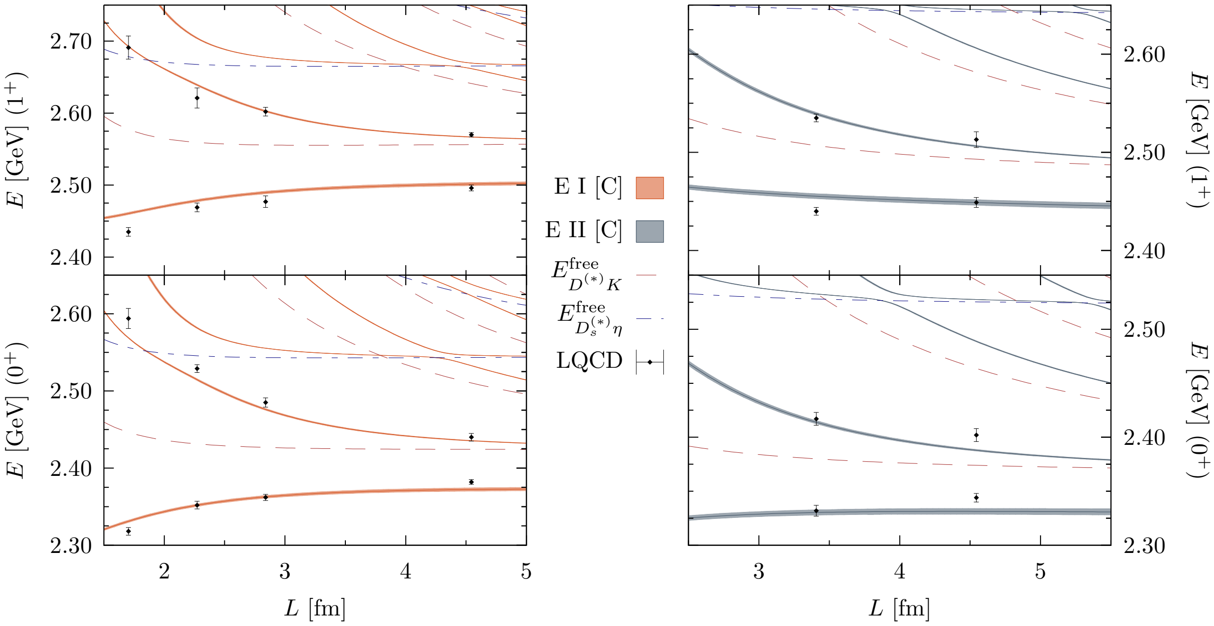

**Figure 8.3:** Same as Fig. 8.1, but in this case the predictions have been obtained after neglecting the contribution to the amplitudes of the exchange of intermediate even-parity charmed-strange CQM mesons, *i.e.*, setting $c = 0$ and evaluating the energy-levels using finite-volume unitarized LO HM$\chi$PT amplitudes. The best fit UV cutoff in this scenario and some derived quantities are given in the Set C rows of Table 8.3.

## 8.3.2 LO and NLO unitarized HMChPT analysis

### LO HMChPT energy-levels

In addition to the results shown in the previous sections, where a CQM pole was added to the LO $D^{(*)}K$ interaction, it is enlightening to discuss whether we are able to describe the lattice data without any CQM $c\bar{s}$ contribution. To explore this scenario, we have performed an additional one-parameter (UV cutoff $\Lambda$)-fit, where the LQCD energy-levels are described using finite-volume unitarized LO HM$\chi$PT amplitudes. Thus the LEC $c$ is set to zero, and consequently the contribution to the amplitudes of the exchange of the CQM mesons vanish as well. This fit is labelled as Set C in Table 8.3, and the obtained $0^+$ and $1^+$ energy-levels, as a function of the box-size, are shown in Fig. 8.3.

We find a quite reasonable description of the LQCD data, and the infinite volume properties of the lowest-lying states agree well with those deduced using the Set A of CQM bare masses, though molecular probabilities and couplings of the $D_{s1}(2460)$ and $D^*_{s0}(2317)$ are now much more similar.[13] Note that the CQM exchange potential induces some HQSS breaking corrections, driven by the $0^+$ and $1^+$ $c\bar{s}$ bare mass-shift, and the fact that these contributions have been eliminated might explain the found pattern of probabilities and couplings. The more distinctive difference, however, is that the UV cutoff is around 1100 MeV. This is to say, the new UV cutoff is around 400 MeV higher than the values needed when the contribution of the CQM meson exchanges are kept. That reveals that higher order chiral corrections, previously effectively accounted for by

---

[13] We find $P_{D^{(*)}K} \sim 65\%$ and $P_{D_s^{(*)}\eta} \sim 6\%$ for both states, and adding the probabilities, we obtain molecular components above 70% in the wave-functions of both mesons. On the other hand, the higher $D_s^{(*)}\eta$ channel becomes also more important in their dynamics.

means of the CQM pole, are not negligible. Conversely, taking into account explicitly the exchange of (bare) CQM mesons is not crucial to describe the $D^*_{s0}(2317)$ and $D_{s1}(2460)$ states, because such contributions can be accommodated by appropriately modifying the finite contributions derived from short-distance physics. This is expected since the CQM bare states lie far from the latter physical states, for which the unitarity meson loops play a fundamental role.

The UV cutoff $\Lambda$ is expected to be larger than the wave number of the states ($\sim 200$ MeV) and, at the same time, small enough to prevent it from inducing large HQSS breaking corrections. From this perspective, one might think that values in the range of 1.1 GeV, comparable to the mass of the charm quark, do not seem appropriate within the spirit of an EFT based on HQSS. However, one should bear in mind that here we are using a Gaussian UV regulator, which will approximately correspond to a sharp-cutoff, $q_{\rm max}$, smaller by a factor[14] $\sqrt{\pi/8}$ [347]. Thus, in terms of a sharp-cutoff, we are dealing with values of the order of 700 MeV that are more acceptable from the point of view of a HQSS EFT.

The Set A of Gaussian regulators found in Sec. 8.3.1 would correspond to sharp cutoffs of the order of 400-450 MeV, which are still larger than the wave number of the $D^*_{s0}(2317)$ and $D_{s1}(2460)$ states. Nevertheless, we should remind here that the CQM bare masses are not observables, and they depend on the UV renormalization. Here we have fixed the CQM masses, and thus the fitted cutoffs should be understood as those needed to effectively account for higher order chiral corrections, when these bare poles are incorporated [341]. This also hints to a certain scale for which the CQM of Ref. [342] might match the chiral EFT.

### NLO HMChPT energy-levels

Within this context, it seems appropriate to calculate the energy-levels obtained from the unitarized HM$\chi$PT NLO amplitudes [198] described in Sec. 8.2.4. As in the previous subsection, the exchanges of CQM bare poles are not included. Indeed, as we have discussed above, considering such contributions, together with the NLO corrections, might lead to some double-counting problems.

The UV divergences are renormalized in Ref. [198] by using subtracted meson loop functions instead of a sharp-cutoff. However, both schemes can be related (see for instance the discussion in Sec. 4.5.1 in Chapter 4), and the subtraction constants determined in [205] correspond, in good approximation, to a sharp-cutoff $q_{\rm max} = 0.72^{+0.07}_{-0.06}$ GeV, similar to the values mentioned in the previous discussion.

Results are shown in Fig. 8.4, where we see that this scheme provides a more than acceptable description of the $0^+$ and $1^+$ LQCD data, for both pion mass ensembles, despite having set all LECs to the values determined in Ref. [205]. We emphasize that, therefore, the energy levels shown in the different panels of the figure are predictions and do not imply any fine adjustment of any type of parameter.[15] We find this remarkable, and

---

[14] Note that the Gaussian regulator introduced in [347] and that used here are related by an extra factor $1/\sqrt{2}$.

[15] We should mention that the unitarized NLO HM$\chi$PT description of the LQCD energy levels shown in Fig. 8.4 might be improved by allowing for a slight variation of the LECs, which could, for example, effectively account for some discretization/finite volume errors etc. Note that, in addition, these systematic errors could be also different to those affecting the lattice study of scattering lengths carried out in Ref. [205]. Nevertheless, the second levels are quite far from the thresholds, and one might need to

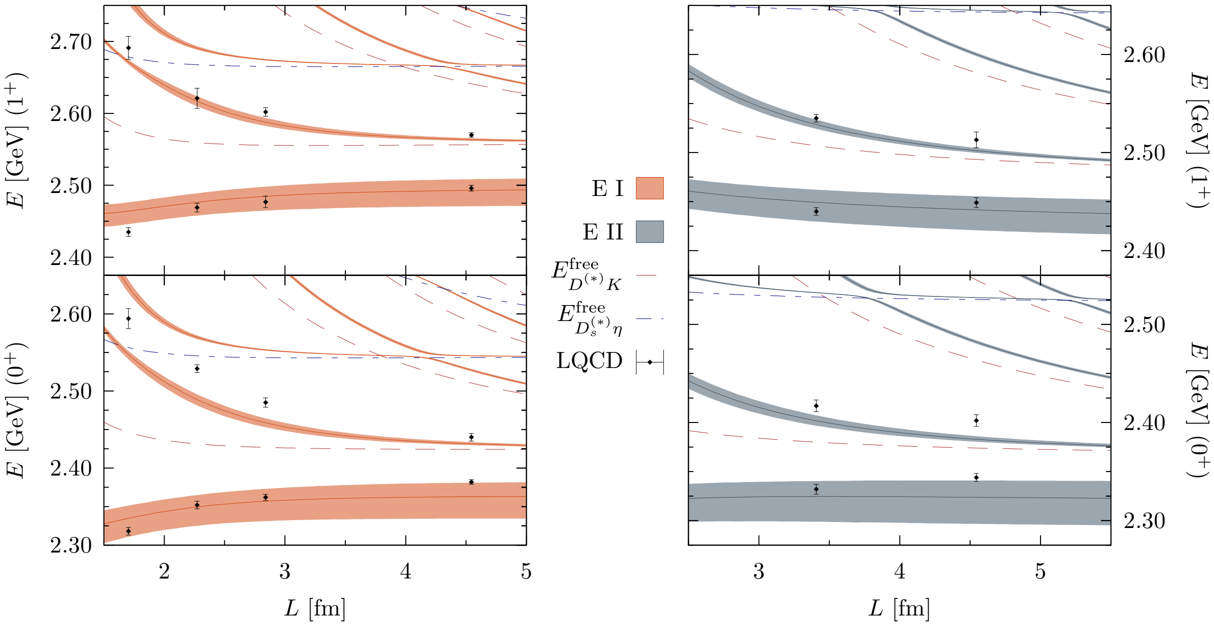

**Figure 8.4:** Volume dependence of the energy levels predicted using the unitarized NLO HM$\chi$PT amplitudes of Refs. [198, 205] compared to the lattice results of Ref. [45]. Exchanges of intermediate CQM mesons are not included, and the distribution of panels is the same as in Fig 8.1. There are no fitted parameters involved in these predictions since all LECs that appear in the definition of the chiral amplitudes were determined from the lattice calculation [205] of the $S$-wave scattering lengths in several $(S, I)$ sectors. The 68% CL uncertainty bands depicted in the plots are inherited from the errors on the LECs quoted in Ref. [205].

together with the similar good description found in Chapter 4 of the $(S, I) = (0, 1/2)$ LQCD low-lying energy levels calculated in Ref. [81], provides a great support for the UHM$\chi$PT amplitudes derived in Refs. [198,205]. Hence, the $D^*_0(2400)$ two-pole structure and the SU(3) pattern $D^*_1$ resonance (located at $2240(6) - i93(9)$ MeV) and of the $0^+$ and $1^+$ heavy-light sectors claimed in Chapter 4 seem rather robust from the theoretical point of view. As we have already discussed in Chapter 5, all these results reinforce the new paradigm to study the spectrum of heavy-light mesons [6], and that questions its traditional interpretation in terms of constituent $Q\bar{q}$ degrees of freedom.

### 8.3.3 $DK$ $S$-wave phase shifts

Here we will show predictions for $DK$ $S$-wave scattering phase shifts [see Eq. (2.64)], and will take the opportunity to discuss few aspects of the renormalization dependence of the scheme. For the sake of brevity, we will not address the rest of channels. In this subsection, we will always show results obtained for infinite volume, using physical meson masses, and the Set A of bare masses to incorporate the CQM degrees of freedom.

The behaviour of the phase shifts at threshold depends strongly on the position of the $S$-wave $DK$ pole, as can be seen in the bottom panel of Fig. 8.5. Thus, and to make the discussion meaningful, we will consider approaches leading to the same $D^*_{s0}(2317)$ mass value, $2315^{+18}_{-28}$, obtained in the NLO UHM$\chi$PT approach [198, 205], and whose central value is quite close to the experimental one. Details can be found in Table 8.5, while the related phase shifts are shown in the left panels of the first two rows in Fig. 8.5.

**NLO vs CQM+LO: Poles, couplings and compositeness.** Looking at the results of Table 8.5, we first stress the dependence of the UV cutoff on the LEC $c$, or *viceversa* the dependence of $c$ on $\Lambda$, for a fixed CQM bare mass. The latter should be also understood as a renormalization scheme dependent quantity. All these three parameters $(c, \Lambda, \overset{\circ}{m}_{c\bar{s}})$ should effectively incorporate higher order chiral corrections beyond LO, and not accounted by the unitarity loops. One expects that these further corrections should be rather independent of the short distance physics at energies moderately far from threshold. However predictions might significantly differ, lets us say above 2450 or 2500 MeV. Indeed, we have an indication from the masses and widths of the possible second (higher resonance) state compiled in the table. We see that for $c = 0.3$, a narrow resonance (28 MeV) is generated at around 2557 MeV, that would produce clear signatures, not seen, in the second energy level calculated in Ref. [45]. The other schemes either do not generate any resonance ($c = 0$ and NLO) or it is located close to 2700 GeV ($c = 0.61$) and it is sufficiently broad to become unnoticed for energies below 2600 MeV. The conclusion is that the $c = 0.3$ predictions above 2500 MeV are unreliable, and that the exact location of the resonance generated for $c = 0.61$ is not well constrained by the data of Ref. [45]. On the other hand, we appreciate a variation pattern for $c$ consistent with the physical interpretation of this LEC, and thus the total molecular probability decreases from $(67 \pm 10)\%$ down to $(60 \pm 9)\%$, when $c$ varies from 0 to 0.61. Scattering lengths are mostly determined by the common $D^*_{s0}(2317)$ mass and do not show statistically significant variations, as it also occurs for the couplings. Paying attention now to the NLO results, we find that they

---

explicitly include higher order chiral corrections. Otherwise, the re-fitted NLO LECs would be biased, since they would effectively account for those contributions. All of this is beyond the scope of the present work.

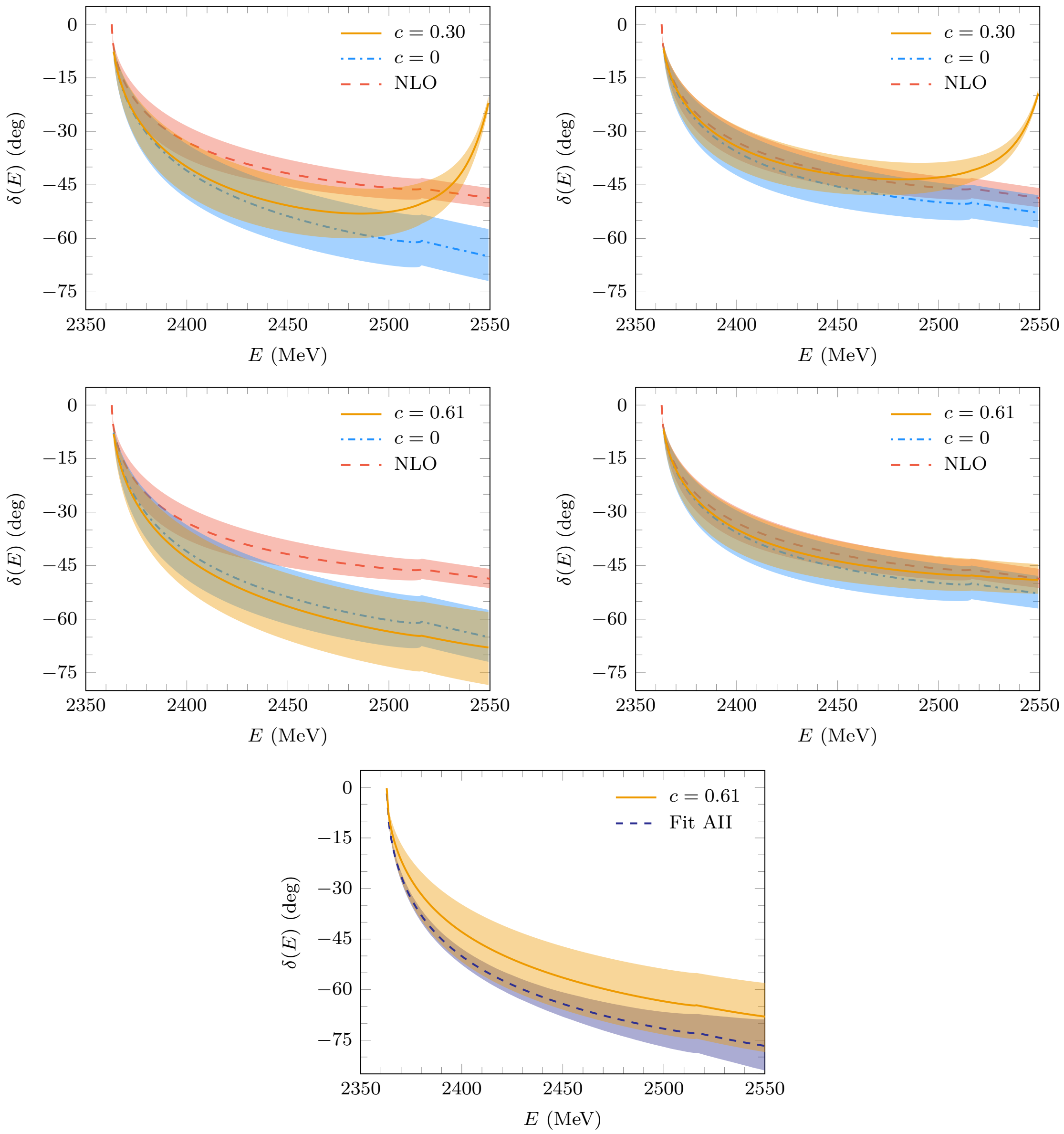

**Figure 8.5:** First two rows of plots: energy dependence of the $DK$ $S$-wave phase shifts obtained using the chiral unitarized approach of Refs. [198, 205] (NLO) compared with the results deduced including the exchange of a CQM state of mass 2511 MeV (Set A). Predictions for three different values of the dimensionless LEC $c$, that controls the strength of the coupling of the bare CQM meson and the $P\phi$−pair, are depicted. Note that in the case $c = 0$, the approach reduces to unitarized LO HM$\chi$PT. In the left (right) panels the UV divergences, that appear in the unitarization of the LO HM$\chi$PT +CQM amplitudes, have been renormalized using a Gaussian cutoff (subtraction constant). For details see Tables 8.5 and 8.6. The UV behaviour of the NLO unitarized amplitudes is always renormalized using subtraction constants [198, 205]. Statistical 68%-CL error-bands are generated from the uncertainties of the LECs that enter in each scheme. Bottom plot: comparison of phase shifts for $c = 0.61$ using two different UV Gaussian cutoffs, $0.71^{+0.07}_{-0.06}$ GeV and $0.81^{+0.17}_{-0.12}$ GeV. The first value corresponds to Fit AII of Table 8.3, and the uncertainty of ±0.09 quoted there for the the LEC $c$ is also considered to obtain the statistical 68%-CL error-band. The second UV cutoff is that associated to $c = 0.61$ in Table 8.5, and the deduced phase shifts are also shown in the left panel of the second row of plots in this figure. Both sets of LECs produce different $D_{s0}^*(2317)$ masses, $2331 \pm 3$ MeV (Table 8.3) and $2315^{+18}_{-28}$ MeV (Table 8.5), respectively. In all cases, physical masses have been used.

**Table 8.5:** Three different sets of $c-\Lambda$ pairs leading to the same $D_{s0}^*(2317)$ mass ($2315^{+18}_{-28}$) obtained from the unitarized LO HM$\chi$PT +CQM approach. The UV cutoff $\Lambda$ is fitted to reproduce the above mass, that it is deduced from the unitarized NLO HM$\chi$PT $T-$matrix [205]. The uncertainties in the $D_{s0}^*(2317)$ mass, inherited from the errors on the LECs, are taken into account and lead to the errors on $\Lambda$. We first generate synthetic sets of LECs, according to the correlated error distributions given in Ref. [205]. Next, we find the position of the $D_{s0}^*(2317)$ pole for each set of LECs, and finally, for each parameter $c$, we tune the UV cutoff to reproduce this mass. In this way, we determine the error distributions of the cutoffs that are also used to estimate the uncertainties on the derived quantities ($S$-wave $DK$ scattering length, mass and width of the higher—dressed—resonance, $D_{s0}^*(2317)$ molecular probabilities and couplings) given in the table. Predictions for the latter quantities from the unitarized NLO HM$\chi$PT approach [198, 205] are compiled in the last row. Finally note that the choice $c = 0.61$ is motivated by the Set A of results in Table 8.3, which $0^+$ CQM bare mass is always employed in this table.

| $c$ | $\Lambda$ [GeV] | $M_{D_{s0}^*}$ [MeV] | $g_{DK}$ [GeV] | $g_{D_s\eta}$ [GeV] | $P_{DK}$ [%] | $P_{D_s\eta}$ [%] | $a_{DK}$ [fm] | $M_R$ [MeV] | $\Gamma_R$ [MeV] |
|---|---|---|---|---|---|---|---|---|---|
| 0 | $1.19^{+0.18}_{-0.13}$ | $2315^{+18}_{-28}$ | $11.3^{+0.7}_{-1.0}$ | $6.7^{+0.2}_{-0.4}$ | $61^{+8}_{-10}$ | $5.9^{+0.3}_{-0.7}$ | $-1.00^{+0.23}_{-0.30}$ | – | – |
| 0.30 | $1.05^{+0.18}_{-0.13}$ | $2315^{+18}_{-28}$ | $11.2^{+0.7}_{-1.0}$ | $6.3^{+0.3}_{-0.4}$ | $58^{+8}_{-9}$ | $4.7^{+0.4}_{-0.7}$ | $-0.98^{+0.23}_{-0.30}$ | $2557^{+1}_{-2}$ | $28^{+2}_{-4}$ |
| 0.61 | $0.81^{+0.17}_{-0.12}$ | $2315^{+18}_{-28}$ | $11.7^{+0.7}_{-1.0}$ | $6.0^{+0.3}_{-0.5}$ | $57^{+8}_{-9}$ | $3.0^{+0.6}_{-0.7}$ | $-1.04^{+0.24}_{-0.31}$ | $2686^{+7}_{-5}$ | $90^{+2}_{-6}$ |
| NLO | | $2315^{+18}_{-28}$ | $9.5^{+1.2}_{-1.1}$ | $7.5 \pm 0.5$ | $54 \pm 4$ | $13^{+6}_{-10}$ | $-0.84^{+0.17}_{-0.23}$ | – | – |

coincide reasonably well with those found using LO HM$\chi$PT amplitudes, thanks to the freedom in the latter to re-adjust the cutoff. Finally, it could be surprising that the $DK$ molecular probability, obtained within the NLO scheme, is only $54 \pm 4\%$, when a value of $\sim 70\%$ was claimed in the original work of Ref. [205]. This discrepancy is due to the use in the latter work of the Weinberg compositeness rule [244], that provides the molecular probability in terms of the scattering length and the $DK$ wave number $\gamma_B$,

$$P_{DK} \sim -\frac{a_{DK}}{a_{DK} + 2/\gamma_B}, \quad \gamma_B = \sqrt{2\mu B}, \tag{8.17}$$

which leads to one, in the limiting case when the scattering length is approximated by $-\gamma_B^{-1}$ (very loosely bound states), neglecting finite effective range corrections. Indeed, using the relation of Eq. (8.17), one obtains $P_{DK} \sim 70 \pm 4$ %, as obtained in Ref. [205]. Note, however, that Eq. (8.17) has corrections due to the $D_{s0}^*(2317)$ binding energy [245], which is not too small ($\sim 46$ MeV), and possible inelastic effects [358], which should bring the 70% down to the more accurate estimate found in the present work.

**NLO vs LO+CQM: phase shifts.** Coming back to the phase shifts shown in the left panels of Fig. 8.5, we see that different schemes produce compatible phase shifts close to threshold, while the differences become larger as the energy increases. Thus for instance, the $c = 0.3$ phase shifts suddenly change curvature above 2500 MeV, but as we discussed above such behaviour, produced for a narrow resonance at 2557 MeV (see Table 8.5), is not compatible with the higher $0^+$ LQCD energy level reported in Ref. [45]. Above 2450 MeV the rest of schemes lead to differences in the phase shifts of few degrees, and at most of around 15° at 2550 MeV. However, taking into account the uncertainties of the different predictions, phase shifts are almost compatible up to this latter energy.

**Regularization dependence.** We now discuss about the dependence of the analysis on the regulator scheme. To this end, instead of the Gaussian form factor UV regulator (Eq. (A.2)), we consider a LO+CQM scheme where the loop matrix function $G$ is renormalized by one subtraction (see Eq. (A.1) in Appendix A)—as in the case of NLO UHM$\chi$PT amplitudes. Suppressing the indices, the loop function is equivalently written for each channel as,

$$G(s) = \bar{G}(s) + G[(M+m)^2]. \tag{8.18}$$

The finite function $\bar{G}(s)$ can be found in Eq. (A9) of Ref. [133]. On the other hand, the constant $G[(M+m)^2]$ contains the UV logarithmic divergence. After renormalizing using dimensional regularization, one finds,

$$\begin{aligned} G[(M+m)^2] &= \frac{1}{16\pi^2}\Big(a(\nu) + \\ &\quad \frac{1}{M+m}[M \ln\frac{M^2}{\nu^2} + m \ln\frac{m^2}{\nu^2}]\Big) \end{aligned} \tag{8.19}$$

where $\nu$ is the scale of the dimensional regularization. Changes in the scale are, in principle, reabsorbed in the subtraction constant $a(\nu)$, so that the results remain scale independent. Here we have taken $\nu = 1$ GeV and a common subtraction constant $a(1 \text{ GeV}) = \alpha$ for both $DK$ and $D_s\eta$ channels, as in Refs. [198, 205]. We have now constrained the LEC $\alpha$ to obtain the same $D_{s0}^*(2317)$ mass ($2315^{+18}_{-28}$), as in Table 8.5, for each value of the parameter $c$. The results are presented in Table 8.6. Comparing these latter results

**Table 8.6:** Same as Table 8.5, but using a different procedure to renormalize the meson loop matrix $G(s)$. Here, as in Refs. [198, 205], we have used dimensional regularization with a subtraction constant $\alpha$ (see Eq. (8.19) and the related discussion), which is adjusted to reproduce the $D_{s0}^*(2317)$ mass.

| $c$ | $\alpha$ | $M_{D_{s0}^*}$ [MeV] | $g_{DK}$ [GeV] | $g_{D_s\eta}$ [GeV] | $P_{DK}$ [%] | $P_{D_s\eta}$ [%] | $a_{DK}$ [fm] | $M_R$ [MeV] | $\Gamma_R$ [MeV] |
|---|---|---|---|---|---|---|---|---|---|
| 0 | $-1.87^{+0.10}_{-0.13}$ | $2315^{+18}_{-28}$ | $10.2^{+0.7}_{-0.9}$ | $6.6^{+0.2}_{-0.3}$ | $63^{+7}_{-8}$ | $10^{+0.1}_{-0.4}$ | $-0.90^{+0.21}_{-0.27}$ | – | – |
| 0.30 | $-1.77^{+0.11}_{-0.14}$ | $2315^{+18}_{-28}$ | $10.0^{+0.7}_{-0.9}$ | $6.2^{+0.2}_{-0.3}$ | $60^{+6}_{-7}$ | $9.0^{+0.1}_{-0.4}$ | $-0.87^{+0.20}_{-0.27}$ | $2559.8^{+0.2}_{-0.4}$ | $23^{+2}_{-3}$ |
| 0.61 | $-1.60^{+0.11}_{-0.14}$ | $2315^{+18}_{-28}$ | $10.1^{+0.8}_{-0.9}$ | $5.8^{+0.2}_{-0.3}$ | $61^{+6}_{-7}$ | $8.0^{+0.1}_{-0.4}$ | $-0.88^{+0.20}_{-0.27}$ | $2704^{+3}_{-2}$ | $88^{+5}_{-7}$ |
| NLO | | $2315^{+18}_{-28}$ | $9.5^{+1.2}_{-1.1}$ | $7.5 \pm 0.5$ | $54 \pm 4$ | $13^{+6}_{-10}$ | $-0.84^{+0.17}_{-0.23}$ | – | – |

with those in Table 8.5, we see that the predictions, within uncertainties, are consistent in the two renormalization schemes. There is a slight dependence, and the $D_{s0}^{*}(2317)$ coupling to $DK$ and the modulus of the scattering length are smaller and closer to those deduced from the NLO approach. Molecular probabilities are somewhat larger, specially $P_{D_s\eta}$ that becomes almost twice bigger. As a consequence, the total hadronic molecular component is now roughly $70 \pm 10\%$. The dependence on $c$ follows a similar pattern as in Table 8.5, and the importance of the $D_s\eta$ channel decreases as the value of the LEC $c$ increases. Finally, the results concerning the higher—dressed—resonance pole position are similar in the two renormalization schemes. Thus from the previous discussion, the $c = 0.3$ predictions for energies above 2500 MeV turn out to be little reliable also in this scheme.

The phase shifts deduced from the various possibilities discussed in Table 8.6 are shown in the right panels of the first two rows in Fig. 8.5. We see, the $c = 0.3$ phase shift above 2500 MeV presents the same pathologies as in the left top panel, where an UV Gaussian cutoff is used. It is interesting to note that the $c = 0$ and $c = 0.61$ phase shifts have smaller errors, the two sets of phase shifts are still statistically compatible, but in addition, they now agree quite well with the NLO predictions, and also qualitatively with those found in Ref. [285]. Thus, the renormalization scheme dependence, while it is not much relevant for the $D_{s0}^{*}(2317)$ properties, turns out more important for the phase shift at energies above 2450 MeV, as one could reasonably expect from the previous discussions. This clearly could be regarded as a source of systematic uncertainty, though up to 2550 MeV remains smaller/comparable to the other uncertainties of the predictions accounted for the error bands depicted in Fig. 8.5.

## 8.4 Summary and concluding remarks

In this chapter we have first carried out a coupled channel study of the $0^+$ and $1^+$ charm-strange meson sectors employing a chiral unitary approach based on LO HM$\chi$PT $P^{(*)}\phi$ interactions, and that incorporates, consistently with HQSS, the interplay between intermediate CQM bare $c\bar{s}$ and $P^{(*)}\phi$ degrees of freedom. We have extended the scheme to finite volumes and fixed the strength of the coupling between both types of degrees of freedom to the available $0^+$ and $1^+$ LQCD energy-levels [45], which we have successfully described. On the other hand and at variance with the situation in the bottom-sector reported in Ref. [4]—which will be presented in the next chapter—, we have found that the $0^+$ and $1^+$ CQM bare masses (denoted as Set B in this work) obtained in Ref. [356] using the one-loop corrections to the CQM OGE potential proposed in Ref. [354], lead to a really poor description of the LQCD data. This is because the HQSS breaking corrections induced by this modification of the OGE potential are inconsistent with the LQCD energy levels calculated in Ref. [45].

We have estimated the size of the the $D^{(*)}K$ two-meson components in the $D_{s0}^{*}(2317)$ and $D_{s1}(2460)$, and conclude that these states have a predominantly hadronic-molecular structure. Furthermore, we have observed a quite significant dependence of the lowest-lying LQCD energy-levels of Ref. [45] on the pion mass, which is difficult to accommodate by a dominant CQM $c\bar{s}$ component. This is, however, consistent with having a large influence of the $P^{(*)}\phi$ loops in the $D_{s0}^{*}(2317)$ and $D_{s1}(2460)$ structure.

In addition, we have found one extra resonance, in both the $0^+$ and $1^+$ sectors, arising from the dressed CQM states. Our predictions for these states are not as robust as those for the low lying $D^*_{s0}(2317)$ and $D_{s1}(2460)$, and moreover they are relatively broad, which might complicate their discovery. Some experimental efforts are needed to clarify their possible existence.

The LEC $c$ depends on the radial quantum number, but not on the heavy flavour, up to $\Lambda_{QCD}/m_Q$ corrections. Thus, the value determined here for this parameter should be similar to the value which would be found in the bottom-strange sector. As we have already advanced, we shall undertake the case of bottom-strange sector in the forthcoming chapter. Nevertheless, we anticipate here that in the bottom sector a value $c = 0.75(6)$ will be obtained, which is quite compatible with the values in the range 0.52–0.70 found in this work for the Set A of CQM bare masses. Note that in addition to heavy flavour symmetry breaking corrections, there might be also some discretization errors. Nevertheless, we have shown that taking into account explicitly the exchange of (bare) CQM mesons is not fundamental to describe the $D^*_{s0}(2317)$ and $D_{s1}(2460)$ states, since such contributions can be accommodated by appropriately modifying the finite contributions derived from short-distance physics. This is natural because the CQM bare states lie far from the latter physical states, for which the unitarity meson loops play a fundamental role.

We have discussed how the approach followed here, where the two meson loop function is computed in a finite volume, the unknown LECs are determined from fits to the LQCD data, and finally poles are searched for in the infinite volume unitarized amplitudes using physical meson masses, provides a theoretically sound tool to analyze the LQCD energy-levels. We have shown that such procedure leads to more precise predictions that those obtained via the Lüscher's relation using the effective range approximation.

We have also calculated the energy-levels obtained from the unitarized HM$\chi$PT NLO amplitudes presented in Chapter 4, without including any contribution from the exchanges of CQM bare poles. We have shown (Fig. 8.4) that this scheme provides a more than acceptable description of the $0^+$ and $1^+$ LQCD energy levels of Ref. [45], despite having fixed all LECs to the values previously determined in Ref. [205] (not fitted to the energy levels). These findings, together with the similar good description found in Chapter 4 of the $(S, I) = (0, 1/2)$ LQCD low-lying energy levels of the Hadron Spectrum Collaboration [81], provide a great support for the aforementioned amplitudes. Hence, the $D^*_0(2400)$ two-pole structure and the SU(3) pattern of the $0^+$ and $1^+$ heavy-light sectors claimed in Chapter 4 seem rather robust from the theoretical point of view. All these results, as we have discussed in former Chapter 5, reinforce a new paradigm to study the spectrum of heavy-light mesons, that questions its traditional interpretation in terms of constituent $Q\bar{q}$ degrees of freedom.

# Chapter 9

# LOWEST LYING EVEN-PARITY $\bar{B}_s$ MESONS: HEAVY QUARK SPIN-FLAVOR SYMMETRY, CHIRAL DYNAMICS, AND CONSTITUENT QUARK MODEL BARE MASSES

## 9.1 Introduction

In the previous Chapter 8, we discussed the effects of incorporating CQM $c\bar{s}$ degrees of freedom into a HM$\chi$PT molecular description of the charm-strange $D_{s0}^*(2317)$ and $D_{s1}(2460)$ states. In this chapter, we shall apply the same formalism to study the bottom analogues of these resonances, although currently there are not experimental evidences of their existence. A brief exposition of their expected properties as well as previous research on these states can be found in Sec. 1.2.1.

Henceforth, we will pay attention to the $0^+$ and $1^+$ isoscalar bottom-strange sector. We will use a UHM$\chi$PT scheme to describe the isoscalar $S$-wave elastic $\bar{B}^{(*)}K \to \bar{B}^{(*)}K$ $T-$matrix. The scattering amplitudes will be obtained by solving a renormalized BSE with an interaction kernel determined from LO HM$\chi$PT [183, 184, 288, 299]. We will couple the two-meson $BK$ and $B^*K$ channels with the CQM $P$-wave $\bar{B}_s$ scalar and axial mesons using the same effective interaction consistent with HQSS that we employed in Chapter 8 (see Sec. 8.2 for details). Finally, as in the preceding chapter, we will use the LQCD information—in this case the energy levels reported in Ref. [58]—to constrain the undetermined LECs of the approach. In contrast with the previous study on charm mesons, we will not consider the influence of coupled $\bar{B}_s^{(*)}\eta$ channels, as in Ref. [58], since in this case the bare CQM bare masses that will be used lie far enough from the $\bar{B}_s^{(*)}\eta$ energy thresholds. As a final outcome, we will present robust predictions for the lowest-lying $b\bar{s}$ $J^P = 0^+$ and $1^+$ states, that can serve as an important guidance for experimental searches and to shed light into the situation in the analogue charm sector. This chapter is based on Ref. [4].

## 9.2 Isoscalar $\bar{B}^{(*)}K \to \bar{B}^{(*)}K$ scattering

The formalism introduced in previous Sec. 8.2 for $S$-wave scattering of pNGBs off charm mesons is readily extended to the case of bottom $\bar{B}$ mesons with the identification $D \leftrightarrow \bar{B}$, *i.e.*, the SU(3) anti-triplet of heavy nonrelativistic fields $P^{(*)Q}$ is now $(B^{0(*)}, B^{-(*)}, \bar{B}_s^{0(*)})$. In the following, we will nevertheless review a few distinct key points with respect to the situation in Chapter 8.

### 9.2.1 Interactions

In $S$-wave, the spin-parity quantum numbers of the $\bar{B}K$ $\left(\bar{B}^*K\right)$ meson pair are $0^+(1^+)$, while the light degrees of freedom are coupled to spin-parity $1/2^+$. As in Ref. [58], we will neglect the $\bar{B}_s^{(*)}\eta$ channels, and thus the (elastic) isoscalar $\bar{B}^{(*)}K \to \bar{B}^{(*)}K$ interaction potential $V(s)$ consists of a chiral contact term $[V_{\rm c}(s)]$ plus the exchange $[V_{\rm ex}(s)]$ of a bare $b\bar{s}$ state as in Eq. (8.10). At LO in the chiral counting, $V_{\rm c}(s)$ is given by the WTL [183, 184, 288, 299] that reads as given in Eq. (3.105). The isoscalar contact term contribution $V_{\rm c}(s)$ can be easily derived, and the result after projecting into $S$-wave reads:[1]

$$V_{\rm c}(s) = \frac{-3s + (m^2_{\bar{B}^{(*)}} - m^2_K)^2/s + 2(m^2_{\bar{B}^{(*)}} + m^2_K)}{4f^2} \,. \tag{9.1}$$

Neglecting the $\bar{B}^* - \bar{B}$ mass difference, the interactions in the $J = 0$ and 1 sectors are identical, as expected from HQSS because they correspond to the same configuration ($j^P_{\bar{s}} = 1/2^+$) of the light degrees of freedom.

As before, the exchange term in Eq. (8.10) is determined by the coupling between the $\bar{B}^{(*)}K$ meson pairs and the $P$-wave bare quark model states described by the matrix field $J^{(Q)}_a$ introduced in Eq. (3.50). The LO term in the chiral and heavy quark expansion was presented in Eq. (3.107) (subsec. 3.4.1 of Chapter 3), depending on the dimensionless undetermined LEC, $c$, that controls the strength of the vertex. See the discussion in the paragraph after Eq. (8.2) for further details. Paying attention to the isoscalar (see isospin conventions in Eqs. (3.43) and (3.49)) bottom-strange sector, we find a $b\bar{s} \to \bar{B}^{(*)}K$ coupling in $S$-wave,

$$V_{b\bar{s}}(s) = \frac{ic}{f}\sqrt{\frac{m_{\bar{B}^{(*)}}\,\overset{\circ}{m}_{b\bar{s}}}{s}}\left(s - m^2_{\bar{B}^{(*)}} + m^2_K\right), \tag{9.2}$$

where now $\overset{\circ}{m}_{b\bar{s}}$ is nothing but the mass of the $b\bar{s}$ meson without the effect of the $\bar{B}^{(*)}K$ meson loops. This mass is the same, up to small HQSS breaking corrections, for both $J = 0$ and $J = 1$ sectors, and it can be in principle obtained from CQMs. In what follows, we will denote it as the *bare mass* of the state.[2] We reinforce here the interpretation that, by bare mass, we mean the mass of the CQM states when the LEC $c$ is set to zero, and thus it is not a physical observable. In the sector studied in this work, the coupling to the $\bar{B}^{(*)}K$ meson pairs renormalizes this bare mass, as we will discuss below. We remark that since, in the effective theory, the UV regulator is finite, the difference between the bare and the physical resonance masses is a finite renormalization. This shift depends on the UV regulator since the bare mass itself depends on the renormalization scheme. The value of the bare mass, which is thus a free parameter, can either be indirectly fitted to experimental observations, or obtained from schemes that ignore the coupling to the mesons, such as some CQMs. In this latter case, the issue certainly would be to set the

---

[1] For $J = 1$, as already discussed in the paragraph after Eq. (8.7), there appears the product of the polarization vectors of the initial and final $\bar{B}^*$ mesons, which is approximated by $-1$, after neglecting corrections suppressed by the heavy meson mass.

[2] Owing to SU(3) light flavor-symmetry, the bare mass would present also a soft pattern of isospin and strangeness corrections.

UV regulator to match the quark model and the EFT approaches. We will come back to this point later.

From Eq. (9.2), we can compute the $V_{\rm ex}(s)$ term contribution to the full potential, (analogous to Eq. (8.10)), that accounts for $\bar{B}^{(*)}K$ scattering via the exchange of intermediate even-parity bottom-strange mesons [341]:

$$V_{\rm ex}(s) = \frac{V_{b\bar{s}}(s)V^{\dagger}_{b\bar{s}}(s)}{s - \mathring{m}^{2}_{b\bar{s}}} \ . \tag{9.3}$$

The potential $V(s)$ detailed above is consistent with HQSS, and it is used to obtain the $\bar{B}^{(*)}K$ elastic unitary amplitude, $T(s)$. This is done as explained in Sec. 8.2.2, solving the BSE within the so-called on-shell approximation ( [132], see Sec. 2.5), with a loop function regularized using a Gaussian form factor suppressing the UV three-momenta (see Eqs. (A.2) and (A.4)).

### 9.2.2 Bound, resonant states, couplings and the compositeness condition for bound states

We follow, as in Chapter 8, the $T$-matrix prescription of Sec. 2.5. In this case, since we have elastic scattering, we have only two RSs which are straightforwardly interpreted as the FRS and SRS. For details on the analytic continuation to the SRS as well as definition of bound and resonant poles, and their couplings, we refer to Sec. 2.5 and subsec. 8.2.5.

We will follow the approach described in Sec. 8.2.5 in order to get information on the compositeness of the bound states from the derivative of the meson loop function and the residue at the pole position. The probability of finding the $\bar{B}^{(*)}K$ molecular component in the bound state wave function is given by Eq. (8.11) particularized for the present elastic case. We shall not extend the compositeness discussion to resonances, restricting it to the case of bound states.

### 9.2.3 Finite volume

In the present case, the comparison with the LQCD results is similar to the one explained in subsec. 8.2.6. To obtain the volume the energy levels in our scheme, we consider the finite volume prescription for the $T$-matrix introduced in subsec. 2.5.1, and compare the eigenenergies obtained with those reported in Ref. [58]. We use finite volume loop functions, $\widetilde{G}(s,L)$ [167, 169], introduced in Eq. (8.12), but adapting them to the case of intermediate $\bar{B}^{(*)}K$ states considered here.

To better describe the energy levels reported in the LQCD simulation carried out in Ref. [58], we use the masses and the energy-momentum dispersion relations given in that work. In particular, we will employ in Eq. (8.12) a modified energy-momentum dispersion relation for the $\bar{B}^{(*)}$ mesons,

$$\omega(\vec{q}\,) \rightarrow \omega^{\rm lat}(\vec{q}\,) = m_1 + \frac{\vec{q}^{\,2}}{2m_2} - \frac{(\vec{q}^{\,2})^2}{8m_4^3} \ , \tag{9.4}$$

where the parameters appearing in the above equation can be found in Table 1 of Ref. [58]. The lattice size and spacing in that simulation are $32^3 \times 64$ and $a = 0.0907 \pm 0.0013$ fm, respectively, while the pion mass is $156 \pm 7$ MeV. For the kaon, the ordinary relativistic

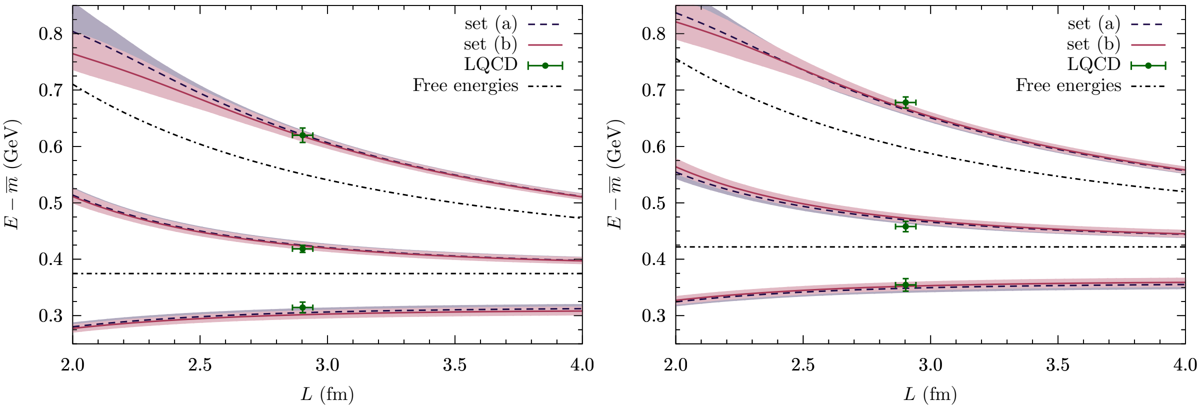

**Figure 9.1:** LQCD energy levels for $J^P = 0^+$ (left) and $J^P = 1^+$ (right), as a function of the box size $L$. We compare our predictions for the difference $E - \bar{m}$ with the results of Ref. [58], given also in Table 3 of that work. We have used $\bar{m}a = 1.62897(43)$, as in Ref. [58]. We have evaluated energy levels ($\widetilde{T}(s, L)$ presents poles at $\sqrt{s} = E$ for a given $L$, when the lattice masses are employed) using both sets of parameters compiled in Table 9.1, which are shown by dashed blue and solid red lines for sets (a) and (b), respectively. Black lines stand for the first and second non-interacting $\bar{B}^{(*)}K$ levels, while the data points show the lattice levels reported in Ref. [58]. The uncertainty bands in the predicted energy levels mark 68% CLs obtained from a Monte Carlo simulation considering the parameter distributions of Table 9.1.

dispersion relation is used with an unphysical mass of $m_K^{\text{lat}}a = 0.2317 \pm 0.0006$ ($m_K^{\text{lat}} = 504 \pm 7$ MeV) [47]. Thus, the $\bar{B}^{(*)}K$ free energies are given by $E^{\text{free}}(\vec{q}) = \omega^{\text{lat}}(\vec{q}) + \omega_K(\vec{q})$ whereas $\omega_K(\vec{q}) = [(m_K^{\text{lat}})^2 + \vec{q}^2]^{1/2}$. To compute the potentials (chiral+exchange) at finite volume, we set the $\bar{B}^{(*)}$ mass to $m_1$, introduced in the modified dispersion relation of Eq. (9.4). Finally $\vec{k}^2$, that appears in the Gaussian regulator needed to render $\widetilde{G}(s, L)$ finite is obtained from Eq. (A.3) using the lattice masses.

## 9.3 Results

We will fit our model to the levels 1,2,3 and 1,3,4 given in Table 3 of Ref. [58] for the $0^+$ and $1^+$ sectors, respectively.[3] We will consider the energy-levels in lattice units. Hence, and to properly take into account the uncertainty on this scale, we introduce it as an additional best-fit parameter, $a^{\text{th}}$, constrained by the central value and error quoted above and taken from Ref. [58]. Thus, we minimize the following $\chi^2$,

$$\chi^2 = \sum_i \left( \frac{(Ea)_i^{\text{lat}} - (Ea)_i^{\text{th}}}{\Delta\left[(Ea)_i^{\text{lat}}\right]} \right)^2 + \left( \frac{a^{\text{lat}} - a^{\text{th}}}{\Delta\left[a^{\text{lat}}\right]} \right)^2 . \tag{9.5}$$

The sum runs over the six $0^+$ and $1^+$ energy-levels (given in lattice units) specified above. We could instead have fitted directly to the energy levels in physical units, but in that case, the errors on the levels inherited from the lattice spacing need to be treated as correlated ones, since variations in the lattice spacing affect to all the energy levels in the same manner. In addition to the use of correlated errors, one would have also to

---

[3] Note that the $1^+$ level 2 is interpreted in [58] to be the $j_{\bar{q}}^P = \frac{3}{2}^+$ state with $J^P = 1^+$, which does not couple to $B^*K$ in $S$-wave in the heavy quark limit.

**Table 9.1:** Parameters of the model fitted to the energy levels of Ref. [58], together with masses and properties of the low-lying $j_{\bar{q}}^P = \frac{1}{2}^+$ $\bar{B}_s$ meson doublets deduced from these parameters in the infinite volume case. In this latter case, physical $\bar{B}^{(*)}$ and $K$ masses have been used, and we have searched for poles in the FRS (bound states) and SRS (resonances) of the isoscalar $S$-wave $\bar{B}^{(*)}K$ amplitudes. Besides, we find $a^{\rm th} = 0.0909 \pm 0.0013$ fm and $0.0910 \pm 0.0013$ fm for sets (a) and (b), respectively, which compare rather well with the lattice spacing ($a = 0.0907 \pm 0.0013$ fm) quoted in Ref. [58]. The isoscalar $0^+$ and $1^+$ scattering lengths ($a_0$) and the isoscalar $S$-wave $\bar{B}^{(*)}K \to \bar{B}^{(*)}K$ amplitudes at threshold are related by $T(s_+) = -8\pi a_0 \sqrt{s_+}$, with $s_+ = (m_{\bar{B}^{(*)}} + m_K)^2$. The $\bar{B}^{(*)}K$ molecular probability $P_{\bar{B}^{(*)}K}$ is calculated using Eq. (8.11) and it is given only for bound states. The coupling $g$, defined in Eq. (2.93), is also calculated only for the bound state. Errors on the fitted parameters show 68% confidence levels (CLs), which are obtained from distributions computed by performing a large number of best fits to Monte Carlo synthetic datasets. The synthetic datasets are generated from the original energy levels of Ref. [58] and the lattice spacing assuming that the data points are Gaussian distributed. The 68% CLs are obtained by discarding the higher and the lower 16% tails of the appropriate distributions. These parameter distributions are used to estimate the uncertainties on the derived quantities in the infinite volume case.

| | | Parameters | | | | Infinite volume predictions | | | | | |
|---|---|---|---|---|---|---|---|---|---|---|---|
| set | $J^P$ | $\overset{\circ}{m}_{b\bar{s}}$ [MeV] | $c$ | $\Lambda$ [MeV] | $\chi^2$/d.o.f. | $M_b$ [MeV] | $P_{\bar{B}^{(*)}K}$ [%] | $g$ [GeV] | $a_0$ [fm] | $M_R$ [MeV] | $\Gamma_R$ [MeV] |
| (a) | $0^+$ | 5851 | $0.74 \pm 0.05$ | $730 \pm 40$ | 1.5 | $5711 \pm 6$ | $51.8 \pm 1.5$ | $31.8 \pm 0.9$ | $-0.90 \pm 0.05$ | $6300 \pm 100$ | $70^{+30}_{-40}$ |
| | $1^+$ | 5883 | | | | $5752 \pm 6$ | $49.7 \pm 1.4$ | $32.3 \pm 0.9$ | $-0.87 \pm 0.04$ | $6300 \pm 100$ | $80^{+30}_{-50}$ |
| (b) | $0^+$ | 5801 | $0.75 \pm 0.04$ | $650 \pm 30$ | 1.6 | $5707 \pm 6$ | $45.8 \pm 1.1$ | $32.3 \pm 0.8$ | $-0.88 \pm 0.05$ | $6220 \pm 70$ | $80^{+30}_{-40}$ |
| | $1^+$ | 5858 | | | | $5757 \pm 6$ | $48.3 \pm 1.3$ | $32.3 \pm 0.8$ | $-0.92 \pm 0.05$ | $6280 \pm 70$ | $70^{+30}_{-40}$ |

consider that the lattice meson masses, appearing in the theoretical $\widetilde{T}(s,L)$, will change with $a$ as well because of their conversion into physical units. The $\chi^2$ introduced in Eq. (9.5) accounts for all these correlations. Indeed, the latter make the uncertainties on $(Ea)_i^{\rm lat}$ to become the most relevant ones. Note that if these correlations induced by the lattice spacing are not taken into account, one will end up with large and unrealistic errors. On the other hand, one might treat $m_K a$, $(m_{1,2,4})a$ also as best-fit parameters, supplementing appropriately the $\chi^2$. Results do not change significantly and for simplicity we have fixed all these masses in lattice units to the central values reported in Ref. [58]. This little sensitivity can be expected since the errors on $m_K a$ and $m_1 a$, which determine the threshold and the chiral potential, are much smaller than those on $a$. Indeed, the largest uncertainty in the magnitude of these quantities is induced from the error on the lattice spacing.

Besides the lattice spacing, the parameters of the model are the bare masses of the CQM $b\bar{s}$ $0^+$ and $1^+$ mesons, $\overset{\circ}{m}_{b\bar{s}}$, the LEC $c$ that gives us the strength of the coupling of the latter states with the two-meson $\bar{B}^{(*)}K$ channels, and the UV Gaussian regulator $\Lambda$. We expect to get reasonable estimates for the bare masses from the predictions of CQMs [26, 51, 52]. These kind of models find masses in the ranges $5800 - 5850$ MeV and $5840 - 5880$ MeV for the $J^P = 0^+$ and $J^P = 1^+$ sectors, respectively. The $\bar{B}K$ and $\bar{B}^*K$ thresholds are located approximately at 5775 MeV and 5820 MeV, respectively. Thus, in principle, we expect the quark model states to be relatively close to, but above, the respective $\bar{B}^{(*)}K$ thresholds, which would produce attractive $\bar{B}^{(*)}K$ interactions for energies below the bare masses [341].

We will explore the ranges of bare masses mentioned above, and we will perform two independent fits using $\overset{\circ}{m}_{b\bar{s}}$ values close to their respective lower and upper limits. To maintain a consistent $0^+ - 1^+$ mass splitting, we will use the predictions of a widely used non-relativistic CQM [343–345]. This quark model was already employed to study the low-lying $P$-wave charmed-strange mesons [342]. In that reference, since the $D_{s0}^*$ $1^3P_0$ ($n^{2S+1}L_J$) bare state was found significantly above the experimental level (2511 versus 2317.7 MeV), an additional one-loop correction to the OGE potential was introduced. This extra term was motivated from the studies of Refs. [29, 354], where a spin-dependent term was added to the quark-antiquark potential affecting only mesons in the case of unequal quark masses. Such correction is in general rather small, except for the $0^+$ sector, where a large mass shift was found (around 128 MeV in the case of the $D_{s0}^*$). Hence, as commented above, we will consider two sets of bare masses $\overset{\circ}{m}_{b\bar{s}}$. In the set (a), we will use bare masses of 5851 MeV and 5883 MeV for the $0^+$ and $1^+$ states, respectively, as deduced from the CQM of Refs. [343–345] without including any correction to the OGE potential. For the second set, (b), we will fix the $0^+$ and $1^+$ bare masses to 5801 MeV and 5858 MeV, as obtained when the latter CQM is supplemented with the OGE one-loop terms discussed in Ref. [29, 354, 365]. Since the LQCD simulation carried out in Ref. [58] uses non-physical meson masses, the CQM bare masses have been corrected using the difference between the experimental and the prediction of Ref. [58] for the spin-average mass $\bar{m} = \frac{1}{4}(m_{\bar{B}_s} + 3m_{\bar{B}_s^*})$.

For each set of bare masses, the values of the other two parameters, $c$ and $\Lambda$, are obtained from a simultaneous fit to the first three $J^P = 0^+$ and $1^+$ energy levels reported in the LQCD study of Ref. [58]. In Fig. 9.1, we present the predicted energy levels as a function of the lattice size $L$, and the values of the fitted parameters are compiled in Table 9.1. As can be seen, we find an excellent description of the LQCD levels of Ref. [58]

in both $J^P$ sectors, despite the large deviations from the free levels. The LEC $c$ is rather insensitive to the used bare masses, taking a value about 0.75 with an error of around 6%. The central values of the UV regulator present however a mild dependence, and we find $\Lambda = 730 \pm 40$ MeV for set (a), while for set (b) the fitted value is $\Lambda = 650 \pm 30$ MeV. We should remind that the CQM bare masses depend on the renormalization scheme, in particular on the UV regulator, or equivalently the UV regulator is expected to depend on the bare masses. Nevertheless, set (a) and (b) UV regulators turn out to be almost compatible within errors.

When the loop function is renormalized by a suitable subtraction, instead of using a Gaussian regulator, the physical results showed in Table 9.1 and Fig. 9.1 do not appreciably change, besides some variation of the renormalization-scheme-dependent low energy constant $c$. Thus, a similar good reproduction of the LQCD energy levels is achieved. Note that the finite volume loop function, in both renormalization schemes, is related to the Lüscher function [163, 164], as it is shown in Refs. [167, 169]. Hence, the continuous volume dependent curves in Fig. 9.1 are essentially the Lüscher curves obtained from the phase shift by solving

$$\delta(q) + \phi(\hat{q}) = n\pi \tag{9.6}$$

with $\hat{q} = qL/2\pi$ and $\phi(\hat{q})$ determined by the Lüscher function (see Eq. (6.13) of Ref. [164]).

Next, and once the parameters have been fixed, we search for poles in the FRS (bound states) and SRS (resonances) of the isoscalar $S$-wave $\bar{B}^{(*)}K$ amplitudes for the infinite volume case. Pole positions are also compiled in Table 9.1, together with the $0^+$ and $1^+$ isoscalar scattering lengths and the probabilities of the molecular $\bar{B}^{(*)}K$ component in the bound states. For both sets of parameters, and for both $J^P = 0^+$ and $1^+$ sectors, we find a bound state (FRS) and a resonance (SRS).

In all cases, the mass of the bound state is rather independent of the UV regulator, or equivalently of the bare quark model mass, and it is located more than 100 MeV below the corresponding bare pole, consequence of the strong attraction produced by the chiral potential. This is a first hint of the importance of the meson loops in the dynamics of the bound state, which can be also inferred from its large ($\sim 50\%$) molecular component. From the results of the Table 9.1, we predict masses of $5709 \pm 8$ MeV and $5755 \pm 8$ MeV for the $\bar{B}^*_{s0}$ and $\bar{B}_{s1}$ states, respectively. These states are the heavy flavor partners of the charmed-strange $D^*_{s0}(2317)$ and $D_{s1}(2460)$ resonances, and are clear candidates for future experimental searches. The masses obtained in this work are in excellent agreement with the estimations given in Ref. [58], and mentioned in the introduction.[4] They are also quite compatible within errors with other HM$\chi$PT predictions, where the explicit coupling (LEC $c$) of the two-meson channel and the bare quark model state is not considered[5] [3, 37, 42, 54, 55]. In all cases a similar binding energy around $60 - 70$ MeV is obtained, which favours a molecular interpretation of such states, where one would expect a $(\bar{B}_{s1} - \bar{B}^*_{s0})$

---

[4] Note that the uncertainties obtained here are smaller than those quoted in Ref. [58] because we go beyond the effective range approximation and determine a potential (see the discussion in Ref. [169]).

[5] In these schemes, such effect is encoded either in the renormalization subtraction constants or in higher order LECs, appearing at NLO in the HM$\chi$PT expansion. (Note that in the present work, we obtain reasonable UV cutoff values $\sim 700$ MeV, which do not hide large higher order contributions [215, 216].) Despite the bare quark model pole was located above, and relatively close to, the $\bar{B}^{(*)}K$ threshold, we find the bound state significantly below $\overset{\circ}{m}_{b\bar{s}}$. Hence, the bare pole induces a mild energy dependence in the vicinity of the physical bound states, which can be accounted for by means of local terms in the potential [341]. The bare pole, however, should produce a relevant energy dependence in the amplitudes above threshold and close to its position.

mass splitting similar to the $(\bar{B}^* - \bar{B})$ one. The latter is around 45 MeV, while in our calculation we find $(m_{\bar{B}_{s1}} - m_{\bar{B}^*_{s0}}) \sim 41$ MeV for set (a) and $\sim 49$ MeV for set (b), around 4 MeV below and above the pseudoscalar-vector mass splitting, respectively. This is a clear indication of the non-canonical quark model nature of the $\bar{B}_{s1}$ and $\bar{B}^*_{s0}$ states. It is interesting, though, to note that the molecular proportion in the $0^+$ state ($\sim 50\%$) is below the EFT estimations for the $D^*_{s0}(2317)$, predicted to be around 70% of $D^{(*)}K$ [44,205,245].

In Ref. [365] two-meson loops and CQM bare poles are also coupled. For the latter, the values of the bare masses are the same as those used here. The $\bar{B}^{(*)}K$ interactions are derived from the same CQM used to compute the bare states, instead of using HM$\chi$PT. The $^3P_0$ model is employed to couple both types of degrees of freedom, and the quark model wave functions provide form-factors that regularize the meson loops. The $0^+$ and $1^+$ states reported in Ref. [365] are around $30-40$ MeV less bound than those found here and in the LQCD study of Ref. [58]. Presumably, this is because the $\bar{B}^{(*)}K$ interactions derived in the CQM of Ref. [365] are weaker than those used here. Molecular probabilities are reported in Ref. [365] to be around $30-40\%$, which are smaller than those found in the present approach.

Regarding the isoscalar scattering lengths, we predict (combining the results of both sets) $a_0 = -0.89 \pm 0.07$ fm for both $J^P = 0^+$ and $1^+$ sectors, which compares well with the results $a_0^{\bar{B}K} = -0.85 \pm 0.10$ fm and $a_0^{\bar{B}^*K} = -0.97 \pm 0.16$ fm, obtained in the analysis carried out in the LQCD study of Ref. [58]. In the approach of Ref. [365], the $0^+$ and $1^+$ scattering lengths turn out to be $\sim -1.18$ fm and $-1.35$ fm, respectively, which are larger (in absolute value) than those found here and in Ref. [58]. This is expected, since the bound states in Ref. [365] lie closer to the respective thresholds.

We now pay attention to the extra poles found in the SRS, located well above ($\sim$ 400-500 MeV) their respective thresholds. From the very beginning we should take these results with some caution, since most likely they should be affected by sizeable NLO and higher threshold-channels corrections. In other words, they are not as theoretically robust as those concerning the lowest-lying $\bar{B}_{s1}$ and $\bar{B}^*_{s0}$ states. These resonances, likely, are originated from the bare $b\bar{s}$-quark-model poles that are dressed by the $\bar{B}^{(*)}K$ meson loops. In that case, the bare pole has been highly renormalized, moving to significant higher masses ($\sim 6.2-6.3$ GeV) and acquiring a significant $\bar{B}^{(*)}K$ width ($\sim 70-80$ MeV). We should also bear in mind that radial excitations of the CQM states or $\bar{B}^{(*)}K^*$ two-meson loops, neither of them taken into account in this study, might lie in this region of energies. Further theoretical and experimental studies will be helpful in shedding light on the possible existence and properties of these resonant states.

## 9.4 Conclusions

We have adopted a chiral unitary approach, based on leading-order HM$\chi$PT $\bar{B}^{(*)}K$ interactions, and for the very first time in this context, the two-meson channels have been coupled to the corresponding CQM $P$-wave $\bar{B}_s$ scalar and axial mesons using an effective interaction consistent with HQSS. We have examined two different sets of masses for the bare quark model poles, and in each case, successfully fitted the rest of parameters to the recently reported LQCD isoscalar $b\bar{s}$ $0^+$ and $1^+$ energy-levels [58]. Results turned out to be rather independent of the bare masses, showing that the changes can be easily re-absorbed by means of reasonable variations of the UV regulator.

We have focused on the scalar and axial $\bar{B}^*_{s0}$ and $\bar{B}_{s1}$ states, which form a HQSS

$j_{\bar{q}}^P = 1/2^+$ meson doublet, heavy-flavor partner of that in the charmed-strange sector integrated by the $D_{s0}^*(2317)$ and $D_{s1}(2460)$ resonances. We have searched for bound states (poles in the FRS) of the isoscalar $S$-wave $\bar{B}^{(*)}K$ amplitudes and found masses of $5709 \pm 8$ MeV ($0^+$) and $5755 \pm 8$ MeV ($1^+$) for these states. Therefore, the $\bar{B}_{s0}^*$ and $\bar{B}_{s1}$ appear well below the $\bar{B}K$ and $\bar{B}^*K$ thresholds, being in this way the lowest-lying mesons with these quantum numbers and stable through strong interactions. These states are clear candidates for experimental search in the LHCb experiment, $B-$factories or future high-luminosity proton-antiproton experiments.

We have also predicted the isoscalar elastic $S$-wave $\bar{B}K$ and $\bar{B}^*K$ scattering lengths to be similar and approximately equal to $-0.89 \pm 0.07$ fm, in good agreement with the findings of Ref. [58].

We have obtained sensible UV cutoff values $\sim 700$ MeV, which do not hide large higher order contributions. In addition, and within the renormalization scheme adopted in this work, we have determined the dimensionless LEC $c$ that controls the strength of the coupling between the $\bar{B}^{(*)}K$ meson pairs and the $P$-wave bare quark model states. This LEC, though it depends on the orbital angular momentum and radial quantum numbers of the CQM state, is in principle independent of both the heavy-quark flavor and the light SU(3) flavor structure of the vertex. Thus, up to $\Lambda_{\text{QCD}}/m_Q$ corrections, it can for example be also used to address the interplay between meson-loops and CQM degrees of freedom in the case of the $D_{s0}^*(2317)$ and $D_{s1}(2460)$ resonances. Indeed, we found in Chapter 8 values for this parameter in reasonable agreement with those found here in the bottom sector. Moreover, the same LEC governs the interplay between two-meson and quark model degrees of freedom in all isospin and strangeness channels. Next, we have looked at the Weinberg compositeness condition. Thanks to this admixture between CQM and two-meson degrees of freedom, we could realistically estimate the molecular component ($\bar{B}^{(*)}K$) of the $\bar{B}_{s0}^*$ and $\bar{B}_{s1}$, which turned out to be of the order of 50%. This is a clear indication of the non-canonical quark model nature of these states.

Finally, we have further predicted the volume dependence of the isoscalar $b\bar{s}$ $0^+$ and $1^+$ energy-levels, which could be useful for future LQCD simulations.

# Chapter 10

# THE $D_{s0}^*(2317)$ IN THE DECAY $B_c \to DKJ/\psi$

## 10.1 Introduction

In the present chapter, we shall study the $DK$ invariant mass distribution in the decay $B_c \to J/\psi DK$, from which information on the internal structure of the $D_{s0}^*(2317)^+$ state will be obtained. Besides the weak decay of the $B_c$ meson and hadronization of the quark-antiquark pair to two mesons, the final state interaction is involved. In order to describe the final state interaction, by which the $D_{s0}^*(2317)^+$ state is generated, we use the chiral unitary approach which makes use of the on-shell version of the factorized Bethe-Salpeter equation which has successfully explained the existence of some resonances (see [129, 131, 204, 219, 220, 366–372]).

The chapter is organized as follows. In Section 10.2 we present the formalism to study the decay of $B_c \to J/\psi DK$ and $B_c \to J/\psi D_{s0}^*(2317)$. The numerical results of the $DK$ invariant mass distribution are given in Section 10.3. Finally, in Sec. 10.3, we present a brief conclusion. The results of this chapter are based on the findings of Ref. [2].

## 10.2 Formalism

In this work, we will discuss the decay mechanism of the $B_c$ meson into $J/\psi DK$ and also into $J/\psi D_{s0}^*(2317)$. In Refs. [373–377], the weak decay mechanisms of the $B$ and $B_s$ mesons were studied. We can take many elements from those works, but there are also some important differences. The works of [373, 374] relied upon diagrams with a structure as the one shown in the left panel of Fig. 10.1, which we have adapted to the present problem. Essentially a $d$ quark from the $B^0$ meson is replaced now by a $c$ quark in the $B_c^+$ case here. This mechanism is addressed as internal emission in the nomenclature of Ref. [378, 379]. However we can also have a mechanism of external emission as depicted in the right diagram in Fig. 10.1.

The right diagram of Fig. 10.1 is colored favored and dominates the transition, but in both cases we have a primary $J/\psi c\bar{s}$ production assuming a $c\bar{c}$ pair combining into $J/\psi$. This is all that we need in the present case, since the matrix element for this transition will be factorized and assumed to be constant in the small range of the $KD$ invariant mass that we need in our problem. The smoothness of the weak plus hadronization form factors is supported by calculations [280] and phenomenology (see a detailed discussion in [380]). The next step consists of the hadronization of the $c\bar{s}$ pair into two mesons. This is depicted in Fig. 10.2 and is implemented introducing an extra $\bar{q}q$ pair with the quantum numbers of the vacuum, $\bar{u}u + \bar{d}d + \bar{s}s$. In a third step, the two mesons produced in the second process may interact with themselves in coupled channels, which is shown

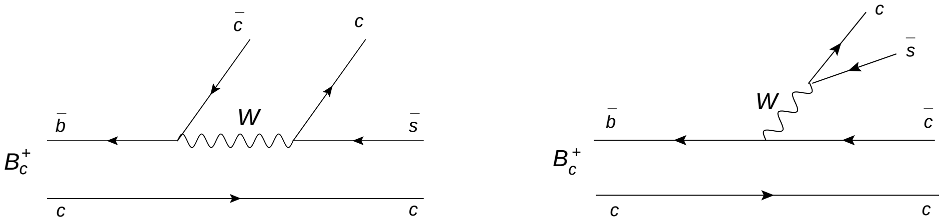

**Figure 10.1:** Diagrams for the decay of $B_c^+$ into $J/\psi$ and the quark pair $c\bar{s}$ with internal (left) and external (right) $W$-emission [378].

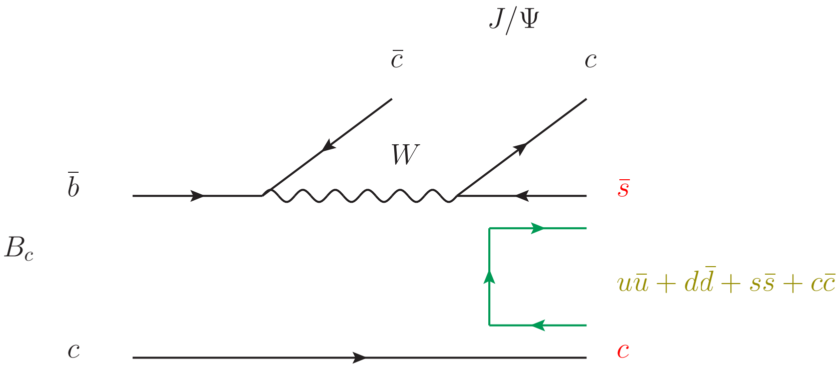

**Figure 10.2:** The hadronization of $c\bar{s} \to c\bar{s}(u\bar{u} + d\bar{d} + s\bar{s})$.

in Fig. 10.3.

It should be noted that apart from the necessary $bc$ transition in the weak process, the other weak vertex is $V_{cs}$ in both mechanisms. As mentioned before, we will include the matrix elements for the weak plus hadronization processes into a constant factor that we call $V_p$. The $c\bar{s}$ then recombine with the $q\bar{q}$ created from the vacuum producing two mesons. In order to calculate it, we first consider the $q\bar{q}$ matrix $M$

$$M = \begin{pmatrix} u\bar{u} & u\bar{d} & u\bar{s} & u\bar{c} \\ d\bar{u} & d\bar{d} & d\bar{s} & d\bar{c} \\ s\bar{u} & s\bar{d} & s\bar{s} & s\bar{c} \\ c\bar{u} & c\bar{d} & c\bar{s} & c\bar{c} \end{pmatrix} = \begin{pmatrix} u \\ d \\ s \\ c \end{pmatrix} \begin{pmatrix} \bar{u} & \bar{d} & \bar{s} & \bar{c} \end{pmatrix}, \tag{10.1}$$

which has the property,

$$\begin{aligned} M \cdot M &= \begin{pmatrix} u \\ d \\ s \\ c \end{pmatrix} \begin{pmatrix} \bar{u} & \bar{d} & \bar{s} & \bar{c} \end{pmatrix} \begin{pmatrix} u \\ d \\ s \\ c \end{pmatrix} \begin{pmatrix} \bar{u} & \bar{d} & \bar{s} & \bar{c} \end{pmatrix} \\ &= \begin{pmatrix} u \\ d \\ s \\ c \end{pmatrix} \begin{pmatrix} \bar{u} & \bar{d} & \bar{s} & \bar{c} \end{pmatrix} (\bar{u}u + \bar{d}d + \bar{s}s + \bar{c}c) \\ &= M \times (\bar{u}u + \bar{d}d + \bar{s}s + \bar{c}c). \end{aligned} \tag{10.2}$$

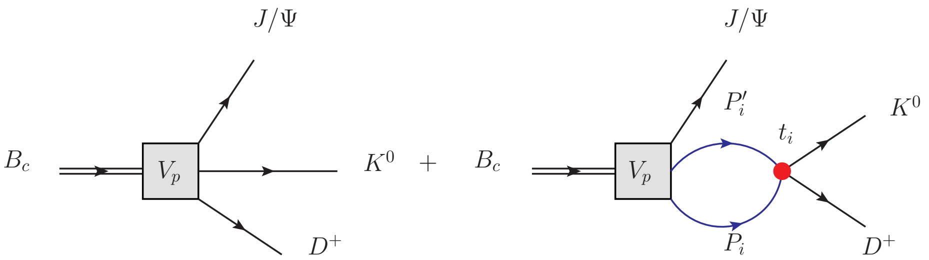

**Figure 10.3:** The diagrams of the decay $B_c^+ \to J/\psi D^+ K^0$ at hadronic level. Note that the intermediate $P_i P_i'$ loops involve the channels $D^+K^0$, $D^0K^+$ and $D_s^+\eta$ ($i = 1, 2, 3$).

On the hadron level, the $M$ matrix corresponds to a hadron $q\bar{q}$ matrix ($\phi$), which has the form,

$$\phi = \begin{pmatrix} \frac{\eta}{\sqrt{3}} + \frac{\pi^0}{\sqrt{2}} + \frac{\eta'}{\sqrt{6}} & \pi^+ & K^+ & \bar{D}^0 \\ \pi^- & \frac{\eta}{\sqrt{3}} - \frac{\pi^0}{\sqrt{2}} + \frac{\eta'}{\sqrt{6}} & K^0 & D^- \\ K^- & \bar{K}^0 & \frac{\sqrt{2}\eta'}{\sqrt{3}} - \frac{\eta}{\sqrt{3}} & D_s^- \\ D^0 & D^+ & D_s^+ & \eta_c \end{pmatrix}, \tag{10.3}$$

where the standard $\eta - \eta'$ mixing is used [349]—see Eqs. (8.5).

Then, we get

$$\begin{aligned}(\bar{u}u + \bar{d}d + \bar{s}s + \bar{c}c)(c\bar{s}) \to (\phi\phi)_{43} &= \eta_c D_s^+ + D^0K^+ + D^+K^0 \\ &\quad -\frac{1}{\sqrt{3}}\eta D_s^+ + \sqrt{\frac{2}{3}} D_s^+\eta'.\end{aligned} \tag{10.4}$$

In this work, we neglect the contribution of $\eta'$ and $\eta_c$ because of their large mass compared with the $K$ and $\eta$ masses.

### 10.2.1 Rescattering

As it is shown in Fig. 10.3, the two mesons produced from the ($c\bar{s}$) (see Fig. 10.2) may interact with themselves and the coupled channels. The amplitude of the $B_c^+ \to J/\psi D^+ K^0$ decay is

$$t(B_c^+ \to J/\psi D^+ K^0) = V_p \left( h_1 + \sum_i h_i G_i t_{i1} \right). \tag{10.5}$$

Here $i$ = 1, 2, 3 label the channels $D^+K^0$, $D^0K^+$ and $D_s^+\eta$ respectively. In Eq. (10.5), $h_1 = h_2 = 1$ and $h_3 = -\frac{1}{\sqrt{3}}$. $G_i$ is the loop function of two meson propagators, which is calculated using dimensional regularization and renormalized by means of a subtraction constant $\alpha(\mu)$. The explicit expressions of the loop function can be found in Eq. (A.1). In Eq. (10.5) $t_{ij}$ is the scattering matrix element for the transition channel $i \to j$, obtained solving the on-shell BSE [130, 204]—see Eq. (2.86) and Sec. 2.5. The kernel potential, $V$, is taken from the LO HM$\chi$PT Lagrangian (see Eq. (3.93)). As in Ch. 8, we take into account the ideal $\eta - \eta'$ mixing (8.5). On the other hand, here we are interested in transitions involving the $D^+K^0$, $D^0K^+$ and $D_s\eta$ states, while in Ch. 8 the interaction kernel amplitudes of Eq. (8.4) were obtained in terms of isospin states. In the particle basis the kernel $V$ is expressed as

$$V(s) = C_{\text{LO}} \left. \frac{s-u}{4f^2} \right|_{S\text{-wave}}, \tag{10.6}$$

where the $S$-wave projection of Eq. (8.6) is implicit, $f \sim 93$ MeV is the pion decay constant and the coefficients $C_{\text{LO}}$ read

$$C_{\text{LO}} = \begin{pmatrix} -1 & -1 & \frac{2}{\sqrt{3}} \\ -1 & -1 & \frac{2}{\sqrt{3}} \\ \frac{2}{\sqrt{3}} & \frac{2}{\sqrt{3}} & 0 \end{pmatrix}. \tag{10.7}$$

Since the process depicted in Fig. 10.1 is a $0^- \to 1^-0^+$ transition, the angular momentum between the $J/\psi$ and the quark pair ($c\bar{s}$) is $L = 1$ due to the total angular momentum conservation. So $V_p$ should have the form of

$$V_p = \sqrt{3} A p_{J/\psi} \cos\theta. \tag{10.8}$$

Thus, we can get the expression of the $K^0D^+$ invariant mass distribution of the decay, $\mathrm{d}\Gamma/\mathrm{d}M_{\text{inv}}$:

$$\frac{\mathrm{d}\Gamma}{\mathrm{d}M_{\text{inv}}} = \frac{A^2}{(2\pi)^3} \frac{1}{4m_{B_c}^2} p_{J/\psi}^3 \tilde{p}_{DK} \bar{\sum}\sum \left| \frac{t_{B_c^+ \to J/\psi D^+ K^0}}{V_p} \right|^2, \tag{10.9}$$

where $M_{\text{inv}}$ is the invariant mass of the $D^+K^0$ system. In Eq. (10.9), the factor $\frac{1}{3}$ which comes from the integral of $\cos\theta^2$ cancels the $\sqrt{3}^2$ in the definition of $V_p$ of Eq. (10.8). The value of $A$ is chosen to normalize the invariant mass distribution and it will cancel in the ratios that we shall construct. In Eq. (10.9) $p_{J/\psi}$ is the momentum of the $J/\psi$ in the global CM frame and $\tilde{p}_{DK}$ is the kaon momentum in the $D^+K^0$ rest frame.

### 10.2.2 Coalescence production of the $D_{s0}^*(2317)^+$ resonance

In the former subsection we have studied the production of $DK$ in the final state. Here we study the production of the resonance $D_{s0}^*(2317)^+$ under the assumption that it is dynamically generated from the $DK$ and $\eta D_s$ channels. Diagrammatically, the reaction proceeds as shown in Fig. 10.4.

The amplitude for the production of the resonance $R$ (in this case the $D_{s0}^*(2317)^+$) is given by

$$\begin{aligned} t(B_c^+ \to J/\psi R) &= V_p \sum_i h_i G_i g_i \Big|_{pole} \\ &= \sqrt{3} A p_{J/\psi} \cos\theta \sum_i h_i G_i g_i \Big|_{pole}, \end{aligned} \tag{10.10}$$

where the index $i$ sums over $K^+D^0$, $K^0D^+$, $\eta D_s$, and $g_i$ is the coupling of the resonance to the channel $i$ (2.93). We remove the kinematic $V_p$ factor from the decay amplitude

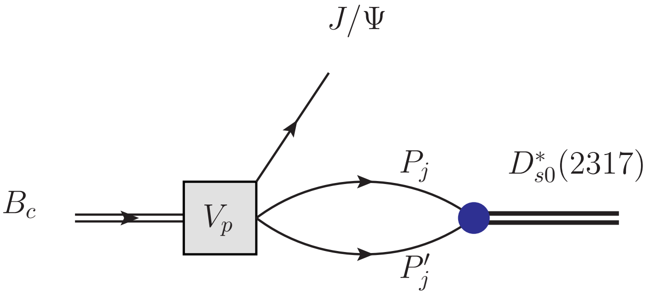

**Figure 10.4:** Diagrammatic presentation of $B_c^+ \to J/\psi R$. One sums over all intermediate mesons $P_i$ and $P_i'$ that generate the resonance ($K^+D^0$, $K^0D^+$ and $\eta D_s^+$).

defining $\tilde{t}(B_c^+ \to J/\psi R) = t(B_c^+ \to J/\psi R)/V_p$. Eqs. (10.10) and (10.5) are different, but under the assumption that the resonance is dynamically generated by the channels included in Eq. (10.5), the two expressions are related and are fixed, up to the common factor $V_p$. The width for the production of the resonance $R$, irrelevant of which decay channel it has, is given by

$$\Gamma(B_c^+ \to J/\psi R) = \frac{A^2}{8\pi}\frac{1}{m_{B_c^+}^2}\left|\tilde{t}(B_c^+ \to J/\psi D_{s0}^*(2317)^+)\right|^2 p_{J/\psi}^3\Big|_{pole}\,. \tag{10.11}$$

It is then interesting to study the ratio [381] of the $KD$ invariant mass distribution (10.9) and the width of direct resonance production (10.11)

$$\begin{aligned}\frac{\mathrm{d}\tilde{\Gamma}}{\mathrm{d}M_{\rm inv}} &= M_R^2\frac{(\mathrm{d}\Gamma/\mathrm{d}M_{\rm inv})/p_{J/\psi}^3\tilde{p}_{DK}}{\Gamma(B_c^+ \to J/\psi R)/\left.p_{J/\psi}^3\right|_{pole}}\\ &= \frac{M_R^2}{4\pi^2}\frac{\left|\tilde{t}(B_c^+ \to J/\psi D^+K^0)\right|^2}{\left|\tilde{t}(B_c^+ \to J/\psi D_{s0}^*(2317)^+)\right|^2}\\ &= \frac{M_R^2}{4\pi^2}\frac{|h_{D^+K^0}+\sum h_iG_it_i|^2}{|\sum h_iG_ig_i|^2|_{pole}},\end{aligned} \tag{10.12}$$

where the factor $M_R^2$ is put in the formula for convenience in order to have a dimensionless quantity. In this ratio the common factor $V_p$ (or $A$) cancels and we obtain a magnitude with no free parameters, tied to the nature of the $D_{s0}^*(2317)^+$ as a dynamically generated resonance.

## 10.3 Results

As mentioned above, the $G_i$ function is calculated analytically by dimensional regularization. In this work the parameter $\alpha(\mu)$ is fixed as $-1.852$ and $\mu$ as 1 GeV, in order to get the resonance $D_{s0}^*(2317)^+$ from the $DK$ and $\eta D_s$ interaction as a bound state pole. The very small width of this state comes from the decay into the isospin forbidden $\pi D_s$

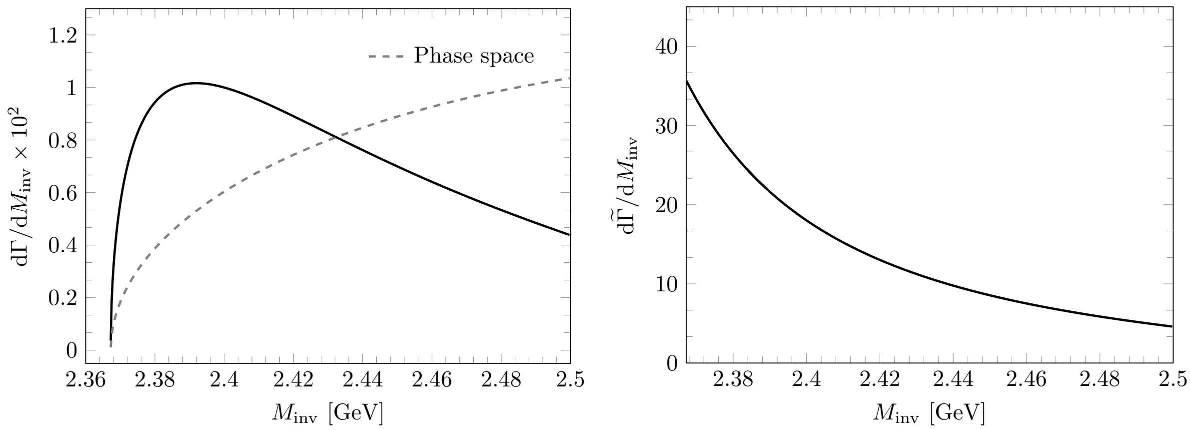

**Figure 10.5:** (Left) Differential decay width for the reaction $B_c^+ \to J/\psi D^+ K^0$. The solid curve corresponds to $(\alpha(\mu), \mu) = (-1.852, 1 \text{ GeV})$. The dash curve is the phase space. Note that the two curves have been normalized in the range of $M_{\mathrm{inv}}$ shown in the figure. (Right) The plot of $\mathrm{d}\tilde{\Gamma}/\mathrm{d}M_{\mathrm{inv}}$ defined in Eq. (10.12).

channel, which we do not consider since it has a negligible role in the generation of the $D^*_{s0}(2317)^+$ mass. We also calculate the couplings of the $D^*_{s0}(2317)^+$ to the $DK$ and the $D_s\eta$ channels, which can be extracted from the behavior of the $T$ matrix near the pole (see Eq. (2.93)). The values of the couplings that we get are $g_{D^+K^0} = g_{D^0K^+} = 7.1$ GeV, $g_{D_s^+\eta} = -6.5$ GeV. This corresponds to a coupling $-\sqrt{2} \times 7.1 = -10.1$ GeV to the $DK$ $I = 0$ channel $-\frac{1}{\sqrt{2}}(K^+D^0 + K^0D^+)$. We see then that the $D^*_{s0}(2317)^+$ resonance couples to the $DK$ channel more strongly.

Using the values of $\alpha(\mu)$ and $\mu$ mentioned above, we can get the differential decay width for the reaction of $B_c^+ \to J/\psi D^+ K^0$ (see left plot in Fig. 10.5). There the line shape of the differential decay width and the phase space have been normalized to unity over the range of the $DK$ invariant mass in the figure, which have been done in the same way as that in Ref. [377]. We clearly see that both curves have a different behaviour near the threshold. Even if the phase space is relatively small, we observe a remarkable enhancement in the $KD$ invariant mass distribution. This enhancement has been also observed experimentally, see for example in Ref. [243] the $B_s$ decay into $KD$ final states. We present a new reaction where this feature is also predicted, but in our approach is due to the dynamically generation of the $D^*_{s0}(2317)$.

In the right panel of Fig. 10.5 we plot $\mathrm{d}\tilde{\Gamma}/\mathrm{d}M_{\mathrm{inv}}$ of Eq. (10.12). We see a fall down of the distribution as a function of the $K^+D^0$ invariant mass. This is a clear indication of the presence of a resonance below threshold since we have divided the original invariant mass distribution by the phase space. Hence, essentially we are plotting $|t(B_c^+ \to J/\psi D^+ K^0)|^2$, which peaks at the mass of the $D^*_{s0}(2317)^+$ and we are seeing the tail of the resonance. In Ref. [2] we considered uncertainties tied to the possibility that the state $D^*_{s0}(2317)$ contains some $q\bar{q}$ component in addition to the $KD$ and $\eta D_s$ molecular channels. This possibility was investigated in Ref. [245] when analyzing the lattice QCD spectra for $KD$ and related channels, including $q\bar{q}$ components, and also has been thoroughly contemplated in Chapter 8. In Ref. [2] it was done by means of adding a Castillejo-Dalitz-Dyson pole [364] to the kernel potential, as in Ref. [245]. We found that, in the energy regime close to the $K^0D^+$ threshold, the consideration of such contribution would lead to differences in $\mathrm{d}\tilde{\Gamma}/\mathrm{d}M_{\mathrm{inv}}$ ranging from 5 to 20% at most, with respect to those shown in the

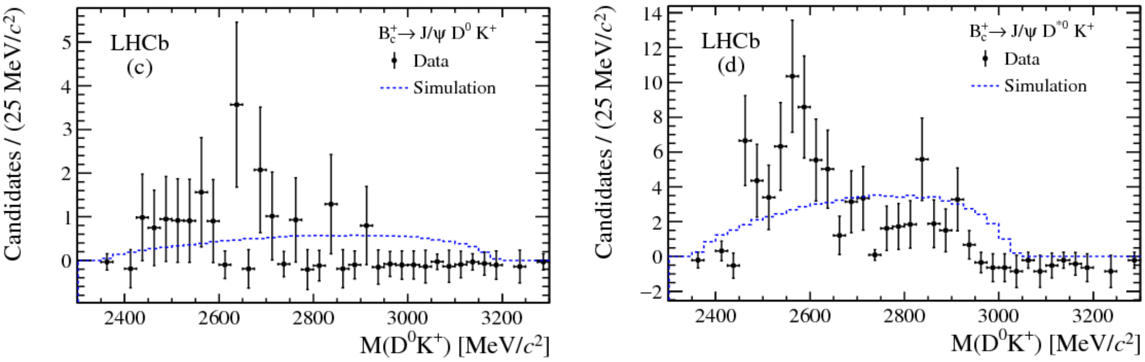

**Figure 10.6:** The event distribution for the decay $B_c \to J/\psi K^+ D^{(*)0}$ as a function of the $K^+D^0$ invariant mass measured by LHCb [382]. These data were published after finishing the results included in the present chapter, based on Ref. [2]. Unfortunately, we consider that neither the precision nor the accumulated statistic are sufficient to extract conclusions regarding the features discussed in the present chapter.

right plot of Fig. 10.5. This is a margin of uncertainty that we can assume, however, the main features discussed above remain.

## 10.4 Conclusion

In this work we have studied the $B_c^+$ decay into $J/\psi D^+ K^0$. The mechanism is: $B_c^+$ decays into $J/\psi$ and the quark pair $c\bar{s}$ via weak interaction; then the quark pair $c\bar{s}$ hadronizes into $D^+K^0$, $D^0K^+$ or $D_s^+\eta$ components which can interact among themselves generating the $D^*_{s0}(2317)^+$ resonance. In the scheme of the chiral unitary approach, we are able to choose the proper parameters $\alpha(\mu)$ and $\mu$ appearing in the loop function by matching the pole position of the $D^*_{s0}(2317)^+$. If $\alpha(1\text{ GeV}) = -1.852$, the couplings of $DK$ and $D_s\eta$ channels are $g_{D^+K^0} = g_{D^0K^+} = 7.1$ GeV and $g_{D_s^+\eta} = -6.5$ GeV, respectively. Later we have calculated the differential decay width of the reaction $B_c^+ \to J/\psi D^+ K^0$. One can appreciate that the shape of the distribution peaks closer to the $DK$ threshold than the phase space, indicating the coupling of $DK$ to a resonance below threshold (the $D^*_{s0}(2317)^+$ in this case). We also evaluated the rate of production of the $D^*_{s0}(2317)^+$ resonance and then constructed the ratio of $\mathrm{d}\Gamma/\mathrm{d}M_{\mathrm{inv}}(B_c^+ \to J/\psi D^+ K^0)$ to the width for $D^*_{s0}(2317)^+$ production, where the unknown factor $V_p$ of our theory cancels. The new normalized distribution obtained is then a prediction of the theory, only tied to the fact that the $D^*_{s0}(2317)^+$ is dynamically generated from the $DK$ and $\eta D_s$ channels. As to the feasibility of the reaction we think this is at reach in present facilities. Indeed in the PDG [383] one finds half of the known decay channels of the $B_c^+$ going to a $J/\psi$, one has also decays into $J/\psi$ and three pions, $J/\psi$ plus two kaons and one pion, and also decays into $J/\psi D_s^+$ and $J/\psi D_s^{*+}$. The study done here, showing how one can learn about the nature of the $D^*_{s0}(2317)^+$ from the measurements proposed, should serve as an incentive to perform these experiments in the near future. Actually, by the time of writing this dissertation there has been a measurement of this reaction by the LHCb collaboration in Ref. [382], though, as can be seen from Fig. 10.6, without enough resolution to test low energy enhancement predicted within our approach.

# Chapter 11

# A STUDY OF THE $Z_c(3900)$ STATE IN FINITE VOLUME

## 11.1 Introduction

The present chapter is devoted to the analysis of the LQCD information on the $Z_c(3900)$ resonance reported in Ref. [384], and it is based on [3]. For a brief introduction to this exotic meson we refer to Sec. 1.2.2. Here, we shall explore the results for finite volumes of a model based on a unitary HQSS $D^*\bar{D}$ interaction, previously constrained in Ref. [385] using experimental information. In this way, we will further test the predictions of the approach by comparing with the LQCD results of Prelovsek *et al* of Ref. [384], in the same spirit as previous research presented in Chapters 4, 8 and 9.

In Ref. [385], which constitutes the theoretical basis of the present manuscript, a $J/\psi\pi$–$D^*\bar{D}$ coupled-channels scheme was proposed to describe the observed peaks associated to the $Z_c(3900)$, which is assumed to have $I(J^{PC}) = 1(1^{+-})$ quantum numbers.[1] Within this coupled channel scheme, it was possible to successfully describe simultaneously the BESIII $J\psi\pi$ [86] and $D^*\bar{D}$ [90] invariant mass spectra, in which the $Z_c(3900)^{\pm}$ structure has been seen. Interestingly, two different fits with similar quality were able to reproduce the data. In each of them, the origin of the $Z_c(3900)^{\pm}$ was different:

1. In the first scenario, it corresponded to a resonance originated from a pole above the $D^*\bar{D}$ threshold.
2. Whereas in the second one the structure was produced by a virtual pole below the threshold (see Ref. [385] for more details).

Hadron interactions are governed by the non-perturbative regime of QCD and, for this reason, LQCD is an essential theoretical tool in hadron physics. In particular, one of the aims of LQCD is to obtain the hadron spectrum from quarks and gluons and their interactions (see *e.g.* Ref. [386] for a review focused on the light sector, and Refs. [387–390] for results concerning the charmonium sector).

LQCD simulations devoted to find the $Z_c(3900)$ state are still scarce [384, 391–395]. Exploratory theoretical studies for hidden charm molecules have been performed in Refs. [169,396], while actual LQCD simulations [384,391–394] find energy levels showing a weak interaction in the $Z_c(3900)^{\pm}$ quantum-numbers sector (either attractive or repulsive), and no evidence is found for its existence. The work of Ref. [395] employs LQCD to obtain a coupled-channel $S$-matrix, which shows an interaction dominated by off-diagonal terms, and, according to Ref. [395], this does not support a usual resonance picture for the $Z_c(3900)$. This $S$-matrix contains a pole located well below threshold in an unphysical

---

[1] Through all this chapter, charge conjugation refers only to the neutral element of the $Z_c(3900)$ isotriplet.

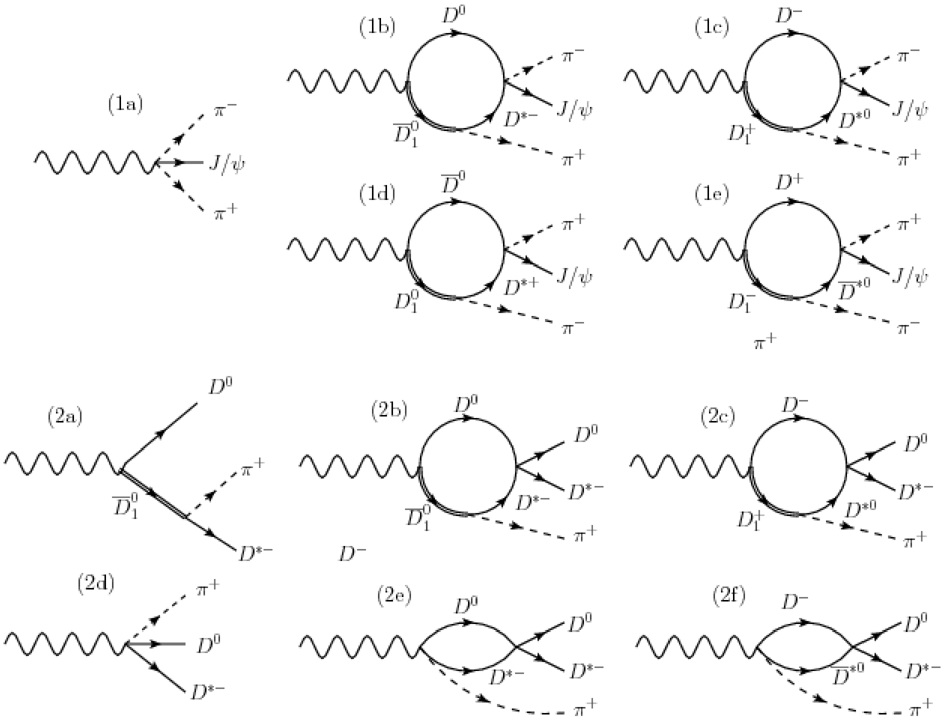

**Figure 11.1:** The diagrams contributing to the $Y(4260) \to D\bar{D}^*\pi$ and $Y(4260) \to J/\psi\pi\pi$ decay mechanisms.

RS, *i.e.*, a virtual pole. It is worth to note that this possibility could be in agreement with the second scenario advocated in Ref. [385], and mentioned above.

Our objective in the present work is to implement the coupled channel $T$-matrix—fitted to data in Ref. [385]—in a finite volume and study its spectrum. Thus, we will be able to compare the energy levels obtained with this finite volume $T$-matrix with those obtained in LQCD simulations, in particular those reported in Ref. [384]. This chapter is organized as follows. The formalism is presented in Sec. 11.2, while the $T$-matrix of Ref. [385] is briefly discussed in Sec. 11.2.1, and its extension for a finite volume is outlined in Sec. 11.2.2. Results are presented and discussed in Sec. 11.3, and the conclusions of this work, together with a brief summary are given in Sec. 11.4.

## 11.2 Formalism

### 11.2.1 Infinite volume

We first briefly review the model of Ref. [385] (where the reader is referred for more details) that we are going to employ here. There, the $Y(4260)$ decays to $D\bar{D}^*\pi$ and $J/\psi\pi\pi$ are studied with a model shown diagrammatically in Fig. 11.1, taken from this reference. Final state interactions among the outgoing $D\bar{D}^*$ and $J/\psi\pi$ produce the peaks observed by the BESIII collaboration, which are associated to the $Z_c(3900)$ state. The two channels involved in the $1(1^+)$ $T$-matrix are denoted as $1 \equiv J/\psi\pi$ and $2 \equiv D\bar{D}^*$. The authors of Ref. [385] solve the on-shell BSE (2.86) using as input kernel potential ($V$) the

**Table 11.1:** Values of the parameters employed in Eq. (11.7), taken from Ref. [385], together with the $Z_c$ pole positions found in that work. The errors account for statistical (first) and systematic (second) uncertainties (see Ref. [385] for details).

| $\Lambda_2$ (GeV) | $C_{1Z}$ (fm$^2$) | $b$ (fm$^3$) | $\widetilde{C}$ (fm$^2$) | $M_{Z_c}$ (MeV) | $\Gamma_{Z_c}/2$ (MeV) |
|---|---|---|---|---|---|
| 1.0 | $-0.19 \pm 0.08 \pm 0.01$ | $-2.0 \pm 0.7 \pm 0.4$ | $0.39 \pm 0.10 \pm 0.02$ | $3894 \pm 6 \pm 1$ | $30 \pm 12 \pm 6$ |
| 0.5 | $0.01 \pm 0.21 \pm 0.03$ | $-7.0 \pm 0.4 \pm 1.4$ | $0.64 \pm 0.16 \pm 0.02$ | $3886 \pm 4 \pm 1$ | $22 \pm 6 \pm 4$ |
| 1.0 | $-0.27 \pm 0.08 \pm 0.07$ | 0 (fixed) | $0.34 \pm 0.14 \pm 0.01$ | $3831 \pm 26^{+\ 7}_{-28}$ | virtual state |
| 0.5 | $-0.27 \pm 0.16 \pm 0.13$ | 0 (fixed) | $0.54 \pm 0.16 \pm 0.02$ | $3844 \pm 19^{+12}_{-21}$ | virtual state |

following matrix elements in the coupled-channel space:

$$V_{ij} = 4\sqrt{m_{i,1}m_{i,2}m_{j,1}m_{j,2}}\; C_{ij}\; e^{-k_i^2/\Lambda_i^2} e^{-k_j^2/\Lambda_j^2}. \tag{11.1}$$

with $m_{i,1}$ and $m_{i,2}$ the masses of the particles of the $i$th channel. Besides, $k_i^2$ is the relative three-momenta squared in the c.m. frame, implicitly defined in each channel through the relations

$$E = \omega_\psi(k_1) + \omega_\pi(k_1), \tag{11.2}$$

$$E = \omega_{D^*\bar{D}}(k_2)\ , \tag{11.3}$$

where,

$$\omega_\psi(q) = \sqrt{m_{J/\psi}^2 + q^2}\ , \tag{11.4}$$

$$\omega_\pi(q) = \sqrt{m_\pi^2 + q^2}\ , \tag{11.5}$$

$$\omega_{D^*\bar{D}}(q) = m_D + m_{D^*} + \frac{m_D + m_{D^*}}{2m_D m_{D^*}} q^2\ . \tag{11.6}$$

with $q \equiv |\vec{q}\,|$. The Gaussian form factors $e^{-k_i^2/\Lambda_i^2}$ are introduced to regularize the BSE, and thus, for each channel, an UV cut-off $\Lambda_i$ is introduced. In Ref. [385] $\Lambda_1 = 1.5$ GeV and two values for $\Lambda_2 = 0.5$ and 1 GeV [397, 398] were used. The $C_{ij}$ matrix stands for the $S$-wave interaction in the coupled-channels space, and it is given by [385]:

$$C = \begin{bmatrix} 0 & \widetilde{C} \\ \widetilde{C} & C_{22}\,(E) \end{bmatrix}. \tag{11.7}$$

In Eq. (11.7) the $J/\psi\pi \to J/\psi\pi$ interaction is neglected, $C_{11} = 0$, the inelastic transition is approximated by a constant, $\widetilde{C}$, while the $D^*\bar{D} \to D^*\bar{D}$ potential $C_{22}(E)$ is parametrized as:

$$C_{22}(E) = C_{1Z} + b\,(E - m_D - m_{D^*})\,. \tag{11.8}$$

In a momentum expansion, the lowest order contact potential for this elastic transition would be simply a constant, $C_{22} \equiv C_{1Z}$. However, it is easy to prove that two coupled channels with contact potentials cannot generate a resonance above threshold. Thus and for the sake of generality, the model of Ref. [385] allows for an energy dependence in Eq. (11.8), driven by the $b$ parameter. The diagonal matrix elements of the loop matrix $G = \mathrm{diag}(G_1, G_2)$ (2.87) associated to $J/\psi\pi$ and $D^*\bar{D}$ channels are given by the following relativistic and nonrelativistic loop functions, respectively, regularized with a Gaussian cutoff (A.2),

$$G_{11}(E) = \int_{\mathbb{R}^3} \frac{\mathrm{d}^3q}{(2\pi)^3} \frac{\omega_\psi(q) + \omega_\pi(q)}{2\omega_\psi(q)\omega_\pi(q)} \frac{e^{-2\left(q^2-k_1^2\right)/\Lambda_1^2}}{E^2 - \left(\omega_\psi(q) + \omega_\pi(q)\right)^2 + i\epsilon}\ , \tag{11.9}$$

$$G_{22}(E) = \frac{1}{4m_D m_{D^*}} \int_{\mathbb{R}^3} \frac{\mathrm{d}^3q}{(2\pi)^3} \frac{e^{-2\left(q^2-k_2^2\right)/\Lambda_2^2}}{E - \omega_{D\bar{D}^*}(q) + i\epsilon}\ . \tag{11.10}$$

These loop functions account for the right-hand cut of the $T$-matrix, that satisfies in this way the optical theorem. The $D^*\bar{D}$ channel loop function $G_{22}$ is computed in the non-relativistic approximation.

Resonances, bound states or virtual states are found as poles in one or more of the different RSs of the amplitude, which are reached by analytical continuation of the loop functions [Eqs. (11.9) and (11.10)] that enter in the evaluation of the $T$-matrix [Eq. (2.86)]. As discussed in Sec. 2.5, the different RSs $(\xi_1, \xi_2)$ are defined by the following continuations (2.89):

$$G_{11}(E) \to G_{11}(E) + \xi_1 i \frac{k_1(E)}{4\pi E} \ , \tag{11.11}$$

$$G_{22}(E) \to G_{22}(E) + \xi_2 i \frac{k_2(E)}{4\pi(m_D + m_{D^*})} \ , \tag{11.12}$$

where $\xi_{1,2}$ take the values 0 or 1. The physical RS is thus denoted by $(0,0)$, as usual.

The free parameters in the interaction matrix $C$ ($\widetilde{C}$, $C_{1Z}$ and $b$) were fitted in Ref. [385] to the experimental $J/\psi\pi^-$ and $D^+D^{*-}$ invariant mass distributions in the $Y(4260) \to J/\psi\pi\pi$ and $Y(4260) \to D\bar{D}^*\pi$ decays [86,90]. The fitted parameters are compiled here in Table 11.1, where we can see the two different scenarios investigated in Ref. [385]. In the first one, $b \neq 0$, the $Z_c$ appears as a $D^*\bar{D}$ resonance, *i.e.*, a pole above the $D^*\bar{D}$ threshold in the $(1,1)$ RS, connected with the physical one above this threshold. In the second one, where $b = 0$, a pole appeared below the $D\bar{D}^*$ threshold in the $(0,1)$ RS, which gives rise to the $Z_c(3900)$ structure, peaking exactly at the $D^*\bar{D}$ threshold in this case [385]. As mentioned, the pole is placed below the $D\bar{D}^*$ threshold, but it is above the $J/\psi\pi$ one, so it has an small imaginary part (about 8 MeV). We still regard it as a virtual pole, since, if the $J/\psi\pi$ channel is switched off (by setting the $D\bar{D}^* \to J/\psi\pi$ transition potential to zero, $\widetilde{C} = 0$), it moves to the real axis in the unphysical RS of the $D\bar{D}^*$ elastic amplitude, $T_{22}$ (see also Ref. [399]). In both scenarios, $b \neq 0$ and $b = 0$, only one pole appears, and it does in only one RS.

### 11.2.2 Finite volume

In this section, the coupled channel $T$-matrix described above is studied in a finite volume. Following the approach introduced in Sec. 2.5.1 the integrals in Eqs. (11.9) and (11.10) will be replaced by sums over all the possible discrete values of $\vec{q}$ ($\vec{q} = \frac{2\pi}{L}\vec{n}$, $\vec{n} \in \mathbb{Z}^3$):

$$\widetilde{G}_{11}(E) = \frac{1}{L^3}\sum_{\vec{n}} \frac{\omega_\psi(q) + \omega_\pi(q)}{2\omega_\psi(q)\omega_\pi(q)} \frac{e^{-2\left(q^2-k_1^2\right)/\Lambda_1^2}}{E^2 - \left(\omega_\psi(q) + \omega_\pi(q)\right)^2} \ , \tag{11.13}$$

$$\widetilde{G}_{22}(E) = \frac{1}{4\left(m_D m_{D^*}\right)} \frac{1}{L^3}\sum_{\vec{n}} \frac{e^{-2\left(q^2-k_2^2\right)/\Lambda_2^2}}{E - \omega_{D\bar{D}^*}(q)} \ , \tag{11.14}$$

(see Ref. [169] for further details). The $T$-matrix in a finite volume, $\widetilde{T}$, is then obtained as illustrated in Eq. (2.97), using the $\widetilde{G}$ matrix elements given by Eqs. (11.13) and (11.14). The discrete energy levels in the finite box are determined by the poles of the $\widetilde{T}$-matrix. As already discussed in Sec. 2.5.1, if the interaction is switched off, $V \to 0$, the free (or non-interacting) energy levels are identified with the poles of the $\widetilde{G}_{ii}$ functions, that in this particular case read,

$$E^{(\vec{n}^{\,2})}_{J/\psi\pi} = \omega_\psi(q_L n) + \omega_\pi(q_L n) \ , \tag{11.15}$$

$$E^{(\vec{n}^{\,2})}_{D^*\bar{D}} = \omega_{D\bar{D}^*}(q_L n) \ , \tag{11.16}$$

**Table 11.2:** Lattice parameters taken from Refs. [47, 384], and employed in this work.

| Lengths (fm) | |
|---|---|
| $a$ | 0.1239(13) |
| $L = 16a$ | 1.982(21) |
| **Masses (lattice units)** | |
| $am_\pi$ | 0.1673(16) |
| $am_{J/\psi}$ | 1.54171(43) |
| $am_{\eta_c}$ | 1.47392(31) |
| $am_{D,1}$ | 0.9801(10) |
| $am_{D,2}$ | 1.107(12) |
| $am_{D,4}$ | 1.107(27) |
| $am_{D^*,1}$ | 1.0629(13) |
| $am_{D^*,2}$ | 1.267(21) |
| $am_{D^*,4}$ | 1.325(68) |

where we use the shorthand $q_L = 2\pi/L$, and $n = \sqrt{\vec{n}^{\,2}}$.

Our purpose is to make contact with the results reported in the LQCD simulation of Ref. [384], and hence we will employ the masses and the energy-momentum dispersion relations used in that work. For the $J/\psi\pi$ channel the dispersion relation in Eq. (11.2) is still appropriate, but for the case of the $D^*\bar{D}$ channel, in Eqs. (11.3) and (11.6), $\omega_{D\bar{D}^*}(q)$ must be replaced by [47, 384]:

$$\omega^{\rm lat}_{D\bar{D}^*}(q) = m_{D,1} + m_{D^*,1} + \frac{m_{D,2} + m_{D^*,2}}{2m_{D,2}m_{D^*,2}}q^2 - \frac{m^3_{D,4} + m^3_{D^*,4}}{8m^3_{D,4}m^3_{D^*,4}}q^4 \, . \tag{11.17}$$

This lattice energy of the $D^*\bar{D}$ pair suffers from discretization errors and it must be used in Eq. (11.14). The non-interacting energy levels in Eq. (11.16) should be also modified accordingly. Notice that, because of the factor $e^{-q^2/\Lambda^2}$, the sum in Eq. (11.14) is exponentially suppressed in $\vec{n}^{\,2}$. For the range of energies considered in this work, it is sufficient to add terms up to $\vec{n}^{\,2} = 6$.[2] Finally, the discrete, interacting energy levels reported in Ref. [384] are actually the result of applying the following shift:

$$E \to E^* = E - m^{\rm lat}_{\rm s.a.} + m^{\rm exp}_{\rm s.a.} \, , \tag{11.18}$$

where the spin-average mass $m_{\rm s.a.}$ is given by $m_{\rm s.a.} = \frac{1}{4}(m_{\eta_c} + 3m_{J/\psi})$. For this reason, we will also present our energy levels shifted as in Eq. (11.18). The parameters involved in our calculations, taken from Refs. [47, 384], are collected in Table 11.2. In particular, one has $m_\pi = 266 \pm 4$ MeV and $L = 16\,a = 1.98 \pm 0.02$ fm, being $a$ the lattice spacing.

### 11.2.3 Further comments

With all the ingredients presented in Sec. 11.2.2, we can compare our predictions for the energy levels in a box with those reported in Ref. [384]. But before presenting our results

---

[2] We have checked that the numerical differences are negligible if larger values, say $\vec{n}^{\,2} = 8$, are used.

we would like to discuss some technical details concerning two differences that could affect the comparison.

First, we would like to note that the LQCD simulation in Ref. [384] includes the $J/\psi\pi$ and $D^*\bar{D}$ channels that are present in our $T$-matrix analysis, but it also includes other channels, like $\eta_c\rho$ or $D^*\bar{D}^*$, the thresholds of which are located 120 MeV below and 140 MeV above the $D\bar{D}^*$ threshold, respectively. However, according to Ref. [385], it is sufficient to include the $J/\psi\pi$ and $D^*\bar{D}$ channels to achieve a good reproduction of the experimental information concerning the $Z_c(3900)$. For this reason, we expect that, in a first approximation, these other channels could be safely neglected in the calculations. It must be stated that there are also three-meson channels with thresholds below the $D^*\bar{D}$ one, like $\eta_c\pi\pi$ ($\sim 3260$ MeV) or $J/\psi\pi\pi$ ($\sim 3370$ MeV) among others, and also above the $D^*\bar{D}$ threshold, such as $D^*\bar{D}\pi$ ($\sim 4015$ MeV), which could give rise to energy levels in the region we are exploring. These channels are neither explicitly taken into account in Ref. [384] nor in the present approach.

Next, we would like to briefly mention the $m_\pi$ dependence of our predictions and of LQCD simulations. In general, the properties of resonances vary, to a larger or lesser extent, with the quark masses. LQCD simulations are usually performed with quark masses different from the physical ones, and hence the resonance parameters extracted from them can also be different from the experimental ones.[3] From a theoretical point of view, the pion mass dependence (in general, the quark mass dependence) will manifest itself both in the kinematics of the processes and in the dynamics of the interactions. In our particular case, there could be a pion mass dependence in the parameters of the potential, Eq. (11.7). Nonetheless, the LQCD simulation of Ref. [384] is performed for a relatively low pion mass, $m_\pi = 266 \pm 4$ MeV, and we thus expect the eventual dependence to be mild, so we have ignored it. Furthermore, we are going to compare several sets of these parameters (presented in Table 11.1), which somewhat compensates this effect.

## 11.3 Results and discussion

In Fig. 11.2, we show the $L$ dependence of some energy levels close to the $D^*\bar{D}$ threshold. They have been computed from the poles of the finite volume $\widetilde{T}$-matrix, Eq. (2.97), by using the parameters of Table 11.1 for $\Lambda_2 = 1$ GeV, and the lattice setup given in Table 11.2. The levels obtained in the $Z_c(3900)^\pm$ resonance (virtual) scenario, calculated using the entries of the first (third) row of Table 11.1, are displayed in the left (right) panel. The blue dashed lines stand for the $J/\psi\pi$–$D^*\bar{D}$ coupled-channel-analysis results, and the red solid lines show the energy levels obtained when the inelastic $J/\psi\pi$–$D^*\bar{D}$ transition is neglected ($\tilde{C} = 0$). This latter case corresponds to consider a single, elastic channel

---

[3] As an example, let us consider the works of Refs. [400, 401], where LQCD simulations concerning the light sector are performed for pion and kaon masses $m_\pi = 391$ MeV and $m_K = 549$ MeV. Although the spectrum found there cannot be easily compared with the physical (experimental) one because of the large masses used, qualitative comparisons can still be made, which are in good agreement with the observed spectrum or with theoretical expectations. In particular, in Ref. [401] the $\eta\pi$, $K\bar{K}$ interaction is studied and a cusp behaviour in the $\eta\pi$ elastic amplitude is traced back to the $a_0(980)$ resonance. In Ref. [400], where the $\eta K$, $\pi K$ interactions are considered, resonances are found alongside with a virtual state and a bound state. The virtual state in the sector $J^P = 0^+$ is expected to evolve to a resonance with decreasing quark masses, and may thus be identified with the $\kappa$ resonance. This is in agreement with the theoretically expected behaviour for the $\kappa$ resonance [402], and also for the $\sigma$ [134, 207], the $I = 0$ member of the octet.

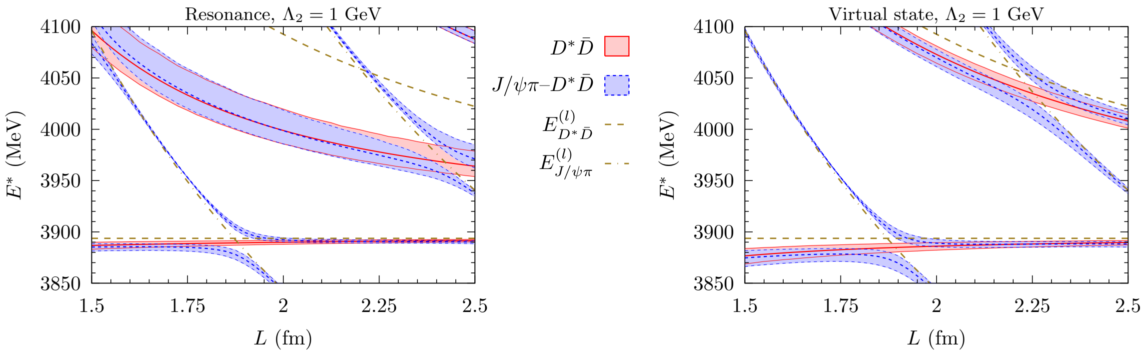

**Figure 11.2:** Volume dependence of some energy levels located close to the $D^*\bar{D}$ threshold, and obtained when the $Z_c$ is described as a resonance (left) or as a virtual state (right) in the $L \to \infty$ limit. The blue dashed lines have been obtained from the $J/\psi\pi$–$D^*\bar{D}$ coupled channel analysis, and the red solid lines show the single elastic channel ($D^*\bar{D}$) case, in both cases $\Lambda_2$ has been fixed to 1 GeV. The error bands are obtained from the uncertainties of the parameters introduced in the theoretical model of Ref. [385] (Table 11.1), adding in quadratures the statistical and systematic errors. The green dashed (dotted-dashed) lines are the free $D^*\bar{D}$ ($J/\psi\pi$) energy levels $E^{(l)}_{D^*\bar{D}}$ ($E^{(l)}_{J/\psi\pi}$).

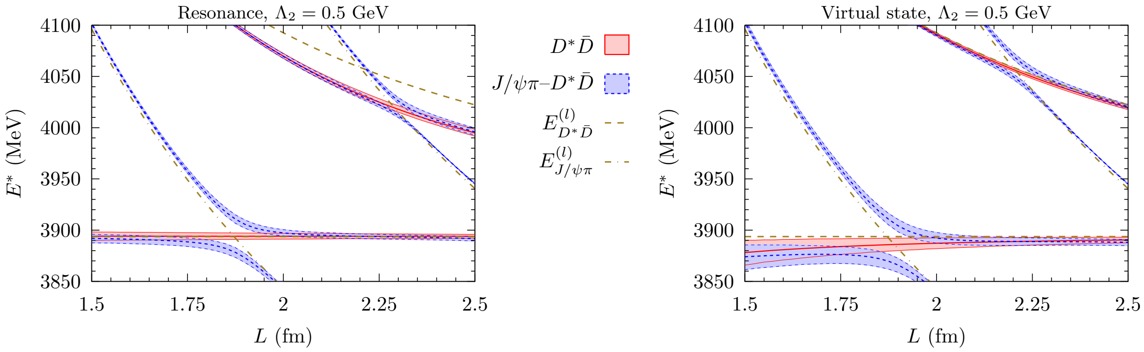

**Figure 11.3:** Same as in Fig. 11.2, but for the case $\Lambda_2 = 0.5$ GeV.

($D^*\bar{D}$). The error bands account for the uncertainties on the energy levels inherited from the errors in the parameters of Ref. [385], quoted in Table 11.1 (statistical and systematic errors are added in quadrature for the calculations). The green dashed (dotted-dashed) lines stand for the non-interacting $D^*\bar{D}$ ($J/\psi\pi$) energy levels. In Fig. 11.3, the same results are shown but for the case $\Lambda_2 = 0.5$ GeV. The qualitative $L$ behaviour of both Figs. 11.2 and 11.3 is similar, so we discuss first Fig. 11.2 and, later on, the specific differences between them will be outlined.

For both resonant and virtual scenarios, there is always an energy level very close to a free energy of the $J/\psi\pi$ state, $E^{(l)}_{J/\psi\pi}$, which reveals that the interaction driven by this meson pair is weak. Furthermore, the energy levels for the coupled–channel $\widetilde{T}$-matrix basically follow those obtained within the elastic $D^*\bar{D}$ approximation, except in the neighbourhood of the $J/\psi\pi$ free energies. This also corroborates that the role of the $J/\psi\pi$ is not essential.

Let us pay attention to the levels placed in the vicinity of the $D^*\bar{D}$ threshold. For simplicity, we first look at the single elastic channel case. There appears always a state just below threshold, as it should occur since we are putting an attractive interaction in a finite box. As the size of the box increases, and since there is no bound state in the infinite volume limit (physical case), this level approaches to threshold.[4] When the $J/\psi\pi$ channel is switched on, the $L-$behaviour of this level will be modified, specially when it is close to a discrete $J/\psi\pi$ free energy. Note that the slopes of the $J/\psi\pi$ free levels, in the range of energies considered here, are larger (in absolute value) than those of the $D\bar{D}^*$ ones, because the threshold of the $J/\psi\pi$ channel is far from the region studied.

From the above discussion, one realizes that the next coupled channel energy level, located between the two $D^*\bar{D}$ free ones ($E^{(0)}_{D^*\bar{D}}$ and $E^{(1)}_{D^*\bar{D}}$), could be more convenient to extract details of the $Z_c(3900)^{\pm}$ dynamics. Indeed, in the resonance scenario, this second energy level is very shifted downwards with respect to $E^{(1)}_{D^*\bar{D}}$, since it is attracted towards the $Z_c$ resonance energy.[5] In this context, it should be noted that the presence of $Z_c(3900)^{\pm}$ does not induce the appearance of an additional energy level, but a sizeable shift of the energy levels with respect to the non-interacting ones. Therefore, even if no extra energy level appears, it would not be possible to completely discard the existence of a physical state (resonance). The energy shift, however, can be quite large and, only in this sense, one might speak of the appearance of an additional energy level. The correction of the second energy level in the virtual state scenario is much less pronounced. We should note here that the elastic phase shift computed with the $T$-matrix in Ref. [385] does not follow the pattern of a standard BW distribution associated to a narrow resonance. Indeed, the phase shift does not change quickly from 0 to $\pi$ in the vicinity of the $Z_c(3900)$ mass, and actually it does not even reach $\pi/2$. This is mostly due to a sizeable background in the amplitude.

We now compare the cases $\Lambda_2 = 1$ GeV (Fig. 11.2) and $\Lambda_2 = 0.5$ GeV (Fig. 11.3). For $\Lambda_2 = 0.5$ GeV, the relevant (second) energy level is more shifted with respect to $E^{(1)}_{D^*\bar{D}}$ in the resonance scenario (Fig. 11.3, left) than in the virtual scenario (Fig. 11.3, right). This is the same behaviour already discussed for $\Lambda_2 = 1$ GeV. However, the shift for the resonance scenario is smaller in the $\Lambda_2 = 0.5$ GeV case (Fig. 11.3, left) than in the $\Lambda_2 = 1$ GeV one (Fig. 11.2, left). This is due to the fact that the $Z_c(3900)^{\pm}$ is closer to the threshold and the coupling to $D^*\bar{D}$ is smaller for the $\Lambda_2 = 0.5$ GeV case. Another important difference between the $\Lambda_2 = 1$ GeV and $\Lambda_2 = 0.5$ GeV results is that the error band of the relevant energy level is smaller when the lighter cutoff is used. This is due to the different relative errors in both cases, and the fact that for $\Lambda_2 = 0.5$ GeV, the relevant level is closer to the $E^{(1)}_{D^*\bar{D}}$ free energy than in the $\Lambda_2 = 1$ GeV case.

After having explored the volume dependence of the energy levels predicted with our $\widetilde{T}$-matrix and scrutinized its physical meaning, we can now compare our results with those reported in Ref. [384]. The energy levels in the latter work are obtained from a single volume simulation, $L = 1.98 \pm 0.02$ fm, and are shown in Fig. 11.4 with black squares. In the figure, we also show the results obtained in this work for $L = 2$ fm, for both the resonance (filled circles) and virtual state (empty circles) scenarios for the $Z_c(3900)$. Besides, the energy levels calculated with $\Lambda_2 = 1$ GeV and $\Lambda_2 = 0.5$ GeV are represented in blue and green, respectively. We provide two different error bars for our results, considering only the uncertainties of the parameters entering in the $T$-matrix (Table 11.1), or additionally taking into account the errors of the lattice parameters (Table 11.2). We clearly see three distinct regions, the lowest energies are very close to

---

[4] This is also discussed in more detail in Ref. [169].

[5] For physical pions ($m_\pi \sim 140$ MeV), the $Z_c$ resonance mass, ignoring errors, is 3894 MeV (3886 MeV) for $\Lambda_2 = 1$ GeV (0.5 GeV), as seen from Table 11.1. For $m_\pi = 266$ MeV as used in Ref. [384], and taking into account the shift in Eq. (11.18), one might estimate that mass to be around 3912 MeV (3902 MeV).

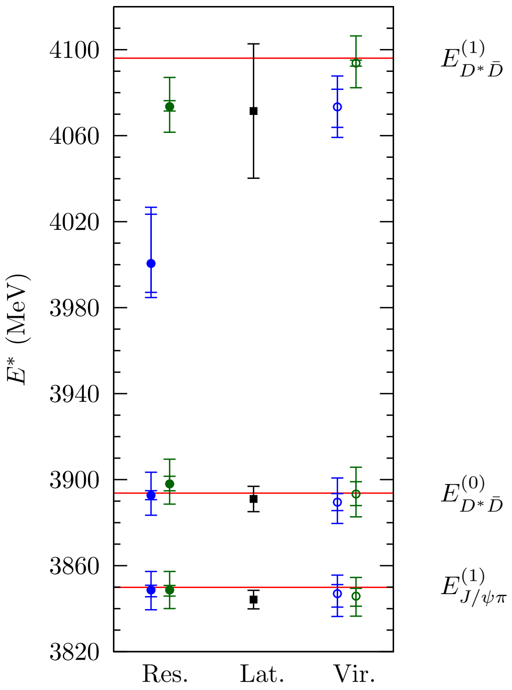

**Figure 11.4:** Comparison of the energy levels of Ref. [384], shown with black squares, with our results for $L \simeq 2$ fm. Full (empty) circles stand for the energy levels obtained in the resonance (virtual state) scenario for the $Z_c(3900)$ state. On the other hand, the energy levels for the $\Lambda_2 = 1$ GeV (0.5 GeV) case are shown by blue (green) circles. The energy levels calculated in this work are displayed with two types of error bars: the smaller ones have been obtained considering only the errors of the parameters entering in the $T$-matrix (Table 11.1), whereas the larger ones additionally take into account the errors of the lattice parameters (Table 11.2).

the $D\bar{D}^*$ threshold ($E^{(0)}_{D^*\bar{D}}$) and to the first $J/\psi\pi$ free energy level ($E^{(1)}_{J/\psi\pi}$). These free energies are shown in Fig. 11.4 with red solid horizontal lines. As expected, the two lowest lattice levels agree well with our results for both cutoffs and the two $Z_c(3900)$ state interpretations examined in this work. The higher energy levels are the relevant ones, and, as already mentioned, our results are significantly shifted to lower energies with respect to $E^{(1)}_{D^*\bar{D}}$ for the resonant scenario, while this shift is much smaller for the virtual state one. In general, the lattice results are in very good agreement with the virtual state scenario level for both $\Lambda_2 = 0.5$ GeV and $\Lambda_2 = 1$ GeV cases, whereas in the resonance scenario the agreement is also very good for $\Lambda_2 = 0.5$ GeV, and it is not so good for $\Lambda_2 = 1$ GeV. However, in the latter case, we find $E_{\rm th} = 4000^{+24}_{-13}$ MeV, while the lattice energy is $E_{\rm lat} = 4070 \pm 30$ MeV [384], and hence this non-compatibility is small, the difference being $E_{\rm lat} - E_{\rm th} = 70 \pm 40$ MeV. The comparison of our results with those of Ref. [384] support the conclusions given in the latter work: from the energy levels found in that LQCD simulation one cannot deduce the existence of a resonance (a truly physical state, instead of a virtual state), namely $Z_c(3900)$. But also from this comparison, putting this conclusion in the other way around, one cannot discard its existence either.

Finally, as can be seen in Fig. 11.4, a comparison of the relevant energy level obtained in the resonance scenario for $\Lambda_2 = 0.5$ GeV (green filled circle) with that obtained in the virtual scenario for $\Lambda_2 = 1$ GeV (blue empty circle) shows that, within theoretical uncertainties (the smallest error bars), both cases are indistinguishable. This fact can

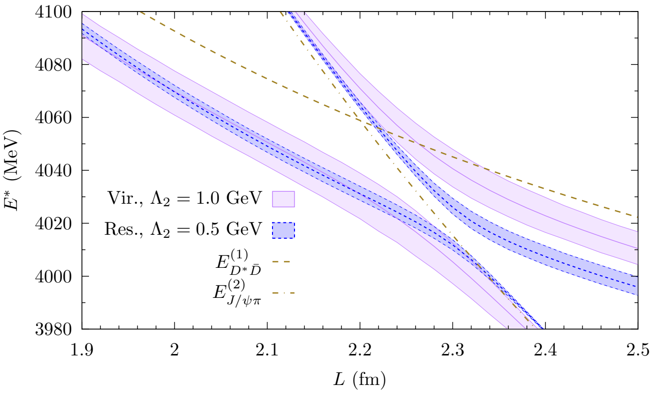

**Figure 11.5:** Comparison of the relevant energy level for the $\Lambda_2 = 1$ GeV virtual state (solid purple lines) and the $\Lambda_2 = 0.5$ GeV resonance scenarios (dashed blue lines) around $L \simeq 2$ fm. The green dashed and dashed-dotted lines represent $E^{(1)}_{D^*\bar{D}}$ and $E^{(2)}_{J/\psi\pi}$ non-interacting energies, respectively.

already be seen by comparing the left panel of Fig. 11.3 and the right panel of Fig. 11.2 around $L \simeq 2$ fm. These energy levels are shown together in Fig. 11.5. It can be seen that, although these two scenarios cannot be distinguished at $L \simeq 2$ fm (the volume used in Ref. [384]), they lead to appreciably different energies already at $L \simeq 2.5$ fm. This means that one cannot elucidate the nature of this intriguing $Z_c(3900)$ state with LQCD simulations performed in a single volume. Rather, it would be useful to perform simulations at different values of the box size, to properly study the volume dependence of the energy levels. Of course, as discussed in Ref. [384], this would bring in a technical problem –the appearance of more $J/\psi\pi$ free energy levels in the energy region of interest,[6] as can be seen in Fig. 11.5 ($E^{(2)}_{J/\psi\pi}$). Notwithstanding these difficulties, our work should stimulate this kind of studies.

It must be also stated that there are certainly other ways to perform LQCD simulations to gain further insight on the nature of the $Z_c(3900)$ that do not require the use of several volumes. One can perform, for example, simulations in a single volume but with the two-meson systems moving with several non-zero momentum [403–406] (examples of such type of simulations can be found *e.g.* in Refs. [400, 401, 407]). Results of such approaches could not be directly compared, however, with our results presented in Sec. 11.3, where we have focused on the volume dependence of the discrete spectrum obtained in LQCD calculations. Although beyond the scope of this work, we would like to mention that it is also possible to make predictions from unitary effective field theories for such simulations [408].

## 11.4 Summary

With the aim of shedding light into the nature of the $Z_c(3900)$ state, we have implemented the $J/\psi\pi$, $D^*\bar{D}$ coupled channel $T$-matrix of Ref. [385] in a finite volume, and we have compared our predictions with the results obtained in the LQCD simulation of Ref. [384]. The model of Ref. [385] provides a similar good description of the experimental informa-

---

[6] It should be noted that recent analysis of LQCD simulations (*e.g.* Refs. [400, 401]) are able to obtain detailed spectra involving a large number of energy levels, overcoming this difficulty.

tion concerning the $Z_c(3900)$ structure in two different scenarios. In the first one, the $Z_c(3900)$ structure is due to a resonance originating from the $D^*\bar{D}$ interaction, while in the second one it is produced by the existence of a virtual state. We have studied the dependence of the energy levels on the size of the finite box for both scenarios. For the volume used in Ref. [384], our results compare well with the energy levels obtained in the LQCD simulation of Ref. [384]. However, the agreement is similar in both scenarios (resonant and virtual) and hence it is not possible to privilege one over the other. Therefore and in order to clarify the nature of the $Z_c(3900)$ state, we suggest performing further LQCD simulations at different volumes to study the volume dependence of the energy levels.

# Chapter 12

# THE $\rho(\omega)B^*(B)$ INTERACTION AND STATES OF $J = 0, 1, 2$

## 12.1 Introduction

Chiral symmetry, reflecting the QCD dynamics at low energies, has played a crucial role in the description of the hadron interactions. Originally developed for the interaction of pseudoscalar mesons [178] and of the meson nucleon system [409, 410], the need to incorporate vector mesons into the framework gave rise to the local hidden gauge approach [202, 411, 412], which incorporates the information of the chiral Lagrangians of [178] and extends it to accommodate the vector interaction with pseudoscalars and with themselves. Another important step to understand the dynamics of hadrons at low and intermediate energies was given by incorporating elements of non-perturbative physics, restoring two body unitarity in coupled channels, which gave rise to the chiral unitary approach, that has been instrumental in explaining many properties of hadronic resonances, mesonic [130, 132, 153–155] and baryonic [128, 131, 133, 204, 220, 361, 366, 413–417]. Concerning the interaction of vector mesons in this unitary approach, the first work was done in [368], where surprisingly the $f_2(1270)$ and $f_0(1370)$ resonances appeared as a consequence of the interaction of $\rho$ mesons from the solution of the BSE equation with the potential generated from the LHG Lagrangians [202, 411, 412]. The generalization to SU(3) of that work was done in [369] and further resonances came from this approach, the $f_2'(1525)$ and $f_0(1710)$ among others. Most of these findings were confirmed in the SU(6) spin-flavor symmetry scheme followed by [211]. The step to incorporate charm in the LHG approach of Refs. [368, 369] was given in [219], and the interaction of $\rho$, $\omega$ and $D^*$ was studied extrapolating to the charm sector the LHG approach. Three $D$ states with spin $J = 0, 1, 2$ were obtained, the second one identified with the $D^*(2640)$ and the last one with the $D_2^*(2460)$. The first state, with $J = 0$, was predicted at 2600 MeV with a width of about 100 MeV. This state is also in agreement with the $D(2600)$, with a similar width, reported after the theoretical work in [418]. The properties of these resonances are well described by the theoretical approach.

The success in the predictions of this theoretical framework in the light and the charm sectors suggests to give the step to the bottom sector and make predictions in this chapter. The extension is straightforward, because the interaction in the local hidden gauge approach is provided by the exchange of vector mesons. The exchange of light vectors is identical to the case of the $\rho D^*$ interaction, since the $c$ or $b$ quarks act as spectators. In the exchange of heavy vectors, the form and the coefficients are also the same, since the $\bar{B}$ meson can be obtained from the $D$ simply replacing the $c$ quark by the $b$ quark. However, instead of exchanging a $D^*$ in the sub-dominant terms, one exchanges now a $B^*$ meson. These terms are anyway sub-dominant. Hence, it is not surprising that the predictions that we obtain in this work in the bottom sector are very similar to those obtained in [219] in the charm sector.

We shall also discuss some implications derived from HQSS, which we show is satisfied by the dominant terms of the interaction, and then discuss the relevance of the sub-dominant HQSS breaking terms. We make predictions for three states from the $\rho/\omega\, B^*$ interaction and compare with available experimental states. As we shall see, the role played by the $\omega$ meson is minor and it is not as important as that of the $\rho$ meson.

In a similar way, we also deal with the interaction of $\rho B$ in $S$-wave, which gives rise to a state of $J = 1$ which we can identify with a state already existing. This interaction follows also from the LHG approach, although equivalent chiral Lagrangians have been used in the light sector [211, 223, 419] and in the $D$ sector [80, 355]. The contents of this chapter are based on the results of Ref. [1]

## 12.2 Formalism

We are going to use the LHG approach where the interaction is given mainly by the exchange of vector mesons. We follow closely the approach of [219] and with minimal changes we can obtain most of the equations.

### 12.2.1 Vector-vector interaction

We take the vector-vector interaction from [202] as

$$\mathcal{L}_{III} = -\frac{1}{4}\langle V_{\mu\nu}V^{\mu\nu}\rangle\,. \tag{12.1}$$

where the symbol $\langle\rangle$ represents the trace in SU(4) flavor space (we consider $u, d, s$ and $b$ quarks), with

$$V_{\mu\nu} = \partial_\mu V_\nu - \partial_\nu V_\mu - ig[V_\mu, V_\nu] \tag{12.2}$$

and

$$V_\mu = \left(\begin{array}{cccc} \frac{\rho^0}{\sqrt{2}} + \frac{\omega}{\sqrt{2}} & \rho^+ & K^{*+} & B^{*+} \\ \rho^- & -\frac{\rho^0}{\sqrt{2}} + \frac{\omega}{\sqrt{2}} & K^{*0} & B^{*0} \\ K^{*-} & \bar{K}^{*0} & \phi & B_s^{*0} \\ B^{*-} & \bar{B}^{*0} & \bar{B}_s^{*0} & \Upsilon \end{array}\right)_\mu \tag{12.3}$$

standing for the vector representation of the different $q\bar{q}$ pairs, and the coupling $g$ is given by

$$g = \frac{m_V}{2f} \tag{12.4}$$

with the pion decay constant $f \simeq 93$ MeV, and $m_V \simeq 770$ MeV. One may wonder why still the value of $g$ in SU(3) is used in the heavy sector. We give a justification at the end of section 12.3 when we discuss the implications of HQSS for the $B^*B\pi$ vertex.

The LHG Lagrangians also contains a four vector contact term

$$\mathcal{L}_{III}^{(c)} = \frac{g^2}{2}\langle V_\mu V_\nu V^\mu V^\nu - V_\nu V_\mu V^\mu V^\nu\rangle, \tag{12.5}$$

which in the $\rho/\omega B^*$ channel gives rise to the term depicted in Fig. 12.1(a).

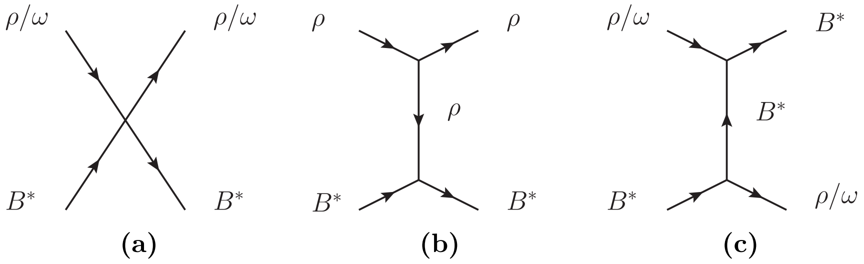

**Figure 12.1:** The model for the $\rho/\omega\, B^*$ interaction.

From Eq. (12.1) we also get a three vector interaction term

$$\mathcal{L}_{III}^{3V} = ig\langle (V^\mu \partial_\nu V_\mu - \partial_\nu V_\mu V^\mu)\, V^\nu \rangle . \tag{12.6}$$

This latter Lagrangian gives rise to a $VV$ interaction term through the exchange of a virtual vector meson, as depicted in Figs. 12.1(b) and 12.1(c). As in [219] we also assume that the three momenta of the particles are small compared to the vector masses. This helps to simplify the formalism.

We consider the $\rho/\omega\, B^*$ states

$$\begin{aligned} |\rho B^*; I=1/2, I_3=1/2\rangle &= -\sqrt{\frac{2}{3}}\left|\rho^+ B^{*0}\right\rangle - \sqrt{\frac{1}{3}}\left|\rho^0 B^{*+}\right\rangle , \\ |\rho B^*; I=3/2, I_3=3/2\rangle &= -\left|\rho^+ B^{*+}\right\rangle , \\ |\omega B^*; I=1/2, I_3=1/2\rangle &= \left|\omega B^{*+}\right\rangle . \end{aligned} \tag{12.7}$$

Where the isospin doublets are $(K^{*+}, K^{*0})$, $(\bar{K}^{*0}, -K^{*-})$, $(B^{*+}, B^{*0})$, $(\bar{B}^{*0}, -B^{*-})$ and the rho triplet is $(-\rho^+, \rho^0, \rho^-)$.

The contact terms are all of the type

$$\begin{aligned} -it^{(c)}_{\rho B^* \to \rho B^*} = -ig^2 (&\alpha \epsilon^{(1)}_\mu \epsilon^{(2)}_\nu \epsilon^{(3)\nu} \epsilon^{(4)\mu} \\ &+ \beta \epsilon^{(1)}_\mu \epsilon^{(2)\mu} \epsilon^{(3)\nu} \epsilon^{(4)\nu} \\ &+ \gamma \epsilon^{(1)}_\nu \epsilon^{(2)}_\mu \epsilon^{(3)\nu} \epsilon^{(4)\mu}), \end{aligned} \tag{12.8}$$

with $\epsilon^\mu$ the polarization vectors of the vector mesons in the order 1, 2, 3, 4, where these indices are used in the reaction $1+2 \to 3+4$ ($\rho B^* \to \rho B^*$). Note that we are using real polarization vectors.

Analogously, the terms associated to vector exchange of the type of Fig. 12.1(b) are particularly easy, since, neglecting the external three momenta, these terms are of the type

$$t^{(ex)} = \frac{g^2}{m_V^2} \alpha' (k_1 + k_3)\cdot(k_2+k_4) \epsilon^{(1)}_\mu \epsilon^{(2)}_\nu \epsilon^{(3)\mu} \epsilon^{(4)\nu} . \tag{12.9}$$

The form of Eq. (12.9) stems from Eq. (12.6) assuming the $\epsilon^0$ component of the external vector mesons to be zero, and neglecting the linear terms in three momentum coming from Eq. (12.6), which is quite reasonable for $S$-wave. An explicit evaluation of these latter extra terms was done in [420], in the study of the $\gamma p \to K^0 \Sigma^+$ reaction, which showed the relevance of the VB intermediate states, where one finds the same three vector vertex of Fig. 12.1 (see section 2 of [420]). The center of mass photon momentum in the reaction of [420] is about 780 MeV/c in spite of which, the linear terms in three momentum neglected in Eq. (12.9) were found to be of the order of 15%. This could also explain why in the decay of resonances like the $f_2(1270)$ into two mesons, which rely upon the same vertices and approximations [421], the widths are obtained in good agreement with experiment, in spite of having two photons with momentum of 635 MeV/c. Note that in this case, the $f_2(1270)$, that comes as a two $\rho$ bound state, is bound by about 270 MeV. Since the $\epsilon^0$ component goes as $|\vec{k}|/M_V$, the ratio for the $\rho B^*$ and $\rho\rho$ bound states would be about $M_\rho \sqrt{\mu(\rho B^*)B(\rho B^*)}/M_{B^*} \sqrt{\mu(\rho\rho)B(\rho\rho)}$, with $\mu(\rho B^*)$, $\mu(\rho\rho)$ the reduced mass and $B(\rho B^*)$, $B(\rho\rho)$ the binding energy of the bound state in the $\rho B^*$ and $\rho\rho$ systems respectively. Taking into account that we get about 350 MeV binding for the $\rho B^*$ system, this ratio is of the order of about 0.22, which reinforces neglecting the $\epsilon^0$ component of the external vectors assumed in Eq. (12.9). One should also keep in mind that small changes in the kernel of Eq. (12.9) can be reabsorbed by suitable changes in the cut off, since the combination $[V]^{-1} - G$ ($V$ would sum contributions from $t^{(c)}$ and $t^{(ex)}$ from Eqs. (12.8) and (12.9)) is what appears in the evaluation of the final $T$-matrix, and one finally always tunes the cut off to some experimental data. We shall come back to this point in Section 12.5.2.

It is interesting to point out that the dominant vector exchange terms (with light vector exchange, Fig. 12.1(b)) contribute neither to the $\omega B^* \to \omega B^*$ nor to the $\omega B^* \to \rho B^*$ transitions. Indeed, the $\omega\omega\omega$ vertex is forbidden by $C-$parity. Similarly, $\omega\omega\rho^0$ is also forbidden for the same reason, and isospin. Finally, the $\rho\rho\omega$ (even with charged $\rho$) is not allowed by $G$ parity conservation. The only way to have a contribution to the $\omega B^* \to \omega B^*$ transitions is through intermediate steps that involve the exchange of heavy vector mesons (12.1(c)).[1]

With the polarization structure of the amplitudes we can separate these terms into different spin contributions (we work only with angular momentum $L = 0$) which are given by [368]

$$\mathcal{P}(0) = \frac{1}{3}\epsilon_\mu^{(1)}\epsilon^{(2)\mu}\epsilon_\nu^{(3)}\epsilon^{(4)\nu}, \tag{12.10}$$

$$\mathcal{P}(1) = \frac{1}{2}(\epsilon_\mu^{(1)}\epsilon_\nu^{(2)}\epsilon^{(3)\mu}\epsilon^{(4)\nu} - \epsilon_\mu^{(1)}\epsilon_\nu^{(2)}\epsilon^{(3)\nu}\epsilon^{(4)\mu}), \tag{12.11}$$

$$\begin{aligned}\mathcal{P}(2) = {} & \frac{1}{2}(\epsilon_\mu^{(1)}\epsilon_\nu^{(2)}\epsilon^{(3)\mu}\epsilon^{(4)\nu} + \epsilon_\mu^{(1)}\epsilon_\nu^{(2)}\epsilon^{(3)\nu}\epsilon^{(4)\mu}) \\ & - \frac{1}{3}\epsilon_\mu^{(1)}\epsilon^{(2)\mu}\epsilon_\nu^{(3)}\epsilon^{(4)\nu}.\end{aligned} \tag{12.12}$$

We can see that, while the contact terms give rise to different combinations of spin, the vector exchange term of type of Fig. 12.1(b), contains the sum $\mathcal{P}(0) + \mathcal{P}(1) + \mathcal{P}(2)$, with equal weights for the different spins. This combination, corresponding to the exchange of a light vector meson ($\rho$, $\omega$, $\phi$, $K^*$) if allowed, satisfies HQSS to which we shall come back later on. On the other hand, the exchange of a heavy vector meson contains the combination

$$\epsilon_\mu^{(1)}\epsilon_\nu^{(2)}\epsilon^{(3)\nu}\epsilon^{(4)\mu} = \mathcal{P}(0) - \mathcal{P}(1) + \mathcal{P}(2) \tag{12.13}$$

---

[1] We recall the quantum numbers of $\omega$ and $\rho$ states, which respectively are $I^G(J^{PC}) = 0^-(1^{--})$ and $1^+(1^{--})$; whereas those of $B$ and $B^*$ mesons are $I(J^P) = \frac{1}{2}(0^-)$ and $\frac{1}{2}(1^-)$.

and does not satisfy leading order HQSS constraints, as we shall see in Section 12.4. This goes in line with HQSS, since the exchange of heavy vectors is penalized versus the exchange of light ones by a factor $m_V^2/m_{B*}^2$ from the propagators and become sub-dominant. The contact term is also sub-dominant since it goes like $m_V/m_{B*}$ of the dominant term from the exchange of a light vector. HQSS is unbroken only for the dominant term in the $\mathcal{O}(\frac{1}{m_{B*}})$ counting, as it should be expected.

### 12.2.2 Vector-pseudoscalar interaction

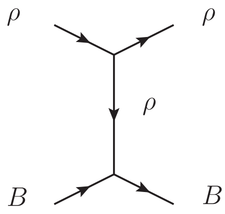

**Figure 12.2:** Interaction of $\rho B$ with vector exchange.

We shall also consider the $\rho B$ interaction. This proceeds via the exchange of a vector meson as in Fig. 12.2 and in this case there is no contact term. One can see that in the limit (which we also take) that $q^2/m_V^2 \to 0$, where $q$ is the momentum transfer, one obtains the chiral Lagrangian of [419]. The lower vertex $VBB$ is given by the Lagrangian provided by the extended LHG approach

$$\mathcal{L} = -ig \langle (\phi\partial_\mu\phi - \partial_\mu\phi\phi) V^\mu \rangle , \tag{12.14}$$

where now $\phi$ is the corresponding matrix of Eq. (12.3) for $q\bar{q}$ in the pseudoscalar representation. We obtain the same expression as for $\rho B^* \to \rho B^*$ (direct term in Fig. 12.1(b)) replacing

$$\epsilon_\mu^{(1)}\epsilon_\nu^{(2)}\epsilon^{(3)\mu}\epsilon^{(4)\nu} \to -\epsilon_\mu^{(1)}\epsilon^{(3)\mu}. \tag{12.15}$$

Then up to the factor $-\epsilon_\mu\epsilon^\mu \to \vec{\epsilon}\cdot\vec{\epsilon}'$, a scalar factor, that becomes unit in the only possible spin state here which is $J = 1$ with $L = 0$, we find the same potential for $\rho B \to \rho B$ as for $\rho B^* \to \rho B^*$ with the dominant light vector exchange in any spin channel.

## 12.3 Decay modes of the $\rho B^*$ and $\rho B$ channels

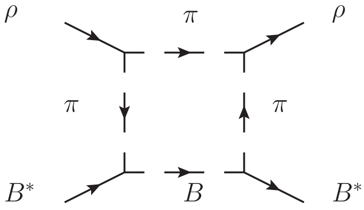

**Figure 12.3:** Box diagram to account for the decay of $\rho B^*$ into $\pi B$ state.

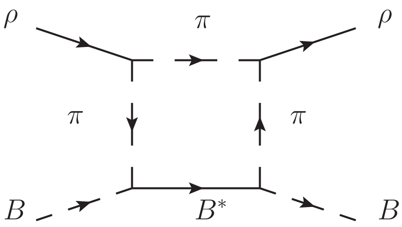

**Figure 12.4:** Box diagram for $\rho B \to \rho B$ with $B^*\pi$ intermediate state.

As in [219] we take into account the box diagrams of the type of Fig. 12.3. The details are identical as those in [219] (Section VI) by simply changing the masses of the particles $D^*$, $D$ by those of the $B^*$, $B$ mesons. Concerning to the $\rho B \to \rho B$ interaction, the decay modes that we will consider are those with a pion and a vector meson $B^*$ as intermediate state[2], which will lead to the kind of box diagrams depicted in Fig. 12.4. The evaluation of these diagrams is very similar to the case of Fig. 12.3 but with some subtle differences that we will deal with in Section 12.5.3.

From the time of Ref. [219] some clarification [422] has come concerning the $B^*B\pi$ vertex, the formalism that we use and HM$\chi$PT. In this latter formalism this coupling is given by $g_H$ which is flavor independent in the heavy quark limit. The width for the $B^* \to B\pi$ decay (formally, since there is no phase space here, unlike the case of $D^* \to D\pi$) is given by

$$\Gamma = \frac{g_H^2}{6\pi \tilde{f}_\pi^2}|\vec{p}_\pi|^3, \ \tilde{f}_\pi = \sqrt{2} f_\pi, \tag{12.16}$$

and according to [423] $g_H$ is heavy flavor independent at leading order. On the other hand, in our normalization [166] we have

$$\Gamma = \frac{g_{B^*B\pi}^2}{6\pi m_{B^*}^2}|\vec{p}_\pi|^3. \tag{12.17}$$

Hence we must identify,

$$g_{B^*B\pi} = \frac{g_H}{\tilde{f}_\pi} m_{B^*} \tag{12.18}$$

It is interesting to obtain that from our formalism. If we take the diagrams of Fig. 12.5 one may accept that the $d\bar{d}$ hadronization acts in the same way in the case of $K^* \to K\pi$ or $B^* \to B\pi$, such that the matrix elements are the same at the quark level. Yet, in the relativistic normalization of the fields that we use [166] we would have at the microscopic level,

$$S^{\text{mic}} = 1 - \mathrm{i}t \sqrt{\frac{2m_l}{2\omega_l}} \sqrt{\frac{2m_l'}{2\omega_l'}} \sqrt{\frac{1}{2\omega_\pi}} \frac{1}{\mathcal{V}^{3/2}} (2\pi)^4 \delta^{(4)}(P_i - P_f), \tag{12.19}$$

where $m_l$ and $m_l'$ are the masses of the incoming and outgoing light quarks respectively, $\omega_l$ and $\omega_l'$ their energies, $\omega_\pi$ the pion energy and $\mathcal{V}$ the volume of the box where the states

---

[2] Note that these diagrams, with an intermediate $B$ meson, do not exist for the case of the $\rho B \to \rho B$ interaction, because we would need a strong $\pi BB$ vertex which does not exist.

are normalized to 1. However, in our normalization, we have at the macroscopic level,

$$S^{\rm mac}_{K^*} = 1 - {\rm i}t_{K^*}\frac{1}{\sqrt{2\omega_{K^*}}}\frac{1}{\sqrt{2\omega_K}}\frac{1}{\sqrt{2\omega_\pi}}\frac{1}{\mathcal{V}^{3/2}}(2\pi)^4\delta^{(4)}(P_i - P_f), \tag{12.20}$$

$$S^{\rm mac}_{B^*} = 1 - {\rm i}t_{B^*}\frac{1}{\sqrt{2\omega_{B^*}}}\frac{1}{\sqrt{2\omega_B}}\frac{1}{\sqrt{2\omega_\pi}}\frac{1}{\mathcal{V}^{3/2}}(2\pi)^4\delta^{(4)}(P_i - P_f). \tag{12.21}$$

This means that in our normalization we would have

$$\frac{t_{B^*}}{t_{K^*}} \simeq \frac{\sqrt{m_{B^*}m_B}}{\sqrt{m_{K^*}m_K}} \simeq \frac{m_{B^*}}{m_{K^*}}, \tag{12.22}$$

which gives us

$$g_{B^*B\pi} = g\frac{m_{B^*}}{m_{K^*}}. \tag{12.23}$$

If we go now to Eq. (12.18) we find

$$g_H = \frac{g_{B^*B\pi}\tilde{f}_\pi}{m_{B^*}} = \frac{g\tilde{f}_\pi}{m_{K^*}} = \frac{m_V}{2f_\pi}\frac{1}{m_{K^*}}\tilde{f}_\pi = \frac{1}{\sqrt{2}}. \tag{12.24}$$

As one can see, our argumentation naturally leads to a flavor independent $g_H$, as required by heavy quark symmetry at leading order. The value of Eq. (12.24) is relatively close to the one obtained in a lattice simulation [424] of $g_H \simeq 0.57 \pm 0.1$, and using it, one also gets a good result for the $D^* \to D^0\pi^+$ decay width. Then we use this vertex in the box diagram instead of the empirical one $g'_{D^*D\pi}$ used in [219]. In the former argumentation we are implicitly assuming that both the strange quark in the $K^*$ and the $b$ quark in the $B^*$ meson act as spectators. Recoil corrections when going from the strange sector to the $D$ or $B$ sector seem to be small in this case, since the results obtained within the spectator assumption agree quite well with both the empirical and lattice QCD values of the $g_H$ coupling.

The same argument can be applied for the $B^*B^{*\prime}\rho$ vertices, but the Weinberg-Tomozawa coupling is proportional to the sum of the $B^*$, $B^{*\prime}$ energies and then the normalization factor of Eq (12.23) is automatically implemented.

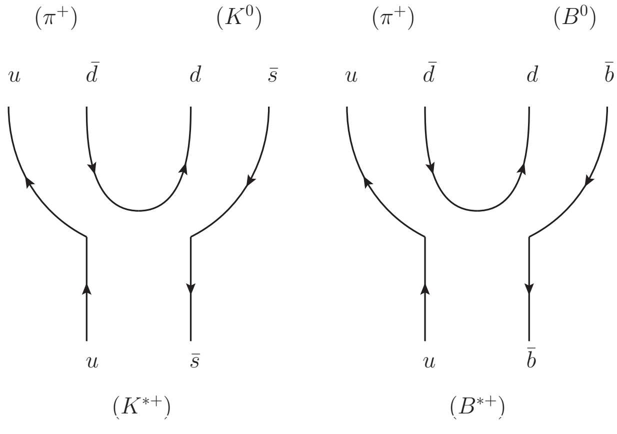

**Figure 12.5:** Diagram of the $K^{*+} \to K^0\pi$ and $B^{*+} \to B^0\pi$ decay at the quark level.

## 12.4 Heavy quark spin symmetry considerations

Let us consider the $\rho B^{(*)}$ meson pair in $S$-wave. In the particle basis we have four states for each isospin combination, namely $|\rho B,\ J = 1\rangle$, $|\rho B^*,\ J = 0\rangle$, $|\rho B^*,\ J = 1\rangle$ and $|\rho B^*,\ J = 2\rangle$. In the HQSS basis [425], the states are classified in terms of the quantum numbers: $J$, total spin of the meson pair system and $\mathcal{L}$, total spin of the light quark degrees of freedom. In addition, for this particular simple case in the HQSS basis, the total spin of the heavy quark subsystem, $S_Q$, is fixed to 1/2. The spin of the light quarks in each of the two mesons is also trivially fixed. Thus, the four orthogonal states in the HQSS basis are given by $|\mathcal{L} = 1/2,\ J = 0\rangle$, $|\mathcal{L} = 1/2,\ J = 1\rangle$, $|\mathcal{L} = 3/2,\ J = 1\rangle$ and $|\mathcal{L} = 3/2,\ J = 2\rangle$. In all the cases the spin of the $\bar{b}$-antiquark, $S_Q$, is coupled to $\mathcal{L}$ to give $J$. The approximate HQSS of QCD leads at LO, i.e., neglecting $\mathcal{O}\left(\Lambda_{\rm QCD}/m_Q\right)$ to important simplifications when the HQSS basis is used,

$$\langle \mathcal{L}', J'; \alpha' |\, H^{\rm QCD}\, | \mathcal{L}, J; \alpha\rangle = \delta_{\alpha\alpha'}\delta_{\mathcal{L}\mathcal{L}'}\delta_{JJ'}\mu^{\alpha}_{2\mathcal{L}} \tag{12.25}$$

where $\alpha$ stands for other quantum numbers (isospin and hypercharge), which are conserved by QCD. The reduced matrix elements, labelled by $\mu^{\alpha}_{2\mathcal{L}}$, depend only on the spin (parity) of the light quark subsystem, $\mathcal{L}$, and on the additional quantum numbers, $\alpha$, that for the sake of simplicity we will omit in what follows. We thus have two irreducible matrix elements $\mu_1$ and $\mu_3$ in the heavy quark limit.

The particle and HQSS bases are easily related through 9-j symbols (see [425]), and one finds

$$\begin{aligned}
|\rho\, B,\ J = 1\rangle &= -\sqrt{\frac{1}{3}}\,|\mathcal{L} = 1/2,\ J = 1\rangle \\
&\quad + \sqrt{\frac{2}{3}}\,|\mathcal{L} = 3/2,\ J = 1\rangle, \\
|\rho\, B^*,\ J = 0\rangle &= |\mathcal{L} = 1/2,\ J = 0\rangle, \\
|\rho\, B^*,\ J = 1\rangle &= \sqrt{\frac{2}{3}}\,|\mathcal{L} = 1/2,\ J = 1\rangle \\
&\quad + \sqrt{\frac{1}{3}}\,|\mathcal{L} = 3/2,\ J = 1\rangle, \\
|\rho\, B^*,\ J = 2\rangle &= |\mathcal{L} = 3/2,\ J = 2\rangle.
\end{aligned} \tag{12.26}$$

In the infinite heavy quark mass limit we obtain,

$$\langle \rho B|\, H^{\rm QCD}\, |\rho B\rangle = \frac{1}{3}\mu_1 + \frac{2}{3}\mu_3, \tag{12.27}$$

$$\langle \rho B^*, J = 0|\, H^{\rm QCD}\, |\rho B^*, J = 0\rangle = \mu_1, \tag{12.28}$$

$$\langle \rho B^*, J = 1|\, H^{\rm QCD}\, |\rho B^*, J = 1\rangle = \frac{2}{3}\mu_1 + \frac{1}{3}\mu_3, \tag{12.29}$$

$$\langle \rho B^*, J = 2|\, H^{\rm QCD}\, |\rho B^*, J = 2\rangle = \mu_3, \tag{12.30}$$

$$\langle \rho B| H^{\rm QCD} |\rho B^*, J = 1\rangle = -\frac{\sqrt{2}}{3}\mu_1 + \frac{\sqrt{2}}{3}\mu_3. \tag{12.31}$$

Since we have not coupled the $\rho B$ with $\rho B^*$ in our model because it involves anomalous terms which are very small in this case, then $\mu_1 = \mu_3$ and we conclude that all the matrix elements are equal for $\rho B^*$ in $J = 0, 1, 2$ and also for $\rho B$. An explicit evaluation of the box diagrams involving those transitions, and particularly considering $\rho$, $\omega$ transitions was done in [368] and their contribution was found very small. We can see that the dominant term for the light vector exchange (Eq. (12.9)) fulfils the rules of HQSS relations, but the contact term and $B^*$ exchange, which are sub-dominant in the $\left(\frac{1}{m_{B^*}}\right)$ counting, do not satisfy those relations, since they do not have to. Note that when rewriting this potential in the usual normalization of HQSS, we would have an extra $\left(\frac{1}{2\omega_{B^*}}\right)$ factor that makes the $\rho$ exchange to go like $\left(\frac{1}{m_{B^*}}\right)^0$, the contact term like $\frac{1}{m_{B^*}}$ and the $B^*$ exchange like $\frac{1}{m_{B^*}}$.

In the present approach the $\rho B^* \to \rho B$ transition would be subdominant. There are other models where this might not be the case. For instance, in Ref. [211] a model is used imposing SU(6) spin-flavor symmetry that, extended to the present problem, could have this transition non suppressed.

We should note that the approach followed here is consistent with HQSS, as discussed above, despite the $\rho B^* \to \rho B$ transition being suppressed. Treating on equal footing $B$ and $B^*$, as HQSS requires, does not imply that a model where the $\rho B^* \to \rho B$ transition is suppressed necessarily breaks HQSS. Examples of this can also be seen in the work of [426] for the $B^*\bar{B}^*$ interaction and in [425] for the meson baryon system.

## 12.5 Results

### 12.5.1 Bethe Salpeter resummation

We restore exact unitary performing the diagrammatic resummation of BSE series. We solve Eq. (2.86) to obtain the scattering matrix $T$ in coupled channels by using an input kernel matrix $V$, which is the potential describing transition amplitudes $\rho B^* \to \rho B^*$, $\rho B^* \to \omega B^*$, $\omega B^* \to \omega B^*$ and $\rho B \to \rho B$ that one obtains using the former sections (from Eqs. (12.8) and (12.9) after spin projection). All the relevant matrix elements can be obtained from Tables I, II and III of [219]. Additionally, the finite width of the $\rho$ meson is also explicitly taken into account (as in Ref. [219]) by considering the $\rho$ mass distribution in the construction of the $G$ function (2.87).

In the next section we shall discuss our results for both the $\rho/\omega B^*$ and $\rho B$ systems by using the coupled channel unitary approach, where we only consider the contribution of $S$-wave. The interaction in the $I = 3/2$ case is repulsive, and thus in what follows we will focus in the $I = 1/2$ sector.

### 12.5.2 $\rho/\omega\, B^*$ system

In the first step, we introduce the kernel or potential $V$, corresponding to the contact and vector exchange contributions. We can get an intuitive idea of the results by using the results of Table I of [219], adapted to the present case in Table 12.1.

By calculating the potential at the threshold of $\rho B^*$, summing the contact, $\rho$ exchange and $B^*$ exchange contributions we get potentials with weights ($\kappa$ of [219] is now $m_\rho^2/m_{B^*}^2$) $-51g^2$, $-50g^2$, $-58g^2$ for $J = 0, 1, 2$, respectively. These results correspond to $-16g^2$, $-14.5g^2$, $-23.5g^2$ of [219]. The strength is bigger than for the $\rho D^*$ system because of the bigger masses of the heavy quarks and we still find that the strength is bigger for $J = 2$. However, we also see that the weights for different spins are now more similar in accordance with HQSS as discussed in Section 12.4.

With the potentials evaluated as a function of the energy as given in Tables I, II, III of [219] we solve the BSE (2.86) in the $\rho B^*$, $\omega B^*$ coupled channels though the contribution of the $\omega$ channel is fairly small. We need to regularize the $G$ function and use the sharp cut off prescription using $q_{max} = 1.3$ GeV—see Eq. (A.5). The $G$ function is also convoluted with the $\rho$ mass distribution as in [219]. With this prescription we obtain three bound states for $J = 0, 1, 2$ that we plot in Figs. 12.6 and 12.7. The value of $q_{max}$ has been chosen to obtain a mass of 5745 MeV within the range of 5743 ± 5 MeV of the nominal mass of the $B_2^*(5747)$ state [383]. The masses for the other two states are then predictions: we obtain a state with $J = 0$ at 5812 MeV and another one for $J = 1$ at 5817 MeV. Here, we can see that the mass of the spin 1 state is larger than that of spin 2, while in the PDG, the resonance $B_1(5721)$ with spin 1 has a mass smaller than the mass of $B_2^*(5747)$. Henceforth, the state with spin 1 that we obtain presents some difficulties to be identified with the $B_1(5721)$. One possibility is that it could be the resonance generated by $\rho B$ interaction, which we shall discuss later. Note that the LO HQSS relation $\mu_1 = \mu_3$ deduced in Section 12.4 has some $1/m_Q$ corrections.

We have given the rational of choosing the value of the cut off to fit one datum. Nevertheless, we test the sensitivity of the mass of the $J = 2$ state in the cutoff. The results are shown in Table 12.2, where we observe variations of about 40 MeV by varying the cut off in 100 MeV. Changes in other spin channel are similar as can be also seen in Table 12.2.

We have also taken the advantage to make a test of the stability of the results when we change the strength of the potential and readjust the cut off to get the mass of the $J = 2$ resonance at the experimental value. For this we take the diagonal (largest) $\rho B^*$ potential and multiply it by 1.5 or 0.75. The results are shown in Table 12.3. We observe that the variation of the masses for the predicted $J = 0$ and $J = 1$ states are small, quite smaller than the differences found with the changes in $q_{max}$ for fixed potential shown in Table 12.2.

The behaviour of each $T$ matrix element close to a pole $z_R$ can be expressed as in Eq. (2.93), where now $g_i$ is the coupling to channel $i$ ($i = \rho B^*, \omega B^*$). We choose the $\rho B^*$ coupling with positive sign, and for the other channels we use

$$\frac{g_i}{g_j} = \lim_{z \to z_R} \frac{T_{ii}}{T_{ij}}, \tag{12.32}$$

which gives us the relative sign for the $\omega B^*$ channel. The couplings to the different

**Table 12.1:** $V(\rho B^* \to \rho B^*)$ in isospin 1/2 sector and for the different spin channels. Here $\kappa = m_\rho^2/m_{B*}^2$.

| $I$ | $J$ | contact | $\rho$ exchange | $B^*$ exchange |
|---|---|---|---|---|
| 1/2 | 0 | $5g^2$ | $-2\frac{g^2}{m_\rho^2}(k_1+k_3)\cdot(k_2+k_4)$ | $-\frac{1}{2}\frac{\kappa g^2}{m_\rho^2}(k_1+k_4)\cdot(k_2+k_3)$ |
| 1/2 | 1 | $\frac{9}{2}g^2$ | $-2\frac{g^2}{m_\rho^2}(k_1+k_3)\cdot(k_2+k_4)$ | $+\frac{1}{2}\frac{\kappa g^2}{m_\rho^2}(k_1+k_4)\cdot(k_2+k_3)$ |
| 1/2 | 2 | $-\frac{5}{2}g^2$ | $-2\frac{g^2}{m_\rho^2}(k_1+k_3)\cdot(k_2+k_4)$ | $-\frac{1}{2}\frac{\kappa g^2}{m_\rho^2}(k_1+k_4)\cdot(k_2+k_3)$ |

**Table 12.2:** The mass of the states obtained with different values of $q_{max}$. All the masses are in units of MeV.

| $q_{max}$ [MeV] | $J = 0$ | $J = 1$ | $J = 2$ |
|---|---|---|---|
| 1200 | 5845 | 5849 | 5785 |
| 1300 | 5812 | 5817 | 5745 |
| 1400 | 5782 | 5787 | 5710 |

**Table 12.3:** The mass of the states obtained for different strengths of the potential. $CF$ is the multiplicative coefficient of the $\rho B^*$ diagonal potential. The cut off is tuned in every case to reproduce the $J = 2$ experimental mass. All the masses are in units of MeV.

| $CF$ | $q_{max}$ [MeV] | $J = 0$ | $J = 1$ | $J = 2$ |
|---|---|---|---|---|
| 1.5 | 1030 | 5807 | 5812 | 5745 |
| 1 | 1300 | 5812 | 5817 | 5745 |
| 0.75 | 1560 | 5815 | 5821 | 5745 |

channels are listed in Table 12.4.

As commented above, the $\rho$ mass distribution is also involved via the convoluted $G$ function and should give a width different from zero to the states. Nonetheless, we obtain that the widths for $J = 0$, 1 and $J = 2$ are much smaller than one MeV (see Figs. 12.6 and 12.7). However, in the PDG the width of the $B_2^*(5747)$ state is $23^{+5}_{-11}$ MeV, which is much larger than the one obtained here. To reconcile the difference, the $\pi B$ decay channel must be included.

The energies of the resonances are closer to the threshold of $\rho$ and $B^*$ than to that of $\pi$ and $B$. We do not need to treat the $\pi B$ as a coupled channel, since it does not have much weight compared to the $\rho B^*$ and $\omega B^*$ channels. Henceforth, as in [219], one can compute the box diagrams that are mediated by $\pi B$ and put them in the potential $V$ in order to get the width. The $\rho B^*$ contribution corresponding to the box diagram was shown in Fig. 12.3. We use directly the result of Eq. (41) of [219], which is the sum of all the terms after the $q^0$ integration using the Cauchy's residue theorem,

**Table 12.4:** Couplings of the bound states to the $\rho B^*$ and $\omega B^*$ channels with $I = 1/2$ and $J = 0, 1, 2$ in units of GeV. The imaginary parts of the couplings are negligible, less than 0.05 % of the real part in all the cases.

| channel | $J = 0$ | $J = 1$ | $J = 2$ |
|---|---|---|---|
| $\rho B^*$ | 39.6 | 39.3 | 43.6 |
| $\omega B^*$ | 1.0 | $-2.1$ | $-2.4$ |

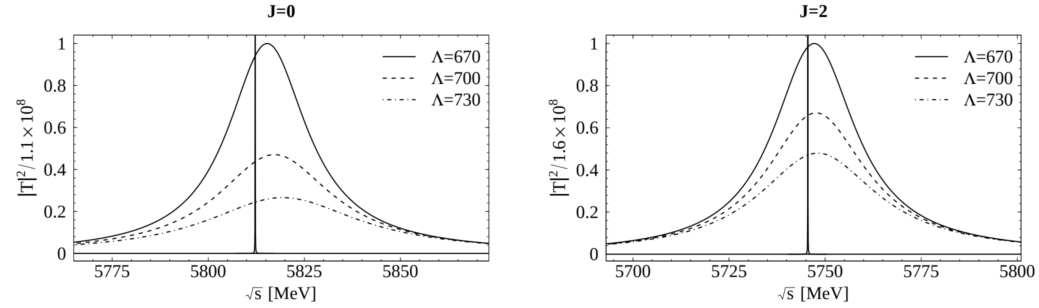

**Figure 12.6:** Squared amplitudes for $J = 0$ and $J = 2$ which depend on the energy in the center of mass including the convolution of $\rho$ mass distribution and the box diagram. The very sharp peaks correspond to the squared amplitude without the box diagram contribution.

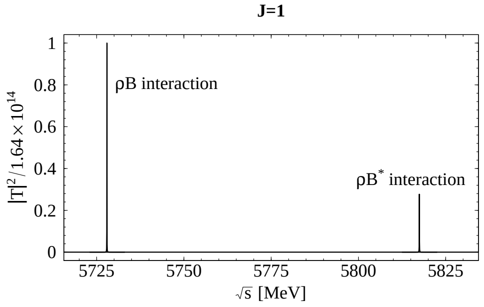

**Figure 12.7:** Squared amplitude for the $\rho B^*$ and the $\rho B$ sector with spin 1.

$$
\begin{aligned}
V^{\pi B} &= g^4(\epsilon_i^{(1)}\epsilon_i^{(2)}\epsilon_j^{(3)}\epsilon_j^{(4)} + \epsilon_i^{(1)}\epsilon_j^{(2)}\epsilon_i^{(3)}\epsilon_j^{(4)} + \epsilon_i^{(1)}\epsilon_j^{(2)}\epsilon_j^{(3)}\epsilon_i^{(4)}) \\
&\times \frac{8}{15\pi^2}\int_0^{q_{max}} dq\vec{q}^{\,6}\left(\frac{1}{2\omega_\pi}\right)^3\left(\frac{1}{k_1^0+2\omega_\pi}\right)^2 \\
&\times \frac{1}{k_2^0-\omega_\pi-\omega_B+i\epsilon}\,\frac{1}{k_4^0-\omega_\pi-\omega_B+i\epsilon}\,\frac{1}{k_1^0-2\omega+i\epsilon} \\
&\times \frac{1}{k_3^0-2\omega_\pi+i\epsilon}\,\frac{1}{P^0-\omega_\pi-\omega_B+i\epsilon}\,\frac{1}{P^0+\omega_\pi+\omega_B} \\
&\times \left(\frac{1}{k_2^0+\omega_\pi+\omega_B}\right)^2\frac{1}{2\omega_B}f(P^0,\vec{q}^{\,2}) \qquad (12.33)
\end{aligned}
$$

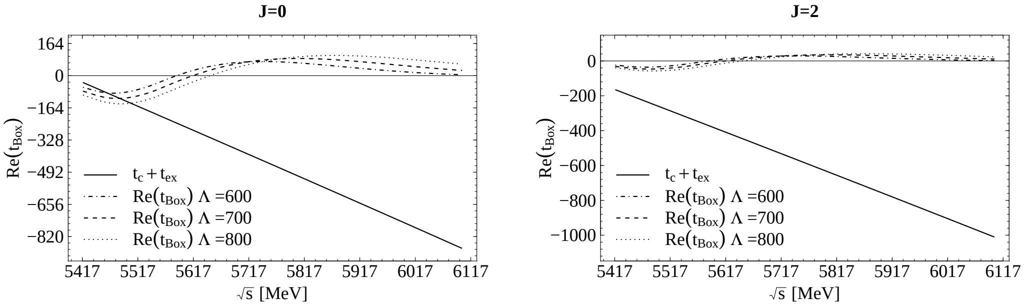

**Figure 12.8:** The real part of box potential for $(I, J) = (1/2, 0)$ and $(I, J) = (1/2, 2)$ compared with those from contact and vector exchange terms.

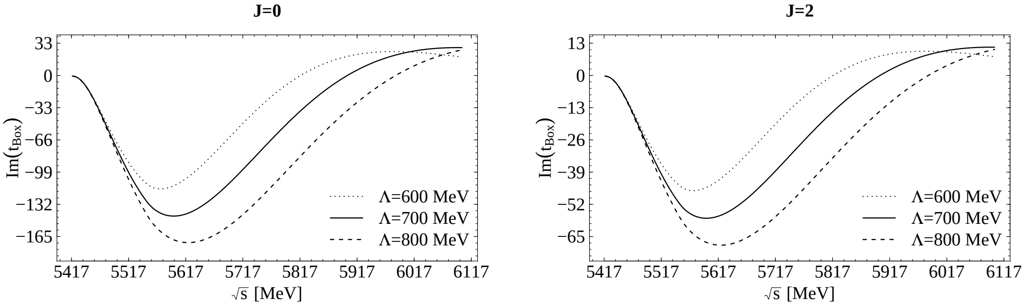

**Figure 12.9:** The imaginary part of box potential for $(I, J) = (1/2, 0)$ and $(I, J) = (1/2, 2)$.

where

$$\begin{aligned} f(P^0, \vec{q}^{\,2}) = 4\{&-32k_3^0P^0\omega_\pi^2\omega_B((P^0)^2 - 2\omega_\pi^2 - 3\omega_\pi\omega_B - \omega_B^2) \\ &+ 2(k_3^0)^3P^0\omega_B((P^0)^2 - 5\omega_\pi^2 - 2\omega_\pi\omega_B - \omega_B^2) \\ &+ (k_3^0)^4(2\omega_\pi^3 - (P^0)^2\omega_B + 3\omega_\pi^2\omega_B + 2\omega_\pi\omega_B^2 + \omega_B^3) \\ &+ 4\omega_\pi^2(8\omega_\pi^5 + 33\omega_\pi^4\omega_B + 54\omega^3\omega_B^2 + 3\omega_B((P^0)^2 \\ &- \omega_B^2)^2 + 18\omega_\pi\omega_B^2(-(P^0)^2 + \omega_B^2) + \omega_\pi^2(-12(P^0)^2\omega_B \\ &+ 44\omega_B^3)) - (k_3^0)^2(16\omega^5 + 63\omega^4\omega_B + 74\omega_\pi^3\omega_B^2 \\ &+ \omega_B((P^0)^2 - \omega_B^2)^2 + 32\omega_\pi^2\omega_B(-(P^0)^2 + \omega_B^2) \\ &+\omega_\pi(-6(P^0)^2\omega_B^2 + 6\omega_B^4))\}\,, \end{aligned} \tag{12.34}$$

$\omega_\pi = \sqrt{\vec{q}^{\,2} + m_\pi^2}$, $\omega_B = \sqrt{\vec{q}^{\,2} + m_B^2}$, and $P^0 = k_1^0 + k_2^0$.

Here, in order to calculate the box diagram amplitude, one has first integrated analytically the $q^0$ variable. Note that the integral is logarithmically divergent, and as in [219] we use a form factor to regularize the loop in addition to the $q_{max}$ value used before. The spin structure only allows $J = 0$ and 2. The reason why $J = 1$ is forbidden is that the parity of the $\rho B^*$ system is positive with $S$-wave, and the angular momentum of the $\pi B$ system has to be $L = 0, 2$. Therefore, the spin of the $\pi B$ pair would be 0 or 2, but not 1. Using again the results of [219] we find the spin projections

$$\delta V^{\pi B, I=1/2, J=0} = 20\tilde{V}^{(\pi B)}, \quad \delta V^{\pi B, I=1/2, J=2} = 8\tilde{V}^{(\pi B)}, \tag{12.35}$$

where $\tilde{V}^{(\pi B)}$ is given in Eq. (12.33) after removing the polarization vectors. As already mentioned, the box diagram is logarithmically divergent and needs regularization. In this

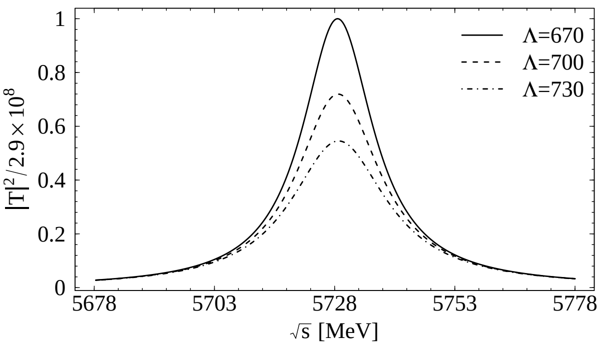

**Figure 12.10:** Squared amplitude of $\rho B$ system as a function of the c.m. energy including the convolution of the $\rho$ mass distribution and the box diagram contribution.

work, we also use a form factor in each vertex of the box diagram, and then finally, $g^4$ is replaced with

$$g^2_{\rho\pi\pi} g^2_{B^*B\pi} \left(e^{-\vec{q}^2/\Lambda^2}\right)^4 \tag{12.36}$$

where $g_{\rho\pi\pi} \equiv g = m_\rho/(2f_\pi)$ and $g_{B^*B\pi} = g m_{B^*}/m_V$ (see Eq. (12.23)), and $\Lambda$ is of the order of 1 GeV.

We take the form factor in exponential form from QCD sum rules calculations carried out in [427]. In that work values of $\Lambda \approx 1.2$ GeV were determined for the $D^*D\pi$ vertex for the case when the pion is virtual (Eq. (17) of Ref. [427]). We allow the value of $\Lambda$ to change when moving to the beauty sector in the present case, and tune it to obtain the phenomenological width. It is thus a free parameter of the theory. The sensitivity of the result to changes in this parameter is discussed below.

The real part of the box diagram contribution is neglected, since it is very small compared with those of the contact and vector exchange terms as we can see in Fig. 12.8. The imaginary part that we focus on is shown in Fig. 12.9. If $\Lambda$ is taken as 0.67 GeV and $q_{max}$ as 1.3 GeV, the width for $J = 2$ is 25.5 MeV which is in agreement with the experimental value in the PDG. For $J = 0$ the width is then 24.7 MeV, while the state with $J = 1$ has no width in our approach. If $\Lambda$ is increased to 0.73 GeV, we obtain a width for $J = 2$ of 37.5 MeV, and 47.8 MeV for $J = 0$. We see that we can obtain a width comparable to experiment using cutoffs or form factors of natural size.

In Fig. 12.6 we show the line shape of $|T|^2$ including the box diagram contribution, which generates a final width for the $J = 0, 2$ states. On the other hand, for $J = 1$ we still have the results of Fig. 12.7, since as discussed above, in this case there is no box diagram.

### 12.5.3 $\rho B$ system

As we have mentioned in the previous subsection, in the PDG the mass of the $B_1(5721)$ is smaller than that of the $B_2^*(5747)$. However, for the $\rho B^*$ systems the mass of the $J = 1$ state is larger than that of the $J = 2$ state. Henceforth, we turn to the $\rho B$ system and investigate its interaction.

For this system there are no contact terms, but we have the vector exchange terms only. In addition, the $\omega$ channel is now inoperative since the $\rho\rho\omega$ vertex is zero by G-parity and $\omega\omega\rho$ is zero by C-parity and isospin. Note that in the case of the vector-vector interaction it is the exchange term of Fig. 12.1 (c) the one that makes $\omega B^*$ mix with $\rho B^*$. The equivalent diagrams would involve anomalous terms which are small. In any case the factor $m_V^2/m_{B*}^2$ of these terms renders them negligible, of the order of 1% also in the case of the vector-vector interaction.

Since the strength of the interaction is the same as in the $\rho B^* \to \rho B^*$ case we expect to find a bound state as before. If the cut off $q_{max}$ in the $G$ function is taken as 1.3 GeV, we find the pole position at 5728 MeV (see Fig. 12.7), which is consistent with the PDG value of the $B_1(5721)$. The coupling to $\rho B$ channel is also computed, and found to be $g_{\rho B} = 41.6$ GeV. It is very interesting to also calculate the width of this state. The dominant decay mode is $B^*\pi$, while the value is found to be $\approx 30$ MeV [428]. This decay mechanism comes out naturally in our approach by means of the box diagram of Fig. 12.4.

It is easy to see the contribution for this new box diagram following the steps of [219]. There we had the combination

$$\begin{aligned}
&\int d^3q\epsilon_i^{(1)}\epsilon_j^{(2)}\epsilon_l^{(3)}\epsilon_m^{(4)}q_iq_jq_lq_m\mathcal{F}(\vec{q}^{\,2})\\
=&\frac{1}{15}\int d^3q\epsilon_i^{(1)}\epsilon_j^{(2)}\epsilon_l^{(3)}\epsilon_m^{(4)}\vec{q}^{\,4}\left(\delta_{ij}\delta_{lm}\right.\\
&\left.+\delta_{il}\delta_{jm}+\delta_{im}\delta_{jl}\right)\mathcal{F}(\vec{q}^{\,2})\\
=&\frac{1}{15}\left(5\mathcal{P}(0)+2\mathcal{P}(2)\right)\int d^3q\vec{q}^{\,4}\mathcal{F}(\vec{q}^{\,2}),
\end{aligned} \tag{12.37}$$

here $\mathcal{F}(\vec{q}^{\,2})$ is a function depending on the square of the three momentum $\vec{q}^{\,2}$, the center of mass energy and the masses of the mesons appearing in Fig. 12.4 .

Now we have the same original form as in the beginning of the equation but we must sum over the $B^*$ polarization of the intermediate $B^*$ state. Since we are only concerned about the imaginary part, the on-shell approximation for the intermediate $B^*$ is sufficient and the contraction of $\epsilon_j^{(2)}\epsilon_m^{(4)}$ gives $\delta_{jm}$. Then the remaining structure is

$$\int d^3q\epsilon_i^{(1)}\epsilon_l^{(3)}q_iq_l\vec{q}^{\,2}\tilde{\mathcal{F}}(\vec{q}^{\,2}) = \epsilon_i^{(1)}\epsilon_i^{(3)}\int d^3q\frac{1}{3}\vec{q}^{\,4}\tilde{\mathcal{F}}(\vec{q}^{\,2}), \tag{12.38}$$

where $\tilde{\mathcal{F}}(\vec{q}^{\,2})$ has the same form as $\mathcal{F}(\vec{q}^{\,2})$ after making the change $m_{B*} \to m_B$ and $m_B \to m_{B*}$, up to a constant factor that we shall discuss right now. The interaction Lagrangian of Eq. (12.14) involves derivatives of the pseudoscalar fields. In comparison with the previous situation which is depicted in the box diagram of Fig. 12.3, now the $B^*B\pi$ vertex does not have a $B$ meson carrying the $q$ momenta of the integral, since this meson is external (see Fig. 12.4). Before we had in the incoming $B^*B\pi$ vertex a factor,

$$\propto \left((P-q)+(k_1-q)\right)_\mu \xrightarrow{\vec{k}_i\to 0} -2q_i, \tag{12.39}$$

corresponding to the momentum of the $B$ and $\pi$ internal mesons in Fig. 12.3. Now in Fig. 12.4 the incoming $B^*B\pi$ vertex is

$$\propto \left(-k_2+(k_1-q)\right)_\mu \xrightarrow{\vec{k}_i\to 0} -q_i, \tag{12.40}$$

because the derivatives involve the external pseudoscalar $B$ and the internal $\pi$. As a consequence, the amplitudes will lack a factor two in each of the $B^*B\pi$ vertex, so $\tilde{\mathcal{F}} = \mathcal{F}/4$. When we remove the polarization vectors the structure is

$$\int d^3q \frac{1}{3}\vec{q}^{\,4}\tilde{\mathcal{F}}(\vec{q}^{\,2}) = \int d^3q \frac{1}{3}\vec{q}^{\,4}\mathcal{F}(\vec{q}^{\,2})\frac{1}{4}. \tag{12.41}$$

Hence, comparing with Eq. (12.37) we see that the strength of the $\rho B$ box potential is identical to the former one with $J = 0$ of the $\rho B^*$, divided by four (changing the intermediate mass of the $B$ to the present one of $B^*$ and *viceversa*). In Fig. 12.10 we plot $|T|^2$ for this case with the same parameters used before to obtain the width of the $B_2^*(5747)$. We see that we obtain a width around 20 MeV, which is a further prediction of the present work; not far from the experimental results of the CDF collaboration [429] ($23 \pm 5$ MeV for the neutral and $49^{+12}_{-16}$ MeV for the charged state) and $30 \pm 7$ MeV reported by LHCb [428].

## 12.6 Summary

In this chapter we have studied the $\rho B^*$, $\omega B^*$ and $\rho B$ interactions by using the LHG unitary approach. First we have solved the BSE in coupled channels for the $\rho B^*$ and the $\omega B^*$ sectors, using the tree level amplitudes and regularizing the loop function with a cut off of 1.3 GeV. In this way we have found three bound states, with masses 5812, 5817 and 5745 MeV for $I = 1/2$ and $J = 0, 1, 2$, respectively, identifying the $J = 2$ state with the $B_2^*(5747)$ [383] of mass $5743 \pm 5$ MeV. Despite having considered the $\rho$ mass distribution, all the states that we have found show small widths. In order to generate the correct width of the state with $J = 2$ as that of the experimental $B_2^*(5747)$, which is quoted as $23^{+5}_{-11}$ MeV, we have taken into account the box diagram mediated by the $\pi B$ which accounts for this decay channel. We have also considered a form factor for the off-shell pions and a rescaled coupling in the $B^*B\pi$ vertex. In this way, we have obtained the widths $25.5 \sim 37.5$ MeV for $J = 2$ and $24.7 \sim 47.8$ MeV for $J = 0$, taking $\Lambda = 0.67 \sim 0.73$ GeV and $q_{max} = 1.3$ GeV. Since the pole position of $J = 1$ is larger than that of $J = 2$, while in the PDG there is a spin one state $B_1(5721)$ which mass is smaller than the $B_2^*(5747)$ mass, we have considered the $\rho B$ system.

For the $\rho B$ interaction in the LHG approach we have found a bound state of mass 5728 MeV, which is consistent with the experimental value of the $B_1(5721)$. We have also predicted a width for this state considering the box diagram contribution in a similar manner as for the $\rho B^*$ system. The width that we have obtained is around 20 MeV. We summarize our results in Table 12.5.

The free parameters in the present approach have been fixed in the $J = 2$ sector. The same parameters have been used in the $J = 0, 1$ sectors to make predictions. We should acknowledge some uncertainties in the predictions obtained for these two latter channels. Quantifying these systematic errors is difficult, although we can make an educated guess by accepting as uncertainties the differences found in Table 12.2 when the cut off was changed by ±100 MeV. This tells us that about 30 MeV, and smaller, uncertainties in the masses of the $J = 0, 1$ states seem reasonable.

Finally we have investigated if there is some aspect in the interaction which can be related to the heaviness of the system under consideration. The fact that the $B$ mesons have a large mass can justify the study of the $\rho B$ and $\rho B^*$ systems under the frame of

**Table 12.5:** Summary of the states found in the $\rho(\omega)B^*$ and $\rho B$ sectors. The experimental values of the $B_2^*(5747)$ [383] and $B_1(5721)$ [428] may slightly differ from the current updated RPP average values [14] appearing in Table 1.1.

| Main channel | $I(J^P)$ | $M$ [Mev] | $\Gamma$ [MeV] | Main decay channel | Exp $(M, \Gamma)$ [MeV] |
|---|---|---|---|---|---|
| $\rho B^*$ | $\frac{1}{2}(0^+)$ | 5812 | $25-45$ | $\pi B$ | |
| $\rho B^*$ | $\frac{1}{2}(1^+)$ | 5817 | 0 | | |
| $\rho B^*$ | $\frac{1}{2}(2^+)$ | 5745 | $25-35$ | $\pi B$ | $(5743 \pm 5\,,\, 23^{+5}_{-11})$ |
| $\rho B$ | $\frac{1}{2}(1^+)$ | 5728 | $18-24$ | $\pi B^*$ | $(5726 \pm 2\,,\, 30 \pm 7)$ |

heavy quark spin symmetry. We have split these states in terms of eigenstates of total angular momentum of the light quarks as in [425].

We find that the dominant terms in our approach, due to light vector exchange, which go like $\mathcal{O}[(1/m_{B^*})^0]$ fulfil the LO constrains of HQSS, while the contact terms and those coming from the exchange of $B^*$ are sub-dominant ($\mathcal{O}\,(1/m_{B^*})$) and do not fulfil the LO HQSS rules. While in the $D\rho$ sector these terms were not too small, in the present case they are much smaller and we have a near degeneracy in the $\rho B^*$ states with $J = 0, 1, 2$.

It is interesting trying to interpret the results in Table 12.5 on the light of HQSS. As it has been discussed in Sec. 1.2.1, the experimental information about the $j_{\bar{q}}^P = 1/2^+$ $(0^+, 1^+)$ and $j_{\bar{q}}^P = 3/2^+$ $(1^+, 2^+)$ doublets is scarce. The two experimental states appearing in the last column of Table 12.5 are those included in Table 1.1 associated to the $j_{\bar{q}}^P = 3/2^+$ doublet—although the values in table 1.1 correspond to isospin masses using the updated averages from the RPP [14]. Note that the identification of those states as the $j_{\bar{q}}^P = 3/2^+$ doublet might be justified by the relations among the $\left|\rho B^{(*)}, J\right\rangle$ and $|\mathcal{L}, J\rangle$ states, and the HQSS matrix elements of Eqs. (12.27)-(12.31). From Eq. (12.26) we learn that the $\rho B$ $J = 1$ state has a major contribution from the light-degrees of freedom configuration associated to $\mathcal{L} = 3/2$, and in the case of $\rho B^*$ $J = 2$ we see that it is exclusively related to $\mathcal{L} = 3/2$. By fixing the interaction in the $J^P = 2^+$ sector we are constraining in great measure the $\rho B$ interaction in the $J^P = 1^+$ sector, and the fair reproduction of the $B_1(5721)$ may indicate that they are indeed in good accuracy HQSS partners. The situation of the additional $0^+$ and $1^+$ states is not so clear. On the other hand, we might be tempted to relate them with the higher poles (members of the HQSS $1/2^+$ doublet) which were predicted in Chapter 4. By looking at Table 4.4 we see that the masses of the higher $B_0^*$ and $B_1$ are not far from those reported above in Table 12.5. Although, the widths of the higher $B_0^*$ and $B_1$ are larger, they are comparable to the ones given Table 12.5. Nevertheless, as we already mentioned in Chapter 4, the higher poles might be affected by $\rho$ physics, conversely, the results discussed here concerning the $\mathcal{L} = 1/2$ $\rho B^*$ states would be influenced by $B^{(*)}\pi$, $B^{(*)}\eta$ and $B_s^{(*)}K$ channels.

# Chapter 13

# CONCLUSIONS

In the following pages we give a brief summary of the major findings obtained in this thesis, paying a special attention to the main results presented in each chapter.

We have studied the $D\pi$, $D\eta$ and $D_s\bar{K}$ scattering in the $J^P = 0^+$ and $(S, I) = (0, 1/2)$ sector, where so far only one meson, the $D_0^*(2400)$, has been reported in experiments [14, 206]. We showed in Chapter 4, within the framework of NLO UHM$\chi$PT, that in the region of the $D_0^*(2400)$ there are in fact two poles in the coupled-channel scattering amplitudes. The two poles are located at $\left(2105^{+6}_{-8} - i\,102^{+10}_{-12}\right)$ MeV and $\left(2451^{+36}_{-26} - i\,134^{+7}_{-8}\right)$ MeV, with the largest couplings to the $D\pi$ and $D_s\bar{K}$ channels, respectively. With all the parameters previously fixed, we predicted the energy levels for the coupled-channel system in finite volumes, finding that they agree remarkably well with the lattice QCD calculation of Ref. [81]. This successful description of the lattice data is regarded as a strong evidence for the two-pole structure of the $D_0^*(2400)$. Since the higher pole is close to the $D_s\bar{K}$ threshold, we expect it to show up as a threshold enhancement in the $D_s\bar{K}$ invariant mass distribution. This could be checked by high-statistic data in future experiments. We also showed that the lower pole belongs to the same SU(3) multiplet as the $D_{s0}^*(2317)$ state. We found a similar two-pole resonance pattern in the $J^P = 1^+$ as well as in the $J^P = 0^+$ and $1^+$ bottom sectors. Besides the two-pole structure, we stress the possible existence of a near-threshold bound or virtual state in the $\bar{B}\bar{K}$ (or $BK$) channel, both in the $0^+$ and $1^+$ sectors. These exotic states, with quark content $bs\bar{d}\bar{u}$, would have a large impact in the scattering length, and if they were bound, they could only decay through weak and/or electromagnetic interactions.

In Chapter 5, we have shown how the NLO UHM$\chi$PT amplitudes of Chapter 4 solve various puzzles in the charm-meson spectrum. These questions find a natural resolution if the SU(3) multiplets for the lightest scalar and axial-vector states, among them the $D_{s0}^*(2317)$ and the $D_{s1}(2460)$, owe their existence to the nonperturbative dynamics of Goldstone-boson scattering off $D_{(s)}$ and $D_{(s)}^*$ mesons. Most importantly the mass ordering of the lightest strange and nonstrange scalars becomes natural. We also demonstrated for the first time that this mechanism is strongly supported by the high quality data on the $B^- \to D^+\pi^-\pi^-$ reaction provided by the LHCb experiment [240]. These findings led us to conclude that the lightest quark-model positive-parity charm mesons, together with their bottom counterparts, if realized in nature, do not form the ground-state multiplet. In a broader view, the results reinforce the interpretation that the hadron spectrum should not be viewed as a collection of quark-model states. Instead, it should be regarded as a manifestation of complex dynamics, leading to an intricate and diverse pattern of states that can only be understood by a joint effort from experiment, LQCD and phenomenology.

In Chapter 6, we simultaneously studied the scalar form factors of the semileptonic heavy meson decays $D \to \pi\bar{\ell}\nu_\ell$, $D \to \bar{K}\bar{\ell}\nu_\ell$, $\bar{B} \to \pi\ell\bar{\nu}_\ell$ and $\bar{B}_s \to K\ell\bar{\nu}_\ell$, solving the MO integral equations. As input, we employed NLO UHM$\chi$PT amplitudes, used also in Chapters 4 and 5, for the energy regions not far from thresholds, while, at high energies, adequate asymptotic conditions were imposed. The scalar form factors were expressed in terms of Omnès matrices multiplied by vector polynomials, which contain some undetermined dispersive subtraction constants. We made use of heavy quark and chiral symmetries to constrain these constants, which were fitted to lattice QCD results both in the charm and the bottom sectors. Besides, in this latter sector we used the LCSR predictions close to $q^2 = 0$ as well. We found a good simultaneous description of the scalar form factors for the four semileptonic decay reactions. From this combined fit, and taking advantage that scalar and vector form factors are equal at $q^2 = 0$, we have obtained $|V_{cd}| = 0.244 \pm 0.022$, $|V_{cs}| = 0.945 \pm 0.041$ and $|V_{ub}| = (4.3 \pm 0.7) \times 10^{-3}$ for the involved CKM matrix elements. In addition, we showed predictions of the following vector form factors at $q^2 = 0$: $|f_+^{D\to\eta}(0)| = 0.01 \pm 0.05$, $|f_+^{D_s\to K}(0)| = 0.50 \pm 0.08$, $|f_+^{D_s\to\eta}(0)| = 0.73 \pm 0.03$ and $|f_+^{\bar{B}\to\eta}(0)| = 0.82 \pm 0.08$, which might serve as alternatives to determine the CKM elements when experimental measurements of the corresponding differential decay rates become available. Finally, we predicted the different form factors above the $q^2$-regions accessible in the semileptonic decays, up to moderate energies amenable to be described using the unitarized coupled-channel chiral approach.

Next in Chapter 7, we have presented a new model-independent parametrization for the hadronic form factors in the semi-leptonic $\bar{B} \to D\ell\bar{\nu}_\ell$ decay, although the formalism can be applied to any other semileptonic processes induced by the weak $b \to c$ transition. This is also inspired in the MO dispersive representation of the form factors. The coefficients in this parametrization are related to the form factor phases by sumrule-like dispersion relations, and hence, are called phase moments. They encode important scattering information of the $\bar{B}\bar{D}$ interactions which, currently, are not well known. Using recent experimental and lattice QCD data on this reaction [319, 321], we determined the phase moments, the CKM matrix element $|V_{cb}| = 41.01(75) \times 10^{-3}$, and predicted the ratio $\mathcal{R}_D = \mathcal{BR}(\bar{B} \to D\tau\bar{\nu}_\tau)/\mathcal{BR}(\bar{B} \to D\ell\bar{\nu}_\ell) = 0.301(5)$. We found an excellent simultaneous reproduction of the lattice and experimental data. Our results provide strong hints about the existence of at least one bound and one virtual $\bar{B}\bar{D}$ $S$-wave $0^+$ states, subject to uncertainties due to the possible influence of inelastic channels.

The structure of the $D_{s0}^*(2317)$ and $D_{s1}(2460)$ resonances has been studied in Chapter 8. There, LO HM$\chi$PT amplitudes are improved by incorporating the interplay between $S$-wave $D^{(*)}K$ meson-meson degrees of freedom and bare $P$-wave $c\bar{s}$ states predicted by CQM. We have extended the formalism to finite volumes, and fitted the strength of the coupling between both types of degrees of freedom to the lattice levels [45], which we successfully described. We have estimated the size of the $D^{(*)}K$ two-meson components in the $D_{s0}^*(2317)$ and $D_{s1}(2460)$ resonances, concluding that these states have a predominantly hadronic-molecular structure ($\sim$ 60-70%), and that it should not be tried to accommodate these mesons within $c\bar{s}$ constituent quark model patterns. We have also used this formalism in Chapter 9 to investigate the bottom counterparts of the $D_{s0}^*(2317)$ and $D_{s1}(2460)$ resonances. We used the LQCD results on the $b\bar{s}$ $J^P = 0^+$ and $1^+$ sectors of Ref. [58] to fix the strength of the coupling between bare $P$-wave $b\bar{s}$ states and $S$-wave $B^{(*)}K$ two-meson components. We have found candidates of scalar $\bar{B}_{s0}^*$ and axial $\bar{B}_{s1}$ states with masses of $5709 \pm 8$ MeV and $5755 \pm 8$ MeV, respectively, and estimated the molecular component of the $\bar{B}_{s0}^*$ and $\bar{B}_{s1}$ to be of the order of 50%. Thus, as in the case of the charm siblings, we interpret these findings as a clear indication of the non-canonical quark model nature of these states.

We have also studied (Chapter 10) the relationship between the $D_{s0}^*(2317)^+$ resonance and the decay of the $B_c^+$ meson into $J/\psi D^+ K^0$. The final state interaction of the $S$-wave $D^+ K^0$ pair was described by a LO UHM$\chi$PT amplitude, and generated the $D_{s0}^*(2317)^+$ resonance as a bound state pole. With the parameters which allowed us to match the pole position to the experimental mass of the $D_{s0}^*(2317)^+$, we have obtained the $D^+ K^0$ invariant mass distribution of the decay $B_c \to J/\psi D^+ K^0$, and also the rate for $B_c \to J/\psi D_{s0}^*(2317)^+$. We have predicted the ratio of these two magnitudes. We have found that both the $D^+ K^0$ invariant mass distribution and the ratio present a characteristic enhancement for energies close to the $D^+ K^0$ threshold, which is tightly related to the dynamical generation of the $D_{s0}^*(2317)^+$ pole in the amplitude. This low energy behaviour of the invariant mass distribution is very different from the energy dependence of the phase space and, in principle, this difference should show up in experiments.

We have also investigated the signatures produced by the $Z_c(3900)^\pm$ in a LQCD simulation. We considered in Chapter 11 a $T$-matrix analysis [385], which accounts for the $J/\psi\pi$ and $D^*\bar{D}$ coupled-channels dynamics, and which successfully describes the experimental information concerning the $Z_c(3900)^\pm$. Within such scheme, the data can be similarly well described in two different scenarios, where $Z_c(3900)$ is either a resonance or a virtual state. To shed light into the nature of this state, we have applied this formalism in a finite box with the aim of comparing with most recent LQCD simulations. We see that the energy levels obtained for both scenarios agree well with those obtained in the single-volume LQCD simulation reported in [384], thus making it difficult to disentangle the two possibilities. We have also studied the volume dependence of the energy levels obtained with our formalism and suggested that LQCD simulations performed at several volumes could help in discerning the actual nature of the intriguing $Z_c(3900)$ state.

Finally, we have studied in Chapter 12 the $\rho/\omega$ and $B^*$ scattering in $S$-wave using unitarized LHG amplitudes. We have found evidence of three bound states in $(I, J^P) = (1/2, 0^+)$, $(1/2, 1^+)$ and $(1/2, 2^+)$. The state with $J = 2$ can be a good candidate for the $B_2^*(5741)$. We have also studied the $\rho B$ system in $S$-wave, and a bound state with mass 5728 MeV and with 20 MeV is obtained, which could be identified with the $B_1(5721)$ resonance. In the case of $I = 3/2$ the interaction was found repulsive, and thus, no exotic meson resonances are generated in the approach.

# Appendix A

## Regularized two-meson loop functions

The purpose of this appendix is to collect all the formulae of the different regularized loop functions employed throughout the previous chapters. We denote them as $G^{(\mathrm{R})}(s, m_1, m_2)$, where "R" corresponds to the type of regularization, $s$ is the invariant mass squared of the external particles, and $m_1$ and $m_2$ are the masses of the pair of virtual mesons.

**Dimensional regularization.** This loop function [242, 430] is obtained by means of Feynman integration in the so-called modified minimal subtraction scheme. Therefore, its real part depends on the remaining subtraction constant $a(\mu)$, and the associated scale $\mu$ introduced during the integration process,

$$\begin{aligned}16\pi^2 G^{(\mathrm{D})}(s, m_1, m_2) = a(\mu) + \ln\frac{m_2^2}{\mu^2} + \frac{m_1^2 - m_2^2 + s}{s}\ln\frac{m_1}{m_2} + \sigma(s)\times \\ \left[\ln\left(\frac{+s - m_1^2 + m_2^2 + 2s\sigma(s)}{-s + m_1^2 - m_2^2 + 2s\sigma(s)}\right) + \ln\left(\frac{+s + m_1^2 - m_2^2 + 2s\sigma(s)}{-s - m_1^2 + m_2^2 + 2s\sigma(s)}\right)\right]\end{aligned} \tag{A.1}$$

with $\sigma(s)$ given in Eq. (2.38). We refer to App. A in Ref. [133] for the phase conventions when Eq. (A.1) is evaluated in the complex $s$-plane.

**Gaussian cut-off.** In this case, the divergent part is removed by introducing an exponential suppression of the higher momenta in the integrand, affecting the real part exclusively. This is achieved as follows. We add in Eq. (2.78), with the integral of the zero-th component already performed, an extra $e^{2(\vec{p}^{\,2} - \vec{k}^2)/\Lambda^2}$ suppressing factor, which becomes 1 when $\vec{k}^2$ is on-shell ($\vec{k}^2 = \vec{p}^{\,2}$),

$$G^{(\mathrm{G})}(s, m_1, m_2) = \int \frac{\mathrm{d}^3 k}{(2\pi)^3}\frac{E_1 + E_2}{2E_1E_2}\frac{e^{2\left(\vec{p}^{\,2} - \vec{k}^2\right)/\Lambda^2}}{s - (E_1 + E_2)^2 + i\epsilon}. \tag{A.2}$$

with meson energies $E_1$ and $E_2$ given by $E_i = \sqrt{m_i^2 + \vec{k}^2}$ and the square of the on-shell three-momentum $\vec{p}$ related with $s$ and the meson masses by

$$\vec{p}^{\,2} = \frac{\lambda(s, m_1^2, m_2^2)}{4s}. \tag{A.3}$$

The parameter $\Lambda$ is the cut-off scale, which suppresses three momentum contributions with magnitudes $|\vec{k}| > \Lambda$. Its specific value is undetermined, though in practice its accepted values are expected to lie in the $\sim 1$ GeV region (see Eq. (1.3) and related discussion). For numerical applications, to compute the loop function on the scattering line, $s + i\epsilon$ ($s > (m_1 + m_2)^2$), it is convenient to split Eq. (A.2) into its real and imaginary contributions,

$$\begin{aligned} G^{(\mathrm{G})}(s, m_1, m_2) = \mathrm{P} \int \frac{\mathrm{d}^3 k}{(2\pi)^3} \frac{E_1 + E_2}{2E_1 E_2} \frac{e^{2\left(\vec{p}^2 - \vec{k}^2\right)/\Lambda^2}}{s - (E_1 + E_2)^2} \\ - i \frac{\sigma(s)}{8\pi} \Theta \left[ s - (m_1 + m_2)^2 \right], \end{aligned} \tag{A.4}$$

where the real part has to be numerically performed.

**Sharp-cutoff regularization.** The last method consists on bounding the range of integration on the three momentum integral in Eq. (2.78), integrating up to some maximum magnitude $|\vec{k}| = q_{\max}$:

$$G^{(\mathrm{SC})}(s, m_1, m_2) = \int_0^{q_{\max}} \frac{|\vec{k}|^2 \mathrm{d}|\vec{k}|}{2\pi^2} \frac{E_1 + E_2}{2E_1 E_2} \frac{1}{s - (E_1 + E_2)^2 + i\epsilon}. \tag{A.5}$$

as opposed to Eq. (A.4), it has the advantage that there is an analytic expression for Eq. (A.5) which can be found in Ref. [431] (note the Erratum).

The three regularization/renormalization schemes provide similar results close to the threshold energy, and the choice may be based on practical grounds. In terms of computation performance, the sharp-cutoff prescription as well as dimensional regularization are very suitable due to their analytic form. On the other hand, for calculations in a finite box, one finds that their finite volume versions (4.4) turn out to be computationally costly. This is not the case of the Gaussian regularization [169], since its finite volume implementation is rather straightforward and converges faster than the others. As a final comment, it should be considered that the application of the sharp cutoff prescription should be restricted to values of $\sqrt{s}$ below $E_1(q_{\max}) + E_2(q_{\max})$, since at this value $G^{(\mathrm{SC})}$ becomes singular [432].

# Bibliography

[1] P. Fernandez-Soler, Z.-F. Sun, J. Nieves and E. Oset, *The* $\rho(\omega)B^*(B)$ *interaction and states of* $J = 0, 1, 2$, Eur. Phys. J. **C76** (2016) 82, [`1507.06787`].

[2] Z.-F. Sun, M. Bayar, P. Fernandez-Soler and E. Oset, $D^*_{s0}(2317)^+$ *in the decay of* $B_c$ *into* $J/\psi DK$, Phys. Rev. **D93** (2016) 054028, [`1510.06316`].

[3] M. Albaladejo, P. Fernandez-Soler, F.-K. Guo and J. Nieves, *Two-pole structure of the* $D^*_0(2400)$, Phys. Lett. **B767** (2017) 465–469, [`1610.06727`].

[4] M. Albaladejo, P. Fernandez-Soler, J. Nieves and P. G. Ortega, *Lowest-lying even-parity* $\bar{B}_s$ *mesons: heavy-quark spin-flavor symmetry, chiral dynamics, and constituent quark-model bare masses*, Eur. Phys. J. **C77** (2017) 170, [`1612.07782`].

[5] M. Albaladejo, P. Fernandez-Soler and J. Nieves, $Z_c(3900)$*: Confronting theory and lattice simulations*, Eur. Phys. J. **C76** (2016) 573, [`1606.03008`].

[6] M.-L. Du, M. Albaladejo, P. Fernández-Soler, F.-K. Guo, C. Hanhart, U.-G. Meißner et al., *Towards a new paradigm for heavy-light meson spectroscopy*, Phys. Rev. **D98** (2018) 094018, [`1712.07957`].

[7] M. Albaladejo, P. Fernandez-Soler, J. Nieves and P. G. Ortega, *Contribution of constituent quark model* $c\bar{s}$ *states to the dynamics of the* $D^*_{s0}(2317)$ *and* $D_{s1}(2460)$ *resonances*, Eur. Phys. J. **C78** (2018) 722, [`1805.07104`].

[8] D. L. Yao, P. Fernandez-Soler, M. Albaladejo, F. K. Guo and J. Nieves, *Heavy-to-light scalar form factors from Muskhelishvili–Omnès dispersion relations*, Eur. Phys. J. **C78** (2018) 310, [`1803.03171`].

[9] D.-L. Yao, P. Fernandez-Soler, F.-K. Guo and J. Nieves, *New parametrization of the form factors in* $\bar{B} \to D\ell\bar{\nu}_\ell$ *decays*, `1906.00727`.

[10] M. Gell-Mann, *A Schematic Model of Baryons and Mesons*, Phys. Lett. **8** (1964) 214–215.

[11] S. Godfrey and N. Isgur, *Mesons in a Relativized Quark Model with Chromodynamics*, Phys. Rev. **D32** (1985) 189–231.

[12] S. Capstick and N. Isgur, *Baryons in a Relativized Quark Model with Chromodynamics*, Phys. Rev. **D34** (1986) 2809.

[13] L. D. Roper, *Evidence for a* $P_{11}$ *Pion-Nucleon Resonance at 556 MeV*, Phys. Rev. Lett. **12** (1964) 340–342.

[14] Particle Data Group collaboration, M. Tanabashi et al., *Review of Particle Physics*, Phys. Rev. **D98** (2018) 030001.

[15] BaBar collaboration, B. Aubert et al., *Observation of a narrow meson decaying to* $D^+_s\pi^0$ *at a mass of 2.32-GeV/*$c^2$, Phys. Rev. Lett. **90** (2003) 242001, [`hep-ex/0304021`].

[16] CLEO collaboration, D. Besson et al., *Observation of a narrow resonance of mass 2.46-GeV/*$c^2$ *decaying to* $D^{*+}_s\pi^0$ *and confirmation of the* $D^*_{sJ}(2317)$ *state*, Phys. Rev. **D68** (2003) 032002, [`hep-ex/0305100`].

[17] N. Isgur and M. B. Wise, *Weak Decays of Heavy Mesons in the Static Quark Approximation*, Phys. Lett. **B232** (1989) 113–117.

[18] N. Isgur and M. B. Wise, *Weak Transition Form Factors between Heavy Mesons*, Phys. Lett. **B237** (1990) 527–530.

[19] H. Georgi, *An Effective Field Theory for Heavy Quarks at Low-energies*, Phys. Lett. **B240** (1990) 447–450.

[20] N. Isgur and M. B. Wise, *Spectroscopy with heavy quark symmetry*, Phys. Rev. Lett. **66** (1991) 1130–1133.

[21] A. V. Manohar and M. B. Wise, *Heavy quark physics*, Camb. Monogr. Part. Phys. Nucl. Phys. Cosmol. **10** (2000) 1–191.

[22] ARGUS collaboration, H. Albrecht et al., *Observation of a New Charmed - Strange Meson*, Phys. Lett. **B230** (1989) 162.

[23] CLEO collaboration, J. P. Alexander et al., *Production and decay of the* $D_{s1}^{+}(2536)$, Phys. Lett. **B303** (1993) 377–384.

[24] CLEO collaboration, Y. Kubota et al., *Observation of a new charmed strange meson*, Phys. Rev. Lett. **72** (1994) 1972–1976, [`hep-ph/9403325`].

[25] S. Godfrey and R. Kokoski, *The Properties of p Wave Mesons with One Heavy Quark*, Phys. Rev. **D43** (1991) 1679–1687.

[26] M. Di Pierro and E. Eichten, *Excited heavy - light systems and hadronic transitions*, Phys. Rev. **D64** (2001) 114004, [`hep-ph/0104208`].

[27] Fayyazuddin and Riazuddin, *Some comments on narrow resonances* $D_{s1}^{*}$ *(2.46-GeV /* $c^2$*) and* $D_{s0}$ *(2.317-GeV/* $c^2$*)*, Phys. Rev. **D69** (2004) 114008, [`hep-ph/0309283`].

[28] M. Sadzikowski, *The Masses of* $D_{sj}^{*}(2317)$ *and* $D_{sj}^{*}(2463)$ *in the MIT bag model*, Phys. Lett. **B579** (2004) 39–42, [`hep-ph/0307084`].

[29] O. Lakhina and E. S. Swanson, *A Canonical* $D_s(2317)$*?*, Phys. Lett. **B650** (2007) 159–165, [`hep-ph/0608011`].

[30] T. Barnes, F. E. Close and H. J. Lipkin, *Implications of a DK molecule at 2.32-GeV*, Phys. Rev. **D68** (2003) 054006, [`hep-ph/0305025`].

[31] H. J. Lipkin, *New predictions for multiquark hadron masses*, Phys. Lett. **B580** (2004) 50–53, [`hep-ph/0306204`].

[32] A. P. Szczepaniak, *Description of the* $D_s^{*}(2320)$ *resonance as the* $D\pi$ *atom*, Phys. Lett. **B567** (2003) 23–26, [`hep-ph/0305060`].

[33] E. E. Kolomeitsev and M. F. M. Lutz, *On Heavy light meson resonances and chiral symmetry*, Phys. Lett. **B582** (2004) 39–48, [`hep-ph/0307133`].

[34] J. Hofmann and M. F. M. Lutz, *Open charm meson resonances with negative strangeness*, Nucl. Phys. **A733** (2004) 142–152, [`hep-ph/0308263`].

[35] T. E. Browder, S. Pakvasa and A. A. Petrov, *Comment on the new* $D_s^{*+}\pi^0$ *resonances*, Phys. Lett. **B578** (2004) 365–368, [`hep-ph/0307054`].

[36] P. Bicudo, *The Family of strange multiquarks as kaonic molecules bound by hard core attraction*, Nucl. Phys. **A748** (2005) 537–550, [`hep-ph/0401106`].

[37] F.-K. Guo, P.-N. Shen, H.-C. Chiang, R.-G. Ping and B.-S. Zou, *Dynamically generated* $0^+$ *heavy mesons in a heavy chiral unitary approach*, Phys. Lett. **B641** (2006) 278–285, [`hep-ph/0603072`].

[38] D. Gamermann, E. Oset, D. Strottman and M. J. Vicente Vacas, *Dynamically generated open and hidden charm meson systems*, Phys. Rev. **D76** (2007) 074016, [`hep-ph/0612179`].

[39] A. Faessler, T. Gutsche, V. E. Lyubovitskij and Y.-L. Ma, *Strong and radiative decays of the* $D^*_{s0}(2317)$ *meson in the* $DK$*-molecule picture*, Phys. Rev. **D76** (2007) 014005, [`0705.0254`].

[40] J. M. Flynn and J. Nieves, *Elastic s-wave* $B\pi$, $D\pi$, $DK$ *and* $K\pi$ *scattering from lattice calculations of scalar form-factors in semileptonic decays*, Phys. Rev. **D75** (2007) 074024, [`hep-ph/0703047`].

[41] A. Martinez Torres, L. R. Dai, C. Koren, D. Jido and E. Oset, *The* $KD$, $\eta D_s$ *interaction in finite volume and the nature of the* $D_{s*0}(2317)$ *resonance*, Phys. Rev. **D85** (2012) 014027, [`1109.0396`].

[42] M. Altenbuchinger, L. S. Geng and W. Weise, *Scattering lengths of Nambu-Goldstone bosons off* $D$ *mesons and dynamically generated heavy-light mesons*, Phys. Rev. **D89** (2014) 014026, [`1309.4743`].

[43] M. Altenbuchinger and L.-S. Geng, *Off-shell effects on the interaction of Nambu-Goldstone bosons and* $D$ *mesons*, Phys. Rev. **D89** (2014) 054008, [`1310.5224`].

[44] M. Albaladejo, D. Jido, J. Nieves and E. Oset, $D^*_{s0}(2317)$ *and* $DK$ *scattering in* $B$ *decays from BaBar and LHCb data*, Eur. Phys. J. **C76** (2016) 300, [`1604.01193`].

[45] G. S. Bali, S. Collins, A. Cox and A. Schäfer, *Masses and decay constants of the* $D^*_{s0}(2317)$ *and* $D_{s1}(2460)$ *from* $N_f = 2$ *lattice QCD close to the physical point*, Phys. Rev. **D96** (2017) 074501, [`1706.01247`].

[46] D. Mohler, C. B. Lang, L. Leskovec, S. Prelovsek and R. M. Woloshyn, $D^*_{s0}(2317)$ *Meson and D-Meson-Kaon Scattering from Lattice QCD*, Phys. Rev. Lett. **111** (2013) 222001, [`1308.3175`].

[47] C. B. Lang, L. Leskovec, D. Mohler, S. Prelovsek and R. M. Woloshyn, $D_s$ *mesons with* $DK$ *and* $D^*K$ *scattering near threshold*, Phys. Rev. **D90** (2014) 034510, [`1403.8103`].

[48] CDF collaboration, T. Aaltonen et al., *Observation of orbitally excited* $B_s$ *mesons*, Phys. Rev. Lett. **100** (2008) 082001, [`0710.4199`].

[49] D0 collaboration, V. M. Abazov et al., *Observation and properties of the orbitally excited* $B^*_{s2}$ *meson*, Phys. Rev. Lett. **100** (2008) 082002, [`0711.0319`].

[50] T. Matsuki, K. Mawatari, T. Morii and K. Sudoh, $0^+$ *and* $1^+$ *states of* $B$ *and* $B_s$ *mesons*, Phys. Lett. **B606** (2005) 329–334, [`hep-ph/0411034`].

[51] D. Ebert, R. N. Faustov and V. O. Galkin, *Heavy-light meson spectroscopy and Regge trajectories in the relativistic quark model*, Eur. Phys. J. **C66** (2010) 197–206.

[52] Y. Sun, Q.-T. Song, D.-Y. Chen, X. Liu and S.-L. Zhu, *Higher bottom and bottom-strange mesons*, Phys. Rev. **D89** (2014) 054026.

[53] W. A. Bardeen, E. J. Eichten and C. T. Hill, *Chiral multiplets of heavy-light mesons*, Phys. Rev. **D68** (2003) 054024, [`hep-ph/0305049`].

[54] F.-K. Guo, P.-N. Shen and H.-C. Chiang, *Dynamically generated* $1^+$ *heavy mesons*, Phys. Lett. **B647** (2007) 133–139, [`hep-ph/0610008`].

[55] M. Cleven, F.-K. Guo, C. Hanhart and U.-G. Meissner, *Light meson mass dependence of the positive parity heavy-strange mesons*, Eur. Phys. J. **A47** (2011) 19, [`1009.3804`].

[56] P. Colangelo, F. De Fazio, F. Giannuzzi and S. Nicotri, *New meson spectroscopy with open charm and beauty*, Phys. Rev. **D86** (2012) 054024, [`1207.6940`].

[57] E. B. Gregory et al., *Precise* $B$, $B_s$ *and* $B_c$ *meson spectroscopy from full lattice QCD*, Phys. Rev. **D83** (2011) 014506, [`1010.3848`].

[58] C. B. Lang, D. Mohler, S. Prelovsek and R. M. Woloshyn, *Predicting positive parity* $B_s$ *mesons from lattice QCD*, Phys. Lett. **B750** (2015) 17–21, [`1501.01646`].

[59] BELLE collaboration, K. Abe et al., *Study of* $B^- \to D^{**0}\pi^-(D^{**0} \to D^{*+}\pi^-)$ *decays*, Phys. Rev. **D69** (2004) 112002, [`hep-ex/0307021`].

[60] BABAR collaboration, B. Aubert et al., *Dalitz Plot Analysis of* $B^- \to D^+\pi^-\pi^-$, Phys. Rev. **D79** (2009) 112004, [`0901.1291`].

[61] FOCUS collaboration, J. M. Link et al., *Measurement of masses and widths of excited charm mesons* $D_2^*$ *and evidence for broad states*, Phys. Lett. **B586** (2004) 11–20, [`hep-ex/0312060`].

[62] LHCB collaboration, R. Aaij et al., *Amplitude analysis of* $B^0 \to \bar{D}^0K^+\pi^-$ *decays*, Phys. Rev. **D92** (2015) 012012, [`1505.01505`].

[63] J. M. Flynn and J. Nieves, *Form-factors for semileptonic* $B \to \pi$ *and* $D \to \pi$ *decays from the Omnes representation*, Phys. Lett. **B505** (2001) 82–88, [`hep-ph/0007263`].

[64] UKQCD collaboration, D. R. Burford, H. D. Duong, J. M. Flynn, J. Nieves, B. J. Gough, N. M. Hazel et al., *Form-factors for* $B \to \pi$ *lepton anti-lepton-neutrino and* $B \to K^*$ *gamma decays on the lattice*, Nucl. Phys. **B447** (1995) 425–440, [`hep-lat/9503002`].

[65] P. Ball and R. Zwicky, *New results on* $B \to \pi, K, \eta$ *decay formfactors from light-cone sum rules*, Phys. Rev. **D71** (2005) 014015, [`hep-ph/0406232`].

[66] E. Dalgic, A. Gray, M. Wingate, C. T. H. Davies, G. P. Lepage and J. Shigemitsu, *B meson semileptonic form-factors from unquenched lattice QCD*, Phys. Rev. **D73** (2006) 074502, [`hep-lat/0601021`].

[67] J. M. Flynn and J. Nieves, $|V_{ub}|$ *from Exclusive Semileptonic* $B \to \pi$ *Decays*, Phys. Lett. **B649** (2007) 269–274, [`hep-ph/0703284`].

[68] J. M. Flynn and J. Nieves, $|V_{ub}|$ *from exclusive semileptonic* $B \to \pi$ *decays revisited*, Phys. Rev. **D76** (2007) 031302, [`0705.3553`].

[69] HEAVY FLAVOR AVERAGING GROUP (HFAG) collaboration, Y. Amhis et al., *Averages of b-hadron, c-hadron, and* $\tau$*-lepton properties as of summer 2014*, `1412.7515`.

[70] S. Aoki et al., *Review of lattice results concerning low-energy particle physics*, Eur. Phys. J. **C77** (2017) 112, [`1607.00299`].

[71] CKMFITTER GROUP collaboration, J. Charles, A. Hocker, H. Lacker, S. Laplace, F. R. Le Diberder, J. Malcles et al., *CP violation and the CKM matrix: Assessing the impact of the asymmetric B factories*, Eur. Phys. J. **C41** (2005) 1–131, [`hep-ph/0406184`].

[72] UTFIT collaboration, M. Bona et al., *The Unitarity Triangle Fit in the Standard Model and Hadronic Parameters from Lattice QCD: A Reappraisal after the Measurements of* $\Delta m_s$ *and* $BR(B \to \tau\nu_\tau)$, JHEP **10** (2006) 081, [`hep-ph/0606167`].

[73] A. Bevan et al., *Standard Model updates and new physics analysis with the Unitarity Triangle fit*, Nucl. Phys. Proc. Suppl. **241-242** (2013) 89–94.

[74] S. Narison, *Open charm and beauty chiral multiplets in QCD*, Phys. Lett. **B605** (2005) 319–325, [`hep-ph/0307248`].

[75] I. W. Lee, T. Lee, D. P. Min and B.-Y. Park, *Chiral radiative corrections and* $D_s(2317)/D(2308)$ *mass puzzle*, Eur. Phys. J. **C49** (2007) 737–741, [`hep-ph/0412210`].

[76] E. van Beveren and G. Rupp, *Observed* $D_s(2317)$ *and tentative* $D(2100-2300)$ *as the charmed cousins of the light scalar nonet*, Phys. Rev. Lett. **91** (2003) 012003, [`hep-ph/0305035`].

[77] H.-Y. Cheng and W.-S. Hou, *B decays as spectroscope for charmed four quark states*, Phys. Lett. **B566** (2003) 193–200, [`hep-ph/0305038`].

[78] K. Terasaki, *BABAR resonance as a new window of hadron physics*, Phys. Rev. **D68** (2003) 011501, [`hep-ph/0305213`].

[79] M. E. Bracco, A. Lozea, R. D. Matheus, F. S. Navarra and M. Nielsen, *Disentangling two- and four-quark state pictures of the charmed scalar mesons*, Phys. Lett. **B624** (2005) 217–222, [`hep-ph/0503137`].

[80] D. Gamermann and E. Oset, *Axial resonances in the open and hidden charm sectors*, Eur. Phys. J. **A33** (2007) 119–131, [`0704.2314`].

[81] G. Moir, M. Peardon, S. M. Ryan, C. E. Thomas and D. J. Wilson, *Coupled-Channel* $D\pi$*,* $D\eta$ *and* $D_s\bar{K}$ *Scattering from Lattice QCD*, JHEP **10** (2016) 011, [`1607.07093`].

[82] BELLE collaboration, S. K. Choi et al., *Observation of a narrow charmonium - like state in exclusive* $B^+ \to K^+\pi^+\pi^- J/\psi$ *decays*, Phys. Rev. Lett. **91** (2003) 262001, [`hep-ex/0309032`].

[83] S. L. Olsen, *A New Hadron Spectroscopy*, Front. Phys.(Beijing) **10** (2015) 121–154, [`1411.7738`].

[84] H.-X. Chen, W. Chen, X. Liu and S.-L. Zhu, *The hidden-charm pentaquark and tetraquark states*, Phys. Rept. **639** (2016) 1–121, [`1601.02092`].

[85] A. Hosaka, T. Iijima, K. Miyabayashi, Y. Sakai and S. Yasui, *Exotic hadrons with heavy flavors: X, Y, Z, and related states*, PTEP **2016** (2016) 062C01, [`1603.09229`].

[86] BESIII collaboration, M. Ablikim et al., *Observation of a Charged Charmoniumlike Structure in* $e^+e^- \to \pi^+\pi^- J/\Psi$ *at* $\sqrt{s} = 4.26$ *GeV*, Phys. Rev. Lett. **110** (2013) 252001, [`1303.5949`].

[87] BELLE collaboration, Z. Q. Liu et al., *Study of* $e^+e^- \to \pi^+\pi^- J/\Psi$ *and Observation of a Charged Charmoniumlike State at Belle*, Phys. Rev. Lett. **110** (2013) 252002, [`1304.0121`].

[88] T. Xiao, S. Dobbs, A. Tomaradze and K. K. Seth, *Observation of the Charged Hadron* $Z_c^{\pm}(3900)$ *and Evidence for the Neutral* $Z_c^0(3900)$ *in* $e^+e^- \to \pi\pi J/\psi$ *at* $\sqrt{s} = 4170$ *MeV*, Phys. Lett. **B727** (2013) 366–370, [`1304.3036`].

[89] BESIII collaboration, M. Ablikim et al., *Observation of a charged* $(D\bar{D}^*)^{\pm}$ *mass peak in* $e^+e^- \to \pi D\bar{D}^*$ *at* $\sqrt{s} = 4.26$ *GeV*, Phys. Rev. Lett. **112** (2014) 022001, [`1310.1163`].

[90] BESIII collaboration, M. Ablikim et al., *Confirmation of a charged charmoniumlike state* $Z_c(3885)^{\mp}$ *in* $e^+e^- \to \pi^{\pm}(D\bar{D}^*)^{\mp}$ *with double D tag*, Phys. Rev. **D92** (2015) 092006, [`1509.01398`].

[91] BESIII collaboration, M. Ablikim et al., *Observation of* $Z_c(3900)^0$ *in* $e^+e^- \to \pi^0\pi^0 J/\psi$, Phys. Rev. Lett. **115** (2015) 112003, [`1506.06018`].

[92] M. B. Voloshin, $Z_c(3900)$ *- what is inside?*, Phys. Rev. **D87** (2013) 091501, [`1304.0380`].

[93] Q. Wang, C. Hanhart and Q. Zhao, *Decoding the riddle of* $Y(4260)$ *and* $Z_c(3900)$, Phys. Rev. Lett. **111** (2013) 132003, [`1303.6355`].

[94] F.-K. Guo, C. Hidalgo-Duque, J. Nieves and M. P. Valderrama, *Consequences of Heavy Quark Symmetries for Hadronic Molecules*, Phys. Rev. **D88** (2013) 054007, [`1303.6608`].

[95] E. Wilbring, H. W. Hammer and U. G. Meißner, *Electromagnetic Structure of the* $Z_c(3900)$, Phys. Lett. **B726** (2013) 326–329, [`1304.2882`].

[96] Y. Dong, A. Faessler, T. Gutsche and V. E. Lyubovitskij, *Strong decays of molecular states* $Z_c^+$ *and* $Z_c'^+$, Phys. Rev. **D88** (2013) 014030, [`1306.0824`].

[97] J.-R. Zhang, *Improved QCD sum rule study of* $Z_c(3900)$ *as a* $\bar{D}D^*$ *molecular state*, Phys. Rev. **D87** (2013) 116004, [`1304.5748`].

[98] H.-W. Ke, Z.-T. Wei and X.-Q. Li, *Is* $Z_c(3900)$ *a molecular state*, Eur. Phys. J. **C73** (2013) 2561, [`1307.2414`].

[99] F. Aceti, M. Bayar, E. Oset, A. Martinez Torres, K. P. Khemchandani, J. M. Dias et al., *Prediction of an* $I = 1$ $D\bar{D}^*$ *state and relationship to the claimed* $Z_c(3900)$*,* $Z_c(3885)$, Phys. Rev. **D90** (2014) 016003, [`1401.8216`].

[100] J. He, *The* $Z_c(3900)$ *as a resonance from the* $D\bar{D}^*$ *interaction*, Phys. Rev. **D92** (2015) 034004, [`1505.05379`].

[101] E. Braaten, *How the* $Z_c(3900)$ *Reveals the Spectra of Quarkonium Hybrid and Tetraquark Mesons*, Phys. Rev. Lett. **111** (2013) 162003, [`1305.6905`].

[102] J. M. Dias, F. S. Navarra, M. Nielsen and C. M. Zanetti, $Z_c^+$ *(3900) decay width in QCD sum rules*, Phys. Rev. **D88** (2013) 016004, [`1304.6433`].

[103] Z.-G. Wang and T. Huang, *Analysis of the* $X(3872)$*,* $Z_c(3900)$ *and* $Z_c(3885)$ *as axial-vector tetraquark states with QCD sum rules*, Phys. Rev. **D89** (2014) 054019, [`1310.2422`].

[104] C.-F. Qiao and L. Tang, *Estimating the mass of the hidden charm* $1^+(1^+)$ *tetraquark state via QCD sum rules*, Eur. Phys. J. **C74** (2014) 3122, [`1307.6654`].

[105] C. Deng, J. Ping and F. Wang, *Interpreting* $Z_c(3900)$ *and* $Z_c(4025)/Z_c(4020)$ *as charged tetraquark states*, Phys. Rev. **D90** (2014) 054009, [`1402.0777`].

[106] A. Esposito, A. L. Guerrieri, F. Piccinini, A. Pilloni and A. D. Polosa, *Four-Quark Hadrons: an Updated Review*, Int. J. Mod. Phys. **A30** (2015) 1530002, [`1411.5997`].

[107] L. Maiani, F. Piccinini, A. D. Polosa and V. Riquer, *The* $Z(4430)$ *and a New Paradigm for Spin Interactions in Tetraquarks*, Phys. Rev. **D89** (2014) 114010, [`1405.1551`].

[108] Z.-Y. Zhou and Z. Xiao, *Distinguishing near-threshold pole effects from cusp effects*, Phys. Rev. **D92** (2015) 094024, [`1505.05761`].

[109] D.-Y. Chen, X. Liu and T. Matsuki, *Reproducing the* $Z_c(3900)$ *structure through the initial-single-pion-emission mechanism*, Phys. Rev. **D88** (2013) 036008, [`1304.5845`].

[110] E. S. Swanson, $Z_b$ *and* $Z_c$ *Exotic States as Coupled Channel Cusps*, Phys. Rev. **D91** (2015) 034009, [`1409.3291`].

[111] A. P. Szczepaniak, *Triangle Singularities and XYZ Quarkonium Peaks*, Phys. Lett. **B747** (2015) 410–416, [`1501.01691`].

[112] S. Coito, *Radially excited axial mesons and the enigmatic* $Z_c$ *and* $Z_b$ *in a coupled-channel model*, Phys. Rev. **D94** (2016) 014016, [`1602.07821`].

[113] F.-K. Guo, C. Hanhart, Q. Wang and Q. Zhao, *Could the near-threshold* $XYZ$ *states be simply kinematic effects?*, Phys. Rev. **D91** (2015) 051504, [`1411.5584`].

[114] M. Cleven, F.-K. Guo, C. Hanhart, Q. Wang and Q. Zhao, *Employing spin symmetry to disentangle different models for the XYZ states*, Phys. Rev. **D92** (2015) 014005, [`1505.01771`].

[115] T. Muta, *Foundations of Quantum Chromodynamics: An Introduction to Perturbative Methods in Gauge Theories, (3rd ed.)*, vol. 78 of *World scientific Lecture Notes in Physics*. World Scientific, Hackensack, N.J., 2010.

[116] D. J. Gross and F. Wilczek, *Asymptotically Free Gauge Theories - I*, Phys. Rev. **D8** (1973) 3633–3652.

[117] S. Weinberg, *Nonabelian Gauge Theories of the Strong Interactions*, Phys. Rev. Lett. **31** (1973) 494–497.

[118] H. D. Politzer, *Asymptotic Freedom: An Approach to Strong Interactions*, Phys. Rept. **14** (1974) 129–180.

[119] S. Bethke, *Experimental tests of asymptotic freedom*, Prog. Part. Nucl. Phys. **58** (2007) 351–386, [`hep-ex/0606035`].

[120] C. G. Callan, Jr., R. F. Dashen and D. J. Gross, *Toward a Theory of the Strong Interactions*, Phys. Rev. **D17** (1978) 2717.

[121] W. Heisenberg, *Die 'beobachtbaren Größen' in der Theorie der Elementarteilchen*, Zeitschrift für Physik **120** (Jul, 1943) 513–538.

[122] J. T. Cushing, *The Importance of Heisenberg's S-Matrix Program for the Theoretical High-Energy Physics of the 1950's*, Centaurus **29** (07, 2007) 110 – 149.

[123] J. A. Wheeler, *On the Mathematical Description of Light Nuclei by the Method of Resonating Group Structure*, Phys. Rev. **52** (1937) 1107–1122.

[124] R. J. Eden, *The Analytic S-Matrix.* Cambridge University Press, 2002.

[125] A. Martin and T. Spearman, *Elementary particle theory.* North-Holland Pub. Co., 1970.

[126] H. M. Nussenzveig, *Causality and dispersion relations.* Math. Sci. Eng. Academic Press, New York, NY, 1972.

[127] S. Mandelstam, *Determination of the Pion-Nucleon Scattering Amplitude from Dispersion Relations and Unitarity. General Theory*, Phys. Rev. **112** (Nov, 1958) 1344–1360.

[128] N. Kaiser, P. B. Siegel and W. Weise, *Chiral dynamics and the* $S_{11}(1535)$ *nucleon resonance*, Phys. Lett. **B362** (1995) 23–28, [`nucl-th/9507036`].

[129] N. Kaiser, P. B. Siegel and W. Weise, *Chiral dynamics and the low-energy kaon - nucleon interaction*, Nucl. Phys. **A594** (1995) 325–345, [`nucl-th/9505043`].

[130] J. A. Oller and E. Oset, *Chiral symmetry amplitudes in the S wave isoscalar and isovector channels and the* $\sigma$*,* $f_0$*(980),* $a_0$*(980) scalar mesons*, Nucl. Phys. **A620** (1997) 438–456, [`hep-ph/9702314`].

[131] E. Oset and A. Ramos, *Nonperturbative chiral approach to s wave anti-K N interactions*, Nucl. Phys. **A635** (1998) 99–120, [`nucl-th/9711022`].

[132] J. Nieves and E. Ruiz Arriola, *Bethe-Salpeter approach for unitarized chiral perturbation theory*, Nucl. Phys. **A679** (2000) 57–117, [`hep-ph/9907469`].

[133] J. Nieves and E. Ruiz Arriola, *The* $S_{11} - N(1535)$ *and* $-N(1650)$ *resonances in meson baryon unitarized coupled channel chiral perturbation theory*, Phys. Rev. **D64** (2001) 116008, [`hep-ph/0104307`].

[134] M. Albaladejo and J. A. Oller, *On the size of the sigma meson and its nature*, Phys. Rev. **D86** (2012) 034003, [`1205.6606`].

[135] R. H. Dalitz and S. F. Tuan, *A possible resonant state in pion-hyperon scattering*, Phys. Rev. Lett. **2** (1959) 425–428.

[136] J. R. Pelaez, *From controversy to precision on the sigma meson: a review on the status of the non-ordinary* $f_0(500)$ *resonance*, Phys. Rept. **658** (2016) 1, [`1510.00653`].

[137] F. Giacosa, *Dynamical generation and dynamical reconstruction*, Phys. Rev. **D80** (2009) 074028, [`0903.4481`].

[138] T. N. Truong, *Chiral Perturbation Theory and Final State Theorem*, Phys. Rev. Lett. **61** (1988) 2526.

[139] T. N. Truong, *Remarks on the unitarization methods*, Phys. Rev. Lett. **67** (1991) 2260–2263.

[140] A. Dobado and J. R. Pelaez, *A Global fit of* $\pi\pi$ *and* $\pi K$ *elastic scattering in ChPT with dispersion relations*, Phys. Rev. **D47** (1993) 4883–4888, [`hep-ph/9301276`].

[141] A. Dobado and J. R. Pelaez, *The Inverse amplitude method in chiral perturbation theory*, Phys. Rev. **D56** (1997) 3057–3073, [`hep-ph/9604416`].

[142] G. F. Chew and S. Mandelstam, *Theory of low-energy pion pion interactions*, Phys. Rev. **119** (1960) 467–477.

[143] R. M. E, *Elementary Theory of Angular Momentum.* New York: Wiley, 1957.

[144] Fayyazuddin and Riazuddin, *A Modern Introduction to Particle Physics: Third Edition.* World Scientific Pub Co Inc, 2011.

[145] H. Pilkuhn, *Relativistic Particle Physics (Theoretical and Mathematical Physics).* Springer, 1979.

[146] J. Taylor, *Scattering Theory: The Quantum Theory of Nonrelativistic Collisions.* Dover Books on Engineering. Dover Publications, 2006.

[147] D. I. Olive, *Unitarity and the evaluation of discontinuities*, Il Nuovo Cimento (1955-1965) **26** (Oct, 1962) 73–102.

[148] J. R. Taylor, *Unitarity, hermiticity and discontinuity relations*, Nuclear Physics **58** (1964) 580 – 592.

[149] Ablowitz, M.J. and Fokas, A.S. and Crighton, D.G. and Davis, S.H. and Hinch, E.J. and Iserles, A., *Complex Variables: Introduction and Applications.* Cambridge Texts in Applied Mathematics. Cambridge University Press, 2003.

[150] G. Breit and E. Wigner, *Capture of Slow Neutrons*, Phys. Rev. **49** (1936) 519–531.

[151] A. Galindo and P. Pascual, *Quantum Mechanics II (Theoretical and Mathematical Physics).* Springer, 2012.

[152] R. H. Landau, *Quantum Mechanics II: A Second Course in Quantum Theory.* Wiley-VCH, 1995.

[153] N. Kaiser, *$\pi\pi$ S wave phase shifts and nonperturbative chiral approach*, Eur. Phys. J. **A3** (1998) 307–309.

[154] M. P. Locher, V. E. Markushin and H. Q. Zheng, *Structure of $f_0(980)$ from a coupled channel analysis of S wave $\pi\pi$ scattering*, Eur. Phys. J. **C4** (1998) 317–326, [`hep-ph/9705230`].

[155] J. R. Pelaez and G. Rios, *Nature of the $f_0(600)$ from its $N_c$ dependence at two loops in unitarized Chiral Perturbation Theory*, Phys. Rev. Lett. **97** (2006) 242002, [`hep-ph/0610397`].

[156] J. A. Oller, E. Oset and A. Ramos, *Chiral unitary approach to meson meson and meson - baryon interactions and nuclear applications*, Prog. Part. Nucl. Phys. **45** (2000) 157–242, [`hep-ph/0002193`].

[157] E. E. Salpeter and H. A. Bethe, *A Relativistic equation for bound state problems*, Phys. Rev. **84** (1951) 1232–1242.

[158] Flavour Lattice Averaging Group collaboration, S. Aoki et al., *FLAG Review 2019*, `1902.08191`.

[159] S. M. Ryan, *Lattice Methods for Hadron Spectroscopy*, Lect. Notes Phys. **889** (2015) 35–67.

[160] K. G. Wilson, *Confinement of Quarks*, Phys. Rev. **D10** (1974) 2445–2459.

[161] L. Maiani and M. Testa, *Final state interactions from Euclidean correlation functions*, Phys. Lett. **B245** (1990) 585–590.

[162] M. Luscher, *Volume Dependence of the Energy Spectrum in Massive Quantum Field Theories. 1. Stable Particle States*, Commun. Math. Phys. **104** (1986) 177.

[163] M. Luscher, *Volume Dependence of the Energy Spectrum in Massive Quantum Field Theories. 2. Scattering States*, Commun. Math. Phys. **105** (1986) 153–188.

[164] M. Luscher, *Two particle states on a torus and their relation to the scattering matrix*, Nucl. Phys. **B354** (1991) 531–578.

[165] R. Gupta, *Introduction to lattice QCD: Course*, in *Probing the standard model of particle interactions. Proceedings, Summer School in Theoretical Physics, NATO Advanced Study Institute, 68th session, Les Houches, France, July 28-September 5, 1997. Pt. 1, 2*, pp. 83–219, 1997, `hep-lat/9807028`.

[166] F. Mandl and G. Shaw, *Quantum Field Theory.* Chichester, UK: Wiley (A Wiley-interscience Publication), 1985.

[167] M. Doring, U.-G. Meissner, E. Oset and A. Rusetsky, *Unitarized Chiral Perturbation Theory in a finite volume: Scalar meson sector*, Eur. Phys. J. **A47** (2011) 139, [`1107.3988`].

[168] M. Doring, J. Haidenbauer, U.-G. Meissner and A. Rusetsky, *Dynamical coupled-channel approaches on a momentum lattice*, Eur. Phys. J. **A47** (2011) 163, [`1108.0676`].

[169] M. Albaladejo, C. Hidalgo-Duque, J. Nieves and E. Oset, *Hidden charm molecules in finite volume*, Phys. Rev. **D88** (2013) 014510, [`1304.1439`].

[170] A. Pich, *Effective field theory: Course*, in *Probing the standard model of particle interactions. Proceedings, Summer School in Theoretical Physics, NATO Advanced Study Institute, 68th session, Les Houches, France, July 28-September 5, 1997. Pt. 1, 2*, pp. 949–1049, 1998, `hep-ph/9806303`.

[171] S. R. Coleman, J. Wess and B. Zumino, *Structure of phenomenological Lagrangians. 1.*, Phys. Rev. **177** (1969) 2239–2247.

[172] C. G. Callan, Jr., S. R. Coleman, J. Wess and B. Zumino, *Structure of phenomenological Lagrangians. 2.*, Phys. Rev. **177** (1969) 2247–2250.

[173] S. Weinberg, *Phenomenological Lagrangians*, Physica **A96** (1979) 327–340.

[174] S. Weinberg, *The Quantum theory of fields. Vol. 1: Foundations.* Cambridge University Press, 2005.

[175] S. Weinberg, *The quantum theory of fields. Vol. 2: Modern applications.* Cambridge University Press, 2013.

[176] J. F. Donoghue, E. Golowich and B. R. Holstein, *Dynamics of the Standard Model.* Cambridge Monographs on Particle Physics, Nuclear Physics and Cosmology. Cambridge University Press, 2 ed., 2014, 10.1017/CBO9780511803512.

[177] J. Gasser and H. Leutwyler, *On the Low-energy Structure of QCD*, Phys. Lett. **125B** (1983) 321–324.

[178] J. Gasser and H. Leutwyler, *Chiral Perturbation Theory to One Loop*, Annals Phys. **158** (1984) 142.

[179] J. Gasser and H. Leutwyler, *Chiral Perturbation Theory: Expansions in the Mass of the Strange Quark*, Nucl. Phys. **B250** (1985) 465–516.

[180] S. Scherer and M. R. Schindler, *A Primer for Chiral Perturbation Theory*, Lect. Notes Phys. **830** (2012) pp.1–338.

[181] U. G. Meissner, *Recent developments in chiral perturbation theory*, Rept. Prog. Phys. **56** (1993) 903–996, [`hep-ph/9302247`].

[182] A. Pich, *Chiral perturbation theory*, Rept. Prog. Phys. **58** (1995) 563–610, [`hep-ph/9502366`].

[183] B. Grinstein, E. E. Jenkins, A. V. Manohar, M. J. Savage and M. B. Wise, *Chiral perturbation theory for $f_{D_s}/f_D$ and $f_{B_s}/f_B$*, Nucl. Phys. **B380** (1992) 369–376, [`hep-ph/9204207`].

[184] M. B. Wise, *Chiral perturbation theory for hadrons containing a heavy quark*, Phys. Rev. **D45** (1992) R2188.

[185] M. Neubert, *Heavy quark symmetry*, Phys. Rept. **245** (1994) 259–396, [`hep-ph/9306320`].

[186] Gell-Mann, M., *The Eightfold Way: A Theory Of Strong Interaction Symmetry*, CTSL-20, TID-12608 (1961) 11–57.

[187] J. Goldstone, *Field Theories with Superconductor Solutions*, Nuovo Cim. **19** (1961) 154–164.

[188] J. Goldstone, A. Salam and S. Weinberg, *Broken Symmetries*, Phys. Rev. **127** (1962) 965–970.

[189] Y. Nambu, *Quasiparticles and Gauge Invariance in the Theory of Superconductivity*, Phys. Rev. **117** (1960) 648–663.

[190] Y. Nambu, *Axial vector current conservation in weak interactions*, Phys. Rev. Lett. **4** (1960) 380–382.

[191] T. Mannel, W. Roberts and Z. Ryzak, *A Derivation of the heavy quark effective Lagrangian from QCD*, Nucl. Phys. **B368** (1992) 204–217.

[192] J. D. Bjorken, *New symmetries in heavy flavor physics*, Conf. Proc. **C900318** (1990) 583–596.

[193] A. F. Falk, *Hadrons of arbitrary spin in the heavy quark effective theory*, Nucl. Phys. **B378** (1992) 79–94.

[194] Howard Georgi, *Weak Interactions and Modern Particle Theory (Dover Books on Physics).* Dover Publications, 2009.

[195] J. C. Ward, *An identity in quantum electrodynamics*, Phys. Rev. **78** (Apr, 1950) 182–182.

[196] Y. Takahashi, *On the generalized ward identity*, Il Nuovo Cimento (1955-1965) **6** (Aug, 1957) 371–375.

[197] S. Okubo, *Note on unitary symmetry in strong interactions*, Prog. Theor. Phys. **27** (1962) 949–966.

[198] F.-K. Guo, C. Hanhart, S. Krewald and U.-G. Meissner, *Subleading contributions to the width of the* $D^*_{s0}(2317)$, Phys. Lett. **B666** (2008) 251–255, [`0806.3374`].

[199] F.-K. Guo, C. Hanhart and U.-G. Meissner, *Interactions between heavy mesons and Goldstone bosons from chiral dynamics*, Eur. Phys. J. **A40** (2009) 171–179, [`0901.1597`].

[200] U. G. Meissner and S. Steininger, *Isospin violation in pion nucleon scattering*, Phys. Lett. **B419** (1998) 403–411, [`hep-ph/9709453`].

[201] G. Muller and U.-G. Meissner, *Virtual photons in baryon chiral perturbation theory*, Nucl. Phys. **B556** (1999) 265–291, [`hep-ph/9903375`].

[202] M. Bando, T. Kugo, S. Uehara, K. Yamawaki and T. Yanagida, *Is the* $\rho$ *Meson a Dynamical Gauge Boson of Hidden Local Symmetry?*, Phys. Rev. Lett. **54** (1985) 1215.

[203] J. A. Oller, E. Oset and J. R. Pelaez, *Nonperturbative approach to effective chiral Lagrangians and meson interactions*, Phys. Rev. Lett. **80** (1998) 3452–3455, [`hep-ph/9803242`].

[204] J. A. Oller and U. G. Meissner, *Chiral dynamics in the presence of bound states: Kaon nucleon interactions revisited*, Phys. Lett. **B500** (2001) 263–272, [`hep-ph/0011146`].

[205] L. Liu, K. Orginos, F.-K. Guo, C. Hanhart and U.-G. Meissner, *Interactions of charmed mesons with light pseudoscalar mesons from lattice QCD and implications on the nature of the* $D^*_{s0}(2317)$, Phys. Rev. **D87** (2013) 014508, [`1208.4535`].

[206] Particle Data Group collaboration, C. Patrignani et al., *Review of Particle Physics*, Chin. Phys. **C40** (2016) 100001.

[207] C. Hanhart, J. R. Pelaez and G. Rios, *Quark mass dependence of the rho and sigma from dispersion relations and Chiral Perturbation Theory*, Phys. Rev. Lett. **100** (2008) 152001, [`0801.2871`].

[208] BaBar collaboration, B. Aubert et al., *Observation of tree-level B decays with s anti-s production from gluon radiation.*, Phys. Rev. Lett. **100** (2008) 171803, [`0707.1043`].

[209] Belle collaboration, J. Wiechczynski et al., *Measurement of* $B \to D^*_s K\pi$ *branching fractions*, Phys. Rev. **D80** (2009) 052005, [`0903.4956`].

[210] O. Antipin and G. Valencia, *The Role of* $D^{**}_0$ *in* $B^- \to D^+_s K^- \pi^-$, Phys. Lett. **B647** (2007) 164–172, [`hep-ph/0611085`].

[211] C. Garcia-Recio, L. S. Geng, J. Nieves and L. L. Salcedo, *Low-lying even parity meson resonances and spin-flavor symmetry*, Phys. Rev. **D83** (2011) 016007, [`1005.0956`].

[212] D0 collaboration, V. M. Abazov et al., *Evidence for a* $B^0_s \pi^\pm$ *state*, Phys. Rev. Lett. **117** (2016) 022003, [`1602.07588`].

[213] LHCb collaboration, R. Aaij et al., *Search for Structure in the* $B^0_s \pi^\pm$ *Invariant Mass Spectrum*, Phys. Rev. Lett. **117** (2016) 152003, [`1608.00435`].

[214] C. Collaboration, *Search for the* $X(5568)$ *state in* $B^0_s \pi^+$*-decays*, CMS-PAS-BPH-16-002 (2016) 10.

[215] M. Albaladejo, J. Nieves, E. Oset, Z.-F. Sun and X. Liu, *Can* $X(5568)$ *be described as a* $B_s\pi$, $B\bar{K}$ *resonant state?*, Phys. Lett. **B757** (2016) 515–519, [`1603.09230`].

[216] F.-K. Guo, U.-G. Meißner and B.-S. Zou, *How the $X(5568)$ challenges our understanding of QCD*, Commun. Theor. Phys. **65** (2016) 593–595, [`1603.06316`].

[217] X.-W. Kang and J. A. Oller, *P-wave coupled-channel scattering of $B_s\pi$, $B_s^*\pi$, $B\overline{K}$, $B^*\overline{K}$ and the puzzling $X(5568)$*, Phys. Rev. **D94** (2016) 054010, [`1606.06665`].

[218] Z. Yang, Q. Wang and U.-G. Meißner, *Where does the X(5568) structure come from?*, Phys. Lett. **B767** (2017) 470–473, [`1609.08807`].

[219] R. Molina, H. Nagahiro, A. Hosaka and E. Oset, *Scalar, axial-vector and tensor resonances from the $\rho D^*$, $\omega D^*$ interaction in the hidden gauge formalism*, Phys. Rev. **D80** (2009) 014025, [`0903.3823`].

[220] D. Jido, J. A. Oller, E. Oset, A. Ramos and U. G. Meissner, *Chiral dynamics of the two $\Lambda(1405)$ states*, Nucl. Phys. **A725** (2003) 181–200, [`nucl-th/0303062`].

[221] C. Garcia-Recio, M. F. M. Lutz and J. Nieves, *Quark mass dependence of s wave baryon resonances*, Phys. Lett. **B582** (2004) 49–54, [`nucl-th/0305100`].

[222] V. K. Magas, E. Oset and A. Ramos, *Evidence for the two pole structure of the $\Lambda(1405)$ resonance*, Phys. Rev. Lett. **95** (2005) 052301, [`hep-ph/0503043`].

[223] L. Roca, E. Oset and J. Singh, *Low lying axial-vector mesons as dynamically generated resonances*, Phys. Rev. **D72** (2005) 014002, [`hep-ph/0503273`].

[224] L. S. Geng, E. Oset, L. Roca and J. A. Oller, *Clues for the existence of two $K_1(1270)$ resonances*, Phys. Rev. **D75** (2007) 014017, [`hep-ph/0610217`].

[225] H.-X. Chen, W. Chen, X. Liu, Y.-R. Liu and S.-L. Zhu, *A review of the open charm and open bottom systems*, Rept. Prog. Phys. **80** (2017) 076201, [`1609.08928`].

[226] R. F. Lebed, R. E. Mitchell and E. S. Swanson, *Heavy-Quark QCD Exotica*, Prog. Part. Nucl. Phys. **93** (2017) 143–194, [`1610.04528`].

[227] A. Esposito, A. Pilloni and A. D. Polosa, *Multiquark Resonances*, Phys. Rept. **668** (2016) 1–97, [`1611.07920`].

[228] F.-K. Guo, C. Hanhart, U.-G. Meißner, Q. Wang, Q. Zhao and B.-S. Zou, *Hadronic molecules*, Rev. Mod. Phys. **90** (2018) 015004, [`1705.00141`].

[229] A. Ali, J. S. Lange and S. Stone, *Exotics: Heavy Pentaquarks and Tetraquarks*, Prog. Part. Nucl. Phys. **97** (2017) 123–198, [`1706.00610`].

[230] S. L. Olsen, T. Skwarnicki and D. Zieminska, *Nonstandard heavy mesons and baryons: Experimental evidence*, Rev. Mod. Phys. **90** (2018) 015003, [`1708.04012`].

[231] R. N. Cahn and J. D. Jackson, *Spin orbit and tensor forces in heavy quark light quark mesons: Implications of the new $D_s$ state at 2.32-GeV*, Phys. Rev. **D68** (2003) 037502, [`hep-ph/0305012`].

[232] Y.-Q. Chen and X.-Q. Li, *A Comprehensive four-quark interpretation of $D_s(2317)$, $D_s(2457)$ and $D_s(2632)$*, Phys. Rev. Lett. **93** (2004) 232001, [`hep-ph/0407062`].

[233] M. A. Nowak, M. Rho and I. Zahed, *Chiral doubling of heavy light hadrons: BABAR 2317-MeV/$c^2$ and CLEO 2463-MeV/$c^2$ discoveries*, Acta Phys. Polon. **B35** (2004) 2377–2392, [`hep-ph/0307102`].

[234] T. Mehen and R. P. Springer, *Even- and odd-parity charmed meson masses in heavy hadron chiral perturbation theory*, Phys. Rev. **D72** (2005) 034006, [`hep-ph/0503134`].

[235] M. H. Alhakami, *Mass Spectra of Heavy-Light Mesons in Heavy Hadron Chiral Perturbation Theory*, Phys. Rev. **D93** (2016) 094007, [`1603.08848`].

[236] H.-Y. Cheng and F.-S. Yu, *Masses of Scalar and Axial-Vector B Mesons Revisited*, Eur. Phys. J. **C77** (2017) 668, [`1704.01208`].

[237] M.-L. Du, F.-K. Guo, U.-G. Meißner and D.-L. Yao, *Study of open-charm* $0^+$ *states in unitarized chiral effective theory with one-loop potentials*, Eur. Phys. J. **C77** (2017) 728, [`1703.10836`].

[238] D. Wilson, *Private communication*, .

[239] C. Hanhart, J. R. Pelaez and G. Rios, *Remarks on pole trajectories for resonances*, Phys. Lett. **B739** (2014) 375–382, [`1407.7452`].

[240] LHCb collaboration, R. Aaij et al., *Amplitude analysis of* $B^- \to D^+\pi^-\pi^-$ *decays*, Phys. Rev. **D94** (2016) 072001, [`1608.01289`].

[241] M. J. Savage and M. B. Wise, *SU(3) Predictions for Nonleptonic B Meson Decays*, Phys. Rev. **D39** (1989) 3346.

[242] J. A. Oller and E. Oset, *N/D description of two meson amplitudes and chiral symmetry*, Phys. Rev. **D60** (1999) 074023, [`hep-ph/9809337`].

[243] LHCb COLLABORATION collaboration, R. Aaij et al., *Dalitz plot analysis of* $B_s^0 \to \bar{D}^0 K^- \pi^+$ *decays*, Phys. Rev. **D90** (2014) 072003, [`1407.7712`].

[244] S. Weinberg, *Evidence That the Deuteron Is Not an Elementary Particle*, Phys. Rev. **137** (1965) B672–B678.

[245] A. Martínez Torres, E. Oset, S. Prelovsek and A. Ramos, *Reanalysis of lattice QCD spectra leading to the* $D_{s0}^*(2317)$ *and* $D_{s1}^*(2460)$, JHEP **05** (2015) 153, [`1412.1706`].

[246] F.-K. Guo and U.-G. Meissner, *More kaonic bound states and a comprehensive interpretation of the* $D_{sJ}$ *states*, Phys. Rev. **D84** (2011) 014013, [`1102.3536`].

[247] M. F. M. Lutz and M. Soyeur, *Radiative and isospin-violating decays of* $D_s$*-mesons in the hadrogenesis conjecture*, Nucl. Phys. **A813** (2008) 14–95, [`0710.1545`].

[248] CLEO collaboration, S. B. Athar et al., *Study of the* $q^2$ *dependence of* $B \to \pi\ell\nu$ *and* $B \to \rho(\omega)\ell\nu$ *decay and extraction of* $|V_{ub}|$, Phys. Rev. **D68** (2003) 072003, [`hep-ex/0304019`].

[249] Belle collaboration, T. Hokuue et al., *Measurements of branching fractions and* $q^2$ *distributions for* $B \to \pi\ell\nu$ *and* $B \to \rho\ell\nu$ *decays with* $B \to D^*\ell\nu$ *decay tagging*, Phys. Lett. **B648** (2007) 139–148, [`hep-ex/0604024`].

[250] BaBar collaboration, B. Aubert et al., *Measurement of the* $B^0 \to \pi^-\ell^+\nu$ *form-factor shape and branching fraction, and determination of* $|V_{ub}|$ *with a loose neutrino reconstruction technique*, Phys. Rev. Lett. **98** (2007) 091801, [`hep-ex/0612020`].

[251] BaBar collaboration, B. Aubert et al., *Measurement of the* $B \to \pi\ell\nu$ *Branching Fraction and Determination of* $|V_{ub}|$ *with Tagged B Mesons*, Phys. Rev. Lett. **97** (2006) 211801, [`hep-ex/0607089`].

[252] BELLE collaboration, L. Widhalm et al., *Measurement of $D^0 \to \pi\ell\nu(K\ell\nu)$ Form Factors and Absolute Branching Fractions*, Phys. Rev. Lett. **97** (2006) 061804, [`hep-ex/0604049`].

[253] CLEO collaboration, D. Besson et al., *Improved measurements of $D$ meson semileptonic decays to $\pi$ and $K$ mesons*, Phys. Rev. **D80** (2009) 032005, [`0906.2983`].

[254] BABAR collaboration, P. del Amo Sanchez et al., *Study of $B \to \pi\ell\nu$ and $B \to \rho\ell\nu$ Decays and Determination of $|V_{ub}|$*, Phys. Rev. **D83** (2011) 032007, [`1005.3288`].

[255] BELLE collaboration, H. Ha et al., *Measurement of the decay $B^0 \to \pi^-\ell^+\nu$ and determination of $|V_{ub}|$*, Phys. Rev. **D83** (2011) 071101, [`1012.0090`].

[256] BABAR collaboration, J. P. Lees et al., *Branching fraction and form-factor shape measurements of exclusive charmless semileptonic $B$ decays, and determination of $|V_{ub}|$*, Phys. Rev. **D86** (2012) 092004, [`1208.1253`].

[257] BABAR collaboration, J. P. Lees et al., *Measurement of the $D^0 \to \pi^- e^+ \nu_e$ differential decay branching fraction as a function of $q^2$ and study of form factor parameterizations*, Phys. Rev. **D91** (2015) 052022, [`1412.5502`].

[258] G. Duplancic, A. Khodjamirian, T. Mannel, B. Melic and N. Offen, *Light-cone sum rules for $B \to \pi$ form factors revisited*, JHEP **04** (2008) 014, [`0801.1796`].

[259] G. Duplancic and B. Melic, *$B, B_s \to K$ form factors: An Update of light-cone sum rule results*, Phys. Rev. **D78** (2008) 054015, [`0805.4170`].

[260] A. Bharucha, *Two-loop Corrections to the $B \to \pi$ Form Factor from QCD Sum Rules on the Light-Cone and $|V_{ub}|$*, JHEP **05** (2012) 092, [`1203.1359`].

[261] H. Na, C. T. H. Davies, E. Follana, G. P. Lepage and J. Shigemitsu, *The $D \to K, l\nu$ Semileptonic Decay Scalar Form Factor and $|V_{cs}|$ from Lattice QCD*, Phys. Rev. **D82** (2010) 114506, [`1008.4562`].

[262] H. Na, C. T. H. Davies, E. Follana, J. Koponen, G. P. Lepage and J. Shigemitsu, *$D \to \pi, l\nu$ Semileptonic Decays, $|V_{cd}|$ and $2^{nd}$ Row Unitarity from Lattice QCD*, Phys. Rev. **D84** (2011) 114505, [`1109.1501`].

[263] C. M. Bouchard, G. P. Lepage, C. Monahan, H. Na and J. Shigemitsu, *$B_s \to K\ell\nu$ form factors from lattice QCD*, Phys. Rev. **D90** (2014) 054506, [`1406.2279`].

[264] FERMILAB LATTICE, MILC collaboration, J. A. Bailey et al., *$|V_{ub}|$ from $B \to \pi\ell\nu$ decays and (2+1)-flavor lattice QCD*, Phys. Rev. **D92** (2015) 014024, [`1503.07839`].

[265] J. M. Flynn, T. Izubuchi, T. Kawanai, C. Lehner, A. Soni, R. S. Van de Water et al., *$B \to \pi\ell\nu$ and $B_s \to K\ell\nu$ form factors and $|V_{ub}|$ from 2+1-flavor lattice QCD with domain-wall light quarks and relativistic heavy quarks*, Phys. Rev. **D91** (2015) 074510, [`1501.05373`].

[266] ETM collaboration, V. Lubicz, L. Riggio, G. Salerno, S. Simula and C. Tarantino, *Scalar and vector form factors of $D \to \pi(K)\ell\nu$ decays with $N_f = 2 + 1 + 1$ twisted fermions*, Phys. Rev. **D96** (2017) 054514, [`1706.03017`].

[267] D. Scora and N. Isgur, *Semileptonic meson decays in the quark model: An update*, Phys. Rev. **D52** (1995) 2783–2812, [`hep-ph/9503486`].

[268] T. Becher and R. J. Hill, *Comment on form-factor shape and extraction of $|V_{ub}|$ from $B \to \pi\ell\nu$*, Phys. Lett. **B633** (2006) 61–69, [`hep-ph/0509090`].

[269] J. F. Donoghue, J. Gasser and H. Leutwyler, *The Decay of a Light Higgs Boson*, Nucl. Phys. **B343** (1990) 341–368.

[270] M. Jamin, J. A. Oller and A. Pich, *Strangeness changing scalar form-factors*, Nucl. Phys. **B622** (2002) 279–308, [`hep-ph/0110193`].

[271] M. Albaladejo and B. Moussallam, *Form factors of the isovector scalar current and the* $\eta\pi$ *scattering phase shifts*, Eur. Phys. J. **C75** (2015) 488, [`1507.04526`].

[272] J. T. Daub, C. Hanhart and B. Kubis, *A model-independent analysis of final-state interactions in* $\overline{B}^0_{d/s} \to J/\psi\pi\pi$, JHEP **02** (2016) 009, [`1508.06841`].

[273] M. Albaladejo, J. T. Daub, C. Hanhart, B. Kubis and B. Moussallam, *How to employ* $\overline{B}^0_d \to J/\psi\left(\pi\eta, \overline{K}K\right)$ *decays to extract information on* $\pi\eta$ *scattering*, JHEP **04** (2017) 010, [`1611.03502`].

[274] G. Burdman and J. Kambor, *Dispersive approach to semileptonic form-factors in heavy to light meson decays*, Phys. Rev. **D55** (1997) 2817–2826, [`hep-ph/9602353`].

[275] C. Albertus, J. M. Flynn, E. Hernandez, J. Nieves and J. M. Verde-Velasco, *Semileptonic* $B \to \pi$ *decays from an Omnes improved nonrelativistic constituent quark model*, Phys. Rev. **D72** (2005) 033002, [`hep-ph/0506048`].

[276] J. M. Flynn and J. Nieves, *Extracting* $|V_{ub}|$ *from* $B \to \pi\ell\nu$ *decays using a multiply-subtracted Omnes dispersion relation*, Phys. Rev. **D75** (2007) 013008, [`hep-ph/0607258`].

[277] U.-G. Meißner and W. Wang, $B_s \to K^{(*)}\ell\bar{\nu}$*, Angular Analysis, S-wave Contributions and* $|V_{ub}|$, JHEP **01** (2014) 107, [`1311.5420`].

[278] C. Albertus, E. Hernández, C. Hidalgo-Duque and J. Nieves, $\bar{B}_s \to K$ *semileptonic decay from an Omnès improved constituent quark model*, Phys. Lett. **B738** (2014) 144–149, [`1404.1001`].

[279] J. M. Flynn, Y. Nakagawa, J. Nieves and H. Toki, $|V_{ub}|$ *from Exclusive Semileptonic* $B \to \rho$ *Decays*, Phys. Lett. **B675** (2009) 326–331, [`0812.2795`].

[280] X.-W. Kang, B. Kubis, C. Hanhart and U.-G. Meißner, $B_{l4}$ *decays and the extraction of* $|V_{ub}|$, Phys. Rev. **D89** (2014) 053015, [`1312.1193`].

[281] C. Albertus, E. Hernández and J. Nieves, $B \to \rho$ *semileptonic decays and* $|V_{ub}|$, Phys. Rev. **D90** (2014) 013017, [`1406.7782`].

[282] P. Wang and X. G. Wang, *Study on* $0^+$ *states with open charm in unitarized heavy meson chiral approach*, Phys. Rev. **D86** (2012) 014030, [`1204.5553`].

[283] D.-L. Yao, M.-L. Du, F.-K. Guo and U.-G. Meißner, *One-loop analysis of the interactions between charmed mesons and Goldstone bosons*, JHEP **11** (2015) 058, [`1502.05981`].

[284] Z.-H. Guo, U.-G. Meißner and D.-L. Yao, *New insights into the* $D^*_{s0}(2317)$ *and other charm scalar mesons*, Phys. Rev. **D92** (2015) 094008, [`1507.03123`].

[285] X.-Y. Guo, Y. Heo and M. F. M. Lutz, *On chiral extrapolations of charmed meson masses and coupled-channel reaction dynamics*, Phys. Rev. **D98** (2018) 014510, [`1801.10122`].

[286] L. Liu, H.-W. Lin and K. Orginos, *Charmed Hadron Interactions*, PoS **LATTICE2008** (2008) 112, [`0810.5412`].

[287] D. Mohler, S. Prelovsek and R. M. Woloshyn, *$D\pi$ scattering and $D$ meson resonances from lattice QCD*, Phys. Rev. **D87** (2013) 034501, [`1208.4059`].

[288] G. Burdman and J. F. Donoghue, *Union of chiral and heavy quark symmetries*, Phys. Lett. **B280** (1992) 287–291.

[289] H.-n. Li, Y.-L. Shen and Y.-M. Wang, *Next-to-leading-order corrections to $B \to \pi$ form factors in $k_T$ factorization*, Phys. Rev. **D85** (2012) 074004, [`1201.5066`].

[290] W.-F. Wang and Z.-J. Xiao, *The semileptonic decays $B/B_s \to (\pi, K)(\ell^+\ell^-, \ell\nu, \nu\bar{\nu})$ in the perturbative QCD approach beyond the leading-order*, Phys. Rev. **D86** (2012) 114025, [`1207.0265`].

[291] J. Gasser and H. Leutwyler, *Low-Energy Expansion of Meson Form-Factors*, Nucl. Phys. **B250** (1985) 517–538.

[292] R. Omnes, *On the Solution of certain singular integral equations of quantum field theory*, Nuovo Cim. **8** (1958) 316–326.

[293] K. M. Watson, *Some general relations between the photoproduction and scattering of $\pi$ mesons*, Phys. Rev. **95** (1954) 228–236.

[294] B. Moussallam, *$N_f$ dependence of the quark condensate from a chiral sum rule*, Eur. Phys. J. **C14** (2000) 111–122, [`hep-ph/9909292`].

[295] N. Muskhelishvili, *Singular integral equations. Boundary problems of function theory and their application to mathematical physics.* Wolters-Noordhoff Publishing, 1958.

[296] S. Waldenstrom, *S-Matrix and Unitarity Bounds for Three Channel Systems, with Application to Low-Energy Photoproduction of Pions from Nucleons*, Nucl. Phys. **B77** (1974) 479–493.

[297] L. Lesniak, *Meson spectroscopy and separable potentials*, Acta Phys. Polon. **B27** (1996) 1835–1847.

[298] G. P. Lepage and S. J. Brodsky, *Exclusive Processes in Perturbative Quantum Chromodynamics*, Phys. Rev. **D22** (1980) 2157.

[299] T.-M. Yan, H.-Y. Cheng, C.-Y. Cheung, G.-L. Lin, Y. C. Lin and H.-L. Yu, *Heavy quark symmetry and chiral dynamics*, Phys. Rev. **D46** (1992) 1148–1164.

[300] H. Ohki, H. Matsufuru and T. Onogi, *Determination of $B^*B\pi$ coupling in unquenched QCD*, Phys. Rev. **D77** (2008) 094509, [`0802.1563`].

[301] P. Colangelo and F. De Fazio, *On Three body $B^0 \to D^{*-}D^{(*)0}K^+$ decays and couplings of heavy mesons to light pseudoscalar mesons*, Phys. Lett. **B532** (2002) 193–201, [`hep-ph/0201305`].

[302] F. de Soto and C. Roiesnel, *On the reduction of hypercubic lattice artifacts*, JHEP **09** (2007) 007, [`0705.3523`].

[303] B. Yoon, Y.-C. Jang, C. Jung and W. Lee, *Covariance fitting of highly correlated data in lattice QCD*, J. Korean Phys. Soc. **63** (2013) 145–162, [`1101.2248`].

[304] Fermilab Lattice, MILC collaboration, J. A. Bailey et al., *Semileptonic decays of K and D mesons in 2+1 flavor QCD*, PoS **LATTICE2010** (2010) 306, [`1011.2423`].

[305] T. Bhattacharya, S. Chandrasekharan, R. Gupta, W.-J. Lee and S. R. Sharpe, *Nonperturbative renormalization constants using Ward identities*, Phys. Lett. **B461** (1999) 79–88, [`hep-lat/9904011`].

[306] MILC collaboration, C. Bernard, S. Datta, T. A. DeGrand, C. E. DeTar, S. A. Gottlieb, U. M. Heller et al., *Lattice calculation of heavy light decay constants with two flavors of dynamical quarks*, Phys. Rev. **D66** (2002) 094501, [`hep-lat/0206016`].

[307] D.-L. Yao, M. Albaladejo, P. Fernández-Soler, F.-K. Guo and J. Nieves, *Scalar form factors of semi-leptonic $D \to \pi/\bar{K}$ transitions with coupled-channel effects*, PoS **Hadron2017** (2018) 089, [`1711.11515`].

[308] HFLAV collaboration, Y. Amhis et al., *Averages of b-hadron, c-hadron, and $\tau$-lepton properties as of summer 2016*, Eur. Phys. J. **C77** (2017) 895, [`1612.07233`].

[309] P. Ball, *$|V_{ub}|$ from UTangles and $B \to \pi\ell\nu$*, Phys. Lett. **B644** (2007) 38–44, [`hep-ph/0611108`].

[310] C. Bourrely, I. Caprini and L. Lellouch, *Model-independent description of $B \to \pi l \nu$ decays and a determination of $|V_{ub}|$*, Phys. Rev. **D79** (2009) 013008, [`0807.2722`].

[311] D. Becirevic and A. B. Kaidalov, *Comment on the heavy → light form-factors*, Phys. Lett. **B478** (2000) 417–423, [`hep-ph/9904490`].

[312] C. G. Boyd and M. J. Savage, *Analyticity, shapes of semileptonic form-factors, and $\bar{B} \to \pi\ell\bar{\nu}$*, Phys. Rev. **D56** (1997) 303–311, [`hep-ph/9702300`].

[313] M.-L. Du, F.-K. Guo, U.-G. Meißner and D.-L. Yao, *Aspects of the low-energy constants in the chiral Lagrangian for charmed mesons*, Phys. Rev. **D94** (2016) 094037, [`1610.02963`].

[314] C. G. Boyd, B. Grinstein and R. F. Lebed, *Precision corrections to dispersive bounds on form-factors*, Phys. Rev. **D56** (1997) 6895–6911, [`hep-ph/9705252`].

[315] I. Caprini, L. Lellouch and M. Neubert, *Dispersive bounds on the shape of $\bar{B} \to D^{(*)}$ lepton anti-neutrino form-factors*, Nucl. Phys. **B530** (1998) 153–181, [`hep-ph/9712417`].

[316] A. Alberti, P. Gambino, K. J. Healey and S. Nandi, *Precision Determination of the Cabibbo-Kobayashi-Maskawa Element $V_{cb}$*, Phys. Rev. Lett. **114** (2015) 061802, [`1411.6560`].

[317] S. Descotes-Genon and P. Koppenburg, *The CKM Parameters*, Ann. Rev. Nucl. Part. Sci. **67** (2017) 97–127, [`1702.08834`].

[318] G. Ricciardi, *Selected updates on semileptonic B decays and $|V_{xb}|$ determination*, in *13th Conference on Quark Confinement and the Hadron Spectrum (Confinement XIII) Maynooth, Ireland, July 31-August 6, 2018*, 2018, `1812.00065`.

[319] Belle collaboration, R. Glattauer et al., *Measurement of the decay $B \to D\ell\nu_\ell$ in fully reconstructed events and determination of the Cabibbo-Kobayashi-Maskawa matrix element $|V_{cb}|$*, Phys. Rev. **D93** (2016) 032006, [`1510.03657`].

[320] Belle collaboration, A. Abdesselam et al., *Measurement of CKM Matrix Element $|V_{cb}|$ from $\bar{B} \to D^{*+}\ell^-\bar{\nu}_\ell$*, `1809.03290`.

[321] HPQCD collaboration, H. Na, C. M. Bouchard, G. P. Lepage, C. Monahan and J. Shigemitsu, *$B \to Dl\nu$ form factors at nonzero recoil and extraction of $|V_{cb}|$*, Phys. Rev. **D92** (2015) 054510, [`1505.03925`].

[322] MILC collaboration, J. A. Bailey et al., *$B \to D\ell\nu$ form factors at nonzero recoil and $|V_{cb}|$ from 2+1-flavor lattice QCD*, Phys. Rev. **D92** (2015) 034506, [`1503.07237`].

[323] D. Bigi and P. Gambino, *Revisiting $B \to D\ell\nu$*, Phys. Rev. **D94** (2016) 094008, [`1606.08030`].

[324] S. Jaiswal, S. Nandi and S. K. Patra, *Extraction of $|V_{cb}|$ from $B \to D^{(*)}\ell\nu_\ell$ and the Standard Model predictions of $R(D^{(*)})$*, JHEP **12** (2017) 060, [`1707.09977`].

[325] D. Bigi, P. Gambino and S. Schacht, *A fresh look at the determination of $|V_{cb}|$ from $B \to D^*\ell\nu$*, Phys. Lett. **B769** (2017) 441–445, [`1703.06124`].

[326] B. Grinstein and A. Kobach, *Model-Independent Extraction of $|V_{cb}|$ from $\bar{B} \to D^*\ell\bar{\nu}$*, Phys. Lett. **B771** (2017) 359–364, [`1703.08170`].

[327] S. Sakai, L. Roca and E. Oset, *Charm-beauty meson bound states from $B(B^*)D(D^*)$ and $B(B^*)\bar{D}(\bar{D}^*)$ interaction*, Phys. Rev. **D96** (2017) 054023, [`1704.02196`].

[328] CMS collaboration, A. M. Sirunyan et al., *Observation of Two Excited $B_c^+$ States and Measurement of the $B_c^+$(2S) Mass in pp Collisions at $\sqrt{s} = 13$ TeV*, Phys. Rev. Lett. **122** (2019) 132001, [`1902.00571`].

[329] LHCb collaboration, R. Aaij et al., *Observation of an excited $B_c^+$ state*, `1904.00081`.

[330] N. Mathur, M. Padmanath and S. Mondal, *Precise predictions of charmed-bottom hadrons from lattice QCD*, Phys. Rev. Lett. **121** (2018) 202002, [`1806.04151`].

[331] J. G. Korner and G. A. Schuler, *Exclusive Semileptonic Heavy Meson Decays Including Lepton Mass Effects*, Z. Phys. **C46** (1990) 93.

[332] A. Sirlin, *Large $m(W)$, $m(Z)$ Behavior of the $O(\alpha)$ Corrections to Semileptonic Processes Mediated by $W$*, Nucl. Phys. **B196** (1982) 83–92.

[333] G. P. Lepage and S. J. Brodsky, *Exclusive Processes in Quantum Chromodynamics: Evolution Equations for Hadronic Wave Functions and the Form-Factors of Mesons*, Phys. Lett. **87B** (1979) 359–365.

[334] S. J. Brodsky and G. P. Lepage, *Large Angle Two Photon Exclusive Channels in Quantum Chromodynamics*, Phys. Rev. **D24** (1981) 1808.

[335] K. M. Watson, *The Effect of final state interactions on reaction cross-sections*, Phys. Rev. **88** (1952) 1163–1171.

[336] BaBar collaboration, B. Aubert et al., *Measurement of $|V_{cb}|$ and the Form-Factor Slope in $\bar{B} \to D\ell\bar{nu}_\ell$ Decays in Events Tagged by a Fully Reconstructed B Meson*, Phys. Rev. Lett. **104** (2010) 011802, [`0904.4063`].

[337] BaBar collaboration, J. P. Lees et al., *Evidence for an excess of $\bar{B} \to D^{(*)}\tau^-\bar{\nu}_\tau$ decays*, Phys. Rev. Lett. **109** (2012) 101802, [`1205.5442`].

[338] Belle collaboration, M. Huschle et al., *Measurement of the branching ratio of $\bar{B} \to D^{(*)}\tau^-\bar{\nu}_\tau$ relative to $\bar{B} \to D^{(*)}\ell^-\bar{\nu}_\ell$ decays with hadronic tagging at Belle*, Phys. Rev. **D92** (2015) 072014, [`1507.03233`].

[339] M. Neubert, *Short distance expansion of heavy quark currents*, Phys. Rev. **D46** (1992) 2212–2227.

[340] M. Neubert, *Renormalization of heavy quark currents*, Nucl. Phys. **B371** (1992) 149–176.

[341] E. Cincioglu, J. Nieves, A. Ozpineci and A. U. Yilmazer, *Quarkonium Contribution to Meson Molecules*, Eur. Phys. J. **C76** (2016) 576, [`1606.03239`].

[342] P. G. Ortega, J. Segovia, D. R. Entem and F. Fernandez, *Molecular components in P-wave charmed-strange mesons*, Phys. Rev. **D94** (2016) 074037, [`1603.07000`].

[343] J. Vijande, F. Fernandez and A. Valcarce, *Constituent quark model study of the meson spectra*, J. Phys. **G31** (2005) 481, [`hep-ph/0411299`].

[344] A. Valcarce, H. Garcilazo, F. Fernandez and P. Gonzalez, *Quark-model study of few-baryon systems*, Rept. Prog. Phys. **68** (2005) 965–1042, [`hep-ph/0502173`].

[345] J. Segovia, D. R. Entem, F. Fernandez and E. Hernandez, *Constituent quark model description of charmonium phenomenology*, Int. J. Mod. Phys. **E22** (2013) 1330026, [`1309.6926`].

[346] A. Le Yaouanc, L. Oliver, O. Pene and J. Raynal, *Naive quark pair creation model of strong interaction vertices*, Phys. Rev. **D8** (1973) 2223–2234.

[347] D. Gamermann, J. Nieves, E. Oset and E. Ruiz Arriola, *Couplings in coupled channels versus wave functions: application to the $X(3872)$ resonance*, Phys. Rev. **D81** (2010) 014029, [`0911.4407`].

[348] BaBar collaboration, J. P. Lees et al., *Dalitz plot analyses of $b^0 \to d^- d^0 k^+$ and $b^+ \to \bar{D}^0 d^0 k^+$ decays*, Phys. Rev. **D91** (2015) 052002, [`1412.6751`].

[349] A. Bramon, A. Grau and G. Pancheri, *Intermediate vector meson contributions to $V_0 \to P_0 P_0 \gamma$ decays*, Phys. Lett. **B283** (1992) 416–420.

[350] F. Ambrosino et al., *A Global fit to determine the pseudoscalar mixing angle and the gluonium content of the $\eta'$ meson*, JHEP **07** (2009) 105, [`0906.3819`].

[351] Z.-H. Guo and J. A. Oller, *Resonances from meson-meson scattering in U(3) CHPT*, Phys. Rev. **D84** (2011) 034005, [`1104.2849`].

[352] D. Ebert, V. O. Galkin and R. N. Faustov, *Mass spectrum of orbitally and radially excited heavy - light mesons in the relativistic quark model*, Phys. Rev. **D57** (1998) 5663–5669, [`hep-ph/9712318`].

[353] T. A. Lahde, C. J. Nyfalt and D. O. Riska, *Spectra and M1 decay widths of heavy light mesons*, Nucl. Phys. **A674** (2000) 141–167, [`hep-ph/9908485`].

[354] S. N. Gupta and J. M. Johnson, *Quantum chromodynamic potential model for light heavy quarkonia and the heavy quark effective theory*, Phys. Rev. **D51** (1995) 168–175, [`hep-ph/9409432`].

[355] M. Cleven, H. W. Grießhammer, F.-K. Guo, C. Hanhart and U.-G. Meißner, *Strong and radiative decays of the $D_{s0}^*(2317)$ and $D_{s1}(2460)$*, Eur. Phys. J. **A50** (2014) 149, [`1405.2242`].

[356] J. Segovia, C. Albertus, E. Hernandez, F. Fernandez and D. R. Entem, *Nonleptonic $B \to D^{(*)} D_{sJ}^{(*)}$ decays and the nature of the orbitally excited charmed-strange mesons*, Phys. Rev. **D86** (2012) 014010, [`1203.4362`].

[357] S. Weinberg, *Elementary particle theory of composite particles*, Phys. Rev. **130** (1963) 776–783.

[358] V. Baru, J. Haidenbauer, C. Hanhart, Yu. Kalashnikova and A. E. Kudryavtsev, *Evidence that the $a_0(980)$ and $f_0(980)$ are not elementary particles*, Phys. Lett. **B586** (2004) 53–61, [`hep-ph/0308129`].

[359] F. Aceti, L. R. Dai, L. S. Geng, E. Oset and Y. Zhang, *Meson-baryon components in the states of the baryon decuplet*, Eur. Phys. J. **A50** (2014) 57, [`1301.2554`].

[360] T. Hyodo, *Structure and compositeness of hadron resonances*, Int. J. Mod. Phys. **A28** (2013) 1330045, [`1310.1176`].

[361] T. Hyodo, D. Jido and A. Hosaka, *Origin of the resonances in the chiral unitary approach*, Phys. Rev. **C78** (2008) 025203, [`0803.2550`].

[362] Z.-H. Guo and J. A. Oller, *Probabilistic interpretation of compositeness relation for resonances*, Phys. Rev. **D93** (2016) 096001, [`1508.06400`].

[363] J. A. Oller, *New results from a number operator interpretation of the compositeness of bound and resonant states*, Annals Phys. **396** (2018) 429–458, [`1710.00991`].

[364] L. Castillejo, R. H. Dalitz and F. J. Dyson, *Low's scattering equation for the charged and neutral scalar theories*, Phys. Rev. **101** (1956) 453–458.

[365] P. G. Ortega, J. Segovia, D. R. Entem and F. Fernández, *Threshold effects in P-wave bottom-strange mesons*, Phys. Rev. **D95** (2017) 034010, [`1612.04826`].

[366] T. Hyodo, S. I. Nam, D. Jido and A. Hosaka, *Flavor SU(3) breaking effects in the chiral unitary model for meson baryon scatterings*, Phys. Rev. **C68** (2003) 018201, [`nucl-th/0212026`].

[367] C. Garcia-Recio, J. Nieves and L. L. Salcedo, *SU(6) extension of the Weinberg-Tomozawa meson-baryon Lagrangian*, Phys. Rev. **D74** (2006) 034025, [`hep-ph/0505233`].

[368] R. Molina, D. Nicmorus and E. Oset, *The $\rho\rho$ interaction in the hidden gauge formalism and the $f_0(1370)$ and $f_2(1270)$ resonances*, Phys. Rev. **D78** (2008) 114018, [`0809.2233`].

[369] L. S. Geng and E. Oset, *Vector meson-vector meson interaction in a hidden gauge unitary approach*, Phys. Rev. **D79** (2009) 074009, [`0812.1199`].

[370] P. Gonzalez, E. Oset and J. Vijande, *An Explanation of the $\Delta_{5/2^-}(1930)$ as a $\rho\Delta$ bound state*, Phys. Rev. **C79** (2009) 025209, [`0812.3368`].

[371] S. Sarkar, B.-X. Sun, E. Oset and M. J. Vicente Vacas, *Dynamically generated resonances from the vector octet-baryon decuplet interaction*, Eur. Phys. J. **A44** (2010) 431–443, [`0902.3150`].

[372] E. Oset and A. Ramos, *Dynamically generated resonances from the vector octet-baryon octet interaction*, Eur. Phys. J. **A44** (2010) 445–454, [`0905.0973`].

[373] W. H. Liang and E. Oset, *$B^0$ and $B_s^0$ decays into $J/\psi\ f_0(980)$ and $J/\psi\ f_0(500)$ and the nature of the scalar resonances*, Phys. Lett. **B737** (2014) 70–74, [`1406.7228`].

[374] M. Bayar, W. H. Liang and E. Oset, *$B^0$ and $B_s^0$ decays into $J/\psi$ plus a scalar or vector meson*, Phys. Rev. **D90** (2014) 114004, [`1408.6920`].

[375] J.-J. Xie and E. Oset, *$\bar{B}^0$ and $\bar{B}_s^0$ decays into $J/\psi$ and $f_0(1370)$, $f_0(1710)$, $f_2(1270)$, $f_2'(1525)$, $K_2^*(1430)$*, Phys. Rev. **D90** (2014) 094006, [`1409.1341`].

[376] W. H. Liang, J.-J. Xie and E. Oset, *$\bar{B}^0$ decay into $D^0$ and $f_0(500)$, $f_0(980)$, $a_0(980)$, $\rho$ and $\bar{B}_s^0$ decay into $D^0$ and $\kappa(800)$, $K^{*0}$*, Phys. Rev. **D92** (2015) 034008, [`1501.00088`].

[377] M. Albaladejo, M. Nielsen and E. Oset, *$D_{s0}^{*\pm}(2317)$ and $KD$ scattering from $B_s^0$ decay*, Phys. Lett. **B746** (2015) 305–310, [`1501.03455`].

[378] L.-L. Chau, *Quark Mixing in Weak Interactions*, Phys. Rept. **95** (1983) 1–94.

[379] H.-Y. Cheng and C.-W. Chiang, *Hadronic D decays involving even-parity light mesons*, Phys. Rev. **D81** (2010) 074031, [`1002.2466`].

[380] T. Sekihara and E. Oset, *Investigating the nature of light scalar mesons with semileptonic decays of D mesons*, Phys. Rev. **D92** (2015) 054038, [`1507.02026`].

[381] W.-H. Liang, J.-J. Xie, E. Oset, R. Molina and M. Döring, *Predictions for the $\bar{B}^0 \to \bar{K}^{*0}X(YZ)$ and $\bar{B}_s^0 \to \phi X(YZ)$ with $X(4160), Y(3940), Z(3930)$*, Eur. Phys. J. **A51** (2015) 58, [`1502.02932`].

[382] LHCb collaboration, R. Aaij et al., *Observation of $B_c^+ \to J/\psi D^{(*)}K^{(*)}$ decays*, Phys. Rev. **D95** (2017) 032005, [`1612.07421`].

[383] Particle Data Group collaboration, K. A. Olive et al., *Review of Particle Physics*, Chin. Phys. **C38** (2014) 090001.

[384] S. Prelovsek, C. B. Lang, L. Leskovec and D. Mohler, *Study of the $Z_c^+$ channel using lattice QCD*, Phys. Rev. **D91** (2015) 014504, [`1405.7623`].

[385] M. Albaladejo, F.-K. Guo, C. Hidalgo-Duque and J. Nieves, *$Z_c(3900)$: What has been really seen?*, Phys. Lett. **B755** (2016) 337–342, [`1512.03638`].

[386] Z. Fodor and C. Hoelbling, *Light Hadron Masses from Lattice QCD*, Rev. Mod. Phys. **84** (2012) 449, [`1203.4789`].

[387] J. J. Dudek, R. G. Edwards, N. Mathur and D. G. Richards, *Charmonium excited state spectrum in lattice QCD*, Phys. Rev. **D77** (2008) 034501, [`0707.4162`].

[388] G. S. Bali, S. Collins and C. Ehmann, *Charmonium spectroscopy and mixing with light quark and open charm states from $n_F = 2$ lattice QCD*, Phys. Rev. **D84** (2011) 094506, [`1110.2381`].

[389] Hadron Spectrum collaboration, L. Liu, G. Moir, M. Peardon, S. M. Ryan, C. E. Thomas, P. Vilaseca et al., *Excited and exotic charmonium spectroscopy from lattice QCD*, JHEP **07** (2012) 126, [`1204.5425`].

[390] C. B. Lang, L. Leskovec, D. Mohler and S. Prelovsek, *Vector and scalar charmonium resonances with lattice QCD*, JHEP **09** (2015) 089, [`1503.05363`].

[391] S. Prelovsek and L. Leskovec, *Search for $Z_c^+(3900)$ in the $1^{+-}$ Channel on the Lattice*, Phys. Lett. **B727** (2013) 172–176, [`1308.2097`].

[392] Y. Chen et al., *Low-energy scattering of the* $(D\bar{D}^*)^{\pm}$ *system and the resonance-like structure* $Z_c(3900)$, Phys. Rev. **D89** (2014) 094506, [`1403.1318`].

[393] L. Liu et al., *Search for* $Z_c(3900)$ *on the lattice with twisted mass fermions*, PoS **LATTICE2014** (2014) 117.

[394] Fermilab Lattice, MILC collaboration, S.-h. Lee, C. DeTar, H. Na and D. Mohler, *Searching for the* $X(3872)$ *and* $Z_c^+(3900)$ *on HISQ Lattices*, `1411.1389`.

[395] HAL QCD collaboration, Y. Ikeda, S. Aoki, T. Doi, S. Gongyo, T. Hatsuda, T. Inoue et al., *Fate of the Tetraquark Candidate* $Z_c(3900)$ *from Lattice QCD*, Phys. Rev. Lett. **117** (2016) 242001, [`1602.03465`].

[396] E. J. Garzon, R. Molina, A. Hosaka and E. Oset, *Strategies for an accurate determination of the* $X(3872)$ *energy from QCD lattice simulations*, Phys. Rev. **D89** (2014) 014504, [`1310.0972`].

[397] J. Nieves and M. P. Valderrama, *The Heavy Quark Spin Symmetry Partners of the* $X(3872)$, Phys. Rev. **D86** (2012) 056004, [`1204.2790`].

[398] C. Hidalgo-Duque, J. Nieves and M. P. Valderrama, *Light flavor and heavy quark spin symmetry in heavy meson molecules*, Phys. Rev. **D87** (2013) 076006, [`1210.5431`].

[399] M. Albaladejo, F. K. Guo, C. Hidalgo-Duque, J. Nieves and M. P. Valderrama, *Decay widths of the spin-2 partners of the X(3872)*, Eur. Phys. J. **C75** (2015) 547, [`1504.00861`].

[400] D. J. Wilson, J. J. Dudek, R. G. Edwards and C. E. Thomas, *Resonances in coupled* $\pi K, \eta K$ *scattering from lattice QCD*, Phys. Rev. **D91** (2015) 054008, [`1411.2004`].

[401] Hadron Spectrum collaboration, J. J. Dudek, R. G. Edwards and D. J. Wilson, *An* $a_0$ *resonance in strongly coupled* $\pi\eta$, $K\overline{K}$ *scattering from lattice QCD*, Phys. Rev. **D93** (2016) 094506, [`1602.05122`].

[402] J. Nebreda and J. R. Pelaez., *Strange and non-strange quark mass dependence of elastic light resonances from SU(3) Unitarized Chiral Perturbation Theory to one loop*, Phys. Rev. **D81** (2010) 054035, [`1001.5237`].

[403] K. Rummukainen and S. A. Gottlieb, *Resonance scattering phase shifts on a nonrest frame lattice*, Nucl. Phys. **B450** (1995) 397–436, [`hep-lat/9503028`].

[404] C. h. Kim, C. T. Sachrajda and S. R. Sharpe, *Finite-volume effects for two-hadron states in moving frames*, Nucl. Phys. **B727** (2005) 218–243, [`hep-lat/0507006`].

[405] Z. Fu, *Rummukainen-Gottlieb's formula on two-particle system with different mass*, Phys. Rev. **D85** (2012) 014506, [`1110.0319`].

[406] L. Leskovec and S. Prelovsek, *Scattering phase shifts for two particles of different mass and non-zero total momentum in lattice QCD*, Phys. Rev. **D85** (2012) 114507, [`1202.2145`].

[407] S. Prelovsek, L. Leskovec, C. B. Lang and D. Mohler, $K\,\pi$ *scattering and the* $K^*$ *decay width from lattice QCD*, Phys. Rev. **D88** (2013) 054508, [`1307.0736`].

[408] M. Doring, U. G. Meissner, E. Oset and A. Rusetsky, *Scalar mesons moving in a finite volume and the role of partial wave mixing*, Eur. Phys. J. **A48** (2012) 114, [`1205.4838`].

[409] G. Ecker, *Chiral perturbation theory*, Prog. Part. Nucl. Phys. **35** (1995) 1–80, [`hep-ph/9501357`].

[410] V. Bernard, N. Kaiser and U.-G. Meissner, *Chiral dynamics in nucleons and nuclei*, Int. J. Mod. Phys. **E4** (1995) 193–346, [`hep-ph/9501384`].

[411] M. Bando, T. Kugo and K. Yamawaki, *Nonlinear Realization and Hidden Local Symmetries*, Phys. Rept. **164** (1988) 217–314.

[412] U. G. Meissner, *Low-Energy Hadron Physics from Effective Chiral Lagrangians with Vector Mesons*, Phys. Rept. **161** (1988) 213.

[413] D. Gamermann, C. Garcia-Recio, J. Nieves and L. L. Salcedo, *Odd Parity Light Baryon Resonances*, Phys. Rev. **D84** (2011) 056017, [`1104.2737`].

[414] Y. Ikeda, T. Hyodo and W. Weise, *Chiral SU(3) theory of antikaon-nucleon interactions with improved threshold constraints*, Nucl. Phys. **A881** (2012) 98–114, [`1201.6549`].

[415] B. Borasoy, R. Nissler and W. Weise, *Chiral dynamics of kaon-nucleon interactions, revisited*, Eur. Phys. J. **A25** (2005) 79–96, [`hep-ph/0505239`].

[416] J. A. Oller, J. Prades and M. Verbeni, *Surprises in threshold antikaon-nucleon physics*, Phys. Rev. Lett. **95** (2005) 172502, [`hep-ph/0508081`].

[417] B. Borasoy, U. G. Meissner and R. Nissler, *$K^-p$ scattering length from scattering experiments*, Phys. Rev. **C74** (2006) 055201, [`hep-ph/0606108`].

[418] BaBar collaboration, P. del Amo Sanchez et al., *Observation of new resonances decaying to $D\pi$ and $D^*\pi$ in inclusive $e^+e^-$ collisions near $\sqrt{s}$ =10.58 GeV*, Phys. Rev. **D82** (2010) 111101, [`1009.2076`].

[419] M. C. Birse, *Effective chiral Lagrangians for spin 1 mesons*, Z. Phys. **A355** (1996) 231–246, [`hep-ph/9603251`].

[420] A. Ramos and E. Oset, *The role of vector-baryon channels and resonances in the $\gamma p \to K^0\Sigma^+$ and $\gamma n \to K^0\Sigma^0$ reactions near the $K^*\Lambda$ threshold*, Phys. Lett. **B727** (2013) 287–292, [`1304.7975`].

[421] H. Nagahiro, J. Yamagata-Sekihara, E. Oset, S. Hirenzaki and R. Molina, *The $\gamma\gamma$ decay of the $f_0(1370)$ and $f_2(1270)$ resonances in the hidden gauge formalism*, Phys. Rev. **D79** (2009) 114023, [`0809.3717`].

[422] W. H. Liang, C. W. Xiao and E. Oset, *Baryon states with open beauty in the extended local hidden gauge approach*, Phys. Rev. **D89** (2014) 054023, [`1401.1441`].

[423] R. Casalbuoni, A. Deandrea, N. Di Bartolomeo, R. Gatto, F. Feruglio and G. Nardulli, *Phenomenology of heavy meson chiral Lagrangians*, Phys. Rept. **281** (1997) 145–238, [`hep-ph/9605342`].

[424] J. M. Flynn, P. Fritzsch, T. Kawanai, C. Lehner, C. T. Sachrajda, B. Samways et al., *The $B^*B\pi$ coupling with relativistic heavy quarks*, PoS **LATTICE2013** (2014) 408, [`1311.2251`].

[425] C. W. Xiao, J. Nieves and E. Oset, *Combining heavy quark spin and local hidden gauge symmetries in the dynamical generation of hidden charm baryons*, Phys. Rev. **D88** (2013) 056012, [`1304.5368`].

[426] A. Ozpineci, C. W. Xiao and E. Oset, *Hidden beauty molecules within the local hidden gauge approach and heavy quark spin symmetry*, Phys. Rev. **D88** (2013) 034018, [`1306.3154`].

[427] F. S. Navarra, M. Nielsen and M. E. Bracco, *$D^*D\pi$ form-factor revisited*, Phys. Rev. **D65** (2002) 037502, [`hep-ph/0109188`].

[428] LHCb collaboration, R. Aaij et al., *Precise measurements of the properties of the $B_1(5721)^{0,+}$ and $B_2^*(5747)^{0,+}$ states and observation of $B^{+,0}\pi^{-,+}$ mass structures*, JHEP **04** (2015) 024, [`1502.02638`].

[429] CDF collaboration, T. A. Aaltonen et al., *Study of Orbitally Excited $B$ Mesons and Evidence for a New $B\pi$ Resonance*, Phys. Rev. **D90** (2014) 012013, [`1309.5961`].

[430] E. Oset, A. Ramos and C. Bennhold, *Low lying $S = -1$ excited baryons and chiral symmetry*, Phys. Lett. **B527** (2002) 99–105, [`nucl-th/0109006`].

[431] J. A. Oller, E. Oset and J. R. Pelaez, *Meson meson interaction in a nonperturbative chiral approach*, Phys. Rev. **D59** (1999) 074001, [`hep-ph/9804209`].

[432] F.-K. Guo, R.-G. Ping, P.-N. Shen, H.-C. Chiang and B.-S. Zou, *$S$ wave $K\pi$ scattering and effects of $\kappa$ in $J/\psi \to \bar{K}^{*0}(892)K^+\pi^-$*, Nucl. Phys. **A773** (2006) 78–94, [`hep-ph/0509050`].

# GLOSSARY

**$\chi$PT** Chiral Perturbation Theory. xxi, 13, 14, 29, 40, 76

**$\chi$Sym** Chiral Symmetry. xvii, xviii, xx, 6, 40, 42–44, 51

**2PI** two-particle irreducible. 29–32, 36, 39

**BGL** Boyd-Grinstein-Lebed. 127, 130, 131

**BSE** Bethe-Salpeter Equation. 29, 32, 136, 140, 163, 165, 175, 182, 184, 193, 201, 202, 208

**BW** Breit Wigner. 76, 80, 81, 189

**CKM** Cabibbo–Kobayashi–Makawa. xix, 73, 91–94, 108, 111, 116, 118–120, 122, 124, 127, 130, 212

**CLN** Caprini-Lellouch-Neubert. 127, 130, 132, 133

**cm** center of momentum or zero momentum. 17–19, 23, 33, 36, 37, 63, 80, 82

**CQM** Constituent Quark Model. xvii, xviii, xx, 1–4, 6, 7, 13, 14, 49, 59, 135–143, 145, 146, 148–154, 156, 159, 161–164, 168–171, 212

**EFT** Effective Field Theory. xvii, xviii, 7, 13, 57, 75, 154, 165, 170

**FLAG** Flavour Lattice Averaging Group. 91, 120

**FRS** first Riemann sheet. 142, 149, 165, 169, 171

**HM$\chi$PT** Heavy Meson Chiral Perturbation Theory. 54, 63, 64, 71, 77, 116, 121, 124, 136, 137, 140, 142, 143, 150, 151, 153, 154, 159, 161–163, 169, 170, 175, 198, 212

**HQET** Heavy Quark Effective Theory. 132

**HQFS** Heavy Quark Flavour Symmetry. xvii, xviii, xx, 4, 45, 46, 48, 58, 59, 70, 92–94, 104, 115, 135

**HQSS** Heavy Quark Spin Symmetry. xvii, xviii, xx, xxi, 4, 6, 7, 45, 48–51, 57–59, 72, 135, 138, 140, 146, 149, 151–154, 161, 163–165, 170, 181, 194, 196, 197, 200–202, 209

**irrep** irreducible representation. 68, 70

**LCSR** light-cone sum rules. xix, 91, 93, 102, 103, 108–112, 116, 119–122, 212

**LEC** Low Energy Constant. 40, 56, 57, 59, 63, 70, 71, 79, 81, 86, 92, 103, 105–111, 115, 116, 118, 122, 124, 136–139, 141, 142, 145, 146, 148–150, 153, 154, 156, 159, 161–164, 168, 169, 171

**LHG** Local Hidden Gauge. xxi, 193, 194, 197, 208, 213

**LO** Leading Order. xx, 55, 58, 64, 65, 136, 138–140, 142, 150, 153, 156, 159, 161, 163, 164, 175, 200, 202, 209, 212, 213

**LQCD** Lattice Quantum Chromodynamics. xvii–xxi, 1, 3, 6–8, 13, 14, 34, 35, 37, 63, 65, 67, 72, 75, 76, 78, 88, 89, 91–93, 102, 103, 108–112, 115, 116, 118–122, 124, 127–133, 135–137, 141, 143–145, 148–154, 156, 159, 161–163, 165, 168–171, 181, 182, 186, 187, 190–192, 211–213

**MO** Muskhelishvili–Omnès. xix, 91–94, 97, 99–111, 116, 118, 120–122, 124, 211, 212

**NLO** Next-to-Leading Order. xviii–xx, 56, 58, 59, 64, 65, 70, 76, 86, 92, 93, 105–107, 109, 121, 122, 136, 137, 142, 154, 156, 159, 161, 162, 170, 211

**NNLO** Next-to-next-to-Leading Order. 118, 124

**OGE** one-gluon exchange. 141, 149, 161, 168

**PDG** Particle Data Group. 67, 91, 93, 119–121, 136, 179, 202, 203, 206–208

**pNGB** pseudo Nambu-Goldstone boson. 39, 44, 46, 48, 53, 65, 88, 95, 137, 138, 163

**QCD** Quantum Chromodynamics. xvii, xix, 1, 2, 4, 7, 13, 14, 34, 39–45, 52, 53, 75–77, 88, 91–93, 105, 121, 128, 141, 181, 193, 199, 200, 206, 211, 212

**RPP** Review of Particle Physics. 4, 76, 77, 88, 209

**RS** Riemann Sheet. 21, 65, 67, 69, 142, 165, 182, 185

**SM** Standard Model. xvii, xix, 1, 13, 91

**SRS** second Riemann sheet. 142, 149, 152, 165, 169, 170

**U$\chi$PT** Unitarized Chiral Perturbation Theory. 76

**UHM$\chi$PT** Unitary Heavy Meson Chiral Perturbation Theory. xviii–xx, 65, 67, 76, 81, 86, 135, 142, 156, 159, 163, 211, 213

**UV** ultraviolet. 30–32, 37, 40, 140, 148, 149, 153, 154, 156, 159, 161, 164, 165, 169–171, 184

**WTL** Weinberg-Tomozawa Lagrangian. 138, 139, 145, 164